Propriétés spectroscopiques et structure électronique du vanadium dans des matériaux complexes: Implications géologiques et technologiques

Amélie Bordage

To cite this version:

Amélie Bordage. Propriétés spectroscopiques et structure électronique du vanadium dans des matériaux complexes: Implications géologiques et technologiques. Physique [physics]. Université Pierre et Marie Curie - Paris VI, 2009. Français. NNT : . tel-00459909

HAL Id: tel-00459909

https://theses.hal.science/tel-00459909

Submitted on 25 Feb 2010

HAL is a multi-disciplinary open access archive for the deposit and dissemination of scientific research documents, whether they are published or not. The documents may come from teaching and research institutions in France or abroad, or from public or private research centers.

L'archive ouverte pluridisciplinaire **HAL**, est destinée au dépôt et à la diffusion de documents scientifiques de niveau recherche, publiés ou non, émanant des établissements d'enseignement et de recherche français ou étrangers, des laboratoires publics ou privés.

UPMC
PARISUNIVERSITAS

THESE DE DOCTORAT DE
L'UNIVERSITE PIERRE ET MARIE CURIE

Spécialité :

Physique et chimie des matériaux

Présentée par :

Amélie Bordage

Pour obtenir le grade de :

DOCTEUR DE L'UNIVERSITE PIERRE ET MARIE CURIE

Propriétés spectroscopiques et structure electronique du vanadium dans des matériaux complexes: Implications géologiques et technologiques.

Soutenue publiquement le 1er décembre 2009 devant le jury composé de:

M.	Jean-Pierre JOLIVET	Président du jury
MM.	John REHR	Rapporteur
	Jérôme ROSE	Rapporteur
Mme	Sakura PASCARELLI	Examinatrice
MM.	Johan DE VILLIERS	Examinateur
	Michael TOPLIS	Examinateur
M.	Christian BROUDER	Directeur de thèse
M.	Etienne BALAN	Co-directeur de thèse

Institut de Minéralogie et de Physique des Milieux Condensés – UMR 7590

The spectroscopic properties and electronic structure of the vanadium in complex materials: Geological and technological implications.

Cherche encore
Le pourquoi de la Terre
Le pourquoi de la guerre
Le pourquoi de la pluie
Le pourquoi du parce que
Le puisque du pourquoi
Du comment du bonheur
Du pourquoi de la vie
Cherche encore

Jusqu'au bout de l'enfer
Jusqu'au bout de tes nerfs
Jusqu'au bout de tes nuits
Jusqu'au bout de la mort
Jusqu'au bout de l'amer
Jusqu'au bout de la vie
Et jusqu'à l'infini
Cherche encore

Pourquoi c'est important de chercher Alec ? Pour trouver !

La Chanson du Dimanche

Remerciements

Avant de remercier tous ceux qui ont joué un rôle important dans cette thèse, je voudrais la dédicacer à celui sans lequel elle n'aurait jamais eu lieu : Monsieur Bazin, mon professeur de physique au collège. En début de quatrième, je lui ai dit que la physique était la matière la plus nulle du monde et que je la détestais. Il m'a alors dit "Tu verras, tu seras docteur en physique un jour. J'en suis sûr". Il a travaillé dur pendant deux ans afin me faire aimé cette matière. Et aujourd'hui, je suis docteur en physique...

Pour les mercis qui vont suivre, j'espère n'avoir oublié personne. Si c'est le cas, je m'engage à organiser un "beer-time" pour rattrapper cette erreur!

Je voudrais remercier en tout premier Delphine Cabaret. En licence, j'avais un module intitulé "physique numérique ". Delphine y enseignait et m'a permis de survivre à des heures de torture de programmation Fortran. En M1, je cherchais un stage et elle m'a présenté son colocataire de bureau, Etienne Balan. Qui m'a ensuite proposé un stage en M2 puis une thèse, avec Christian Brouder comme directeur. Je vous remercie d'avoir cru en moi tous les trois, de m'avoir fait confiance tout au long de ma thèse. Encadrée par Etienne pour la géologie, Chrisitan pour la théorie et Delphine pour les calcouls, j'ai appris énormément au milieu de vous. Etienne, merci de m'avoir laissé libre de choisir l'orientation que je souhaitais donner à mon travail, même si ce n'était pas celle que tu préférais. Merci aussi de m'avoir fait découvrir pendant les manips à l'ESRF tout un pan de la musique que je ne connaissais pas et d'avoir enrichie ma connaissance de blagues nulles. Christian, je n'ai qu'une seule chose à te dire : Aaaaaargrrrrrggggghhhhhhhhhdslfkjdsgùsmfgkjkzouuuuuuuuuu. Delphine, merci pour ton amitié, ton soutien et tout le temps que tu m'as consacré (même enceinte jusqu'au cou), pour tes conseils, pour ton aide dans la rédaction de ma thèse. Et tout le reste encore.

Je remercie les membres du jury pour l'attention qu'ils ont porté à ma thèse: Jean-Pierre Jolivet, John Rehr, Jérôme Rose, Sakura Pascarelli, Mike Toplis et Johan de Villiers. Merci Jérôme d'avoir accepté de raccourcir tes nuits pour lire le manuscrit. Thank you John for your review and the danse at the XAFS 14 dinner. Merci Mike d'avoir tout lu, car je sais que certains chapitres t'ont fait peur au début! Merci Sakura pour tes conseils.

Ma thèse a été très riche en collaborations. Je tiens à remercier toutes les personnes avec qui j'ai eu la chance de travailler et qui ont permis à ce travail d'avancer. Je remercie très chaleuresement toute l'équipe de la ligne ID26 à l'ESRF (même si à trois heures du matin il fait un peu froid dans la hutch), pour m'avoir fait découvrir le synchrotron et pour leur aide pendant les expériences HERFD: Pieter Glatzel, Sigrid Eeckhout, Marcin Sikora, Tsu-Chien Weng, Janine Grattage, Kristina Kvashnina, Roberto Alonso-Mori et (the last but not the least) Christophe

Lapras. Thank you for all the funny times on the beamline and during the Users'meetings and conferences (HERFD is a spectroscopy also called "It-which-must-not-be-named", isn't it?...). Thank you Janine for your help during my thesis writing and all your advices concerning the english grammar and spelling. And Pieter, a special thanks for you, because you patiently answered to all my "why" and "how" about the beamline and HERFD, and you were the only one I can speak soccer and F1 with during the experiments! Je suis allée deux mois en Afrique du Sud, à l'Université de Pretoria et je souhaiterais donc remercier tous ceux qui se sont occupés de moi là-bas: Johan (and all his family), Robert, Maggie, Sabine, Wiepke, Allison, Sean, Teresa, Lizelle, Sanet and Eva. I thank you all for your welcome and your kindness and all the time you took for me. Thanks for having taken care of me during these two months, for the coffee-times in the Stonemen Building and and for having made me discovered South Africa. Johan, a special thank you for giving me the oppurtunity to come . Robert, thank you for your support during my experiments. I will never forget to say the "h" at the beginning of the words and the "s" at the end. I also hope all the little fairies have left your pump... J'ai eu de plus l'occasion de travailler avec Yves Joly (Institut Néel), pour faire des calculs sur la magnétite. Je le remercie pour son aide, ses explications et toutes les discussions sur le vanadium dans la magnétite. Je remercie enfin Andrea Di Cicco et Adriano Filipponi, pour avoir organisé le congrès XAFS 14 à Camerino. C'est le meilleur congrès auquel je suis allée, aussi bien pour les conférences que pour l'ambiance!

Je voudrais maintenant revenir en France pour remercier l'IMPMC, et en particulier Bernard Capelle, son directeur, pour son écoute, sa disponibilité, son imprimante couleurs et pour m'avoir permis d'assister à un grand nombre de congrès. Je remercie aussi toute l'équipe Théorie Quantique des Matériaux, la dreamteam des calcouls. Je remercie en particulier Matteo Calandra pour son aide sur les calcouls *ab initio* et l'utilisation de Xspectra, ainsi que Michele Lazzeri pour son aide sur les calcouls et LateX. Je remercie fortement (au propre comme au figuré) Philippe Sainctavit pour son aide sur l'absorption des rayons X, que ce soit la préparation des expériences, les nuits à l'ESRF ou la théorie, Marie-Anne Arrio pour m'avoir initiée aux calculs multiplets et Claire Carvallo, qui est venue faire des nuits avec moi à l'ESRF.

Mes remerciements vont aussi à Gaëlle Dufour, Danielle Raddas, Ouafa Faouzi et Danielle Thomas pour leur aide et leur efficacité dans la préparation de toutes mes mission et la vie pratique du labo; Michelle Jacquet et Mélanie Escudé de l'INSP, pour leur aide dans la préparation d'échantillons; Alain-Jeanne Michaud, pour mon affiche de thèse. J'ai eu la chance d'être monitrice pendant ma thèse. Alors merci Jocelyne, Seb et Alex pour votre aide pendant les TPs, les cafés et croissants avant les TPs du matin. Merci Ismaïl pour ton aide dans la préparation des TDs. Je suis ravie aussi que mes préparations de TDs et TPs soient venues grossir ton tas de photocopies de mes cours et TDs que tu collectionnes précieusement depuis la licence! Merci Maître Claire d'avoir été ma tutrice pour le monitorat et de m'avoir acceptée comme padawan. Je remercie très chaleuresement Annick Whüler, pour son aide pendant mon DEA et qui m'a soutenue pour obtenir une bourse de thèse. Enfin, merci à Stéphanie de m'avoir parlé du poste d'ATER que j'ai aujourd'hui au Laboratoire en Géomatériaux et Environnement. Cela m'a permis de découvrir un nouveau labo et d'autres aspects de la recherche.

Et maintenant que tous les remerciements "sérieux" sont faits, je voudrais passer à ceux plus rigolos.

Merci Jam. Sans toi, ma thèse n'aurait pas été la même. Je pourrais détailler tout ce pour quoi je te remercie, mais en fait, je trouve qu'un clin d'oeil en dit beaucoup plus... Et merci à toi aussi Simon, mon cothésard préféré, pour ton aide et ton soutien en toutes circonstances, tes blagues vaseuses auxquelles je suis la seule à rigoler et tes demandes en mariage.

Je voudrais remercier plus particulièrement certains membres de l'IMPMC : Philippe, pour avoir épargné des maux de tête à l'IMPMC en trouvant un surnom à chaque Amélie; Marie-Anne, pour ton soutien et toutes les discussions sur les dessins animés; Michele pour Fiorentino, le crapaud-en-peluche-futur-prince-charmant, et les discussions footballisitques (oui Michele, un jour, la Fiorentina gagnera); Matteo (Calandra) pour les discussions sportives, qui peuvent se résumer par "Forza Ferrari!" ; Feriel, pour ton soutien et toutes nos discussions; Nicolas et Thierry pour leurs blagues et leur bonne humeur à la cantine et à la cafèt; Claire et Federica, pour leur amitié et toutes les discussions sur les beaux gosses; Niels, Olivier D, Mathieu, Tobias, Marc, Gérald, Eglantine, Guillaume, Tobias, Fabien, Olivier V, Marie, Boris B, Haruka, Boris V, Chloé, Coralie, Marion, Merlin et tous les adeptes des tea-times et beer-times; les producteurs de café du monde entier, grâce à qui j'ai pu fournir l'IMPMC en café pendant trois ans (parce que un chercheur sans caféine, c'est comme... un manouche sans guitare, un château sans la Loire, un martien sans soucoupe,un pâté sans la croûte (merci Thomas Dutronc pour ces belles paroles)); AC DC, pour leurs chansons, énorme soutien pendant les traitements de données un peu longs et répétitifs; et enfin Clive Owen, pour tous ses excellents films sortis avant et pendant ma thèse, et en particulier "King Arthur" (n'est-ce-pas, Jam?).

Merci Fanny, ma "co-docteur", pour ton amitié. et ton soutien. Je te remercie en particulier pour ton soutien pendant ma rédaction et surtout aprés, puisque tu as fait plus de cauchemars que moi avant ma soutenance!

Merci à Stéphanie et Nico de m'avoir présenté la "Suricate Family" (Karim, Jess, Clélia, Champy, Caro), qui m'a accueillie à bras ouvert dans mon nouveau laboratoire (ils le regrettent peut-être maintenant...). Grâce notamment à Stéphanie, j'ai pu rencontré deux personnes au moins aussi bavardes que moi (Stéph et Jess), et une espèce que je croyais en voie de disparition: un vrai supporter du PSG (si si, ça existe). Merci Nico de m'avoir expliqué ta ligne et vivement nos manips ensemble! Merci à Carambar (sponsor officiel de LGE) pour tous les fous rires qu'il m'a déjà permis de partager avec Rossana et Valérie, et qui promettent d'être encore nombreux!

Un merci spécial à Maya d'avoir été ma cavalière à la soirée de XAFS 14 et d'avoir transformé mon lion en lion-baba-cool, ainsi qu' à Gaspard pour ses beaux dessins et sa "cool-attitude" avec sa baby-sitter préférée. Un merci en avance pour Octave, pour qu'il soit comme son grand-frère avec sa future baby-sitter (aussi préférée).

Enfin, je souhaiterais remercier vraiment beaucoup très ènormément tous ceux qui n'ont pas forcément de lien direct avec ma thèse mais qui en entendent parler depuis trois ans, et qui m'ont soutenue pendant tout ce temps: mes parents, mes soeurs Mathilde et Elise, Loic-le-chevelu, mes grand-parents/oncles/tantes/cousins et mes amis (Elsa, Sab la Chacale, Oliv, Jul', Maciej, Tom, Camille, Jam, Delphine et Cétéra). Sans oublier tous ceux des Scouts et Guides de France qui eux aussi m'ont soutenue, en particulier la dernière année : David, Charles, Aude, Jonathan, Clément (l'équipe des "calories-party", tous fans de coin-coins), ainsi que tout le groupe Notre Dame des Ailes. Parmi eux, il faut que je mentionne Eric, qui a découvert avec étonnement (et incrédulité) qu'on pouvait travailler pendant trois ans sur (je cite) "la physique des cailloux"...

PS: Merci aussi à tous ceux qui sont repartis avec des restes du pot! Grâce à vous, on a évité d'en manger matin, midi et soir pendant une semaine...

Résumé

Cette thèse a pour but d'étudier les propriétés spectroscopiques et la structure électronique du vanadium dans différents minéraux d'intérêt géologique et/ou technologique. Une approche expérimentale basée sur la spectroscopie HERFD-XAS au seuil K du vanadium a été combinée à une approche théorique. Cette dernière couple calculs ab initio et calculs multiélectroniques des spectres XANES, permettant une interprétation plus fine des spectres expérimentaux. Des développements théoriques basés sur les tenseurs sphériques et la méthode des cosets ont été effectués puis appliqués au cas de la section efficace d'absorption des rayons X, afin d'extraire les propriétés spectroscopiques du cristal à partir de celles d'un site individuel.

La signature spectrale de V^{3+} dans le grossulaire ($Ca_3Al_2(SiO_4)_3$) a été déterminée grâce à la dépendance angulaire du préseuil de son spectre XANES. Ce minéral peut donc être utilisé de manière fiable comme composé de référence dans l'étude du degré d'oxydation du vanadium dans des verres, de minéraux et de composés synthétiques. Le vanadium peut être incorporé comme dopant dans l'anatase (TiO_2) sous forme de vanadium tétravalent. Son environnement local dans l'anatase a été sondé, montrant que le vanadium n'est pas incorporé en substitution du titane. Enfin, le degré d'oxydation du vanadium dans les titanomagnétites ($Fe_{3-x}Ti_xO_4$:V) du Bushveld (Afrique du Sud) a été déterminé pour des échantillons naturels et synthétiques. La coexistence de deux degrés d'oxydation (+III et +IV) a été montrée mais les implications de leur variations relatives sur la formation des couches géantes de magnétite dans le Bushveld restent encore mal comprises.

Mots-clés

Vanadium, impuretés, titanomagnétite, degré d'oxydation, HERFD-XAS, calculs *ab initio*

Abstract

The aim of this thesis is the investigation of the spectroscopic properties and the electronic structure of vanadium in minerals with a geological and/or technological interest. V K-edge HERFD-XAS experiments were combined with a theoretical determination of the measured spectra. Two approaches were complementary used to calculate the spectra: an ab initio approach and a multielectronic one. Theoretical developments based on a spherical tensor analysis and the coset method were achieved and applied to the X-ray absorption cross-section, in order to extract the spectroscopic properties of the crystal from those of a single site.

The spectral signature of V^{3+} in grossular ($Ca_3Al_2(SiO_4)_3$) was determined using the angular dependence of the XANES pre-edge features. This mineral is therefore a reliable reference compound for further study of the vanadium oxidation state in glasses, minerals and synthetic compounds. Vanadium is also used as a dopant in anatase (TiO_2) in which it is incorporated under the +IV oxidation state. The investigation of its local environment showed that vanadium is not incorporated in the Ti-substitutional site but may be incorporated in the interstitial one. Finally, the oxidation state of vanadium in natural and synthetic samples of titanomagnetite ($Fe_{3-x}Ti_xO_4$:V) from the Bushveld Complex (South Africa) was determined and the +III and +IV oxidation states were shown to coexist. Despite this detailed investigation, the geological implication of their relative variations on the crystallization of the giant magnetite layers is still not well understood.

Key words

Vanadium, impureties, titanomagnetite, oxidation state, HERFD-XAS, *ab initio* calculations

Contents

II Applications 85

Remarks

In the manuscript, the name tsavorite is used for a V-bearing grossular ($Ca_3Al_2(SiO_4)_3$:V^{3+}). This name was fixed by usage at the beginning of my thesis and I thus used it. The International Mineralogical Association discredited it and "tsavorite" must not be used anymore. However, the name is used in this thesis for simplicity and clarity.

The bibliography is sorted in the alphabetical order of authors. The references given in the publications are not included in the bibliography.

A part of the theoretical work presented here (DFT calculations) was granted access to the HPS resources of IDRIS (Institut du Développement et de Recherche en Informatique Scientifique) under the allocations 2007, 2008 and 2009 - 2015 made by GENCI (Grand Equipement National de Calcul Intensif).

A summary of the manuscript is written in French and incorporated in the the manuscript. This summary is needed by the Pierre and Marie Curie University administration since the manuscript is written in English. Some words in the summary remain in English as they are widely use in French. They are written in italic.

Have fun!

Introduction

The subject of this thesis is the study of the spectroscopic properties and the electronic structure of vanadium in complex materials. This work was focused on three V-bearing minerals which present a geological or technological interest. Minerals are inorganic natural compounds occuring as crystalline solids. In mineralogy, elements present in small concentration in the mineral are said to be minor or trace elements, and impurity in materials science. The presence of a transition element in a host-mineral modifies several of its properties, notably the color: corundum α-Al_2O_3 is neutral but ruby α-Al_2O_3:Cr^{3+} is red, α-Al_2O_3:Fe^{3+} yellow, α-Al_2O_3:V^{3+} purple and sapphire α-Al_2O_3:Fe^{2+}, Ti^{4+} blue. The mechanisms of the trace element incorporation and the impact on the mineral properties are thus widely studied in gemology, Earth sciences or materials science.

Vanadium is a transition metal from the first row and is present in several minerals as an impurity or a major constituent. It was discovered in 1831 by Nils Gabriel Sefström and named after Vanadis[1], the goddess of beauty and fertility in the scandinavian mythology, because of the wide range of colored chemical compounds produced with vanadium [188]. Vanadium is indeed responsible for the colour of several minerals, *e.g.* green for tsavorite $Ca_3Al_2(SiO_4)_3$:V^{3+}, blue for cavansite $CaVOSi_4O_{10}\cdot 4H_2O$, orange for lasalite $Na_2Mg_2[V_{10}O_28] \cdot 20H_2O$ or red for vanadinite $Pb_5(VO_4)_3Cl$ (Fig. 1).

In addition to its role as a coloring impurity in natural minerals, vanadium has also many technological applications. It is used as a catalyst , *e.g.* in manufacturing sulfuric acid [73] or maleic anhydride [1], and as a coloring impurity in synthetic crystals and pigments. For instance, vanadium is used to obtain a range of yellow colours for ceramic pigments based on ZrO_2 [61]. The blue or green color of V-doped zircons ($ZrSiO_4$:V) depends on the synthesis conditions which can modify the incorporation of vanadium in zircon and the resulting color [6]. Vanadium is also used to make high-performance steel for application in axles, bicycle frames, crankshafts, gears, surgical instruments, among other applications. The first industrial use of vanadium in steel was found in the gears and the chassis of the Ford Model T: using vanadium high-strength steel allowed the reduction of the weight of the chassis by a third for the same strength [17] (Fig. 2). However, vanadium does not form ore mineral by itself but needs to be extracted from minerals or chemically isolated. The first chemical preparation of pure vanadium metal was done in 1927 [144].

The main natural source of vanadium is V-bearing titanomagnetite $Fe_{3-x}Ti_xO_4$:V. The largest ore in the world is the monomineralic layers of massive titanomagnetite from the Bushveld Complex, in South Africa [215, 176, 54]. These magnetite layers range from a few centimeters to several meters in thickness, and some extend for more than 100 km along the strike of the bed [54]. Outcrops of these layers are visible in the Bushveld Complex and the layers can be

---

[1] Vanadis is also called Freya

Figure 1: Vanadium is responsible for a wide range of colors in chemical compounds and minerals. Some examples are presented here: the green tsavorite, the blue cavansite, the yellow lasalite and the red vanadinite.

Figure 2: The first industrial use of steels with vanadium was to make the chassis of the Ford T.

well-observed in open-cast mines (Fig. 3). The vanadium-bearing nature of the titaniferous iron ores was first recognized in 1923 [2] but the commercial production of the vanadium extraction from magnetite in the Bushveld Complex only began in 1957 [19].

The Bushveld Complex, discovered in 1897 [150], is the largest known layered intrusion in the world, with a total area of about 66000 km^2 [222]. It is approximately 2058.9 ± 0.8 Ma old [26] and is situated within the Transvaal basin, in South Africa. A layered intrusion is a large sill-like body of igneous rock which exhibits vertical layering or differences in composition and texture, and an igneous rock is formed by a magma which slowly cools and becomes solid.

Figure 3: (*Left*) The outcrop of a titanomagnetite layer, at Mapochs Mine. (*Right*) A titanomagentite layer at the Vametco mine, situated in the Eastern limb of the Bushveld Complex.

In other words, the Bushveld Complex was a giant magmatic chamber which slowly cooled and became solid below the Earth's crust. The Bushveld Complex consists of five limbs connected together at depth [53, 57]: the Far Western, the Western, the Southeastern (or Bethal) , the Eastern and the Northern (or Potgietesrus) limbs (Fig. D.3) [56]. The layered rocks are divided into Lower, Critical, Main and Upper zones, depending on their stratigraphic height [187]. Two major groups of oxide minerals are present in the layered rocks of the Bushveld Complex. The first one consists of chromitites (igneous cumulate rock composed mostly of chromite $FeCr_2O_4$) in the Critical Zone. The second consists of vanadium-bearing titanomagnetite deposits in the upper part of the Complex [38]. The magnetite-rich rocks of the Western Lobe are collectively referred as the Bierkraal Magnetite Gabbro[2].

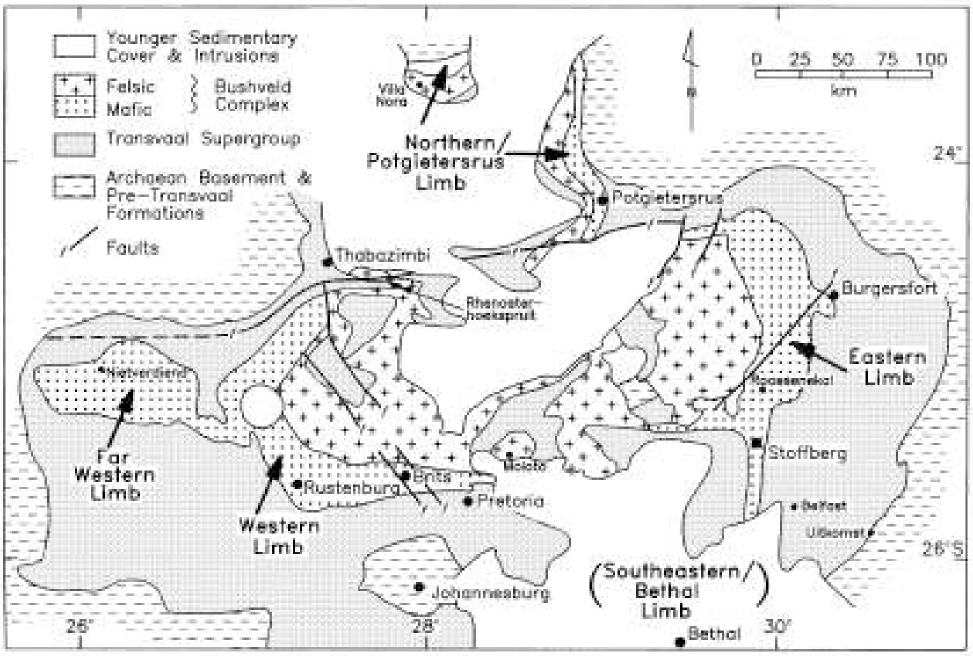

Figure 4: General geology of the Bushveld Complex, showing outcrops of the northern, eastern, western and far western limbs, and the position of the unexposed southeastern limb (it is completely covered by younger sedimentary rocks). The map is reproduced from Ref. [56].

---

[2] Gabbro refers to a large group of dark, corse-grained igneous mafic rocks, *i.e.* mafic rocks being rocks with a low silicon contents and a high content in magnesium and iron.

Despite numerous studies on the formation of the Bushveld Complex, the crystallization of the titanomagnetite layers is still poorly understood. Any proposed model for the genesis of titanomagnetite layers is indeed constrained by their petrological, mineralogical and geochemical characteristics as well as those of their host silicate rocks. It must explain not only the mechanisms that are responsible for the precipitation of large quantitites of titanomagnetite and the development of ore-rich layers, but also the mechanisms by which primary precipitates are converted into essentially monomineralic ores. Several models have thus been proposed, but no one has found a general agreement yet. The first models invoked mechanisms involving separation and gravitational accumulation of titanomagnetite crystals at the bottom of the magmatic chamber or postulated the existence of discrete Fe-Ti oxide liquids that was intruded from below and spread laterally along certain lithological contact [13, 63, 205, 141, 215]. Reynolds presented in 1985 a review and synthesis of the proposed models [175], concluding that most models recognize that precipitation of copious quantities of titanomagnetite required for the development of ore-rich layers is triggered by episodic increase in oxygen fugacity, f_{O_2} [113, 172, 173, 152, 130, 129], but that the process whereby this occurs is not well understood. The increase in oxygen fugacity must have been indeed more or less simultaneous over the entire width of the magma chamber to allow for the uniform thickness and lateral continuity of individual ore-rich layers. Similarly, a magma-mixing model [114, 103] can not effectively account for the common presence of numerous titanomagnetite rich-layers within small vertical intervals and variations in silicate mineral content within individual layers [175]. A change in pressure caused by a fracturing through to the surface would explain a quite homogeneous increase of the oxygen fugacity [50, 210]. Tegner *et al.* have published recently a review on the previous models and proposed that the magnetite layers were formed by fractional crystallization, *i.e.* the removal and segregation from a melt of mineral precipitates, of a huge stratified magma sheet [202]. The fractional crystallization was previously proposed [176] but invoked a mixing of numerous injections of magma [56]. Analogies were often made between chromite and magnetite layers to explain the formation of the titanomagnetite layers [37, 39, 49, 71].

To propose the models on the layer crystallization and explain the process whereby the oxygen fugacity would increase in the whole magmatic chamber, chromium in chromite and titanomagnetite was widely investigated [28, 36, 52, 51, 50, 136, 148, 147]. Vanadium in V-bearing titaniferous magnetite was also studied but received less attention than chromium [54, 55, 175]. A detailed study of vanadium in V-rich titanomagnetite is required. In particular, the oxidation state of vanadium may provide information on the processes that led to the crystallization of these huge V-rich titanomagnetite layers.

Vanadium may indeed occur under several oxidation states: +II, +III, +IV and +V. V^{3+}, V^{4+} and V^{5+} are known to exist in a wide range of geological environment, whereas V^{2+} is observed only in highly reduced systems such as those that existed in the early solar nebula [192, 199]. The determination of the oxygen fugacity for magmas derived by the melting of planetary mantles is critical to the understanding of the genesis and differentiation of magmas and to the nature and evolution of planetary interiors [46, 11]. The several oxidation states of vanadium make it a valuable geochemical indicator providing information on the oxygen fugacity prevailing during the formation of Earth and planetary rocks. Vanadium was indeed shown to be redox-sensitive during melting or crystallization [21, 191] and the relative proportions of the different oxidation states depends on the oxygen fugacity of the melt [41, 42]. The abundance of V^{4+} is small in melts, but the proportion of V^{3+} and thus the V^{4+}/V^{3+} ratio decreases substantially with an increasing oxygen fugacity [44]. For instance, in conditions of oxygen fugacity relevant to terrestrial basaltic systems, V^{4+} is predicted to be the main valence in a ferrobasaltic magma, whereas at more oxidizing conditions, V^{5+} becomes the dominant valence (Fig. 5) [206].

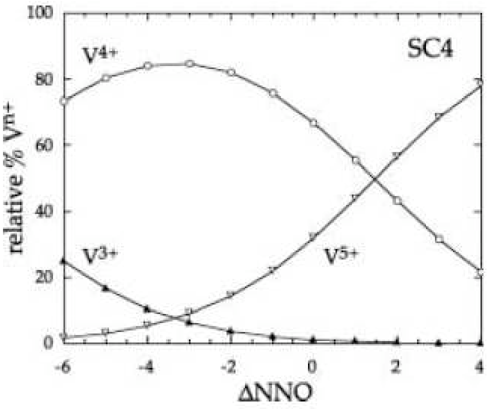

Figure 5: Calculated variations of the relative proportions of V^{n+} as a function of the oxygen fugacity for a ferrobasaltic melt. The conditions of oxygen fugacity relevant to terretrial basaltic systems correspond to ΔNNO = -3 to ΔNNO = +1, where ΔNNO represents the oxidizing conditions with respect to the Nickel-Nickel Oxide (NNO) buffer. The figure is reproduced from Ref. [206].

Considering these relations between the vanadium oxidation states and the oxygen fugacity, vanadium valence oxybarometers has been developed [107, 158]. They are based on the variation of the partition coefficient between a mineral and the parent liquid magma, which represents the affinity of an element during a crystallization or a melting to incorporate the solid or liquid phase [40, 43, 143]. The vanadium valence oxybarometers can record at least eight orders of magnitude in oxygen fugacity, allowing for applicability to both oxidized and reduced magmas from planetary bodies. The applicability at low oxygen fugacity conditions is especially important because traditional Fe^{2+}/Fe^{3+} barometers are ineffectual if no Fe^{3+} is present in these environments [125] and because unaltered Fe-Ti oxides used in the traditional geobarometers are rarely preserved. Some vanadium valence oxybarometers are concentrated on basaltic glasses [197, 127], spinels [157, 177, 178], olivines [198, 190] and pyroxenes [125, 126]. The vanadium oxidation state is therefore a potential window into the processes leading to the formation of the V-rich titanomagnetite layers in the Bushveld Complex and could bring information on the oxygen fugacity during the layer crystallization.

Nevertheless, at the present time, the oxidation state of vanadium in titanomagnetite from layered intrusions is still unknown and has to be determined. The first study on the vanadium oxidation state in the titanomagnetite was done in 2006 by Balan *et al.* using X-ray Absorption Spectroscopy (XAS). XAS is indeed a powerful tool to determine the oxidation state of an atom in a compound, since it is a chemically sensitive technique and that the structures observed in an X-ray Absorption spectrum depend on the crystallographic and electronic structures of the investigated element. These structures are the result of the interaction between an X-ray beam and the electrons of the investigated atoms. In particular, the features situated at an energy just below the edge, said to be "the pre-edge", provide information on the oxidation state and local environment of the absorbing atom [35]. To infer the oxidation state from the pre-edge features, the most widely used method is to compare the spectrum of the investigated element to those of reference compounds, in which the oxidation state and coordination number is well known. This "fingerprint" method was used in minerals and glasses to investigate several elements, such as titanium [79, 75, 78, 217], iron [35, 83, 116, 161, 218, 219, 221], chromium [72], nickel [77], manganese [59, 76, 110] or magnesium [168, 207]. Particular attention has been given to vanadium, since its several oxidation states makes it a potential geochemical probe. The first detailed analysis of the vanadium pre-edge in minerals as a function of the oxidation state and coordination number was done by Wong *et al.* [224] and numerous studies followed, *e.g.* Ref [18, 10, 60, 93, 127, 149, 156, 166, 171, 197].

To correctly interpret the pre-edge features of an investigated element, its spectral signature for a given oxidation state and coordination number needs to be well-known. Indeed, the pre-edge energy and intensity depend on both of them. Detailed knowledge of the pre-edge can be obtained experimentally and theoretically. XAS experiments on single-crystals are prefered in order to get a fine interpretation of the pre-edge features. Indeed, measurements on powder samples give access only to the average spectrum and therefore provide information averaged over all the angles. To get more accurate information on the electronic structure and on the local environment of an absorbing atom, the single-crystal has to be cut and oriented, so its orientation with respect to the polarization and direction of the incident beam can be varied. Indeed, in most cases, crystals present a natural anisotropy, the advantage of which can be taken. This effect is called X-ray Natural Linear Dichroism. The angular dependence of the XAS spectrum can also be observed for the pre-edge of cubic crystals [24] and was well observed in the case of pyrite FeS_2 [32] and Cr^{3+}-bearing spinel [122].

However, XAS measurements on a single-crystal are not simple to perform. The theoretical determination of the XAS spectrum can come to the rescue and provide additional quantitative and qualitative information. For instance, the structural relaxation around an impurity incorporated in a host-structure can be theoretically determined by the energy minimization of the structure. To calculate the spectrum itself, two theoretical approaches can be used, depending whether the final states are localized or delocalized. In the case of localized final states, for instance for transitions from occupied $1s$ orbitals to the $3d$ empty ones, the Ligand Field Multiplet Theory is used to simulate the pre-edge and was successfully applied to several cases [9, 89, 122, 94, 95, 219]. This approach has the main advantage to take into account the multielectronic interactions and to give access to quantitative parameters, for instance the crystal field parameter or the p-d hybridization. In the case of delocalized final states, a monoelectronic approach based on the Density Functional Theory is used. This monoelectronic method is widely used and is applied in several codes, Quantum Espresso [12, 92, 99], PARATEC [163], FDMNES [118], FEFF [169, 170] (and many others), the choice of which depends on the user. The DFT calculations have also shown satisfactory results for the calculations of K pre-edges [34, 85, 99, 120, 122, 223], which corresponds to localized final states. The monoelectronic approach has the advantage to be parameter-free and to allow the calculation of the complete XAS spectrum, and not only the pre-edge as with the LFM theory. Spin-polarized calculations can also be performed, hence providing additional information on the involved transitions. To calculate the pre-edge region of a XAS spectrum, only one approach (monoelectronic or multielectronic) is often exclusively chosen but recent calculations on the Cr *K* pre-edge in spinel $MgAl_2O_4$ showed that they provide complementary information when used together [121, 122]. This coupling of the two theoretical approaches permits the maximum of information to be obtained from the pre-edge.

In my thesis work, the crystallographic and electronic structure of vanadium as an impurity in some minerals has been investigated. The main question was indeed the speciation, *i.e.* the oxidation state and coordination number, of vanadium in the titanomagnetites from the Bushveld Complex. The vanadium oxidation state and the ratio between the different oxidation states present in magnetite, if oberved at all, may provide information on the crystallization of the giant magnetite layers in the Bushveld Complex which is still poorly understood. The determination of the vanadium oxidation state is a potential benchmark since vanadium was proved to be a reliable geochemical probe, its oxidation state being related to the oxygen fugacity at the crystallization time. This study has mainly used X-ray Absorption Spectroscopy, which is a powerful experimental method to investigate the oxidation state and local environment of an atom in a structure. The spectra analyses were done by a fingerprint method, which consists of the comparison between the investigated spectrum and those of reference compounds for which the oxidation state and coordination number is well defined. A precise knowledge of the latter is therefore required and can be obtained by a detailed experimental and theoretical study of the reference compound. The study of tsavorite, a mineral incorporating V^{3+} in an octahedral site, was thus undertaken. A coupling of several theoretical methods providing complementary information was used to calculate the experimental XAS spectra in the pre-edge region and hence give a fine interpretation of the measured features and a detailed knowledge of its spectral signature. In parallel, an experimental and theoretical study was then done to determine the speciation of vanadium in V-doped anatase, which is a material of technological interest used as a photocatalyst. This study enabled to study the incorporation of vanadium as an impurity in a larger view.

The manuscript is divided in two parts. The first part consists of two chapters dedicated respectively to the experimental and theoretical methods I used. The second part presents the results obtained in the study of three minerals: tsavorite, V-doped anatase and V-bearing (titano)magnetite, each mineral corresponding to a chapter.

- **Chapter 1** presents the main information of the studied minerals (magnetite Fe_3O_4, tsavorite $Ca_3Al_2(SiO_4)_3$ and anatase TiO_2) and gives their main crystallographic data. The experimental tools are also presented, with a particular emphasis on High-Energy Resolution Fluorescence Detected X-ray Absorption Spectroscopy (HERFD-XAS), which is the main experimental technique used to study the electronic structure of vanadium.
- **Chapter 2** presents the theoretical methods used to model the crystallographic environment and electronic structure of vanadium in different minerals. In a first part, I present the monoelectronic approach. The reader is reminded about the principles of Density Functional Theory (DFT) calculations and the details of the calculations performed in the reciprocal space are described. This approach was used to study tsavorite and V-doped anatase. The principles of calculations performed in the real space are also briefly exposed, since they were used to model the V *K*-edge in magnetite. In a second part, I present the multielectronic approach, based on the Ligand Field Multiplet (LFM) theory

and used to simulate the K pre-edge of vanadium in tsavorite. In a third part, theoretical developments based on a spherical tensor analysis are presented as an article published in *Journal of Physics: Condensed Matter* [25]. Finally, a study on Cr^{3+} in spinel $MgAl_2O_4$ is presented as an article published in *Physical Review B* [122] to illustrate the use of these three theoretical methods (the monoelectronic approach, the multielectronic one and the formalism of spherical tensors).

- **Chapter 3** deals with a detailed study of the electronic structure of vanadium in tsavorite, which is used as a reference compound in the study of titanomagnetite. In tsavorite, vanadium occurs under the +III oxidation state in a slighty distorted octahedral site. Its spectral signature is determined experimentally and theoretically by an analysis of the angular dependence of the pre-edge features. The results obtained with HERFD-XAS experiments and DFT calculations are presented as an article submitted to *American Mineralogist*. Then additional materials to the article are detailed and finally the results obtained with LFM calculations are given.

- **Chapter 4** is dedicated to the incorporation of vanadium in anatase TiO_2. Vanadium is incorporated under the +IV oxidation state in anatase but its incorporation site has to be determined. A HERFD-XAS analysis is thus presented with DFT calculations that were performed at the Ti K-edge of anatase and at the VK-edge of V-doped anatase (with vanadium substituted for titanium).

- **Chapter 5** is dedicated to the study of the vanadium oxidation state in the titanomagnetites from the Bushveld Complex, with an investigation of natural titanomagnetite and synthetic magnetite samples. Syntheses of V-bearing magnetite were performed during my thesis and the experimental protocol is described. The oxidation state of vanadium is analyzed with V K-edge HERFD-XAS experiments and the oxygen fugacity with microprobe analyses. Then these two kinds of results are then compared to get information on the crystallization of the titanomagnetite layer of the Bushveld Complex.

Part I

Methods

Chapter 1

Minerals and experiments

During my thesis, I was interested in determining the oxidation state of vanadium in titanomagnetites from the Bushveld Complex (South Africa) and I thus studied a series of eleven natural samples taken at different depths in a borehole. As titanomagnetite is a complex system, I synthesized V-bearing magnetite samples to obtain information from a close but simpler system. The study of these titanomagnetite samples also led me to study reference compounds in which the oxidation state of vanadium is well-known. This chapter is thus dedicated to the description of the V-bearing minerals studied: magnetite, tsavorite and anatase. Their structure and main crystallographic data are presented in the first section. The second section is dedicated to the experimental tools I used to chemically analyze natural and synthetic magnetite samples: the principles of X-ray diffraction, electron microprobe analyses and scanning electron microscopy are briefly reminded. Finally, the third section is dedicated to the main technique I used: the X-ray absorption Spectroscopy (XAS). I performed XAS measurements at the V K-edge of the reference minerals and of the natural titanomagnetite samples, in order to characterize the crystallographic and electronic structures of vanadium. The XAS principle is explained, with the particular measurement modes I used, and the experimental setup is described.

1.1 Presentation of the studied minerals

I studied three minerals during my thesis:

- magnetite Fe_3O_4:V (and titanomagnetite $Fe_{3-x}Ti_xO_4$:V),
- tsavorite $Ca_3Al_2(SiO_4)_3$:V^{3+},
- anatase TiO_2:V^{4+}.

Vanadiferous titanomagnetite presents economical and geological interests, as it is the main vanadium source. Tsavorite was used as a V^{3+} reference compound in the determination of the oxidation state of vanadium in natural and synthetic (titano)magnetite samples. Therefore, the electronic structure of V^{3+} in this mineral was studied in detail. In addition to its interest as a reference compound, tsavorite is a good candidate for the study of the angular dependence of the XAS spectrum in cubic minerals. This angular dependence of XAS was also studied for a non-cubic mineral, anatase, which shows a different behaviour than tsavorite. The study of V-doped anatase was first motivated by a collaboration with chemists, who study the V-doped anatase synthesis for slications in photocatalysis. I present here their structure and main crystallographic data which are needed for the experimental and theoretical studies.

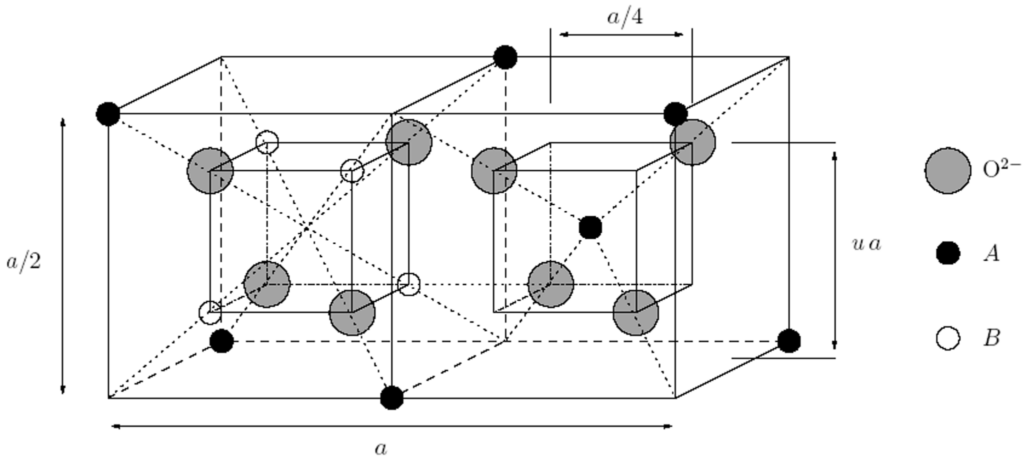

Figure 1.1: Positions of the cations and anions in two neighboring octants in the spinel cubic cell.

1.1.1 Magnetite Fe_3O_4

The AB_2O_4 spinel structure

The AB_2O_4 spinel structure includes several oxides. The O^{2-} anions form a face-centered cubic system and their spatial arrangement defines tetrahedral and octahedral cationic sites, denoted respectively A and B. The conventional cell used to describe the spinel structure is cubic. It has a multiplicity four and it contains 32 oxygen atoms, for 32 A and 64 B sites. Only 8 A and 16 B sites are occupied by cations. The cubic cell therefore contains eight AB_2O_4 formula units (56 atoms).

The conventional cubic cell (parameter a) is divided into eight subcubes, called octants, with a $a/2$ edge length. Fig. 1.1 shows the positions of the cations and anions in two neighboring octants. The oxygen atoms form the corners of a tetrahedron which fits in a cube with a edge length $a/4$. Sites A are situated at the center of every two octants and on half the corners of all the octants. Sites B occupy one octant out of two and sit on the four corners of the $a/4$ cube which are not occupied by oxygen atoms. The A-O bonds are aligned with the [111] direction whereas the B-O ones are along the [001] one. Along the [001] direction, planes of only A sites alternate with planes of B sites, with a distance of $a/8$ between two planes. Fig. 1.2 represents the spatial arrangement of octahedral and tetrahedral sites in the cubic cell. The octahedra share edges and form chains along the [110] direction and each octahedron shares corners with six tetrahedra.

Usually, the A sites are too small with respect to the ionic radii of the incorporated cations. The oxygen atoms are therefore shifted along the [111] direction of the tetrahedra towards the cubes with occupied B sites. This displacement is quantified by the u parameter ($u = 3/8$ in the case of no displacement) [213, 108].

The reference mineral in the spinel family is $MgAl_2O_4$, which is given the name "spinel". The other spinels are classified with respect to spinel $MgAl_2O_4$, as a function of the site occupied by the divalent cation. If the divalent cation is incorporated in the tetrahedral A site, the structure of the spinel is said to be "normal". On the contrary, if it sits in an octahedral B site, the spinel is said to be "inverse". The incorporation of the cations in a site depends on its size and its crystal-field stabilization energy. For instance, the following minerals have the normal spinel structure: hercynite $FeAl_2O_4$, chromite $FeCr_2O_4$, magnesiochromite $MgCr_2O_4$, galaxite

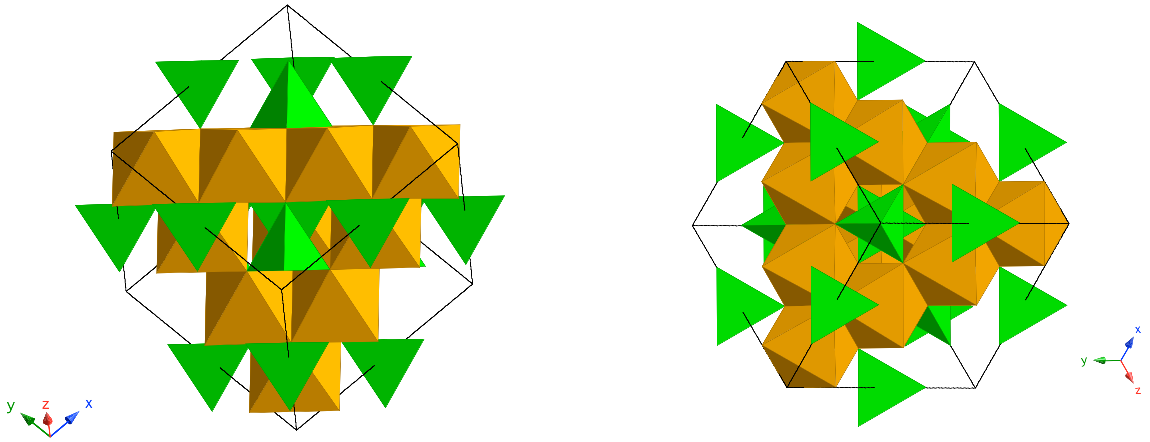

Figure 1.2: Spatial organisation of the tetrahedra and octahedra in the spinel structure.

$MnAl_2O_4$. On the contrary , magnetite Fe_3O_4, jacobsite $MgFe_2O_4$ and ulvospinel $TiFe_2O_4$ have the inverse spinel structure.

The crystallographic structure of spinel

The space group of spinel is $Fd\bar{3}m$ (no.227). Table 1.1 gives the main crystallographic information for the spinel structure. Fig. 1.3 presents all the information on equivalent positions and the group symmetry operations. The structure is described in the International Tables of Crystallography [7] with two possible choices for the origin. For choice 1, the A site is taken as the origin. For choice 2, the origin sits in the B site. The second description is deduced from the first one by a (-1/8, -1/8, -1/8) translation. The local point group of the octahedral site is $\bar{3}m$ (D_{3d} in the Schönflies notation). It corresponds to a slightly distorted octahedron with an inversion center: the six Al-O distances are identical but the angles slightly deviate from 90°.

Site	Local point group	Wyckoff position	Origin choice 1			Origin choice 2		
			x	y	z	x	y	z
A	$\bar{4}3m$	$8a$	0	0	0	1/8	1/8	1/8
B	$\bar{3}m$	$16d$	1/8	1/8	1/8	1/2	1/2	1/2
O	$3m$	$32e$	0.375	0.375	0.375	0.25	0.25	0.25

Table 1.1: Atomic reduced coordinates, Wyckoff positions and local symmetry for each site in the spinel, for the two origin choices.

Magnetite Fe_3O_4 and titanomagnetite $Fe_{3-x}Ti_xO_4$

Magnetite Fe_3O_4 is an inverse spinel: half Fe^{3+} cations sit in tetrahedral sites, the second half and the Fe^{2+} cations in the octahedral ones. The magnetite is therefore written $(Fe^{3+})[Fe^{2+}Fe^{3+}]O_4$. The unit-cell parameter of magnetite is a = 8.377 Å [81]. Magnetite has a ferrimagnetic structure: the ions are antiferromagnetically aligned between the A and B sites, and ferromagnetically in the B sites. Magnetite presents a first-order phase transition at T_V = 120 K, called the Verwey transition [212]. Verwey proposed that below this temperature,

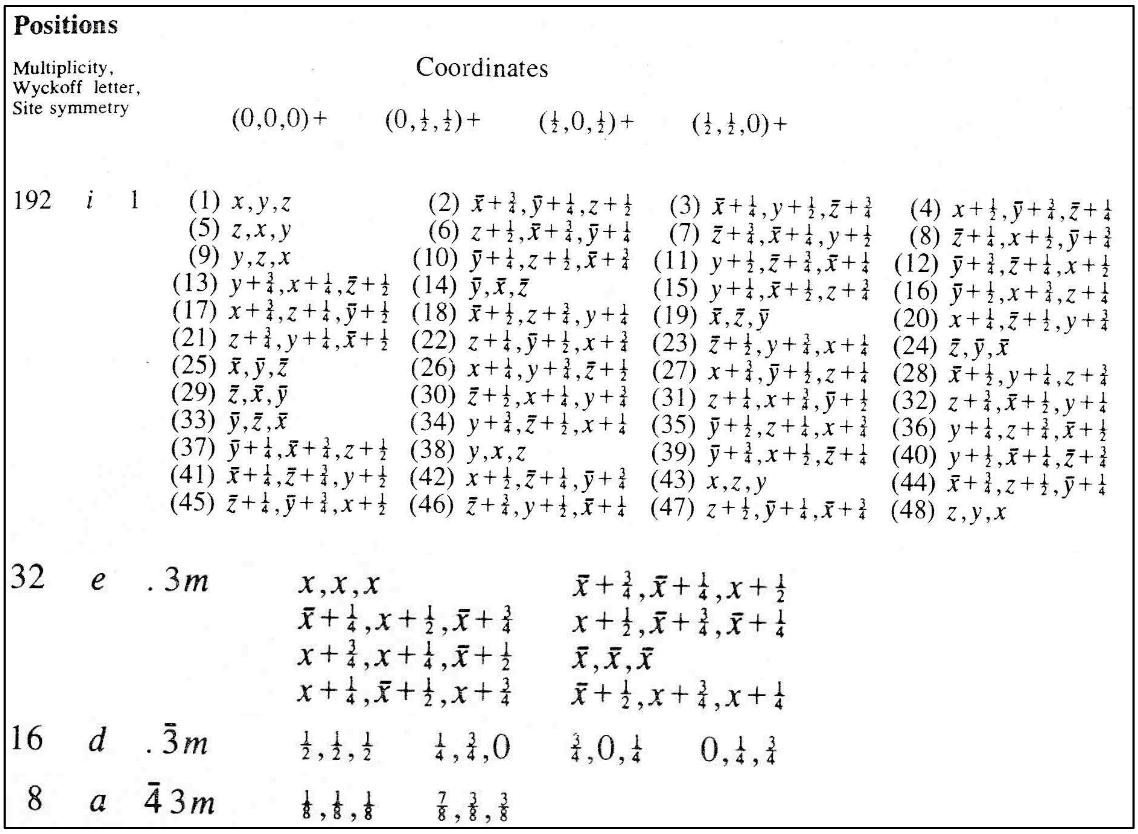

Positions

Multiplicity, Wyckoff letter, Site symmetry			Coordinates			
			$(0,0,0)+$	$(0,\frac{1}{2},\frac{1}{2})+$	$(\frac{1}{2},0,\frac{1}{2})+$	$(\frac{1}{2},\frac{1}{2},0)+$
192	i	1	(1) x,y,z	(2) $\bar{x}+\frac{3}{4},\bar{y}+\frac{1}{4},z+\frac{1}{2}$	(3) $\bar{x}+\frac{1}{4},y+\frac{1}{2},\bar{z}+\frac{3}{4}$	(4) $x+\frac{1}{2},\bar{y}+\frac{3}{4},\bar{z}+\frac{1}{4}$
			(5) z,x,y	(6) $z+\frac{1}{2},\bar{x}+\frac{3}{4},\bar{y}+\frac{1}{4}$	(7) $\bar{z}+\frac{3}{4},\bar{x}+\frac{1}{4},y+\frac{1}{2}$	(8) $\bar{z}+\frac{1}{4},x+\frac{1}{2},\bar{y}+\frac{3}{4}$
			(9) y,z,x	(10) $\bar{y}+\frac{1}{4},z+\frac{1}{2},\bar{x}+\frac{3}{4}$	(11) $y+\frac{1}{2},\bar{z}+\frac{3}{4},\bar{x}+\frac{1}{4}$	(12) $\bar{y}+\frac{3}{4},\bar{z}+\frac{1}{4},x+\frac{1}{2}$
			(13) $y+\frac{3}{4},x+\frac{1}{4},\bar{z}+\frac{1}{2}$	(14) $\bar{y},\bar{x},\bar{z}$	(15) $y+\frac{1}{4},\bar{x}+\frac{1}{2},z+\frac{3}{4}$	(16) $\bar{y}+\frac{1}{2},x+\frac{3}{4},z+\frac{1}{4}$
			(17) $x+\frac{3}{4},z+\frac{1}{4},\bar{y}+\frac{1}{2}$	(18) $\bar{x}+\frac{1}{2},z+\frac{3}{4},y+\frac{1}{4}$	(19) $\bar{x},\bar{z},\bar{y}$	(20) $x+\frac{1}{4},\bar{z}+\frac{1}{2},y+\frac{3}{4}$
			(21) $z+\frac{3}{4},y+\frac{1}{4},\bar{x}+\frac{1}{2}$	(22) $z+\frac{1}{4},\bar{y}+\frac{1}{2},x+\frac{3}{4}$	(23) $\bar{z}+\frac{1}{2},y+\frac{3}{4},x+\frac{1}{4}$	(24) $\bar{z},\bar{y},\bar{x}$
			(25) $\bar{x},\bar{y},\bar{z}$	(26) $x+\frac{1}{4},y+\frac{3}{4},\bar{z}+\frac{1}{2}$	(27) $x+\frac{3}{4},\bar{y}+\frac{1}{2},z+\frac{1}{4}$	(28) $\bar{x}+\frac{1}{2},y+\frac{1}{4},z+\frac{3}{4}$
			(29) $\bar{z},\bar{x},\bar{y}$	(30) $\bar{z}+\frac{1}{2},x+\frac{1}{4},y+\frac{3}{4}$	(31) $z+\frac{1}{4},x+\frac{3}{4},\bar{y}+\frac{1}{2}$	(32) $z+\frac{3}{4},\bar{x}+\frac{1}{2},y+\frac{1}{4}$
			(33) $\bar{y},\bar{z},\bar{x}$	(34) $y+\frac{3}{4},\bar{z}+\frac{1}{2},x+\frac{1}{4}$	(35) $\bar{y}+\frac{1}{2},z+\frac{1}{4},x+\frac{3}{4}$	(36) $y+\frac{1}{4},z+\frac{3}{4},\bar{x}+\frac{1}{2}$
			(37) $\bar{y}+\frac{1}{4},\bar{x}+\frac{3}{4},z+\frac{1}{2}$	(38) y,x,z	(39) $\bar{y}+\frac{3}{4},x+\frac{1}{2},\bar{z}+\frac{1}{4}$	(40) $y+\frac{1}{2},\bar{x}+\frac{1}{4},\bar{z}+\frac{3}{4}$
			(41) $\bar{x}+\frac{1}{4},\bar{z}+\frac{3}{4},y+\frac{1}{2}$	(42) $x+\frac{1}{2},\bar{z}+\frac{1}{4},\bar{y}+\frac{3}{4}$	(43) x,z,y	(44) $\bar{x}+\frac{3}{4},z+\frac{1}{2},\bar{y}+\frac{1}{4}$
			(45) $\bar{z}+\frac{1}{4},\bar{y}+\frac{3}{4},x+\frac{1}{2}$	(46) $\bar{z}+\frac{3}{4},y+\frac{1}{2},\bar{x}+\frac{1}{4}$	(47) $z+\frac{1}{2},\bar{y}+\frac{1}{4},\bar{x}+\frac{3}{4}$	(48) z,y,x
32	e	$.3m$	x,x,x		$\bar{x}+\frac{3}{4},\bar{x}+\frac{1}{4},x+\frac{1}{2}$	
			$\bar{x}+\frac{1}{4},x+\frac{1}{2},\bar{x}+\frac{3}{4}$		$x+\frac{1}{2},\bar{x}+\frac{3}{4},\bar{x}+\frac{1}{4}$	
			$x+\frac{3}{4},x+\frac{1}{4},\bar{x}+\frac{1}{2}$		$\bar{x},\bar{x},\bar{x}$	
			$x+\frac{1}{4},\bar{x}+\frac{1}{2},x+\frac{3}{4}$		$\bar{x}+\frac{1}{2},x+\frac{3}{4},x+\frac{1}{4}$	
16	d	$.\bar{3}m$	$\frac{1}{2},\frac{1}{2},\frac{1}{2}$	$\frac{1}{4},\frac{3}{4},0$	$\frac{3}{4},0,\frac{1}{4}$	$0,\frac{1}{4},\frac{3}{4}$
8	a	$\bar{4}3m$	$\frac{1}{8},\frac{1}{8},\frac{1}{8}$	$\frac{7}{8},\frac{3}{8},\frac{3}{8}$		

Figure 1.3: Symmetry operations and equivalent positions of the $Fd\bar{3}m$ group (Origin choice 2). The first line gives the lattice translations. The first unit (with the multiplicity 192) gives the group symmetry operations. The three units, with multiplicity 32, 16 and 8, indicates the equivalent positions in the cell of the A, B and O atoms respectively. Extracted from the International Tables of Crystallography [7].

a charge ordering takes place among the Fe^{2+} and Fe^{3+} cations on the B sites. In its ordering scheme, the [110] and $[1\bar{1}0]$ rows of B sites on the (001) planes are occupied alternatively by Fe^{2+} and Fe^{3+} [213]. During the transition, the conductivity is reduced by a factor 2 and the residual magnetisation also decreases. The crystallographic structure also changes: below T_V, the space group becomes Cc (monoclinic cell) [112, 226].

Titanomagnetite is an intermediate member of the magnetite-ulvospinel solid-solution. The Ti^{4+} ions substitute for iron ions in the octahedral sites. Consequently, to maintain the charges equilibrium, two Fe^{3+} cations are replaced by one Ti^{4+} cation and one Fe^{2+} cation. The detailed formula of titanomagnetite can thus be written as $Fe^{3+}_{2-2x}Fe^{2+}_{1+x}Ti^{4+}_{x}O_4$, where x is the Ti^{4+} substitution rate.

1.1.2 Tsavorite $Ca_3Al_2(SiO_4)_3$:V^{3+}

The $X_3Y_2Z_3O_{12}$ garnet structure

In the garnet $X_3Y_2Z_3O_{12}$ structure, the O^{2-} anions form a body-centered cubic system. The cationic sites are dodecahedra, octahedra and tetrahedra, corresponding respectively to sites X, Y and Z. The most common garnets are the silicate ones, with Z=Si^{4+}. Divalent cations sit in the X sites and trivalent ones in the Y sites. The unit cell contains eight formula units (160 atoms). Garnets are nesosilicates and their structure can be described as a tridimensional network of

SiO_4 tetrahedra connected by corner to YO_6 octahedra (Fig. 1.4). Cavities are distorted XO_8 dodecahedra. Each tetrahedron shares its corners with four different YO_6 octahedra. Each octahedron is linked to six SiO_4 tetrahedra by corner and to six XO_8 dodecahedra by edges. Each dodecahedron shares its edges with four other dodecahedra, four octahedra and two tetraheda, leaving only two free edges.

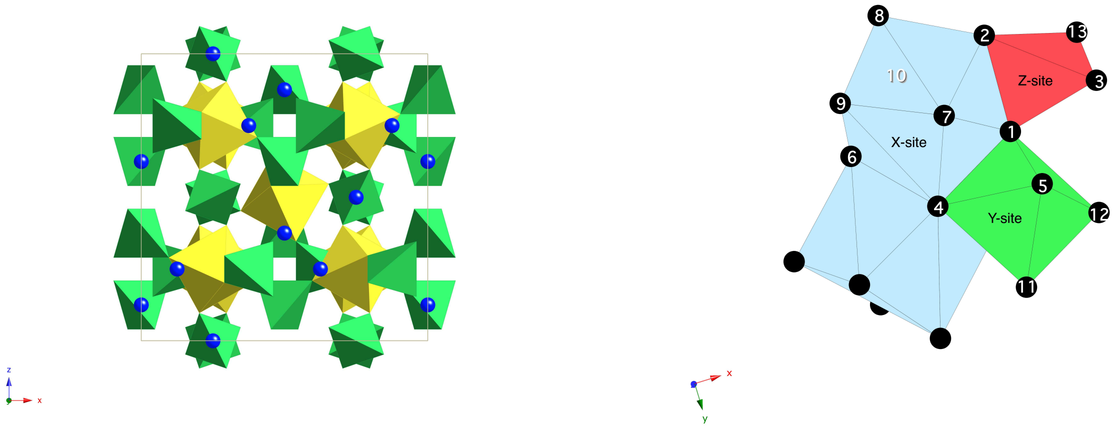

Figure 1.4: The garnet structure. *Left*: the structure in the cubic cell (the blue points represent the center of the dodecahedra). *Right*: A portion of the structure, showing the connection between the tetrahedra and the octahedra. The oxygen atoms are labelled after [155].

The silicate garnets are separated into two families, depending on the presence of Ca^{2+} cations in the X sites. The calcic garnets ($Ca_3Y_2Si_3O_{12}$) form the ugrandite family (Uvarovite GRossular ANDradite): grossular $Ca_3Al_2Si_3O_{12}$, uvarovite $Ca_3Cr_2Si_3O_{12}$, andradite $Ca_3Fe_2Si_3O_{12}$, goldmanite $Ca_3V_2Si_3O_{12}$, etc. The other garnets ($X_3Y_2Si_3O_{12}$, with $X \neq Ca$) form the pyralspite family (PYRope ALmandine SPessartine): pyrope $Mg_3Al_2Si_3O_{12}$, almandine $Fe_3Al_2Si_3O_{12}$, knorringite $Mg_3Cr_2Si_3O_{12}$, spessartine $Mn_3Al_2Si_3O_{12}$, etc.

The crystallographic structure of garnet

The space group of garnet is $Ia\bar{3}d$ (no.230). Table 1.2 gives the main crystallographic information for the garnet structure. Fig. 1.5 presents all the information on equivalent positions and the group symmetry operations. The local point group of the octahedral site is $\bar{3}$ (C_{3i} in the Schönflies notation), which corresponds to a slightly distorted octahedron with an inversion center. The six Al-O distances are identical but the angles slightly deviate from 90°.

Site	Local point group	Wyckoff position	x	y	z
X	222	24c	1/8	0	1/4
Y	$\bar{3}$	16a	0	0	0
Z	$\bar{4}$	24d	3/8	0	1/4
O	1	96h	x	y	z

Table 1.2: Atomic reduced coordinates, Wyckoff positions and local symmetry for each site in the garnet structure.

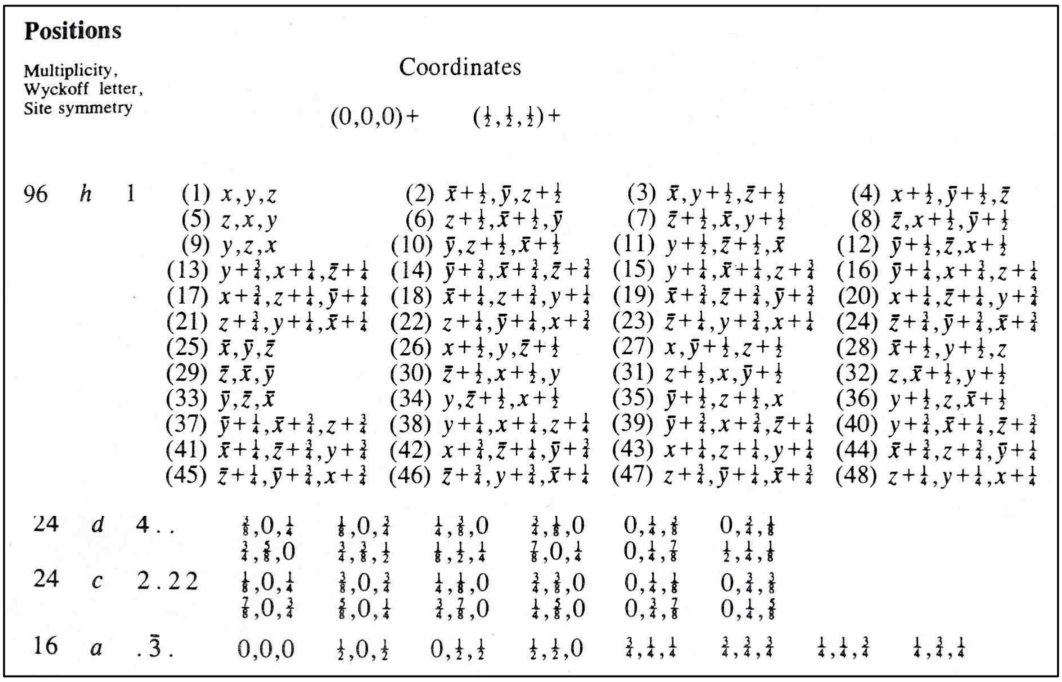

Positions

Multiplicity,	Wyckoff letter,	Site symmetry	Coordinates							
			$(0,0,0)+$	$(\frac{1}{2},\frac{1}{2},\frac{1}{2})+$						
96	*h*	1	(1) x,y,z	(2) $\bar{x}+\frac{1}{2},\bar{y},z+\frac{1}{2}$	(3) $\bar{x},y+\frac{1}{2},\bar{z}+\frac{1}{2}$	(4) $x+\frac{1}{2},\bar{y}+\frac{1}{2},\bar{z}$				
			(5) z,x,y	(6) $z+\frac{1}{2},\bar{x}+\frac{1}{2},\bar{y}$	(7) $\bar{z}+\frac{1}{2},\bar{x},y+\frac{1}{2}$	(8) $\bar{z},x+\frac{1}{2},\bar{y}+\frac{1}{2}$				
			(9) y,z,x	(10) $\bar{y},z+\frac{1}{2},\bar{x}+\frac{1}{2}$	(11) $y+\frac{1}{2},\bar{z}+\frac{1}{2},\bar{x}$	(12) $\bar{y}+\frac{1}{2},\bar{z},x+\frac{1}{2}$				
			(13) $y+\frac{3}{4},x+\frac{1}{4},\bar{z}+\frac{1}{4}$	(14) $\bar{y}+\frac{3}{4},\bar{x}+\frac{3}{4},\bar{z}+\frac{3}{4}$	(15) $y+\frac{1}{4},\bar{x}+\frac{1}{4},z+\frac{3}{4}$	(16) $\bar{y}+\frac{1}{4},x+\frac{3}{4},z+\frac{1}{4}$				
			(17) $x+\frac{3}{4},z+\frac{1}{4},\bar{y}+\frac{1}{4}$	(18) $\bar{x}+\frac{1}{4},z+\frac{3}{4},y+\frac{1}{4}$	(19) $\bar{x}+\frac{3}{4},\bar{z}+\frac{3}{4},\bar{y}+\frac{3}{4}$	(20) $x+\frac{1}{4},\bar{z}+\frac{1}{4},y+\frac{3}{4}$				
			(21) $z+\frac{3}{4},y+\frac{1}{4},\bar{x}+\frac{1}{4}$	(22) $z+\frac{1}{4},\bar{y}+\frac{1}{4},x+\frac{3}{4}$	(23) $\bar{z}+\frac{1}{4},y+\frac{3}{4},x+\frac{1}{4}$	(24) $\bar{z}+\frac{3}{4},\bar{y}+\frac{3}{4},\bar{x}+\frac{3}{4}$				
			(25) $\bar{x},\bar{y},\bar{z}$	(26) $x+\frac{1}{2},y,\bar{z}+\frac{1}{2}$	(27) $x,\bar{y}+\frac{1}{2},z+\frac{1}{2}$	(28) $\bar{x}+\frac{1}{2},y+\frac{1}{2},z$				
			(29) $\bar{z},\bar{x},\bar{y}$	(30) $\bar{z}+\frac{1}{2},x+\frac{1}{2},y$	(31) $z+\frac{1}{2},x,\bar{y}+\frac{1}{2}$	(32) $z,\bar{x}+\frac{1}{2},y+\frac{1}{2}$				
			(33) $\bar{y},\bar{z},\bar{x}$	(34) $y,\bar{z}+\frac{1}{2},x+\frac{1}{2}$	(35) $\bar{y}+\frac{1}{2},z+\frac{1}{2},x$	(36) $y+\frac{1}{2},z,\bar{x}+\frac{1}{2}$				
			(37) $\bar{y}+\frac{1}{4},\bar{x}+\frac{3}{4},z+\frac{3}{4}$	(38) $y+\frac{1}{4},x+\frac{1}{4},z+\frac{1}{4}$	(39) $\bar{y}+\frac{3}{4},x+\frac{3}{4},\bar{z}+\frac{1}{4}$	(40) $y+\frac{3}{4},\bar{x}+\frac{1}{4},\bar{z}+\frac{3}{4}$				
			(41) $\bar{x}+\frac{1}{4},\bar{z}+\frac{3}{4},y+\frac{3}{4}$	(42) $x+\frac{3}{4},\bar{z}+\frac{1}{4},\bar{y}+\frac{3}{4}$	(43) $x+\frac{1}{4},z+\frac{1}{4},y+\frac{1}{4}$	(44) $\bar{x}+\frac{3}{4},z+\frac{3}{4},\bar{y}+\frac{1}{4}$				
			(45) $\bar{z}+\frac{1}{4},\bar{y}+\frac{3}{4},x+\frac{3}{4}$	(46) $\bar{z}+\frac{3}{4},y+\frac{3}{4},\bar{x}+\frac{1}{4}$	(47) $z+\frac{3}{4},\bar{y}+\frac{1}{4},\bar{x}+\frac{3}{4}$	(48) $z+\frac{1}{4},y+\frac{1}{4},x+\frac{1}{4}$				
24	*d*	4 . .	$\frac{3}{8},0,\frac{1}{4}$	$\frac{1}{8},0,\frac{3}{4}$	$\frac{1}{4},\frac{3}{8},0$	$\frac{3}{4},\frac{1}{8},0$	$0,\frac{1}{4},\frac{3}{8}$	$0,\frac{3}{4},\frac{1}{8}$		
			$\frac{3}{4},\frac{5}{8},0$	$\frac{3}{4},\frac{3}{8},\frac{1}{2}$	$\frac{1}{8},\frac{1}{2},\frac{1}{4}$	$\frac{7}{8},0,\frac{1}{4}$	$0,\frac{1}{4},\frac{7}{8}$	$\frac{1}{2},\frac{1}{4},\frac{1}{8}$		
24	*c*	2 . 22	$\frac{1}{8},0,\frac{1}{4}$	$\frac{3}{8},0,\frac{3}{4}$	$\frac{1}{4},\frac{1}{8},0$	$\frac{3}{4},\frac{3}{8},0$	$0,\frac{1}{4},\frac{1}{8}$	$0,\frac{3}{4},\frac{3}{8}$		
			$\frac{7}{8},0,\frac{3}{4}$	$\frac{5}{8},0,\frac{1}{4}$	$\frac{3}{4},\frac{7}{8},0$	$\frac{1}{4},\frac{5}{8},0$	$0,\frac{3}{4},\frac{7}{8}$	$0,\frac{1}{4},\frac{5}{8}$		
16	*a*	$.\bar{3}.$	$0,0,0$	$\frac{1}{2},0,\frac{1}{2}$	$0,\frac{1}{2},\frac{1}{2}$	$\frac{1}{2},\frac{1}{2},0$	$\frac{3}{4},\frac{1}{4},\frac{1}{4}$	$\frac{3}{4},\frac{3}{4},\frac{3}{4}$	$\frac{1}{4},\frac{1}{4},\frac{3}{4}$	$\frac{1}{4},\frac{3}{4},\frac{1}{4}$

Figure 1.5: Symmetry operations and equivalent positions of the $Ia\bar{3}m$ group. Extracted from the International Tables of Crystallography [7].

Tsavorite $Ca_3Al_2Si_3O_{12}$:V^{3+} is a grossular with vanadium present as a substituted minor element in the Al site. The cell parameter of grossular is a = 11.847 Å. The Al-O distance is 1.926 Å, the Al-Ca and Al-Si ones are 3.31 Å and the Al-Al one 5.130 Å. The oxygen reduced coordinates (x,y,z) are (0.03823, 0.04528, 0.65137) [91]. Fig. 1.6 presents the cubic cell of tsavorite, *i.e.* the grossular one with a V^{3+} ion substituted for an Al^{3+} ion in an octahedral site.

In the grossular cubic cell, the aluminum atoms sit in sixteen equivalent sites, but differently oriented with respect to the cubic frame. They are divided into two groups of eight atoms equivalent by a $(\frac{1}{2}, \frac{1}{2}, \frac{1}{2})$ translation. The eight sites of each group are equivalent by space group symmetry operations. Vanadium can substitute for aluminum in any of these eight sites. This point is important for the theoretical study of tsavorite (Chap. 3).

1.1.3 Anatase TiO_2

Anatase is one of the three polymorphs of titanium dioxide (TiO_2), the two other being rutile and brookite. Anatase and rutile are both tetragonal forms of TiO_2, whereas brookite crystallizes in the orthorombic system. Rutile, which is the more abundant phase, is stable above 700° and anatase is the stable form at low temperature. Both anatase and rutile are of great interest in catalysis, material sciences [142] and geological sciences [79]. Rutile is prefered over anatase in pigmentary applications as it has a higher refractive index and is less photoactive [22]. Anatase is more efficient than rutile for catalysis applications, such as photocatalysis or dye-sensitized solar cells [137] as it has a high photoreactivity [186]. Both of them have the advantages of being inexpensive, non-toxic, resistant to photo-corrosion and to have an high oxidative power [211].

In anatase, the titanium atoms are at the center of an oxygen octahedron. Each oxygen atom is coordinated to three titanium atoms. Each octahedron is connected to eight octahedra, four by edges and four by corners. Between the occupied octahedra exist vacant tetrahedral and

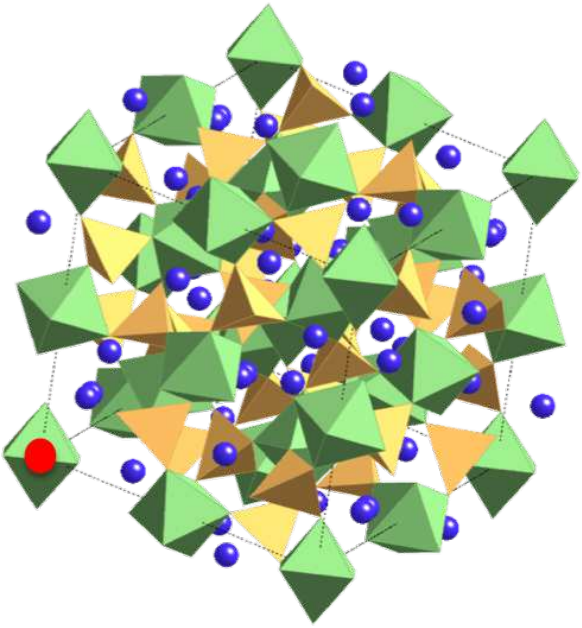

Figure 1.6: The cubic cell of tsavorite. The substituted atom of vanadium is represented by the red point.

octahedral sites. The unit cell is a body-centered tetragonal lattice and contains four formula units per unit cell. The cell parameters are $a = 3.78$ Å and $c = 9.51$ Å [111]. The main structural differences between rutile and anatase are the cell parameters (a = 4.59 Å and c = 2.96 Å in rutile) [111] and the secondary coordination: in rutile, the titanium octahedra are joined by sharing only two edges (four edges in anatase).

The space group of anatase is $I4_1/amd$ (no.141). Table 1.3 gives the main crystallographic information for the anatase structure. Fig. 1.8 presents all the information on equivalent positions and the group symmetry operations. The local point group of the octahedral site is $\bar{4}m2$ (D_{2d} in the Schönflies notation), which corresponds to a distorted octahedron without an inversion center. There are two Al-O distances at 1.937 Å and four at 1.965 Å. The angles deviate from 90° by ±12.6°. In anatase, Ti is located at (0,0,0) and O at (0,0,z), with $z = 0.20806$ [111].

Site	Local point group	Wyckoff position	x	y	z
Ti	$\bar{4}m2$	$4a$	0	0	0
O	$2mm$	$8e$	0	0	z

Table 1.3: Atomic reduced coordinates, Wyckoff positions and local symmetry for the Ti and O sites in the anatase structure, with the origin at $\bar{4}m2$ (origin choice 1).

1.2 Chemical analyses

The magnetite samples investigated during this thesis were chemically analyzed by several techniques. The synthetic magnetite samples were first analyzed by X-ray diffraction (XRD). Both synthetic and natural samples were characterized by electron microprobe (EMP) analyses and scanning electron microscopy (SEM). The principles of each technique is explained in brief

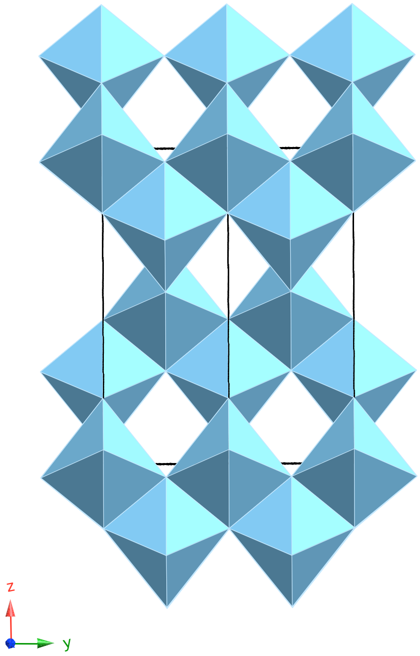

Figure 1.7: Anatase structure

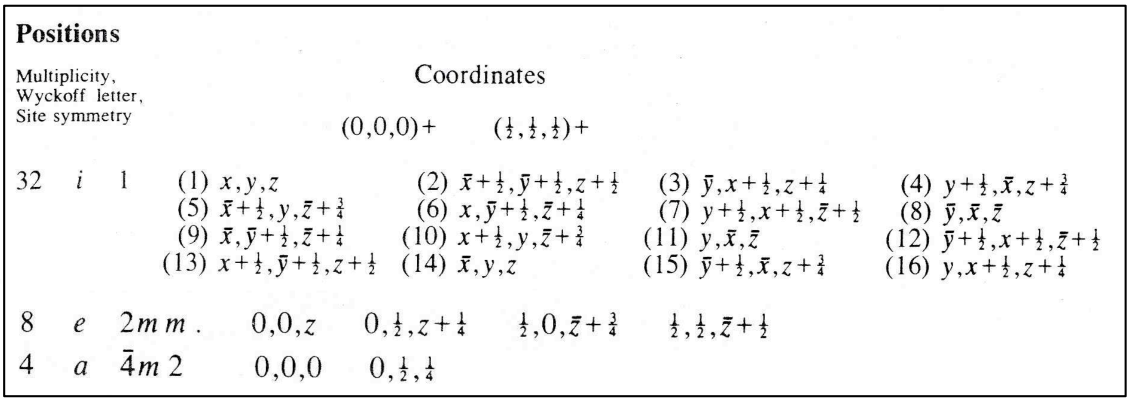

Positions

Multiplicity, Wyckoff letter, Site symmetry			Coordinates			
			$(0,0,0)+$	$(\frac{1}{2},\frac{1}{2},\frac{1}{2})+$		
32	i	1	(1) x,y,z	(2) $\bar{x}+\frac{1}{2},\bar{y}+\frac{1}{2},z+\frac{1}{2}$	(3) $\bar{y},x+\frac{1}{2},z+\frac{1}{4}$	(4) $y+\frac{1}{2},\bar{x},z+\frac{3}{4}$
			(5) $\bar{x}+\frac{1}{2},y,\bar{z}+\frac{3}{4}$	(6) $x,\bar{y}+\frac{1}{2},\bar{z}+\frac{1}{4}$	(7) $y+\frac{1}{2},x+\frac{1}{2},\bar{z}+\frac{1}{2}$	(8) $\bar{y},\bar{x},\bar{z}$
			(9) $\bar{x},\bar{y}+\frac{1}{2},\bar{z}+\frac{1}{4}$	(10) $x+\frac{1}{2},y,\bar{z}+\frac{3}{4}$	(11) $y,\bar{x},\bar{z}$	(12) $\bar{y}+\frac{1}{2},x+\frac{1}{2},\bar{z}+\frac{1}{2}$
			(13) $x+\frac{1}{2},\bar{y}+\frac{1}{2},z+\frac{1}{2}$	(14) $\bar{x},y,z$	(15) $\bar{y}+\frac{1}{2},\bar{x},z+\frac{3}{4}$	(16) $y,x+\frac{1}{2},z+\frac{1}{4}$
8	e	$2mm.$	$0,0,z$	$0,\frac{1}{2},z+\frac{1}{4}$	$\frac{1}{2},0,\bar{z}+\frac{3}{4}$	$\frac{1}{2},\frac{1}{2},\bar{z}+\frac{1}{2}$
4	a	$\bar{4}m2$	$0,0,0$	$0,\frac{1}{2},\frac{1}{4}$		

Figure 1.8: Symmetry operations and equivalent positions of the $I4_1/amd$ group (Origin choice 1).

as they are standard techniques used in this research as complementary tools to X-ray absorption spectroscopy.

1.2.1 X-ray diffraction

XRD is a powerful tool to identify mineral phases present in a sample and to determine a crystallographic structure. It gives access to structural parameters (cell parameters, atomic positions, ...) and provides information also on the sample microstructure (size and shape of the coherent domains). To study crystallized samples, X-rays are particularly suitable as their wavelength is similar the interatomic distances in a crystal. Experiments can be performed on single crystals or powders.

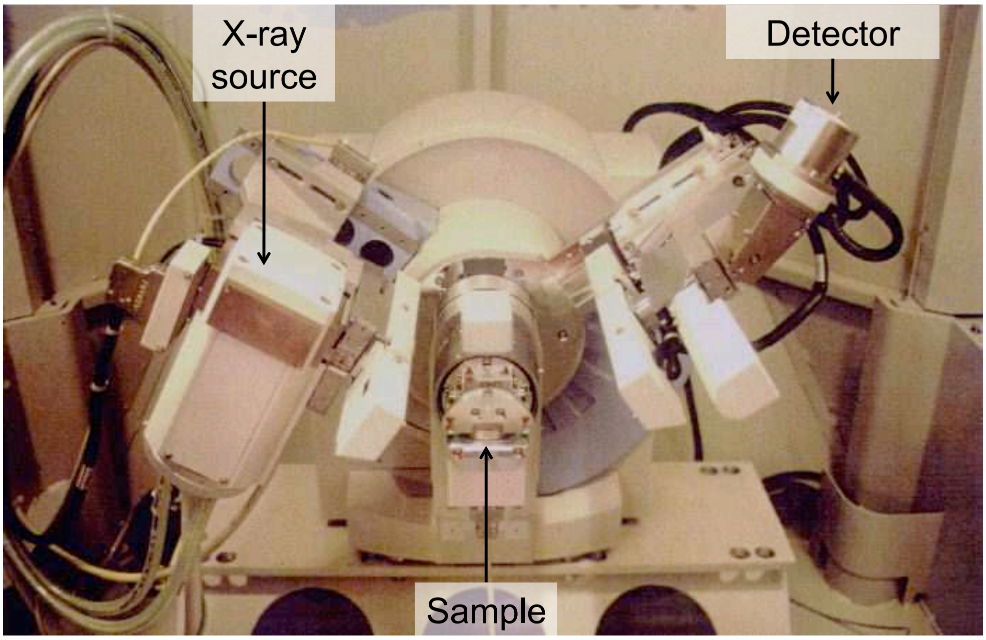

Figure 1.9: Picture of the θ-θ diffractometer. The sample is kept fixed while the X-rays source and the detector rotate by an angle θ.

The choice of the X-ray source used in XRD experiments depends on the elements present in the sample. It must be done so that no fluorescence radiation creates a high background in the XRD pattern which would obscure weak peaks. This fluorescence baseline is present if the energy of the incident beam is higher but close to the absorption edge energy of an element present in a significant concentration in the sample. In the case of iron oxides, a Co source ($E = 7709$ eV) is used. As the detector (Fig. 1.9) records the corresponding fluorescence, *i.e.* the Co K_{α_1} (6930 eV) and K_{α_2} (6915 eV) fluorescence lines, the fluorescence of iron ($K_{\alpha_1} = 6403$ eV, $K_{\alpha_1} = 6390$ eV) is filtered out.

The information in a XRD pattern comes from the angles where the diffraction peaks are observed, from their intensity and from their width. The position of the diffraction peaks is determined by Bragg's law, which gives the relation between the peak postition ($\sin\theta$) to the incident beam wave-length (λ) and the interreticular distances for the ($hk\ell$) plane family ($d_{hk\ell}$):

$$2d_{h,k,\ell}sin\theta = n\lambda \tag{1.1}$$

This position is determined only by the cell parameters. For a peak related to a ($hk\ell$) planes family, the diffracted intensity is given by the structure factor, $F_{hk\ell}$, which depends on the atomic reduced coordinates in the cell (f_i is the diffusion factor of the i^{th} atom):

$$F_{hk\ell} = \sum f_i \ \exp(2i\pi(x_i h + Y_i k + z_i \ell)), \tag{1.2}$$

and by the Debye-Waller factor. Finally, the peak width depends on three parameters: the intrinsic diffractometer instrumental broadening, the presence of elastic constraints in crystals and the size of the coherent domains.

Only the synthesized samples were analyzed by XRD. The measurements were performed at the institute on a θ-θ diffractometer (XpertPro MD, by Panalytical). The diffractometer is shown in Fig. 1.9.

1.2.2 Electron microprobe

The electron microprobe (EMP) provides the chemical composition of the sample under investigation. It is a non-destructive method which permits all the elements of the periodic classification from beryllium to be detected with a sensitivity of ∼100ppm. The major and minor elements of the sample can thus be determined. The results are obtained in wt% oxides. The EMP measures the fluorescence yield of the elements present in the sample due to their excitation under an electron beam. As the fluorescence line intensities are proportional to the mass concentration of the corresponding element, the relative proportion of the latter be determined.

The EMP analyses were performed at the CAMPARIS facility of the University Pierre and Marie Curie (Paris, France), with a CAMECA SX50 device. It was operated at 15kV and 40nA, with a counting time varying between 10 and 30 s, depending on the element.

1.2.3 Scanning Electron Microscopy

The scanning electron microscopy (SEM) analysis provides topographical and chemical information on the sample (grain size, surface roughness, porosity, particle size distribution, material homogeneity, ...). A finely focused electron beam scans across the surface of the samples. The electrons interact with the sample atoms and thus generate several signals, which are collected by different detectors to form 3D images of the sample. The backscattered (or primary) electrons are beam electrons that bounce off nuclei of atoms in the sample; they are used to determine the spatial distribution of elements. The secondary electron imaging provide information on the topography of surface features a few nm across. The interactions between the sample and the beam electrons can also result in a X-ray emission. These fluorescence lines, as for microprobe, provide quantitative information about the elements present in the sample. The determination of the chemical composition with a SEM is called energy-dispersive spectroscopy (EDS).

The SEM analyses of the natural and synthesized magnetite samples were done at the "Laboratoire Interfaces et Systèmes Electrochimiques" of the University Pierre and Marie Curie (Paris, France) using a LEICA S440. Analyses were also performed at the Industrial Minerals and Metals Research Institute, of the Department of Materials Science and Metallurgical Engineering, at the University of Pretoria (South Africa). The microscope was a Jeol JSM 6300. Both microscopes have a tungsten filament electron gun. The images were taken using a Centaurus backscattered electron detector, with an accelerating voltage of 15kV.

1.3 X-ray Absorption Spectroscopy

X-ray absorption spectroscopy (XAS) is a powerful tool to study the electronic and crystallographic structures around an atom in a structure, whether an impurity in a host-mineral or a major component element of the mineral. The first advantage of XAS is that this technique is chemically selective: each element has its own edge energy, and the energy shift between two edges is significant enough so that two successive edges do not superimpose (Fig. 1.10). All the chemical species are accessible by XAS. The second advantage of XAS is its orbital selectivity: as the binding energies of the core levels are different, one can choose the level where the electron is excited and consequently which empty states are probed. In the electric dipole approximation, the transitions must obey this selection rule: $\Delta\ell = \pm 1$. In this approximation, K edge thus corresponds to transitions from $1s$ to p states, L_1 edge from $2s$ to p, $L_{2,3}$ edges from $2p$ levels to d ones, M_1 edge from $3s$ to p, $M_{2,3}$ edge from $3p$ to d, $M_{4,5}$ edge from $3d$ to f... The electric quadrupole approximation is defined by $\Delta\ell = \pm 2$ or 0 (except if the ground state is an s one). Therefore, in this approximation, K edge also corresponds to transitions from $1s$ to d states. These chemical and orbital selectivities permit access to the electronic structure of the absorbing atom (oxidation state, type of the chemical bindings, ...). XAS is also a structural probe that does not need long-range order. Hence both crystals and amorphous materials can be studied equally well using this technique, and the local and medium-range orders around the absorbing atom can be determined.

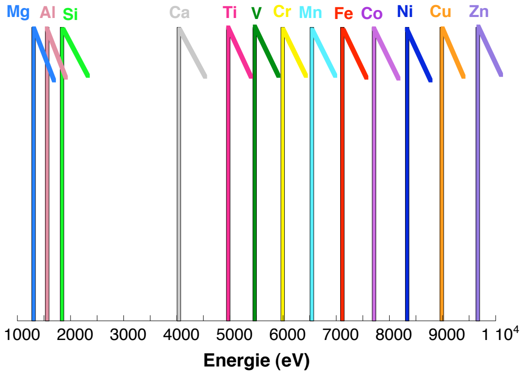

Figure 1.10: Representation of the K-edge position of various elements, illustrating the chemical selectivity of XAS.

1.3.1 Principle

During the XAS process, a core electron is excited by absorbing a photon with an energy $\hbar\omega$. The excited electron is called photoelectron. The variation of the X-ray absorption coefficient is measured as a function of the incident radiation energy (E). The Bouguer law describes the absorption of the X-rays by matter:

$$I = I_0 \cdot \exp(-\mu(E)x) \tag{1.3}$$

where I_0 is the incident beam intensity, I the one of the transmitted beam, μ the absorption coefficient of the probed element and x the sample thickness.

During my thesis, I performed measurements on dilute samples at the V K-edge. In that case, the fluorescence detection mode is used and a fluorescence yield, proportional to $\frac{I_f}{I_0}$ (I_f is the fluorescence intensity), is determined. If the samples had been concentrated (*i.e.* if the concentration of vanadium had exceeded a few percents in oxide weight), the absorption coefficient would have been calculated with the previous equation (1.3) and transmission would have been used as a detection mode. These different detection modes are presented in Fig. 1.11.

Fig. 1.12 presents a XAS spectrum recorded at the V K-edge of tsavorite. The structures that compose a XAS spectrum are due to the interactions of the photoelectron with the neighboring atoms of the absorbing atom. The spectrum can be divided in three regions, depending on the incident X-rays energy.

- In the region before the edge, the incident photoelectron energy E is too weak to excite core electrons. A continuous background is recorded, due to the presence in the sample of other elements with a lower edge-energy than the one of the probed element (Fig. 1.12a). This background of the absorption coefficient constitutes the spectrum baseline.

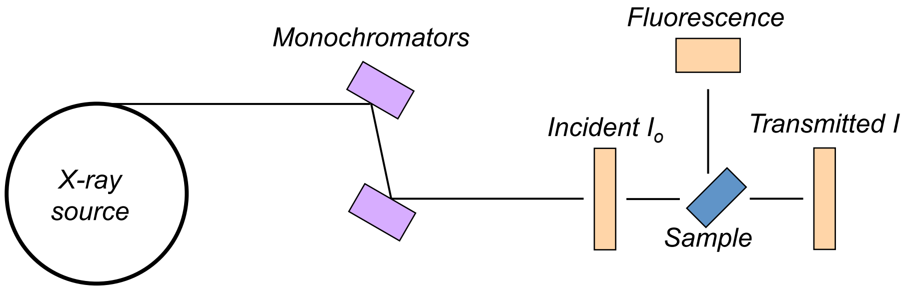

Figure 1.11: Schematic view of an absorption beamline where the different detection modes are shown. The monochromator is used to select the incident energy.

- The following region, called XANES (X-ray Absorption Near-Edge Structure), expands up to approximateky 50 eV after the edge. As long as the X-rays energy is slightly below the absorption edge energy, a photoelectron is promoted to the first empty or partially occupied states, which are localized states. At K-edge of transition elements, structures can usually observed in the so-called pre-edge region, also called pre-peak (Fig. 1.12b). If the X-rays have an energy above the edge, the electron is then promoted in the continuum and it is involved in multiple scattering processes with neighbouring atoms (Fig. 1.12c). Its kinetic energy is small and its mean free-path (the distance covered without energy loss) is significant. In the case of K-edges, the structures of a XANES spectrum result from transitions of the photoelectron from $1s$ core orbitals to different shells, depending on the edge and the pre-edge. The edge part consists of $1s \rightarrow p$ (electric dipole) transitions. The pre-edge consists of contributions from both $1s \rightarrow p$ and $1s \rightarrow 3d$ (electric quadrupole) transitions. Electric dipole transitions contribute to the pre-edge only if one of these situations is encountered: (i) there is p-d intrasite hybridization (*i.e.* the crystallographic site does not show an inversion center), (ii) there is p-d intersite hybridization (in samples highly concentrated in the investigated element), (iii) the thermally activated vibrations remove the inversion center. The XANES part of the spectrum gives access to the crystallographic and electronic structures of the absorbing atom. The edge part provides information on the short and medium-range order around the absorbing atom and on the electronic structure. The pre-edge can give information on the coordination number of the absorbing atom, its site symmetry, its oxidation state and the hybridization of the p and d orbitals.

- The EXAFS (Extended X-ray Absorption Fine Structure) region expands above the XANES one. The X-ray energy is sufficient to promote the electron in the delocalized states of the continuum (Fig. 1.12d). Therefore the ejected electron has a high kinetic energy, its mean free-path is short and it is therefore mainly involved in simple diffusion phenomena with the neighboring atoms. The analysis of EXAFS oscillations provides local information on the absorbing atom: the coordination number, the nature of its neighbors, the distance with them and the structural disorder.

The XANES and EXAFS regions are distinguished because their analysis methods are completely different. Two approaches are possible to interpret the XANES spectra. The phenomenological approach, also called fingerprint method, is based on the direct comparison between the spectrum and those of reference compounds. It is used to get simple or preliminary information concerning the absorbing atom, for instance its oxidation state or coordination number. To get richer information, theoretical XANES computations are needed. Two kinds of methods can be

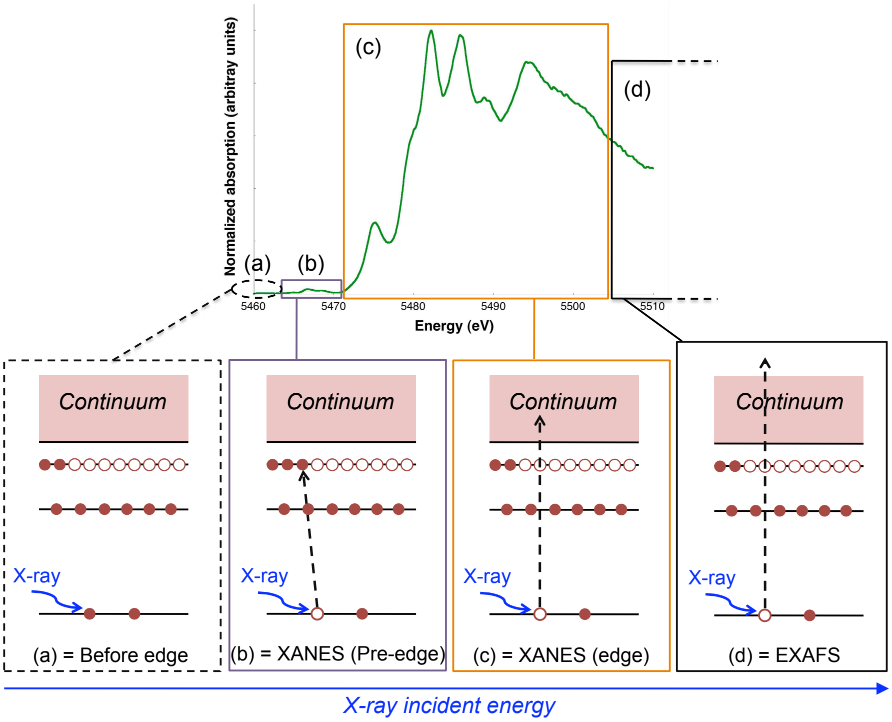

Figure 1.12: The different regions of a XAS spectrum (here : the V K-edge spectrum of tsavorite) with the transitions of the photoelectron in the different regions.

distinguished to compute XANES spectra : the monoelectronic approach, which is more dedicated to the study of delocalized final states, and the multielectronic one, which is usually used in the case of localized final states. These two appraoches will be described in Chap. 2.

1.3.2 High Energy Resolution Fluorescence Detected X-ray Absorption Spectroscopy

Under certain conditions (impurity present at a very low concentration, atom in a centrosymmetric site,...), the intensity of the pre-edge may be small compared to that of the main edge. To get reliable information on the oxidation state and local symmetry from the pre-edge features, the background in the pre-edge region must be as weak as possible. In this way the structures are related only to the local symmetry and oxidation state of the absorbing atom, and no additional feature due to the background interferes.

The background results from the fluorescence of the elements present in the sample which have an edge-energy lower than the one of the probed element. I consider here the example of vanadiferous titanomagnetites but it can be applied to other minerals. These chemically complex samples contain between 1 and 2 wt% V_2O_3 and about 15 wt% TiO_2. The Ti K-edge is at 4966 eV and the V one at 5465 eV. Fig. 1.13 shows the XANES spectrum recorded at the Ti K-edge and then at the V one in the conventional fluorescence detection mode. The background in the pre-edge of the V spectrum sits on the top of the Ti EXAFS and is really significant. Consequently the V pre-edge structures are not clearly defined.

In order to filter out the Ti fluorescence, a particular detection mode can be used: a specificic fluorescence line is recorded while scanning the incident energy range. Hence, by recording the V Kα_1 fluorescence line (4952 eV), the Ti fluorescence is filtered out (Fig. 1.14). Only the V

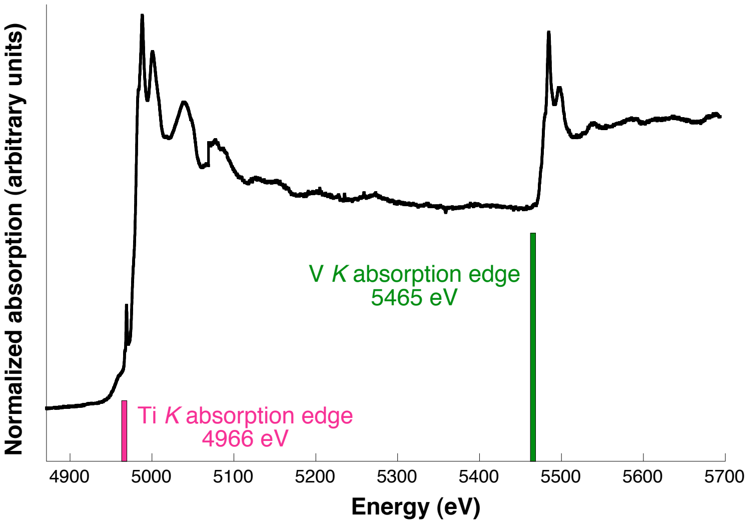

Figure 1.13: Conventional XANES spectrum of a vanadiferous titanomagnetite at the Ti and V *K*-edges.

signal is recorded and the pre-edge structures are well defined. The special detection mode is called high energy-resolution fluorescence detected X-ray absorption spectroscopy (HERFD-XAS) [66, 69, 97, 96]. A second effect of this detection mode is a sharpening effect on the features, leading to better resolved spectra [94, 65, 104, 102].

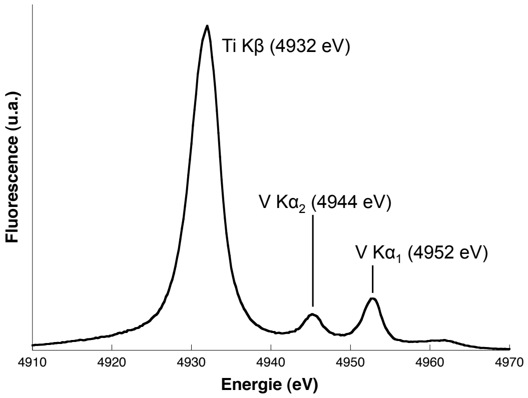

Figure 1.14: Fluorescence lines of Ti and V.

HERFD-XAS experiments need a high-resolution spectrometer. Fig. 1.15 (left) shows the experimental setup used to perform all the XAS experiments during the thesis. The spectra presented in this thesis were recorded during three experiments between January 2007 and June 2008 at the European Synchroron Radiation Facilty (ESRF, Grenoble, France) on the ID26 beamline [90]. The fluorescence emitted by the sample after interaction with X-rays is analyzed by the high-resolution spectrometer. The central spectrometer component is a Bragg crystal that analyses the fluorescence from the sample and reflects it on a photon counter. The spectrometer has an energy resolution similar to the core hole lifetime broadening. The sample, the analyzer crystal and the detector are set in a Rowland geometry (Fig. 1.15 right). The choice of the analyzer crystal depends on the energy of the fluorescence line that has to be selected. An helium bag is put between the sample, the analyzer and the detector so that the X-ray photons are not absorbed by the air.

Room-temperature V K-edge HERFD-XAS spectra were recorded with the high-resolution spectrometer. We selected the V Kα_1 line with a Ge(331) analyzer crystal, with R=855 mm for the Rowland circle diameter. The energy of the incident radiation was selected using a pair of ℓN_2-cooled Si crystals with a (311) orientation. The spot size of the incident X-ray beam on the sample was approximately 250×50 μm^2. The incident flux was monitored by detecting the X-ray scattering from a thin Kapton foil in the incident beam path. An avalanche photodiode was used as a fast photon detector for emission detection to avoid non-linear effects.

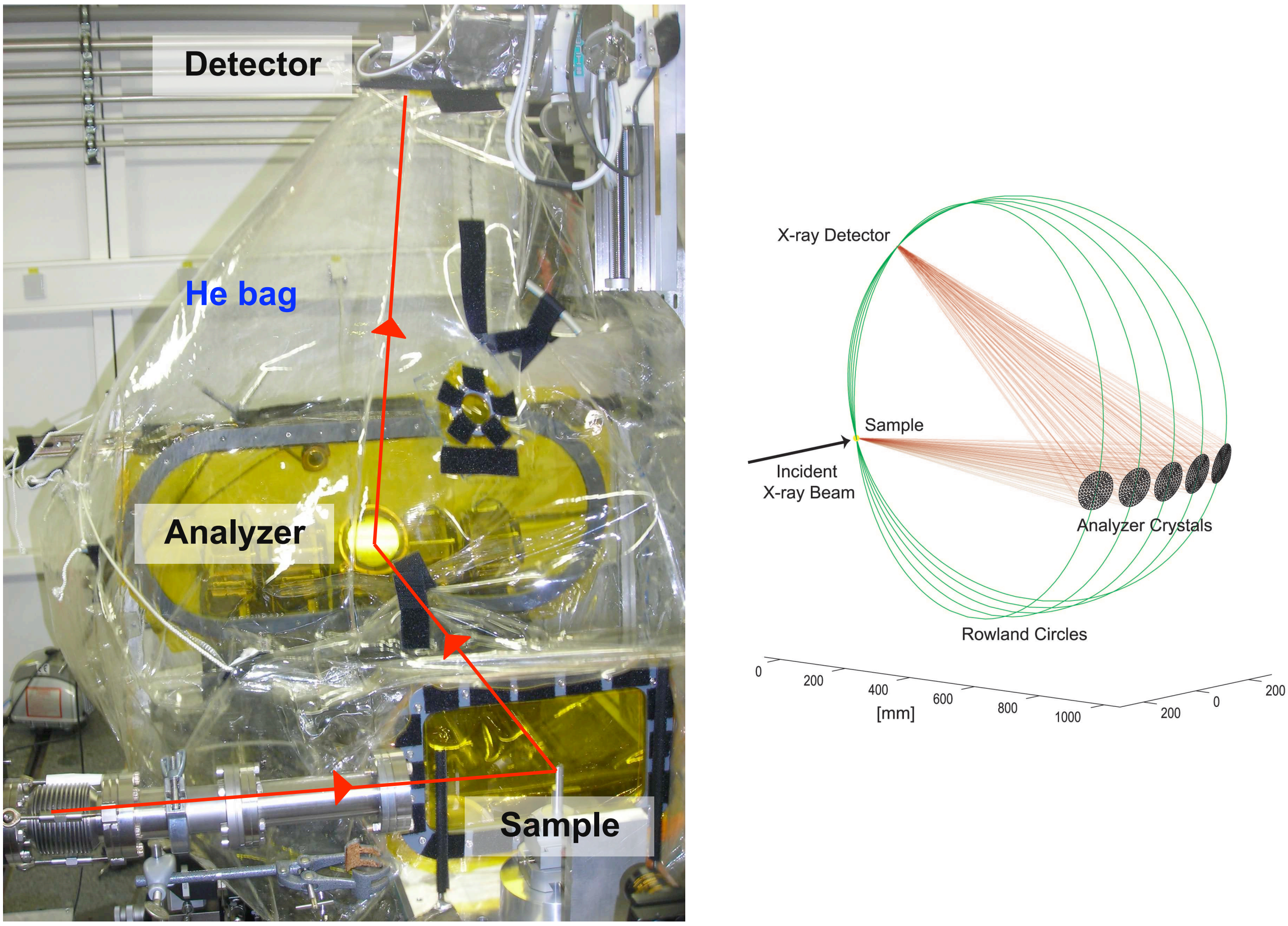

Figure 1.15: Experimental setup on ID26 beamline (left), with the geometry of the high-resolution spectrometer (right). During our experiments, we used only one crystal. The figure of the spectrometer is extracted from [97].

1.3.3 HERFD-XAS *vs.* conventional XAS

HERFD-XAS might differ from conventional XAS in total fluorescence yield with respect to the peak broadening and also with respect to the number of peaks and the intensity ratios. An additional peak can for instance appear on a HERFD-XAS spectrum compared to a conventional one [94, 66]. Then it is useful to record a full Resonant Inelastic X-ray Scattering (RIXS) plane to determine whether the HERFD-XAS spectrum is equivalent to a conventional XANES spectrum in term of number of features and energy positions [97, 96]. Reference [94] is a review by P. Glatzel and U. Bergmann concerning the 1s core hole X-ray spectroscopy in 3d

transition metal complexes and how it provides electronic and structural information.The basic theoretical and experimental aspects of RIXS are explained, with a particular emphasis on the differences bewteen a HERFD-XAS spectrum (called Constant Emission Energy (CEE) scan in the reference) and a conventional XANES spectrum.

Resonant Inelastic X-ray Scattering is a two-step process separated into a resonant excitation to an intermediate state and a subsequent decay into a final state. Fig. 4.2 illustrates what happens in the pre-edge region. First a photoelectron is ejected from the 1s shell to a 3d empty one and then the 1s core-hole is filled with a (2,3)p electron. In RIXS, the intermediate state is the final state of XANES, and the one-step transition from the ground state to the final state corresponds to the soft X-ray absorption spectroscopy ($L_{2,3}$, $M_{4,5}$ edges). The Kα fluorescence lines result from this 2p→1s transitions and the Kβ main lines from the 3p→1s ones (Fig. 1.17 left). The Kα lines are the most intense lines whereas the Kβ main ones are approximately eight times weaker (Fig. 1.17 right).

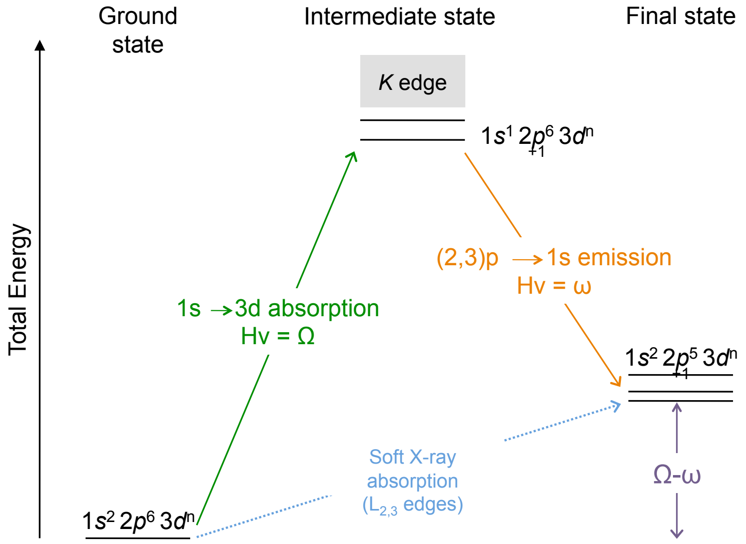

Figure 1.16: RIXS energy scheme for 1s(2,3)p RIXS in a 3d transition metal. The vertical axis describes the total energy of the electron configuration. For simplicity, only 1s→3d excitations are shown.

In RIXS spectroscopy, both incident energy Ω and emission energy ω are varied. A second energy axis, the transfer energy (Ω-ω) or the emission energy (ω) is added to that of the incident photon. These three energies (incident, emission and transfer) are illustrated in Fig. 4.2. The recorded intensity is thus plotted in a two-dimensional grid. Single line scans can be done in one direction of the RIXS plane, providing information on the different states reached during the RIXS process. For instance, a vertical scan in the (Ω,Ω-ω) RIXS plane means that a $1s^1 3d^{n+1}$ intermediate state (or Ω) is kept fixed while the final states (or Ω-ω) are varied. Such a scan shows all the final states that are reached via one particular resonance.

Line plots can also be obtained by integrating the intensity in the RIXS plane along the incident or transfer energy. If we integrate over the transfer energy and plot the resulting line as a function of the incident energy, the resulting spectrum is called a constant energy transfer (CET) spectrum. It is identical to a regular K-edge XANES spectrum if the integrated range extends over all final state energies. If the integration of the intensity is done over the incident energy and the resulting line plot as a function of the transfer energy, the resulting spectrum is

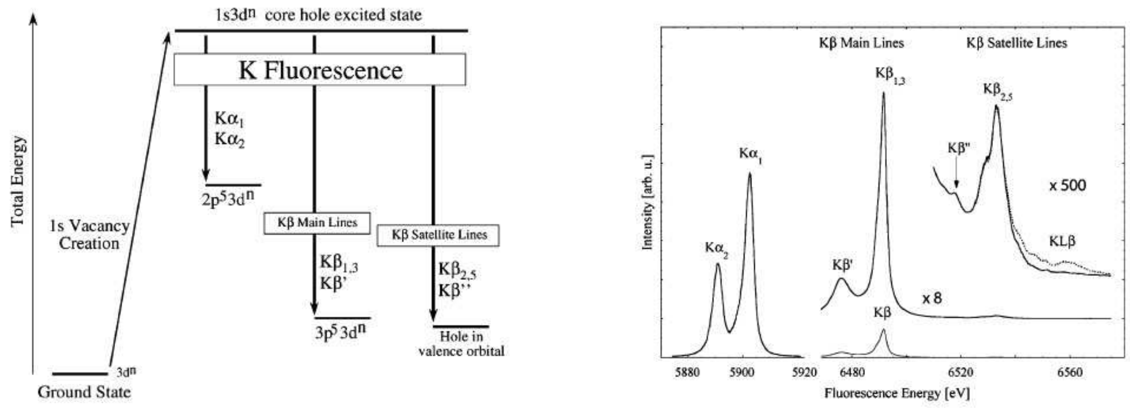

Figure 1.17: Simplified energy scheme for K fluorescence emission (left) and K emission lines in MnO. Both figures are from [94].

called a constant incident energy (CIE) spectrum. A CIE plot in the $1s2p$ ($1s3p$) is formed by the same final state configuration as an $L_{2,3}$-edges ($M_{4,5}$-edges) absorption spectrum.

But for these studies, the most useful cut of the (Ω,Ω-ω) RIXS plane is along the diagonal. A cut along the diagonal corresponds indeed to a constant emission energy (CEE) scan. That means that a diagonal cut corresponds to recording the intensity at a constant emission energy (ω) while scanning the incident energy, which is identical to a HERFD-XAS spectrum. If the structures on the RIXS plane are only on the diagonal, with no broadening in the vertical and/or horizontal direction, all the structures that would be present on a conventional XANES spectrum are also present on the HERFD-XAS spectrum (or the CEE scan). However, if some off-diagonal structures are present in the RIXS plane, the HERFD-XAS spectrum will be significanty different from a conventional XANES spectrum [68].

Recording a RIXS plane in addition to the HERFD-XAS spectra provides thus useful information on the reliability of the HERFD spectrum compared to the conventional XANES one. However, even if a number of decay channels, *e.g.* Kβ lines are neglected in the Kα HERFD-XAS measurements, it is reasonable to assume that the resulting spectrum deviates only slightly from a conventional XANES spectrum by weakly different relative intensity as the Kα fluorescence lines represent nearly 90% of the total fluorescence emission (Fig. 1.17 right) [94]. A comparison between HERFD-XAS and conventional XAS spectra was done in detail for tsavorite, and is presented in Chap. 3.

1.3.4 Angular dependence of the XAS measurements

In a K-edge XANES spectrum, electric dipole ($1s \rightarrow p$) transitions contribute mainly to the edge. The associated electric dipole cross-section is a function of the polarization $\hat{\boldsymbol{\epsilon}}$ of the incident beam. The pre-edge consists of contributions from both electric dipole and quadrupole ($1s \rightarrow 3d$) transitions, depending on the local symmetry. The electric quadrupole cross-section is a function of both the polarization $\hat{\boldsymbol{\varepsilon}}$ and direction $\hat{\boldsymbol{k}}$ of the incident X-ray beam.

Both electric dipole and quadrupole cross-sections are thus expressed as functions of the incident X-ray beam. An angular dependence of the spectrum, *i.e.* changes in the spectrum features, is expected when the orientation of the sample with respect to the incident beam varies. This angular dependence of the XANES spectrum depends on the point group of the investigated crystal and its description for each point group is done in [24]. For instance, the electric dipole absorption cross-section is isotropic for a cubic crystal but anisotropic for the other class of crystals. Moreover, the angular dependence of the electric dipole and quadrupole cross-sections are different. In the case of a cubic crystal, the electric dipole cross-section is isotropic but the electric quadrupole one is not. This different behaviour is due to the dependence on both $\hat{\varepsilon}$ and $\hat{\boldsymbol{k}}$ of the electric quadrupole cross-section, whereas the electric dipole one depends only on $\hat{\varepsilon}$. This angular dependence effect is observed most of the time in the case of single-crystals, but it has also been measured on textured powder samples [162].

On the one hand the angular dependence of the XANES spectrum is an interesting tool to study the electronic structure of an atom. It allows us for instance to differentiate the electric dipole and quadrupole contributions in the pre-edge, as they have a different angular dependence with respect to the incident beam. But on the other hand, if a careful attention is not given to it, the angular dependence can lead to a wrong interpretation of the spectral features when the fingerprint method is used to analyze the spectra. The angular dependence can indeed be an important effect.

Angular dependence measurements were performed in the case of tsavorite. I present here two configurations (Fig. 1.18) of the sample with respect to the incident beam just to illustrate the angular dependence measurements. The details will be given in Chap. 3. To perform reliable angular dependence measurements, it is necessary to study a single-crystal orientated by the Laue method. The preparation of the tsavorite single-crystal was done by Michelle Jacquet and Mélanie Escudier at the "Atelier d'optique cristalline" of the University Pierre et Marie Curie (Paris, France).

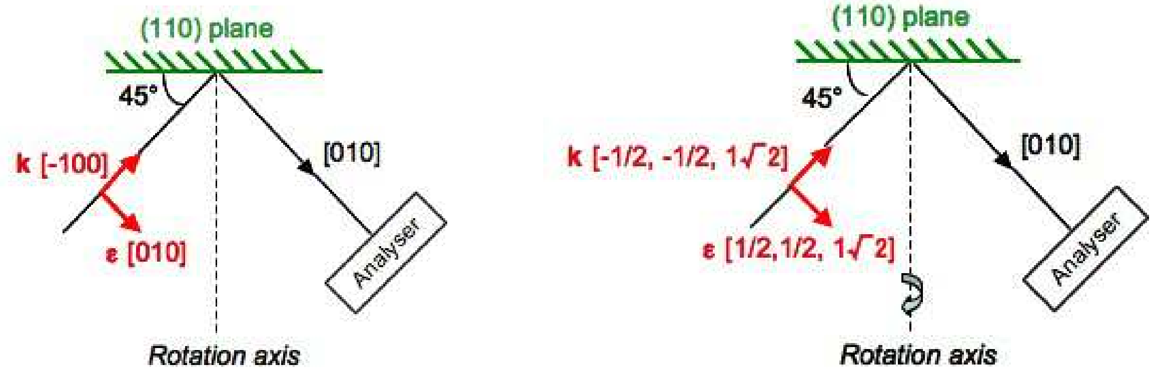

Figure 1.18: Two experimental configurations of a tsavorite single-crystal and of the incident X-ray beam. The sample was rotated by 90° between the two configurations. These two orientations were measured in the study of the angular dependence of the pre-edge of tsavorite.

Chapter 2

Theoretical methods

In this chapter, I present the theoretical tools I used during my thesis. The first section presents the monoelectronic approach, based on the Density Functional Theory (DFT). A reciprocal space method was used to determine, by a energy minimization calculation, a structural model of a mineral with a substituted impurity. From this structural model, the XANES spectrum, including the pre-edge, was computed. The calculations allowed the validation of the theoretical structural models and provided information on the electronic and crystallographic structures around the absorbing atom. This approach was used to study two minerals: tsavorite $Ca_3Al_2(SiO_4)_3$:V^{3+}, with calculations at the V K-edge, and anatase TiO_2, with calculations at both V and Ti K-edges. Calculations were also performed with a direct space method to investigate the V K pre-edge in magnetite Fe_3O_4. Then, the second section presents the multielectronic approach, based on the Ligand Field Multiplet (LFM) theory, used to perform a complementary study of the V K pre-edge in tsavorite. This method provides information on the crystal field and on the electronic interactions. In both cases (the monoelectronic and multielectronic approaches) the angular dependence of the pre-edge of tsavorite, *i.e.* its modifications when the direction and the polarization of the incident X-ray beam vary, was investigated. In the third section, general theoretical developments using spherical tensors are presented. They were done to link the spectroscopic properties of a single crystallographic site and those of the crystal, which may be different. These theoretical developments were published in *Journal of Physics: Condensed Matter* [25]. Finally, an application of these three methods (the monoelectronic approach, the multielectronic one and the spherical tensor analysis) is presented with a study on the Cr K pre-edge in spinel $MgAl_2O_4$, the results of which were published in *Physical Review B* [122]. The results for V in tsavorite, V in magnetite, and V and Ti in anatase will be presented respectively in Chap. 3, 4 and 5.

2.1 Monoelectronic approach

2.1.1 Density Functional Theory

Density Functional Theory (DFT) is an exact theory that allows the determination of the ground state of a system with N electrons. The determination of its electronic properties comes down theoretically to calculate the wave-function $\psi(\boldsymbol{r_1}, ..., \boldsymbol{r_N})$ solution of the Schrödinger equation: $H\psi = E\psi$ and where $\boldsymbol{r_i}$ represents the position of each electron i. H is the Hamiltonian of the system constituted by interacting electrons in an external potential V_{ext}, while the nuclei are considered to be fixed. DFT is indeed developed within the Born-Oppenheimer approximation, which assumes that the nuclear movement can be decoupled from the electronic one because of the difference between their respective masses. The Hamiltonian H is a sum of three contributions : a kinetic energy term, T, the interaction potential between electrons, V_{ee}, and external potential V_{ext} which results from the Coulomb interactions between the electrons and the nuclei. Because of the V_{ee} term, the resolution of the Schrödinger equation becomes quickly complicated. DFT is an alternative to this problem.

DFT is based on the two theorems of Hohenberg and Kohn [109] which concern a generic system of N interacting electrons in an external potential $V_{ext}(\boldsymbol{r})$ and with a non-degenerate ground state. In such a situation, the total electronic density of the system in the ground state, $\rho(\boldsymbol{r})$, unequivocally determines the external potential $V_{ext}(\boldsymbol{r})$ and becomes the basic variable. Hence the total energy of the system is a density functional. Its minimal value is obtained for the electronic density of the ground state and thus gives the total energy of the system in its ground state. The Hohenberg and Kohn theorems were expressed for non spin-polarized systems but their extension to polarized systems is immediate: the total energy of the system and the ground state properties become functionals of each spin (up and down) densities.

Using the Hohenberg and Kohn theorems, Kohn and Sham had the idea to consider a system of N independent electrons whose ground state is the Slater determinant formed by the N monoelectronic orbitals ψ_i. The electronic density of this system is identical to the one of the interacting electrons system [131]. If we apply the variational principle to these orbitals ψ_i, we get the Kohn-Sham equations:

$$\left(\frac{\hbar^2}{2m}\Delta + V_{\text{eff}}\right)\psi_i = \epsilon_i\psi_i. \tag{2.1}$$

$V_{\text{eff}}(\boldsymbol{r})$ is the Kohn-Sham potential, also called effective potential. It contains the external potential, the interelectronic repulsion and an exchange-correlation term, $V_{xc}(\boldsymbol{r})$. In the DFT-based codes dedicated to electronic structure calculations, the minimization of the total energy of the system is performed by resolving self-consistently the Kohn-Sham equations. They are Schrödinger-type equations with monoelectronic orbitals as solutions.

DFT is an exact theory as far as the density which minimizes the total energy is also the density of the N interacting electrons system [101]. Nevertheless the exact expression of the exchange-correlation potential $V_{xc}(\boldsymbol{r})$ is not known. The local density approximation (LDA) or the general gradient approximation (GGA) permits the transformation of the DFT from an abstract exact theory to an approximate practical one.

2.1.2 Absorption cross-section, the PAW method and the recursive method of Haydock, Heine and Kelly

In a DFT-based approach, the X-ray absorption cross-section is expressed as:

$$\sigma(\hbar\omega) = 4\pi^2\alpha\hbar\omega\sum_{i,f}|\langle\psi_f|\hat{O}|\psi_i\rangle|^2\delta(E_f - E_i - \hbar\omega), \tag{2.2}$$

where α is the fine structure constant ($\alpha = \frac{e^2}{4\pi\epsilon_0\hbar c}$(S.I. units) and $\alpha \simeq \frac{1}{137}$), $\hbar\omega$ the energy of the incident photons and $\hat{O}$ a transition operator coupling the initial state $|\psi_i\rangle$ of energy E_i and the final states $|\psi_f\rangle$ of energy E_f. The Dirac function $\delta(E_f - E_i - \hbar\omega)$ ensures the conservation of the energy. The monoelectronic wave functions $\psi_i(\boldsymbol{r})$ and $\psi_f(\boldsymbol{r})$ are orbitals solution of the Kohn-Sham equations. In the case of K edges, the $\psi_i(\boldsymbol{r})$ determination does not pose problems because it is a core orbital and it can be calculated by considering an isolated (neutral) absorbing atom. The $\psi_f(\boldsymbol{r})$ wave functions are obtained through the self-consistent resolution of the Kohn-Sham equations for a system of atoms with a core hole on the absorbing atom.

In X-ray absorption spectroscopy, the transition operator is described in two different approximations. In the electric dipole approximation($\Delta\ell = \pm 1$), the transition operator only depends on the polarization of the incident beam $\hat{\boldsymbol{\varepsilon}}$ and is expressed as :

$$\hat{O}_{dip} = \hat{\boldsymbol{\varepsilon}} \cdot \boldsymbol{r} \tag{2.3}$$

The second approximation corresponds to the electric quadrupole approximation ($\Delta\ell = \pm 2$ or 0, except if the ground state is a s one). In this approximation, the transition operator depends on the polarization $\hat{\boldsymbol{\varepsilon}}$ and direction $\hat{\mathbf{k}}$ of the incident beam. The electric quadrupole transition operator is therfore:

$$\hat{O}_{quad} = \frac{i}{2}(\hat{\boldsymbol{\varepsilon}} \cdot \boldsymbol{r})(\hat{\boldsymbol{k}} \cdot \boldsymbol{r}) \tag{2.4}$$

The transition operators in these two approximations are derived from the general expression of the Hamiltonian describing the matter-radiation interaction. The derivation is given in details in Ref. [24].

The Kohn-Sham orbitals must be developed on a specific basis. The codes I used develop the orbitals on a plane-wave basis which forms a complete and simple basis. So theoretically, an arbitrary precision can be obtained by increasing the number of plane-waves in the basis and the calculation convergence can be controlled by varying the plane-waves *cutoff* energy. Even so, plane-waves are badly adapted to the direct resolution of the Kohn-Sham equations because the potential, and consequently the wave-functions, rapidly vary near the atomic nuclei. An important number of plane-waves is therefore necessary to well describe these wave functions.

Pseudopotentials allow this problem to be circumvented. The first idea of pseudopotentials is to separate the electrons into core and valence electrons. The valence electrons belong to external shells which play a part in the chemical bond. The core electrons are in the internal shells, close to the nucleus and therefore are not very sensitive to the chemical environment around the atom. They are considered as frozen and so the pseudopotentials are defined in the frozen-core approximation. The rigid ion then consists of a nucleus and core electrons and it interacts with valence electrons. The second idea of pseudopotentials is to build valence electron potentials in such a way that the associated pseudowave functions vary as little as possible near the core. The pseudopotentials thus distinguish the pseudowave function and the *all electron* wave function, which is the wave function of the true potential without using the frozen-core approximation. The pseudopotential characteristics are:

- The Hamiltonian eigenvalues built from pseudopotentials must be identical to the *all electron* Hamiltonian eigenvalues (for the valence states energies).
- Outside the core region, pseudo and *all electron* wave functions coincide. The size of the core region is delimited by the core radii, r_{cut}.

Fig. 2.1 illustrates the differences between the pseudo and *all electron* wave functions with the example of the vanadium. The *all electron* wave function has no more nodes in the core region once it has been transformed in pseudowave function. Above r_{cut}, the two wave functions coincide.

But at first sight, pseudopotentials may pose problems for XANES spectra calculations. The initial state $|\psi_i\rangle$, contributing to the matrix element $\langle\psi_f|\hat{O}|\psi_i\rangle$, is a core wave function which rapidly vanishes far from the nucleus. Hence this wave function is non-zero where the

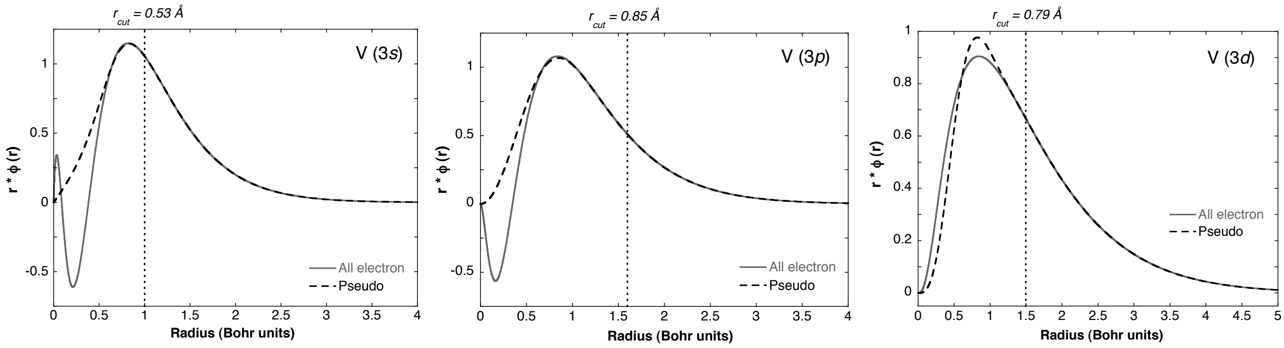

Figure 2.1: The pseudo and *all electron* wave functions in the example of the vanadium.

pseudopotential approximation is done. Before the calculation of the matrix elements, the final state *all electron* wave function has to be reconstructed from the pseudowave function. The Projector Augmented Wave (PAW) method [20] allows this reconstruction by applying a linear operator to the pseudo wave function. It acts inside spherical core regions centered on each atomic site. The absorption cross-section can then be expressed as a function of pseudowave function for the final state $|\widetilde{\psi}_f\rangle$ and a function resulting from the reconstruction [31, 85, 200].

Nevertheless, the calculation of the XANES spectrum requires the determination of many empty states pseudo wave-funtion, which limits the size of the supercell used to describe the structure in the calculation. The recursive method of Haydock, Heine and Kelly [105, 106] uses the Green formalism to rewrite the absorption cross-section $\sigma(\hbar\omega)$ as a continued fraction, so that only the occupied bands have to be calculated. This requires the construction of a Lanczos basis where the pseudo Hamiltonian has a tridiagonal symmetric representation. The continued fraction is then expressed as a function of diagonal and subdiagonal terms of the Hamiltonian matrix in the Lanczos basis.

The formalism of the PAW method and of the recursive method of Haydock, Heine and Kelly are detailed in references [31, 85, 200].

2.1.3 Practical details about the pseudopotentials and the used codes

Two computation codes were used to calculate the XANES spectra : PARATEC (PARAllel Total Energy Code) [163] and the packages PWscf [12] and Xspectra [99] of the Quantum-Espresso suite of codes [92]. They are both total energy codes, the wave functions are developed on a plane waves basis and they use pseudopotentials. The calculations are done in the reciprocal space and use periodic boundary conditions, which are particularly adapted to the study of crystalline structures thanks to the Bloch theorem. The Kohn-Sham equations are solved through a loop over all the $\boldsymbol{k}$ points of the first Brillouin zone. The derivation of the electric dipole and quadrupole X-ray absorption cross-sections as a continued fraction is implemented in both of them. The calculations of tsavorite were performed in the LSDA approximation and V-doped anatase in the spin-polarized GGA approximation in the Perdew-Burke-Ernzerhof (PBE) formulation [160].

Norm-conserving pseudopotentials, *i.e.* they conserve the electronic density norm inside the core region, were used. They are Troullier-Martins pseudopotentials [208] in the Kleinman-Bylander form [128]. The parameters for the pseudopotentials generation are given in Table 2.1. They are identical in both LDA and GGA approximation.

Element	V	Ca	Al	Si	O	Ti
Valence state	$3s$ (0.53) $3p$ (0.85) $3d$ (0.79)	$3s$ (0.77) $3p$ (1.06) $3d$ (0.77)	$3s$ (1.06) $3p$ (1.06) $3d$ (1.06)	$3s$ (1.06) $3p$ (1.06) $3d$ (1.06)	$2s$ (0.77) $2p$ (0.77)	$3s$ (0.53) $3p$ (0.85) $3d$ (0.79)
Elec. config.	$3s^2\ 3p^6\ 3d^2$	$3s^2\ 3p^6\ 3d^0$	$3s^3\ 3p^0\ 3d^0$	$3s^2\ 3p^{1.3}\ 3d^{0.2}$	$2s^2\ 2p^3$	$3s^2\ 3p^6\ 3d^0$
Local part	s	d	d	d	p	s

Table 2.1: Parameters used for the generation of the pseudopotentials. The core radii (r_{cut} of the valence state are indicated between parentheses in Å.

2.1.4 Calculation steps

The monoelectronic calculations I performed during my thesis comprise of two main steps. First a structural model is determined by a minimization energy calculation. This step was performed with the PARATEC code. The next step, which is done in two steps, corresponds to the X-ray absorption spectrum itself and was done with the Quantum-Espresso code.

Structural relaxation

First of all, a structural relaxation of the system with the impurity is performed. The determination of the crystallographic environment around the impurity is essential so that a theoretical reliable structural model is known. Only the case of impurities is described here but it can be applied to any material under investigation.

The structural relaxation is done through an energy minimization calculation. The system, defined by the impurity in the host structure, relaxes towards its ground state by minimizing the total energy of the system and the interatomic forces. In a first time, a supercell is defined from the unit cell of the host structure without the impurity: its dimensions are, for instance, doubled or tripled in one or several space directions so the supercell contains at least one hundred atoms. One impurity atom is then substituted in the supercell, which must be large enough to isolate the impurity when the periodic boundary conditions are applied. The (fictional) interactions between impurities belonging to neighbouring cells must indeed be negligible. Moreover, the supercell composition, and especially the quantity of impurities, should be realistic with respect to the sample which was used to perform experiments. For instance, in the case of tsavorite, the V/Al ratio is 0.067 in the supercell and 0.036 in the sample. This difference may appear important but convergence difficulties due to the size of the cell (160 atoms in the case of tsavorite) prevented us to increase the size of the supercell. Table 2.2 summarizes the composition and the size of the supercells used in the calculation of tsavorite and TiO_2:V^{4+}. Before relaxing, the impurity is slightly moved from its site so that no constraint forces it to stay in its high-symmetrical position. All the atomic positions are allowed to vary while the lattice parameters are kept fixed to the experimental host-structure values.

Nevertheless, the Vegard law holds that a linear relation exists between the crystal lattice parameters of a mineral and the concentration of the constitutive elements. For instance, the cell parameters of hematite Fe_2O_3 and goethite FeOOH decrease when Al atoms are substituted for Fe atoms [183, 185]. Hence a variation of the lattice parameters of the experimental structure, a_{exp}, could be expected. Another possibility to determine the structural model is thus to allow both the atomic positions and the lattice parameters to vary. A calculated value of the lattice parameter, a_{calc}, is determined during the relaxation process. This approach was adopted by A.

Mineral	Supercell	Number of atoms	Composition
$Ca_3Al_2Si_3O_{12}$:V^{3+}	Cubic 1×1×1	160	1 V, 15 Al, 24 Ca, 24 Si, 96 O
TiO_2:V^{4+}	Tetragonal 1×1×3	108	1 V, 35 Ti, 72 O

Table 2.2: Size and composition of the substituted supercells used to perform calculations.

Juhin for the calculations of Cr-bearing spinel $MgAl_2O_4$:Cr^{3+} [121]. To evaluate the influence of the lattice parameters variations, she also relaxed the experimental structure with the lattice parameter kept fixed, as I did. She compared a_{calc} to a_{exp} , and the interatomic distances determined by the two relaxation approaches. She observed that a_{calc} was smaller by 1.6 %, as were the interatomic distances in the relaxed calculated structure. However, after increasing the a_{calc} and the interatomic distances by 1.6 %, the difference between the interatomic distances is smaller than 0.001Å and the one between the angles than 0.01°. She then computed the XANES spectrum for the relaxed calculated and experimental structures. She observed that the differences between the two spectra relate to a small shift ($\sim$ 1 eV) of the structures at high energy. The comparison between the theoretical spectra and the experimental one showed that the agreement is better for the relaxed structure obtained with a_{exp}, *i.e.* when the relaxation process is performed with the lattice parameters kept fixed. Therefore, the relaxation of the cell parameter is not crucial to get a reliable structural model. The relaxation approach I used allows a good determination of a structural model and of the XANES spectrum.

The determination of the relaxed structure is considered to be converged if the three following operations do not change the interatomic distances and the total energy of the system:

- the increase of the supercell size
- the increase of the *cutoff* energy
- the increase of the number of $\boldsymbol{k}$ points used in the Brillouin zone integration.

The Kohn-Sham wave functions are developed in a plane wave basis that has a kinetic energy lower than the *cutoff*. The $\boldsymbol{k}$ points are chosen on a grid according to the Monkhorst-Pack scheme [153]. In the relaxation process, the calculation were done at the Γ point.

XANES spectrum computation

The second step consists of computing the charge density of the relaxed supercell with a 1*s* core hole on the absorbing atom. The Kohn-Sham equations are self-consistently resolved for this supercell with a 1*s* hole. If the calculation is performed in the LDA approximation, the Xspectra code uses the Ceperley-Alder formulation [58], and the Perdew-Burke-Ernzerhof one [160] in the case of the GGA approximation. The spin polarization can be taken into account. There are two important convergence parameters in this step: the *cutoff* energy and the number of $\boldsymbol{k}$ points used in the Brillouin zone integration. The Kohn-Sham wave functions are developed in a plane wave basis that has a kinetic energy lower than the *cutoff*. The $\boldsymbol{k}$ points are chosen on a grid according to the Monkhorst-Pack scheme [153].

The calculation of the absorption cross-section in the electric dipole and quadrupole approximation is the last step. The calculation is considered as converged if the following operations have no effect on the spectra:

- Addition of plane waves in the basis (through the increase of the *cutoff* energy)

- Addition of $\boldsymbol{k}$ points in the Brillouin zone
- Addition of vectors in the Lanczos basis (the number of vectors is self-consistently determined in the code).

The continued fraction method requires a broadening parameter γ, which conditioned the required number of Lanczos vectors (typically, $\sim$ 2000 Lanczos vectors correspond to a broadening factor of $\sim$ 0.5 eV). It is equivalent to a convolution by a Lorentzian $L(E) = \frac{\gamma}{\pi(\gamma^2+(E-E_0)^2)}$, with a full-width at half-maximum Γ=2γ. The broadening parameter Γ can be chosen as a constant which corresponds to the 1s core hole lifetime [134]. In order to account for the different photoelectrons damping-modes, due to the different mean-free path with the incident energy [182], we can use a linear variation of γ with the energy. At low energy (approximately up to the edge energy), the mean-free path of the photoelectron is only limited by the core hole lifetime. Therefore γ is set to a constant equal to half the core hole lifetime. At higher energy, the photoelectron kinetic energy is high enough to interact with the electron gas of the system and the mean-free path is attenuated, provoking a sharp decrease in the lifetime behaviour. A rapid linear variation of γ near the edge (during about 15 eV) followed by a constant value is chosen.

The chosen convergence and convolution parameters will be given for each application.

2.1.5 Calculations methods in the direct space

To better understand the variations in the V K pre-edge in titanomagnetite samples (Chap. 5), I spent one week at the Neel Institut (Grenoble, France) to perform with Yves Joly some calculations at the V K-edge in magnetite with its FDMNES code (Finite Difference Method for Near-Edge Structure) [118]. As it is only a complementary part of the study on the Bushveld Complex and a study still under progress, I only give here the main features of the code I used and its formalism. I did not use the previously described codes (PARATEC and Quantum-Espresso) because reproducing the magnetic structure of magnetite is too challenging for band-structure codes and requires too much computation time. The FDMNES code is developed for the XANES and Diffraction Anomalous Fine Structure (DAFS) spectra calculations. An important point of the FDMNES code is that calculations are performed in the real space and so it uses a cluster approach, on the contrary to two former codes that perform the calculations in the reciprocal space. Two methods are developed in the code to solve the Schrödinger equation: the multiple-scattering theory and the finite difference method [117]. They are both *ab initio* methods based on DFT in the LDA approximation. Details concerning these two methods and their applications with the FDMNES code can be found in references [118] and [119].

Multiple-scattering theory

The multiple scattering theory (MST) can be introduced by two ways: the scattered wave method and the Green function method. In the scattered wave method, the final state of the wave function is computed as the sum of two parts: an outgoing wave plus a scattered wave. This approach of MST is described in reference [181]. A detailed description of the Green function formalism can be found in reference [30], but I mention here the main characteristics as this approach is the one used in FDMNES for the multiple scattering calculations. The Green function method is more straightforward than the scattered wave method but partially relies on the knowledge of the resolvant of a linear equation. The essential point of this approach is that the imaginary part of the Green function is related to the density of state $\delta(H - E_i - \hbar\omega)$

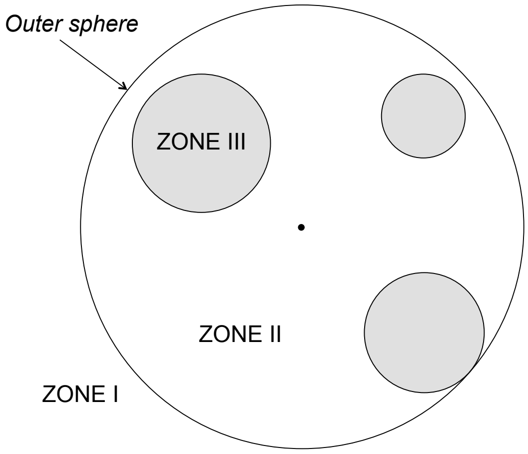

Figure 2.2: Definition of the various zones in a *muffin-tin* potential.

present in the absorption cross-section formulation. The Schrödinger equation is rewritten in its integral form (Lippmann-Schwinger equation) with Green functions and is then resolved in the *muffin-tin* approximation, which is a particular geometrical form of the potential of the system of atoms (here a cluster). In this approximation, the potential is divided into three regions (Fig. 2.2):

- The outer region (zone I): it is situated outside the "outer sphere", that is the smallest sphere containing all the atomic spheres. The potential in this region is usually spherical and tends toward zero at infinity.
- The interstitial region (zone II): it is inside the outer sphere and outside the atomic sphere. The interstitial potential is constant in this zone.
- The atomic sphere (zone III): the atomic potentials are spherical potentials delimited by finite atomic spheres. There is only one atom in each atomic sphere and it is at the center of the sphere. There is no overlap between the atomic spheres. The radii of the atomic sphere are called the *muffin-tin* radii.

A drawback of *muffin-tin* potentials is a discontinuity at the border of the atomic spheres due to the constant interstitial potential in the interstitial region. This is why large *muffin-tin* spheres or an overlap factor between them are often used, in order to reduce the volume of the interstitial zone where the potential is not really well described. The discontinuities at the limit of the atomic spheres in the *muffin-tin* approximation is well shown on Fig. 2.3 (left).

There are two important parameters in a multiple-scattering calculation:

- The size of the system, which is a convergence parameter : a system with a finite number of atoms, the absorbing atom being at its center, must be defined because the computational resources are limited.
- The *muffin-tin* radius of the atomic spheres, which is an adjustable parameter: it is related to the potential and must be defined with care.

As for the reciprocal space calculations described previously, the calculation is converged when changing these parameters does not change the XANES spectrum.

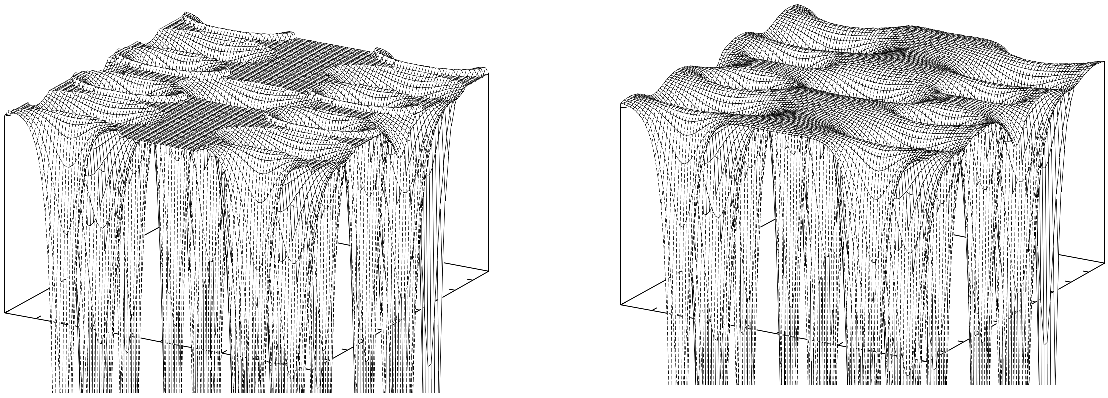

Figure 2.3: Comparison of a *muffin-tin* potential (left) and the corresponding full one (right) for the (110) plane of the TiO_2-rutile structure.

Finite Difference Method

The finite difference method was developed by Y. Joly to go beyond the *muffin-tin* approximation. This method solves the Schrödinger in a spherical volume centered on the absorbing atom and extended over a sufficiently large cluster. The volume is divided in three zones:

- The external zone surrounding the atoms cluster (similar to zone I of the *muffin-tin* potential), with a constant potential.
- The interstitial zone
- The atomic zone: it is constituted by very small atomic spheres, much smaller than the *muffin-tin* ones. The potential has a spherical symmetry in this zone.

In the interstitial zone, the complex form of the potential is discretized, which defines a meshing of space, and the Schrödinger equation is discretized on the mesh nodes. The finite difference method is indeed a general way to solve differential equations by discretizing them over a grid of points in the whole volume where the calculation is made. The potential is better described here than in the *muffin-tin* approximation because no assumption on the potential geometry is done. The difference between this full potential and a *muffin-tin* one is illustrated in Fig. 2.3 in the case of the (110) plane of the TiO_2-rutile structure. The finite difference method is simpler and more precise than the multiple-scattering theory but really time-consuming. Indeed, the time needed to perform a calculation is related to the meshing: the denser it is, the more precise is the description of the potential and consequently the calculation.

2.2 Multielectronic approach

For systems with important multielectronic interactions, the monoelectronic approach may fail in properly calculating the XAS spectra. The Ligand Field Multiplet (LFM) theory can give better results when the absorption happens toward a localized state. This theory was first applied to calculate the spectra $M_{4,5}$ edges of rare-earth elements ($3d \rightarrow 4f$ absorption) [98] and $L_{2,3}$ edges of transition metal elements ($2p \rightarrow 3d$ absorption) [8, 67]. Afterwards the LFM theory has been successfully applied to K pre-edge of $3d$ transition elements ($1s \rightarrow 3d$ absorption) [9, 85, 219]. In this section, I recall the general principles of the LFM theory and the absorption cross-section calculation in the case of a $3d$ elements, with a presentation of the calculations steps. The calculations were performed using the method developed by Thole [203] in the framework established by Cowan [64] and Butler [29]. During this thesis, multiplet calculations were performed only in the case of the K pre-edge of vanadium in tsavorite.

2.2.1 Principle

Characteristics of the LFM method and absorption cross-section

The first characteristic of the LFM approach is that it uses multielectronic wave functions: the absorption cross-section is calculated for the ion with its N electrons. The absorbing atom is indeed considered with all its electrons in both the initial and final states. As an example, concerning the electric quadrupole transitions for the K pre-edge of V^{3+}, the electronic configurations used in the calculations are $1s^2 2s^2 2p^6 3s^2 3p^6 3d^2$ and $1s^1 2s^2 2p^6 3s^2 3p^6 3d^3$ for the initial and final states, respectively. All the interelectronic interactions are considered in the initial state and the final state, as well as the interaction with the core-hole. The full shells ($2s^2 2p^6 3s^2 3p^6$) contribute only to the average energy of the ion.

Its second characteristic is that the absorbing atom is considered as an isolated ion embedded in a crystal-field potential. The structural parameters used in the multielectronic approach are the ligand field and the local point group and no more the complete crystal structure as in the monoelectronic calculations. The calculation for only the absorbing atom site can be done in the case of edges with localized orbitals, as the $3d$ orbitals. The $1s \rightarrow p$ transitions involved in the K-edges can not be computed in the LFM approach because the p orbitals are delocalized and consequently the structure at a longer range is needed.

Finally this approach is semi-empirical: some parameters of the calculated spectrum need to be fitted to the experimental ones. These parameters are the crystal field potential, the distortion of the site and its intensity, the spin-orbit coupling and the scaling factor of the Slater integrals (related to the B and C Racah parameters). Therefore it is possible to extract quantitative information from the LFM calculations through these fitted parameters. Most of them can be derived from optical absorption spectroscopy, which allows their LFM values to be validated.

The absorption cross-section is almost identical to the one for the monoelectronic approach:

$$\sigma(\hbar\omega) = 4\pi^2\alpha\hbar\omega \sum_{i,f} \frac{1}{d_i} |\langle f|\hat{O}|i\rangle|^2 \delta(E_f - E_i - \hbar\omega). \tag{2.5}$$

The additional term is $\frac{1}{d_i}$, where d_i is the degeneracy of the ground state. In monoelectronic calculations, the ground state is non-degenerate as it is necessary for the Kohn-Sham implementation of DFT and d_i=1. On the contrary, in multielectronic calculations, the multielectronic state is often degenerate so the degeneracy has to be taken into account in the cross-section formula.

The absorption cross-section is calculated as the sum of all possible discrete transitions from the ground state $|i\rangle$ to the final states $|f\rangle$ through the transition operator $\hat{O}$. These transitions occur at the energies $\hbar\omega = E_f - E_i$. The transitions are broadened because of the $1s$ core-hole lifetime and of the instrumental resolution. At T = 0K, only the lowest energy state contributes to the absorption cross-section. At T > 0K, the relative contribution of the different accessible ground states $|i\rangle$ is governed by the Boltzmann law and is taken into account in the multiplet calculation.

As for the monoelectronic calculations, the determination of the absorption cross-section can be performed in both electric dipole and quadrupole approximations. Nevertheless, the LFM theory can not be applied to the main edge calculation since the band structure is not taken into account and so transitions to delocalized states can not be calculated. In other words, the multielectronic approach can be used to calculate the K pre-edge spectra, but the edge region cannot be reproduced.

Calculation of the multielectronic states $|i\rangle$ and $|f\rangle$

To calculate the multielectronic states, the Schrödinger equation is solved for the ion with its N electrons, in its initial configuration and its final one: $H_{ion}\ \psi_{ion} = E_{ion}\ \psi_{ion}$, where H_{ion} is the Hamiltonian of the system in the chosen configuration, E_{ion} its eigenvalue and ψ_{ion} its eigenfunction.

In the abscence of a magnetic field, the Hamiltonian can be written as:

$$H_{ion} = H_{kin} + H_{e-N} + H_{e-e} + H_{SO} + H_{crystal} \tag{2.6}$$

H_{kin} is the kinetic energy of the electrons, H_{e-N} the electrostatic interaction of the electrons with the nucleus, H_{e-e} the electron-electron repulsion, H_{SO} is the spin-orbit coupling interaction and $H_{crystal}$ is the crystal-field Hamiltonian, which takes into account the local environment around the absorbing atom. The Hamiltonian terms are expressed as kth-rank spherical tensors $\mathcal{T}_{\mathrm{q}}^{(\mathrm{k})}$. The initial states are determined by the diagonalization of the matrix constituted by the $\langle\psi'|\mathcal{T}_{\mathrm{q}}^{(\mathrm{k})}|\psi\rangle$ elements, where $|\psi\rangle$ and $|\psi'\rangle$ are basis functions. The initial state is the lowest energy state. The same operations are done to determine the final states.

The adapted $|\psi\rangle$ functions are $|\alpha(L,S)JM_J\rangle$ functions, where $J(J+1)$ is the eigenvalue of the J^2 and M_J the one of the J_z operator. The total moment of the shell, $\mathbf{J}$, is obtained by coupling $\mathbf{L}$ and $\mathbf{S}$ ($\mathbf{J}$=$\mathbf{L}$+$\mathbf{S}$). Their associated quantum numbers, respectively J, L and M are defined by the relation $|\mathrm{L}-\mathrm{S}| \leq \mathrm{J} \leq \mathrm{L}+\mathrm{S}$. The total orbital moment of the ion L and its total spin moment S correspond respectively to the coupling of the N electrons individual orbital moments, $\boldsymbol{\ell}_i$, through the operator

$$\mathbf{L} = \sum_{i=1}^{N} \boldsymbol{\ell}_i,$$

and to the N electrons individual spin moments, $\mathbf{s}_i$, through the operators

$$\mathbf{S} = \sum_{i=1}^{N} \mathbf{s}_i.$$

The orbital and spin moment are coupling shell by shell, for all the shells implied in the electronic configuration. The details of the (L,S) coupling is given in Ref. [8]. The operator $\mathbf{J}$ projected on the quantification axis z gives the component J_z characterized by the M quantum number, with $-\mathrm{J} \leq \mathrm{M} \leq \mathrm{J}$. The number α represents all the quantum numbers needed to completely identify the basis functions.

The kinetic energy of the electrons and the Coulomb interaction of the electrons with the nucleus are fixed for a given atomic configuration and they contribute only to the average energy of the configuration. We take advantage of the spherical symmetry of the interelectronic interactions and of the spin-orbit coupling to determine them in the initial and final states. In the case of a spherical symmetry, the matrix elements $\langle\alpha'(L',S')J'M_J'|\mathcal{T}_{\mathrm{q}}^{(\mathrm{k})}|\alpha(L,S)JM_J\rangle$ are evaluated in the irreducible representation of the spherical SO_3 group. The functions $|\alpha(L,S)JM_J\rangle$ and $|\alpha'(L',S')J'M'_J\rangle$ represents two initial (or two final) states and the matrix elements are evaluated with the Wigner-Eckart theorem:

$$\langle\alpha'J'M'|\mathcal{T}^{(\mathrm{k})}_{\mathrm{q}}|\alpha JM\rangle = (-1)^{J'-M'}\begin{pmatrix} J' & \mathrm{k} & J \\ -M' & \mathrm{q} & M \end{pmatrix}\langle\alpha'J'||\mathcal{T}^{(\mathrm{k})}||\alpha J\rangle \tag{2.7}$$

where $\langle\alpha'J'||\mathcal{T}^{(\mathrm{k})}||\alpha J\rangle$ is called reduced matrix element and $\begin{pmatrix} J' & \mathrm{k} & J \\ -M' & \mathrm{q} & M \end{pmatrix}$ is a $3j$ symbol, the values of which are tabulated in Ref. [64]. If the $3j$ symbol is zero, the corresponding matrix element is zero too so that the expression of the Hamiltonian matrix in the chosen basis is simpler and its diagonalization easier. The rank of the tensor is zero for the spherical Hamiltonian and $\mathrm{k}\geq 0$ in the case of the crystal-field Hamiltonian.

Nevertheless, the crystal field Hamiltonian has to be determined in the local symmetry of the absorbing atom, the local point group of which is noted S_{abs}. The functions $|\alpha jm\rangle$ previously chosen, adapted to the SO_3 group, are no more suitable for the new local point group. The functions of the initial and final states must indeed have the same symmetry than the irreducible representations of the S_{abs} group. The subduction theory permits to establish relations between the functions in the SO_3 and S_{abs} groups. It consists of determining a succession of irreducible representations in a suite of subgroups of the spherical group, SO_3, till the local point group of the absorbing atom, S_{abs}. When the suite defines all the functions, the Wigner-Eckart theorem is used in its expression generalized by Butler to finite groups, which depends on the reduced matrix elements [29]. Examples of the use of the subduction theory are given in Sec. 2.2.2 (Step 3) and 2.2.3.

2.2.2 Calculation steps

Four steps are necessary to perform the calculation of the absorption cross-section:

- Step 1: the calculation of the atomic parameters (the average enegy of the initial and final states, the direct F^k and exchange G^k Slater integrals and the spin-orbit coupling ζ_j)
- Step 2: the calculation of the reduced matrix elements (Eq. 2.7) in a spherical symmetry for the initial and final states, respectively denoted $\langle\alpha'_iJ'_i||\mathcal{T}^{(\mathrm{k})}||\alpha_iJ_i\rangle$ and $\langle\alpha'_fJ'_f||\mathcal{T}^{(\mathrm{k})}||\alpha_fJ_f\rangle$, and for the quadrupolar transitions between the initial and final state, denoted $\langle\alpha_fJ_f||\mathcal{T}^{(2)}||\alpha_iJ_i\rangle$ (the electric quadrupole transition operator is expressed as a 2^{nd}-rank tensor),
- Step 3: the calculation of the initial and final states and of the transitions in the symmetry of the absorbing atom site,
- Step 4: the spectrum convolution.

The different steps will be illustrated through the example of the V^{3+} ion in a O_h symmetry and in the case of electric quadrupole transitions $1s \to 3d$. The case of a lower symmetry (C_{3i}) is described in section 2.2.3.

Step 1: Atomic parameters calculation

The V^{3+} atomic orbitals are calculated for the initial and final configurations in an *ab initio* self-consistent and atomic Hartree-Fock model. The electronic configuration in the initial state

$1s^22s^22p^63s^23p^63d^2$, written $1s^23d^2$, and in the final state $1s^12s^22p^63s^23p^63d^3$, written $1s^13d^3$, are used. The first atomic parameters determined in the code are their average energy.

The matrix elements for the electron-electron repulsion can be expressed as the product of the integral over its radial part, corresponding to the f_k and g_k integrals (numerical part), and its angular part, corresponding to the F^k and G^k Slater integrals:

$$\langle \alpha jm|H_{e-e}|\alpha' j' m'\rangle = \sum_{i,j}\sum_{k=0}^{\infty} f_k(\ell_j,\ell_j)F^k(\ell_j,\ell_j)+f_k(\ell_i,\ell_j)F^k(\ell_i,\ell_j)+g_k(\ell_i,\ell_j)G^k(\ell_i,\ell_j). \quad (2.8)$$

The (i,j) index indicate the shells of the ion configuration and ℓ_i and ℓ_j the orbital momentum of each shell. In the case of the purely quadrupolar K pre-edge, ℓ_i corresponds to the $1s$ shell ($\ell_i = 0$) and ℓ_i to the $3d$ one ($\ell_i = 2$). F^k is the direct Slater integral and G^k the exchange Slater integral. The functions f_k and g_k depend on the orbital moment of the empty shells and of the shell filling and they have an analytical value [64]. The product $f_k(\ell_j,\ell_j)F^k(\ell_j,\ell_j)$ represents the direct Coulomb repulsion between electrons from the same shell, $f_k(\ell_i,\ell_j)F^k(\ell_i,\ell_j)$ the direct Coulomb repulsion between electrons from different shells and $g_k(\ell_i,\ell_j)G^k(\ell_i,\ell_j)$ the Coulomb exchange interaction between electrons from different shells.

The calculated values of F^k and G^k are obtained for a free ion in a spherical symmetry. In a solid, the chemical bond delocalizes the electrons and tends to reduce the electronic repulsion. The atomic values of F^k and G^k determined in the Hartree-Fock model are therefore multiplied by a coefficient $\kappa<1$. It is to be noted that the Slater integrals F^k and G^k are calculated by the code and the coefficient κ is an adjustable given parameter. For the initial configuration $1s^23d^2$, the Slater integrals can be expressed with the Racah parameters used in optical absorption spectroscopy [139]. The coefficient κ is equal to $\frac{B}{B_0}=\frac{C}{C_0}$, where B_0 and C_0 are the Racah parameters of the free ion in its initial configuration, defined by: $B_0=\frac{1}{49}F^2(3d,3d)$-$\frac{5}{441}F^4(3d,3d)$ and $C_0=\frac{35}{441}F^4(3d,3d)$. The parameters B and C are those of the ion in the solid and can be obtained from optical spectroscopy [27].

Concerning the spin-orbit coupling, the matrix element of the Hamiltonian can be written as:

$$\langle \alpha jm|H_{SO}|\alpha' j' m'\rangle = \sum_{j=1}^{q} \zeta_j d_j \quad (2.9)$$

where ζ_j is a radial integral and the spin-orbit coupling constant. The term d_j is an angular integral whose value depends mainly on the shell filling and on the orbital moment of the empty shells. When a shell is complete, there is no spin-orbit coupling for this shell.

In the case of electric quadrupole transitions for V^{3+}, the atomic parameters determined by the code are summarized in table 2.3.

Step 2: Calculation of the reduced matrix elements in a spherical symmetry

The reduced matrix elements $\langle \alpha j||\mathcal{T}^{(\mathrm{k})}||\alpha' j'\rangle$ are determined in a spherical symmetry for all the Hamiltonian terms (Eq. 2.6). They then be used to determine the Hamiltonian terms in the symmetry of the absorbing atom site. The notation used hereafter are those determined by Butler (App. A) [29].

The electron-electron repulsion term H_{e-e} and the spin-orbit coupling one H_{SO} (Eq. 2.6) are taken into account through a 0^{th}-rank spherical tensor in the SO_3 group, written $\boldsymbol{T}^{(\mathbf{0})}(SO_3)$ [8]. This tensor is associated to the completely symmetric representation $\mathbf{0}(SO_3)$.

Electronic configuration	$1s^2 3d^2$	$1s^1 3d^3$
E_{av}	0	5475.224
$F^2(3d,3d)$ (eV)	10.127	10.863
$F^4(3d,3d)$ (eV)	6.354	6.809
$G^2(1s,3d)$ (eV)	0	0.045
ζ_{3d} (eV)	0.027	0.036

Table 2.3: Atomic parameters and configuration energies determined by in the Hartree-Fock model. E_{av} is the average energy of the configuration, $F^2(3d,3d)$, $F^4(3d,3d)$ and $G^2(1s,3d)$ the Slater integrals and ζ_{3d} the spin-orbit coupling. The enrgy of the initial configuration was set to zero.

The crystal-field term is determined by an electrostatic potential, the symmetry of which is given by the point group of the atom. The Hamiltonian is developed in a basis of spherical harmonics as:

$$H_{crystal} = \sum_{i=1}^{N} \sum_{k=0}^{\infty} \sum_{q=-k}^{+k} b_{kq}(r_i) C_k^q(\hat{r}_i),$$

where i is the index of the N^{th} electron and $\mathrm{C}_k^q(\hat{r}_i)$= $\sqrt{\frac{4\pi}{2k+1}}\mathrm{Y}_k^q(\hat{r}_i)$ are the renormalized spherical harmonics. The spherical harmonic Y_k^q is the qth component of a k^{th}-rank spherical tensor. The crystal-field Hamiltonian can be rewritten as a sum of k^{th}-rank spherical tensors:

$$H_{crystal} = \sum_{k=0, k \ even}^{2\ell} \sum_{q=-k}^{k} \sum_{j=1}^{n} X_j^{kq} U_{(j)}^{(kq)}. \tag{2.10}$$

The X_j^{kq} terms are the crystal-field parameters (they must be given in the input of the code) and the U_j^{kq} ones are k^{th}-rank irreducible unit-tensors[1] associated to the irreducible representation **k** of the SO_3 group. In the case of the transition elements, the crystal field acts only on the $3d$ states so $\ell = 2$. The U_j^{kq} tensor has thus an even rank as it couples $3d$ states and only the values $k = 0$, 2, 4 are taken into account in the sum. In the case of V^{3+}, the crystal-field parameter is thus taken into account in SO_3 by the sum of a 4^{th}-rank spherical tensor, denoted $U^{(4)}(SO_3)$, and a 2^{th}-rank spherical tensor, denoted $U^{(2)}(SO_3)$. [2]

Step 3: Calculation of the initial and final states, and of the transitions in the site symmetry of the absorbing atom

The eigenstates and eigenenergies of the system in its initial and final states have to be determined in the symmetry of the absorbing atom site, using the reduced matrix elements determined in step 2. These reduced matrix elements were calculated in the chosen symmetry using the subduction theory and the Wigner-Eckart theorem in its expression generalized to finite groups. The Hamiltonian has therefore the symmetry of the local point group, S_{abs}. If the absorbing atom is, for instance, in a O_h-symmetry site, the $O_3 \supset O_h$ subduction is used. To get complete functions, it is necessary to be in a O_h subgroup where all the representations are of dimension 1 (it is not the case for O_h). For instance, the $O_3 \supset O_h \supset D_{4h} \supset C_{4h}$ subduction can be chosen. Then the $|\langle f|\hat{O}|i\rangle|^2$ quantities are evaluated for all the initial eigenstates $|i\rangle$,

---

[1] The definition of the irreducible unit-tensor is given in Ref.[64].

[2] $k = 0$ contributes only to the average energy of the configuration.

filled at the temperature T, and for all the final states $|f\rangle$. The calculation parameters are the crystal-field potentials.

In a O_h symmetry, $H_{e^- - e^-}$ and H_{SO} (Eq. 2.6) are expressed in O_3 as functions of a 0^{th}-rank tensor. The corresponding branching is $\mathbf{0}^+(O_3) \rightarrow \mathbf{0}^+(O_h) \rightarrow \mathbf{0}^+(D_{4h}) \rightarrow \mathbf{0}^+(C_{4h})$. $\mathbf{0}^+$ is the representation of the group of subgroup, the + sign indicating an even parity. They are thus functions of the irreducible tensor $T^{0^+(O_3)0^+(O_h)0^+(D_{4h})0^+(C_{4h})}$, which is associated to the $\mathbf{0}$ representation in all the groups and subgroups of the subduction.

As explained in step 2, in the case of a transition metal ion, the crystal-field acts on the d electrons and the crystal-field parameter is thus taken into account in SO_3 by the sum of a 4^{th}-rank spherical tensor, denoted $U^{(4)}(SO_3)$, and a 2^{th}-rank spherical tensor, denoted $U^{(2)}(SO_3)$. In a O_h symmetry, the crystal-field Hamiltonian has the same symmetry as the site of the absorbing atom and is hence associated to the $\mathbf{0}^+(O_h)$ representation. Therefore, only the branchings of the irreducible representations $\mathbf{2}^+(O_3)$ and $\mathbf{4}^+(O_3)$ which allow to get the $\mathbf{0}^+(O_h)$ representation are taken into account in the calculation. If the $\mathbf{2}^+(O_3)$ representation is considered, its decomposition contains the following branchings (the branching rules are given in chapter 12 of Ref. [29]):

$$\begin{gathered}
\mathbf{2}^+(O_3) \rightarrow \tilde{\mathbf{1}}^+(O_h) \rightarrow \mathbf{1}^+(D_{4h}) \rightarrow \mathbf{1}^+(C_{4h}) \\
\mathbf{2}^+(O_3) \rightarrow \tilde{\mathbf{1}}^+(O_h) \rightarrow \mathbf{1}^+(D_{4h}) \rightarrow -\mathbf{1}^+(C_{4h}) \\
\mathbf{2}^+(O_3) \rightarrow \tilde{\mathbf{1}}^+(O_h) \rightarrow \tilde{\mathbf{2}}^+(D_{4h}) \rightarrow \mathbf{2}^+(C_{4h}) \\
\mathbf{2}^+(O_3) \rightarrow \mathbf{2}^+(O_h) \rightarrow \mathbf{0}^+(D_{4h}) \rightarrow \mathbf{0}^+(C_{4h}) \\
\mathbf{2}^+(O_3) \rightarrow \mathbf{2}^+(O_h) \rightarrow \mathbf{2}^+(D_{4h}) \rightarrow \mathbf{2}^+(C_{4h})
\end{gathered}$$

None of them are retained because there is no $\mathbf{0}^+(O_h)$ representation. If the $\mathbf{4}^+(O_3)$ representation is now considered, the following branchings are possible:

$$\begin{gathered}
\mathbf{4}^+(O_3) \rightarrow \mathbf{0}^+(O_h) \rightarrow \mathbf{0}^+(D_{4h}) \rightarrow \mathbf{0}^+(C_{4h}) \\
\mathbf{4}^+(O_3) \rightarrow \mathbf{1}^+(O_h) \rightarrow \tilde{\mathbf{0}}^+(D_{4h}) \rightarrow \mathbf{0}^-(C_{4h}) \\
\mathbf{4}^+(O_3) \rightarrow \mathbf{1}^+(O_h) \rightarrow \mathbf{1}^+(D_{4h}) \rightarrow \mathbf{1}^+(C_{4h}) \\
\mathbf{4}^+(O_3) \rightarrow \mathbf{1}^+(O_h) \rightarrow \mathbf{1}^+(D_{4h}) \rightarrow -\mathbf{1}^+(C_{4h}) \\
\mathbf{4}^+(O_3) \rightarrow \tilde{\mathbf{1}}^+(O_h) \rightarrow \mathbf{1}^+(D_{4h}) \rightarrow \mathbf{1}^+(C_{4h}) \\
\mathbf{4}^+(O_3) \rightarrow \tilde{\mathbf{1}}^+(O_h) \rightarrow \mathbf{1}^+(D_{4h}) \rightarrow -\mathbf{1}^+(C_{4h}) \\
\mathbf{4}^+(O_3) \rightarrow \tilde{\mathbf{1}}^+(O_h) \rightarrow \tilde{\mathbf{2}}^+(D_{4h}) \rightarrow -\mathbf{2}^+(C_{4h}) \\
\mathbf{4}^+(O_3) \rightarrow \mathbf{2}^+(O_h) \rightarrow \mathbf{0}^+(D_{4h}) \rightarrow \mathbf{0}^+(C_{4h}) \\
\mathbf{4}^+(O_3) \rightarrow \mathbf{2}^+(O_h) \rightarrow \mathbf{2}^+(D_{4h}) \rightarrow \mathbf{2}^+(C_{4h})
\end{gathered}$$

Only the first branching contains the $\mathbf{0}^+(O_h)$ representation and is thus taken into account in the calculations. The crystal-field Hamiltonian in a O_h symmetry is hence expressed as:

$$H_{crystal} = X^{4^+(O_3)0^+(O_h)0^+(D_{4h})0^+(C_{4h})} U^{4^+(O_3)0^+(O_h)0^+(D_{4h})0^+(C_{4h})}. \tag{2.11}$$

For clarity, the + signs and the group are omitted and the crystal-field parameter is denoted X^{4000} (the same notation will be used in the section 2.2.3). The crystal-field parameter X^{4000}

is proportional to $10D_q$, which is usually used in optical absorption spectroscopy[3]:

$$X^{4000} = \frac{18}{\sqrt{30}}\ 10Dq$$

Step 4: Spectrum convolution

The peaks corresponding to the discrete transitions, at the energies $E = \hbar\omega = E_f - E_i$ and with an intensity $|\langle f|\hat{O}|i\rangle|^2$, are convoluted by a Lorentzian and a Gaussian.

The Lorentzian $L(E)$ represents the core-hole lifetime broadening of the final state and is given by:

$$L(E) = \frac{\gamma}{\pi(\gamma^2 + (E - E_0)^2)} \tag{2.12}$$

The full-width at half-maximum is $\Gamma = 2\gamma$ and the parameter in the calculation γ. In the case of the K pre-edge of V^{3+}, the core-hole lifetime of the final state is the one of the $1s$ core-hole: $\gamma = 0.55$ eV [134].

The Gaussian takes into account the instrumental broadening and is expressed as:

$$G(E) = \frac{1}{\sigma\sqrt{2\pi}} e^{-\frac{(E-E_0)^2}{2\sigma^2}} \tag{2.13}$$

The full-width at half-maximum is $2\sigma\sqrt{2\ln 2}$ and the parameter in the calculation $\sigma\sqrt{2\ln 2}$ (σ is the standard deviation). Concerning the experiments on ID26 at the ESRF, σ is calculated from the intrinsic resolution of the monochromator:

$$\frac{\Delta E}{E} = 1,4.10^{-4}$$

At the V K edge ($E = 5465$ eV), we have $\Delta E = 0.76$ eV$= 2\sigma\sqrt{2\ln 2}$ and so $\sigma = 0.38$ eV.

2.2.3 Use of the subduction theory

The case of a C_{3i} symmetry

The subduction in the case of an O_h symmetry was described with the third step of the calculations. However, the site symmetry of V^{3+} in tsavorite is C_{3i} and another subduction has thus to be used. I describe here the use of the subduction theory in the case of a C_{3i} symmetry and for the electric quadrupole transition operator.

For an ion in the C_{3i} symmetry, the subduction $O_3 \supset O_h \supset D_{3d} \supset C_{3i}$ was chosen.

The H_{e-e} and H_{SO} terms (Eq. 2.6) are expressed as a function of the 0^{th}-rank irreducible spherical tensor $T^{0^+(O_3)0^+(O_h)0^+(D_{3d})0^+(C_{3i})}$, which is associated to the **0** representation in all the groups and subgroups of the subduction.

In a C_{3i} symmetry, the Hamiltonian of the crystal field which acts on the d electrons has the same symmetry as the site of the absorbing atom. Hence it is associated to the $\mathbf{0}^+(C_{3i})$ representation. The crystal-field Hamiltonian is expressed in SO_3 by the sum of a 4^{th}-rank spherical tensor, denoted $U^{(4)}(SO_3)$, and a 2^{th}-rank spherical tensor, denoted $U^{(2)}(SO_3)$. Therefore, only the branchings of the irreducible representations $\mathbf{2}^+(O_3)$ and $\mathbf{4}^+(O_3)$ which allow to get the

---

[3] $10D_q$ is the energy splitting of the $3d$ orbitals (t_{2g} and e_g) in the O_h crystal-field potential.

$\mathbf{0}^{+}(C_{3i})$ representation are taken into account in the O_h subgroup. If I consider the $\mathbf{2}^{+}(O_3)$ representation, the following branchings are possible [29]:

$$\begin{aligned}
&\mathbf{2}^{+}(O_3) \rightarrow \tilde{\mathbf{1}}^{+}(O_h) \rightarrow \mathbf{1}^{+}(D_{3d}) \rightarrow \mathbf{1}^{+}(C_{3i})\\
&\mathbf{2}^{+}(O_3) \rightarrow \tilde{\mathbf{1}}^{+}(O_h) \rightarrow \mathbf{1}^{+}(D_{3d}) \rightarrow \mathbf{-1}^{+}(C_{3i})\\
&\mathbf{2}^{+}(O_3) \rightarrow \tilde{\mathbf{1}}^{+}(O_h) \rightarrow \mathbf{0}^{+}(D_{3d}) \rightarrow \mathbf{0}^{+}(C_{3i})\\
&\mathbf{2}^{+}(O_3) \rightarrow \mathbf{2}^{+}(O_h) \rightarrow \mathbf{1}^{+}(D_{3d}) \rightarrow \mathbf{1}^{+}(C_{3i})\\
&\mathbf{2}^{+}(O_3) \rightarrow \mathbf{2}^{+}(O_h) \rightarrow \mathbf{1}^{+}(D_{3d}) \rightarrow \mathbf{-1}^{+}(C_{3i})
\end{aligned}$$

Only the third branching has the $\mathbf{0}$ representation in C_{3i} and is therefore taken into account in the calculation.

If I consider now the $\mathbf{4}^{+}(O_3)$ representation, the following branchings are possible [29]:

$$\begin{aligned}
&\mathbf{4}^{+}(O_3) \rightarrow \mathbf{0}^{+}(O_h) \rightarrow \mathbf{0}^{+}(D_{3d}) \rightarrow \mathbf{0}^{+}(C_{3i})\\
&\mathbf{4}^{+}(O_3) \rightarrow \mathbf{1}^{+}(O_h) \rightarrow \tilde{\mathbf{0}}^{+}(D_{3d}) \rightarrow \mathbf{0}^{-}(C_{3i})\\
&\mathbf{4}^{+}(O_3) \rightarrow \mathbf{1}^{+}(O_h) \rightarrow \mathbf{1}^{+}(D_{3d}) \rightarrow \mathbf{1}^{+}(C_{3i})\\
&\mathbf{4}^{+}(O_3) \rightarrow \mathbf{1}^{+}(O_h) \rightarrow \mathbf{1}^{+}(D_{3d}) \rightarrow \mathbf{-1}^{+}(C_{3i})\\
&\mathbf{4}^{+}(O_3) \rightarrow \tilde{\mathbf{1}}^{+}(O_h) \rightarrow \mathbf{0}^{+}(D_{3d}) \rightarrow \mathbf{0}^{+}(C_{3i})\\
&\mathbf{4}^{+}(O_3) \rightarrow \tilde{\mathbf{1}}^{+}(O_h) \rightarrow \mathbf{1}^{+}(D_{3d}) \rightarrow \mathbf{1}^{+}(C_{3i})\\
&\mathbf{4}^{+}(O_3) \rightarrow \tilde{\mathbf{1}}^{+}(O_h) \rightarrow \mathbf{1}^{+}(D_{3d}) \rightarrow \mathbf{-1}^{+}(C_{3i})\\
&\mathbf{4}^{+}(O_3) \rightarrow \mathbf{2}^{+}(O_h) \rightarrow \mathbf{1}^{+}(D_{3d}) \rightarrow \mathbf{1}^{+}(C_{3i})\\
&\mathbf{4}^{+}(O_3) \rightarrow \mathbf{2}^{+}(O_h) \rightarrow \mathbf{1}^{+}(D_{3d}) \rightarrow \mathbf{-1}^{+}(C_{3i})
\end{aligned}$$

Only the first, second and fifth branchings have the $\mathbf{0}$ representation in C_{3i} and are therefore taken into account in the calculation.

Consequently, the four retained branching in the $O_3 \supset O_h \supset D_{3d} \supset C_{3i}$ subduction are:

$$\begin{aligned}
&\mathbf{4}^{+}(O_3) \rightarrow \mathbf{0}^{+}(O_h) \rightarrow \mathbf{0}^{+}(D_{3d}) \rightarrow \mathbf{0}^{+}(C_{3i})\\
&\mathbf{4}^{+}(O_3) \rightarrow \tilde{\mathbf{1}}^{+}(O_h) \rightarrow \mathbf{0}^{+}(D_{3d}) \rightarrow \mathbf{0}^{+}(C_{3i})\\
&\mathbf{4}^{+}(O_3) \rightarrow \mathbf{1}^{+}(O_h) \rightarrow \tilde{\mathbf{0}}^{+}(D_{3d}) \rightarrow \mathbf{0}^{+}(C_{3i})\\
&\mathbf{2}^{+}(O_3) \rightarrow \tilde{\mathbf{1}}^{+}(O_h) \rightarrow \mathbf{0}^{+}(D_{3d}) \rightarrow \mathbf{0}^{+}(C_{3i})
\end{aligned}$$

So the crystal-field Hamiltonian in a C_{3i} symmetry is:

$$\begin{aligned}
H_{crystal} = {} & X^{4^{+}(O_3)0^{+}(O_h)0^{+}(D_{3d})0^{+}(C_{3i})}U^{4^{+}(O_3)0^{+}(O_h)0^{+}(D_{3d})0^{+}(C_{3i})}\\
& + X^{4^{+}(O_3)\tilde{1}^{+}(O_h)0^{+}(D_{3d})0^{+}(C_{3i})}U^{4^{+}(O_3)\tilde{1}^{+}(O_h)0^{+}(D_{3d})0^{+}(C_{3i})}\\
& + X^{4^{+}(O_3)1^{+}(O_h)\tilde{0}^{+}(D_{3d})0^{+}(C_{3i})}U^{4^{+}(O_3)1^{+}(O_h)\tilde{0}^{+}(D_{3d})0^{+}(C_{3i})}\\
& + X^{2^{+}(O_3)\tilde{1}^{+}(O_h)0^{+}(D_{3d})0^{+}(C_{3i})}U^{2^{+}(O_3)\tilde{1}^{+}(O_h)0^{+}(D_{3d})0^{+}(C_{3i})}.
\end{aligned} \tag{2.14}$$

The $X^{4\tilde{1}00}$ and $X^{41\tilde{0}0}$ crystal-field parameters are not independent because they are joined by the choice of the C_2 axis in the $O_h \supset D_{3d}$ branching [29]. We can choose $X^{4\tilde{1}00} = 0$ or $X^{41\tilde{0}0} = 0$ [23]. This dependence will be explained in detail in Chap. 3.

In the case of a C_{3i} symmetry, the relations between the (X^{4000}, $X^{4\tilde{1}00}$, $X^{2\tilde{1}00}$) crystal-field parameters and the (Dq, $D\sigma$, $D\tau$) parameters used in optical absorption are:

$$\begin{aligned} X^{4000} &= \frac{\sqrt{10}}{\sqrt{3}}(18Dq + 7D\tau), \\ X^{4\tilde{1}00} &= \frac{10\sqrt{14}}{\sqrt{3}}D\tau, \\ X^{2\tilde{1}00} &= -\sqrt{70}D\sigma. \end{aligned} \tag{2.15}$$

The parameters used by the code are X^{4000}, $X^{4\tilde{1}00}$ and $X^{2\tilde{1}00}$.

The case of a D_{3d} symmetry

I will show in Chap. 3 that instead of performing the calculations in a C_{3i} symmetry, the calculations can be done in a D_{3d} symmetry. A geometrical parameter thus reappears but the crystal-field Hamiltonian is simpler. Only the branchings of the irreducible representations $\mathbf{2}^+(O_3)$ and $\mathbf{4}^+(O_3)$ which allow to get the $\mathbf{0}^+(D_{3d})$ representation are taken into account in the O_h subgroup. The same subduction is chosen as for the C_{3i} symmetry. Three branchings are retained in the $O_3 \supset O_h \supset D_{3d} \supset C_{3i}$ subduction:

$$\begin{aligned} &\mathbf{4}^+(O_3) \to \mathbf{0}^+(O_h) \to \mathbf{0}^+(D_{3d}) \to \mathbf{0}^+(C_{3i}) \\ &\mathbf{4}^+(O_3) \to \tilde{\mathbf{1}}^+(O_h) \to \mathbf{0}^+(D_{3d}) \to \mathbf{0}^+(C_{3i}) \\ &\mathbf{2}^+(O_3) \to \tilde{\mathbf{1}}^+(O_h) \to \mathbf{0}^+(D_{3d}) \to \mathbf{0}^+(C_{3i}) \end{aligned}$$

The crystal-field Hamiltonian in a D_{3d} symmetry is therefore given by:

$$\begin{aligned} H_{crystal} &= X^{4^+(O_3)0^+(O_h)0^+(D_{3d})0^+(C_{3i})}U^{4^+(O_3)0^+(O_h)0^+(D_{3d})0^+(C_{3i})} \\ &+ X^{4^+(O_3)\tilde{1}^+(O_h)0^+(D_{3d})0^+(C_{3i})}U^{4^+(O_3)\tilde{1}^+(O_h)0^+(D_{3d})0^+(C_{3i})} \\ &+ X^{2^+(O_3)\tilde{1}^+(O_h)0^+(D_{3d})0^+(C_{3i})}U^{2^+(O_3)\tilde{1}^+(O_h)0^+(D_{3d})0^+(C_{3i})}. \end{aligned} \tag{2.16}$$

The relations between the (X^{4000}, $X^{4\tilde{1}00}$, $X^{2\tilde{1}00}$) crystal-field parameters and the (Dq, $D\sigma$, $D\tau$) parameters used in optical absorption are identical to the relations given in Eq. 2.15.

Expression of the electric quadrupole operator

The crystal-field Hamiltonian is used in the third step of the calculations to determine the initial and final states. To calculate the transitions between theses two states, the transition operator must also be expressed in the symmetry of the absorbing site. I concentrate here on the electric quadrupole operator as I performed multielectronic calculations only in the case of K pre-edge of tsavorite, which arises from pure electric quadrupole transitions because of the centrosymmetrical site of vanadium. The electric quadrupole operator, $\hat{O}= \frac{i}{2}(\hat{\boldsymbol{\epsilon}}.\boldsymbol{r})(\hat{\boldsymbol{k}}.\boldsymbol{r})$, is a 2nd-rank tensor in the SO_3 group. It is associated to the irreducible representations $\mathbf{2}(SO_3)$ and $\mathbf{2}^+(O_3)$ and the considered branchings are those given in Eq. 2.14.

To express the electric quadrupole operator as a function of irreducible tensors in the given subduction, its expression is determined from the coordinates of $\hat{\boldsymbol{\epsilon}}$ and $\hat{\boldsymbol{k}}$ in the chosen basis. In the case of the C_{3i} group and the $O_3 \supset O_h \supset D_{3d} \supset C_{3i}$ subduction, the (x, y, z) axes of the absorbing atom site are implicitly chosen so that the z axis is aligned with the 3-fold axis of the cube. Then the electric quadrupole is expressed as a functions of the $|\alpha\ell M_\ell\rangle$ functions and finally as a function of the $|k(SO_3)\rho(O)\sigma(D_{3d})\lambda(C_{3i})\rangle$ states. The expressions of the electric quadrupole transition operator are thus determined as a function of irreducible tensors in the chosen subduction. All the relations needed to determine the electric quadrupole transition operator are given by Butler [29] and they are given here in the case of the $O_3 \supset O_h \supset D_{3d} \supset C_{3i}$ subduction.

The transition operator is a linear combination of xy, xz, yz, (x^2-y^2) and ($3z^2$-r^2). It can be written as a function of operators that change as $|\alpha\ell M_\ell\rangle$ partners ($\ell = 2$ in the case of $3d$ orbitals) with the following relations [29]:

$$\begin{aligned}
d_{xy} &= \frac{i}{\sqrt{2}}(|2^+{-2}^+\rangle - |2^+2^+\rangle),\\
d_{yz} &= \frac{i}{\sqrt{2}}(|2^+{-1}^+\rangle + |2^+1^+\rangle),\\
d_{xz} &= \frac{1}{\sqrt{2}}(|2^+{-1}^+\rangle - |2^+1^+\rangle),\\
d_{3z^2-r^2} &= |2^+0^+\rangle,\\
d_{x^2-y^2} &= \frac{1}{\sqrt{2}}(|2^+2^+\rangle + |2^+{-2}^+\rangle).
\end{aligned} \tag{2.17}$$

The relations between the $|\alpha\ell M_\ell\rangle$ partners and the $|k(SO_3)\rho(O)\sigma(D_{3d})\lambda(C_{3i})\rangle$ states are (the + signs are omitted for a better clarity):

$$\begin{aligned}
|2{-2}\rangle &= \frac{1}{\sqrt{3}}\,|2211\rangle - \frac{\sqrt{2}}{\sqrt{3}}\,|2\tilde{1}11\rangle\\
|2{-1}\rangle &= \frac{\sqrt{2}}{\sqrt{3}}\,|221{-1}\rangle + \frac{1}{\sqrt{3}}\,|2\tilde{1}1{-1}\rangle\\
|20\rangle &= -|2\tilde{1}001\rangle\\
|21\rangle &= -\frac{\sqrt{2}}{\sqrt{3}}\,|2211\rangle - \frac{1}{\sqrt{3}}\,|2\tilde{1}11\rangle\\
|22\rangle &= \frac{1}{\sqrt{3}}\,|221{-1}\rangle - \frac{\sqrt{2}}{\sqrt{3}}\,|2\tilde{1}1{-1}\rangle
\end{aligned} \tag{2.18}$$

As the electric quadrupole transition operator is a function of the ($\hat{\boldsymbol{\epsilon}}$,$\hat{\boldsymbol{k}}$) configuration, the transition operators used in the multielectronic calculations of tsavorite will be detailed in Chap. 3.

2.3 Symmetry considerations: The coset method

The calculation of the absorption cross-section has been described in the two previous sections for two approaches. In the monoelectronic approach, the calculations are performed for the crystal and it is not straightforward to get electronic and structural information on the site of the absorbing atom. On the contrary, in the multielectronic approach, the calculations are done for a single site and the spectrum for the full crystal has to be determined from that of the single site. An additional complication arises from the fact that, in a crystal, a crystallographic site is usually not unique. For the concrete example of tsavorite, aluminum atoms sit in sixteen equivalent sites in the cubic cell, divided into two equal groups equivalent by a $(\frac{1}{2},\frac{1}{2},\frac{1}{2})$ translation. Inside each group, the eight sites are equivalent by rotation but they are differently orientated with respect to the cubic frame. When a vanadium atom is incorporated in tsavorite, it can substitute for the aluminum atom in any of these sixteen sites. The experimental spectrum corresponds to the average of the spectra of vanadium atoms occupying the sixteen sites and whatever the chosen approach, the calculations need to take these different sites into account. Some relations can be determined by symmetry considerations to deduce the crystal spectrum from that of a single site, or on the contrary to get information on a single site from the crystal spectrum. However, these relations between sites and between a site and the crystal are not trivial and require an important theoretical development, based on spherical tensor analysis.

The mathematical tools needed to this development were detailed in a publication in *Journal of Physics: Condensed Matter*, which is reproduced here in the entirety. A general presentation of spherical tensors is given, as well as the general formulas of the spherical tensor coupling, which are illustrated with the example of the electric dipole and quadrupole transitions in X-ray absorption spectroscopy. After the generalities, the case of crystals is considered: the way that the symmetry of a crystal constrains the spherical tensor components in the reference frame of the site and in the reference frame of the crystal. The formulas relating these reference frames are given. The examples of the Al site in spinel and garnet is treated as an illustration of the general formula. Finally, the spherical tensor describing the full crystal from those of the sites is determined. A powerful way to calculate the tensor averaged over the crystal from the tensor symmetrized over a single site is the coset method.

IOP PUBLISHING JOURNAL OF PHYSICS: CONDENSED MATTER
J. Phys.: Condens. Matter **20** (2008) 455205 (15pp) doi:10.1088/0953-8984/20/45/455205

Site symmetry and crystal symmetry: a spherical tensor analysis

Christian Brouder, Amélie Juhin, Amélie Bordage and Marie-Anne Arrio

Institut de Minéralogie et de Physique des Milieux Condensés, CNRS UMR 7590,
Universités Paris 6 et 7, IPGP, 140 rue de Lourmel, 75015 Paris, France

E-mail: christian.brouder@impmc.jussieu.fr

Received 10 June 2008, in final form 15 September 2008
Published 13 October 2008
Online at stacks.iop.org/JPhysCM/20/455205

Abstract
The relation between the properties of a specific crystallographic site and the properties of the full crystal is discussed by using spherical tensors. The concept of spherical tensors is introduced and the way it transforms under the symmetry operations of the site and from site to site is described in detail. The law of spherical tensor coupling is given and illustrated with the example of the electric dipole and quadrupole transitions in x-ray absorption spectroscopy. The main application of the formalism is the reduction of computation time in the calculation of the properties of crystals by band-structure methods. The general approach is illustrated by the examples of substitutional chromium in spinel and substitutional vanadium in garnet.

(Some figures in this article are in colour only in the electronic version)

1. Introduction

This paper deals with the relation between the properties of specific sites in a crystal and the properties of the crystal itself. We shall discuss in particular the case of x-ray absorption spectroscopy, but many of our results are general.

The aim of this paper is to introduce x-ray physicists, experimentalists and theoreticians, to the use of spherical tensors for analyzing theoretical and experimental spectra. Therefore, our presentation is as pedagogical as we can manage. As the manipulation of spherical tensors can be quite complicated, we have tried to reduce it to the simplest possible rules.

An atom in a crystal generally occupies a crystallographic site that is not unique. If we take the concrete example of a chromium atom substituting for aluminum in spinel ($MgAl_2O_4$), the chromium atom can occupy 16 equivalent trigonal sites in the cubic cell [1]. The (normalized) x-ray absorption spectrum of chromium is the average of the spectra of the chromium atoms occupying the 16 sites. To calculate the spectrum of chromium, we need to put a chromium atom at an aluminum site, relax the environment, carry out a self-consistent band-structure calculation with and without a core hole, and calculate the spectrum of this site. In a straightforward approach, we need then to repeat the procedure for all equivalent sites and take the average spectrum. A considerable amount of time can be saved if we calculate the spectrum of a single site and deduce the spectrum of the other sites by symmetry considerations. The present paper gives all the required tools to do so.

Let us first defend the case of spherical tensors, that will be precisely defined in the next section. Most physical properties are tensors and they are usually considered as Cartesian tensors. Spherical tensors consist of a ‘refinement’ of Cartesian tensors in the sense that a Cartesian tensor is generally the sum of several spherical tensors. For example, a second-rank Cartesian tensor is the sum a zeroth-rank, a first-rank and a second-rank spherical tensor. This refinement enables us to discard irrelevant contributions. For example, the electric quadrupole contribution to an x-ray absorption spectrum is represented by a symmetric fourth-rank Cartesian tensor with 36 components, whereas it is represented by the sum of a zeroth-rank, a second-rank and a fourth-rank spherical tensor with 15 components altogether. Moreover, the spherical average used to represent powder samples is obtained by taking only one spherical tensor component, whereas it is the sum of 12 Cartesian components. Thus, using spherical tensors can save computing time.

The drawback of the spherical tensor analysis is that some subtleties enter its practical use. One purpose of this paper is to give a detailed presentation of these problems and of their solutions.

0953-8984/08/455205+15$30.00 © 2008 IOP Publishing Ltd Printed in the UK

In practice, one faces the frustrating task of sorting out the various conventions used by the authors and to determine whether a rotation is active or passive, whether the row index of the Wigner matrix increases from left to right as in a normal matrix or decreases as in [2], which definition of the Wigner matrix is used (seven inequivalent definitions are found in the literature [3]), how tensors transform under complex conjugation, etc.

The paper starts with a presentation of the Cartesian and spherical tensors and a detailed description of our notation. Then, the concept of tensor coupling is introduced and a simple formula is given to change the coupling order. This formula is applied to the calculation of electric dipole and quadrupole transitions. This completes the generalities on spherical tensors. Then, we consider the case of crystals. We show how the symmetry of a crystal site constrains the spherical tensor components in the reference frame of the site and in the reference frame of the crystal. We also give the precise formula relating these reference frames. As an illustration, we treat the example of the Al site in spinel and garnet. Finally, we determine the spherical tensor describing the full crystal from those of the sites. An appendix gathers the formulae that were used to calculate rotation matrices, Wigner matrices and solid harmonics.

2. Cartesian and spherical tensors

A Cartesian tensor is the generalization of a scalar, a vector or a matrix. A three-dimensional vector $\mathbf{r} = (x, y, z) = (\mathbf{r}_1, \mathbf{r}_2, \mathbf{r}_3)$ is transformed by a rotation R into a vector $\mathbf{r}' = R\mathbf{r}$, so that $\mathbf{r}'_i = \sum_{j=1}^{3} R_{ij}\mathbf{r}_j$. A vector is also called a first-rank tensor. A matrix A defined by $A_{ij} = \mathbf{r}_i\mathbf{r}_j$ transforms under rotation into

$$A'_{ij} = \mathbf{r}'_i\mathbf{r}'_j = \sum_{lm} R_{il}R_{jm}A_{lm}. \qquad (1)$$

Any matrix A_{ij} that transforms under rotation as in equation (1) is called a second-rank Cartesian tensor. More generally, an nth-rank Cartesian tensor is a generalized matrix $A_{i_1\ldots i_n}$ that transforms under rotation as in equation (1), but with the product of n matrices R instead of just two. Cartesian tensors are ubiquitous in physics. For example, electric dipole transition amplitudes are described by a first-rank tensor, electric dipole transition intensities and electric quadrupole transition amplitudes by a second-rank tensor, and electric quadrupole transition intensities by a fourth-rank tensor.

Cartesian tensors have very simple transformation rules under rotation, but they suffer from a severe drawback: they are not irreducible. To see what this means, consider a second-rank tensor A_{ij}. Its trace is $t = \sum_{i=1}^{3} A_{ii}$ and transforms under rotation into

$$t' = \sum_{i=1}^{3} A'_{ii} = \sum_{ilm} R_{il}R_{im}A_{lm} = \sum_{lm} \delta_{lm}A_{lm} = t,$$

where we used the fact that $RR^{\mathrm{T}} = \mathrm{Id}$, where R^{T} is the transpose of R. We recover the fact that the trace of a matrix is invariant: it transforms into itself under rotation. A second-order Cartesian tensor gives another interesting object, the vector $\mathbf{v}$ defined by $\mathbf{v}_i = \sum_{jk} \epsilon_{ijk}A_{jk}$, where j and k run from 1 to 3. The Levi-Civita symbol ϵ_{ijk} is 1 if (i, j, k) is a cyclic permutation of $(1, 2, 3)$, it is -1 if (i, j, k) is another permutation of $(1, 2, 3)$, and it is 0 if two indices are identical. Then, using the identity $\sum_{jk} \epsilon_{ijk}R_{jl}R_{km} = \sum_j R_{ij}\epsilon_{jlm}$, we see that $\mathbf{v}$ transforms under rotation as a vector: $\mathbf{v}' = R\mathbf{v}$. Therefore, from a second-rank Cartesian tensor, we can build a linear combination of its elements (the trace) that is invariant under rotation, and three linear combinations of its elements that transform into each other as the components of a vector. More generally, a tensor is said to be *reducible* when there are linear combinations of its elements that transform into each other under rotation. When a tensor is not reducible, it is called irreducible. Thus, a vector is irreducible but a second-rank Cartesian tensor is reducible. The irreducible tensors are called *spherical tensors* and will be the main topic of this paper.

The first spherical tensors were the spherical harmonics Y_ℓ^m. For each ℓ, there are $2\ell + 1$ spherical harmonics Y_ℓ^m that transform into each other under rotation. More precisely, for each rotation R, there is a unitary matrix D^ℓ, called a *Wigner matrix* (to be precisely defined in the next section), such that the rotation of Y_ℓ^m by R is

$$RY_\ell^m = \sum_{m'=-\ell}^{\ell} Y_\ell^{m'} D^\ell_{m'm}(R).$$

Spherical tensors are defined in analogy with spherical harmonics. An ℓth-rank spherical tensor, denoted by T^ℓ, is a set of $2\ell + 1$ components, written T^ℓ_m, where $m = -\ell, -\ell + 1, \ldots, \ell - 1, \ell$, that transform under rotation as

$$RT^\ell_m = \sum_{m'=-\ell}^{\ell} T^\ell_{m'} D^\ell_{m'm}(R). \qquad (2)$$

This definition is rather abstract, but we shall see how spherical tensors are built in practice. It is an unfortunate but historical fact that the position of ℓ and m is different in the spherical harmonics Y_ℓ^m and the spherical tensors T^ℓ_m.

When many spherical tensors are involved in a formula, we use also the notation P^a, Q^b, etc. For notational convenience, we shall often write $RT^\ell = T^\ell D^\ell(R)$ for equation (2), as for the product of a matrix and a vector. Moreover, the product of two Wigner matrices will be denoted by $D^\ell(R)D^\ell(R')$.

2.1. Further symmetries

A spherical tensor is a basis of an irreducible representation of the rotation group $SO(3)$. A different group leads to a different concept of irreducibility. For example, an irreducible representation of $SO(3)$ is generally reducible for a subgroup of $SO(3)$ (e.g. $SO(2)$ or a point symmetry group). In many applications we have to consider a group larger than $SO(3)$, for example $O(3)$, the direct product of the rotation group and the group $\mathcal{I} = \{1, I\}$, where I is the inversion symmetry operation: $I\mathbf{r} = -\mathbf{r}$. An element of $O(3)$ is called a *rotoinversion*. By definition, for any rotoinversion g, there is a unique rotation R_g such that either $g = R_g$ (g is a pure rotation) or $g = IR_g$ (g contains the inversion). It can be checked that $R_{gg'} = R_g R_{g'}$ and that $R_{g^{-1}} = R_g^{-1}$. The group $\mathcal{I}$ is of order 2 and commutative. It has two one-dimensional irreducible representations, where the inversion is represented by the factor 1 or -1, respectively. Therefore, according to a general theorem ([4], p 115), spherical tensors become bases of the irreducible representations of $O(3)$ if they are provided with a definite parity: the parity of T^ℓ is even if $IT^\ell = T^\ell$; it is odd if $IT^\ell = -T^\ell$. For instance, the spherical tensor representing electric dipole transition amplitudes is odd; the one representing electric quadrupole transition amplitudes is even. We denote the action of a rotoinversion on a tensor T^ℓ with a definite parity by

$$gT_m^\ell = \epsilon(g) \sum_{m'=-\ell}^{\ell} T_{m'}^\ell D_{m'm}^\ell(g), \tag{3}$$

where $D^\ell(g)$ is a simplified notation for $D^\ell(R_g)$ and where ϵ is the *parity operator* associated with T^ℓ: $\epsilon(g) = -1$ if T^ℓ is odd and g contains the inversion, $\epsilon(g) = 1$ otherwise. We have $\epsilon(gg') = \epsilon(g)\epsilon(g') = \epsilon(g'g)$ and $\epsilon(g^{-1}) = \epsilon(g)$.

Time-reversal symmetry is more subtle because of its antiunitary nature [5]. It is taken into account by considering that the spherical tensors are built from Hermitian operators (see equation (4), p 61 of [3]):

$$(T_m^\ell)^\dagger = (-1)^m T_{-m}^\ell. \tag{4}$$

In this paper, the only tensors that do not satisfy time-reversal symmetry are those built from the polarization vector $\boldsymbol{\epsilon}$, that can possibly be complex. In this case we have $(T_m^\ell(\boldsymbol{\epsilon}))^\dagger = (-1)^m T_{-m}^\ell(\boldsymbol{\epsilon}^*)$. This happens for instance when T^ℓ is a solid harmonic built from a vector with complex coordinates (see appendix B.2).

3. Notation

The fact that many conventions are found in the literature leads us to precisely describe our notation. We consider *active* rotations, i.e. rotations that move the points and not the reference frame. For example the rotation through an angle ψ about the z-axis is represented by

$$R_z(\psi) = \begin{pmatrix} \cos\psi & -\sin\psi & 0 \\ \sin\psi & \cos\psi & 0 \\ 0 & 0 & 1 \end{pmatrix}.$$

After an active rotation R, the coordinates $(\mathbf{r}_1, \mathbf{r}_2, \mathbf{r}_3)$ of the vector $\mathbf{r}$ are transformed into the coordinates $\mathbf{r}'_i = \sum_j R_{ij}\mathbf{r}_j$ of $\mathbf{r}' = R\mathbf{r}$. In a *passive* rotation, the reference frame is rotated: the basis vectors $\mathbf{e}_i$ are transformed into the basis vectors $\mathbf{e}'_i = \sum_j R_{ij}\mathbf{e}_j$. Thus, the coordinates of a point $\mathbf{r}$ are transformed by the inverse matrix: $\mathbf{r}' = R^{-1}\mathbf{r}$.

To describe the transformation of the properties of a crystal under rotation, we consider the case of its charge density $\rho(\mathbf{r})$. After a rotation changing $\mathbf{r}$ into $\mathbf{r}' = R\mathbf{r}$, the charge density ρ is transformed into a 'rotated' charge density ρ' of the rotated crystal. To determine ρ', we require the value of the charge density to be invariant under rotation. More precisely, we want $\rho'(\mathbf{r}') = \rho(\mathbf{r})$. Therefore, the rotated function ρ' is defined by $\rho'(\mathbf{r}') = \rho(R^{-1}\mathbf{r}')$. For later convenience, we denote the rotated function ρ' by $R\rho$. The use of the same symbol R to denote the rotation of both the vectors and the functions should not bring too much confusion. The presence of the inverse rotation R^{-1} in the definition of $R\rho$ ensures that $R'(R\rho) = (R'R)\rho$ (see [6], p 59).

3.1. Wigner rotation matrices

We denote by $D_{m'm}^\ell(R)$ the Wigner rotation matrix corresponding to the rotation R (see appendix B.3 for a definition). For example, $D_{m'm}^\ell(R_z(\psi)) = \delta_{mm'}\mathrm{e}^{-\mathrm{i}m\psi}$. The Wigner rotation matrices define a unitary representation of the rotation group, so that

$$D_{m'm}^\ell(R^{-1}) = (D_{mm'}^\ell(R))^*, \tag{5}$$

and

$$D_{m'm}^\ell(RR') = \sum_{m''=-\ell}^{\ell} D_{m'm''}^\ell(R) D_{m''m}^\ell(R'). \tag{6}$$

3.2. Spherical harmonics

The spherical harmonics are defined by (see [2], p 68)

$$Y_\ell^m(\theta,\phi) = \sqrt{\frac{2\ell+1}{4\pi}}(D_{m0}^\ell(R_{\theta\phi}))^*, \tag{7}$$

where $R_{\theta\phi}$ is the rotation described by the Euler angles $(\phi, \theta, 0)$ (see appendix B.1.2). For notational convenience, we denote by $\mathbf{n}$ the vector $(\sin\theta\cos\phi, \sin\theta\sin\phi, \cos\theta)$ and we write $Y_\ell^m(\mathbf{n})$ and $R_\mathbf{n}$ for $Y_\ell^m(\theta,\phi)$ and $R_{\theta\phi}$, respectively. This notation is justified by the fact that $Y_\ell^m(\mathbf{n})$ can be defined for any (not necessarily normalized) vector $\mathbf{r}$. The resulting functions are called *solid harmonics* and are described in appendix B.2. Solid harmonics are required, for example, in the case of elliptically polarized x-rays because $\mathbf{n}$ has then complex coordinates. A three-dimensional Cartesian vector $\mathbf{r} = (x, y, z)$ can be turned into a set of three solid harmonics

$$Y_1^{-1}(\mathbf{r}) = \sqrt{\frac{3}{8\pi}}(x - \mathrm{i}y), \tag{8}$$

$$Y_1^0(\mathbf{r}) = \sqrt{\frac{3}{4\pi}}z, \tag{9}$$

$$Y_1^1(\mathbf{r}) = -\sqrt{\frac{3}{8\pi}}(x + \mathrm{i}y). \tag{10}$$

The definition of spherical harmonics implies

$$Y_\ell^m(R\mathbf{n}) = \sum_{m'} Y_\ell^{m'}(\mathbf{n}) D_{m'm}^\ell(R^{-1}).$$

This relation is proved by noticing that the argument $R\mathbf{n}$ of the spherical harmonics corresponds to the argument $RR_\mathbf{n}$ of the Wigner matrix in equation (7). From equation (5), we have $(D_{m0}^\ell(RR_\mathbf{n}))^* = D_{0m}^\ell((RR_\mathbf{n})^{-1})$. The result follows from $(RR_\mathbf{n})^{-1} = R_\mathbf{n}^{-1}R^{-1}$ and the group representation property defined by equation (6). The same property is true for solid harmonics. Therefore,

$$(RY_\ell^m)(\mathbf{r}) = Y_\ell^m(R^{-1}\mathbf{r}) = \sum_{m'} Y_\ell^{m'}(\mathbf{r}) D_{m'm}^\ell(R). \tag{11}$$

The presence of the spherical harmonics on the left of the Wigner rotation matrices ensures that $R'(RY_\ell^m) = (R'R)Y_\ell^m$. To show this, equation (11) is multiplied on the left by R':

$$\begin{aligned}(R'(RY_\ell))(\mathbf{r}) &= (R'Y_\ell)(\mathbf{r})D^\ell(R) = Y_\ell(\mathbf{r})D^\ell(R')D^\ell(R)\\ &= Y_\ell(\mathbf{r})D^\ell(R'R) = (R'R)Y_\ell(\mathbf{r}).\end{aligned}$$

In the foregoing proof, we simplified the notation by omitting the component index m, as described at the end of section 2.

4. Building tensor operators

Physical properties can be represented by spherical tensors, that can often be built by coupling lower rank tensors. We illustrate this construction by the example of electric dipole and quadrupole transitions. We shall use the remarkable toolbox for spherical tensor calculations elaborated by Varshalovich *et al* [3].

The basic elements of this construction are first-rank spherical tensors. Any three-dimensional Cartesian vector $\mathbf{v} = (x, y, z)$ can be turned into a first-rank spherical tensor $\mathbf{v}^1$ by defining

$$\begin{aligned}\mathbf{v}^1_{-1} &= (x - \mathrm{i}y)/\sqrt{2},\\ \mathbf{v}^1_0 &= z,\\ \mathbf{v}^1_1 &= -(x + \mathrm{i}y)/\sqrt{2}.\end{aligned} \tag{12}$$

Note that solid harmonics $Y_\ell^m(\mathbf{v})$ are also spherical tensors built from $\mathbf{v}$ and that $\mathbf{v}^1 = Y_1(\mathbf{v})\sqrt{4\pi/3}$. However, the factor $\sqrt{4\pi/3}$ is cumbersome and the definition $\mathbf{v}^\ell = Y_\ell(\mathbf{v})\sqrt{4\pi/(2\ell+1)}$ is often preferred.

An ath-rank spherical tensor P^a can be *coupled* to a bth-rank spherical tensor Q^b into a cth-rank spherical tensor, denoted by $\{P^a \otimes Q^b\}^c$, and defined by

$$\{P^a \otimes Q^b\}^c_\gamma = \sum_{\alpha=-a}^{a} \sum_{\beta=-b}^{b} (a\alpha b\beta|c\gamma) P^a_\alpha Q^b_\beta.$$

The symbol $(a\alpha b\beta|c\gamma)$ denote Clebsch–Gordan coefficients [2, 3], which are zero when $\gamma \neq \alpha + \beta$ or when c does not satisfy the triangle relation $|a - b| \leqslant c \leqslant a + b$. For example, the coupling of two vectors (i.e. $a = b = 1$) gives a zeroth-rank, a first-rank and a second-rank spherical tensor (i.e. $c = 0, 1, 2$). The zeroth-rank tensor obtained by coupling two vectors is proportional to the scalar product of these vectors: $\{\mathbf{u}^1 \otimes \mathbf{v}^1\}^0 = -\mathbf{u} \cdot \mathbf{v}/\sqrt{3}$, because $(1\alpha 1 -\alpha|00) = -(-1)^\alpha/\sqrt{3}$. More generally, we define the *scalar product* of two spherical tensors P^a and Q^a of the same rank to be (see [3], p 64 and 65)

$$P^a \cdot Q^a = \sum_{\alpha=-a}^{a} (-1)^\alpha P^a_{-\alpha} Q^a_\alpha = (-1)^a \sqrt{2a+1}\{P^a \otimes Q^a\}^0. \tag{13}$$

If we consider the group $O(3)$, then let ϵ_P and ϵ_Q be the parity operators of P^a and Q^b, respectively. The parity operator ϵ_T of the coupled tensor $T^c = \{P^a \otimes Q^b\}^c$ is defined by $\epsilon_T(g) = \epsilon_P(g)\epsilon_Q(g)$.

It is often necessary to modify the coupling order of the tensors. For example, to evaluate electric dipole transition intensities, we have to calculate $|\langle f|\boldsymbol{\epsilon} \cdot \mathbf{r}|i\rangle|^2$, where $\mathbf{r}$ is coupled to $\boldsymbol{\epsilon}$ by the scalar product, and the result is multiplied by its complex conjugate. As we shall see in the next section, it is more convenient from the physical point of view to directly couple the x-ray polarization vectors $\boldsymbol{\epsilon}$ and $\boldsymbol{\epsilon}^*$. For this purpose, we use the recoupling identity

$$\{P^a \otimes Q^a\}^0 \cdot \{R^d \otimes S^d\}^0 = \sum_g (-1)^g \frac{\{P^a \otimes R^d\}^g \cdot \{Q^a \otimes S^d\}^g}{\sqrt{(2a+1)(2d+1)}}, \tag{14}$$

where g runs from $|a - d|$ to $a + d$ by the triangle relation. This identity is proved in appendix C.

In the next two sections, we illustrate the recoupling methods with the calculation of electric dipole and quadrupole transitions. Similar methods were used to investigate the interference of electric and quadrupole transitions [7–10] or to calculate x-ray scattering cross-sections [11].

4.1. Dipole

The electric dipole transition amplitudes are given by the formula $T_{fi} = \langle f|\boldsymbol{\epsilon} \cdot \mathbf{r}|i\rangle$. If we denote $\langle f|\mathbf{r}|i\rangle$ by $\mathbf{r}_{fi}$, equation (13) gives us $T_{fi} = \boldsymbol{\epsilon} \cdot \mathbf{r}_{fi} = -\sqrt{3}\{\boldsymbol{\epsilon}^1 \otimes \mathbf{r}^1_{fi}\}^0$. For notational convenience, we remove the exponent 1 in the spherical tensors $\boldsymbol{\epsilon}^1$ and $\mathbf{r}^1_{fi}$. This should not bring confusion: if a vector takes part in a coupling, it is a first-rank spherical tensor. Using the recoupling identity (14), we find the expression of the dipole transition intensity

$$\begin{aligned}|T_{fi}|^2 &= 3\{\boldsymbol{\epsilon}^* \otimes \mathbf{r}^*_{fi}\}^0\{\boldsymbol{\epsilon} \otimes \mathbf{r}_{fi}\}^0\\ &= \sum_{a=0}^{2} (-1)^a \{\boldsymbol{\epsilon}^* \otimes \boldsymbol{\epsilon}\}^a \cdot \{\mathbf{r}^*_{fi} \otimes \mathbf{r}_{fi}\}^a.\end{aligned} \tag{15}$$

Note that, for elliptic polarization, $\boldsymbol{\epsilon}$ is complex. Each term of a decomposition over spherical tensors often has a clear physical meaning. In equation (15), the variables concerning the incident x-ray (i.e. $\boldsymbol{\epsilon}$ and $\boldsymbol{\epsilon}^*$) are gathered in $\{\boldsymbol{\epsilon}^* \otimes \boldsymbol{\epsilon}\}^a$; the variables concerning the crystal are in $\{\mathbf{r}^*_{fi} \otimes \mathbf{r}_{fi}\}^a$. Thus, we can easily investigate the influence of a rotation R of the crystal on the absorption cross-section

$$\begin{aligned}R|T_{fi}|^2 &= \sum_{a=0}^{2} (-1)^a \{\boldsymbol{\epsilon}^* \otimes \boldsymbol{\epsilon}\}^a \cdot (R\{\mathbf{r}^*_{fi} \otimes \mathbf{r}_{fi}\}^a)\\ &= \sum_{a=0}^{2} (-1)^a \{\boldsymbol{\epsilon}^* \otimes \boldsymbol{\epsilon}\}^a \cdot (\{\mathbf{r}^*_{fi} \otimes \mathbf{r}_{fi}\}^a D^a(R)),\end{aligned}$$

where we used equation (2) and the fact that $\{\mathbf{r}^*_{fi} \otimes \mathbf{r}_{fi}\}^a$ is an ath-rank spherical tensor. In particular, the spectrum of a powder sample is given by the average over all orientations, i.e. over all rotations R. This average is very simple when performed with spherical tensors: $\langle D^a(R)\rangle = \delta_{a,0}$. Thus, the term $a = 0$ gives the spectrum of a powder, called the isotropic spectrum.

$$\langle |T_{fi}|^2\rangle = \{\boldsymbol{\epsilon}^* \otimes \boldsymbol{\epsilon}\}^0 \cdot \{\mathbf{r}^*_{fi} \otimes \mathbf{r}_{fi}\}^0 = \frac{1}{3}(\boldsymbol{\epsilon}^* \cdot \boldsymbol{\epsilon})(\mathbf{r}^*_{fi} \cdot \mathbf{r}_{fi}) = \frac{|\mathbf{r}_{fi}|^2}{3},$$

where we used equation (13) and $|\boldsymbol{\epsilon}|^2 = 1$.

To interpret the term $a = 1$, we use the relation between vectors $\mathbf{u}$, $\mathbf{v}$ and the corresponding first-rank spherical tensors

$\mathbf{u}^1$, $\mathbf{v}^1$ (we restore the tensor rank in $\mathbf{u}^1$, $\mathbf{v}^1$ for clarity): according to equation (C.1), $\{\mathbf{u}^1\otimes\mathbf{v}^1\}^1$ is the first-rank tensor corresponding to the vector $(\mathrm{i}/\sqrt{2})\mathbf{u}\times\mathbf{v}$. Therefore,

$$\{\boldsymbol{\epsilon}^*\otimes\boldsymbol{\epsilon}\}^1\cdot\{\mathbf{r}^*_{fi}\otimes\mathbf{r}_{fi}\}^1 = -\tfrac{1}{2}(\boldsymbol{\epsilon}^*\times\boldsymbol{\epsilon})\cdot(\mathbf{r}^*_{fi}\times\mathbf{r}_{fi}).$$

The first cross-product is related to the rate of circular polarization P_{c} and to the wavevector direction $\hat{k}$ of the incident x-ray by $\boldsymbol{\epsilon}^*\times\boldsymbol{\epsilon} = -\mathrm{i}P_{\mathrm{c}}\hat{k}$ [8]. Moreover, the second cross-product is zero for a non-magnetic sample because time-reversal symmetry implies $\mathbf{r}^*_{fi} = \mathbf{r}_{fi}$. Therefore, the term $a = 1$ describes magnetic circular dichroism.

The term $a = 2$ describes the linear dichroism of x-ray spectra. The number of non-zero components of $\{\mathbf{r}^*_{fi}\otimes\mathbf{r}_{fi}\}^2$ depends on the symmetry of the crystal [12]. We shall determine this number in the case of spinel and garnet.

4.2. Quadrupole

We consider the case of electric quadrupole transitions. We start from the quadrupole transition operator $T = \boldsymbol{\epsilon}\cdot\mathbf{r}\mathbf{k}\cdot\mathbf{r}$ and we rewrite it in terms of spherical tensors using equation (C.2): $T = 3\{\{\boldsymbol{\epsilon}\otimes\mathbf{r}\}^0\otimes\{\mathbf{k}\otimes\mathbf{r}\}^0\}^0$. In this expression $\boldsymbol{\epsilon}$ is coupled with $\mathbf{r}$, and $\mathbf{k}$ with $\mathbf{r}$. As in the case of electric dipole transitions, we want to gather all the terms concerning the crystal into a single tensor. For this purpose, we use equation (14) with the sum over g changed into a sum over a

$$T = \sum_{a=0}^{2}(-1)^a\{\boldsymbol{\epsilon}\otimes\mathbf{k}\}^a\cdot\{\mathbf{r}\otimes\mathbf{r}\}^a.$$

The term $a = 0$ is zero because, according to equation (13), $\{\boldsymbol{\epsilon}\otimes\mathbf{k}\}^0 = -(1/\sqrt{3})\boldsymbol{\epsilon}\cdot\mathbf{k} = 0$ since the polarization and wavevectors are perpendicular. The term $a = 1$ is zero because equation (C.1) gives us $\{\mathbf{r}\otimes\mathbf{r}\}^1 = (\mathrm{i}/\sqrt{2})\mathbf{r}\times\mathbf{r} = 0$. Thus, T is reduced to the single term

$$T = \{\boldsymbol{\epsilon}\otimes\mathbf{k}\}^2\cdot\{\mathbf{r}\otimes\mathbf{r}\}^2 = \sqrt{5}\{\{\boldsymbol{\epsilon}\otimes\mathbf{k}\}^2\otimes\{\mathbf{r}\otimes\mathbf{r}\}^2\}^0.$$

The tensor $\{\mathbf{r}\otimes\mathbf{r}\}^2$ can be expressed in terms of spherical harmonics (equation (23), p 67 of [3])

$$\{\mathbf{r}\otimes\mathbf{r}\}^2_m = \sqrt{\frac{8\pi}{15}}Y_2^m(\mathbf{r}) = \sqrt{\frac{8\pi}{15}}r^2Y_2^m(\theta,\phi),$$

where r, θ and ϕ are the spherical coordinates of $\mathbf{r}$. For completeness, we give the components of $\{\boldsymbol{\epsilon}\otimes\mathbf{k}\}^2$:

$$\{\boldsymbol{\epsilon}\otimes\mathbf{k}\}^2_{\pm2} = \frac{(\epsilon_x\pm\mathrm{i}\epsilon_y)(k_x\pm\mathrm{i}k_y)}{2},$$

$$\{\boldsymbol{\epsilon}\otimes\mathbf{k}\}^2_{\pm1} = \mp\frac{(\epsilon_x\pm\mathrm{i}\epsilon_y)k_z+\epsilon_z(k_x\pm\mathrm{i}k_y)}{2},$$

$$\{\boldsymbol{\epsilon}\otimes\mathbf{k}\}^2_{0} = \frac{3\epsilon_zk_z-\boldsymbol{\epsilon}\cdot\mathbf{k}}{\sqrt{6}} = \sqrt{\frac{3}{2}}\epsilon_zk_z.$$

The electric quadrupole transition intensities are proportional to $|T_{fi}|^2$, where the transition amplitude is $T_{fi} = \langle f|T|i\rangle$. Therefore, $|T_{fi}|^2 = 5\{P^2\otimes Q^2\}^0\{R^2\otimes S^2\}^0$, with $P^2 = \{\boldsymbol{\epsilon}^*\otimes\mathbf{k}\}^2$, $Q^2 = \langle f|\{\mathbf{r}\otimes\mathbf{r}\}^2|i\rangle^*$, $R^2 = \{\boldsymbol{\epsilon}\otimes\mathbf{k}\}^2$ and $S^2 = \langle f|\{\mathbf{r}\otimes\mathbf{r}\}^2|i\rangle$. The recoupling identity gives us

$$\begin{aligned}|T_{fi}|^2 &= 5\{P^2\otimes Q^2\}^0\{R^2\otimes S^2\}^0\\ &= \sum_{a=0}^{4}(-1)^a\{P^2\otimes R^2\}^a\cdot\{Q^2\otimes S^2\}^a.\end{aligned} \qquad (16)$$

The apparent simplicity of this calculation is essentially due to the powerful tools given in [3]. A straightforward approach is quite heavy [12].

As in the electric dipole case, the term $a = 0$ corresponds to the isotropic spectrum obtained by measuring a powder. Equation (C.3) gives us $\{P^2\otimes R^2\}^0 = k^2/(2\sqrt{5})$ and the isotropic spectrum is

$$\langle|T_{fi}|^2\rangle = k^2\frac{\{Q^2\otimes S^2\}^0}{2\sqrt{5}}.$$

The calculation of this average in Cartesian coordinates is discussed in appendix A.

If $P^2 = R^2$ (i.e. the x-rays are linearly polarized) or $Q^2 = S^2$ (i.e. the sample is non-magnetic), then the terms $a = 1$ and $a = 3$ are zero. More generally, for any tensor T^a with integer rank a, $\{T^a\otimes T^a\}^c$ is zero if c is odd. This is due to the symmetry of the Clebsch–Gordan coefficients [2, 3] $(b\beta a\alpha|c\gamma) = (-1)^{a+b-c}(a\alpha b\beta|c\gamma)$:

$$\begin{aligned}\{T^a\otimes T^a\}^c_\gamma &= \sum_{\alpha,\beta}(a\alpha a\beta|c\gamma)T^a_\alpha T^a_\beta\\ &= (-1)^{2a-c}\sum_{\beta,\alpha}(a\alpha a\beta|c\gamma)T^a_\beta T^a_\alpha\\ &= (-1)^c\{T^a\otimes T^a\}^c_\gamma,\end{aligned}$$

where we first exchanged the summation variables α and β, then used the symmetry of the Clebsch–Gordan coefficients, the commutativity of T^a_α and T^a_β, and the fact that a is an integer.

Therefore, if we consider the case of linearly polarized x-rays or non-magnetic samples, only the terms $a = 0$, 2 and 4 are possibly non-zero. The number of independent components depends on the crystal symmetry and is tabulated in [12]. The spherical tensors of [12] are related to the present spherical tensors by

$$\sigma^D(\ell,m) = -4\pi^2\alpha_0\hbar\omega\sum_f\frac{\{\mathbf{r}_{fi}\otimes\mathbf{r}_{fi}\}^\ell_m}{\sqrt{3}}\delta(E_{\mathrm{f}}-E_{\mathrm{i}}-\hbar\omega),$$

$$\sigma^Q(\ell,m) = \pi^2\alpha_0\hbar\omega k^2\sum_f\frac{\{Q^2\otimes S^2\}^\ell_m}{2\sqrt{5}}\delta(E_{\mathrm{f}}-E_{\mathrm{i}}-\hbar\omega),$$

where α_0 is the fine-structure constant.

5. Site symmetry

We now describe how to calculate the spherical tensor of a crystallographic site, assuming that it is invariant under the symmetry of the site. We recall that the symmetry group of a site consists of the operations of the space group that leave the site invariant. In a reference frame where the site is the origin, the symmetry group is isomorphic to a point group (i.e. a group of rotoinversions). We can work in a reference frame corresponding either to the site symmetry or to the crystal symmetry. If we take the example of spinel ($MgAl_2O_4$), the crystal symmetry is cubic and a natural crystal frame is defined by three orthonormal vectors along the edges of the conventional cubic unit cell of the lattice. In spinel, the aluminum site with reduced coordinates $(0, 1/4, 3/4)$ has a threefold symmetry axis along the $(-1, 1, 1)$ direction. Therefore, it is natural to take the unit basis vector $\mathbf{e}'_3$ of the site frame along this direction. The unit basis vector $\mathbf{e}'_2$ is along the $(1, 1, 0)$ direction, which is a twofold symmetry axis of the site. The three vectors $\mathbf{e}'_1 = \mathbf{e}'_2 \times \mathbf{e}'_3$, $\mathbf{e}'_2$ and $\mathbf{e}'_3$ define the orthonormal site frame. In general, the orthonormal reference frames naturally associated with the crystal and with a specific site are different. Symmetrized tensors usually have fewer non-zero components in the site frame, but they are easier to calculate in the crystal frame. We shall describe the way to go from one reference frame to the other. Two examples are treated in detail: a spinel and a garnet.

5.1. Symmetrized tensor

If G is the space group of the crystal, then a site has a symmetry group G', which is a subgroup of G. The number of elements of G' is denoted by $|G'|$. To know the form of a spherical tensor invariant under the site symmetry, we start from an arbitrary spherical tensor T^ℓ (having the parity of the property we investigate) and we calculate the symmetrized tensor $\langle T^\ell \rangle$ by using the classical formula [6]

$$\langle T^\ell_m \rangle = \frac{1}{|G'|} \sum_g \epsilon(g) \sum_{m'=-\ell}^{\ell} T^\ell_{m'} D^\ell_{m'm}(g), \qquad (17)$$

where g runs over the rotoinversion parts of the symmetry operations of the subgroup G'. In this section, the arguments g or h of D^ℓ and ϵ stand for the rotoinversion parts of the space group operations g and h.

From the physical point of view, equation (17) means that the tensor $\langle T^\ell \rangle$ is obtained by averaging over all the symmetry operations that leave the site invariant. From the mathematical point of view, we project onto the subspace that is invariant under any symmetry operation of G'. To check this, take any operation g in G' and evaluate the action of g on the symmetrized tensor. Using equation (17), where the elements of G' are now denoted by h, we find

$$\begin{aligned} g\langle T^\ell_m \rangle &= \frac{1}{|G'|} \sum_h \epsilon(h)\epsilon(g) \sum_{m'm''} T^\ell_{m''} D^\ell_{m''m'}(g) D^\ell_{m'm}(h) \\ &= \frac{1}{|G'|} \sum_h \epsilon(gh) \sum_{m''} T^\ell_{m''} D^\ell_{m''m}(gh) = \langle T^\ell_m \rangle. \end{aligned}$$

Indeed, G' being a group, the set of operations gh where h runs over G' is the same as the set of operations of G'.

5.2. Site and crystal frames

The rotoinversions g can be expressed either in the site frame or in the crystal frame. We shall see in our two examples that symmetrized tensors are simpler when expressed in the site frame. Moreover, some computer programs need to be used in the site frame[1]. However, the action of the rotoinversions on a vector $\mathbf{r}$ is easier to determine in the crystal frame, because they belong to the tabulated symmetry operations of the crystal [18]. Both cases will be treated in the examples of the following sections.

It is also necessary to describe precisely how to go from one reference frame to the other. If $\mathbf{e}_1$, $\mathbf{e}_2$, $\mathbf{e}_3$ are the orthonormal axes of the crystal frame and $\mathbf{e}'_1$, $\mathbf{e}'_2$, $\mathbf{e}'_3$ those of the site frame, there is an orthogonal matrix M such that $\mathbf{e}'_i = \sum_j M_{ij}\mathbf{e}_j$. This matrix defines a rotoinversion g by $(g\mathbf{r})_i = \sum_j M_{ij}\mathbf{r}_j$. If we take the example of spinel discussed at the beginning of section 5, if $\mathbf{e}_i$ are the orthonormal axes of the cubic unit cell and $\mathbf{e}'_i$ are the orthonormal axes of the site frame, then M is the rotation matrix representing the pure rotation g with Euler angles $(0, \arccos(1/\sqrt{3}), \pi/4)$. It is the inverse of the rotation matrix of equation (B.2). It can be checked that $\mathbf{e}'_3 = (-\mathbf{e}_1 + \mathbf{e}_2 + \mathbf{e}_3)/\sqrt{3}$ (i.e. the threefold axis is the z-axis of the site along the $(-1, 1, 1)$ direction of the cube) and $\mathbf{e}'_2 = (\mathbf{e}_1 + \mathbf{e}_2)/\sqrt{2}$ (i.e. the y axis of the site is along the $(1, 1, 0)$ direction of the cube). If h is a symmetry operation in the (cubic) crystal frame leaving the site invariant, the basis change formula of linear algebra implies that ghg^{-1} is the same symmetry operation in the (trigonal) site frame. A spherical tensor T^ℓ will be denoted by $T^\ell(3)$ when expressed in the trigonal site frame and by $T^\ell(4)$ when expressed in the cubic crystal frame. The arguments 3 and 4 mean that the z axis is along a threefold axis for a trigonal basis and a fourfold axis for a cubic basis. The relation between $T^\ell(3)$ and $T^\ell(4)$ is given by the formula

$$T^\ell_m(4) = \sum_{m'} T^\ell_{m'}(3) D^\ell_{m'm}(g). \qquad (18)$$

We now give two examples.

5.3. The example of spinel

We illustrate this method with the example of the aluminum site in spinel $MgAl_2O_4$, which is the prototype of the spinel structural family. The spinel structure is derived from a face-centered-cubic close-packing of oxygen atoms with a space group symmetry $Fd\bar{3}m$. The conventional cubic cell contains eight formula units, i.e. 32 oxygen atoms with 24 cations in tetrahedral and pseudo-octahedral interstices. With origin choice 2 [18], the Mg^{2+} cations occupy eight tetrahedral sites, which are located at the special 8a Wyckoff positions $(1/8, 1/8, 1/8)$, with $\bar{4}3m$ (T_d) point symmetry. The Al^{3+} cations occupy 16 pseudo-octahedral sites at the special 16d Wyckoff positions $(0, 1/4, 3/4)$, with $\bar{3}m$ (D_{3d}) point symmetry. This symmetry corresponds to a small elongation of the octahedron along the trigonal axis, arising from a small departure of the position of the oxygen atoms from the perfect fcc arrangement. The O^{2-} ions are located at the Wyckoff positions 32e (u, u, u) with point symmetry $3m$.

---

[1] The most prominent example is the package of multiplet programs written by Cowan, Butler, Thole, Ogasawara and Searle [13–17].

5.3.1. The site frame. The simplest expressions are obtained when the reference frame of the site is used. The point group of the site we consider is D_{3d}. The group D_{3d} has six pure rotations and the same six rotations multiplied by the inversion. We assume that the property we investigate is represented by an even tensor, so that we only have to consider the six pure rotations. It is natural to take the z-axis along the threefold axis and the y axis along one of the C_2 axes. The formulae do not depend on which C_2 axis is chosen. However, they would be different if the y axis were chosen, for example, between two C_2 axes. The six pure rotations are the unit, the C_3 rotation about the z-axis through the angle $2\pi/3$, its square C_3^2, the C_2 rotation about the y-axis through the angle π and the other two rotations C_3C_2 and $C_3^2C_2$. These rotations have Euler angles $(0,0,0)$, $(0,0,2\pi/3)$, $(0,0,4\pi/3)$, $(0,\pi,0)$, $(0,\pi,4\pi/3)$ and $(0,\pi,2\pi/3)$, respectively. These rotations will be denoted by $R_1,\ldots,R_6$, respectively.

To calculate the symmetrized tensors for this site, we use equation (17). The special cases given in appendix B.3.1 enable us to show that $D^{\ell}_{m'm}(R_1) = \delta_{m'm}$, $D^{\ell}_{m'm}(R_2) = \delta_{m'm}\mathrm{e}^{-2mi\pi/3}$ and $D^{\ell}_{m'm}(R_3) = \delta_{m'm}\mathrm{e}^{-4mi\pi/3}$. Therefore, the sum $\sum_{j=1}^{3} D^{\ell}_{m'm}(R_j)$ is $3\delta_{m'm}$ if m is an integer multiple of 3, and zero otherwise. We calculate the Wigner matrices for the other three rotations and we obtain

$$\frac{1}{|G'|}\sum_{R'} D^{\ell}_{m'm}(R') = \frac{1}{6}\sum_{j=1}^{6} D^{\ell}_{m'm}(R_j) = \frac{\delta_{m'm} + (-1)^{\ell-m}\delta_{m,-m'}}{2}$$

if m and m' are integer multiples of 3, and zero otherwise. Equation (17) is then applied to a general fourth-rank tensor $T^4_m(3)$, where the argument (3) denotes the trigonal axes, and we obtain the non-zero components of the symmetrized tensor $\langle T^4_m(3)\rangle$,

$$\langle T^4_0(3)\rangle = T^4_0(3),$$

$$\langle T^4_3(3)\rangle = -\langle T^4_{-3}(3)\rangle = \frac{T^4_3(3) - T^4_{-3}(3)}{2}.$$

For the second-rank tensor, all symmetrized components are zero, except for $\langle T^2_0(3)\rangle = T^2_0(3)$. Of course, we also have the relation $\langle T^0_0(3)\rangle = T^0_0(3)$, which is valid for any group. We now show that time-reversal symmetry implies that the symmetrized tensors are real. According to equation (4) $(T^{\ell}_0)^* = T^{\ell}_0$, so that T^{ℓ}_0 is real. Still, by equation (4) we have $(T^{\ell}_3)^* = -T^{\ell}_{-3}$. Thus, $\langle T^4_3(3)\rangle^* = (-T^4_{-3}(3) + T^4_3(3))/2 = \langle T^4_3(3)\rangle$ is real as well.

In x-ray absorption spectra, the symmetrized tensors are spectral functions depending on the photon energy. For the example of the electric quadrupole transitions we take, for each energy $\hbar\omega$,

$$T^{\ell} = \pi^2\alpha_0\hbar\omega \times \sum_f \{\langle f|\{\mathbf{r}\otimes\mathbf{r}\}^2|i\rangle^*\otimes\langle f|\{\mathbf{r}\otimes\mathbf{r}\}^2|i\rangle\}^{\ell}\delta(E_{\mathrm{f}} - E_{\mathrm{i}} - \hbar\omega),$$

where α_0 is the fine-structure constant and E_{i} and E_{f} the energies of the initial and final states. The symmetrized tensors $\langle T^{\ell}(3)\rangle$ can be calculated by multiplet programs. The value of these tensors for a chromium atom substituting for aluminum in spinel is given in figure 1 (see [1] for more details).

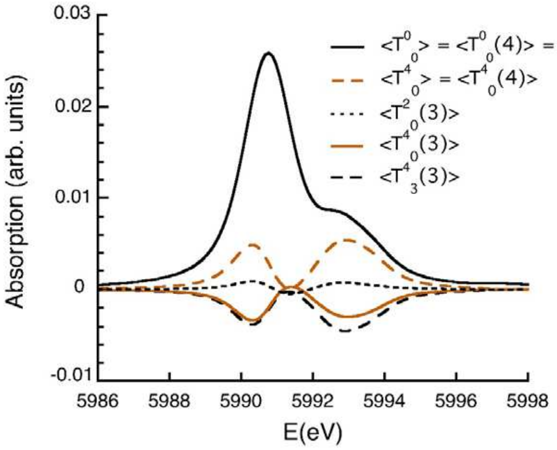

Figure 1. The symmetrized tensors $\langle T^0_0(3)\rangle$, $\langle T^2_0(3)\rangle$, $\langle T^4_0(3)\rangle$ and $\langle T^4_3(3)\rangle$ in the site frame, for the electric quadrupole transitions of the K edge of a chromium atom substituting for aluminum in spinel. After averaging over the sites, only the symmetrized tensors $\langle T^0_0\rangle$ and $\langle T^4_0\rangle$ remain as independent parameters.

5.3.2. The crystal frame. We consider now the same average in the crystal frame. The Al site with reduced coordinates $(0, 1/4, 3/4)$ has a threefold axis along the $(-1,1,1)$ direction and a twofold axis along the $(0,1,0)$ direction. Therefore, the six pure rotations of D_{3d} are now (i) the identity, denoted by (x,y,z), (ii) a C_3 rotation about $(-1,1,1)$, denoted by $(-y,z,-x)$, (iii) its square $(-z,-x,y)$, (iv) a rotation of π about $(1,1,0)$ denoted by $(y,x,-z)$, (v) a rotation of π about $(1,0,1)$ denoted by $(z,-y,x)$ and (vi) a rotation of π about $(0,1,-1)$ denoted by $(-x,-z,-y)$. The notation used for the rotations is the result of the operation $R\mathbf{r}$ in the cubic axes. For example, the C_3 rotation gives

$$R\mathbf{r} = \begin{pmatrix} 0 & -1 & 0 \\ 0 & 0 & 1 \\ -1 & 0 & 0 \end{pmatrix}\begin{pmatrix} x \\ y \\ z \end{pmatrix} = \begin{pmatrix} -y \\ z \\ -x \end{pmatrix}.$$

The corresponding Euler angles are $(0,0,0)$, $(\pi/2,\pi/2,0)$, $(\pi,\pi/2,\pi/2)$, $(0,\pi,\pi/2)$, $(0,\pi/2,\pi)$ and $(3\pi/2,\pi/2,3\pi/2)$.

We apply again equation (17) to the general second-rank tensor $T^2_m(4)$, where the argument (4) stands for the cubic axes. This gives us the symmetrized tensor $\langle T^2(4)\rangle$

$$\begin{aligned} \langle T^2_0(4)\rangle &= 0, \\ \langle T^2_{-2}(4)\rangle &= \langle T^2_2(4)\rangle^* = -\mathrm{i}\lambda, \\ \langle T^2_{-1}(4)\rangle &= -\langle T^2_1(4)\rangle^* = (1+i)\lambda, \end{aligned} \tag{19}$$

with

$$\lambda = \frac{\mathrm{Im}\, T^2_2(4) - \mathrm{Re}\, T^2_1(4) + \mathrm{Im}\, T^2_1(4)}{3},$$

where we have used time-reversal symmetry as in equation (4).

Note that λ is real. For the tensor $\langle T^4(4)\rangle$,

$$\begin{aligned}\langle T^4_0(4)\rangle = \sqrt{\tfrac{14}{5}}\langle T^4_4(4)\rangle = \sqrt{\tfrac{14}{5}}\langle T^4_{-4}(4)\rangle^* = \xi,\\ \langle T^4_{-3}(4)\rangle = -\langle T^4_3(4)\rangle^* = (1-i)\sqrt{7}\zeta,\\ \langle T^4_{-2}(4)\rangle = \langle T^4_2(4)\rangle^* = 2i\sqrt{2}\zeta,\\ \langle T^4_{-1}(4)\rangle = -\langle T^4_1(4)\rangle^* = (1+i)\zeta,\end{aligned} \tag{20}$$

with

$$\xi = \frac{7T^4_0(4) + \sqrt{70}\,\mathrm{Re}\,T^4_4(4)}{12},$$
$$\zeta = -\{\sqrt{7}(\mathrm{Re}\,T^4_3(4) + \mathrm{Im}\,T^4_3(4)) + 2\sqrt{2}\,\mathrm{Im}\,T^4_2(4) + \mathrm{Re}\,T^4_1(4) - \mathrm{Im}\,T^4_1(4)\}/24.$$

Note that ξ and ζ are real.

5.3.3. From site to crystal frame. From this example, it is clear that the symmetrized tensor $\langle T^\ell(3)\rangle$ in the site frame is much simpler than the same tensor $\langle T^\ell(4)\rangle$ in the crystal frame. The relation between the trigonal and cubic axes is worked out in appendix B.4.

To go from one to the other we apply equation (18) and we obtain the relations

$$\langle T^4_0(4)\rangle = -\frac{7\langle T^4_0(3)\rangle + 2\sqrt{70}\langle T^4_3(3)\rangle}{18}, \tag{21}$$

$$\langle T^4_{-2}(4)\rangle = \mathrm{i}\frac{\sqrt{10}\langle T^4_0(3)\rangle - \sqrt{7}\langle T^4_3(3)\rangle}{9}. \tag{22}$$

We recover equations (20) with

$$\zeta = \frac{2\sqrt{5}\langle T^4_0(3)\rangle - \sqrt{14}\langle T^4_3(3)\rangle}{36},$$
$$\xi = -\frac{7\langle T^4_0(3)\rangle + 2\sqrt{70}\langle T^4_3(3)\rangle}{18}.$$

For the second-rank tensor we find equations (19) with $\lambda = -\langle T^2_0(3)\rangle/\sqrt{6}$. For the zeroth-rank tensor we have obviously $\langle T^0_0(4)\rangle = \langle T^0_0(3)\rangle$.

5.4. The example of garnet

We consider now the Al site in garnet with the example of grossular $Ca_3Al_2(SiO_3)_4$, which is a cubic mineral with the space group $Ia\bar{3}d$. The conventional cubic cell contains 96 oxygen, 24 calcium, 24 silicium and 16 aluminum atoms. The Al^{3+} cations are at the 16a Wyckoff positions. We put vanadium at the Al site (1/2, 1/2, 0), which is a slightly distorted octahedron, with a small elongation along the (−1, 1, 1) axis of the cube, and has the $\bar{3}$ (C_{3i}) point symmetry.

We calculate the symmetrized tensor in the site frame as for spinel, but with the smaller symmetry group C_{3i}.

We find that the non-zero tensor components are [12] $\langle T^4_{-3}(3)\rangle$, $\langle T^4_0(3)\rangle$, $\langle T^4_3(3)\rangle$, $\langle T^2_0(3)\rangle$ and $\langle T^0_0(3)\rangle$, as illustrated in figure 2 (see [19] for more details).

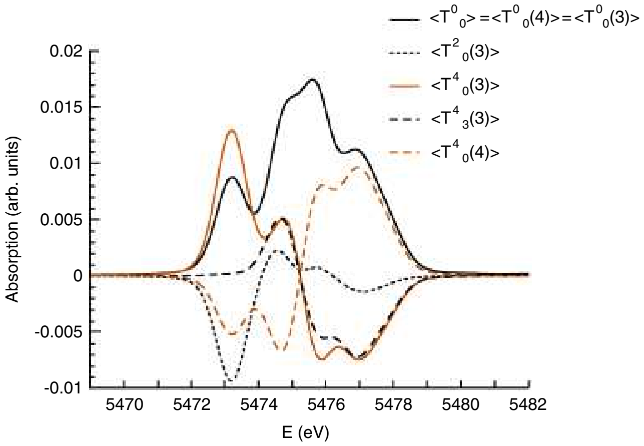

Figure 2. The symmetrized tensors $\langle T^0_0(3)\rangle$, $\langle T^2_0(3)\rangle$, $\langle T^4_0(3)\rangle$ and $\langle T^4_3(3)\rangle$ in the site frame, as well as $\langle T^4_0(4)\rangle$ (for $\alpha = 0$) in the crystal frame, for the electric quadrupole transitions at the K edge of a vanadium atom substituting for aluminum in grossular garnet.

It would not be very illuminating to calculate directly the symmetrized tensor in the crystal frame. It is more interesting to rotate the tensor. Indeed, when the site has a C_{3i} symmetry group, the z-axis of the orthonormal site frame is specified by the rotation axis, but the y-axis is arbitrary in the plane perpendicular to the rotation axis. This arbitrariness can be quite useful. For instance, the parametrization of the crystal-field Hamiltonian is simplified by choosing the y-axis so that a crystal-field parameter is set to zero (see [14] p 184). This simplifies the calculation of the eigenstates but the parameter reappears as the angle α between the y-axis and the (1, 1, 0) direction of the cube in the plane perpendicular to the (−1, 1, 1) direction.

The corresponding rotation matrix is

$$R = \sqrt{\frac{2}{3}}\begin{pmatrix}\cos(\alpha+\pi/3) & \cos(\alpha+2\pi/3) & \cos\alpha\\ \sin(\alpha+\pi/3) & \sin(\alpha+2\pi/3) & \sin\alpha\\ -1/\sqrt{2} & 1/\sqrt{2} & 1/\sqrt{2}\end{pmatrix}.$$

The Euler angles are α, $\beta = \arccos(1/\sqrt{3})$ and $\gamma = \pi/4$. The angle α describes a rotation about the axis (−1, 1, 1). Therefore, the α dependence of the result is very simple: $T^\ell_m(\alpha) = T^\ell_m(0)\mathrm{e}^{-mi\alpha}$, because the corresponding Wigner matrix is $D^\ell_{m'm} = \delta_{mm'}\mathrm{e}^{-\mathrm{i}m\alpha}$.

To calculate the symmetrized tensor $\langle T^4_m(4)\rangle$ in the cubic axes, we use equation (18), we put $s = \langle T^4_0(3)\rangle$, $t_r + \mathrm{i}t_i = \mathrm{e}^{-3\mathrm{i}\alpha}\langle T^4_3(3)\rangle$ and we obtain

$$\begin{aligned}\langle T^4_{-4}(4)\rangle = \langle T^4_4(4)\rangle^* = -\frac{\sqrt{70}s + 20t_r - 12\mathrm{i}\sqrt{3}t_i}{36},\\ \langle T^4_{-3}(4)\rangle = -\langle T^4_3(4)\rangle^* = (1-i)\frac{2\sqrt{35}s - 7\sqrt{2}t_r + 3\mathrm{i}\sqrt{6}t_i}{36},\\ \langle T^4_{-2}(4)\rangle = \langle T^4_2(4)\rangle^* = \mathrm{i}\frac{\sqrt{10}s - \sqrt{7}t_r}{9},\\ \langle T^4_{-1}(4)\rangle = -\langle T^4_1(4)\rangle^* = (1+i)\frac{2\sqrt{5}s - \sqrt{14}t_r + 3\mathrm{i}\sqrt{42}t_i}{36},\\ \langle T^4_0(4)\rangle = -\frac{7s + 2\sqrt{70}t_r}{18}.\end{aligned} \tag{23}$$

The symmetrized second-rank tensor in the cubic crystal frame is

$$\langle T_0^2(4)\rangle = 0,$$

$$\langle T_{-2}^2(4)\rangle = \langle T_2^2(4)\rangle^* = -\mathrm{i}\lambda,$$

$$\langle T_{-1}^2(4)\rangle = -\langle T_1^2(4)\rangle^* = (1+i)\lambda,$$

where $\lambda = -\langle T_0^2(3)\rangle/\sqrt{6}$ is real.

The effect of the angle α on the experimental spectrum can be considerable, as is illustrated in figure 3.

6. From site symmetry to crystal symmetry

We consider in this section another type of problem. We assume that we have calculated a symmetrized tensor $\langle T^\ell\rangle$ for a certain site A. We want to know the value of the same tensor for all the sites equivalent to A. In the first section, we describe how this can be done. In an x-ray absorption measurement, we measure the average of the signals coming from all sites of the crystal. We present two ways to calculate the average spectrum: the coset method and the brute force method. Finally, we treat the examples of spinel and garnet.

6.1. Changing site

In general, the symmetry of the crystal generates several equivalent sites. Assume that we have calculated a physical property described by a spherical tensor T^ℓ for a given site A. We want to calculate the same property for the equivalent site B.

If $\mathbf{r}_\mathrm{A}$ and $\mathbf{r}_\mathrm{B}$ are the position vectors of sites A and B, there is a symmetry operation g of the space group such that $\mathbf{r}_\mathrm{B} = g\mathbf{r}_\mathrm{A}$. If we denote by G_A and G_B the symmetry groups of sites A and B, then any rotoinversion h of G_A is transformed by g into the rotoinversion ghg^{-1} of G_B. A word of caution is in order here. There are two ways to consider h. If it is an element of the space group, it is generally not written as a rotoinversion because it can contain a translation when site A is not at (0, 0, 0). If the origin of the crystal frame is translated to A, then h is a rotoinversion but g contains now an additional translation. In practice, we can drop the translation of g and keep only its rotoinversion part. This will be done implicitly in the following (i.e. h and g will stand for the rotoinversion parts of the space group operations h and g).

The tensor $T^\ell(\mathrm{B})$ at site B is related to the tensor $T^\ell(\mathrm{A})$ at site A by the relation

$$T_m^\ell(\mathrm{B}) = \epsilon(g)\sum_{m'=-\ell}^{\ell} T_{m'}^\ell(\mathrm{A}) D_{m'm}^\ell(g^{-1}). \qquad (24)$$

We are now facing a typical subtlety of crystal symmetry. From equation (18), we could have expected the argument of the Wigner matrix to be g instead of g^{-1}. This is actually not the case because, by moving the atoms of the crystal, the operation g transports the reference frame of the site. Therefore, we are in the passive point of view and we need to use g^{-1} since our convention uses the active point of view.

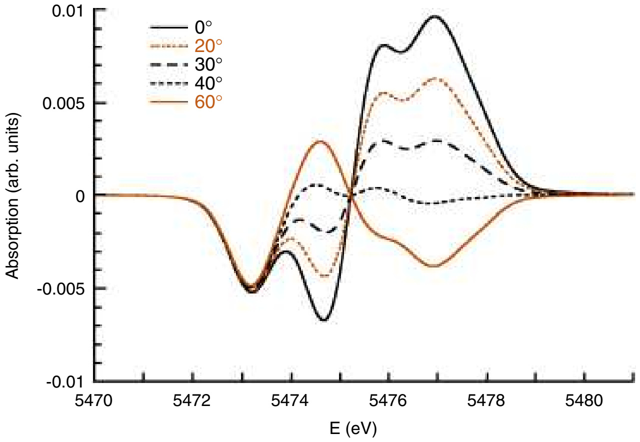

Figure 3. The symmetrized tensor $\langle T_0^4(4)\rangle$ in the crystal frame as a function of α, for the electric quadrupole transitions at the K edge of a vanadium atom substituting for aluminum in grossular garnet.

To check this, we calculate the symmetrized tensor around B.

$$\langle T_m^\ell(\mathrm{B})\rangle = \frac{1}{|G_\mathrm{B}|}\sum_{h_\mathrm{B}\in G_\mathrm{B}} \epsilon(h_\mathrm{B}) \sum_{m'=-\ell}^{\ell} T_{m'}^\ell(\mathrm{B}) D_{m'm}^\ell(h_\mathrm{B}).$$

Now, we can use the fact that, for each rotoinversion h_B of G_B there is a unique rotoinversion h_A of G_A such that $h_\mathrm{B} = gh_\mathrm{A}g^{-1}$. Therefore,

$$\langle T_m^\ell(\mathrm{B})\rangle = \frac{1}{|G_\mathrm{A}|}\sum_{h_\mathrm{A}\in G_\mathrm{A}} \epsilon(gh_\mathrm{A}g^{-1})$$

$$\times \sum_{m'=-\ell}^{\ell} T_{m'}^\ell(\mathrm{B}) D_{m'm}^\ell(gh_\mathrm{A}g^{-1}),$$

where we used $|G_\mathrm{A}| = |G_\mathrm{B}|$, a consequence of the isomorphism between G_A and G_B. We see that this is only compatible with the transformations $T^\ell(\mathrm{B}) = \epsilon(g)T^\ell(\mathrm{A})D^\ell(g^{-1})$ and $\langle T^\ell(\mathrm{B})\rangle = \epsilon(g)\langle T^\ell(\mathrm{A})\rangle D^\ell(g^{-1})$.

6.2. Changing the x-ray beam

If we have calculated the spectrum of site A for a given incident x-ray beam, it is possible to obtain the spectrum of any site equivalent to A by calculating the spectrum of site A for a rotated x-ray beam. This is physically clear because, if you rotate both the crystal and the x-ray, the spectrum does not change. Thus, if site A is measured with a polarization $\boldsymbol{\epsilon}$ and a wavevector $\mathbf{k}$, the spectrum obtained by applying the rotoinversion g on the crystal around A is same as the spectrum of the crystal in its original position, measured with a polarization $g^{-1}\boldsymbol{\epsilon}$ and a wavevector $g^{-1}\mathbf{k}$. To show this, we prove more generally that, if P^a and Q^a are two ath-rank tensors, then $P^a \cdot (gQ^a) = \epsilon_P(g)\epsilon_Q(g)(g^{-1}P^a)\cdot Q^a$. Equations (3) and (13) give us

$$P^a \cdot (gQ^a) = \epsilon_Q(g) P^a \cdot (Q^a D^a(g))$$
$$= \epsilon_Q(g)\sum_{\alpha\beta}(-1)^\alpha P_{-\alpha}^a Q_\beta^a D_{\beta\alpha}^a(g).$$

The symmetry relation (see [3], p 79) $D^a_{\beta\alpha}(g) = (-1)^{\beta-\alpha} D^a_{-\alpha-\beta}(g^{-1})$ enables us to write

$$
\begin{aligned}
P^a \cdot (gQ^a) &= \epsilon_Q(g) \sum_{\alpha\beta} (-1)^\beta P^a_{-\alpha} D^a_{-\alpha-\beta}(g^{-1}) Q^a_\beta \\
&= \epsilon_Q(g) \sum_{\beta} (-1)^\beta (P^a D^a(g^{-1}))_{-\beta} Q^a_\beta \\
&= \epsilon_Q(g)\epsilon_P(g)(g^{-1}P^a) \cdot Q^a,
\end{aligned}
$$

because $g^{-1}P^a = \epsilon(g^{-1})P^a D^a(g^{-1})$ and $\epsilon(g)\epsilon(g^{-1}) = 1$.

For the example of the electric dipole transition probability (15) we find

$$
\{\boldsymbol{\epsilon}^*\otimes\boldsymbol{\epsilon}\}^a \boldsymbol{\cdot} g(\{\mathbf{r}^*_{fi}\otimes\mathbf{r}_{fi}\}^a) = g^{-1}(\{\boldsymbol{\epsilon}^*\otimes\boldsymbol{\epsilon}\}^a) \boldsymbol{\cdot} \{\mathbf{r}^*_{fi}\otimes\mathbf{r}_{fi}\}^a. \tag{25}
$$

It remains to prove that the rotation of $\{\boldsymbol{\epsilon}^*\otimes\boldsymbol{\epsilon}\}^a$ corresponds to the rotation of $\boldsymbol{\epsilon}^*$ and $\boldsymbol{\epsilon}$. This is done by using the following identity:

$$
g\{P^a\otimes Q^b\}^c = \{(gP^a)\otimes(gQ^b)\}^c.
$$

To demonstrate the latter identity, we write the action of a rotoinversion g in terms of the parity operators and the Wigner matrices, and we write the coupled tensor in terms of the Clebsch–Gordan coefficients:

$$
g\{P^a\otimes Q^b\}^c_\gamma = \epsilon_P(g)\epsilon_Q(g) \sum_{\alpha\beta\gamma'} (a\alpha b\beta|c\gamma') P^a_\alpha Q^b_\beta D^c_{\gamma'\gamma}(g). \tag{26}
$$

The classical identity (C.4) transforms this expression into

$$
\begin{aligned}
g\{P^a\otimes Q^b\}^c_\gamma &= \epsilon_P(g)\epsilon_Q(g) \\
&\quad \times \sum_{\alpha\beta\alpha'\beta'} (a\alpha' b\beta'|c\gamma) P^a_\alpha Q^b_\beta D^a_{\alpha\alpha'}(g) D^b_{\beta\beta'}(g) \\
&= \sum_{\alpha'\beta'} (a\alpha' b\beta'|c\gamma)(gP)^a_{\alpha'}(gQ)^b_{\beta'} = \{(gP^a)\otimes(gQ^b)\}^c_\gamma.
\end{aligned}
$$

Equations (25) and (26) yield

$$
\{\boldsymbol{\epsilon}^*\otimes\boldsymbol{\epsilon}\}^a \boldsymbol{\cdot} g(\{\mathbf{r}^*_{fi}\otimes\mathbf{r}_{fi}\}^a) = \{(g^{-1}\boldsymbol{\epsilon}^*)\otimes(g^{-1}\boldsymbol{\epsilon})\}^a \boldsymbol{\cdot} \{\mathbf{r}^*_{fi}\otimes\mathbf{r}_{fi}\}^a.
$$

In other words, transforming the crystal by g gives the same result as transforming the x-ray beam by g^{-1}. The same result is true for the electric quadrupole transition probabilities, except for the fact that $\mathbf{k}$ is rotated by g^{-1} as well.

6.3. The coset method

The coset method is a powerful way to calculate the tensor averaged over the crystal from the tensor symmetrized over a single site. However, to make it work, we first need to modify the space group G. For this purpose, we choose a (not necessarily primitive) unit cell of the crystal. There is a group of translations T such that the action of T on the unit cell generates the crystal. We also assume that the group T is invariant under the operations of the point group of G (i.e. the set of rotoinversion parts of the operations of G). If we take the example of spinel, we can choose as a unit cell the conventional cubic cell, which is not primitive. The group T is generated by the pure translations along three orthogonal edges of the cube. If we choose the primitive rhombohedral cell, the group T will be generated by the rhombohedral axes.

To define the *reduced space group* $\overline{G}$, we first consider an equivalence relation where two space group operations are equivalent if their translational parts differ by an element of T. Then, the elements of $\overline{G}$ are the equivalence classes of G under this equivalence relation. We assume that the group T is invariant under the operations of the point group of the space group G. Thus, the product in G induces a product in $\overline{G}$ and $\overline{G}$ is a group. More intuitively, the operations of $\overline{G}$ can be obtained from the operations of G by applying periodic boundary conditions to the unit cell. Consider for instance the symmetry operation $g\mathbf{r} = (y + 1/4, x + 3/4, -z + 1/2)$. We have $g^2\mathbf{r} = (x + 1, y + 1, z)$ in G but $g^2\mathbf{r} = (x, y, z)$ in $\overline{G}$ because of the periodic boundary conditions. The group $\overline{G}$ has a very handy property: it is finite [4].

6.3.1. Mathematical aspects. We first introduce some mathematical concepts [6]. If g is an element of a group G and H a subgroup of G, the set $gH = \{gh : h \in H\}$ is called a *coset*. If we take two elements g and g' of G, then gH and $g'H$ are either identical or disjoint (i.e. they have no element in common). The number of different cosets is $n = |G|/|H|$ (it is an integer by the Euler–Lagrange theorem [6]), and the number of elements in each coset is $|H|$. Moreover, every element of G belongs to one and only one coset. Therefore, if we pick up an arbitrary element g_i in each coset, we have $G = g_1H \cup \cdots \cup g_nH$ and each g_i is called a *representative* of its coset.

6.3.2. Cosets in a crystal. We now apply these concepts to a crystal. We take the crystal symmetry group to be $\overline{G}$. By definition, the symmetry group of a site A is the set of operations of the space group G that leave site A invariant. It is the same as the set of operations of $\overline{G}$ that leave A invariant [4]. More precisely, if $\mathbf{r}_{\mathrm{A}}$ is the coordinate vector of site A, then $G_{\mathrm{A}} = \{g \in \overline{G} | g(\mathbf{r}_{\mathrm{A}}) = \mathbf{r}_{\mathrm{A}}\}$. It is clear that G_{A} is isomorphic to a subgroup of $\overline{G}$. In the unit cell, the number of sites equivalent to A is $n = |\overline{G}|/|G_{\mathrm{A}}|$. The group $\overline{G}$ is partitioned into n cosets $g_1G_{\mathrm{A}}, \ldots, g_nG_{\mathrm{A}}$. All the elements of a given coset send site A to the *same* equivalent site.

The symmetrized tensor $\langle T^\ell\rangle_X$ over the full crystal is obtained from the site-symmetrized tensor $\langle T^\ell\rangle_{\mathrm{A}}$ by the operation

$$
\langle T^\ell\rangle_X = \frac{1}{n} \sum_{i=1}^{n} \epsilon(g_i)\langle T^\ell\rangle_{\mathrm{A}} D^\ell(g_i^{-1}). \tag{27}
$$

Equation (27) can be described by saying that, starting from the average over the symmetry of site A, we go to all equivalent sites with g_i and we average over the symmetry of these other sites.

We show now that equation (27) gives the same result as an average over all crystal symmetry operations. We already know that

$$
\begin{aligned}
\langle T^\ell\rangle_{\mathrm{A}} &= \frac{1}{|G_{\mathrm{A}}|} \sum_{h\in G_{\mathrm{A}}} \epsilon(h) T^\ell D^\ell(h) \\
&= \frac{1}{|G_{\mathrm{A}}|} \sum_{h\in G_{\mathrm{A}}} \epsilon(h) T^\ell D^\ell(h^{-1}),
\end{aligned}
$$

because the sum over the elements of a group is the same as the sum over the inverse elements of this group and $\epsilon(h^{-1})=\epsilon(h)$. Therefore

$$\begin{aligned}\langle T^\ell\rangle_X &= \frac{1}{n|G_{\rm A}|}\sum_{i=1}^{n}\sum_{h\in G_{\rm A}}\epsilon(h)\epsilon(g_i)T^\ell D^\ell(h^{-1})D^\ell(g_i^{-1})\\ &= \frac{1}{|\overline{G}|}\sum_{i=1}^{n}\sum_{h\in G_{\rm A}}\epsilon(hg_i)T^\ell D^\ell(h^{-1}g_i^{-1})\\ &= \frac{1}{|\overline{G}|}\sum_{i=1}^{n}\sum_{h\in G_{\rm A}}\epsilon(g_ih)T^\ell D^\ell((g_ih)^{-1})\\ &= \frac{1}{|\overline{G}|}\sum_{g\in\overline{G}}\epsilon(g)T^\ell D^\ell(g),\end{aligned}$$

where we used $(g_ih)^{-1}=h^{-1}g_i^{-1}$ and $|\overline{G}|=n|G_{\rm A}|$. Note that the proof holds because we defined cosets to be $g_iG_{\rm A}$ (i.e. left cosets) and not $G_{\rm A}g_i$ (i.e. right cosets).

In other words, the average over the site symmetry followed by the average over the sites gives the average over the crystal symmetry. This can be considered as a factorization of the average, because $\sum_g=\sum_h\sum_{g_i^{-1}}$. It can be checked that the result of equation (27) is the same if we replace g_i by any g_i' in $g_iG_{\rm A}$. We illustrate the coset method with our two favorite examples, spinel and garnet.

6.3.3. The example of spinel. We call the site (0, 1/4, 3/4) of the spinel structure site A. The reduced space group $\overline{G}$ has 192 operations[2]. Twelve of them leave site A invariant: (x,y,z), $(-z+3/4,-x+1/4,y+1/2)$, $(-y+1/4,z-1/2,-x+3/4)$, $(y-1/4,x+1/4,-z+3/2)$, $(-x,1-z,1-y)$, $(z-3/4,-y+1/2,x+3/4)$, $(-x,-y+1/2,-z+3/2)$, $(z-3/4,x+1/4,1-y)$, $(y-1/4,1-z,x+3/4)$, $(-y+1/4,-x+1/4,z)$, $(x,z-1/2,y+1/2)$, and $(-z+3/4,y,-x+3/4)$. This set of 12 operations defines a group isomorphic to $\mathrm{D_{3d}}$. The isomorphism φ is described explicitly as follows. If $\mathbf{r}_{\rm A}$ is the coordinate vector of site A, for any operation g of the set, we define the operation $\varphi(g)$ by $\varphi(g)(\mathbf{r})=g(\mathbf{r}+\mathbf{r}_{\rm A})-\mathbf{r}_{\rm A}$. In practice, $\varphi(g)$ is obtained by removing the translation of g. The map φ is an isomorphism because $\varphi(g'g)=\varphi(g')\varphi(g)$:

$$\begin{aligned}&\varphi(g')\varphi(g)(\mathbf{r})=\varphi(g')(g(\mathbf{r}+\mathbf{r}_{\rm A})-\mathbf{r}_{\rm A})\\ &\quad=(g'g)(\mathbf{r}+\mathbf{r}_{\rm A})-\mathbf{r}_{\rm A}=\varphi(g'g)(\mathbf{r}),\end{aligned}$$

and it can be checked that the images by φ of the first six operations are the rotations listed in section 5.3.2, the images of the other six operations are the same rotations multiplied by the inversion. The space group operations g are selected by the condition that the site is fixed: $g(\mathbf{r}_{\rm A})=\mathbf{r}_{\rm A}$. Thus, the origin is a fixed point of $\varphi(g)$: $\varphi(g)(0)=g(\mathbf{r}_{\rm A})-\mathbf{r}_{\rm A}=0$.

There are 16 sites equivalent to A because the ratio $|Fd\bar{3}m|/|D_{3d}|$ is 16. However, each site is equivalent to three other sites by pure lattice translations with translation vectors (1/2, 1/2, 0), (1/2, 0, 1/2) and (0, 1/2, 1/2). The x-ray spectrum of these sites will be equal because their orientations with respect to the x-ray beam are the same. Therefore, we are left with four equivalent sites: A itself and the sites with coordinates (1/4, 3/4, 0), (3/4, 0, 1/4) and (1/2, 1/2, 1/2). A representative of the coset corresponding to each of these sites is (y,z,x), (z,x,y) and $(-x+1/2,y+1/4,z-1/4)$.

6.3.4. The example of garnet. We consider now site A as the Al site in grossular garnet with coordinates (1/2, 1/2, 0). It is invariant by the following six operations: identity, (x,y,z); rotation through $2\pi/3$ about the $(-1,1,1)$ axis, $(1-y,z+1/2,-x+1/2)$; rotation through $4\pi/3$ about the $(-1,1,1)$ axis, $(-z+1/2,1-x,y-1/2)$; and the same operations multiplied by the inversion, $(1-x,1-y,-z)$, $(y,-z+1/2,x-1/2)$ and $(z+1/2,x,-y+1/2)$. This group is $\mathrm{C_{3i}}$. The number of cosets (i.e. the number of sites equivalent to A) is $|Ia\bar{3}d|/|\mathrm{C_{3i}}|=16$. If we remove the lattice translation (1/2, 1/2, 1/2) we are left with eight equivalent sites.

The approach in terms of cosets is quite powerful in practice because it completely avoids the explicit description of the sites and of the geometric operations that transform a specific site into another one. Many programs compute the symmetry operations of the sites (for example Quantum-ESPRESSO [20]). It is thus enough to take one of these sites, to choose any representative g_i in each coset and to calculate the contribution of all equivalent sites by the formula $\epsilon(g_i)\langle T^\ell\rangle_{\rm A}D^\ell(g_i^{-1})$. The average over the crystal is then obtained with equation (27).

6.4. The brute force method

If one is not interested in the contribution of each site to the spectrum of the crystal, a still simpler solution is to take the average of $\langle T^\ell\rangle_{\rm A}$ over all the symmetry operations of the crystal. This is not very clever because the site operations have already been taken into account and we average over them a second time, but this method can simplify the computer implementation.

We show now that averaging the site-symmetrized tensor over all the symmetry operations of the crystal gives the same result as the coset method.

$$\begin{aligned}&\frac{1}{|\overline{G}|}\sum_{g\in\overline{G}}\epsilon(g)\langle T^\ell\rangle_{\rm A}D^\ell(g)\\ &\quad=\frac{1}{|G_{\rm A}||\overline{G}|}\sum_{h\in G_{\rm A}}\sum_{g\in\overline{G}}\epsilon(h)\epsilon(g)T^\ell D^\ell(h)D^\ell(g)\\ &\quad=\frac{1}{n|G_{\rm A}|^2}\sum_{h,h'\in G_{\rm A}}\sum_{i}\epsilon(h)\epsilon(h')\epsilon(g_i)\\ &\qquad\times T^\ell D^\ell(h)D^\ell(h')D^\ell(g_i^{-1})\\ &\quad=\frac{1}{n|G_{\rm A}|}\sum_{h\in G_{\rm A}}\sum_{i}\epsilon(h)\epsilon(g_i)T^\ell D^\ell(h)D^\ell(g_i^{-1})\\ &\quad=\langle T^\ell\rangle_X,\end{aligned}$$

where we used the identity $\sum_{h,h'\in G_{\rm A}}\epsilon(hh')D^\ell(hh')=|G_{\rm A}|\sum_{h\in G_{\rm A}}\epsilon(h)D^\ell(h)$. This equation is readily established by noting that, in the sum $\sum_{h,h'\in G_{\rm A}}$, each group element appears exactly $|G_{\rm A}|$ times.

Therefore, the average over all the symmetry operations of the crystal gives the same result as the average over the sites, irrespective of the number of equivalent sites.

---

[2] This is because we use the conventional cubic unit cell [18]. Using a primitive (rhombohedral) unit cell reduces this number to 48.

6.5. The case of spinel

We illustrate the coset method with the case of spinel. We first notice that the absorption cross-section is invariant under a translation of the Bravais lattice, because such a translation multiplies the wavefunction by a phase (independent of $\mathbf{r}$) that disappears in the square modulus. Therefore, by removing the translations, we can replace the representatives of the four cosets given in section 6.3.3 by the four rotations about the z-axis of the crystal through angles 0, $\pi/2$, π and $3\pi/2$. For a fourth-rank tensor, the average over these coset operations is rather drastic. The only non-zero elements of the matrix $M = (1/4)\sum_i D^4(g_i^{-1})$ are $M(-4,-4) = M(0,0) = M(4,4) = 1$. Therefore, the crystal-averaged fourth-rank tensor is $\langle T^4\rangle_X = \langle T^4(4)\rangle M$:

$$\langle T^4_0\rangle_X = \sqrt{\tfrac{14}{5}}\langle T^4_4\rangle_X = \sqrt{\tfrac{14}{5}}\langle T^4_{-4}\rangle_X = \langle T^4_0(4)\rangle.$$

The relation between $\langle T^4_0(4)\rangle$ and the site-symmetrized tensor in the trigonal axes is given by equation (21).

For a second-rank tensor, the matrix $M = (1/4)\sum_i D^2(g_i^{-1})$ has a single non-zero element: $M(0,0) = 1$. Therefore $\langle T^2_0\rangle_X = 0$, as expected [12].

6.6. The case of garnet

To calculate the spherical tensor of garnet, we use the brute force method and calculate $M = (1/48)\sum_g D^\ell(g)$, where the sum runs over all the symmetry operations of the cube and the tensor is assumed to be even.

For $\ell = 4$, the only non-zero matrix elements are

$$M(4,4) = M(-4,4) = M(4,-4) = M(-4,-4) = \tfrac{5}{24},$$

$$M(4,0) = M(0,4) = M(0,-4) = M(-4,0) = \tfrac{\sqrt{70}}{24},$$

$$M(0,0) = \tfrac{7}{12}.$$

Therefore, the only non-zero components of a fourth-rank tensor are

$$\begin{aligned}\langle T^4_0\rangle_X &= \sqrt{\frac{14}{5}}\langle T^4_4\rangle_X = \sqrt{\frac{14}{5}}\langle T^4_{-4}\rangle_X = \langle T^4_0(4)\rangle \\ &= -\frac{7s + 2\sqrt{70}t_r}{18},\end{aligned}$$

where we recall that $s = \langle T^4_0(3)\rangle$ and $t_r = (1/2)(\mathrm{e}^{-3\mathrm{i}\alpha}\langle T^4_3(3)\rangle + \mathrm{e}^{3\mathrm{i}\alpha}\langle T^4_3(3)\rangle^*)$.

7. Conclusion

We have tried to provide the main tools required for the calculation of a site-dependent property in a crystal. Although most of these methods are probably known to the expert, we were not able to find them presented in a systematic and pedagogical way. These tools proved quite efficient for the calculation of the x-ray absorption spectra of impurities in crystals [1]. The computation time was approximately divided by the number of equivalent sites of the crystal. Moreover, the group theoretical methods were useful to determine the properties of the spectra, for example the fact that the spectra of two sites have to be equal for a specific direction of the polarization vector.

The property we considered (x-ray absorption spectrum) is relatively simple because translations do not play any role. A similar calculation for x-ray scattering would require an explicit treatment of translations. The tools provided here can be extended to this case.

Acknowledgments

We thank Etienne Balan and Philippe Sainctavit for very constructive comments.

Appendix A. Spherical average

In Cartesian coordinates, the electric dipole absorption cross-section can be written, for linearly polarized x-rays, as

$$\sigma^D(\boldsymbol{\epsilon}) = \sum_{ij} \epsilon_i \epsilon_j \sigma_{ij},$$

with

$$\sigma_{ij} = 4\pi^2\alpha_0\hbar\omega \sum_f \langle i|\mathbf{r}_i|f\rangle\langle f|\mathbf{r}_j|i\rangle\delta(E_\mathrm{f} - E_\mathrm{i} - \hbar\omega).$$

It is well known that the absorption spectrum of a powder is given by the spherical average

$$\langle\sigma^D(\boldsymbol{\epsilon})\rangle = \tfrac{1}{3}(\sigma_{xx} + \sigma_{yy} + \sigma_{zz}).$$

For electric quadrupole transitions, the average is more complicated. If we write the electric quadrupole absorption cross-section for linearly polarized x-rays

$$\sigma(\boldsymbol{\epsilon}, \mathbf{k}) = \sum_{ijlm} \epsilon_i k_j \epsilon_l k_m \sigma_{ijlm}, \tag{A.1}$$

with

$$\sigma_{ijlm} = \pi^2\alpha_0\hbar\omega \sum_f \langle i|\mathbf{r}_i\mathbf{r}_j|f\rangle\langle f|\mathbf{r}_l\mathbf{r}_m|i\rangle\delta(E_\mathrm{f} - E_\mathrm{i} - \hbar\omega), \tag{A.2}$$

the absorption by a powder is given by the spherical average

$$\begin{aligned}\langle\sigma(\boldsymbol{\epsilon}, \mathbf{k})\rangle = \frac{k^2}{30}(&2\sigma_{xxxx} + 2\sigma_{yyyy} + 2\sigma_{zzzz} + 6\sigma_{xyxy} + 6\sigma_{xzxz} \\ &+ 6\sigma_{yzyz} - \sigma_{xxyy} - \sigma_{xxzz} - \sigma_{yyxx} - \sigma_{zzxx} \\ &- \sigma_{yyzz} - \sigma_{zzyy}).\end{aligned}$$

This average was obtained by substituting the second and third columns of the rotation matrix (B.1) for the unit vectors $\boldsymbol{\epsilon}$ and $\mathbf{k}/k$ in the absorption cross-section (A.1) and by averaging over all angles α, β and γ. The result was then simplified by using the symmetries of the tensor σ_{ijlm} that can be read from equation (A.2). If the system is non-magnetic, then $\sigma_{iijj} = \sigma_{jjii}$ and the average further simplifies

$$\begin{aligned}\langle\sigma(\boldsymbol{\epsilon}, \mathbf{k})\rangle = \frac{k^2}{15}(&\sigma_{xxxx} + \sigma_{yyyy} + \sigma_{zzzz} + 3\sigma_{xyxy} + 3\sigma_{xzxz} \\ &+ 3\sigma_{yzyz} - \sigma_{xxyy} - \sigma_{xxzz} - \sigma_{yyzz}).\end{aligned}$$

Appendix B. Formulae

B.1. Rotation matrix

In this section we give several expressions for the rotation matrices.

B.1.1. Axis and angle. The rotation through an angle ψ about the direction $\mathbf{n}$ (a unit vector) is represented by the rotation matrix $R = \mathrm{Id} + \sin\psi N + (1-\cos\psi)N^2$, where N is the skew-symmetric matrix with matrix elements $N_{ij} = -\sum_k \epsilon_{ijk} n_k$, so that $(N^2)_{ij} = n_i n_j - \delta_{ij}$ (see [2], p 10).

Conversely, the rotation angle ψ and the rotation axis $\mathbf{n}$ are determined from the rotation matrix R by the relations $\cos\psi = (\mathrm{tr}\, R - 1)/2$, $n_1 \sin\psi = (R_{32} - R_{23})/2$, $n_2 \sin\psi = (R_{13} - R_{31})/2$ and $n_3 \sin\psi = (R_{21} - R_{12})/2$. This is a corrected version of the relation given in [2] p 20.

B.1.2. Euler angles. The rotation matrix can be expressed in terms of the Euler angles α, β and γ (see [2], p 24)

$$R = \begin{pmatrix} c_\alpha c_\beta c_\gamma - s_\alpha s_\gamma & -c_\alpha c_\beta s_\gamma - s_\alpha c_\gamma & c_\alpha s_\beta \\ s_\alpha c_\beta c_\gamma + c_\alpha s_\gamma & -s_\alpha c_\beta s_\gamma + c_\alpha c_\gamma & s_\alpha s_\beta \\ -s_\beta c_\gamma & s_\beta s_\gamma & c_\beta \end{pmatrix}, \qquad \text{(B.1)}$$

where $0 \leqslant \alpha < 2\pi$, $0 \leqslant \beta \leqslant \pi$ and $0 \leqslant \gamma < 2\pi$, $c_\alpha = \cos\alpha$, $s_\alpha = \sin\alpha$ etc. There is a one-to-one correspondence between rotations and parameters in this range, except for the cases $\beta = 0$ and π, which describe the rotation through the angle $\alpha + \gamma$ and $\alpha - \gamma$, respectively, about the axis $(0, 0, 1)$.

B.1.3. Euler–Rodrigues parameters. Although the Euler angles are more common, the Euler–Rodrigues parameters have the advantage that the relation between these parameters and the rotation matrix elements does not involve trigonometric functions. Thus, they are convenient to derive analytical expressions. From the rotation axis $\mathbf{n}$ and angle ψ, we define the Euler–Rodrigues parameters $\alpha_0 = \cos(\psi/2)$, $\alpha_i = \sin(\psi/2)n_i$ ([2], p 54). In terms of these parameters, the rotation matrix is

$$R = \begin{pmatrix} \alpha_0^2 + \alpha_1^2 - \alpha_2^2 - \alpha_3^2 & 2\alpha_1\alpha_2 - 2\alpha_0\alpha_3 & 2\alpha_1\alpha_3 + 2\alpha_0\alpha_2 \\ 2\alpha_1\alpha_2 + 2\alpha_0\alpha_3 & \alpha_0^2 + \alpha_2^2 - \alpha_3^2 - \alpha_1^2 & 2\alpha_2\alpha_3 - 2\alpha_0\alpha_1 \\ 2\alpha_1\alpha_3 - 2\alpha_0\alpha_2 & 2\alpha_2\alpha_3 + 2\alpha_0\alpha_1 & \alpha_0^2 + \alpha_3^2 - \alpha_1^2 - \alpha_2^2 \end{pmatrix}.$$

Conversely, the Euler–Rodrigues parameters can be obtained from the rotation matrix R ([2], p 54). If $\mathrm{tr}\, R \neq -1$, then $\alpha_0 = \sqrt{\mathrm{tr}\, R + 1}/2$, $\alpha_1 = (R_{32} - R_{23})/(4\alpha_0)$, $\alpha_2 = (R_{13} - R_{31})/(4\alpha_0)$, and $\alpha_3 = (R_{21} - R_{12})/(4\alpha_0)$. If $\mathrm{tr}\, R = -1$, then $\alpha_0 = 0$ and $\alpha_i = (\mathrm{sign}\, \alpha_i)\sqrt{(1 + R_{ii})/2}$ for $i = 1, 2, 3$, with $\mathrm{sign}\, \alpha_1 = 1$, $\mathrm{sign}\, \alpha_2 = \mathrm{sign}\, R_{12}$, and $\mathrm{sign}\, \alpha_3 = \mathrm{sign}\, R_{13}$.

B.2. Solid harmonics

For a vector $\mathbf{r} = (x, y, z)$, the solid harmonics $Y_\ell^m(\mathbf{r})$ are defined by (see [2], p 71)

$$Y_\ell^m(\mathbf{r}) = \sqrt{\frac{(2\ell+1)(\ell+m)!(\ell-m)!}{4\pi}} \times \sum_k \frac{(-x-\mathrm{i}y)^{k+m}(x-\mathrm{i}y)^k z^{\ell-2k-m}}{2^{2k+m}(k+m)!k!(l-m-2k)!},$$

where k runs from $\max(0, -m)$ to the integer part of $(\ell - m)/2$. The most important example of solid harmonics is

$$Y_1(\mathbf{r}) = \sqrt{\frac{3}{4\pi}} \begin{pmatrix} \frac{x-\mathrm{i}y}{\sqrt{2}} \\ z \\ -\frac{x+\mathrm{i}y}{\sqrt{2}} \end{pmatrix},$$

where the upper component is $Y_1^{-1}(\mathbf{r})$.

B.3. Wigner matrices

There are several representations of the Wigner rotation matrices. We present here the expressions in terms of Euler angles and of Euler–Rodrigues parameters. Other formulae have been derived, for example the recent invariant spinor representation [21].

B.3.1. Euler angles. For a rotation R expressed in terms of Euler angles α, β, γ, the Wigner matrix is ([2], p 46)

$$D^\ell_{m'm}(R) = \mathrm{e}^{-\mathrm{i}m'\alpha} d^\ell_{m'm}(\beta) \mathrm{e}^{-\mathrm{i}m\gamma}.$$

Various expressions exist for the reduced Wigner matrix $d^\ell_{m'm}(\beta)$. The following formula (valid for half-integer ℓ) is particularly convenient for computers, because it (almost) avoids the presence of singular terms ([2], p 50, [3], p 78):

$$d^\ell_{m'm}(\beta) = (-1)^\lambda \sqrt{\frac{k!(2\ell-k)!}{(k+\mu)!(k+\nu)!}} \times \left(\sin\frac{\beta}{2}\right)^\mu \left(\cos\frac{\beta}{2}\right)^\nu P_k^{(\mu,\nu)}(\cos\beta),$$

where $\mu = |m - m'|$, $\nu = |m + m'|$, $k = \ell - (\mu + \nu)/2$ and $\lambda = 0$ if $m \geqslant m'$, $\lambda = m - m'$ if $m < m'$. In this expression, the only possible numerical difficulty occurs with 0^0, that should be set to unity. The Jacobi polynomials $P_k^{(\mu,\nu)}(x)$ are given by the formula

$$P_k^{(\mu,\nu)}(x) = \sum_{i=0}^k \binom{k+\mu}{i} \binom{k+\nu}{k-i} \left(\frac{x-1}{2}\right)^{k-i} \left(\frac{x+1}{2}\right)^i.$$

For example, the Wigner matrix for first-rank tensors is

$$D^1 = \begin{pmatrix} \frac{\cos\beta+1}{2}\mathrm{e}^{\mathrm{i}(\alpha+\gamma)} & \frac{\sin\beta}{\sqrt{2}}\mathrm{e}^{\mathrm{i}\alpha} & \frac{1-\cos\beta}{2}\mathrm{e}^{\mathrm{i}(\alpha-\gamma)} \\ -\frac{\sin\beta}{\sqrt{2}}\mathrm{e}^{\mathrm{i}\gamma} & \cos\beta & \frac{\sin\beta}{\sqrt{2}}\mathrm{e}^{-\mathrm{i}\gamma} \\ \frac{1-\cos\beta}{2}\mathrm{e}^{\mathrm{i}(\gamma-\alpha)} & -\frac{\sin\beta}{\sqrt{2}}\mathrm{e}^{-\mathrm{i}\alpha} & \frac{\cos\beta+1}{2}\mathrm{e}^{-\mathrm{i}(\alpha+\gamma)} \end{pmatrix},$$

where the upper left matrix element is D^1_{-1-1}. Two useful special cases are $d^\ell_{m'm}(0) = \delta_{mm'}$ and $d^\ell_{m'm}(\pi) = (-1)^{\ell-m}\delta_{m',-m}$.

B.3.2. Euler–Rodrigues parameters. In terms of the Euler–Rodrigues parameters, the Wigner rotation matrix is ([2], p 54)

$$\begin{aligned} D^\ell_{m'm}(R) = {} & \sqrt{(\ell+m')!(\ell-m')!(\ell+m)!(\ell-m)!} \\ & \times \sum_k \{(\alpha_0 - \mathrm{i}\alpha_3)^{\ell+m-k}(-\mathrm{i}\alpha_1 - \alpha_2)^{m'-m+k} \\ & \times (-\mathrm{i}\alpha_1 + \alpha_2)^k (\alpha_0 + \mathrm{i}\alpha_3)^{\ell-m'-k}\} \\ & \times \{(\ell+m-k)!(m'-m+k)!k!(\ell-m'-k)!\}^{-1}, \end{aligned}$$

where k runs from $\max(0, m - m')$ to $\min(\ell + m, \ell - m')$.

B.4. Butler's orientation

The powerful multiplet program developed by Thole and colleagues is based on Butler's conventions. For the calculation of trigonal sites in cubic crystals, it is necessary to know precisely the relation between the cubic and trigonal reference frames, which is not clearly stated in Butler's book. To determine it, we combine Butler's tables pp 522, 527 and 549 of [14]. This shows that the transition between spherical harmonics $|1m\rangle_3$ in the trigonal axes (i.e. in the O–D_3–C_3 basis) and spherical harmonics $|1m\rangle_4$ in the cubic axes (i.e. in the O–D_4–C_4 basis) is

$$|1-1\rangle_3 = |1-1\rangle_4 \frac{(1-i)(\sqrt{3}+1)}{\sqrt{24}} + |10\rangle_4 \frac{1}{\sqrt{3}} + |11\rangle_4 \frac{(1+i)(\sqrt{3}-1)}{\sqrt{24}},$$

$$|10\rangle_3 = |1-1\rangle_4 \frac{-1+i}{\sqrt{6}} + |10\rangle_4 \frac{1}{\sqrt{3}} + |11\rangle_4 \frac{1+i}{\sqrt{6}},$$

$$|11\rangle_3 = |1-1\rangle_4 \frac{(1-i)(\sqrt{3}-1)}{\sqrt{24}} + |10\rangle_4 \frac{-1}{\sqrt{3}} + |11\rangle_4 \frac{(1+i)(\sqrt{3}+1)}{\sqrt{24}}.$$

This can be rewritten

$$|1m\rangle_3 = \sum_{m'=-1}^{1} |1m'\rangle_4 D^1_{m'm}(R),$$

for the rotation R corresponding to the Euler angles $\alpha = 3\pi/4$, $\beta = \beta_0 = \arccos(1/\sqrt{3})$ and $\gamma = \pi$. This corresponds to the C_{3z} axis of D_3 along the $(-1, 1, 1)$ direction of the cube and the C_{2y} axis of D_3 along the $(1, 1, 0)$ direction of the cube (see figure 11.6 of [14], p 204). The inverse rotation has Euler angles $(0, \beta_0, \pi/4)$. More precisely, the rotation

$$R = R(3\pi/4, \beta_0, \pi) = \begin{pmatrix} 1/\sqrt{6} & 1/\sqrt{2} & -1/\sqrt{3} \\ -1/\sqrt{6} & 1/\sqrt{2} & 1/\sqrt{3} \\ \sqrt{2/3} & 0 & 1/\sqrt{3} \end{pmatrix}, \tag{B.2}$$

transforms any symmetry operation R' in the D_{3d} axes into the symmetry operation $RR'R^{-1}$ in the cubic axes.

Appendix C. Coupling identities

We gather some useful coupling formulae. If $\mathbf{a}$, $\mathbf{b}$, $\mathbf{c}$ and $\mathbf{d}$ are vectors, we denote by $\mathbf{a}^1$, $\mathbf{b}^1$, $\mathbf{c}^1$ and $\mathbf{d}^1$ the corresponding first-rank spherical tensors. Then, according to [3] p 66 and 67,

$$\{\mathbf{a}^1 \otimes \mathbf{b}^1\}^1 = \frac{\mathrm{i}}{\sqrt{2}} (\mathbf{a} \times \mathbf{b})^1. \tag{C.1}$$

$$\{\{\mathbf{a}^1 \otimes \mathbf{b}^1\}^0 \otimes \{\mathbf{c}^1 \otimes \mathbf{d}^1\}^0\}^0 = \tfrac{1}{3} (\mathbf{a} \cdot \mathbf{b})(\mathbf{c} \cdot \mathbf{d}). \tag{C.2}$$

$$\{\{\mathbf{a}^1 \otimes \mathbf{b}^1\}^2 \otimes \{\mathbf{c}^1 \otimes \mathbf{d}^1\}^2\}^0 = \tfrac{1}{\sqrt{5}} \big(\tfrac{1}{2} (\mathbf{a} \cdot \mathbf{c})(\mathbf{b} \cdot \mathbf{d}) + \tfrac{1}{2} (\mathbf{a} \cdot \mathbf{d})(\mathbf{b} \cdot \mathbf{c}) - \tfrac{1}{3} (\mathbf{a} \cdot \mathbf{b})(\mathbf{c} \cdot \mathbf{d})\big). \tag{C.3}$$

To prove equation (14), we start from the identity

$$\{P^a \otimes Q^b\}^c \cdot \{R^d \otimes S^e\}^c = (-1)^{2a+b-d} \sum_g (2c+1) \times \begin{Bmatrix} a & b & c \\ e & d & g \end{Bmatrix} \{P^a \otimes R^d\}^g \cdot \{Q^b \otimes S^e\}^g,$$

where g runs from $\max(|a-d|, |b-e|)$ to $\min(a+d, b+e)$ (see equation (13), p 70 of [3]). Equation (14) corresponds to the case $c = 0$ because of the special value of the $6j$-symbol (equation (1), p 299 of [3]),

$$\begin{Bmatrix} a & b & 0 \\ e & d & g \end{Bmatrix} = (-1)^{a+d+g} \frac{\delta_{ab}\delta_{de}}{\sqrt{(2a+1)(2d+1)}}.$$

The interplay between Wigner matrices and Clebsch–Gordan coefficients is described by the following identity (equation (5), p 85 of [3]):

$$\sum_\gamma (a\alpha b\beta|c\gamma) D^c_{\gamma\gamma'}(R) = \sum_{\alpha'\beta'} (a\alpha' b\beta'|c\gamma') D^a_{\alpha\alpha'}(R) D^b_{\beta\beta'}(R). \tag{C.4}$$

References

[1] Juhin A, Brouder Ch, Arrio M A, Cabaret D, Sainctavit Ph, Balan E, Bordage A, Calas G, Eeckhout S G and Glatzel P 2008 X-ray linear dichroism in cubic compounds: the case of Cr^{3+} in $\mathrm{MgAl_2O_4}$ *Phys. Rev.* B at press arXiv:cond-mat/0806.1586

[2] Biedenharn L and Louck J 1981 *Angular Momentum in Quantum Physics* (*Encyclopedia of Mathematics and its Applications* vol 8) (Reading, MA: Addison-Wesley)

[3] Varshalovich D A, Moskalev A N and Khersonskii V K 1988 *Quantum Theory of Angular Momentum* (Singapore: World Scientific)

[4] Cornwell J F 1984 *Group Theory in Physics* vol 1 (London: Academic)

[5] Wigner E 1959 *Group Theory* (New York: Academic)

[6] Ludwig W and Falter C 1996 *Symmetries in Physics: Group Theory Applied to Physical Problems* 2nd edn (Berlin: Springer)

[7] Goulon J 1989 Systèmes moléculaires: Dichroïsme circulaire naturel et magnétique dans les spectroscopies optiques ou d'excitation des couches internes *Rayonnement Synchrotron Polarisé, Électrons Polarisés et Magnétisme* ed E Beaurepaire, B Carrière and J P Kappler (Strasbourg: IPCMS) pp 333–86

[8] Natoli C, Brouder Ch, Sainctavit Ph, Goulon J, Goulon-Ginet C and Rogalev A 1998 Calculation of x-ray natural circular dichroism *Eur. Phys. J.* B **4** 1–11

[9] Carra P and Benoist R R 2000 X-ray natural circular dichroism *Phys. Rev.* B **62** R7703–6

[10] Carra P, Jerez A and Marri I 2003 X-ray dichroism in noncentrosymmetric crystals *Phys. Rev.* B **67** 045111

[11] Marri I and Carra P 2004 Scattering operators for E1–E2 x-ray resonant diffraction *Phys. Rev.* B **69** 113101

[12] Brouder Ch 1990 Angular dependence of x-ray absorption spectra *J. Phys.: Condens. Matter* **2** 701–38

[13] Cowan R D 1981 *The Theory of Atomic Structure and Spectra* (Berkeley, CA: University of California Press)

[14] Butler P H 1981 *Point Symmetry Group Applications* (New York: Plenum)

[15] Thole B T, van der Laan G, Fuggle J C, Sawatzky G A, Karnatak R C and Esteva J M 1085 3d x-ray-absorption lines and the $3\mathrm{d}^9 4\mathrm{f}^{n+1}$ multiplets of lanthanides *Phys. Rev.* B **32** 5107–18

[16] Kotani A, Ogasawara H, Okada K, Thole B T and Sawatzky G A 1989 Theory of multiplet structure in 4d core photoabsorption spectra of $\mathrm{CeO_2}$ *Phys. Rev.* B **40** 65–73

[17] Kuiper P, Searle B G, Rudolf P, Tjeng L H and Chen C T 1957 X-ray magnetic dichroism of antiferromagnet $\mathrm{Fe_2O_3}$: the

orientation of magnetic moments observed by Fe 2p x-ray-absorption spectroscopy *Phys. Rev. Lett.* **70** 1549–52

[18] Hahn T 2002 *International Tables for Crystallography: Volume A* 5th edn (Dordrecht: Kluwer–Academic)

[19] Bordage A *et al* 2008 Substitutional vanadium in garnet in preparation

[20] Baroni S, De Gironcoli S, Dal Corso A and Giannozzi P 2001 Phonons and related crystal properties from density-functional perturbation theory *Rev. Mod. Phys.* **73** 515

[21] Manakov N L, Meremianin A V and Starace A F 2001 Invariant spinor representations of finite rotation matrices *Phys. Rev.* A **64** 032105

2.4 Example of application

I have presented in this chapter the different theoretical tools I used to model the X-ray absorption spectra measured during my thesis. The monoelectronic and multielectronic approaches are complementary. The DFT approach allows the calculation of both the pre-edge and the edge whereas the multielectronic approach can simulate only the pre-edge. The LFM calculations provide quantitative information on the absorbing atom, such as the *p-d* hybridization mixing. The general formulas given in the spherical tensor development can be used in different ways, depending on the chosen approach, *i.e.* monoelectronic or multielectronic.

In the monoelectronic approach, the absorption cross-section is determined for the full crystal. In tsavorite, the vanadium can be incorporated in sixteen different sites. The average calculated spectra over the sixteen sites can be obtained in two different ways: a "brute force" method or the coset method. The brute force method is a straightforward approach which consists of repeating the calculation procedure for all equivalent sites and take the average spectrum. This method is very time-consuming due to the different calculation steps. It is indeed needed to relax the structure around the substituted vanadium atom in the aluminum site, carry out a self-consistent charge-density calculation with a core-hole on the absorbing atom and finally calculate the spectrum of the site in electric dipole and quadrupole approximations. A considerable amount of time can be saved if we use the coset method, described in the previous section. In the multielectronic approach, the absorption cross-section is determined for a single site. The absorption cross-section is expressed in the local symmetry and not for the crystal symmetry. The coset method permits to reconstruct the spectrum of the full crystal from that of a single site.

The application of these approaches combined with the coset method will be presented for tsavorite in Chap. 3 and for TiO_2:V^{4+} in Chap. 4. A publication I collaborated on summarizes the monoelectronic and multielectronic approaches and give another example with the case of Cr^{3+} in spinel $MgAl_2O_4$ [122]. This study is a part of Amélie Juhin's thesis, on the incorporation of chromium in spinels and garnets. Spinel is a cubic mineral, and Cr^{3+} is incorporated in a site with the D_{3d} symmetry. The structure and crystallographic data are identical to those given in Chap. 1 for the magnetite. The coset method is also used in the two ways described previously in this section, to save computational time in the monoelectronic calculations, and to reconstruct the full crystal spectrum from that of one site in the multielectronic calculations. This publication is included here in full.

PHYSICAL REVIEW B **78**, 195103 (2008)

X-ray linear dichroism in cubic compounds: The case of Cr^{3+} in $MgAl_2O_4$

Amélie Juhin,[1,*] Christian Brouder,[1] Marie-Anne Arrio,[1] Delphine Cabaret,[1] Philippe Sainctavit,[1] Etienne Balan,[1,2]
Amélie Bordage,[1] Ari P. Seitsonen,[1] Georges Calas,[1] Sigrid G. Eeckhout,[3] and Pieter Glatzel[3]
[1]*Institut de Minéralogie et de Physique des Milieux Condensés (IMPMC), UMR CNRS 7590, Université Pierre et Marie Curie, Paris 6 & Paris 7, IPGP, 4 Place Jussieu, 75052 Paris Cedex 05, France*
[2]*Institut de Recherche pour le Développement (IRD), UR T058, 213 rue La Fayette, 75480 Paris Cedex 10, France*
[3]*European Synchrotron Radiation Facility, 6 rue Jules Horowitz, BP 220, 38043 Grenoble Cedex, France*
(Received 9 June 2008; revised manuscript received 25 September 2008; published 7 November 2008)

The angular dependence (x-ray linear dichroism) of the Cr *K* pre-edge in $MgAl_2O_4{:}Cr^{3+}$ spinel is measured by means of x-ray absorption near-edge structure spectroscopy and compared to calculations based on density functional theory (DFT) and ligand field multiplet (LFM) theory. We also present an efficient method, based on symmetry considerations, to compute the dichroism of the cubic crystal starting from the dichroism of a single substitutional site. DFT shows that the electric dipole transitions do not contribute to the features visible in the pre-edge and provides a clear vision of the assignment of the $1s \rightarrow 3d$ transitions. However, DFT is unable to reproduce quantitatively the angular dependence of the pre-edge, which is, on the other side, well reproduced by LFM calculations. The most relevant factors determining the dichroism of Cr *K* pre-edge are identified as the site distortion and 3*d*-3*d* electronic repulsion. From this combined DFT, LFM approach is concluded that when the pre-edge features are more intense than 4% of the edge jump, pure quadrupole transitions cannot explain alone the origin of the pre-edge. Finally, the shape of the dichroic signal is more sensitive than the isotropic spectrum to the trigonal distortion of the substitutional site. This suggests the possibility to obtain quantitative information on site distortion from the x-ray linear dichroism by performing angular dependent measurements on single crystals.

DOI: 10.1103/PhysRevB.78.195103 PACS number(s): 61.72.Bb, 78.70.Dm, 71.15.Mb

I. INTRODUCTION

Transition metal elements play an essential role in physics (magnetic materials, superconductors, etc.), coordination chemistry (catalysis and metalloproteins), or geophysics (3*d* elements are major constituents of the Earth and planets). To understand the properties that transition elements impart to the materials they are inserted in, x-ray absorption near-edge structure (XANES) spectroscopy has been widely used since it provides unique information on their local surrounding and electronic structure. In particular, the position and intensity of the localized transitions observed at the *K* pre-edge ($1s \rightarrow 3d$ transitions) are sensitive to the cation oxidation state, the geometry of its environment (coordination number and symmetry), and the degree of admixture between *p* and *d* orbitals. For example, the shape and area of the pre-edge are commonly used to quantify the redox states of transition elements in crystals, glasses, and coordination complexes by comparison to those recorded on reference compounds.[1–3] However, it is not straightforward to obtain this kind of information on single crystals. Indeed, it is well known that the XANES spectra of noncubic crystals show an angular dependence when the polarization and the direction of the incident x-ray beam (here, designated as unit vectors, $\hat{\varepsilon}$ and $\hat{\mathbf{k}}$, respectively) are varied. For cubic crystals, the problem may seem at first sight more simple. Electric dipole transitions (e.g., $1s \rightarrow p$ transitions) are isotropic. They contribute mainly not only to the edge but also to the pre-edge if one of the three following situations is encountered: (i) there is *p*-*d* intrasite hybridization (e.g., the crystallographic site does not show an inversion center), (ii) the thermally activated vibrations remove the inversion center, and (iii) there is *p*-*d* intersite hybridization (in samples highly concentrated in the investigated element). Electric quadrupole transitions are anisotropic and the cubic crystal thus shows an angular dependence. The information carried by the pre-edge features can be derived for cubic crystals by taking advantage of this angular dependence. In particular, the respective proportion of electric dipole and electric quadrupole transitions in the pre-edge can be derived by measuring XANES spectra for various known orientations $(\hat{\varepsilon},\hat{\mathbf{k}})$ of the incident beam.[4] In addition, the symmetry of the crystallographic sites, which host the investigated element, is often a subgroup of the cubic group. The number of equivalent sites is given by the ratio of the multiplicity of the space group and the multiplicity of the point group. The XANES spectrum of the cubic crystal is thus the average over the equivalent sites of the individual site spectra. Hence, the derivation of structural and electronic information for a single site is not straightforward, which makes the use of group theory and theoretical computations mandatory.

Among cubic oxides, spinels have attracted considerable interest for their optical, electronic, mechanical, and magnetic properties.[5–7] In the Earth's interior, the formation of silicate spinels has major geophysical implications.[8] More specifically, $MgAl_2O_4$ spinels are used in a broad range of applications, including optically transparent materials, catalyst supports, nuclear waste management, and cement castables.[9–12] Cr^{3+} often substitutes for Al^{3+} in $MgAl_2O_4$, which causes a red color and makes natural Cr spinels valuable gemstones. Cr^{3+} is intentionally added to high-temperature refractory materials to improve their thermal and mechanical properties.[13] In $MgAl_2O_4$ spinel ($Fd\bar{3}m$ space-group symmetry), Al^{3+} cations occur at octahedral sites,

©2008 The American Physical Society

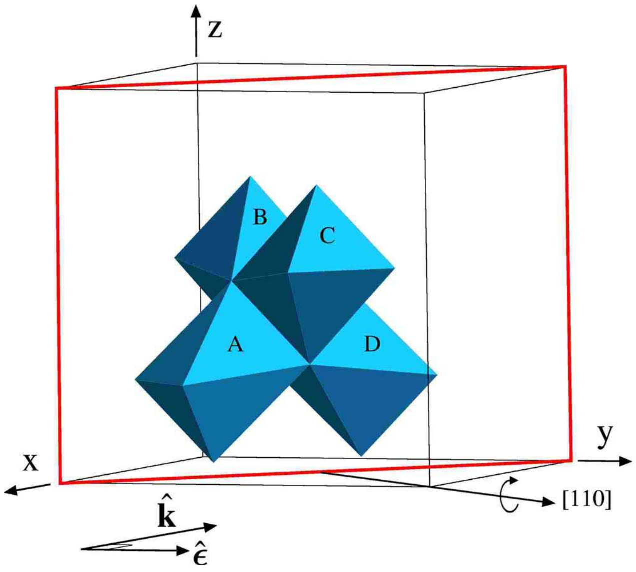

FIG. 1. (Color online) Cubic cell of the spinel structure and experimental setup. The four equivalent octahedral sites are labeled according to the coordinates given in Table I. Site distortion has been slightly exaggerated for clarity. The sample is cut along the (110) plane (red) and rotated along the [110] direction, while $\hat{\epsilon}$ and $\hat{\mathbf{k}}$ are fixed in the laboratory system. The figure corresponds to the experimental setup taken as starting point ($\alpha_{\mathrm{rot}}=0°$). For this configuration, the [001] axis of the cube is in the vertical plane, perpendicular to $\hat{\epsilon}=[010]$ and $\hat{\mathbf{k}}=[\bar{1}00]$.

which exhibit D_{3d} (or $\bar{3}m$) symmetry and build chains aligned along the six twofold axis of the cubic structure.[14] The number of equivalent octahedral sites in the unit cell is four, denoted hereafter as sites A, B, C, and D, depending on their direction of distortion, either $[\bar{1}11]$, $[11\bar{1}]$, [111], or $[1\bar{1}1]$, respectively (Fig. 1 and Table. I). During the Al to Cr substitution, the local D_{3d} symmetry is retained and the relaxed Cr site remains centrosymmetric, which indicates the absence of Cr $3d$-$4p$ mixing.[15] Hence, the K pre-edge features arise from pure electric quadrupole transitions ($1s \rightarrow 3d$) but an experimental evidence of this is still lacking. As the Cr site remains distorted in the same direction as for the Al site, four equivalent relaxed sites are available for Cr. Hence, the electric dipole and electric quadrupole absorption cross sections, for a given single-crystal configuration, are expected to be different for a Cr impurity located at sites A, B, C, or D since their orientations with respect to the incident beam are different.

In this paper, we compare the experimental angular dependence of the Cr K pre-edge $MgAl_2O_4:Cr^{3+}$ to those obtained by theoretical calculations, combining a monoelectronic approach based on density functional theory (DFT) and multielectronic methods based on the ligand field multiplet (LFM) theory. The monoelectronic approach is usually dedicated to the study of delocalized final states (e.g., the calculation of K-edge spectra) but has also provided satisfactory results for the study of Ti K pre-edge in TiO_2 and $SrTiO_3$ (Refs. 16–19) and also for the study of Fe K pre-edge in FeS_2.[20] The multielectronic approach, usually dedicated to the study of localized final states (e.g., K pre-edge and $L_{2,3}$ edges of $3d$ transition elements), has been successfully applied to the case of K pre-edge in several systems.[21,22] Our aim is to determine the factors (site distortion and electronic interactions) prevailing at the angular dependence of Cr K pre-edge in spinel and to provide a comparison between the monoelectronic and multielectronic approaches. We also present a powerful method, based on symmetry considerations, to reduce the number of calculations needed to reconstruct the angular dependence of the cubic crystal from that of a single site. The paper is organized as follows. Section II is dedicated to the experimental work, including the sample description, the x-ray absorption measurements, and analysis. Section III is devoted to the computational work, including the theoretical framework (Sec. III A) and the details of DFT calculations (Sec. III B 1) and of the multiplet calculations (Sec. III B 2). Results are presented in Sec. IV and discussed in Sec. V.

II. EXPERIMENTS

A natural gem-quality red spinel single crystal from Mogok (Burma), with composition $(Mg_{0.95}Fe_{0.01})_{0.96}(Al_{2.02}Cr_{0.01})_{2.03}O_4$, was investigated (for details, see Ref. 15). The single crystal was cut along the (110) plane (plotted in red on Fig. 1) and orientated according to the Laue method.

Cr K-edge (5989 eV) XAS spectra were collected at room temperature at beamline ID26 of the European Synchrotron Radiation Facility (Grenoble, France).[23] The energy of the incident radiation was selected using a pair of He-cooled Si crystals with (111) orientation. The spot size on the sample was approximately 250×50 μm^2. The orientated sample

TABLE I. Coordinates of Cr atom and direction of site distortion for the four equivalent substitutional sites belonging to the rhombohedral unit cell. We also give the coordinates of the 12 other sites obtained from the previous by the three translations of the *fcc* lattice (see text and Fig. 1).

Site identification	Direction of site distortion	Cr coordinates in rhombohedral unit cell	Cr coordinates in cubic cell
A	$[\bar{1}11]$	$(\frac{1}{2},\frac{1}{4},\frac{1}{4})$	$(\frac{1}{2},\frac{3}{4},\frac{3}{4})$, $(0,\frac{3}{4},\frac{1}{4})$, $(0,\frac{1}{4},\frac{3}{4})$
B	$[11\bar{1}]$	$(\frac{1}{4},\frac{1}{4},\frac{1}{2})$	$(\frac{3}{4},\frac{3}{4},\frac{1}{2})$, $(\frac{1}{4},\frac{3}{4},0)$, $(\frac{3}{4},\frac{1}{4},0)$
C	$[111]$	$(\frac{1}{2},\frac{1}{2},\frac{1}{2})$	$(0,0,\frac{1}{2})$, $(0,\frac{1}{2},0)$, $(\frac{1}{2},0,0)$
D	$[1\bar{1}1]$	$(\frac{1}{4},\frac{1}{2},\frac{1}{4})$	$(\frac{3}{4},\frac{1}{2},\frac{3}{4})$, $(\frac{1}{4},0,\frac{3}{4})$, $(\frac{3}{4},0,\frac{1}{4})$

was placed on a rotating holder at 45° with respect to the incident beam and turned around the [110] direction from a rotation angle α_{rot}. The starting configuration ($\alpha_{\text{rot}}=0°$) corresponds to $\hat{\boldsymbol{\varepsilon}}=[010]$ and $\hat{\mathbf{k}}=[\bar{1}00]$ (see Fig. 1). The ($\alpha_{\text{rot}}=90°$) configuration corresponds to $\hat{\boldsymbol{\varepsilon}}=[\frac{1}{2},\frac{1}{2},\frac{1}{\sqrt{2}}]$ and $\hat{\mathbf{k}}=[-\frac{1}{2},-\frac{1}{2},\frac{1}{\sqrt{2}}]$. For this sample cut and this experimental setup, the maximum variation effect is obtained by subtracting the absorption recorded for $\alpha_{\text{rot}}=0°$ from that recorded for $\alpha_{\text{rot}}=90°$. One spectrum was recorded every 15° from $\alpha_{\text{rot}}=0°$ to $\alpha_{\text{rot}}=360°$, which enables us to reconstruct the complete angular dependence of the crystal. The absorption was measured by a photodiode fluorescence detector. For each α_{rot} angle, ten pre-edge spectra ranging from 5987 to 5998 eV were recorded with an energy step of 0.05 eV and averaged. Two additional scans were recorded between 5985 and 6035 eV by step of 0.2 eV in order to merge the pre-edge on the XANES spectrum and two more spectra were recorded between 5950 and 6350 eV by step of 0.5 eV in order to normalize the XANES to the *K*-edge jump far from the edge. Self-absorption effects are negligible because of the low Cr content of the sample.

III. THEORY

In this section, we recall the general expressions of the electric dipole and electric quadrupole absorption cross sections for a cubic crystal and for a site with D_{3d} symmetry (Sec. III A). Then, we use the general method described in Ref. 24 to calculate the angular dependence of the cubic crystal from that of a single site. This framework is illustrated in the particular case of spinel. Finally, we report the details of the monoelectronic and multielectronic calculations performed for substitutional Cr in spinel (Secs. III B 1 and III B 2).

A. Theoretical framework

1. Absorption cross sections for a cubic crystal

The total absorption cross section for a crystal (cubic or noncubic), σ, is expressed as

$$\sigma(\hat{\boldsymbol{\varepsilon}},\hat{\mathbf{k}}) = \sigma^{D}(\hat{\boldsymbol{\varepsilon}}) + \sigma^{Q}(\hat{\boldsymbol{\varepsilon}},\hat{\mathbf{k}}), \tag{1}$$

where σ^D is the electric dipole cross section and σ^Q is the electric quadrupole cross section. The expression given above is valid in the absence of coupling between the electric dipole and the electric quadrupole terms; this condition is fulfilled if the system is either centrosymmetric or if, at the same time, the system is nonmagnetic (no net magnetic moment on the absorbing ion) and one uses exclusively linear polarization. For Cr in $MgAl_2O_4$, the two types of conditions are satisfied. The dipole and quadrupole cross sections can be expressed in function of spherical tensor components, respectively, $[\sigma^D(0,0),\ \sigma^D(2,m)]$ and $[\sigma^Q(0,0),\ \sigma^Q(2,m),\sigma^Q(4,m)]$, which transform under rotation such as the corresponding spherical harmonics (Y_0^0, Y_2^m, and Y_4^m).[25] The tensor components are functions of $\hbar\omega$, omitted for clarity in this paper. The symmetries of the crystal restrict the possible values of $\sigma^D(2,m)$ and $\sigma^Q(4,m)$, as will be precised hereafter for the cubic case.

The electric dipole cross section for a cubic crystal, σ^D_{cub}, is isotropic (e.g., it does not depend on the direction of the polarization vector) and is equal to $\sigma^D_{\text{cub}}(0,0)$,[25]

$$\sigma^D_{\text{cub}}(\hat{\boldsymbol{\varepsilon}}) = \sigma^D_{\text{cub}}(0,0). \tag{2}$$

The electric-quadrupole cross section for a cubic crystal, σ^Q_{cub}, is expressed, according to group theory (Appendix A), as

$$\sigma^Q_{\text{cub}}(\hat{\boldsymbol{\varepsilon}},\hat{\mathbf{k}}) = \sigma^Q_{\text{cub}}(0,0) + \frac{20}{\sqrt{14}}\left(\varepsilon_x^2 k_x^2 + \varepsilon_y^2 k_y^2 + \varepsilon_z^2 k_z^2 - \frac{1}{5}\right)\sigma^Q_{\text{cub}}(4,0), \tag{3}$$

where $\sigma^Q_{\text{cub}}(0,0)$ is the isotropic electric-quadrupole cross section and $\sigma^Q_{\text{cub}}(4,0)$ is a purely anisotropic electric-quadrupole term. The polarization unit vector $\hat{\boldsymbol{\varepsilon}}$ and the wave unit vector $\hat{\mathbf{k}}$ have their coordinates expressed in the Cartesian reference frame of the cube.

2. Absorption cross sections for a site with D_{3d} symmetry

For a site with D_{3d} symmetry, the reference frame is chosen consistently with the symmetry operations of the point group, i.e., with the z axis parallel to the C_3 axis of the D_{3d} group.[26] The polarization and the wave unit vectors are expressed as

$$\hat{\boldsymbol{\varepsilon}} = \begin{pmatrix} \sin\theta\cos\phi \\ \sin\theta\sin\phi \\ \cos\theta \end{pmatrix}$$

and

$$\hat{\mathbf{k}} = \begin{pmatrix} \cos\theta\cos\phi\cos\psi - \sin\phi\sin\psi \\ \cos\theta\sin\phi\cos\psi + \cos\phi\sin\psi \\ -\sin\theta\cos\psi \end{pmatrix}.$$

Hence, θ, which appears in the expression of $\hat{\boldsymbol{\varepsilon}}$ and $\hat{\mathbf{k}}$, is the angle between $\hat{\boldsymbol{\varepsilon}}$ and the C_3 axis.

The electric dipole absorption cross section in D_{3d} is given by[25]

$$\sigma^D_{D_{3d}}(\hat{\boldsymbol{\varepsilon}}) = \sigma^D_{D_{3d}}(0,0) - \frac{1}{\sqrt{2}}(3\cos^2\theta - 1)\sigma^D_{D_{3d}}(2,0). \tag{4}$$

In order to determine $\sigma^D_{D_{3d}}(\hat{\boldsymbol{\varepsilon}})$ for any experimental configuration ($\hat{\boldsymbol{\varepsilon}}$), one needs first to determine $\sigma^D_{D_{3d}}(0,0)$ and $\sigma^D_{D_{3d}}(2,0)$, for example, by performing calculations for at least two independent orientations of $\hat{\boldsymbol{\varepsilon}}$. The isotropic term, $\sigma^D_{D_{3d}}(0,0)$, can be calculated directly by choosing $\theta=\arccos\frac{1}{\sqrt{3}}$.

The electric quadrupole absorption cross section in D_{3d} is given by[25]

$$\begin{aligned}\sigma^Q_{D_{3d}}(\hat{\varepsilon},\hat{\mathbf{k}}) = {} & \sigma^Q_{D_{3d}}(0,0) + \sqrt{\frac{5}{14}}(3\sin^2\theta\sin^2\psi - 1)\sigma^Q_{D_{3d}}(2,0) \\ & + \frac{1}{\sqrt{14}}(35\sin^2\theta\cos^2\theta\cos^2\psi \\ & + 5\sin^2\theta\sin^2\psi - 4)\sigma^Q_{D_{3d}}(4,0) \\ & - \sqrt{10}\sin\theta[(2\cos^2\theta\cos^2\psi - 1)\cos\theta\cos 3\phi \\ & - (3\cos^2\theta - 1)\sin\psi\cos\psi\sin 3\phi]\sigma^Q_{D_{3d}}(4,3).\end{aligned} \tag{5}$$

To determine $\sigma^Q_{D_{3d}}(\hat{\varepsilon},\hat{\mathbf{k}})$ for any experimental configuration $(\hat{\varepsilon},\hat{\mathbf{k}})$, one needs first to determine $\sigma^Q_{D_{3d}}(0,0)$, $\sigma^Q_{D_{3d}}(2,0)$, $\sigma^Q_{D_{3d}}(4,0)$, and $\sigma^Q_{D_{3d}}(4,3)$, for example, by performing calculations for at least four independent orientations $(\hat{\varepsilon},\hat{\mathbf{k}})$.

3. From a single site D_{3d} to the cubic crystal

In order to reconstruct the angular dependence of the cubic crystal from that of a single site with D_{3d} symmetry, the tensor components have to be averaged over the equivalent sites of the cubic cell. For the electric dipole cross section, we need a relation between $[\sigma^D_{D_{3d}}(2,0), \sigma^D_{D_{3d}}(0,0)]$ and $\sigma^D_{\mathrm{cub}}(0,0)$, and for the electric quadrupole cross section, we need a relation between $[\sigma^Q_{D_{3d}}(0,0), \sigma^Q_{D_{3d}}(2,0), \sigma^Q_{D_{3d}}(4,0), \sigma^Q_{D_{3d}}(4,3)]$ and $[\sigma^Q_{\mathrm{cub}}(0,0), \sigma^Q_{\mathrm{cub}}(4,0)]$. To do so, we have used the formulas given in Ref. 24, which have been obtained from a spherical tensor analysis. This general method uses the symmetry operations of the crystal, which exchange the equivalent sites of the cubic cell, and is here illustrated in the case of spinel.

The averages over the four equivalent sites are given by[24]

$$\sigma^D_{\mathrm{cub}}(0,0) = \sigma^D_{D_{3d}}(0,0), \tag{6}$$

$$\sigma^D_{\mathrm{cub}}(2,0) = 0. \tag{7}$$

Similarly, we have[24]

$$\sigma^Q_{\mathrm{cub}}(0,0) = \sigma^Q_{D_{3d}}(0,0), \tag{8}$$

$$\sigma^Q_{\mathrm{cub}}(4,0) = -\frac{1}{18}[7\sigma^Q_{D_{3d}}(4,0) + 2\sqrt{70}\sigma^Q_{D_{3d}}(4,3)]. \tag{9}$$

4. Calculation of the absorption cross sections for the experimental orientations

The electric dipole isotropic cross section of the cubic crystal, $\sigma^D_{\mathrm{cub}}(\hat{\varepsilon})$, does not depend on the direction of the incident polarization vector $\hat{\varepsilon}$. Hence, it will be the same for every experimental configuration,

$$\sigma^D_{\mathrm{cub}}(\alpha_{\mathrm{rot}}) = \sigma^D_{\mathrm{cub}}(0,0). \tag{10}$$

For the sample cut and the experimental setup used in this study, the expression of the electric quadrupole cross section of the cubic crystal is given in function of the rotation angle α_{rot} by

$$\begin{aligned}\sigma^Q_{\mathrm{cub}}(\alpha_{\mathrm{rot}}) = {} & \sigma^Q_{\mathrm{cub}}(0,0) + \frac{1}{16\sqrt{14}}[-19 - 60\cos(2\alpha_{\mathrm{rot}}) \\ & + 15\cos(4\alpha_{\mathrm{rot}})]\sigma^Q_{\mathrm{cub}}(4,0).\end{aligned} \tag{11}$$

The connection between Eqs. (3) and (11) is made following the definition of $\hat{\varepsilon}$ and $\hat{\mathbf{k}}$ as functions of α_{rot} (Appendix B). Equation (11) shows that the total angular dependence of the cubic crystal is a π-periodic function. The fact that the rotation axis might not be perfectly aligned with the x-ray beam or that the sample might not be perfectly homogeneous could have introduced an additional 2π periodic component. This component would be removed from the signal, using a filtering algorithm, based on the angular dependence recorded from 0° to 360°.[20] In our experiments, this 2π periodic component was measured to be very small, and no filtering was applied.

For the present sample cut and experimental setup, the maximum variation in the electric quadrupole cross section is expected between $\alpha_{\mathrm{rot}}=0°$ and $\alpha_{\mathrm{rot}}=90°$.

(i) For $\alpha_{\mathrm{rot}}=0°$,

$$\sigma^Q_{\mathrm{cub}}(\alpha_{\mathrm{rot}}=0°) = \sigma^Q_0 - \frac{4}{\sqrt{14}}\sigma^Q_{\mathrm{cub}}(4,0). \tag{12}$$

(ii) For $\alpha_{\mathrm{rot}}=90°$,

$$\sigma^Q_{\mathrm{cub}}(\alpha_{\mathrm{rot}}=90°) = \sigma^Q_0 + \frac{7}{2\sqrt{14}}\sigma^Q_{\mathrm{cub}}(4,0). \tag{13}$$

(iii) The isotropic cross section is

$$\sigma^Q_{\mathrm{iso}} = \frac{1}{15}[8\sigma^Q_{\mathrm{cub}}(\alpha_{\mathrm{rot}}=90°) + 7\sigma^Q_{\mathrm{cub}}(\alpha_{\mathrm{rot}}=0°)] = \sigma^Q_{\mathrm{cub}}(0,0). \tag{14}$$

(iv) The dichroic term is

$$\sigma^Q_{\mathrm{dichro}} = \sigma^Q_{\mathrm{cub}}(\alpha_{\mathrm{rot}}=90°) - \sigma^Q_{\mathrm{cub}}(\alpha_{\mathrm{rot}}=0°) = \frac{15}{2\sqrt{14}}\sigma^Q_{\mathrm{cub}}(4,0). \tag{15}$$

B. Computational details

1. Density functional theory calculations

The computations of the electric dipole and electric quadrupole absorption cross sections were done using a first-principles total-energy code based on DFT in the local density approximation with spin polarization (LSDA).[27] We used periodic boundary conditions, plane-wave basis set, and norm conserving pseudopotentials[28] in the Kleinman-Bylander form.[29] The parameters for the pseudopotential generation are given in Ref. 15.

We started from a host structure of $MgAl_2O_4$, which is obtained by an *ab initio* energy minimization calculation. In this calculation, the lattice parameter was fixed to its experimental value,[30] while the atomic positions were allowed to vary to minimize the total energy and the interatomic forces. We then relaxed a 2×2×2 rhombohedral supercell containing one Cr atom in substitution for Al (i.e., 1 Cr, 31 Al, 16 Mg, and 64 O), with the basis vectors expressed in a cubic frame. The supercell was large enough to avoid interactions between neighboring Cr atoms. As the Cr impurity is in its high-spin state, the spin multiplet $S_z=\frac{3}{2}$ is imposed for the supercell. The atomic positions in the supercell were allowed to vary in order to minimize the total energy and the interatomic forces. We used a 90 Ry energy cutoff and a single k-point sampling in the Brillouin zone. The Cr site, after relaxation, still exhibits a D_{3d} symmetry, with an inversion center, one C_3 axis and three C_2 axis.

The Cr K-edge absorption cross section was computed using the method described in Refs. 31 and 32. First, we calculated self-consistently the charge density of the system, with a 1s core hole on the substitutional Cr atom. Then, the all-electron wave functions were reconstructed within the projector augmented wave framework.[33] The absorption cross section was computed as a continued fraction using a Lanczos basis constructed recursively.[34,35] We used a 70 Ry energy cutoff for the plane-wave expansion, one k point for the self-consistent spin-polarized charge-density calculation, and a Monkhorst-Pack grid of $3\times3\times3$ k points in the Brillouin zone for the absorption cross-section calculation. For the convolution of the continued fraction, we used an energy-dependent broadening parameter γ, which takes into account the main photoelectron damping modes (core-hole lifetime and imaginary part of the photoelectron self-energy). The energy-dependent γ used in this study is that of Ref. 36. The calculated spectrum was then shifted in energy to the experimental one: the maximum of absorption is set at 6008.5 eV. The absorption edge jump is set to 1, so that experimental and calculated spectra for all figures are normalized absorption. In such a way, the calculated pre-edge could be compared directly to the experimental one. As mentioned previously, the four substitutional sites will exhibit different spectra for the electric dipole and electric quadrupole operators since their orientations are different with respect to the incident beam absorption of x rays with given $(\hat{\varepsilon},\hat{\mathbf{k}})$. The general method to obtain the angular dependence measured for the cubic crystal is to compute the electric dipole and electric quadrupole absorption cross sections for a Cr impurity lying in each of the four trigonally distorted sites A, B, C, and D and then to take the average. However, this heavy *brute force* method requires the calculation of four monoelectronic potentials with core hole (after previous associated structural relaxation). The number of calculations can be drastically reduced if we take advantage of the symmetry properties of the crystal, which enables us to perform the calculations for only one substitutional site (site A, with coordinates of $(0,\frac{1}{4},\frac{3}{4})$ and direction of distortion $[\bar{1}11]$). This method is detailed in Appendix C.

Figure 2 presents the normalized electric quadrupole cross section calculated for the four equivalent sites for $\alpha_{\rm rot}=0°$ and $\alpha_{\rm rot}=90°$. The spectra calculated for $\alpha_{\rm rot}=0°$ (orange line) are equal for the four sites. For $\alpha_{\rm rot}=90°$, sites B and C give the same spectra (black solid line), as well as sites A and D (black dashed line). We observe a slight difference in intensity for the peak at 5993.2 eV; this is indeed a consequence of the fact that sites (A, D) and (B, C) have different orientations with respect to the incident beam and that their symmetry differs from O_h. Because the trigonal distortion of the octahedra is small in spinel, the anisotropic behavior of the sites is limited for the investigated configurations. However, the effect of the trigonal environment can have drastic consequences when the distortion is more pronounced.

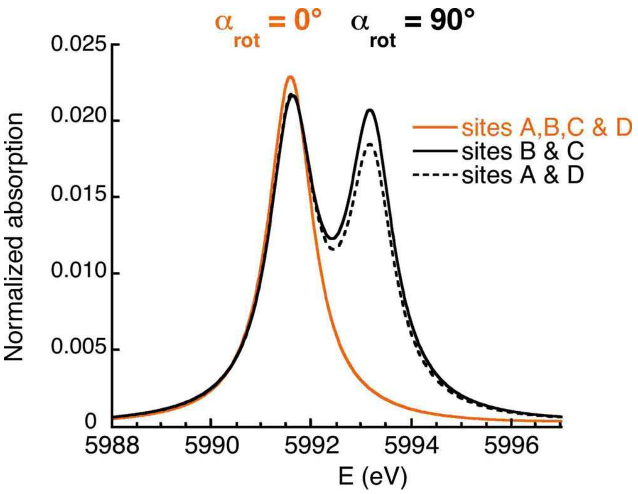

FIG. 2. (Color online) Pre-edge spectra calculated for sites A, B, C, and D in the electric quadrupole approximation. The orange lines present the spectra calculated for $\alpha_{\rm rot}=0°$ $(\hat{\varepsilon}=[010],\ \hat{\mathbf{k}}=[\bar{1}00])$, while the black lines are the spectra calculated for $\alpha_{\rm rot}=90°$ $(\hat{\varepsilon}=[\frac{1}{2},\frac{1}{2},\frac{1}{\sqrt{2}}],\ \hat{\mathbf{k}}=[-\frac{1}{2},-\frac{1}{2},\frac{1}{\sqrt{2}}])$.

2. Ligand field multiplet calculations

In order to extract quantitative information from the angular dependence of the pre-edge, we have performed LFM calculations using the method developed by Thole *et al.*[37] in the framework established by Cowan[38] and Butler.[26] In this approach, Cr^{3+} is considered as an isolated ion embedded in a crystal-field potential. The band structure of the solid is not taken into account, which prevents to calculate transitions to delocalized (i.e., nonatomic) levels. In other words, the LFM approach can be used to calculate K pre-edge spectra, but the edge region cannot be computed. Since the Cr site is centrosymmetric, no hybridization is allowed between the 3d orbitals and the 4p orbitals of Cr. Hence, the pre-edge is described by the transitions from the initial state $1s^2 3d^3$ to the final state $1s^1 3d^4$.[39]

We expose briefly the principles of multiplet calculations but details can be found in other references (see, for example, Ref. 40). This approach takes into account all the 3d-3d and 1s-3d electronic Coulomb interactions, as well as the spin-orbit coupling on every open shell of the absorbing atom, and treats its geometrical environment through a crystal-field potential. In the electric quadrupole approximation, the spectrum is calculated as the sum of all possible transitions for an electron jumping from the 1s level toward one 3d level according to

$$\sigma^Q(\hat{\varepsilon},\hat{\mathbf{k}}) = \pi^2 k^2 \alpha\hbar\omega \sum_{I,F} \frac{1}{d_I} |\langle F|\hat{\varepsilon}\cdot\mathbf{r}\hat{\mathbf{k}}\cdot\mathbf{r}|I\rangle|^2 \delta(E_F - E_I - \hbar\omega), \tag{16}$$

where $|I\rangle$ and $|F\rangle$ are the multielectronic initial and final states of respective energies E_I and E_F and d_I the degeneracy of the initial state.[41]

Once the $|I\rangle$ and $|F\rangle$ states have been calculated, the absolute intensities of the pre-edge spectra are calculated in Å^2 at $T=300$ K. The population of the ground-state levels $|I\rangle$ is given by a Boltzmann law. The spectra are convoluted by a Lorentzian [with half width at half maximum (HWHM) $=0.54$ eV] and a Gaussian [with full width at half maximum (FWHM) $=0.85$ eV], which, respectively, take into account the lifetime of the 1s core hole for Cr and the instrumental resolution. Finally, the transitions are normalized by the edge jump at the Cr K-edge, calculated for a Cr atom from Ref. 42 as 4.48 10^{-4} Å^2. Hence, the calculated spectra can be directly compared to the normalized experimental ones.

The electric quadrupole absorption cross section was calculated for a Cr^{3+} ion lying in D_{3d} symmetry, according to the method described above. The crystal-field parameters used in the calculation are those derived from optical absorption spectroscopy ($D_q=0.226$ eV, $D_\sigma=-0.036$ eV, $D_\tau=0.089$ eV).[43] We used the scaling factor of the Slater integrals ($\kappa=0.7$), related to B and C Racah parameters, given in the same reference. The only adjustable parameter is the absolute position in energy.

As mentioned in Sec. III A 2 [Eq. (5)], one needs first to determine $\sigma^Q_{D_{3d}}(0,0)$, $\sigma^Q_{D_{3d}}(2,0)$, $\sigma^Q_{D_{3d}}(4,0)$, and $\sigma^Q_{D_{3d}}(4,3)$, in order to determine $\sigma^Q_{\text{cub}}(0,0)$ and $\sigma^Q_{\text{cub}}(4,0)$ using Eqs. (8) and (9). This is done by performing four multiplet calculations, which provide four independent values of the electric-quadrupole cross section (Appendix D). Once this first step has been performed, we used Eqs. (8) and (9) to derive $\sigma^Q_{\text{cub}}(0,0)$ and $\sigma^Q_{\text{cub}}(4,0)$. The electric quadrupole cross section of the cubic crystal can then be calculated for any experimental configuration using Eq. (11). The electric quadrupole cross section for $\alpha_{\text{rot}}=0°$ and $\alpha_{\text{rot}}=90°$, the dichroic, and the isotropic spectra were determined, respectively, according to Eqs. (12)–(15).

IV. RESULTS

A. DFT calculations

1. Comparison with experiment

The XANES spectrum, calculated for the cubic crystal by first-principles calculations (solid line), is shown in Fig. 3 and compared to the experimental spectrum (dotted line). As we mentioned above, the main absorption edge is due to electric dipole transitions. Hence, the XANES spectrum does not show any angular dependence except in the pre-edge region. The agreement between the experimental and theoretical spectra is good since all the features are reproduced by the calculation. A more detailed discussion is reported in Ref. 15. The inset of Fig. 3 shows the theoretical isotropic XANES spectrum in the pre-edge region (black solid line).

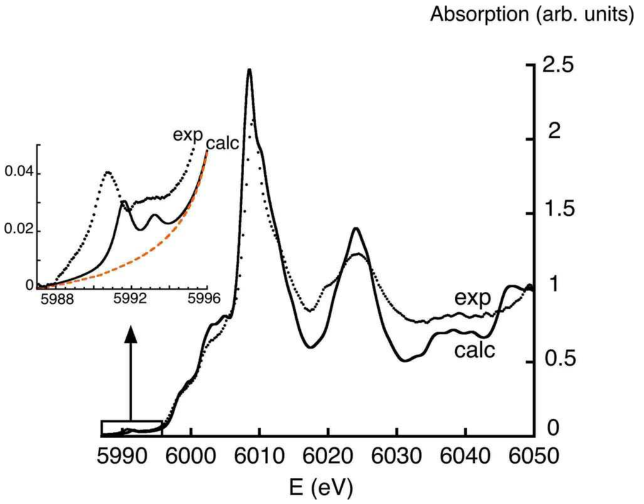

FIG. 3. (Color online) Comparison between experimental (dotted line) and calculated (solid line) isotropic XANES spectra at the Cr K-edge in spinel. The calculation was performed using DFT-LSDA (see Sec. III B 1). The inset presents the spectra in the pre-edge region. The dashed orange line is the calculated electric-dipole contribution.

This spectrum is the sum of the isotropic electric dipole (orange dashed line) and the electric quadrupole contributions. Our calculations show that electric dipole transitions do not contribute to the pre-edge, except by a background, which is actually the tail of the absorption edge ($1s\rightarrow p$ transitions). This is a clear confirmation that Cr K pre-edge features are due to a pure electric quadrupole contribution. In the pre-edge region, the calculated isotropic spectrum is in satisfactory agreement with experiment since the two features visible in the pre-edge are reproduced. Similar calculations have been successfully performed to calculate the K pre-edge for substitutional Cr^{3+} in corundum and beryl,[36,44] with a good agreement between the experimental and theoretical data. This shows that a monoelectronic approach can reproduce pre-edge features, as can be measured on powder spectra. However, the position of the theoretical spectrum is shifted by about 0.9 eV relative to experiment. This shift, which has been already observed in several systems,[17,20,36,44] is due the limitation of DFT-LSDA in the modeling of electron-hole interaction. In the calculation, the effect of the core hole is to shift the 3d levels to lower energy, with respect to the main edge. Unfortunately, this effect is not sufficient to reproduce the experimental data because the core hole seems to be partly screened.[16] This could be improved by taking into account the self-energy of the photoelectron.[45]

The experimental and calculated pre-edge spectra for the two configurations, which give the maximum dichroic signal for the sample cut, are shown in Fig. 4. The number of peaks is well reproduced in both cases by the calculation. For both spectra, the intensity of the first peak at about 5990.7 eV is close to 4% of the absorption edge on the experimental data but underestimated by 25% in the calculation. The relative intensity of the peak at about 5992.7 eV is overestimated in the 90° configuration. Additionally, the energy splitting between the two peaks is underestimated by the calculation

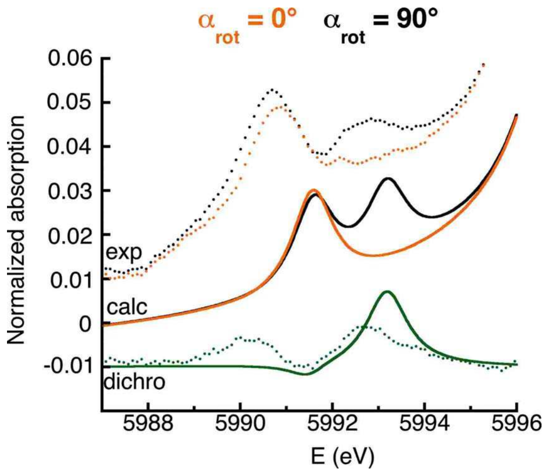

FIG. 4. (Color online) Comparison between experimental (dotted line) and calculated (solid line) Cr K-pre-edge spectra in spinel using DFT-LSDA. The orange lines correspond to $\hat{\varepsilon}=[010]$, $\hat{\mathbf{k}}=[\bar{1}00]$ ($\alpha_{\text{rot}}=0°$). The black lines correspond to $\hat{\varepsilon}=[\frac{1}{2},\frac{1}{2},\frac{1}{\sqrt{2}}]$, $\hat{\mathbf{k}}=[-\frac{1}{2},-\frac{1}{2},\frac{1}{\sqrt{2}}]$ ($\alpha_{\text{rot}}=90°$). The dichroic signal (green lines) is the difference between the black and red lines for the experimental (dotted) and the calculated spectra (solid), respectively.

(1.6 eV vs 2.0 eV experimentally). The small energy shift of the first peak between the two configurations, observed as positive in the experimental data, is calculated as negative. As a consequence of those several discrepancies, the theoretical dichroic signal is not in good agreement with the experimental one. Compared to the Ti K pre-edge calculations in rutile and SrTiO$_3$, using a similar monoelectronic approach and reported in several studies,[16–19] the significant discrepancy observed for Cr in spinel may seem at first sight unexpected. However, we underline the fact that interlectronic repulsions become crucial for localized final states (e.g., for $1s\rightarrow 3d$ transitions) and that Ti has no d electrons in the systems studied. This shows that the electronic interactions on the Cr atom are too significant to reproduce quantitatively the angular dependence of Cr spinel in a monoelectronic approach, although the average description (i.e., the isotropic spectrum) is satisfactory.

Nevertheless, the monoelectronic calculation is able to reproduce the correct number of peaks. Since this monoelectronic approach does not take into account spin-orbit coupling and does not fully describe the $3d$-$3d$ electronic repulsion, a monoelectronic chemical vision of an isolated Cr^{3+} ion can be applied for the interpretation of the calculated features.

2. Assignment of the calculated monoelectronic transitions within an atomic picture

In the following, we shall concentrate on the spectra associated to the local symmetry (i.e., calculated for site A). In the monoelectronic calculations, the spin multiplet $S_z=\frac{3}{2}$ is imposed for the supercell since the Cr impurity is in its high-spin state. Cr^{3+} has an initial electronic configuration $(t_{2g}^{\uparrow})^3(e_g)^0$, which means that Cr^{3+} is a fully magnetized paramagnetic ion in the calculation, while it is paramagnetic in the experiment. Indeed, it is not possible to impose the fourfold-degenerate $S=\frac{3}{2}$ ground state in the DFT calculation, which requires nondegenerate ground states. In order to assign the transitions visible in the experimental spectra, we would need to calculate the average of the spectra for $S_z=\frac{3}{2}$, $S_z=-\frac{3}{2}$, $S_z=\frac{1}{2}$, and $S_z=-\frac{1}{2}$. However, it is not possible to do the calculation for $S_z=\pm\frac{1}{2}$ in the Kohn-Sham formalism since they are linear combinations of three Slater determinants.[46] Nevertheless, the spin-polarized computation of the XANES spectrum for $S_z=\frac{3}{2}$ enables us to understand the origin of the pre-edge features: the contribution of the two spins (↑ and ↓) can be indeed separated, which means that we can deduce whether the $3d$ orbitals have been reached by a $1s$ electron with spin ↑ or ↓, and this for different expressions of the electric quadrupole operator.

As shown in Fig. 1, although the distortion of the octahedra has been slightly exaggerated, the oxygen ligands are located approximately along the fourfold axis of the cube for all the equivalent sites A, B, C, and D. Thus, the analysis made for site A provides an assignment, which is also valid (*mutatis mutandis*) for the equivalent sites. For a given configuration $(\hat{\varepsilon},\hat{\mathbf{k}})$, we can easily deduce from the expression of the electric quadrupole operator which $3d$ orbital has been probed in this transition. The interpretation of the features is possible through group theory in the monoelectronic approach using the branching rules of $O_h\supset D_{3d}$ (Appendix E). The d orbitals belong to the $t_{2g}(O_h)$ and $e_g(O_h)$ irreducible representations within octahedral symmetry. When lowering the symmetry to D_{3d}, the $t_{2g}(O_h)$ irreducible representation is split into the $e_g(D_{3d})$ and $a_{1g}(D_{3d})$ irreducible representations. To indicate that they come from $t_{2g}(O_h)$, they will be written as $e_g(t_{2g})$ and $a_{1g}(t_{2g})$. The $e_g(O_h)$ irreducible representation becomes the $e_g(D_{3d})$ irreducible representation, designed hereafter as $e_g(e_g)$.

The normalized electric quadrupole cross sections calculated for site A are shown in Fig. 5 for three different configurations $(\hat{\varepsilon},\hat{\mathbf{k}})$. For a better understanding of the structures, the electric quadrupole transitions to both occupied and empty states are represented. For $(\hat{\varepsilon}=[\frac{1}{\sqrt{2}},\frac{1}{\sqrt{2}},0]$, $\hat{\mathbf{k}}=[\frac{1}{\sqrt{2}},-\frac{1}{\sqrt{2}},0])$ [Fig. 5(a)], the electric quadrupole operator is expressed as $\hat{O}_a=\frac{1}{2}(x^2-y^2)$, which enables us to probe the $3d$ electronic density in the x^2-y^2 direction, i.e., along Cr-O bonds: the orbitals probed are the $e_g(e_g)$, which are empty for spins ↑ and ↓, since they are coming from the $e_g(O_h)$ levels. Figure 5(a) shows that, indeed, two peaks are obtained at 5991.6 and 5993.2 eV above the Fermi level. Below the Fermi level at 5990 eV, a broad structure is observed between 5982 and 5990 eV, which corresponds to e_g states hybridized with the p orbitals of the oxygens.

For $\alpha_{\text{rot}}=0°$ ($\hat{\varepsilon}=[010]$, $\hat{\mathbf{k}}=[\bar{1}00]$), one single peak is obtained in the empty states at 5991.6 eV for spin ↓ [see Fig. 5(b), black line]. For this orientation, the electric quadrupole operator, expressed as $\hat{O}_b=xy$, enables us to probe the d electronic density, projected on Cr, in the xy direction, i.e., between the Cr-O bonds. The $e_g(t_{2g})$ and $a_{1g}(t_{2g})$ orbitals having a component along xy, as indicated by their expressions in Appendix D [Eq. (E4)], they are probed in the transition. As these states coming from the $t_{2g}^{\uparrow}(\mathrm{O}_h)$ are fully occupied,

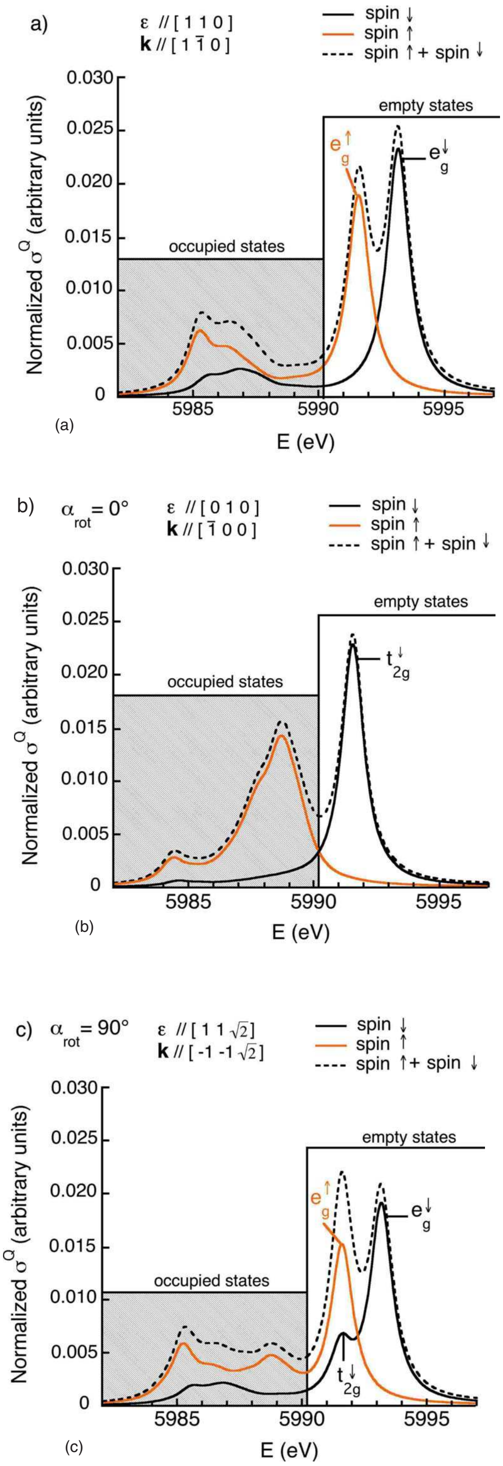

FIG. 5. (Color online) Electric quadrupole transitions calculated for site A using spin polarization. The upper panel (a) presents the spectrum calculated for ($\hat{\boldsymbol{\varepsilon}}=[\frac{1}{\sqrt{2}},\frac{1}{\sqrt{2}},0]$, $\hat{\mathbf{k}}=[\frac{1}{\sqrt{2}},-\frac{1}{\sqrt{2}},0]$). The middle panel (b) presents the spectrum calculated for $\alpha_{\text{rot}}=0°$ ($\hat{\boldsymbol{\varepsilon}}=[010]$, $\hat{\mathbf{k}}=[\bar{1}00]$). Lower panel (c) presents the spectrum calculated for $\alpha_{\text{rot}}=90°$ ($\hat{\boldsymbol{\varepsilon}}=[\frac{1}{2},\frac{1}{2},\frac{1}{\sqrt{2}}]$, $\hat{\mathbf{k}}=[-\frac{1}{2},-\frac{1}{2},\frac{1}{\sqrt{2}}]$). For each configuration, the respective contributions of the two spins are plotted (black solid line for spin down, orange solid line for spin up), as well as the sum (dashed line). The Fermi level is located approximately around 5990 eV.

they can be reached only by a photoelectron with spin ↓. This is indeed consistent with our results. The splitting between $e_g^{\downarrow}$ and $a_{1g}^{\downarrow}$ is not visible, which is an indication of a small trigonal distortion for the Cr site in spinel. Below the Fermi level, a broad structure with an intense peak at 5988.7 eV is observed. The intense peak corresponds to the occupied $e_g^{\uparrow}(t_{2g})$ levels. To interpret the origin of the broad structure, we have to remind that the $e_g(t_{2g})$ states can hybridize with the $e_g(e_g)$ levels since they belong to the same irreducible representation in D_{3d}. As mentioned previously, the hybridization of the mixed e_g states with the p orbitals of the oxygens gives rise to the structures visible below 5988 eV.

For $\alpha_{\text{rot}}=90°$ ($\hat{\boldsymbol{\varepsilon}}=[\frac{1}{2},\frac{1}{2},\frac{1}{\sqrt{2}}]$, $\hat{\mathbf{k}}=[-\frac{1}{2},-\frac{1}{2},\frac{1}{\sqrt{2}}]$) [Fig. 5(c)], two peaks are obtained above the Fermi level. For this orientation, the electric quadrupole operator is expressed as $\hat{O}_c=\frac{3z^2-r^2}{4}-\frac{xy}{2}$, which enables us to probe the $3d$ electronic density both in the xy and $3z^2-r^2$ directions. For the $3z^2-r^2$ component, the levels probed are the $e_g(e_g)$, as for the first orientation studied [Fig. 5(a)]. For the xy component, the levels probed are the $e_g(t_{2g})$ and $a_{1g}(t_{2g})$, as for the second orientation [Fig. 5(b)]. Figure 5(c) shows that the spectrum is a close combination of the transitions visible on the two previous spectra [Figs. 5(a) and 5(b)], and the assignment of the structures is made clear from the two previous cases. The position of the $t_{2g}^{\downarrow}(e_g)$ peak is close to that of the $e_g^{\uparrow}(e_g)$ at 5991.6 eV. The energy difference (1.6 eV) between $t_{2g}^{\downarrow}(e_g)$ and $e_g^{\downarrow}(e_g)$ gives an idea of the $t_{2g}^{\downarrow}(O_h)$-$e_g^{\downarrow}(O_h)$ splitting due to the crystal field. This can be compared to the experimental crystal-field splitting (2.26 eV), derived from optical absorption spectroscopy, but one should keep in mind that the crystal-field splitting in the monoelectronic picture is associated with spin ↑ levels.

For the configuration $\hat{O}_c$, the $3z^2-r^2$ component enables us to probe the $e_g(O_h)$ states, as x^2-y^2. Considering the normalization factors in the expression of the d orbitals, the magnitude of the transition operator along $3z^2-r^2$ is $\sqrt{3}$ times bigger than the magnitude of the transition operator along x^2-y^2, which is two times bigger than the magnitude of the transition operator along xy. $\hat{O}_c$ thus appears as a linear combination of the two operators $\hat{O}_a$ and $\hat{O}_b$, with respective weights of $\frac{\sqrt{3}}{2}$ and $\frac{1}{2}$. If no coupling occurs between $\hat{O}_a$ and $\hat{O}_b$ when calculating the square matrix elements $|\langle F|\hat{\boldsymbol{\varepsilon}}\cdot\mathbf{r}\hat{\mathbf{k}}\cdot\mathbf{r}|I\rangle|^2$, the third cross section (c) should be the linear combination of the two cross sections (a) and (b) obtained for $\hat{O}_a$ and $\hat{O}_b$, with respective weights of $\frac{3}{4}$ and $\frac{1}{4}$. However, the linear combination of the two cross sections (not shown in Fig. 5) and the cross section obtained for the linear combination of the transition operators are slightly different, which indicates a small interference between the xy and $3z^2-r^2$ (or x^2-y^2) components. The interference is a clear evidence of the $e_g^{\downarrow}(e_g)$ and $e_g^{\downarrow}(t_{2g})$ hybridizations due to the D_{3d} local symmetry.

B. LFM calculations

1. Comparison with experiment

For the two experimental configurations, Fig. 6 presents the experimental Cr K pre-edge spectra (dotted line), the the-

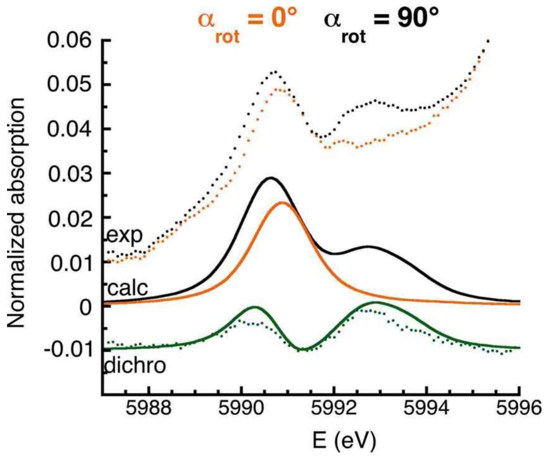

FIG. 6. (Color online) Comparison between experimental (dotted line) and calculated (solid line) Cr *K* pre-edge spectra in spinel using ligand field multiplet theory in D_{3d} symmetry. The orange lines correspond to $\hat{\varepsilon}=[010]$, $\hat{\mathbf{k}}=[\bar{1}00]$ ($\alpha_{\rm rot}=0°$). The black lines correspond to $\hat{\varepsilon}=[\frac{1}{2},\frac{1}{2},\frac{1}{\sqrt{2}}]$, $\hat{\mathbf{k}}=[-\frac{1}{2},-\frac{1}{2},\frac{1}{\sqrt{2}}]$ ($\alpha_{\rm rot}=90°$). The dichroic signal is the difference between the black and orange lines.

oretical spectra obtained by LFM calculations (solid line), and the corresponding dichroic signals. The calculated pre-edges have been obtained for the cubic crystal from a calculation performed for a single site with D_{3d} symmetry. For each configuration, the shape of the spectrum is well reproduced by the calculation. In the experimental data, the position of the first peak is shifted by approximately +0.15 eV for $\alpha_{\rm rot}=0°$, compared to that in the $\alpha_{\rm rot}=90°$ configuration. This relative shift is also well reproduced in the calculated spectra. For $\alpha_{\rm rot}=90°$, the relative intensity of the two peaks is in good agreement with the experimental data. The shape of the dichroic signal is well reproduced by the calculation; in fact, the x-ray linear dichroism of the crystal is well described in the multiplet approach, suggesting that the calculation includes the necessary multielectronic interactions on the Cr atom. We recall that the crystal-field parameters used in the calculation are those obtained from optical absorption spectroscopy (see Appendixes F and G for the correspondence between the experimental crystal-field parameters and the parameters used in the multiplet calculations). However, the intensity of the dichroic signal is overestimated by 20% in the calculation. The first reason for this overestimation is that the calculated spectra have been normalized by the edge jump at the Cr *K*-edge, which was calculated for an isolated Cr without considering the influence of the crystal structure according to Ref. 42. This can account for a few percent in the discrepancy. Another few percent possibly lie in the normalization of the experimental data since we used the average of two spectra, which were recorded between 5950 and 6350 eV with a rather large energy step (0.5 eV). This can introduce limited noise and thus uncertainty on the normalization. A third source of error is that the crystal-field parameters used in the calculation might be slightly different in the excited state than in the ground state because of the influence of the core hole: for example, if D_q is increased by 2% in the excited state, the intensity of the first peak in the dichroic signal decreases by 14%. The shape and intensity of the calculated dichroism are quite sensitive to the crystal-field parameters used in the excited state.

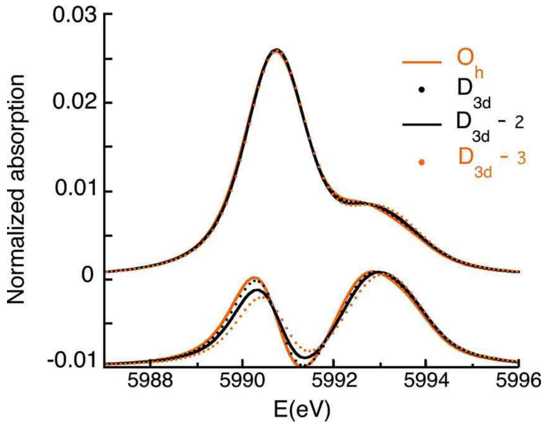

FIG. 7. (Color online) Comparison between calculated Cr *K* pre-edge spectra in spinel in D_{3d} symmetry for increasing trigonal distortion. The orange solid line, labeled O_h, corresponds to a perfect O_h symmetry ($D_\sigma=0$, $D_\tau=0$). The black dotted line, labeled D_{3d}, corresponds to ($D_\sigma=-0.036$ eV, $D_\tau=0.089$ eV), which are the distortion parameters obtained from optical absorption spectroscopy (Ref. 43). The black solid line, labeled $D_{3d}-2$, was obtained for a doubled distortion parameters ($D_\sigma=-0.072$ eV, $D_\tau=0.178$ eV) and the orange dotted line, labeled $D_{3d}-3$, for tripled distortion parameters ($D_\sigma=-0.108$ eV, $D_\tau=0.267$ eV).

Nevertheless, despite this slight intensity mismatch with the experimental data, the angular dependence of the crystal is well reproduced by the calculation, which means that the multielectronic approach takes into account the necessary interactions. Since isotropic and dichroic calculated spectra fit well with experiment, the analysis of the calculation is very likely to yield valuable insight into the origin of the experimental transitions in the pre-edge region. In the following, we shall investigate the influence of the different terms in the Hamiltonian taken into account in the LFM approach (trigonal distortion, fourfold degeneracy of the ground-state trigonal $S=\frac{3}{2}$ ($^4A_{2g}$), and spin-orbit coupling on the 3*d* levels, 3*d*-3*d* or 1*s*-3*d* Coulomb repulsion) on the angular dependence.

2. Influence of trigonal distortion on dichroism

In this paragraph, we investigate the influence of the trigonal distortion on the angular dependence. The isotropic and dichroic spectra in O_h symmetry have been obtained by setting the trigonal distortion of the crystal field to zero. They are compared to those calculated in D_{3d} symmetry using the distortion parameters given by optical absorption spectroscopy ($D_\sigma=-0.036$ eV, $D_\tau=0.089$ eV). As shown in Fig. 7, the difference between the calculations performed in O_h and D_{3d} symmetries (orange solid line and black dotted line, respectively) is weak since the isotropic and dichroic signals have similar shape and intensity. This result is consistent with the small values of the parameters D_σ and D_τ, which quantify the trigonal distortion of the Cr site in spinel. This means that, provided that trigonal distortion is limited, the calculation of pre-edge spectra could have been performed for a single site with O_h symmetry (see Appendix A 2 for simplified formula). This is also in line with the monoelectronic calculation, for which the splitting between $e_g^{\downarrow}(t_{2g})$ and $a_{1g}^{\downarrow}(t_{2g})$ could not be resolved in the calculated spectra.

We have investigated the effect of the intensity of the trigonal distortion on the calculated spectra by choosing two other sets of the distortion parameters. In Fig. 7, the spectra labeled $D_{3d}-i$ $(i=2,3)$ are calculated with the set of distortion parameters $(i\times D_{\sigma},\ i\times D_{\tau})$ for $(D_{\sigma}=-0.036$ eV, $D_{\tau}=0.089$ eV). The crystal-field parameters used are the same in the ground and excited states. As seen in Fig. 7, the intensities of the isotropic spectra (D_{3d}, $D_{3d}-2$, and $D_{3d}-3$) are almost identical, indicating that the isotropic signal is not sensitive to site distortion. The intensity of the maximum at 5990.75 eV remains close to 2.5% of the electric dipole edge jump. On the contrary, the shape and intensity of the linear dichroic signal are highly sensitive to the trigonal distortion. The intensity of the first feature at 5990.25 eV is lowered when the distortion is increased: one observes a 20% decrease when the distortion parameters are doubled (signal labeled $D_{3d}-2$ in Fig. 7) and a 50% decrease when the distortion parameters are tripled (signal labeled $D_{3d}-3$). It should be noticed that, for our parameter sets, the increase in site distortion is accompanied by a rather counterintuitive decrease in the intensity of the linear dichroic signal, thus indicating the relevance of the theoretical developments performed within this paper. This means that site distortion has to be carefully taken into account when calculations are performed to mimic the angular dependence of the pre-edge. In that case, the calculation for a single site with D_{3d} symmetry should follow the method described in Sec. III.

3. Influence of ground-state degeneracy, spin-orbit coupling, and interelectronic repulsion on dichroism

Beyond the site symmetry distortion, the other ingredients of the calculation are the fourfold degeneracy of the $S=\frac{3}{2}$ ground state, the 3*d*-3*d* Coulomb repulsion, the 1*s*-3*d* Coulomb repulsion, and the 3*d* spin-orbit coupling. We shall check the influence of these different parameters. We have performed multiplet calculations restricting the ground state to the nondegenerate $S_z=\frac{3}{2}$ state of the $S=\frac{3}{2}$ multiplet. The calculated electric quadrupole transitions are almost identical to those with the fourfold ground state. Differences are below 0.1% of the maximum intensity of the isotropic electric quadrupole spectrum. This clearly indicates that the procedure followed in monoelectronic calculations to take into account the spin degeneracy is sound and appropriate. The radial integrals for Coulomb interaction and spin-orbit coupling are calculated by relativistic Hartree-Fock atomic calculations. One finds the 1*s*-3*d* exchange Slater integral $G^1_{1s,3d}=0.052$ eV, the direct 3*d*-3*d* Slater integrals $F^2_{3d,3d}=10.78$ eV and $F^4_{3d,3d}=6.75$ eV, and the 3*d* spin-orbit coupling $\zeta_{3d}=0.035$ eV. $G^1_{1s,3d}$ is small compared to $F^2_{3d,3d}$ and $F^4_{3d,3d}$. Using $G^1_{1s,3d}=0$ in the multiplet calculation, we found almost no difference with the isotropic and dichroic signals calculated with the *ab initio* atomic value of $G^1_{1s,3d}$. By calculating the dichroic signal with $\zeta_{3d}=0$, we found a small difference concerning the intensity of isotropic and dichroic signals when compared to the associated spectra with $\zeta_{3d}=0.035$ eV. The maximum relative difference is less than a few percent (2%) of the feature intensity. The observed small dependence of the pre-edge features with $G^1_{1s,3d}$ and ζ_{3d} is in line with results obtained at the Fe *K* pre-edge.[21] We also performed calculations setting $F^2_{3d,3d}$ and $F^4_{3d,3d}$ to zero, and we observed that the isotropic and dichroic calculated spectra (not shown) were in complete disagreement with experimental data. This clearly indicates that the direct Slater integrals on the 3*d* shell and thus the multielectronic 3*d*-3*d* Coulomb interactions are the essential ingredients governing the shape of the isotropic as well as the dichroic signals.

From the preceding analysis, we can unambiguously determine the parameters governing the shape and intensities of the pre-edge features. Spin-orbit coupling on the 3*d* orbitals, ground-state degeneracy, and 1*s*-3*d* Coulomb repulsions have only limited impact on the calculated LFM isotropic spectra. This explains the reasonable agreement between calculation and experiment for isotropic pre-edge in the DFT formulation, where the two first previous ingredients are missing and where the 1*s*-3*d* Coulomb repulsion is taken into account in an approximate way. The D_{3d} distortion has almost no influence on the isotropic pre-edge but can have a large one on the dichroic signal. In the case of Cr in spinel, the trigonal distortion is so small that it does not provide detectable features on the dichroic signal. The major ingredient for the interpretation of the Cr pre-edge features is 3*d*-3*d* Coulomb repulsion. This effect is highly multielectronic and complicates the simple interpretation provided by the monoelectronic scheme. This ingredient is mandatory to get correct intensities and energies for both isotropic and dichroic signals.

V. DISCUSSION AND CONCLUSION

On the one hand, monoelectronic calculations allow us to make contact between electric dipole and electric quadrupole calculations. They show that electric dipole transitions do not contribute to the features visible in the pre-edge and they provide a clear vision of the assignment of the 1*s*-3*d* transitions occurring in the pre-edge. However, they are unable to reproduce quantitatively the linear dichroism in cubic crystals since the interelectronic repulsion on the 3*d* levels of the Cr ion cannot fully be described in the LSDA framework. On the other hand, multielectronic calculations well reproduce the angular dependence of the pre-edge in cubic crystals, as well as the isotropic spectrum, with no adjusted parameters. However, in this approach, the main absorption edge, associated to electric dipole transitions, cannot be reproduced since the band structure (or at least the electronic structure of a large enough cluster around the absorbing atom) is not taken into account. The agreement between experiment and multiplet calculations indicates that the assignment of the transitions is no more straightforward, as could have been expected from a more simple atomic monoelectronic picture. Hence, the two approaches are highly complementary. We wish to stress that we did not consider any electric dipole transitions induced by vibronic coupling.

From this monoelectronic-multielectronic combined approach, our first finding is that the 3*d*-3*d* electronic repulsions and the crystal field are the main interactions prevailing at the *K* pre-edge of Cr in spinel. The multiplet approach seems mandatory to describe quantitatively the *K* pre-edge of 3*d* transition ions and more generally the *K*-edge spectra of elements for which electronic correlations are significant. The effect of the 3*d* spin-orbit coupling and that of the 1*s*-3*d* Coulomb repulsion are very weak; this explains that the monoelectronic approach (which does not fully take into account these interactions) can provide a satisfactory simulation of the isotropic spectrum.

Our second finding concerns the maximum proportion of electric quadrupole transitions in the Cr *K* pre-edge that can be estimated with respect to the edge jump (here, normalized to 1); the intensity of the largest peak (5990.75 eV) on the pre-edge isotropic spectrum is less than 2.5% of the edge jump. From the monoelectronic calculations, we estimate that the nonstructured slope from electric dipole origin contributes to about 0.9% of the edge jump at 5990.75 eV. Thus, the total intensity of the largest pre-edge feature does not exceed 3.5%. We can conclude that, if the pre-edge features are more intense than 4% of the edge jump, pure quadrupole transitions alone cannot explain the origin of the structures. It gives a strong limitation to the often encountered idea that electric quadrupole transitions could explain large pre-edge features. This result, which is consistent with previous studies on Fe^{2+} and Fe^{3+} in minerals and glasses,[21,22,47] can probably be extended to the other 3*d* transition ions.

Our final finding concerns the relation between the spectral features of the pre-edge with the local site distortion of the absorbing ion. The effect of the trigonal distortion does not affect significantly the pre-edge isotropic spectrum. This is a general trend already observed for other related spectra (electric dipole transitions for *K* edge and $L_{2,3}$ edges of 3*d* elements). On the contrary, the dichroic signal is much more sensitive. This indicates the possibility to obtain quantitative information on site distortion from the linear dichroic dependence of the pre-edge feature. This can only be recorded if angular dependent measurements on single crystals are performed to yield the full dependence of the absorption signal. The connection between site distortion and linear dichroism is then made by simulations in the LFM method within the geometrical analysis developed throughout this paper.

ACKNOWLEDGMENTS

The authors warmly acknowledge M. Jacquet and M. Escudier for sample preparation. We are also very grateful to M. Sikora (ID26 beamline) for help during experiment and to F. Mauri, M. Calandra, M. Lazzeri, and C. Gougoussis for fruitful discussions and useful comparison with PWSCF code.[48] The theoretical part of this work was supported by the French CNRS, computational Institut of Orsay (Institut du Développement et de Recherche en Informatique Scientifique), under Projects No. 62015 and No. 72015. This is IPGP Contribution No. 2428.

APPENDIX A: PROOF OF EQUATION (3)

1. General expression of the electric-quadrupole cross section for a cubic crystal

We start from defining formula of the electric quadrupole cross section for linearly polarized x rays,

$$\sigma^Q(\hat{\varepsilon},\hat{\mathbf{k}}) = \pi^2 k^2 \alpha\hbar\omega \sum_{I,F} |\langle F|(\hat{\varepsilon}\ \cdot \mathbf{r}\hat{\mathbf{k}}\cdot\mathbf{r}|I\rangle|^2 \delta(E_I+\hbar\omega-E_F)$$
$$= \sum_{ijlm} \varepsilon_i\varepsilon_j k_l k_m \sigma_{iljm}, \qquad \text{(A1)}$$

where

$$\sigma_{ijlm} = \pi^2 k^2 \alpha\hbar\omega \sum_{I,F} \langle I|r_i r_l|F\rangle\langle F|r_j r_m|I\rangle \delta(E_I+\hbar\omega-E_F)$$

and $\hat{\varepsilon}$ and $\hat{\mathbf{k}}$ are the polarization and wave unit vectors, respectively.

To calculate the form of this sum when the sample has a symmetry group *G*, we use the fact that the absorption cross section is invariant by any symmetry operation that acts on both the sample variables σ_{ijlm} and the x-ray variables $\hat{\varepsilon}$, $\hat{\mathbf{k}}$. Therefore, the cross section is left invariant by the crystal symmetries applied to the x-ray variables. In other words, for any operation *S* of the symmetry group *G* of the sample, we have $\sigma(\hat{\varepsilon},\hat{\mathbf{k}})=\sigma[S(\hat{\varepsilon}),S(\hat{\mathbf{k}})]$. Therefore, if *G* is the symmetry group of the sample or a subgroup of it, we can write

$$\sigma^Q(\hat{\varepsilon},\hat{\mathbf{k}}) = \frac{1}{|G|}\sum_S \sigma[S(\hat{\varepsilon}),S(\hat{\mathbf{k}})], \qquad \text{(A2)}$$

where $|G|$ denotes the number of elements of *G*.

We rewrite Eq. (A1) as

$$\sigma^Q(\hat{\varepsilon},\hat{\mathbf{k}}) = \sum_{i\neq j} \varepsilon_i^2 k_j^2 \sigma_{ijij} + \sum_{i\neq j} \varepsilon_i\varepsilon_j k_i k_j \sigma_{iijj} + \sum_{i\neq j} \varepsilon_i\varepsilon_j k_j k_i \sigma_{ijji}$$
$$+ \sum_i \varepsilon_i^2 k_i^2 \sigma_{iiii} + R. \qquad \text{(A3)}$$

Equation (A3) defines term *R*. The term *R* is the sum of the terms that are not ($i=j$ and $l=m$), ($l=i$ and $m=j$), or ($m=i$ and $l=j$). So *R* is a sum of four terms of the type ($i\neq j$, $i\neq l$, and $i\neq m$) plus the three cyclic permutations of (i,j,l,m) and four terms of the type ($i\neq j$, $j\neq l$, and $l\neq i$) plus the three cyclic permutations of (i,j,l,m). We want to prove Eq. (3) that is valid for a cubic crystal in a reference frame such that *x*, *y*, and *z* axes are taken along the fourfold symmetry of the cubic crystal. We first show that if the sample has three perpendicular mirror planes, the term *R* is zero. Consider the term ($i\neq j$, $i\neq l$, and $i\neq m$) and take the symmetry $[S(\varepsilon_i)=-\varepsilon_i]$ the other variables j,k,l are different from *i*, so the symmetry leaves them invariant and changes only one sign. Therefore, using Eq. (A2), this term disappears from *R*. The same is true for the three cyclic permutations. Consider now the term ($i\neq j$, $j\neq l$, and $l\neq i$). Since the values of the indices are 1, 2, or 3, one of the three indices i,j,k is different from the other two and from *m*. So one index is again different from the other ones and the same reasoning can be applied to show that the corresponding term vanishes. This holds also for the three cyclic permutations and we have shown that, when there are three perpendicular symmetry planes, the absorption cross section is

$$\sigma^{Q}(\hat{\boldsymbol{\varepsilon}},\hat{\mathbf{k}}) = \sum_{i\neq j}\varepsilon_i^2k_j^2\sigma_{ijij} + \sum_{i\neq j}\varepsilon_i\varepsilon_jk_ik_j\sigma_{iijj} + \sum_{i\neq j}\varepsilon_i\varepsilon_jk_jk_i\sigma_{ijji} + \sum_{i}\varepsilon_i^2k_i^2\sigma_{iiii}. \tag{A4}$$

The group O_h has a subgroup made by the six permutations of (x,y,z). An average over this subgroup gives the following result:

$$\sigma^{Q}_{\mathrm{cub}}(\hat{\boldsymbol{\varepsilon}},\hat{\mathbf{k}}) = \sum_{i\neq j}\varepsilon_i^2k_j^2A + \sum_{i\neq j}\varepsilon_i\varepsilon_jk_ik_jB + \sum_{i}\varepsilon_i^2k_i^2C, \tag{A5}$$

where

$$A = \sum_{i\neq j}\frac{\sigma_{ijij}}{6},$$

$$B = \sum_{i\neq j}\frac{\sigma_{iijj}+\sigma_{ijji}}{6},$$

$$C = \sum_{i}\frac{\sigma_{iiii}}{3}.$$

To complete the proof, we use the fact that

$$\sum_{i\neq j}\varepsilon_i^2k_j^2 = \hat{\boldsymbol{\varepsilon}}\cdot\hat{\boldsymbol{\varepsilon}}\hat{\mathbf{k}}\cdot\hat{\mathbf{k}} - \sum_{i}\varepsilon_i^2k_i^2,$$

$$\sum_{i\neq j}\varepsilon_i\varepsilon_jk_ik_j = (\hat{\boldsymbol{\varepsilon}}\cdot\hat{\mathbf{k}})^2 - \sum_{i}\varepsilon_i^2k_i^2,$$

and the identities $\hat{\boldsymbol{\varepsilon}}\cdot\hat{\boldsymbol{\varepsilon}}=1$, $\hat{\mathbf{k}}\cdot\hat{\mathbf{k}}=1$, and $\hat{\boldsymbol{\varepsilon}}\cdot\hat{\mathbf{k}}=0$ to get

$$\sigma^{Q}_{\mathrm{cub}}(\hat{\boldsymbol{\varepsilon}},\hat{\mathbf{k}}) = A + \sum_{i}\varepsilon_i^2k_i^2(C-A-B). \tag{A6}$$

To compare this result with the expansion over spherical tensors, we need to determine the isotropic contribution σ^{Q}_{0}, which is obtained as the average of $\sigma^{Q}_{\mathrm{cub}}(\hat{\boldsymbol{\varepsilon}},\hat{\mathbf{k}})$ over angles. We write $\sigma(\hat{\boldsymbol{\varepsilon}},\hat{\mathbf{k}})$ in terms of θ, ϕ, and ψ as in Sec. III A 2.

Thus,

$$\begin{aligned}\sigma^{Q}_{\mathrm{cub}}(\hat{\boldsymbol{\varepsilon}},\hat{\mathbf{k}}) = A + \frac{C-A-B}{4}\sin^2\theta\,(7\cos^2\theta\cos^2\psi \\ + \cos 4\phi\cos^2\theta\cos^2\psi + 2\sin^2 2\phi\sin^2\psi \\ - \cos\theta\sin 4\phi\sin 2\psi),\end{aligned}$$

and the average over all directions is

$$\begin{aligned}\sigma^{Q}_{0} &= \frac{1}{8\pi^2}\int_0^{\pi}\sin\theta d\theta\int_0^{2\pi}d\phi\int_0^{2\pi}d\psi\sigma^{Q}_{\mathrm{cub}}(\hat{\boldsymbol{\varepsilon}},\hat{\mathbf{k}}) \\ &= A + \frac{C-A-B}{5}.\end{aligned}$$

Therefore,

$$\sigma^{Q}_{\mathrm{cub}}(\hat{\boldsymbol{\varepsilon}},\hat{\mathbf{k}}) = \sigma^{Q}_{0} + \left(\sum_{i}\varepsilon_i^2k_i^2 - \frac{1}{5}\right)(C-A-B)$$

and

$$\sigma^{Q}_{\mathrm{cub}}(\hat{\boldsymbol{\varepsilon}},\hat{\mathbf{k}}) = \sigma^{Q}_{0} + \left(\varepsilon_x^2k_x^2 + \varepsilon_y^2k_y^2 + \varepsilon_z^2k_z^2 - \frac{1}{5}\right)\sigma^{Q}_{1}, \tag{A7}$$

where $\sigma^{Q}_{1}=(C-A-B)$ and k_x, k_y, and k_z are the coordinates of $\hat{\mathbf{k}}$. This expression is valid for any cubic crystal, providing that the reference frame is such that the x, y, and z axes are taken along the fourfold symmetry axis of the cubic crystal.

2. Absorption cross sections in O_h symmetry

For a site with O_h symmetry, the orthonormal reference frame chosen is that of the cubic crystal. The z axis of the reference frame is parallel to the fourfold axis of the cube. The angle θ is thus the angle between the polarization vector and the z axis of the cube.

The cross section calculated for a single site in O_h is equal to the cross section of the cubic crystal since a perfect octahedron and the cube have the same symmetry operations,

$$\sigma^{Q}_{O_h}(\hat{\boldsymbol{\varepsilon}},\hat{\mathbf{k}}) = \sigma^{Q}_{\mathrm{cub}}(\hat{\boldsymbol{\varepsilon}},\hat{\mathbf{k}}), \quad \sigma^{D}_{O_h}(\hat{\boldsymbol{\varepsilon}}) = \sigma^{D}_{\mathrm{cub}}(\hat{\boldsymbol{\varepsilon}}).$$

For a single site with O_h symmetry, the expression of the electric dipole cross section is very simple,

$$\sigma^{D}_{O_h}(\hat{\boldsymbol{\varepsilon}}) = \sigma^{D}(0,0), \tag{A8}$$

where $\sigma^{D}(0,0)$ is the isotropic electric dipole cross section.

For the cubic crystal, one obtains

$$\sigma^{D}_{\mathrm{cub}}(\hat{\boldsymbol{\varepsilon}}) = \sigma^{D}_{O_h}(\hat{\boldsymbol{\varepsilon}}) = \sigma^{D}(0,0). \tag{A9}$$

The electric quadrupole absorption cross section for a site with O_h symmetry is given by

$$\begin{aligned}\sigma^{Q}_{O_h}(\hat{\boldsymbol{\varepsilon}},\hat{\mathbf{k}}) = \sigma^{Q}_{O_h}(0,0) + \frac{1}{\sqrt{14}}[35\sin^2\theta\cos^2\theta\cos^2\psi \\ + 5\sin^2\theta\sin^2\psi - 4 \\ + 5\sin^2\theta(\cos^2\theta\cos^2\psi\cos 4\phi - \sin^2\psi\cos 4\phi) \\ - 2\cos\theta\sin\psi\cos\psi\sin 4\phi]\sigma^{Q}_{O_h}(4,0),\end{aligned} \tag{A10}$$

where $\sigma^{Q}_{\mathrm{cub}}(0,0)$ is the isotropic electric quadrupole cross section and $\sigma^{Q}_{\mathrm{cub}}(4,0)$ a purely anisotropic electric quadrupole term. Using $\sigma^{Q}_{O_h}(\hat{\boldsymbol{\varepsilon}},\hat{\mathbf{k}})=\sigma^{Q}_{\mathrm{cub}}(\hat{\boldsymbol{\varepsilon}},\hat{\mathbf{k}})$ and $(\theta=\frac{\pi}{2},\ \phi=\frac{\pi}{2},\ \psi=\frac{\pi}{2})$, Eq. (A10) is equivalent to Eq. (A7) with

$$\sigma^{Q}_{0} = \sigma^{Q}_{O_h}(0,0) = \sigma^{Q}_{\mathrm{cub}}(0,0), \tag{A11}$$

$$\sigma^{Q}_{1} = \frac{20}{\sqrt{14}}\sigma^{Q}_{O_h}(4,0) = \frac{20}{\sqrt{14}}\sigma^{Q}_{\mathrm{cub}}(4,0). \tag{A12}$$

Equation (A7) can be rewritten as

$$\begin{aligned}\sigma^{Q}_{\mathrm{cub}}(\hat{\boldsymbol{\varepsilon}},\hat{\mathbf{k}}) = \sigma^{Q}_{\mathrm{cub}}(0,0) \\ + \frac{20}{\sqrt{14}}\left(\varepsilon_x^2k_x^2 + \varepsilon_y^2k_y^2 + \varepsilon_z^2k_z^2 - \frac{1}{5}\right)\sigma^{Q}_{\mathrm{cub}}(4,0).\end{aligned} \tag{A13}$$

This is the proof of Eq. (3).

APPENDIX B: EXPRESSION OF $\hat{\varepsilon}(\alpha_{\text{rot}})$ AND $\hat{\mathbf{k}}$ (α_{rot})

For the sample cut and the experimental setup used in this study, we have

$$\hat{\varepsilon}(\alpha_{\text{rot}}) = \begin{pmatrix} \dfrac{1-\cos\alpha_{\text{rot}}}{2} \\ \dfrac{1+\cos\alpha_{\text{rot}}}{2} \\ \dfrac{\sin\alpha_{\text{rot}}}{\sqrt{2}} \end{pmatrix},$$

$$\hat{\mathbf{k}}(\alpha_{\text{rot}}) = \begin{pmatrix} \dfrac{-1-\cos\alpha_{\text{rot}}}{2} \\ \dfrac{-1+\cos\alpha_{\text{rot}}}{2} \\ \dfrac{\sin\alpha_{\text{rot}}}{\sqrt{2}} \end{pmatrix}.$$

APPENDIX C: SYMMETRY ADAPTED METHOD USED IN MONOELECTRONIC CALCULATIONS

First, the absorption cross section was calculated in the electric dipole approximation in order to derive $\sigma^{D}_{\text{cub}}(0,0)$, the isotropic electric dipole cross section. This term can be obtained from a single calculation of the electric dipole absorption cross section performed for site A. The expression of the electric dipole cross section in D_{3d}, σ^{D}_{A}, is given by Eq. (4), where θ is the angle between the polarization vector and the C_3 axis. The program we used for the *ab initio* calculations calculates the average of σ^{D}_{A} $(\hat{\varepsilon})$ for $\hat{\varepsilon}$ along the x, y, and z axes of the cubic frame. The angle θ between the $[\bar{1}11]$ direction (parallel to the C_3 axis of the site) and each of these three directions is $\arccos\frac{1}{\sqrt{3}}$. This implies that, for a polarization vector $\hat{\varepsilon}$ taken along the x, y, or z axis,

$$\sigma^{D}_{\text{cub}}(\hat{\varepsilon}) = \sigma^{D}_{A}(\hat{\varepsilon}) = \sigma^{D}_{D_{3d}}(0,0) = \sigma^{D}_{\text{cub}}(0,0). \tag{C1}$$

This means that the average value calculated by the program is directly equal to $\sigma^{D}_{\text{cub}}(0,0)$. Hence, $\sigma^{D}_{\text{cub}}(0,0)$ was obtained from a single calculation performed at site A.

Second, the calculation was performed in the electric quadrupole approximation in order to derive $\sigma^{Q}_{\text{cub}}(0,0)$ and $\sigma^{Q}_{\text{cub}}(4,0)$. Once these two terms are determined, we will be able to calculate the electric quadrupole absorption cross section for the cubic crystal, according to Eq. (3), for any $(\hat{\varepsilon},\hat{\mathbf{k}})$ configuration. We used a symmetry adapted method to determine $\sigma^{Q}_{\text{cub}}(0,0)$ and $\sigma^{Q}_{\text{cub}}(4,0)$ in order to reduce the number of calculations; this way, it is possible to consider one single substitutional site (site A) and take advantage of the symmetry properties of the crystal. This method allows us to save significant computational time since we perform only two self-consistent calculations (instead of eight with the brute force method): one calculation to do the structural relaxation of the system (substituted at site A) and a second one to calculate the charge density with a core hole on Cr. As mentioned in Ref. 24, assuming that we have calculated the spectrum for a given site X, it is possible to obtain the spectrum for any site Y equivalent to X by calculating the spectrum of site X for a rotated x-ray beam. More precisely, in the case of electric quadrupole transitions, if site Y is the image of site X by a rotation R, the spectrum of site Y for a configuration $(\hat{\varepsilon},\hat{\mathbf{k}})$ is equal to the spectrum of site X for the rotated configuration $[R^{-1}(\hat{\varepsilon}),R^{-1}(\hat{\mathbf{k}})]$. As in Ref. 24, let us consider the site with reduced coordinates (0, 1/4, 3/4), which is a representative of site A. By applying the three rotations about the z axis of the crystal through angles of $\pi/2$, π, and $3\pi/2$, we obtain the positions of three sites, which are, respectively, representative of sites B, D, and C. The three rotations will be denoted as $R_{\pi/2}$, R_{π}, and $R_{3\pi/2}$. This implies that

$$\sigma^{Q}_{B}(\hat{\varepsilon},\hat{\mathbf{k}}) = \sigma^{Q}_{A}[R^{-1}_{\pi/2}(\hat{\varepsilon}),R^{-1}_{\pi/2}(\hat{\mathbf{k}})], \tag{C2}$$

$$\sigma^{Q}_{C}(\hat{\varepsilon},\hat{\mathbf{k}}) = \sigma^{Q}_{A}[R^{-1}_{3\pi/2}(\hat{\varepsilon}),R^{-1}_{3\pi/2}(\hat{\mathbf{k}})], \tag{C3}$$

$$\sigma^{Q}_{D}(\hat{\varepsilon},\hat{\mathbf{k}}) = \sigma^{Q}_{A}[R^{-1}_{\pi}(\hat{\varepsilon}),R^{-1}_{\pi}(\hat{\mathbf{k}})]. \tag{C4}$$

We shall now apply the previous equations to the case of the two experimental configurations, $\alpha_{\text{rot}}=0°$ and $\alpha_{\text{rot}}=90°$, in order to see if additional simplifications can be found. To do so, we need to consider the expression of the electric-quadrupole transition operator $\hat{Q}$,

$$\hat{Q} = \frac{i}{2}\hat{\varepsilon}\cdot\mathbf{r}\hat{\mathbf{k}}\cdot\mathbf{r}. \tag{C5}$$

Note that, in text, the assignment of the calculated monoelectronic transitions is discussed using $\hat{O}=\hat{\varepsilon}\cdot\mathbf{r}\hat{\mathbf{k}}\cdot\mathbf{r}$. We have to consider the absolute value of $\hat{O}$ (or $\hat{Q}$) because the cross section does not depend on the sign of $\hat{O}$.

For $\alpha_{\text{rot}}=0°$ $(\hat{\varepsilon}=[010],\ \hat{\mathbf{k}}=[\bar{1}00])$,

$$\begin{aligned} |\hat{\varepsilon}\cdot\mathbf{r}\hat{\mathbf{k}}\cdot\mathbf{r}| &= |R^{-1}_{\pi/2}(\hat{\varepsilon})\cdot\mathbf{r}R^{-1}_{\pi/2}(\hat{\mathbf{k}})\cdot\mathbf{r}| \\ &= |R^{-1}_{\pi}(\hat{\varepsilon})\cdot\mathbf{r}R^{-1}_{\pi}(\hat{\mathbf{k}})\cdot\mathbf{r}| \\ &= |R^{-1}_{3\pi/2}(\hat{\varepsilon})\cdot\mathbf{r}R^{-1}_{\pi/2}(\hat{\mathbf{k}})\cdot\mathbf{r}| = xy. \end{aligned}$$

Hence, we have

$$\begin{aligned} \sigma^{Q}_{A}(\hat{\varepsilon},\hat{\mathbf{k}}) &= \sigma^{Q}_{A}[R^{-1}_{\pi/2}(\hat{\varepsilon}),R^{-1}_{\pi/2}(\hat{\mathbf{k}})] \\ &= \sigma^{Q}_{A}[R^{-1}_{\pi}(\hat{\varepsilon}),R^{-1}_{\pi}(\hat{\mathbf{k}})] \\ &= \sigma^{Q}_{A}[R^{-1}_{3\pi/2}(\hat{\varepsilon}),R^{-1}_{3\pi/2}(\hat{\mathbf{k}})]. \end{aligned}$$

This means that

$$\sigma^{Q}_{A}(\hat{\varepsilon},\hat{\mathbf{k}}) = \sigma^{Q}_{B}(\hat{\varepsilon},\hat{\mathbf{k}}) = \sigma^{Q}_{C}(\hat{\varepsilon},\hat{\mathbf{k}}) = \sigma^{Q}_{D}(\hat{\varepsilon},\hat{\mathbf{k}}). \tag{C6}$$

For $\alpha_{\text{rot}}=0°$, we thus need to perform one single calculation of the electric quadrupole cross section since

$$\sigma^{Q}_{\text{cub}}(\hat{\varepsilon},\hat{\mathbf{k}}) = \sigma^{Q}_{A}(\hat{\varepsilon},\hat{\mathbf{k}}). \tag{C7}$$

For $\alpha_{\text{rot}}=90°$ $(\hat{\varepsilon}=[\frac{1}{2},\frac{1}{2},\frac{1}{\sqrt{2}}]$ and $\hat{\mathbf{k}}=[-\frac{1}{2},-\frac{1}{2},\frac{1}{\sqrt{2}}])$,

TABLE II. Expression of the electric quadrupole cross section calculated in D_{3d} group for the four independent orientations used to derive $\sigma^Q_{D_{3d}}(0,0)$, $\sigma^Q_{D_{3d}}(2,0)$, $\sigma^Q_{D_{3d}}(4,0)$, and $\sigma^Q_{D_{3d}}(4,3)$ (see text). The coordinates of $\hat{\boldsymbol{\varepsilon}}$ and $\hat{\mathbf{k}}$ are given in the reference frame chosen for D_{3d}, with the z direction parallel to the C_3 axis.

Label	θ	ϕ	ψ	$\hat{\boldsymbol{\varepsilon}}$	$\hat{\mathbf{k}}$	$\sigma^Q_{D_{3d}}(\hat{\boldsymbol{\varepsilon}},\hat{\mathbf{k}})$
$s1$	$\arccos(\frac{1}{\sqrt{3}})$	$-\frac{2\pi}{3}$	$\frac{\pi}{4}$	$(-\frac{1}{\sqrt{6}},-\frac{1}{\sqrt{2}},\frac{1}{\sqrt{3}})$	$(\frac{1}{\sqrt{6}},-\frac{1}{\sqrt{2}},-\frac{1}{\sqrt{3}})$	$\sigma^Q_{D_{3d}}(0,0)+\frac{\sqrt{14}}{9}\sigma^Q_{D_{3d}}(4,0)+\frac{4\sqrt{5}}{9}\sigma^Q_{D_{3d}}(4,3)$
$s2$	$\arccos(\frac{1}{\sqrt{3}}+\frac{1}{\sqrt{6}})$	0	0	$(\frac{-1+\sqrt{2}}{\sqrt{6}},0,\frac{1+\sqrt{2}}{\sqrt{6}})$	$(\frac{1+\sqrt{2}}{\sqrt{6}},0,\frac{1-\sqrt{2}}{\sqrt{6}})$	$\sigma^Q_{D_{3d}}(0,0)-\sqrt{\frac{5}{14}}\sigma^Q_{D_{3d}}(2,0)-\frac{109}{36\sqrt{14}}\sigma^Q_{D_{3d}}(4,0)-\frac{2\sqrt{5}}{9}\sigma^Q_{D_{3d}}(4,3)$
$s3$	$\frac{\pi}{2}$	$\frac{\pi}{2}$	$\frac{\pi}{2}$	(0,1,0)	$(-1,0,0)$	$\sigma^Q_{D_{3d}}(0,0)+\sqrt{\frac{10}{7}}\sigma^Q_{D_{3d}}(2,0)+\frac{1}{\sqrt{14}}\sigma^Q_{D_{3d}}(4,0)$
$s4$	$\frac{3\pi}{4}$	$\frac{\pi}{2}$	π	$(0,\frac{1}{\sqrt{2}},-\frac{1}{\sqrt{2}})$	$(0,\frac{1}{\sqrt{2}},\frac{1}{\sqrt{2}})$	$\sigma^Q_{D_{3d}}(0,0)-\sqrt{\frac{5}{14}}\sigma^Q_{D_{3d}}(2,0)+\frac{19}{4\sqrt{14}}\sigma^Q_{D_{3d}}(4,0)$

$$|\hat{\boldsymbol{\varepsilon}}\cdot\mathbf{r}\hat{\mathbf{k}}\cdot\mathbf{r}| = |R^{-1}_{\pi}(\hat{\boldsymbol{\varepsilon}})\cdot\mathbf{r}R^{-1}_{\pi}(\hat{\mathbf{k}})\cdot\mathbf{r}| = |z^2/2-(x-y)^2/4|$$

and

$$\begin{aligned}&|R^{-1}_{\pi/2}(\hat{\boldsymbol{\varepsilon}})\cdot\mathbf{r}R^{-1}_{\pi/2}(\hat{\mathbf{k}})\cdot\mathbf{r}|\\&\quad=|R^{-1}_{3\pi/2}(\hat{\boldsymbol{\varepsilon}})\cdot\mathbf{r}R^{-1}_{\pi/2}(\hat{\mathbf{k}})\cdot\mathbf{r}| = |z^2/2-(x+y)^2/4|.\end{aligned}$$

This means that

$$\sigma^Q_A(\hat{\boldsymbol{\varepsilon}},\hat{\mathbf{k}}) = \sigma^Q_D(\hat{\boldsymbol{\varepsilon}},\hat{\mathbf{k}}), \tag{C8}$$

$$\sigma^Q_B(\hat{\boldsymbol{\varepsilon}},\hat{\mathbf{k}}) = \sigma^Q_C(\hat{\boldsymbol{\varepsilon}},\hat{\mathbf{k}}). \tag{C9}$$

For $\alpha_{\mathrm{rot}}=90°$, we thus need to perform two calculations of the electric quadrupole cross sections since

$$\sigma^Q_{\mathrm{cub}}(\hat{\boldsymbol{\varepsilon}},\hat{\mathbf{k}}) = \frac{\sigma^Q_A(\hat{\boldsymbol{\varepsilon}},\hat{\mathbf{k}})+\sigma^Q_C(\hat{\boldsymbol{\varepsilon}},\hat{\mathbf{k}})}{2}. \tag{C10}$$

As mentioned previously, instead of doing the calculation for the two sites A and C, it is more convenient to compute the spectrum for site A for the two orientations $(\hat{\boldsymbol{\varepsilon}},\hat{\mathbf{k}})$ and $[R^{-1}_{-3\pi/2}(\hat{\boldsymbol{\varepsilon}}),R^{-1}_{-3\pi/2}(\hat{\mathbf{k}})]$. This corresponds to $(\hat{\boldsymbol{\varepsilon}}=[\frac{1}{2},\frac{1}{2},\frac{1}{\sqrt{2}}]$, $\hat{\mathbf{k}}=[-\frac{1}{2},-\frac{1}{2},\frac{1}{\sqrt{2}}])$ and $(\hat{\boldsymbol{\varepsilon}}=[-\frac{1}{2},\frac{1}{2},\frac{1}{\sqrt{2}}]$, $\hat{\mathbf{k}}=[\frac{1}{2},-\frac{1}{2},\frac{1}{\sqrt{2}}])$, respectively.

APPENDIX D: METHOD USED TO PERFORM THE MULTIPLET CALCULATIONS

As mentioned in Sec. III A 2 [Eq. (5)], one needs first to determine $\sigma^Q_{D_{3d}}(0,0)$, $\sigma^Q_{D_{3d}}(2,0)$, $\sigma^Q_{D_{3d}}(4,0)$, and $\sigma^Q_{D_{3d}}(4,3)$ in order to determine $\sigma^Q_{\mathrm{cub}}(0,0)$ and $\sigma^Q_{\mathrm{cub}}(4,0)$ using Eqs. (8) and (9). This is done by performing four multiplet calculations, which provide four independent values of the electric quadrupole cross section, $s1$, $s2$, $s3$, and $s4$, where $\hat{\boldsymbol{\varepsilon}}$ and $\hat{\mathbf{k}}$ are defined in Table II. The components $\sigma^Q_{D_{3d}}(0,0)$, $\sigma^Q_{D_{3d}}(2,0)$, $\sigma^Q_{D_{3d}}(4,0)$, and $\sigma^Q_{D_{3d}}(4,3)$ are obtained by a combination of $s1$, $s2$, $s3$, and $s4$, according to

$$\sigma^Q_{D_{3d}}(0,0) = \frac{1}{5}s1+\frac{2}{5}s2+\frac{4}{15}s3+\frac{2}{15}s4,$$

$$\sigma^Q_{D_{3d}}(2,0) = -\frac{1}{\sqrt{70}}s1-\sqrt{\frac{2}{35}}s2+\sqrt{\frac{5}{14}}s3-\sqrt{\frac{2}{35}}s4,$$

$$\sigma^Q_{D_{3d}}(4,0) = -\frac{2\sqrt{14}}{35}s1-\frac{4\sqrt{14}}{35}s2+\frac{2\sqrt{14}}{105}s3+\frac{16\sqrt{14}}{105}s4,$$

$$\sigma^Q_{D_{3d}}(4,3) = \frac{2}{\sqrt{5}}s1-\frac{1}{2\sqrt{5}}s2-\frac{2}{3\sqrt{5}}s3-\frac{\sqrt{5}}{6}s4. \tag{D1}$$

These equations have been obtained by inversing the system of equations, which give the expressions of $s1$, $s2$, $s3$, and $s4$, in functions of $\sigma^Q_{D_{3d}}(0,0)$, $\sigma^Q_{D_{3d}}(2,0)$, $\sigma^Q_{D_{3d}}(4,0)$, and $\sigma^Q_{D_{3d}}(4,3)$ (Table II).

Once this first step has been performed, Eq. (8) and (9) are used to derive $\sigma^Q_{\mathrm{cub}}(0,0)$ and $\sigma^Q_{\mathrm{cub}}(4,0)$. The electric quadrupole cross section of the cubic crystal can then be calculated for any experimental configuration using Eq. (11).

APPENDIX E: EXPRESSION OF THE *d* EIGENSTATES IN D_{3d}

The d eigenstates in D_{3d} point group are determined by the branching rules of the irreducible representation $2^{+}(O_3)$ in D_{3d}. In order to get the complete eigenstates, we must consider the $O_3\supset O_h\supset D_{3d}\supset C_{3i}$ subduction. To simplify the notation, we will make no use of the parity (± or g/u) in the rest of the appendix. Hence, we will use the subduction $SO_3\supset O\supset D_3\supset C_3$. In the following, the irreducible representations are labeled according to Ref. 26. For example, in O group, the irreducible representation $\tilde{1}$ designates T_2 in Schönflies notation, while 2 designates E. The complete eigenstates are written as $|k(SO_3)\rho(O)\sigma(D_3)\lambda(C_3)\rangle_3$, where λ is the irreducible representation of C_3 subgroup, coming from the k irreducible representation of SO_3, which becomes ρ in O, σ in D_3, and λ in C_3. The branching rules for $k=2$ are given in Table III.

We recall that in D_3 (or C_3), the reference frame chosen is not the one used in O. Therefore, we need to express the $|k(SO_3)\rho(O)\sigma(D_3)\lambda(C_3)\rangle_3$ in function of $|k(SO_3)\rho(O)\sigma(D_4)\lambda(C_4)\rangle_4$, where $|k(SO_3)\rho(O)\sigma(D_4)\lambda(C_4)\rangle_4$ are determined using the $SO_3\supset O\supset D_4\supset C_4$ subduction. To do so, we use the relations given for $k=2$ in Ref. 26 (p. 549),

$$|2211\rangle_3 = -\frac{1}{\sqrt{2}}|2200\rangle_4 + i\frac{1}{\sqrt{2}}|2222\rangle_4,$$

TABLE III. Branching rules for $k=2$ using the $SO_3 \supset O \supset D_3 \supset C_3$ subduction.

$SO_3 \rightarrow O \rightarrow D_3 \rightarrow C_3$	$\lvert k(SO_3)\rho(O)\sigma(D_3)\lambda(C_3)\rangle$
$2 \rightarrow \tilde{1} \rightarrow 1 \rightarrow 1$	$\lvert e_+(t_2)\rangle$
$2 \rightarrow \tilde{1} \rightarrow 1 \rightarrow -1$	$\lvert e_-(t_2)\rangle$
$2 \rightarrow \tilde{1} \rightarrow 0 \rightarrow 0$	$\lvert a_1(t_2)\rangle$
$2 \rightarrow 2 \rightarrow 1 \rightarrow 1$	$\lvert e_+(e)\rangle$
$2 \rightarrow 2 \rightarrow 1 \rightarrow -1$	$\lvert e_-(e)\rangle$

$$|221-1\rangle_3 = -\frac{1}{\sqrt{2}}|2200\rangle_4 - i\frac{1}{\sqrt{2}}|2222\rangle_4,$$

$$|2\tilde{1}00\rangle_3 = (1+i)\frac{1}{\sqrt{6}}|2\tilde{1}11\rangle_4 + (1-i)\frac{1}{\sqrt{6}}|2\tilde{1}1-1\rangle_4 - \frac{i}{\sqrt{3}}|2\tilde{1}\tilde{2}2\rangle_4,$$

$$|2\tilde{1}11\rangle_3 = (1+i)\left(\frac{1}{2\sqrt{2}} - \frac{1}{2\sqrt{6}}\right)|2\tilde{1}11\rangle_4 + (-1+i)\left(\frac{1}{2\sqrt{2}} + \frac{1}{2\sqrt{6}}\right)|2\tilde{1}1-1\rangle_4 - \frac{i}{\sqrt{3}}|2\tilde{1}\tilde{2}2\rangle_4,$$

$$|2\tilde{1}1-1\rangle_3 = -(1+i)\left(\frac{1}{2\sqrt{2}} + \frac{1}{2\sqrt{6}}\right)|2\tilde{1}11\rangle_4 + (1-i)\left(\frac{1}{2\sqrt{2}} - \frac{1}{2\sqrt{6}}\right)|2\tilde{1}1-1\rangle_4 - \frac{i}{\sqrt{3}}|2\tilde{1}\tilde{2}2\rangle_4. \tag{E1}$$

If we now express the $|k(SO_3)\rho(O)\sigma(D_4)\lambda(C_4)\rangle_4$ as $|JM\rangle$ partners (Ref. 26, p. 527), we obtain

$$|2200\rangle_4 = -|20\rangle,$$

$$|2222\rangle_4 = -\frac{1}{\sqrt{2}}|22\rangle - \frac{1}{\sqrt{2}}|2-2\rangle,$$

$$|2\tilde{1}11\rangle_4 = -|21\rangle,$$

$$|2\tilde{1}1-1\rangle_4 = |2-1\rangle,$$

$$|2\tilde{1}\tilde{2}2\rangle_4 = \frac{1}{\sqrt{2}}|22\rangle - \frac{1}{\sqrt{2}}|2-2\rangle. \tag{E2}$$

In O, the d orbitals are expressed as

$$d_{xy} = \frac{i}{\sqrt{2}}(|2-2\rangle - |22\rangle),$$

$$d_{yz} = \frac{i}{\sqrt{2}}(|2-1\rangle + |21\rangle),$$

$$d_{xz} = \frac{1}{\sqrt{2}}(|2-1\rangle - |21\rangle),$$

$$d_{3z^2-r^2} = |20\rangle,$$

$$d_{x^2-y^2} = \frac{1}{\sqrt{2}}(|22\rangle + |2-2\rangle). \tag{E3}$$

Combining Eqs. (E1)–(E3), we obtain the expression of the d functions, which are basis of the irreducible representations in C_3, in function of the d orbitals in O,

$$e_+(e) = |2211\rangle_3 = \frac{1}{\sqrt{2}}d_{3z^2-r^2} - \frac{i}{\sqrt{2}}d_{x^2-y^2},$$

$$e_-(e) = |221-1\rangle_3 = \frac{1}{\sqrt{2}}d_{3z^2-r^2} + \frac{i}{\sqrt{2}}d_{x^2-y^2},$$

$$a_1(t_2) = |2\tilde{1}00\rangle_3 = \frac{1}{\sqrt{3}}d_{xy} + \frac{1}{\sqrt{3}}d_{xz} - \frac{1}{\sqrt{3}}d_{yz},$$

$$e_+(t_2) = |2\tilde{1}11\rangle_3 = \frac{1}{\sqrt{3}}d_{xy} + \left(-\frac{1}{2\sqrt{3}} + \frac{i}{2}\right)d_{xz} + \left(\frac{1}{2\sqrt{3}} + \frac{i}{2}\right)d_{yz},$$

$$e_+(t_2) = |2\tilde{1}1-1\rangle_3 = \frac{1}{\sqrt{3}}d_{xy} - \left(\frac{1}{2\sqrt{3}} + \frac{i}{2}\right)d_{xz} + \left(\frac{1}{2\sqrt{3}} - \frac{i}{2}\right)d_{yz}. \tag{E4}$$

In D_3, $[e_+(t_2),\ e_-(t_2)]$ is a basis of the irreducible representation $e(t_2)$. Similarly, $[e_+(e),\ e_+(e)]$ is a basis of the irreducible representation $e(e)$. In D_3, a mixing is thus possible between the functions belonging to the two e irreducible representations, originating from the e and t_2 levels in O.

APPENDIX F: DEFINITION OF THE CRYSTAL-FIELD PARAMETERS USED IN THE LFM CALCULATIONS

In SO_3 symmetry, the crystal-field Hamiltonian can be written as a combination of the q components of unit tensors $U^{(k)}$ with rank k. Each tensor $U^{(k)}$ is associated to the k irreducible representation of SO_3. For the Cr^{3+} ion, $k=0$, 2, or 4, the term $k=0$ contributing only to the average energy of the configuration. Again, we will not make use of the parity ($\pm$ or g/u). To study the Cr^{3+} ion in trigonal symmetry D_3, we need to consider the subduction $SO_3 \supset O \supset D_3 \supset C_3$.

The crystal-field Hamiltonian is expressed as

TABLE IV. Branching rules giving 0 as irreducible representation in D_3.

$SO_3 \rightarrow O \rightarrow D_3 \rightarrow C_3$	$X^{k(SO_3)\rho(O)\sigma(D_3)\lambda(C_3)}$
$4 \rightarrow 0 \rightarrow 0 \rightarrow 0$	X^{4000}
$4 \rightarrow \tilde{1} \rightarrow 0 \rightarrow 0$	$X^{4\tilde{1}00}$
$2 \rightarrow \tilde{1} \rightarrow 0 \rightarrow 0$	$X^{2\tilde{1}00}$

$$H_{cc} = \sum_{k=2,4} X^{k(SO_3)\rho(O)\sigma(D_3)\lambda(C_3)} U^{k(SO_3)\rho(O)\sigma(D_3)\lambda(C_3)}.$$

The unit tensor $U^{k(SO_3)\rho(O)\sigma(D_3)\lambda(C_3)}$ is related to the λ irreducible representation of C_3 subgroup, coming from the k irreducible representation of SO_3, which becomes ρ in O, σ in D_3, and λ in C_3. The terms $X^{k(SO_3)\rho(O)\sigma(D_3)\lambda(C_3)}$ are the crystal-field parameters used in the LFM code. Their definitions, in function of (D_σ, D_τ, D_q) or (ν, ν', D_q'), are given in Appendix G.

The branching rules which give 0 as irreducible representation in D_3 are summarized in Table IV. This implies that

$$H_{cc} = X^{4000}U^{4000} + X^{4\tilde{1}00}U^{4\tilde{1}00} + X^{2\tilde{1}00}U^{2\tilde{1}00}. \tag{F1}$$

Using the expression of the d eigenstates in C_3 given in Appendix E and the Wigner-Eckhart theorem (Eq. 4.2.4 of Ref. 26), we can now calculate the matrix elements,

$$\langle k_1(SO_3)\rho_1(O)\sigma_1(D_3)\lambda_1(C_3)|H_{cc}|k_2(SO_3)\rho_2(O)\sigma_2(D_3)\lambda_2(C_3)\rangle.$$

We obtain the following equations:

$$\langle e_\pm(t_2)|H_{cc}|e_\pm(t_2)\rangle = -\frac{\sqrt{2}}{3\sqrt{15}}X^{4000} + \frac{\sqrt{2}}{3\sqrt{21}}X^{4\tilde{1}00} - \frac{1}{\sqrt{70}}X^{2\tilde{1}00},$$

$$\langle a_1(t_2)|H_{cc}|a_1(t_2)\rangle = -\frac{\sqrt{2}}{3\sqrt{15}}X^{4000} - 2\frac{\sqrt{2}}{3\sqrt{21}}X^{4\tilde{1}00} + \frac{2}{\sqrt{70}}X^{2\tilde{1}00},$$

$$\langle e_\pm(e)|H_{cc}|e_\pm(e)\rangle = \frac{1}{\sqrt{30}}X^{4000},$$

$$\langle e_\pm(t_2)|H_{cc}|e_\pm(e)\rangle = \frac{1}{2\sqrt{21}}X^{4\tilde{1}000} + \frac{1}{\sqrt{35}}X^{2\tilde{1}00}. \tag{F2}$$

APPENDIX G: RELATIONS BETWEEN THE CRYSTAL-FIELD PARAMETERS USED IN LFM CALCULATIONS AND THOSE DERIVED FROM OPTICAL ABSORPTION SPECTROSCOPY

As mentioned in Ref. 49, two equivalent parameter sets are available in optical absorption spectroscopy to describe the crystal field in trigonal symmetry: (D_σ, D_τ, D_q) and (ν, ν', D_q'). In the following, we make connection between the two sets.

1. (D_σ, D_τ, D_q) parameter set

H_{cc} is defined as $H_{cc} = H_{\text{cub}} + H_{\text{trig}}$, where H_{cub} and H_{trig} are the Hamiltonian for the cubic and the trigonal contributions to the crystal field, respectively. According to Ref. 49 (Eq. 3.88), we have

$$\langle e_\pm(t_2)|H_{\text{trig}}|e_\pm(t_2)\rangle = D_\sigma + \frac{2}{3}D_\tau,$$

$$\langle a_1(t_2)|H_{\text{trig}}|a_1(t_2)\rangle = -2D_\sigma - 6D_\tau,$$

$$\langle e_\pm(e)|H_{\text{trig}}|e_\pm(e)\rangle = \frac{7}{3}D_\tau,$$

$$\langle e_\pm(t_2)|H_{\text{trig}}|e_\pm(e)\rangle = -\frac{\sqrt{2}}{3}(3D_\sigma - 5D_\tau). \tag{G1}$$

If the cubic term H_{cub} is added, we have

$$\langle e_\pm(t_2)|H_{cc}|e_\pm(t_2)\rangle = -4D_q + D_\sigma + \frac{2}{3}D_\tau,$$

$$\langle a_1(t_2)|H_{cc}|a_1(t_2)\rangle = -4D_q - 2D_\sigma - 6D_\tau,$$

$$\langle e_\pm(e)|H_{cc}|e_\pm(e)\rangle = 6D_q + \frac{7}{3}D_\tau,$$

$$\langle e_\pm(t_2)|H_{cc}|e_\pm(e)\rangle = -\frac{\sqrt{2}}{3}(3D_\sigma - 5D_\tau). \tag{G2}$$

Combining Eqs. (F2) and (G2), we obtain

$$X^{4000} = \frac{\sqrt{10}}{\sqrt{3}}(18D_q + 7D_\tau),$$

$$X^{4\tilde{1}00} = \frac{10\sqrt{14}}{\sqrt{3}}D_\tau,$$

$$X^{2\tilde{1}00} = -\sqrt{70}D_\sigma. \tag{G3}$$

X^{4000} contains only the cubic part of the crystal field, although D_τ appears in its expression. This means that the trigonal distortion, via D_τ, contributes to the $e-t_2$ splitting of the d orbitals. On the contrary, $X^{4\tilde{1}00}$ and $X^{2\tilde{1}00}$ are entirely due to the trigonal distortion. Hence, when we investigated the effect of the trigonal distortion on the XANES spectra in the LFM calculations, the values of $X^{4\tilde{1}00}$ and $X^{2\tilde{1}00}$ were set to zero, while the value of X^{4000} was fixed to the value used in D_{3d} symmetry. Things can be simplified by defining D_q', so that it contains also the contribution of D_τ to the cubic field. This leads to the definition of two other distortion parameters, ν and ν'.

2. (ν, ν', D_q') parameter set

The crystal-field Hamiltonian H_{cc} is now defined as $H_{cc} = H'_{\text{cub}} + H'_{\text{trig}}$, where H'_{cub} contains the contribution of D_τ. According to Ref. 49 (Eq. 3.90), we have

$$\langle e_{\pm}(t_2)|H'_{\text{trig}}|e_{\pm}(t_2)\rangle = -\frac{1}{3}\nu,$$

$$\langle a_1(t_2)|H'_{\text{trig}}|a_1(t_2)\rangle = \frac{2}{3}\nu,$$

$$\langle e_{\pm}(t_2)|H'_{\text{trig}}|e_{\pm}(e)\rangle = \nu'. \qquad (G4)$$

If we add the cubic term H'_{cub}, which is here defined so that the center of gravity is maintained for the trigonally split t_{2g} orbitals, the following equations are obtained:

$$\langle e_{\pm}(t_2)|H_{cc}|e_{\pm}(t_2)\rangle = -4D'_q - \frac{1}{3}\nu,$$

$$\langle a_1(t_2\ |H_{cc}|a_1(t_2)\rangle = -4D'_q + \frac{2}{3}\nu,$$

$$\langle e_{\pm}(t_2)|H_{cc}|e_{\pm}(e)\rangle = \nu'. \qquad (G5)$$

Combining Eqs. (F2) and (G5), we have

$$X^{4000} = 6\sqrt{30}D'_q,$$

$$X^{4\tilde{1}00} = -\frac{2\sqrt{3}}{\sqrt{7}}(\sqrt{2}\nu - 3\nu'),$$

$$X^{2\tilde{1}00} = \frac{4\sqrt{35}}{7}\left(\nu' + \frac{1}{2\sqrt{2}}\nu\right). \qquad (G6)$$

3. Relations between the two parameter sets

Combining Eqs. (G3) and (G6), we obtain the relations given in Ref. 49 (Eq. 3.91),

$$D'_q = D_q + \frac{7}{18}D_\tau,$$

$$\nu = -3D_\sigma - \frac{20}{3}D_\tau,$$

$$\nu' = -\sqrt{2}D_\sigma + 5\frac{\sqrt{2}}{3}D_\tau. \qquad (G7)$$

---

*amelie.juhin@impmc.jussieu.fr

[1] E. Balan, J. P. R. De Villiers, S. G. Eeckhout, P. Glatzel, M. J. Toplis, E. Fritsch, T. Allard, L. Galoisy, and G. Calas, Am. Mineral. **91**, 953 (2006).

[2] S. G. Eeckhout, N. Bolfan-Casanova, C. McCammon, S. Klemme, and E. Amiguet, Am. Mineral. **92**, 966 (2007).

[3] L. Galoisy, G. Calas, and M.-A. Arrio, Chem. Geol. **174**, 307 (2001).

[4] G. Dräger, R. Frahm, G. Materlik, and O. Brummer, Phys. Status Solidi B **146**, 287 (1988).

[5] N. Ueda, T. Omata, N. Hikuma, K. Ueda, H. Mizoguchi, T. Hashimoto, and H. Kawazoe, Appl. Phys. Lett. **61**, 1954 (1992).

[6] W. Schiessl, W. Potzel, H. Karzel, M. Steiner, G. M. Kalvius, A. Martin, M. K. Krause, I. Halevy, J. Gal, W. Schäfer, G. Will, M. Hillberg, and R. Wäppling, Phys. Rev. B **53**, 9143 (1996).

[7] T. Rodriguez-Suarez, S. Lopez-Esteban, J. F. Bartolomé, and J. S. Moya, J. Eur. Ceram. Soc. **27**, 3339 (2007).

[8] P. C. Burnley and H. W. Green, Nature (London) **338**, 753 (1989).

[9] M. Shimada, T. Endo, T. Saito, and T. Sato, Mater. Lett. **28**, 413 (1996).

[10] J. Guo, H. Lou, H. Zhao, X. Wang, and X. Zheng, Mater. Lett. **58**, 1920 (2004).

[11] M. Beauvy, C. Dalmasso, C. Thiriet-Dodane, D. Simeone, and D. Gosset, Nucl. Instrum. Methods Phys. Res. B **242**, 557 (2006).

[12] S. Mukhopadhyay, S. Ghosh, M. K. Mahapatra, R. Mazumder, P. Barick, S. Gupta, and S. Chakraborty, Ceram. Int. **28**, 719 (2002).

[13] D. Levy, G. Artioli, A. Gualtieri, S. Quartieri, and M. Valle, Mater. Res. Bull. **34**, 711 (1999).

[14] Note that the direction of the chains has been incorrectly reported in Ref. 15.

[15] A. Juhin, G. Calas, D. Cabaret, L. Galoisy, and J.-L. Hazemann, Phys. Rev. B **76**, 054105 (2007).

[16] Y. Joly, D. Cabaret, H. Renevier, and C. R. Natoli, Phys. Rev. Lett. **82**, 2398 (1999).

[17] D. Cabaret, B. Couzinet, A.-M. Flank, J.-P. Itié, P. Lagarde, and A. Polian, *XAFS13: 13th International Conference*, AIP Conf. Proc. No. 882 (AIP, New York, 2007), pp. 120-122.

[18] T. Yamamoto, T. Mizoguchi, and I. Tanaka, Phys. Rev. B **71**, 245113 (2005).

[19] J. C. Woicik, E. L. Shirley, C. S. Hellberg, K. E. Anderson, S. Sambasivan, D. A. Fischer, B. D. Chapman, E. A. Stern, P. Ryan, D. L. Ederer, and H. Li, Phys. Rev. B **75**, 140103(R) (2007).

[20] D. Cabaret, Ch. Brouder, M.-A. Arrio, Ph. Sainctavit, Y. Joly, A. Rogalev, and J. Goulon, J. Synchrotron Radiat. **8**, 460 (2001).

[21] M.-A. Arrio, S. Rossano, C. Brouder, L. Galoisy, and G. Calas, Europhys. Lett. **51**, 454 (2000).

[22] T. E. Westre, P. Kennepohl, J. D. DeWitt, B. Hedman, K. O. Hodgson, and E. I. Solomon, J. Am. Chem. Soc. **119**, 6297 (1997).

[23] C. Gauthier, V. A. Solé, R. Signorato, J. Goulon, and E. Moguiline, J. Synchrotron Radiat. **6**, 164 (1999).

[24] Ch. Brouder, A. Juhin, A. Bordage, and M.-A. Arrio, J. Phys.: Condens. Matter **20**, 455205 (2008).

[25] Ch. Brouder, J. Phys.: Condens. Matter **2**, 701 (1990).

[26] P. H. Butler, *Point Symmetry Group Applications* (Plenum, New York, 1981).

[27] Calculations were performed with PARATEC (parallel total-energy code) by B. Pfrommer, D. Raczkowski, A. Canning, S. G. Louie, Lawrence Berkeley National Laboratory (with contribu-

tions from F. Mauri, M. Cote, Y. Yoon, Ch. Pickard, and P. Haynes. For more information, see www.nersc.gov/projects/paratec).

[28] N. Troullier and J. L. Martins, Phys. Rev. B **43**, 1993 (1991).

[29] L. Kleinman and D. M. Bylander, Phys. Rev. Lett. **48**, 1425 (1982).

[30] T. Yamanaka and Y. Takeuchi, Z. Kristallogr. **165**, 65 (1983).

[31] M. Taillefumier, D. Cabaret, A.-M. Flank, and F. Mauri, Phys. Rev. B **66**, 195107 (2002).

[32] D. Cabaret, E. Gaudry, M. Taillefumier, Ph. Sainctavit, and F. Mauri, *Physica Scripta*, Proceedings of the XAFS-12 Conference, 2005, Vol. T115, p. 131.

[33] P. E. Blöchl, Phys. Rev. B **50**, 17953 (1994).

[34] R. Haydock, V. Heine, and M. J. Kelly, J. Phys. C **5**, 2845 (1972).

[35] R. Haydock, V. Heine, and M. J. Kelly, J. Phys. C **8**, 2591 (1975).

[36] E. Gaudry, D. Cabaret, Ph. Sainctavit, Ch. Brouder, F. Mauri, J. Goulon, and A. Rogalev, J. Phys.: Condens. Matter **17**, 5467 (2005).

[37] B. T. Thole, G. van der Laan, J. C. Fuggle, G. A. Sawatzky, R. C. Karnatak, and J. M. Esteva, Phys. Rev. B **32**, 5107 (1985).

[38] R. D. Cowan, *The Theory of Atomic Structure and Spectra* (University of California, Berkeley, 1981).

[39] The matrix elements between $1s^2 3d^3 4p^0$ and $1s^1 3d^3 4p^1$ give transitions only in the region of the main absorption edge and not in the pre-edge region. Any hypothetical Cr displacement from the center would induce $3d$-$4p$ hybridization and then nonzero electric-dipole transitions in the pre-edge region.

[40] F. M. F. de Groot, Coord. Chem. Rev. **249**, 31 (2005).

[41] In monoelectronic calculations, the ground state $|I\rangle$ ($1s^2$ in this case) is nondegenerate, as it is necessary for the Kohn-Sham implementation of DFT ($d_I=1$). In multielectronic calculations applied to $3d$ elements, the multielectronic state $|I\rangle$ ($1s^2 3d^3$) is often degenerate so that the degeneracy has to be taken into account in the cross-section formula.

[42] E. M. Gullikson, X-ray interactions with matter, www-cxro.lbl.gov/optical_constants

[43] D. L. Wood, G. F. Imbusch, R. M. Macfarlane, P. Kisliuk, and D. M. Larkin, J. Chem. Phys. **48**, 5255 (1968).

[44] E. Gaudry, D. Cabaret, Ch. Brouder, I. Letard, A. Rogalev, F. Wilhlem, N. Jaouen, and Ph. Sainctavit, Phys. Rev. B **76**, 094110 (2007).

[45] C. R. Natoli, M. Benfatto, and S. Doniach, Phys. Rev. A **34**, 4682 (1986).

[46] J. C. Slater, *Quantum Theory of Atomic Structure* (McGraw-Hill, New York, 1960).

[47] G. Calas and J. Petiau, Solid State Commun. **48**, 625 (1983).

[48] http://www.pwscf.org; S. Baroni, S. de Gironcoli, A. Dal Corso, and P. Giannozzi, Rev. Mod. Phys. **73**, 515 (2001).

[49] E. König and S. Kremer, *Ligand Field Energy Diagrams* (Plenum, New York, 1977).

Part II

Applications

Chapter 3

Tsavorite $Ca_3Al_2(SiO_4)_3$:V^{3+}

This chapter is dedicated to the study of tsavorite $Ca_3Al_2(SiO_4)_3$:V^{3+}, the V^{3+} reference compound used in the determination of the vanadium oxidation state in the (titano)magnetite samples (Chap. 5). Tsavorite was studied by X-ray absorption spectroscopy, with a particular emphasis on the pre-edge angular dependence. To support the experimental results, calculations were performed. The monoelectronic calculations, as the experiments, are presented as a publication submitted to American Mineralogist. Complementary computational details and results on the calculations presented in the publication are then given. Finally, some multielectronic calculations are presented and discussed. The latter relate to an ongoing study which is not completed yet.

3.1 The angular dependence of the pre-edge

3.1.1 Summary of the publication

In the study of the Bushveld titanomagnetite samples (Chap. 5), the idea was to use vanadium and its several oxidation states as a geochemical probe to get information on the formation of the monomineralic magnetite layers in the Bushveld Complex. HERFD-XAS spectra at the V K-edge were measured and analyzed with a fingerprint method: the spectra were compared with those of reference compounds to infer the speciation of vanadium. For the V^{3+} in a octahedral site, tsavorite was chosen as a reference compound. A precise characterization of its spectral signature was thus needed to correctly interpret the pre-edge features of the titanomagnetites spectra. The energy and relative intensity of the pre-edge features indeed provide information on the oxidation state and site symmetry of the absorbing atom [35].

Nevertheless, the changes in the pre-edge features could be misinterpreted if careful attention is not given to the investigated samples. Variations in the position and relative intensities can indeed arise not from different oxidation states or incorporation sites, but from an angular dependence of the XAS spectrum. This effect is most commonly observed for single crystals but it can be also measured on textured powder samples [162]. The angular dependence of the XAS spectrum is well-known in the case of non-cubic compounds [164, 165, 33, 34, 87, 86, 200] but it can also be observed in the case of cubic compounds [24, 32, 122] (Chap. 1).

Tsavorite is a cubic mineral with vanadium atoms in a C_{3i} symmetry site, which corresponds to a distorted octahedron with an inversion center, as described in Chap. 1. Hence the pre-edge arises from pure electric quadrupole transitions and variations of the spectral features are expected when the sample orientation varies with respect to the incident beam polarization and direction [24]. To evaluate the influence of these variations on the pre-edge features of tsavorite, XAS experiments at the V K-edge were performed to measure the angular dependence. HERFD-XAS spectra were recorded for different orientations on a cut single crystal, oriented by the Laue method. The angular dependence was experimentally well observed. The maximal effect was observed for the two configurations described in figure 3.1. Between them, the crystal was rotated by an angle of 90°. However the measured effect is quite small and does not interfere significantly in the determination of the V^{4+}/V^{3+} ratio of the (titano)magnetite samples.

DFT calculations were then performed to give a fine interpretation of the experimentally observed angular dependence. The methodology described in Chap. 2 was used. In order to reduce the number of calculations, the coset method was used. A concrete application of the general formulas given in Chap. 2 is thus described for the specific case of the garnet structure. The site symmetry (C_{3i}) is retained during the relaxation process, which led to a slight dilatation of the octahedron with the substitution of a vanadium atom for a aluminum. A good agreement was obtained between experimental and theoretical spectra. The calculations confirmed that the electric dipole cross-section does not contribute to the pre-edge features, as expected by the centrosymmetry of the vanadium site in tsavorite. The calculations were spin-polarized, which allowed the interpretation of the transitions within a monoelectronic picture. The splitting between the t_{2g} and e_g orbitals was thus determined. The $t_{2g}^{\uparrow}$-$e_g^{\uparrow}$ splitting was found to be similar to the $10Dq$ crystal-field value determined from optical spectroscopy.

Finally, the importance of the angular dependence and its influence in the determination of the elements speciation in minerals is discussed in a more general picture than the particular case of tsavorite and garnets.

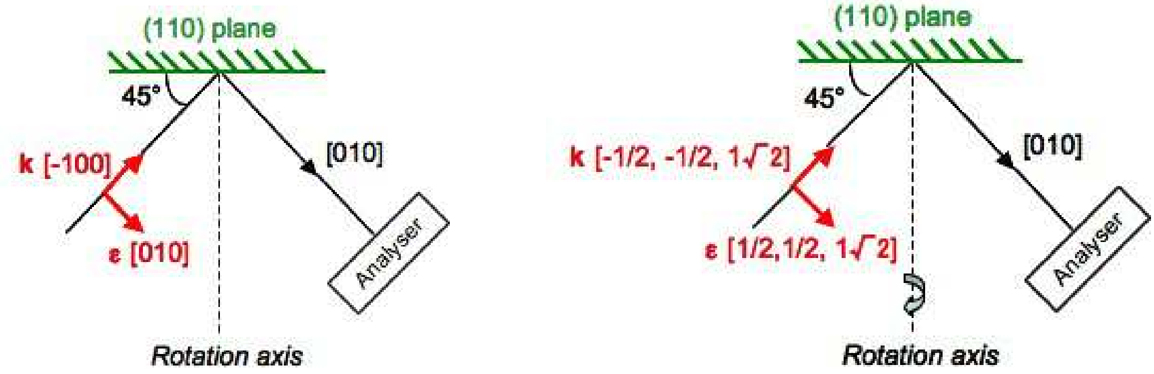

Figure 3.1: The two experimental configurations. The sample was rotated by 90° between them.

3.1.2 Publication

Electronic structure and local environment of substitutional V^{3+} in grossular garnet $Ca_3Al_2(SiO_4)_3$: *K*-edge X-ray Absorption Spectroscopy and first-principles modeling

Amélie Bordage[1,*], Christian Brouder[1], Etienne Balan[1], Amélie Juhin[1, †], Delphine Cabaret[1], Marie-Anne Arrio[1], Philippe Sainctavit[1], Georges Calas[1] and Pieter Glatzel[2]

[1] Institut de Minéralogie et de Physique des Milieux Condensés, UMR CNRS 7590, Université Pierre et Marie Curie, Université Paris Diderot, IRD UMR 206, IPGP, 140 rue de Lourmel, 75015 Paris, France

[2] European Synchrotron Radiation Facility, 6 rue Jules Horowitz, BP 220, 38043 Grenoble Cedex, France

*amelie.bordage@impmc.jussieu.fr

[†] Present address: Debye Institute for Nanomaterials Science, Inorganic Chemistry and Catalysis, Utrecht University, Sorbonnelaan 16, 3584 CA Utrecht, The Netherlands

Abstract

The V *K*-edge spectrum of a V-bearing grossular garnet (tsavorite) single-crystal has been measured by high-energy resolution fluorescence detected X-ray absorption spectroscopy (HERFD-XAS). First-principles calculations based on density functional theory (DFT) reproduce well the experimental spectra, including the angular dependence of the pre-edge. An interpretation of the spectral features is given using a monoelectronic description of the transitions involved in the X-ray absorption process. The assignment of experimental pre-edge peaks in terms of 1*s*-3*d* transitions makes it possible to determine the magnitude of the *3d*-splitting, which is similar to the 10Dq crystal-field value determined from optical absorption spectroscopy. DFT calculations also indicate a full structural relaxation around V^{3+} substituting Al^{3+} in the garnet structure. The angular dependence only causes weak variations of the pre-edge intensity, which supports the use of V-bearing grossular garnet as a reference compound for octahedral V^{3+}.

Keywords: Vanadium, Garnet, HERFD-XAS, DFT calculations, *K* pre-edge, Angular dependence, Structural relaxation, Crystal field splitting

Introduction

Transition elements play an important role in geophysics and Earth sciences, as they are major constituents of the Earth and planets. They may occur under different oxidation states, which makes them valuable geochemical probes. For instance, vanadium oxidation state ranges from +III to +V in terrestrial magmatic systems, which dramatically influences the partitioning of this element between minerals and melts (e.g., Toplis and Corgne 2002, Canil 2002, Papike et al. 2005 , Karner et al. 2006). Vanadium speciation (i.e., oxidation state and local structure) in minerals and glasses has been mostly investigated by V K-edge X-ray absorption near-edge structure (XANES) (Berry et al. 2003, Giuli et al. 2004, Berry et al. 2004, Sutton et al. 2005, Balan et al. 2006). Indeed, the pioneering studies of Wong et al. (1984) have shown a great sensitivity of the XANES features to vanadium speciation in oxides and silicates. Due to the localized character of the associated electronic transitions at the origin of the pre-edge structure (Calas and Petiau 1983, autres?), this important XANES component has received a special attention, as it provides a quantitative information on the speciation of transition elements. In glasses, it has then been possible to quantify vanadium speciation, through an accurate determination of the energy position and relative intensity of pre-edge components (Sutton et al. 2005). This relies on an accurate calibration with reference minerals in which the vanadium oxidation state is known. These crystalline references are among the few minerals in which the V K-edge XANES spectra are known. In magmatic minerals, vanadium is predicted to be preferentially incorporated as V^{3+}, replacing Al^{3+} or Fe^{3+} in octahedral sites (Canil 2002). However few direct information is available on the crystal chemistry of this oxidation state in vanadium-bearing minerals and the incorporation of V^{3+} in rock-forming minerals.

We present new information on vanadium speciation in a V-bearing grossular garnet ($Ca_3Al_2(SiO_4)_3$:V^{3+}, sometimes referred to as tsavorite). As vanadium occurs in minor amounts, this makes this mineral an ideal V^{3+}-diluted reference compound (Balan et al. 2006). In the present work, V K-edge XANES spectra of a V-bearing grossular single-crystal have been obtained using high-energy resolution fluorescence-detected X-ray absorption spectroscopy (HERFD-XAS) (De Groot et al. 2009, Glatzel et al. 2009a,b), to prevent parasitic secondary x-ray emission from Ti impurities, naturally present in the sample investigated. The XANES spectra are modeled using Density Functional Theory in the local density approximation (DFT-LDA). We show that the pre-edge features vary with the orientation of this cubic single crystal with respect to the polarization $\hat{\varepsilon}$ and direction $\boldsymbol{k}$ of the incident X-ray beam, as for any crystal symmetry (Brouder 1990). This angular dependence must be taken into account for the investigation of textured powders (Pettifer et al. 1990) and may have implications for the investigation of vanadium speciation in minerals. The good agreement between experimental and calculated XANES spectra allows the DFT-LDA calculations to be used to get further insight on the local structural relaxation about V^{3+} in the Y-site of garnets, showing a full relaxation around substituted V^{3+}. In addition, these calculations predict V^{3+} crystal-field splitting values in V-bearing grossular that are in agreement with existing optical spectroscopy data.

Experiments

Sample

The chemical composition of the natural single-crystal of V-bearing grossular investigated was analyzed using the Cameca SX50 electron microprobe at the CAMPARIS analytical facility of the University Pierre et Marie Curie, Paris (France). It was operated at 15 kV and 40 nA, with counting time varying from 10 to 30 s, depending on the element. The chemical formula of the tV-bearing grossular studied is approximately $Ca_3(Al_{1.93}V_{0.07})_2(SiO_4)_3$, with 0.42 at% Mn, 0.26 at% Mg, 0.05 at% Cr, 0.12 at% Ti and 0.02 at% Fe. The V-bearing grossular single-crystal was cut along the (110) plane and oriented using the Laue method.

X-ray absorption spectroscopy measurements

The presence of comparable amounts of Ti and V in V-bearing grossular hinders the use of a conventional total fluorescence yield detection. High energy-resolution fluorescence detection X-ray absorption spectroscopy (HERFD-XAS) overcomes this problem. Furthermore it improves substantially the resolution of the pre-edge and edge structures (Glatzel and Bergmann 2005, De Groot et al. 2009, Glatzel et al. 2009a,b). In HERFD-XAS, one fluorescence line is selected to record the spectrum while scanning the incident energy, using a fluorescence detector with an energy resolution similar to the core-hole lifetime broadening. This analyzer is a Bragg crystal positioned in a Rowland geometry (Fig. 1) in the energy range of transition metal *K* edges. A Bragg crystal is a spherically-bent crystal the reflection of which corresponds to the required X-ray emission energy and that focuses the selected X-rays on a photon detector. Room-temperature V *K*-edge HERFD-XAS spectra were recorded at the high-brilliance beamline ID26 of ESRF (European Synchrotron Radiation Facility) (Gauthier et al. 1999). We recorded the $K\alpha_1$ line of vanadium (4952 eV) while scanning the incident energy. The energy of the incident radiation was selected using a pair of lN_2-cooled Si crystals with a (311) orientation. The spot size of the incident X-ray beam on the sample was 250 x 50 μm^2. Spectra ranging from 5460 to 5515 eV incident energy were recorded in a quick scan mode. Additional scans were performed between 5460 and 5815 eV to normalize the XANES spectra to the K-edge jump. The incident flux was monitored by detecting the X-ray scattering from a thin Kapton® foil in the incident beam path. High-resolution emission detection was achieved by employing a spherical bent Ge crystal (R = 855 mm) with a (331) orientation in a Rowland geometry. An avalanche photodiode was used as a fast detector for emission detection to avoid non-linear effects. Self-absorption was negligible because of the low V-content of the samples. We checked carefully during measurements that there was no photoreduction effect. The incident beam had a resolution $\Delta E = 0.2$ eV and the convoluted resolution, i.e. the combined resolutions of the incident beam and the spectrometer is 0.8 eV.

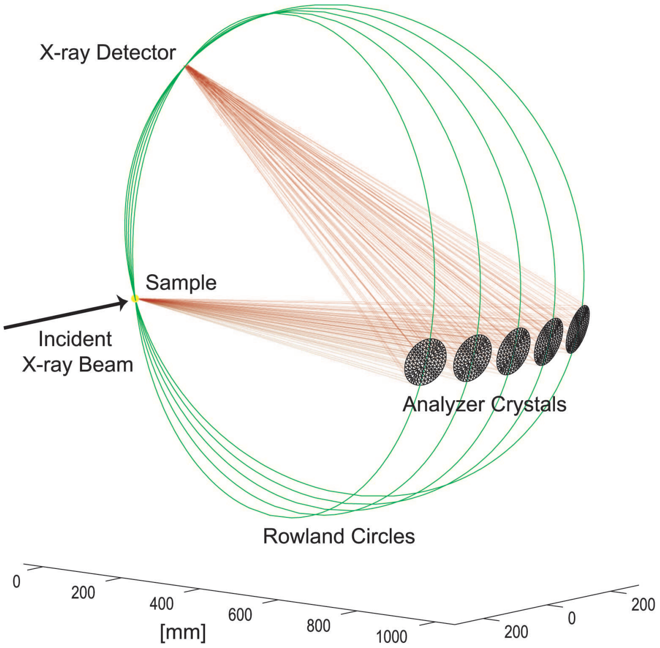

***Figure** 1: Experimental set-up for HERFD-XAS measurements, showing the orientation of the Rowland circles for the five analyzer crystals. Only one crystal was used during the experiments at V K edge of tsavorite. (Figure reproduced from Glatzel et al. 2009a)*

The single crystal was mounted on a rotating holder at 45° with respect to the incident beam, and rotated by an angle α_{rot} about the [110] direction. The starting configuration α_{rot} = 0° corresponds to $\hat{\varepsilon} = [010]$ and $\hat{k} = [\bar{1}00]$. The α_{rot} = 90° configuration corresponds to $\hat{\varepsilon} = \left[\frac{1}{2}, \frac{1}{2}, \frac{1}{\sqrt{2}}\right]$ and $\hat{k} = \left[-\frac{1}{2}, -\frac{1}{2}, \frac{1}{\sqrt{2}}\right]$. For this sample cut and this experimental setup, the maximum variation is obtained by subtracting the absorption recorded for α_{rot} = 0° from that recorded for α_{rot} = 90° (Juhin et al. 2008b). The difference between these two orientations is called X-ray Linear Natural Dichroism (XNLD). A spectrum was recorded every 15° from α_{rot} = 0° to α_{rot} = 360° in order to ensure the reconstruction of the complete angular dependence of the crystal.

A resonant inelastic X-ray scattering (RIXS) plane was also measured for a powder sample. As only one fluorescence line is recorded in the case of HERFD-XAS, the spectrum may differ from a conventional XANES one. Therefore, recording a RIXS plane enables to ensure that the spectra are similar. In RIXS spectroscopy, both incident and emitted energies are simultaneously scanned. A second axis (the energy transfer or emission energy) is added to that of the incident photon so a 2D plane is plotted (Glatzel and Bergmann, 2005). The plane was recorded between 5462 and 5479 eV for the incident energy, and between 4940 and 4960 eV for the emitted energy.

Calculations

Theoretical framework

We adopt here a first-principles approach based on the Density Functional Theory in the local density approximation (DFT-LDA). It has already been successfully used to study the crystallographic and electronic structures of an impurity in a host-structure, e.g., Cr, Ti and Fe in corundum α-Al_2O_3 (Gaudry et al., 2003, 2005), Cr in beryl $Be_3Si_6Al_2O_{18}$ (Gaudry et al. 2007), Cr in spinel $MgAl_2O_4$ (Juhin et al. 2007), Cr in pyrope $Mg_3Al_2(SiO_4)_3$ (Juhin et al. 2008a). The DFT-LDA approach is usually used for the calculation of *K*-edge spectra as the excited 1*s* electron in *K*-edge X-ray absorption spectroscopy probes the *p*-states, i.e. delocalized final states. However several studies have also shown good results for the pre-edges calculations, e.g., Ti in TiO_2-rutile and $SrTiO_3$ (Joly et al. 1999, Cabaret et al. 2007, Yamamoto et al. 2005, Woicik et *al.* 2007), Fe in FeS_2 (Cabaret et al. 2001) or Cr in $MgAl_2O_4$ (Juhin et al. 2008b). The monoelectronic approach is based on the calculation of the absorption cross section, σ, which has the following general expression:

$$\sigma\left(\hat{\varepsilon},\hat{k}\right) = 4\pi^2\alpha\hbar\omega\sum_f \left|\langle f|H|i\rangle\right|^2\delta\left(E_f - E_i - \hbar\omega\right)$$

where $\alpha = e^2/4\pi\varepsilon_0\hbar c$ (in S.I. units) is the fine-structure constant (~1/137), $\hbar\omega$ the energy of the incoming photons, H is the interaction hamiltonian. $|i\rangle$ is the initial state and $|f\rangle$ a final state, with respective energy E_i and E_f. The Dirac function $\delta\left(E_f - E_i - \hbar\omega\right)$ ensures the conservation of the energy. In the electric dipole approximation, H is given by $(\hat{\varepsilon}\cdot r)$ and in the electric quadrupole approximation by $\frac{i}{2}(\hat{\varepsilon}\cdot r)(\hat{k}\cdot r)$. In the absence of coupling between the electric dipole and quadrupole terms, $\sigma\left(\hat{\varepsilon},\hat{k}\right)$ is simply the sum of electric dipole σ^D and electric quadrupole σ^Q contributions:

$$\sigma\left(\hat{\varepsilon},\hat{k}\right) = \sigma^D\left(\hat{\varepsilon}\right) + \sigma^Q\left(\hat{\varepsilon},\hat{k}\right)$$

This expression is valid if the system is centrosymmetric. It is also valid if the system is non-magnetic (no net magnetic moment on the absorbing atom) and one uses exclusively linear polarization.

In a cubic crystal the electric dipole cross section is isotropic, i.e. it does not depend on the direction of the polarization vector. The electric dipole transitions contribute mainly to the edge, but also to the pre-edge if one of the three following situations is encountered: (i) there is *p* - *d* intrasite hybridization (e.g., the crystallographic site does not show an inversion center), (ii) the thermally activated vibrations remove the inversion center, (iii) there is *p* - *d* intersite hybridization, e.g., in samples highly concentrated in the investigated element (Shukla et al. 2006, Gougoussis et al. 2009). Electric quadrupole transitions contribute mainly to the pre-edge. In garnet, the octahedral site shows an inversion center and therefore the pre-edge of the central cation is due to pure electric quadrupole transitions. The latter are anisotropic whatever the crystal symmetry is (Brouder 1990) and variations of the electric quadrupole cross-section are thus expected when the orientation of the sample with respect to the incident X-ray beam is varied. The anisotropy of the electric quadrupole cross section depends on the crystal point group. When the point group is different for the crystal and the absorbing atom site, the parameters of the crystal angular dependence can be expressed as functions of the site point group parameters (Brouder et al. 2008). This angular dependence improves our understanding of the electronic structure of the absorbing atom, e.g., by giving the respective proportion of electric dipole and quadrupole transitions in the pre-edge (Cabaret et al. 2001, Juhin et al. 2008b).

Computational details

The DFT calculations are done in two steps: first a structural model is determined and then the X-ray absorption spectrum is computed. For V-bearing grossular, the structural model is obtained from a grossular host-structure where one aluminum is substituted by one vanadium. Because of the difference between the two ionic radii (r (V^{3+}) = 0.64Å *vs.* r (Al^{3+}) = 0.535Å; Burns 1993), a modification of the local structure around the substituted V^{3+} cation is expected. The substituted structure is thus relaxed by *ab initio* energy minimization calculations. From the relaxed structure, the charge density with a 1*s* core-hole on the absorbing atom is computed and the XANES spectrum is finally calculated in the electric dipole and quadrupole approximations. The PWscf code (Baroni et al. 2001) and the XSpectra code (Gougoussis et al. 2009) from the Quantum-Espresso suite of codes (Giannozzi et al.) were used. PWscf is a first-principles total-energy code based on DFT in the local density approximation with spin polarization (LSDA). It uses periodic boundary conditions, plane-wave basis set and norm-conserving pseudopotentials (Troullier and Martins, 1991) in the Kleinman-Bylander form (Kleinman and Bylander 1982). All the parameters for the pseudopotential generation are given in Table I.

The structural relaxation started from the experimental structure of grossular $Ca_3Al_2(SiO_4)_3$ (Geiger and Armbruster 1997). The cubic cell (a=11.85 Å, Geiger 1997) contains eight $Ca_3Al_2(SiO_4)_3$ formula units, corresponding to 160 atoms: 1 vanadium, 15 aluminum, 24 silicium, 24 calcium and 96 oxygen. With such a large cell, interactions between neighboring cells are negligible. The cell was relaxed using a single *k*-point sampling in the Brillouin zone and a 70 Ry energy cutoff. All the atomic positions are allowed to vary to minimize the total energy and the interatomic forces, while the lattice parameter is kept fixed to the experimental value. Before relaxation, the vanadium was slightly displaced from its position to avoid an artificial conservation of the symmetry around vanadium. This methodology was already adopted to study impurities (Ti, Fe and Cr) in beryl $Be_3Si_6Al_2O_{18}$, corundum α-Al_2O_3 (Gaudry et al. 2007, 2005, 2003) and spinel $MgAl_2O_4$ (Juhin et al. 2007).

The method used for XANES calculations is described by Taillefumier et al. (2002) and Cabaret et al. (2005). The reconstruction of the all-electron wavefunctions is done within the projector augmented wave method (Blöchl 1994). To be able to treat large supercells (more than one hundred of atoms), the scheme uses a recursion method to construct a Lanczos basis and then compute the cross section as a continued fraction (Haydock et al. 1972, 1975). We used a 90 Ry cutoff energy for the plane-wave expansion, one *k*-

point for the self-consistent spin-polarized calculation of the charge density with a core-hole on vanadium and a Monkhorst-Pack grid of 4x4x4 points in the Brillouin zone for the absorption cross-section calculation. An energy dependent broadening parameter γ is used in the continuous fraction in order to account for the two main photoelectron damping-modes. This width γ corresponds to the lifetime of the photoelectron through the time-energy uncertainty relations. At low energy (approximately up to the edge energy), the lifetime of the photoelectron is only limited by the core-hole lifetime. The parameter γ was set to a constant that corresponds to the *K*-level half-width at half-maximum given by Krause and Oliver (1979). At higher energy, the photoelectron is fast enough to interact with the electron gas of the system and consequently its mean free-path is attenuated, inducing a sharp decrease in the lifetime behavior (Sainctavit et al. 1989). We chose rapid variation of γ near the edge, followed by a constant value at higher energy: $\gamma = 0.5$ eV till 5472 eV and $\gamma = 1$ eV from 5485 eV, with a linear variation between these two energies, similar to Kokubun et al. (2004) and Gaudry et al. (2005).

Atom	V	Ca	Al	Si	O
Valence states	$3s^2$ (0.53) $3p^6$ (0.85) $3d^2$ (0.79)	$3s^2$ (0.77) $3p^6$ (1.06) $3d^0$ (0.77)	$3s^2$ (1.06) $3p^0$ (1.06) $3d^0$ (1.06)	$3s^2$ (1.06) $3p^{1.3}$ (1.06) $3d^{0.2}$ (1.06)	$2s^2$ (0.77) $2p^3$ (0.77)
Local part	s	d	d	d	p

Table I. *Parameters used for the generation of the pseudopotentials. The core radii of the valence states are indicated between parentheses in Å.*

Symmetry considerations in order to reduce the number of calculations.

The unit cell of grossular (space group $Ia\overline{3}d$) contains sixteen octahedral sites and the vanadium atoms can enter equally in any of them. These sites are divided in two groups equivalent by a (1/2,1/2,1/2) translation vector. The eight sites of each group are related to each other by space group operations. Each octahedron is distorted (C_{3i} symmetry) and the direction of the distortion with respect to the cubic frame is determined by the orientation of the C_3 axis. As the sites have a different orientation with respect to the cubic frame, the calculation of the XANES spectrum requires the consideration of the different site orientations. As mentioned before, the electric dipole cross-section is isotropic for a cubic crystal and the local symmetry and orientation of the vanadium site has no influence on it. Therefore it will be identical for the eight sites and a single calculation is needed. However the electric quadrupole cross-section, for a given single-crystal experimental configuration, is expected to be different for each site, since their orientation with respect to the incident X-ray beam are different. Consequently the average electric quadrupole cross-section must be determined. Two methods are possible. The “brute force” method consists in successively computing the XANES spectra for each site and average them. To reproduce the angular dependence, two orientations are calculated, which means that 8 charge densities with a core-hole, 1 electric dipole cross-section and 16 electric quadrupole cross sections have to be computed. This method is simple but its cost in computational time is significant. A more elegant way is to use the coset method that takes advantage of the crystal symmetries. This method, based on a spherical tensor analysis (Brouder et al. 2008), determines the general relations between the sites and deduces from these relations whether some electric quadrupole cross-sections are identical. For the case of garnet, we can show that the electric quadrupole cross-section for the $\alpha_{\mathrm{rot}} = 0°$ orientation is identical for the eight sites. For the $\alpha_{\mathrm{rot}} = 90°$ orientation, the electric quadrupole cross-section corresponds to the average of two sites. Hence the use of the coset method allows to limit the calculation to only one charge density, one electric dipole cross-section and three electric quadrupole cross-sections (one for the $\alpha_{\mathrm{rot}} = 0°$ orientation and two for the $\alpha_{\mathrm{rot}} = 90°$ orientation). The detailed formulas are given in the appendix 1.

Results

Structural relaxation

In the unrelaxed garnet structure (Fig. 2), the calcium atoms sit on the 24*c* sites and are eightfold coordinated in an oxygen dodecahedron (site X). The silicon atoms are fourfold coordinated and located at the 24*d* sites with $\bar{4}$ symmetry (site Z). The aluminum atoms occur at the 16*a* sites (site Y), which are distorted octahedral sites with symmetry $\bar{3}$ (or C_{3i}). The oxygen atoms are located at general positions (*x,y,z*). The SiO_4 tetrahedra are connected by corners to AlO_6 octahedra, and the Ca atoms lie in the center of the dodecahedral cavity created by the arrangement of these tetrahedra and octahedra. Figure 3 shows the first atomic shell around the substitutional V atom before and after relaxation when V^{3+} substitutes for Al^{3+} in the grossular structure. The six V-O distances increase from 1.92 Å in the non-relaxed structure to 1.99 Å in the relaxed one. The calculations also show that the V-centered octahedron is slightly more distorted after relaxation than in unsubstituted grossular (Table II). The octahedral angular variance (OAV) (Robinson et *al.* 1971) increases from $2.2^{(°)2}$ to $5.3^{(°)2}$ with the substitution. The O1-O4 distances lengthen (from 2.76 Å to 2.88 Å) more than the O1-O5 ones (from 2.69 to 2.77 Å). A propagation of the relaxation around V^{3+} to the nearest neighbors is observed: the V-Ca distance remains quite the same but the V-Si distance increases during the relaxation process (Table II). The symmetry of the relaxed V site is however retained from the Al site in grossular. The preservation of the trigonal distortion has already been observed in Cr-bearing pyrope and Cr-bearing grossular, where Cr^{3+} substitutes for aluminum (Juhin et al. 2008a).

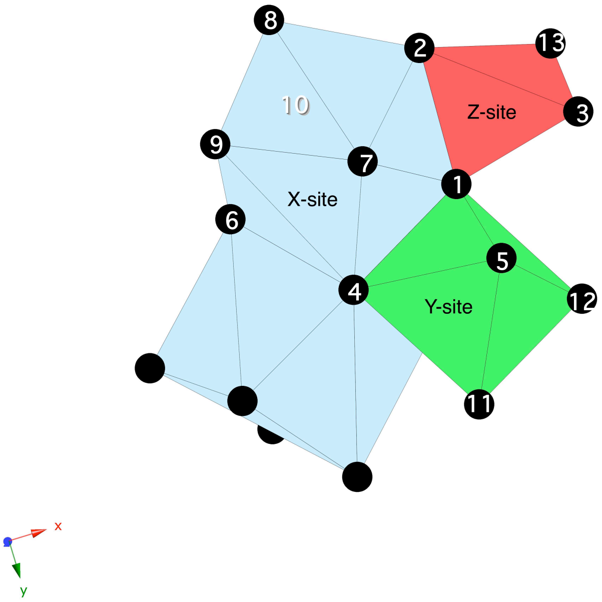

***Figure** 2: Portion of the tsavorite garnet structure, with X=Ca^{2+}, Y=Al^{3+} and V^{3+}, and Z=Si^{4+}. The O atoms are labelled according to Novak and Gibbs (1971). The figure is taken from Juhin et al. (2008a).*

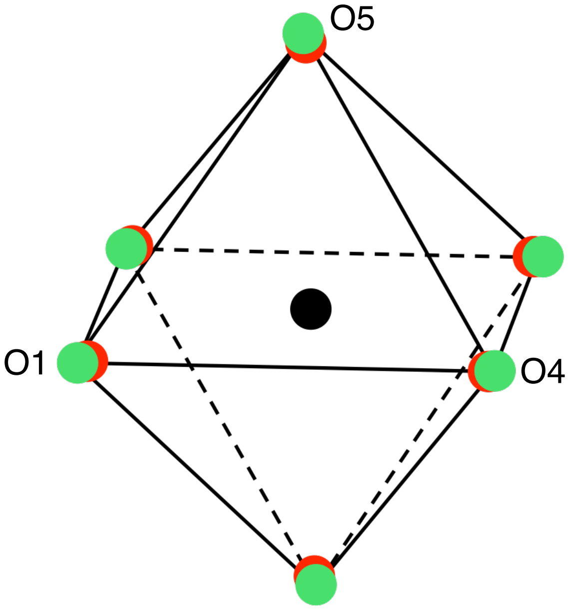

***Figure 3:** V-centered (dark atom) octahedron before (red) and after (green) relaxation.*

	V-O (Å)	Al-O (Å)	Al-Si Al-Ca (Å)	V-Si (Å)	V-Ca (Å)	O1-O4 (Å)	O1-O5 (Å)	Angle O4-V-O5(°)	OAV (°)^2
Before relaxation	-	1.926	3.31	-	-	2.76	2.69	88.6	2.2
After relaxation	1.995	-	-	3.36	3.31	2.88	2.77	87.8	5.3

***Table II.** Structural parameters before and after relaxation. The structure before relaxation is the experimental structure of grossular (Geiger and Armbruster 1997). OAV is the octahedral angular variance, defined by Robinson et al. (1971). The oxygen labels O1, O4 and O5 are those of Fig.3.*

Experiment vs. calculations

The experimental and calculated XANES spectra of V-bearing grossular for the two orientations α_{rot} = 0° and α_{rot} = 90° are shown in Figure 4. The edge presents four structures with two additional ones at lower energy, i.e. in the edge rising. A pre-edge is also observed, characterized by three structures (Fig. 4). A good agreement is obtained between the experimental spectra and the ones calculated from the *ab initio* relaxed structure. All the experimental features are present on the calculated spectrum (Fig. 4a). The position, shape and intensity of the main peaks at 5483.3 (peak C) and 5486.9 eV (peak D) are well reproduced. The A and B features exhibited at lower energy (5476.3 and 5480.6 eV) are also in good agreement with the experimental ones. The splitting of peak A observed in the calculated spectrum is not significant. The edge is identical for the two orientations, as expected for electric dipole transitions in a cubic structure. On the contrary the angular dependence of the pre-edge is well observed on the experimental spectra (Fig. 4b). The relative intensities between the three peaks are different, especially between peaks P2 (5467.8 eV) and P3 (5469.6 eV) from an orientation to another. The relative energy between the three peaks is also reproduced and the overall shape of the pre-edge is well reproduced by the calculation. However, compared with the experiments, the calculated pre-edge is shifted (~2 eV) toward higher energies with respect to the main rising edge. This shift is a well-known effect that has already been observed (Joly et *al.* 1999; Gaudry et *al.* 2005; Juhin et *al.* 2008b) and is related to the limit of DFT within LSDA to model the interaction between the core-hole and the empty *d* states of 3*d* transition metals. However, despite this energy shift, the experimental and calculated pre-edges present the same number of peaks, with the correct relative intensities and energies.

To evaluate the sensitivity of the XANES spectrum to the structural relaxation, the XANES spectrum was computed from the relaxed and non-relaxed structures. The XANES spectra computed from the two structural models are compared with the experimental one in Figure 5. The experimental spectrum is not as well reproduced with the non-relaxed structure as with the relaxed one, especially when considering the shape and relative intensities of peaks C, D and H. Peak A is less satisfactory and peak B is absent on the non-relaxed spectrum. The agreement is also better in the pre-edge region when the XANES spectrum is computed from the relaxed structure. The relaxed structural model is therefore reliable.

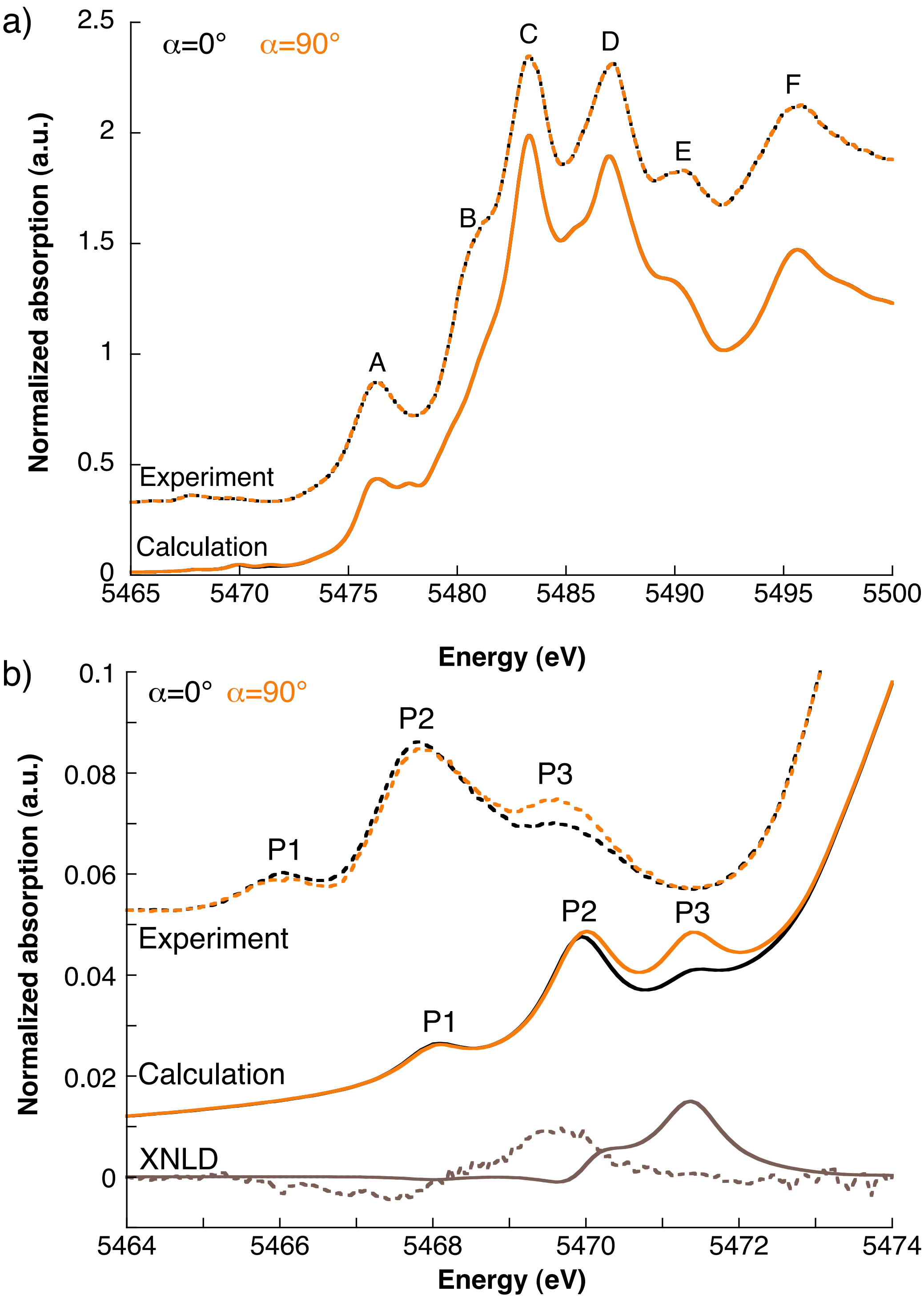

Figure 4: *Comparison between the experimental (dotted line) and calculated (solid line) spectra of V K edge (a). The bottom figure is a zoom of the pre-edge region (b). The black lines correspond to the* α_{rot} = *0° orientation* $\left(\hat{\varepsilon}=\left[010\right],\hat{k}=\left[\bar{1}00\right]\right)$ *and the orange lines to* α_{rot} = *90°* $\left(\hat{\varepsilon}=\left[\frac{1}{2},\frac{1}{2},\frac{1}{\sqrt{2}}\right],\hat{k}=\left[-\frac{1}{2},-\frac{1}{2},\frac{1}{\sqrt{2}}\right]\right)$. *The brown lines (b) represent the XNLD signal, which is the difference between the 90° and 0° orientation signals.*

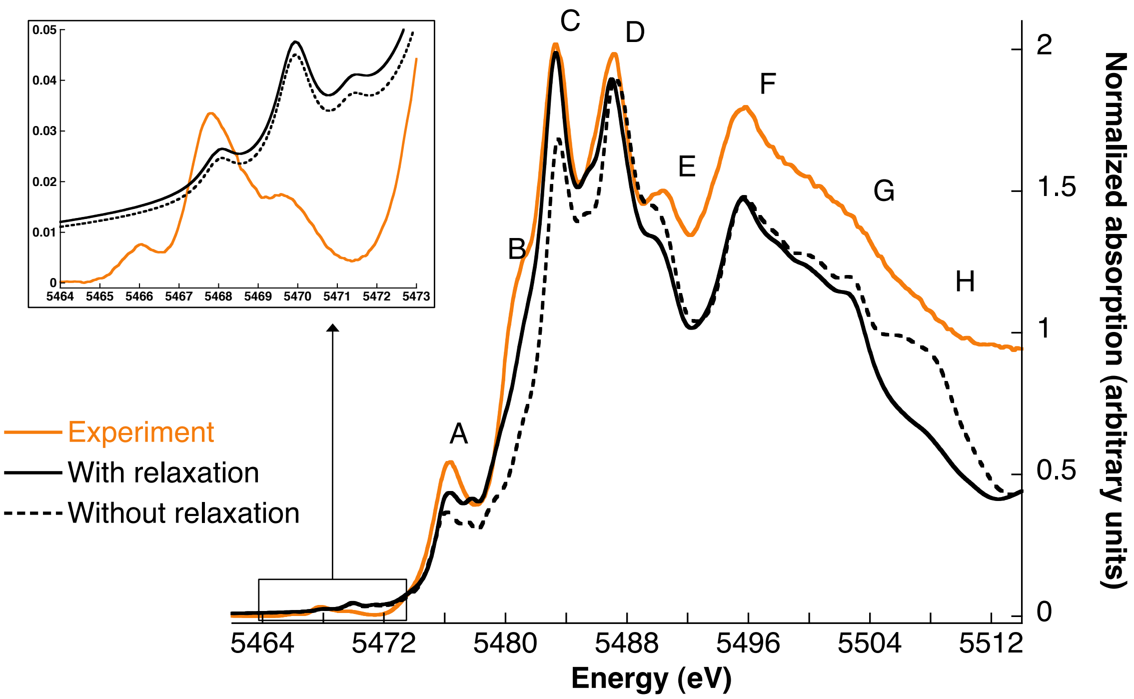

Figure 5: *Comparison between the experimental V K-edge XANES spectra of tsavorite (orange) and the ab initio calculated spectra for the relaxed (solid black line) and non-relaxed (dashed black line) structures for the* α_{rot} *= 0° orientation. The inset presents the spectra in the pre-edge region.*

RIXS plane and HERFD-XAS

A partial fluorescence yield experiment is based on secondary process detection that may not yield true absorption spectra. It has been shown that Kα detected absorption spectroscopy in 3*d* transition metals using energy dispersive solid state detectors provides a very good approximation to the absorption coefficient (Jaklevic et al. 1977). High-energy resolution fluorescence detection further reduces the energy bandwidth as compared to standard fluorescence detected XAS (Hamaläinen et al. 1991). Carra et al. (1995) pointed to problems that may be encountered when the detection energy bandwidth is reduced to a few eV and thus below the magnitude of electron-electron interactions. It is therefore necessary to verify whether electron-electron interactions in the final state cause additional spectral features that may be misinterpreted as absorption features (Glatzel and Bergmann 2005). A full RIXS plane at the V *K* absorption pre-edge of V-bearing grossular was therefore recorded in order to verify the importance of final state interactions (Fig. 6). A HERFD-XAS spectrum corresponds to a horizontal cut through the RIXS plane at a given emission energy.

The Kα_1 and Kα_2 lines are at 4952 eV and 4944 eV emission energy, respectively. The Kα lines present 90% of the total fluorescence yield and the 2*p* spin-orbit split Kα_1 and Kα_2 lines show similar spectral shapes. Three absorption features are observed at 5466 eV, 5468 eV and 5470 eV. They correspond to the three peaks observed on the HERFD-XAS pre-edge spectra that were recorded of the maximum of the Kα_1 line. The more intense feature at 5476 eV corresponds to the A peak (cf. Fig. 4a). The variation of intensity of the Kα_1 and Kα_2 lines as a function of incident energy show the same structure and no strong final state effects with features off the horizontal lines are observed. Therefore, in the case of V-bearing grossular, the selection of the Kα_1 fluorescence line to perform HERFD-XAS measurements results in a spectrum similar to that of conventional XAS.

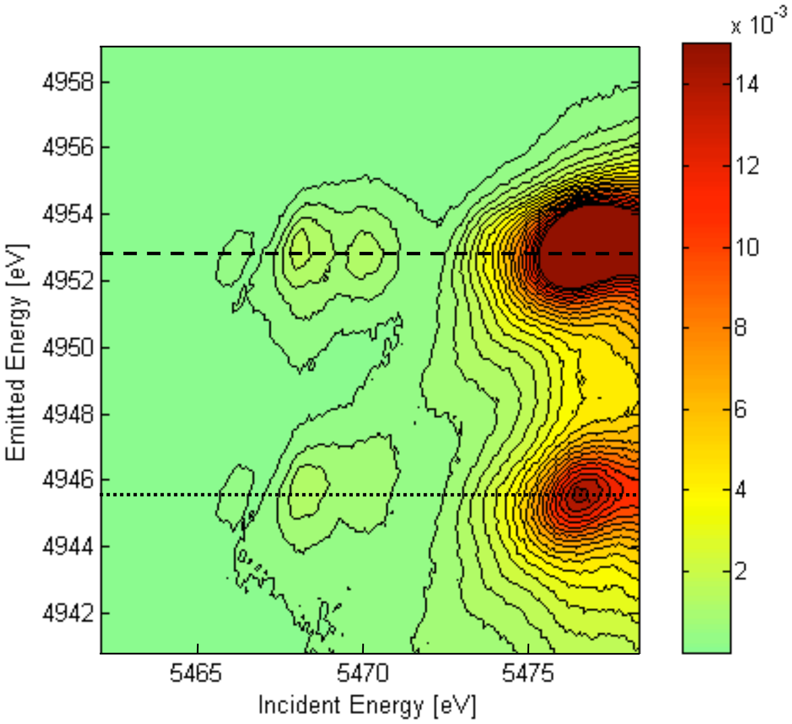

Figure 6: *RIXS plane at the V K edge of tsavorite. The relative spectral intensity is shown on the colour bar on the right. The white lines represent the Kα_1 (dashed) and Kα_2 (dotted) fluorescence lines.*

Interpretation of the pre-edge structures

Figure 7 shows for each experimental orientation the electric dipole and quadrupole contributions of the total theoretical spectra, which is the sum of these two contributions. Concerning the electric dipole transitions, they present no structure in the pre-edge region and contribute only to a background, which is actually the tail of the absorption edge. Therefore it confirms that the pre-edge arises from pure electric quadrupole transitions, as expected from the centrosymmetry of the vanadium site.

The good agreement between experiments and calculations allows a detailed interpretation of the pre-edge structures. The calculated electric quadrupole cross-section, which is proportional to the transition probabilities, corresponds to the sum of the spin up and spin down contributions. By taking advantage of this spin dependence, an interpretation of the involved transitions can be done within a monoelectronic

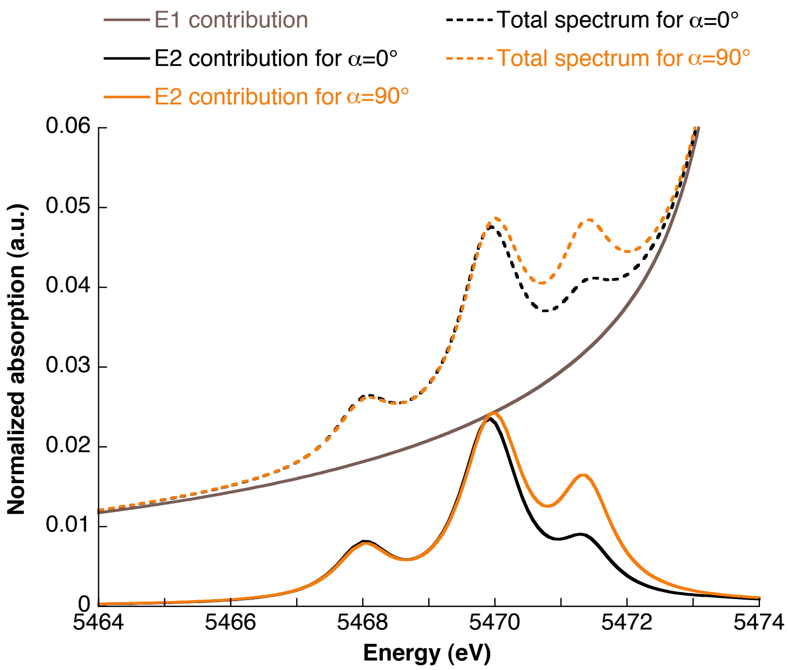

***Figure** 7: Electric dipole (E1) and quadrupole (E2) contributions (solid line) along with the total computed spectra (dashed line) for the two experimental configurations. The black lines correspond to the* α_{rot} *= 0° orientation* $\left(\hat{\varepsilon}=[010],\hat{k}=[\bar{1}00]\right)$ *and the orange lines to* α_{rot} *= 90°* $\left(\hat{\varepsilon}=\left[\frac{1}{2},\frac{1}{2},\frac{1}{\sqrt{2}}\right],\hat{k}=\left[-\frac{1}{2},-\frac{1}{2},\frac{1}{\sqrt{2}}\right]\right)$.

framework. The ion V^{3+} in an octahedral environment has an electronic configuration $t_{2g}^{\uparrow\,2}\ e_g^{\,0}$ (the octahedral field splits the five degenerate *d* orbitals in three $t_{2g}(Oh)$ and two $e_g(Oh)$). Among the three $t_{2g}(Oh)$orbitals, two orbitals are occupied and one is empty (Figure 8). For the two experimental orientations α_{rot} = 0° and α_{rot} = 90°, the pre-edge presents three peaks (Figures 9 a and b). The transition probabilities to both occupied and empty states are represented in figure 9 for a better understanding of the transition assignment. The P1 peak (5468 eV) contains both occupied and empty states and therefore corresponds to transitions from the 1*s* orbital to the $t_{2g}^{\uparrow}$ (Figure 8a). With the trigonal distortion C_{3i}, the three $t_{2g}(Oh)$ states are split into two orbitals e_g and one a_{1g}, denoted hereafter $e_g(C_{3i})$ and $a_{1g}(C_{3i})$, whereas the distortion does not split the two $e_g(Oh)$ orbitals. As no splitting is visible for the P1 peak in figure 9, it is an indication that the two sets of orbitals (the three $t_{2g}(Oh)$ orbitals in ne hand and the two $e_g(Oh)$ ones on the other hand) are close in energy and that the distortion is quite small. Since transitions to both occupied and empty states are shown here, the P1 peak appears to be more intense than in figure 5. Indeed, the occupied states correspond to virtual transitions that are not observed experimentally. As only one $t_{2g}(Oh)$ orbital is empty, the experimental peak is less intense than in calculation where the transitions to the three $t_{2g}(Oh)$ orbitals are represented. The P2 (5469.9 eV) and P3 (5471.4 eV) peaks correspond to transitions to empty states only. For both orientations, a peak is attributed to a transition to the $e_g^{\uparrow}$ state (Figure 8B). Two peaks for the spin down contributions are visible, corresponding to transitions to the $t_{2g}^{\downarrow}$ (Figure 8C) and $e_g^{\downarrow}$ (Figure 8D) states. The three peaks observed experimentally therefore corresponds to the number of transitions to empty states expected in a monoelectronic picture: the P1 peak to transitions to the empty $t_{2g}^{\uparrow}$ orbital, the P2 peak to both transitions to $e_g^{\uparrow}$ and $t_{2g}^{\downarrow}$ orbitals (as the two transitions are close in energy) and finally the P3 peak to transitions to the $e_g^{\downarrow}$ orbital.

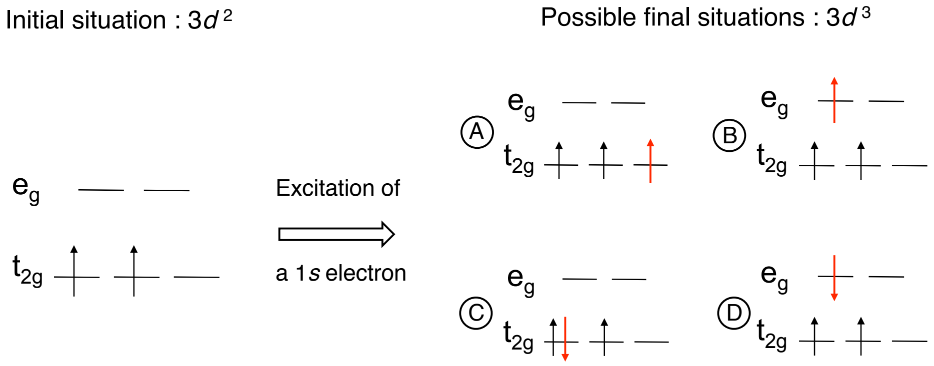

Figure 8: Schematic representation of the 3d orbitals of V^{3+} in a Oh symmetry in the ground state and in the possible final states. Note that in tsavorite, the site symmetry is C_{3i} and that the t_{2g} orbitals are split in a $a_{1g}(t_{2g})$ orbital and two $e_g(t_{2g})$ orbitals. The splitting is not reproduced here because it is small compared to the $t_{2g} – e_g$ splitting.

The splitting of 3*d* orbitals

In an octahedral field, the 3*d* orbitals are split into three t_{2g} and two e_g orbitals. The DFT spin-polarized calculations enable to distinguish the spin up from the spin down contributions. The energy separation between the $t_{2g}^{\uparrow}$ and $e_g^{\uparrow}$ orbitals, or between the $t_{2g}^{\downarrow}$ and $e_g^{\downarrow}$ ones, can thus be determined. For the α_{rot} = 0° configuration, the $t_{2g}^{\uparrow} - e_g^{\uparrow}$ separation is 2.15 eV and the $t_{2g}^{\downarrow} - e_g^{\downarrow}$ one is 1.44 eV (Figure 9). They are similar for the α_{rot} = 90° configuration. In the case of spin up, the energy separation between the occupied $t_{2g}^{\uparrow}$ orbital and the empty $e_g^{\uparrow}$ one can be compared to the crystal field splitting parameter determined by optical spectroscopy. For V-bearing grossular, the available experimental values are 10Dq=1.97 eV=15900 cm^{-1} (Mazurak and Czaja, 1996) and 10Dq=2.03 eV=16390 cm^{-1} (Rossman). The energy separation determined by DFT differs only by 6-7% from the optical absorption values (Table III). These higher DFT-deduced values can be explained by the fact that in the calculation, the core-hole present on the 1*s* orbital attracts the occupied 3*d* orbitals. Hence the energy separation between the occupied $t_{2g}^{\uparrow}$ and empty $e_g^{\uparrow}$ orbitals is more important than in optical absorption spectroscopy where there is no 1*s* core-hole. It is to be noted that the energy separation between the $t_{2g}^{\downarrow}$ and $e_g^{\downarrow}$ is strongly different from the 10Dq values (between 26 and 29%, depending on the orientation). It was expected because the 10Dq value does not represent the energy separation between two empty orbitals with an identical spin. Similar differences were observed for Cr^{3+} in grossular (10Dq=2.06 eV in optical absorption spectroscopy and $t_{2g}^{\downarrow} - e_g^{\downarrow}$ = 1.40 eV in

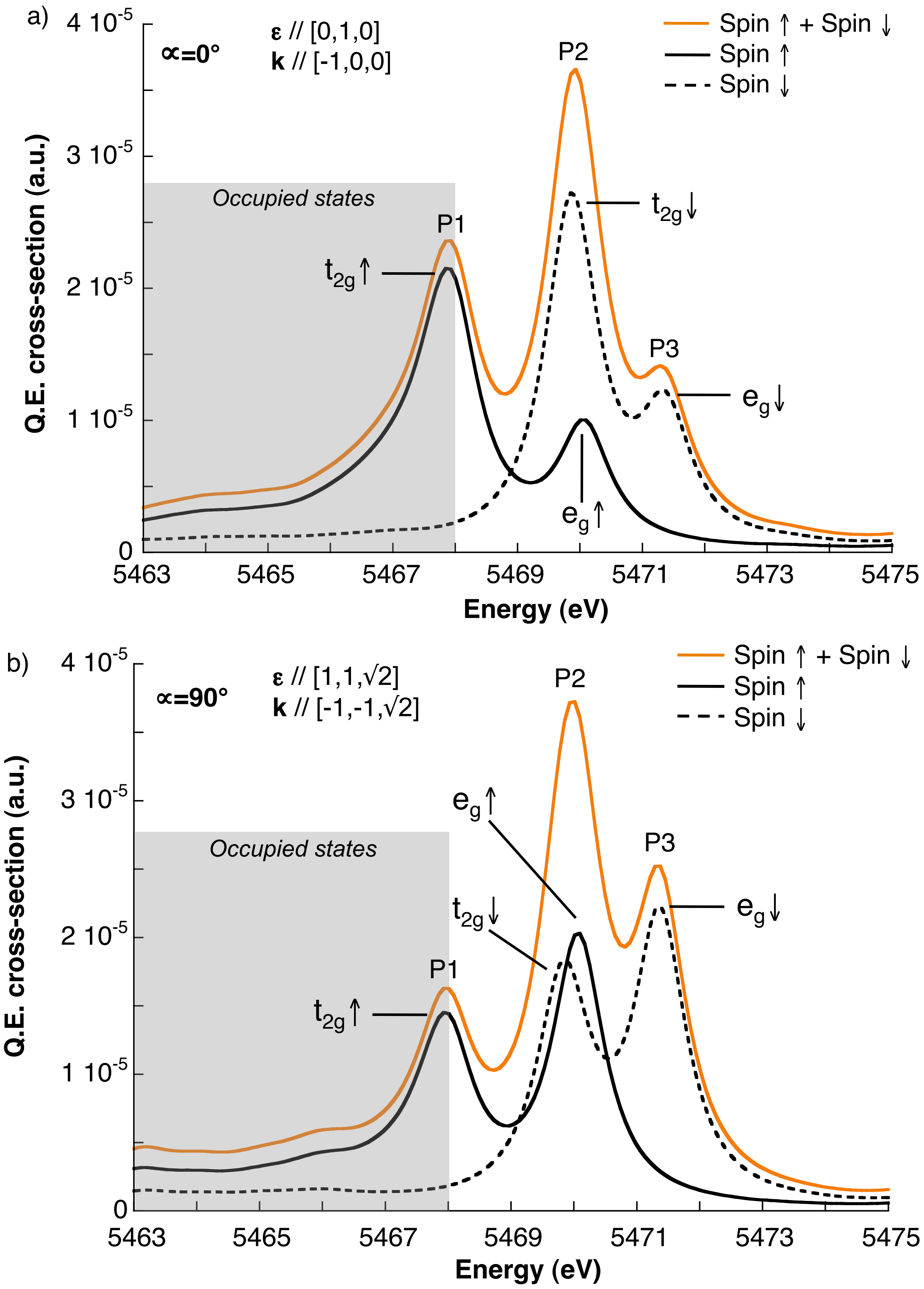

Figure 9: *Calculated electric quadrupole transitions with the spin-polarization. The upper panel (a) represents the spectrum calculated for α_{rot} = 0° and the lower panel (b) for α_{rot} = 90°. For each orientation, the respective contributions of the two spins are plotted (black solid line for spin up, black dashed line for spin down), as well as the sum (orange solid line). The Fermi level is located at 5468 eV. The electric quadrupole cross-sections of the two orientations are plotted with the same scale. The Fermi level is located at 5468 eV and the grey region corresponds to the virtual transitions towards the occupied states.*

DFT calculations) and in pyrope ($Mg_3Al_2(SiO_4)_3$) (10Dq=2.23 eV in optical absorption spectroscopy and $t_{2g}^{\downarrow} - e_g^{\downarrow}$ = 1.54 eV in DFT calculations) (Juhin 2008c). We can also use the peak assigment given by DFT calculations to directly analyze the experimental pre-edges. To do so, the experimental pre-edge was fitted for each configuration with four Gaussian contributions, corresponding to the $t_{2g}^{\uparrow}$, $t_{2g}^{\downarrow}$, $e_g^{\uparrow}$ and $e_g^{\downarrow}$ contributions observed in the DFT calculations. The $t_{2g}^{\uparrow} - e_g^{\uparrow}$ energy separations obtained from the experimental pre-edges are 2.11 eV to 2.16 eV (depending on the orientation), so close to the 10Dq values obtained by optical spectroscopy (Table III).

	0° (DFT)	90° (DFT)	0° (Exp.)	90° (Exp.)	Optical spectroscopy
$t_{2g}^{\uparrow} - e_g^{\uparrow}$ splitting (eV)	2.15	2.17	2.11	2.16	10Dq = 2.03 eV (Rossman)
$t_{2g}^{\downarrow} - e_g^{\downarrow}$ splitting (eV)	1.44	1.49	1.99	2.14	10Dq = 1.97 eV (Mazurak)

Table III. *Comparison between the 10Dq values determined from the DFT calculations and the Gaussian decomposition of the experimental pre-edges with the optical absorption value. The exchange energy is determined by the energy separation between the two peaks of the same orbital but with different spins.*

Discussion and conclusion

Relaxation process around vanadium in V-bearing grossular

Relaxation around impurities in minerals is an important issue for the rationalization of element partitioning between minerals and melts (Blundy and Wood 2003). There is spectroscopic evidence that the local structure often differs from a diffraction-derived average crystal structure: the Vegard law is not obeyed at local scale due to lattice relaxation during element substitution (Galoisy 1996). Cation incorporation in the X or Y sites of silicate garnets has been widely studied to study the chemical dependence of physical properties such as in the solid solutions, pyrope $Mg_3Al_2(SiO_4)_3$ – knorringite $Mg_3Cr_2(SiO_4)_3$ (substitution Al/Cr in the Y site) and pyrope-grossular (substitution of Ca/Mg in the X site; Ungaretti et al. 1995, Oberti et al. 2006). In pyralspites (X=Mg, Fe, Mn) the O1-O4 (numbering in Fig. 1) distances are smaller than the O1-O5 ones so the Y site is elongated along the $\bar{3}$ axis, and substitution at the X site is favored because they tend to flatten the octahedral and decrease the OAV. The opposite trend is observed for ugrandites (X=Ca): the O1-O4 distances are longer than O1-O5 and the Y site is flattened along the $\bar{3}$ axis. They thus predict that with the substitution of a cation larger than Al^{3+} in the Y site, an elongation of the octahedral along the $\bar{3}$ axis should happen, due to the more important increase of the O1-O5 distance than the O1-O4 ones and a decrease in the OAV. However, different relaxation processes have been observed for some ugrandites. In the substitution of Al^{3+} by Cr^{3+} in grossular, no significant variation in the OAV was observed (Juhin 2008c) and the O1-O4 and O1-O5 distances increase with Cr^{3+} incorporation. Wildner and Andrut (2001) described the opposite behavior than Ungaretti et al. (1995) for uvarovite (ugrandite garnet): during the Cr^{3+} substitution in grossular, the OAV of the individual CrO_6 octahedron increases. This observation is in agreement with the variations observed here for V-bearing grossular, when V^{3+} substitutes for Al^{3+} in grossular. Our results are therefore in contradiction with the predictions of Ungaretti et al. (1995) and confirmed the trend observed by Wildner and Andrut (2001). The V-O distance calculated here for V-bearing grossular (1.995 Å) is close to the one in goldmanite $Ca_3V_2(SiO_4)_3$: Novak and Gibbs (1971) measured a V-O distance of 1.988 Å in a natural sample and Milman et al. (2001) calculated a distance of 2.012 Å. This V-O distance is consistent with crystallographic data on V^{3+}-bearing crystals, which indicate individual octahedral V^{3+}-O distances mostly comprised between 1.98 and 2.04 Å, with an average bond length of 2.01(5) Å (Schindler et al. 2000). Previous studies showed the similarities of the Y cation-O distances between a slightly substituted garnet (~2 wt% M_2O_3, where M is the cation incorporated in the Y site) and the end-member of the corresponding solid-solution. The full relaxation observed around V^{3+} in V-bearing grossular is also in agreement with that around Cr^{3+} in garnets, with Cr-O distances of 1.99 Å in Cr-bearing grossular (Juhin 2008c) and 1.994 Å in uvarovite (Andrut and Wildner 2002). In the pyrope-knorringite solid-solution, the Cr-O distance remains constant, at 1.96 Å for both substituted pyrope (Juhin et al. 2008) and knorringite (Juhin et al. 2009).

Implications for the determination of the oxidation state of vanadium in natural samples

Accurate determination of the oxidation state of cations from pre-edge XANES spectroscopy is usually done by comparing the pre-edge with that of reference samples with a known oxidation state. In the case of vanadium, several compounds have been proposed as references for the trivalent state. They include glasses synthesized under reducing conditions (Sutton et al. 2005), V_2O_3 (Wong et al. 1984), V-bearing magnetite (Giuli et al. 2004, Chaurand et al. 2007) and roscoelite (Wong et al. 1984). In the case of crystalline compounds, the pre-edge is affected by several factors, including the local symmetry around the element, possible interactions between cations of transition elements in concentrated samples (e.g., pure oxides) and experimental geometry. For instance, the inversion center of the octahedral site of V-bearing grossular leads to a smaller pre-edge of V^{3+} when compared with V_2O_3. Despite the inversion center of the octahedral site of spinel structure, the pre-edge of V-bearing grossular is also smaller than that of vanadium in magnetite. This suggests that the vanadium speciation in magnetite is more complex and likely involves the occurrence of vanadium ions under several oxidation states and/or in strongly distorted sites (see Balan et al. 2006). V-bearing grossular thus appears as a suitable reference compound for V^{3+} in a slightly distorted octahedron with an inversion center. The good agreement achieved between experiment and theory evidences that only one oxidation state of vanadium occurs in a well-defined site. In addition, the angular dependence of the pre-edge, although observed, remains small enough to use the pre-edge area recorded on a single crystal. As an example, we consider the case of V-bearing titanomagnetites from the Bushveld Complex (Balan et *al.* 2006): the use of the $\alpha_{rot} = 0°$ or $\alpha_{rot} = 90°$ orientation as V^{3+} pre-edge reference changes the V^{4+}/V^{3+} ratio by less than 3%, which remains within the experimental uncertainty. The angular dependence of the pre-edge has also been studied for Cr^{3+} in spinel (Juhin et al. 2008b) where the effect is only slightly more pronounced. This supports the determination of the redox state of transition cations in cubic oxides with uncontrolled crystal orientation, such as spinel grains in thin sections of natural or synthetic samples (e.g., Righter et al. 2006).

Concluding remarks

In this study a detailed investigation of the *K* pre-edge spectrum of vanadium in grossular has been presented, including its angular dependence. This study consisted of *K*-edge HERFD-XAS (De Groot et al. 2009, Glatzel et al. 2009a,b) experiments, coupled with first-principles modeling. The good agreement obtained between theory and experiment made it possible to interpret the pre-edge in terms of monoelectronic 1*s*-3*d* transitions. The computational method developed by Taillefumier et al. (2002) is now implemented in the open-source Quantum Espresso suite of codes (Gianozzi et al.). It offers the opportunity to model X-ray absorption spectra from first-principles using plane-wave basis sets and pseudopotentials, thus providing an ideal link between XAS, crystal structure and the results of other analytical tools that can be modeled within the same theoretical framework (e.g., NMR spectroscopy, vibrational spectroscopy). In addition, the successful modeling of the angular dependence indicates that this theoretical approach, coupled with the use of the spherical tensors analysis (Brouder et al. 2008), can be used to assess this effect in other crystals. In particular, the effect related to the angular dependence may be dramatic in non-cubic crystals because it is observed for both the edge and pre-edge, since the latter arises also from electric dipole transitions in non-cubic crystals (e.g., Poumellec et al. 1991, for Ti in rutile). When a detailed investigation of the angular dependence is difficult (e.g., when thin sections are investigated with a microbeam), first-principles modeling may provide reliable information on the pre-edge intensity variation as a function of the crystal orientation, thus improving the knowledge of the spectral signature and consequently the determination of the oxidation state in complex samples.

Acknowledgments

The authors warmly acknowledge M. Jacquet and M. Escudier for sample preparation. We are also very grateful to M. Sikora and Ch. Lapras (ID26 beamline) for help during experiments, to M. Calandra and C. Gougoussis for help in using Xspectra, and to M. Lazzeri and O. Dargaud for fruitful discussions. The theoretical part of this work was granted access to the HPS resources of IDRIS (Institut du Développement et de Recherche en Informatique Scientifique) under the allocations 2008 and 2009- 2015 made by GENCI (Grand Equipement National de Calcul Intensif).

References

Andrut, M. and Wildner, M. (2002) The crystal chemistry of birefringent natural uvarovites: Part III. Application of the superposition model of crystal fields with a characterization of synthetic cubic uvarovite. Physics and Chemistry of Minerals, 29, 595-608.

Balan, E., de Villiers, J.P.R., Eeckhout, S.G., Glatzel, P., Toplis, M.J., Fritsch, E., Allard, T., Galoisy, L. and Calas, G. (2006) The oxidation state of vanadium in titanomagnetite from layered basic intrusions. American Mineralogist, 91, 953-958.

Baroni, S., De Gironcoli, S., Dal Corso, A. and Giannozzi, P. (2001) Phonons and related crystal properties from density functional perturbation theory. Reviews of Modern Physics, 73, 515-562. http://www.pwscf.org .

Berry, A.J., O'Neill, H.S.C., Jayasuriya, K.D., Campbell, S.J. and Foran, G.J. (2003) XANES calibrations for the oxidation state of iron in a silicate glass. American Mineralogist, 88, 967-977.

Berry, A.J. and O'Neill, H.S.C. (2004) A XANES determination of the oxidation state of chromium in silicate glasses. American Mineralogist, 89, 790-798.

Blöchl, P. E. (1994) Projector augmented-wave method. Physical Review, 50, 17953-17979.

Blundy, J. and Wood, B (2003) Partitioning of trace elements between crystals and melts. Earth and Planetary Science Letters, 210, 383-397.

Brouder, Ch. (1990) Angular dependence of X-ray absorption spectra. Journal of Physics: Condensed Matter, 2, 701-738.

Brouder, Ch., Juhin, A., Bordage, A. and Arrio, M-A. (2008) Site symmetry and crystal symmetry: a spherical tensor analysis. Journal of Physics: Condensed Matter, 20, 455205.

Burns, R.G. (1993) Mineralogical applications of crystal field theory. Volume 5 of Cambridge topics in Mineral Physics and Chemistry. Cambridge University Press, 2nd edition.

Cabaret, D., Brouder, Ch., Arrio, M-A., Sainctavit, Ph., Joly, Y., Rogalev, A. and Goulon, J. (2001) Natural linear dichroism in pyrite (FeS_2): Experiments and calculations. Proceedings XAFS 11, Journal of Synchrotron Radiation, 8, 460-462.

Cabaret, D., Gaudry, E., Taillefumier, M., Sainctavit, Ph. and Mauri, F. (2005) XANES calculations with an efficient "non-muffin tin" method: Application to the angular dependence of the AL *K*-edge in corundum. Physica Scripta, Proceedings XAFS 12 Conference, T115, 131-133.

Cabaret, D., Couzinet, B., Flank, A-M., Itié, J-P., Lagarde, P. and Polian, A. (2007) Ti *K* pre-edge in SrTiO3 under pressure: experiments and full-potential first-principles calculations. Proceedings XAFS 13 Conference, AIP Conference Proceedings, 882, 120.

Calas, G. and Petiau, J. (1983) Coordination of iron in oxide glasses through high-resolution *K*-edge spectra: Information from the pre-edge. Solid state communications, 48 (7), 625-629.

Canil, D. (1999) Vanadium partitioning between orthopyroxene, spinel and silicate melt and the redox states of mantle source regions for primary magmas. Geochimica et Cosmochimica Acta, 63 (3-4), 557-572.

Canil, D. (2002) Vanadium in peridotites, mantle redox and tectonic environments: Archean to present. Earth and Planetary Science Letters, 195, 75-90.

Carra, P., Fabrizio, M. and Thole, B.T. (1995) High resolution X-ray resonant Raman scattering. Physical Review Letters, 74(18), 3700-3703.

Chalmin, E., Farges, F. and Brown, G.E. (2009) A pre-edge analysis of Mn K-edge XANES spectra to help determine the speciation of manganese in minerals and glasses. Contribution to Mineralogy and Petrology, 157, 111-126.

Chaurand, P., Rose, J., Briois, V., Salome, M., Proux, O., Nassif, V., Olivi, L., Susini, J., Hazemann, J-L. and Bottero, J-Y. (2007) New methodological approach for the vanadium *K*-edge X-ray absorption near-edge structure interpretation: Application to the speciation of vanadium in oxide phases from steel slag. The Journal of Physicla Chemistry B, 111(19), 5101-5110.

De Groot, F.M.F., G. Vanko, G. and Glatzel, P. (2009) The 1s X-ray absorption pre-edge structures in transition metal oxides. Journal of Physics: Condensed Matter, 21, 104207.

Eeckhout, S.G., Bolfan-Casanova, N., McCammon, C., Klemme, S. and Amiguet, E. (2007) XANES study of the oxidation state of Cr in lower mantle phases: Periclase and magnesium silicate perovskite. American Mineralogist, 92, 966-972.

Farges, F., Lefrère, Y., Rossano, S., Berthereau, A., Calas, G. and Brown, G.E. (2004) The effect of redox state on the local structural environment of iron in silicate glasses : a combined XAFS spectroscopy, molecular dynamics, and bond valence study. Journal of Non-crystalline Solids, 344, 176-188.

Galoisy, L. (1996) Local versus average structure around cations in minerals from spectroscopic and diffraction measurements. Physics and Chemistry of Minerals, 23, 217-228.

Galoisy, L., Calas, G. and Arrio, M-A. (2001) High-resolution XANES spectra of iron in minerals and glasses: structural information from the pre-edge region. Chemical Geology, 174, 307-319.

Gaudry, E., Kiratisin, A., Sainctavit, Ph., Brouder, Ch., Mauri, F., Ramos, A., Goulon, J. and Rogalev, A. (2003) Structural and electronic relaxations around Substitutional Cr^{3+} and Fe^{3+} ions in corundum. Physical Review B, 67, 094108.

Gaudry, E., Cabaret, D., Sainctavit, Ph., Brouder, Ch., Mauri, F., Goulon, J. and Rogalev, A. (2005) Structural relaxations around Ti, Cr and Fe impurities in α-Al_2O_3 probed by X-ray absorption near-edge structure with first principles calculations. Journal of Physics: Condensed Matter, 17, 5467-5480.

Gaudry, E., Cabaret, D., Brouder, Ch., Letard, I. Rogalev, A., Wilhlem, F., Jaouen, N. and Sainctavit., Ph. (2007) Relaxation around the substitutional chromium site in emerald: X-ray absorption experiments and density functional calculations. Physical Review B, 76, 094110.

Gauthier, C., Solé, V.A., Signorato, R., Goulon, J. and Moguiline. E. (1999) The ESRF beamline ID26: X-ray absorption on ultra dilute sample. Journal of Synchrotron Radiation, 6, 164-166.

Geiger, C.A. and Armbruster, T. (1997) $Mn_3Al_2Si_30_{12}$ spessartine and $Ca_3Al_2Si_3O_{12}$ grossular garnet: Structural dynamic and thermodynamic properties. American Mineralogist, 82, 740-747.

Giannozzi, P., Baroni, S., Bonini, N., Calandra, M., Car, R., Cavazzoni, C., Ceresoli, D., Chiarotti, G.L., Cococcioni, M., Dabo, I., Dal Corso, A., de Gironcoli, S., Gebauer, R., Gerstmann, U., Gougoussis, Ch., Kokalj, A., Lazzeri, M., Martin Samos Colomer, L., Marzari, N., Mauri, F., Paolini, S., Pasquarello, A., Paulatto, L., Sbraccia, C., Scandolo, S., Sclaurezo, G., Seitsonen, A.P., Smogunov, A., Umari, P. and Wentzcovitch, R.M. QUANTUM ESPRESSO: a modular and open-source software project for quantum simulations of materials. arXiv:0906.2569v1 (Journal of Physics: Condensed Matter).

Giuli, G., Paris, E., Mungall, J., Romano, C. and Dingwell, D. (2004) V oxidation state and coordination number in silicate glasses by XAS. American Mineralogist, 89, 1640-1646.

Glatzel, P. and Bergmann, U. (2005) High-resolution 1*s* core-home X-ray spectroscopy in 3*d* transition metal complexes – Electronic and structural information. Coordination Chemistry Review, 249, 65-95.

Glatzel, P., Sikora, M., Smolentsev, G. and Fernandez-Garcia, M. (2009a) Hard X-ray photon-in photon-out spectroscopy. Catalysis Today, 145, 294-299.

Glatzel, P., De Groot, F.M.F. and Bergmann, U. (2009b) Hard X-ray photon-in photon-out spectroscopy. Synchrotron Radiation News, 22(2), 12-16.

Gougoussis, Ch., Calandra, M., Seitsonen, A. Brouder, Ch., Shukla, A. and Mauri, F. (2009) Intrinsic charge transfer gap in NiO from Ni *K* edge X-ray absorption spectroscopy. Physical Review B, 79, 45118.

Hamaläinen, K., Siddons, D.P., Hastings, J.B. and Berman, L.E. (1991) Elimination of the inner-shell lifetime broadeninf in X-ray absorption spectroscopy. Physical Review Letters, 67(20), 2850-2853.

Haydock, R., Heine, V. and Kelly, M.J. (1972) Electronic structure based on the local atomic environment for tight-binding bands. Journal of Physics C: Solid State Physics, 5, 2845-2858.

Haydock, R., Heine, V. and Kelly, M.J. (1975) Electronic structure based on the local atomic environment for tight-binding bands II. Journal of Physics C: Solid State Physics, 8, 2591-2605.

Jaklevic, J., Kirby, J.A., Klein, M.P., Robertson, A.S., Brown, G.S., Elsenberger, P. (1977) Fluorescence detection of EXAFS: Sensitivity enhancement for dilute species and thin films. Solid State Communications, 23, 679-682.

Joly, Y., Cabaret, D., Renevier, H. and Natoli, C.R. (1999) Electron Population Analysis by Full-Potential X-ray absorption. Physical Review Letters, 82 (11), 2398.

Juhin, A., Calas, G., Cabaret, D., Galoisy, L. and Hazemann, J-L. (2007) Structural relaxation around substitutional Cr^{3+} in $MgAl_2O_4$. Physical Review B, 76, 054105.

Juhin, A., Calas, G., Cabaret, D., Galoisy, L. and Hazemann, J-L. (2008a) Structural relaxation around Substitutional Cr^{3+} in pyrope garnet. American Mineralogist, 93, 800-805.

Juhin, A., Brouder, Ch, Arrio, M-A, Cabaret, D., Sainctavit, Ph., Balan, E., Bordage, A., Seitsonen, A.P., Calas, G., Eeckhout, S.G. and Glatzel, P. (2008b) X-ray linear dichroism in cubic compounds : The case of Cr^{3+} in $MgAl_2O_4$. Physical Review B, 78, 195103.

Juhin, A. (2008c) Propriétés électroniques et strucutrales du chrome en impureté dans les cristaux. Approche expérimentale et théorique. PhD thesis, Université Pierre et Marie Curie, Paris (France).

Juhin, A., Morin, G., Elkaim, E., Frost, D.J., Fialin, M., Juillot, F. and Calas, G. (2009) Structure refinement of a synthetic knorringite $Mg_3(Cr_{0.8}\ Mg_{0.1}\ Si_{0.1})_2(SiO_4)_3$. Accepted in American Mineralogist.

Karner, J., Papike, J.J. and Shearer, C.K. (2006) Comparative planetary mineralogy: Pyroxene major- and minor-element chemistry and partitioning of vanadium between pyroxene and melt in planetary basalts. American Mineralogist, 91, 1574-1582.

Kleinman, L. and Bylander, D.M. (1982) Efficacious form for model pseudopotentials. Physical Review Letters, 48, 1425-1428.

Kokubun, J., Ishida, K., Cabaret, D., Mauri, F., Vedrinskii, R.V., Kraizman, V.L., Novakovich, A.A., Ktivitskiin, E.V. and Dmitrienko, V.E. (2004) Resonant diffraction in FeS_2: Determination of the X-ray polarization anisotropy of iron atoms. Physical Review B, 69, 245103.

Krause, M.O. and Oliver, J.H. (1979) Natural widths of atomic K and L levels, K_α X-ray lines and several KLL Auger lines. Journal of Physical and Chemical Reference Data, 8(2), 329-338.

Mazurak, Z. and Czaja, M. (1996) Optical properties of tsavorite $Ca_3Al_2(SiO_4)_3$:Cr^{3+},V^{3+} from Kenya. Journal of Luminescence, 65, 335-340.

Milman, V., Akhmatskaya, E.V., Nobes, R.H., Winkler, B., Pickard, C.J. and White, J.A. (2000) Systematic *ab initio* study of the compressibility of silicate garnets. Acta Crystallographica B, 57, 163-177.

Novak, G.A. and Gibbs, G.V. (1971) The crystal chemistry of the silicate garnets. American Mineralogist, 56, 791-825.

Oberti, R., Quartieri, S., Dalconi, M.C. Boscherini, F., Iezzi, G., Boiocchi, M. (2006) DIstinct local environments for Ca along the non-ideal pyrope-grossular solid solution: A new model based on crystallographic and EXAFS analysis. Chemical Geology, 225, 347-359.

Papike, J.J., Karner, J.M. and Shearer, C.K. (2005) Comparative planetary mineralogy: Valence state partitioning of Cr, Fe, Ti and V among crystallographic sites in olivine, pyroxene, and spinel from planetary basalts. American Mineralogist, 90, 277-290.

Petit, P-E., Farges, F., Wilke, M. and Solé, V.A. (2001) Determination of the iron oxidation state in Earth materials using XANES pre-edge information. Journal of Synchrotron Radiation, 8, 952-954.

Pettifer, R.F., Brouder, Ch., Benfatto, M., Natoli, C.R., Hermes, C. and Ruiz Lopez, M.F. (1990) Magic-angle theorem in powder X-ray absorption spectroscopy. Physical Review B, 42, 37-42.

Poumellec, B., Cortes, R., Tourillon, G. and Berthon, J. (1991) Angular dependence of the Ti K edge in rutile TiO_2. Physics state solid B, 164, 319-326.

Quartieri, S., Triscari, M., Sabatino, G., Boscherini, F. and Sani, A. (2002) Fe and Mn K-edge study of ancient Roman glasses. European Journal of Mineralogy, 14, 749-756.

Robinson, K., Gibbs, G.V. and Ribbe, P.H. (1971) Quadratic elongation: A quantitative measure of distortion in coordination polyhedra. Science, 172, 567-570.

Rossman, G.R. http://minerals.gps.caltech.edu .

Sainctavit, Ph., Petiau, J., Benfatto, M. and Natoli, C.R. (1989) Comparison between XAFS experiment and multiple-scattering calculations in silicon and zincblende. Physica B: Condensed Mater, 158, 347-350.

Schindler, M., Hawthorne, F. C. and Baur, W. H. (2000) Crystal chemical aspects of vanadium: Polyhedral geometries, characteristic bond valences, and polymerization of (VO_n) polyhedra. Chemistry of Materials. 12, 1248-1259

Shukla, A., Calandra, M., Taguchi, M., Kotani, A., Vanko, G. and Cheong, S-W. (2006) Polarized Resonant Inelastic X-ray Scattering as an ultrafine probe of excited states of La_2CuO_4. Physical Review Letters, 96, 077006.

Sutton, S.R., Karner, J., Papike, J., Delaney, J.S., Shearer, C., Newville, M., Eng, P., Rivers, M. and Dyar, D. (2005) Vanadium K edge XANES of synthetic and natural basaltic glasses and application to microscale oxygen barometry. Geochimica et Cosmochimica Acta, 69 (9), 2333-2348.

Taillefumier, M., Cabaret, D., Flank, A-M. and Mauri, F. (2002) X-ray absorption near-edge structure calculations with the pseudopotentials: Application to the *K* edge in diamond and α-quartz. Physical Review B, 66, 195107.

Toplis, M.J. and Corgne, A. An experimental study of element partitioning between magnetite, clinopyroxene and iron-bearing silicate liquids with particular emphasis on vanadium. Contribution to Mineralogy and Petrology, 144, 22-37.

Troullier, N. and Martins, J.L. (1991) Efficient pseudopotentials for plane-wave calculation. Physical Review B, 43, 1993-2006.

Ungaretti, L., Leona, M., Merli, M. and Oberti, R. (1995) Non-ideal solid-solution in garnet: crystal-structure evidence and modeling. European Journal of Mineralogy, 7, 1299-1312.

Waychunas, G.A., Apted, M.J. and Brown, G.E. (1983) X-ray K-edge absorption spectra of Fe minerals and model compounds: Near-edge structure. Physics and Chemistry of Minerals, 10, 1-9.

Waychunas, G.A. (1987) Synchrotron radiation XANES spectroscopy of Ti in minerals: Effects of Ti bonding distances, Ti valence, and site geometry on absorption edge structure. American Mineralogist, 72, 89-101.

Wildner, M. and Andrut, M. (2001) The crystal chemistry of birefringent natural uvarovites: Part II. Single-crystal X-ray structures. American Mineralogist, 86, 1231-1251.

Wilke, M., Farges, F., Petit, P-E., Brown, G.E. and Martin, F. (2001) Oxidation state and coordination of Fe in minerals: An Fe *K*-XANES spectroscopic study. American Mineralogist, 86, 714-730.

Woicik, J. C., Shirley, E.L., Hellberg, C.S., Anderson, K.E., Sambasivan, S., Fischer, D.A., Chapman, B.D., Stern, E.A., Ryan, P., Ederer, D.L. and Li, H. (2007) Ferroelectric distortion in $SrTiO_3$ thin films on Si (001) by X-ray absorption fine structure spectroscopy: Experiment and first-principles calculations. Physical Review B, 75, 140103.

Wong, J., Lytle, F.W., Messmer, R.P. and Maylotte, D.H. (1984) *K*-edge absorption spectra of selected vanadium compounds. Physical Review B, 30 (10), 5596-5610.

Yamamoto, T., Mizoguchi, T. and Tanaka, I. (2005) Core-hole effect on dipolar and quadrupolar transitions of $SrTiO_3$ and $BaTiO_3$ at Ti *K* edge. Physical Review B, 71, 245113.

Appendix 1: The coset method

Given two sites Y$_0$ and Y$_i$ equivalent by rotation, assuming we have calculated the spectrum for the Y$_0$ site, it is possible to obtain the spectrum for the Y$_i$ site by calculating the spectrum of the Y$_0$ site for a fictive "rotated" X-ray beam. Indeed, if the Y$_i$ site is the image of the Y$_0$ site by a rotation R, then the spectrum of the Y$_i$ site for a configuration $\left(\hat{\varepsilon},\hat{k}\right)$ is equal to the spectrum of the Y$_0$ site for the rotated configuration $\left[R^{-1}(\hat{\varepsilon}),R^{-1}\left(\hat{k}\right)\right]$ (Brouder et al. 2008). In the case of the electric quadrupole cross-section $\sigma^Q\left(\hat{\varepsilon},\hat{k}\right)$, the transition operator of the Y$_i$ site is deduced from the one of the Y$_0$ site with the following relation:

$$\left|(\hat{\varepsilon}\cdot r)\left(\hat{k}\cdot r\right)\right|_{Y_i} = \left|\left(R_{Y_0}^{-1}(\hat{\varepsilon})\cdot r\right)\left(R_{Y_0}^{-1}\left(\hat{k}\right)\cdot r\right)\right|$$

In garnet, the eight equivalent sites are denoted here Y$_0$ (1/2,1/2,0), Y$_1$ (0,0,0), Y$_2$ (1/2,0,1/2), Y$_3$ (0,1/2,1/2), Y$_4$ (3/4,1/4,1/4), Y$_5$ (3/4,3/4,3/4), Y$_6$ (1/4,1/4,3/4) and Y$_7$ (1/4,3/4,1/4). As the Y$_0$ site octahedron is orientated along the [-1,1,1] axis of the cube and so has the C_{3i} point symmetry, it is considered as the initial site. The rotation matrix R is determined from the symmetry operations that transform the Y$_0$ site to the Y$_i$ site (i = 1,…,7) and the transition operator is then calculated from the inverse matrix R^{-1} for each site and the two experimental configurations. As an example, for the Y$_1$ site (0,0,0), the symmetry operation (obtained from the International Crystallographic Tables) to go from the Y$_0$ site to the Y$_1$ site is $\left(x+\tfrac{1}{2},\bar{y}-\tfrac{1}{2},\bar{z}\right)$. The corresponding rotation matrix and its inverse are:

$$R_{Y_i} = \begin{pmatrix} 1 & 0 & 0 \\ 0 & -1 & 0 \\ 0 & 0 & -1 \end{pmatrix} \quad \text{and} \quad R_{Y_i}^{-1} = \begin{pmatrix} 1 & 0 & 0 \\ 0 & -1 & 0 \\ 0 & 0 & -1 \end{pmatrix}$$

Note that only the rotation part of the symmetry operation has to be taken into account because the transition operator is invariant by translation.

For the first experimental configuration $\alpha_{\mathrm{rot}} = 0°$ $\left(\hat{\varepsilon}=[010],\hat{k}=[\bar{1}00]\right)$, whatever the Y$_i$ site (i=1,…,7) is, the electric quadrupole transition operator is given by:

$$\left|(\hat{\varepsilon}\cdot r)\left(\hat{k}\cdot r\right)\right|_{Y_0} = \left|\left(R_{Y_i}^{-1}(\hat{\varepsilon})\cdot r\right)\left(R_{Y_i}^{-1}\left(\hat{k}\right)\cdot r\right)\right| = \pm xy$$

The sign of the transition operator is irrelevant because the electric quadrupole cross-section is the squared modulus of the transition amplitude. Hence the electric quadrupole cross-section is expressed as

$$\sigma_{Y_0}^{Q}\left(\hat{\varepsilon},\hat{k}\right) = \sigma_{Y_i}^{Q}\left[R_{Y_i}^{-1}(\hat{\varepsilon}),R_{Y_i}^{-1}\left(\hat{k}\right)\right]$$

meaning that

$$\sigma_{Y_0}^{Q}\left(\hat{\varepsilon},\hat{k}\right)=\sigma_{Y_i}^{Q}\left(\hat{\varepsilon},\hat{k}\right)$$

Therefore, for $\alpha_{\text{rot}} = 0°$, a single calculation of the electric quadrupole cross-section is needed to determine the cross-section of the cubic crystal σ_{cub}^{Q}, i.e. with the eight sites taken into account, as we have:

$$\sigma_{cub}^{Q}\left(\hat{\varepsilon},\hat{k}\right)=\sigma_{Y_0}^{Q}\left(\hat{\varepsilon},\hat{k}\right)$$

For the second experimental configuration $\alpha_{\text{rot}} = 90°$ $\left(\hat{\varepsilon}=\left[\frac{1}{2},\frac{1}{2},\frac{1}{\sqrt{2}}\right],\hat{k}=\left[-\frac{1}{2},-\frac{1}{2},\frac{1}{\sqrt{2}}\right]\right)$, we show that

$$\left|\left(\hat{\varepsilon}\cdot r\right)\left(\hat{k}\cdot r\right)\right|_{Y_0}=\left|\left(R_{Y_i,i=3,6,7}^{-1}\left(\hat{\varepsilon}\right)\cdot r\right)\left(R_{Y_i,i=3,6,7}^{-1}\left(\hat{k}\right)\cdot r\right)\right|=\frac{z^2}{2}-\frac{\left(x+y\right)^2}{4}$$

and

$$\left|\left(R_{Y_i,i=1,2,4,5}^{-1}\left(\hat{\varepsilon}\right)\cdot r\right)\left(R_{Y_i,i=1,2,4,5}^{-1}\left(\hat{k}\right)\cdot r\right)\right|=\frac{z^2}{2}-\frac{\left(x-y\right)^2}{4}$$

This means that

$$\sigma_{Y_0}^{Q}\left(\hat{\varepsilon},\hat{k}\right)=\sigma_{Y_i,i=3,6,7}^{Q}\left(\hat{\varepsilon},\hat{k}\right)\neq\sigma_{Y_i,i=1,2,4,5}^{Q}\left(\hat{\varepsilon},\hat{k}\right)$$

For $\alpha_{\text{rot}} = 90°$ we thus need to perform two calculations to determine the cubic absorption cross-section as:

$$\sigma_{cub}^{Q}\left(\hat{\varepsilon},\hat{k}\right)=\frac{\sigma_{Y_0}^{Q}\left(\hat{\varepsilon},\hat{k}\right)+\sigma_{Y_1}^{Q}\left(\hat{\varepsilon},\hat{k}\right)}{2}$$

Instead of doing the calculation for two different sites, it is more convenient to compute the spectrum for site Y_0 with the two orientations $\left(\hat{\varepsilon},\hat{k}\right)$ and $\left[R_{Y_1}^{-1}\left(\hat{\varepsilon}\right),R_{Y_1}^{-1}\left(\hat{k}\right)\right]$. This corresponds to $\left(\hat{\varepsilon}=\left[\frac{1}{2},\frac{1}{2},\frac{1}{\sqrt{2}}\right],\hat{k}=\left[-\frac{1}{2},-\frac{1}{2},\frac{1}{\sqrt{2}}\right]\right)$ and $\left(\hat{\varepsilon}=\left[\frac{1}{2},-\frac{1}{2},-\frac{1}{\sqrt{2}}\right],\hat{k}=\left[-\frac{1}{2},\frac{1}{2},-\frac{1}{\sqrt{2}}\right]\right)$ respectively.

With the coset method, we thus have to perform only one relaxation, one charge density with a core-hole, one electric dipole and three electric quadrupole cross-sections to obtain the total spectra for the two experimental configurations.

3.2 Additional materials to the publication

Some results were not detailed in the publication and some theoretical DFT calculations were not presented. This choice was made because the article is adressed to mineralogists and the main purpose was to explain the angular dependence of the pre-edge in cubic compounds and how DFT calculations can support the interpretation of the experimental spectra. The first part of this section thus presents complementary materials about the HERFD-XAS experiments. Additional DFT calculations results are presented in a second part.

3.2.1 Complementary results to the HERFD-XAS experiments

In the "Results: RIXS plane and HERFD-XAS" section of the publication, the difference between a HERFD-XAS spectrum and the one measured in a conventional fluorescence detection mode is explained. A complete RIXS plane was recorded to investigate if the HERFD-XAS spectra are enough similar to the conventional XANES to be calculated within the DFT framework. HERFD-XAS spectra were indeed calculated with a method dedicated to the conventional XANES. The (Ω, γ) RIXS plane at the V K-edge of tsavorite is thus presented in the publication. The $(\Omega, \Omega - \gamma)$ plane, which is another way to present a RIXS plane, is shown here in Fig. 3.2. Its axes are the incident energy and the transfer energy. In this kind of RIXS plane, the fluorescence lines correspond to the diagonals. The one situated at lowest transfer energies corresponds the $K\alpha_1$ line.

A RIXS plane can also be plotted with the emission energy as a second axis instead of the transfer energy, as in the publication. In that case, a total fluorescence spectrum can be deduced from the RIXS plane by integrating over the emission energies. The (Ω, γ) RIXS plane and the corresponding integrated spectrum are shown in Fig. 3.3. The pre-edge appears identical to the HERFD-XAS one. The high-intensity structure observed at ∼5476 eV corresponds to the peak present just before the edge (Peak A in Fig. 4 of the publication).

Complementary to the data presented in the RIXS plane, a conventional XANES measurement was also performed. The RIXS plane was indeed recorded only in the pre-edge region and information concerning the edge were also needed. Both HERFD and total fluorescence spectra are displayed in figure 3.4. All the edge features of the total fluorescence spectrum are present on the HERFD spectrum, with correct energy and relative intensities. The HERFD features are sharpened compared with the total fluorescence ones, which is a well-known effect of HERFD-XAS [94].

The comparison of the HERFD-XAS spectrum with, on the one hand, the RIXS plane and, on the other hand, the conventional XANES spectrum clearly demonstrates that in the case of vanadium in tsavorite, all the features are present on the $K\alpha_1$ HERFD-XAS spectrum.

3.2.2 A detailed study of the $3d$ orbitals splitting

By taking advantage of the spin polarization in the DFT calculations, the experimental pre-edge features were interpreted within a monoelectronic framework. The transitions were described with the orbital scheme described in Fig. 8 of the publication and the assignments of the experimental peaks were done by considering the different possible final states. The orbital scheme used for the transition assignments corresponds to a simple view of the $3d$ orbitals splitting where only the crystal-field splitting is taken into account. In the "Results: The

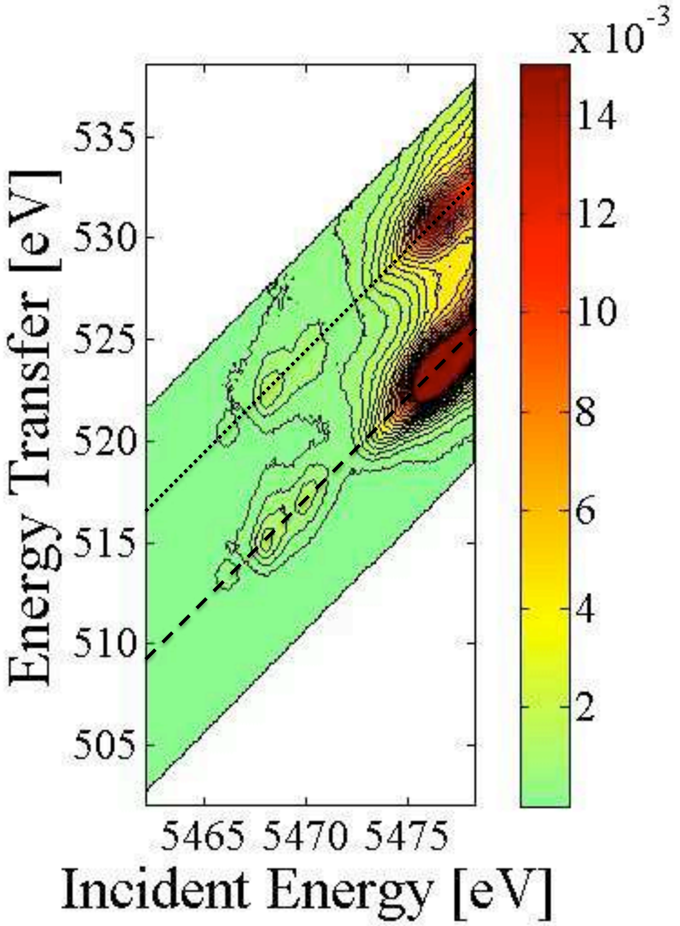

Figure 3.2: V K-edge (Ω, $\Omega - \gamma$) RIXS plane of tsavorite. The dashed line represent the Kα_1 fluorescence line and the dotted one the Kα_2 fluorescence line.

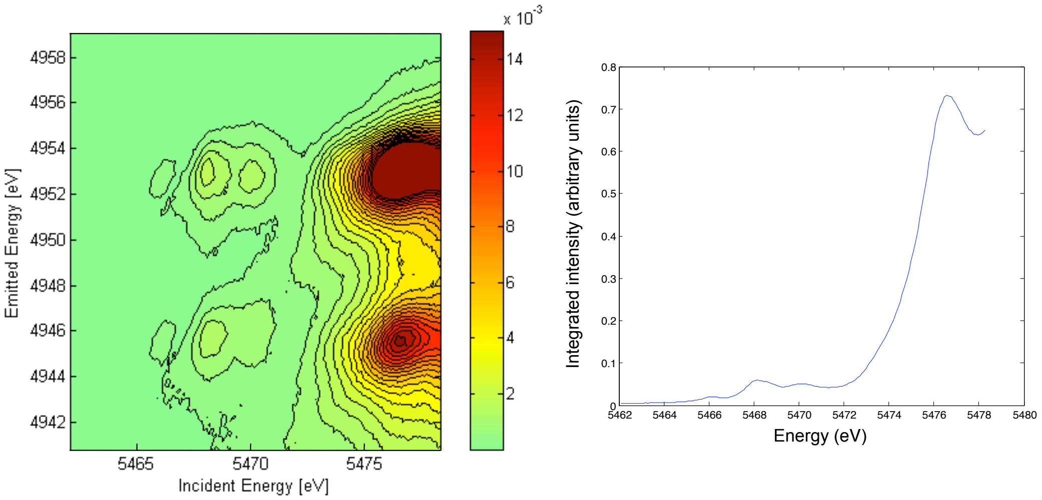

Figure 3.3: V K-edge (Ω, γ) RIXS plane of tsavorite (left), with the spectrum corresponding to an integration of the plane over the emission energies. (right)

splitting of $3d$ orbitals" section of the publication, a comparison was thus done between the crystal-field splitting $10Dq$ derived from optical spectroscopy and the $t_{2g}^{\uparrow}$ - $e_g^{\uparrow}$ energy separation

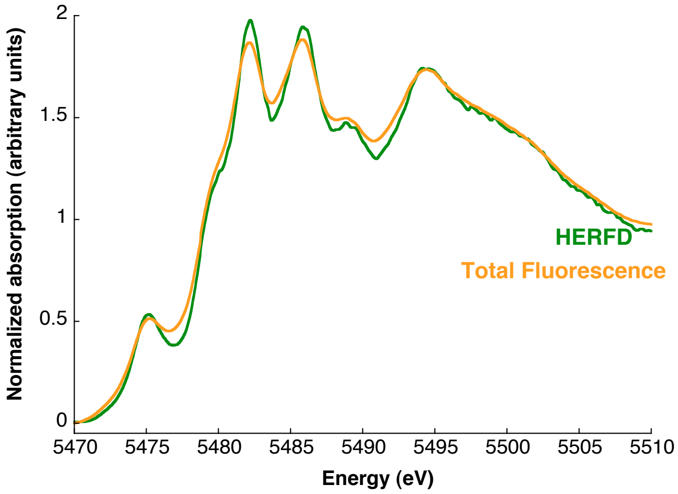

Figure 3.4: V *K*-edge spectrum in tsavorite recorded with the HERFD mode (green line) and the conventional XANES mode (or total fluorescence mode) (orange line).

determined from the DFT calculations. Complementary information on this comparison are first given. Then are presented additional results to the publication on the electronic structure of V^{3+} in tsavorite when the splitting of the $3d$ orbitals due to a C_{3i} symmetry is taken into account.

Complementary information for the comparison between DFT calculation and optical spectroscopy

In an octahedral field, the five $3d$ orbitals are split in three t_{2g} and two e_g orbitals. The octahedral field splitting, $10Dq$, represents the energy separation between these two sets of orbitals and can be measured by optical spectrocopy. In an absorption spectrum, the value of $10Dq$ is directly given by the position of the first broad band or by the second band if the y-axis represents the Kubelka-Munk function. The optical spectrum of tsavorite, reproduced from the data base of Rossman [179], is plotted in Fig. 3.5. Tsavorite is a green V-bearing grossular, and it is clearly indicated on the spectrum, which presents a minimum in the wavelength window corresponding to the green color (∼470 - 570 nm. The value of the octahedral field splitting determined with the spectrum is $10Dq = 610\text{nm} = 16390\ \text{cm}^{-1} = 2.03$ eV. Mazurak and Czaja [145] studied a natural tsavorite from Kenya and deduced from their optical experiments a value of $10Dq = 15900\ \text{cm}^{-1} = 1.97$ eV.

In the spin-polarized DFT calculations, as shown in the publication, the contribution of each spin is determined and the transitions to empty t_{2g} or e_g orbitals can be assigned to the experimental peaks. This is done in the publication. The energy separation between the $t_{2g} \uparrow$ and $e_g \uparrow$ contributions and between the $t_{2g} \downarrow$ and $e_g \downarrow$ contributions is thus given by the calculation. This value can be compared to the crystal field splitting of the optical spectroscopy as it describes the separation between two orbitals with the same spin.

The peak assignment given by the DFT calculations can also be used to directly interpret the experimental pre-edge features. The experimental spectrum of each orientation was fitted with four Gaussian contributions (Tab. 3.1), corresponding to the $t_{2g} \uparrow$, $e_g \uparrow$, $t_{2g} \downarrow$ and $e_g \downarrow$ contributions observed in the calculations. Their positions were used to determine the experimental energy separation between the $t_{2g} \uparrow$ and $e_g \uparrow$ and between the $t_{2g} \downarrow$ and $e_g \downarrow$ contributions.

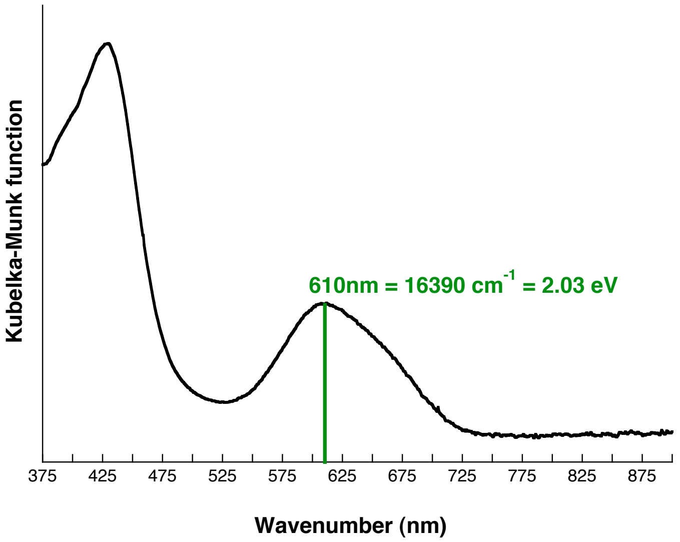

Figure 3.5: Optical spectrum of tsavorite reproduced from the database of Rossman [179].

I give here the parameters used for the fitting (Tab. 3.1) and Fig. 3.6 shows the Gaussian decomposition that has led to the results presented in Tab. III of the publication.

Contributions	$\alpha_{rot} = 0°$			$\alpha_{rot} = 90°$		
	A	x_0	s	A	x_0	s
$t_{2g}\uparrow$	$7.002 \,.\, 10^{-3}$	5464.90	0.450	$6.150 \,.\, 10^{-3}$	5464.92	0.519
$t_{2g}\downarrow$	$2.301 \,.\, 10^{-2}$	5466.56	0.498	$1.744 \,.\, 10^{-2}$	5466.44	0.411
$e_g\uparrow$	$1.200 \,.\, 10^{-2}$	5467.11	0.648	$2.105 \,.\, 10^{-2}$	5467.08	0.536
$e_g\downarrow$	$1.550 \,.\, 10^{-2}$	5468.56	0.816	$2.070 \,.\, 10^{-2}$	5468.58	0.706

Table 3.1: Parameters of the Gaussians used to fit the experimental spectra.

The electronic structure of V^{3+} in tsavorite for a C_{3i} symmetry

The transition assignments from the DFT calculations were done by considering the splitting of the five $3d$ orbitals into three t_{2g} and two e_g ones, which occurs in an pure octahedral field. Nevertheless, vanadium sits in a C_{3i} symmetry site in tsavorite and the trigonal distortion further splits the three t_{2g} orbitals into two e_g and one a_{1g} orbitals, as represented in Fig. 3.7. This splitting was not considered in the publication to interpret the pre-edge features as the splitting between the three t_{2g} orbitals is not visible in the calculated pre-edge (*cf.* "Results: Interpretation of the pre-edge features" section). Additional results with the C_{3i} splitting taken into account are therefore presented here.

The following notation is adopted: the two e_g orbitals resulting from the C_{3i} splitting are denoted $e_g(C_{3i})$ and the a_{1g} orbital $a_{1g}(C_{3i})$. The e_g orbitals denoted $e_g(O_h)$ are the orbitals from the octahedral field splitting that are not further split by the C_{3i} distortion. As the electronic structure of V^{3+} is $3d^2$ (I consider here for the discussion only the valence d electrons), only two of the three t_{2g} orbitals are occupied. Consequently two electronic configurations are possible to describe the ground state of V^{3+} in tsavorite: $a_{1g}^{\uparrow}(C_{3i})^0\ e_g^{\uparrow}(C_{3i})^2\ (e_g)^0(O_h)$ (Fig. 3.7, situation 1) or $a_{1g}^{\uparrow}(C_{3i})^1\ e_g^{\uparrow}(C_{3i})^1\ (e_g)^0(O_h)$ (Fig. 3.7, situation 2).

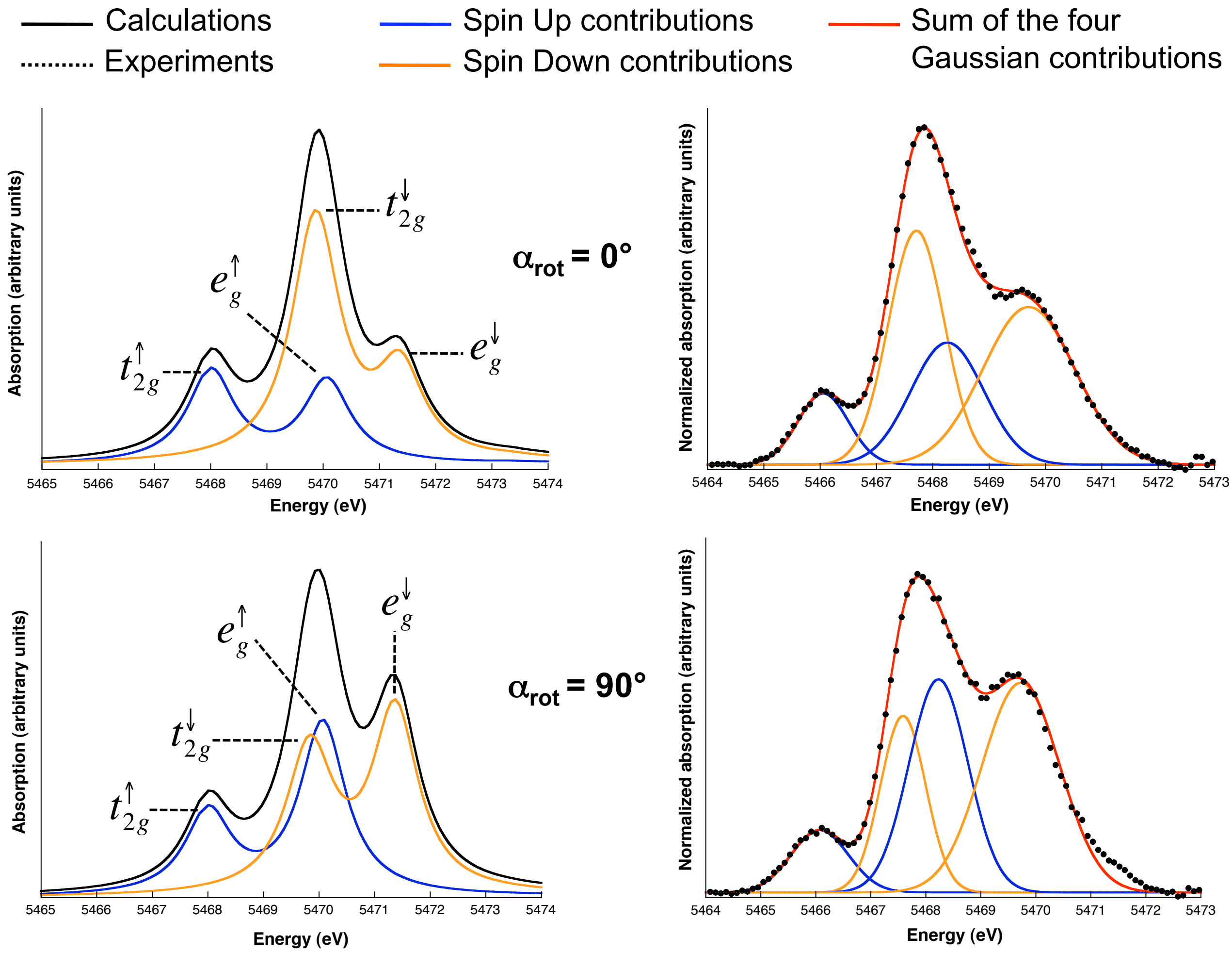

Figure 3.6: Comparison of the $t_{2g} \uparrow$, $e_g \uparrow$, $t_{2g} \downarrow$ and $e_g \downarrow$ contributions between calculations (left) and experiments (right). The upper pannel concerns the $\alpha_{rot} = 0°$ orientation and the lower panel the $\alpha_{rot} = 90°$ orientation.

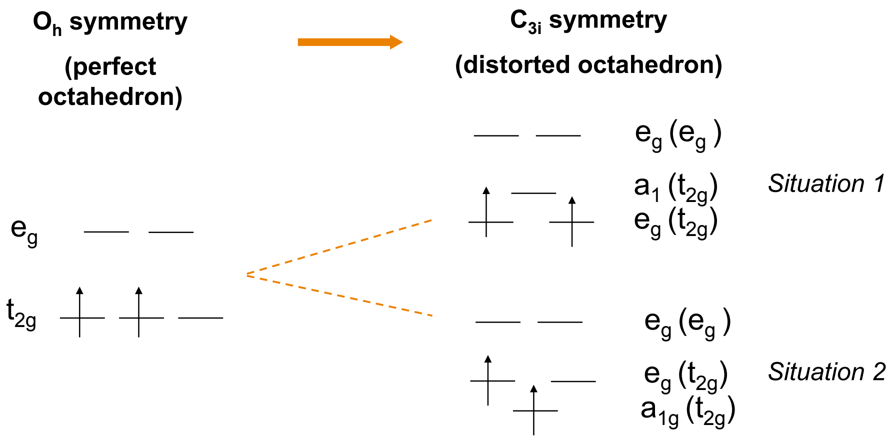

Figure 3.7: Schematic representation of the trigonal splitting (C_{3i}) of the d orbitals with the two possible ground states for V^{3+} in tsavorite.

On the experimental and calculated spectra for the two experimental configurations, no splitting of the t_{2g} orbitals is observed, meaning that the two sets of orbitals are close in energy. In such a case, the angular dependence of the pre-edge can help to determine the electronic configuration. A relevant ($\hat{\boldsymbol{\varepsilon}}$,$\hat{\mathbf{k}}$) configuration can enable to distinguish the two $e_g(C_{3i})$ orbitals from the $a_{1g}(C_{3i})$ one. The different d orbitals are indeed orientated differently with respect to the cubic frame. The electric quadrupole cross-section is calculated for this orientation and the peaks are assigned with respect to the expression of the transition operator.

The vanadium site symmetry is trigonal so the expression of C_{3i} eigenstates as a function of d orbitals in the cubic frame can be used. They are defined by the following relations [122]:

$$\begin{aligned}
d_{xy} &= \frac{1}{\sqrt{3}}(a_{1g}(t_{2g}) + e_{g+}(t_{2g}) + e_{g-}(t_{2g})) && (3.1)\\
d_{xz} &= \frac{1}{\sqrt{3}}a_{1g}(t_{2g}) - \left(\frac{1}{2\sqrt{3}} + \frac{i}{2}\right) e_{g+}(t_{2g}) + \left(-\frac{1}{2\sqrt{3}} + \frac{i}{2}\right) e_{g-}(t_{2g}) && (3.2)\\
d_{yz} &= -\frac{1}{\sqrt{3}}a_{1g}(t_{2g}) + \left(\frac{1}{2\sqrt{3}} - \frac{i}{2}\right) e_{g+}(t_{2g}) + \left(\frac{1}{2\sqrt{3}} + \frac{i}{2}\right) e_{g-}(t_{2g}) && (3.3)\\
d_{3z^2-r^2} &= \frac{1}{\sqrt{2}}\left(e_{g+}(t_{2g}) + e_{g-}(t_{2g})\right) && (3.4)\\
d_{x^2-y^2} &= \frac{i}{\sqrt{2}}\left(e_{g+}(t_{2g}) - e_{g-}(t_{2g})\right) && (3.5)
\end{aligned}$$

The $a_{1g}(C_{3i})$ orbital can be expressed as a linear combination of equations 3.1, 3.2 and 3.3 :

$$a_{1g} = \frac{1}{\sqrt{3}}(d_{xy} - d_{yz} + d_{xz}) \tag{3.6}$$

No ($\hat{\boldsymbol{\varepsilon}}$, $\hat{\mathbf{k}}$) couple allows to probe the $a_{1g}(C_{3i})$ orbital unless the orthogonality condition for $\hat{\boldsymbol{\varepsilon}}$ and $\hat{\mathbf{k}}$ is relaxed. In that case, the ($\hat{\boldsymbol{\varepsilon}}$, $\hat{\mathbf{k}}$) configuration cannot be reached experimentally, as $\hat{\boldsymbol{\varepsilon}}$ and $\hat{\mathbf{k}}$ are not perpendicular and only the theoretical spectrum can be determined. A corresponding orientation to probe the $a_{1g}(C_{3i})$ orbital is ($\hat{\boldsymbol{\varepsilon}} = [-\frac{1}{\sqrt{3}},\frac{1}{\sqrt{3}},\frac{1}{\sqrt{3}}]$, $\hat{\mathbf{k}} = [-\frac{1}{\sqrt{3}},\frac{1}{\sqrt{3}},\frac{1}{\sqrt{3}}]$) and its electric quadrupole transition operator is given by:

$$(\hat{\boldsymbol{\varepsilon}} \cdot \mathbf{r})(\hat{\mathbf{k}} \cdot \mathbf{r}) = \frac{1}{3}(x^2 + y^2 + z^2) - \frac{2}{3}(xy - yz + xz) \tag{3.7}$$

The first term describes the spherical orbitals and the second the linear relation between three $3d$ orbitals. This term corresponds to the linear combination which defines the a_{1g} orbital (Eq. 3.6).

In the general case, the expression of the electric quadrupole operator $(\hat{\boldsymbol{\varepsilon}} \cdot \mathbf{r})(\hat{\mathbf{k}} \cdot \mathbf{r})$ is [85] :

$$(\hat{\boldsymbol{\varepsilon}}\cdot\mathbf{r})(\hat{\mathbf{k}}\cdot\mathbf{r}) = \frac{1}{3}r^2(\hat{\boldsymbol{\varepsilon}}\cdot\hat{\mathbf{k}}) + \left(\frac{4\pi}{3}\right)^2 r^2\sqrt{\frac{3}{10\pi}} \sum_{\lambda,\mu,\nu} \left[(-1)^{\nu} Y_1^{-\lambda}(\hat{\boldsymbol{\varepsilon}})\ \times Y_1^{-\mu}(\hat{\mathbf{k}})(1\lambda 1\mu|2\nu) Y_2^{\nu}(\mathbf{r})\right] \tag{3.8}$$

The first term represents the spherical orbitals and the second one the $3d$ orbitals. The spherical term is zero if $\hat{\boldsymbol{\varepsilon}}$ and $\hat{\mathbf{k}}$ are perpendicular.

Each term of Eq. 3.7 can be identified with those of Eq. 3.8: the spherical term of equation 3.8 is zero in Eq. 3.7 and the $3d$ orbitals term in equation 3.8 corresponds to the a_{1g} term in Eq. 3.7:

$$\frac{1}{3}(x^2 + y^2 + z^2) \Longleftrightarrow \frac{1}{3}r^2(\hat{\boldsymbol{\varepsilon}} \cdot \hat{\mathbf{k}})$$

$$-\frac{2}{3}(xy - yz + xz) \Longleftrightarrow \left(\frac{4\pi}{3}\right)^2 r^2 \sqrt{\frac{3}{10\pi}} \sum_{\lambda,\mu,\nu} \left[(-1)^{\nu} Y_1^{-\lambda}(\hat{\boldsymbol{\varepsilon}}) \times Y_1^{-\mu}(\hat{\mathbf{k}})(1\lambda 1\mu|2\nu) Y_2^{\nu}(\mathbf{r})\right].$$

The Xspectra code was written under the assumption of a fulfilled orthogonality condition for $\hat{\boldsymbol{\varepsilon}}$ and $\hat{\mathbf{k}}$. Therefore the spherical term of the electric quadrupole transition operator is not coded. However the term corresponding to the d orbitals is implemented and can be computed even if the orthogonality condition is not obeyed. The a_{1g} orbital can thus be theoretically probed by the ($\hat{\boldsymbol{\varepsilon}} = [-\frac{1}{\sqrt{3}}, \frac{1}{\sqrt{3}}, \frac{1}{\sqrt{3}}]$, $\hat{\mathbf{k}} = [-\frac{1}{\sqrt{3}}, \frac{1}{\sqrt{3}}, \frac{1}{\sqrt{3}}]$) configuration.

The theoretical absorption cross-section calculated for the configuration that permits the a_{1g} orbitals to be probed is displayed in figure 3.8. Two peaks are visible: one in the occupied state and one in the empty state, corresponding respectively to the spin up and spin down contribution. The presence of the spin ↑ peak in the occupied state is a clear evidence that the $a_{1g}(C_{3i})$ orbital is occupied and that the DFT calculation has led to the situation no. 1 illustrated in Fig. 3.7. Consequently, one $e_g(C_{3i})$ orbital has to be occupied and the second is empty. The initial electronic configuration of V^{3+} in tsavorite, as modelled by the LSDA-DFT calculation, can thus be described as $a_{1g}^{\uparrow}(C_{3i})^1\ e_g^{\uparrow}(C_{3i})^1\ (e_g)^0(O_h)$ (Fig. 3.7 situation 2).

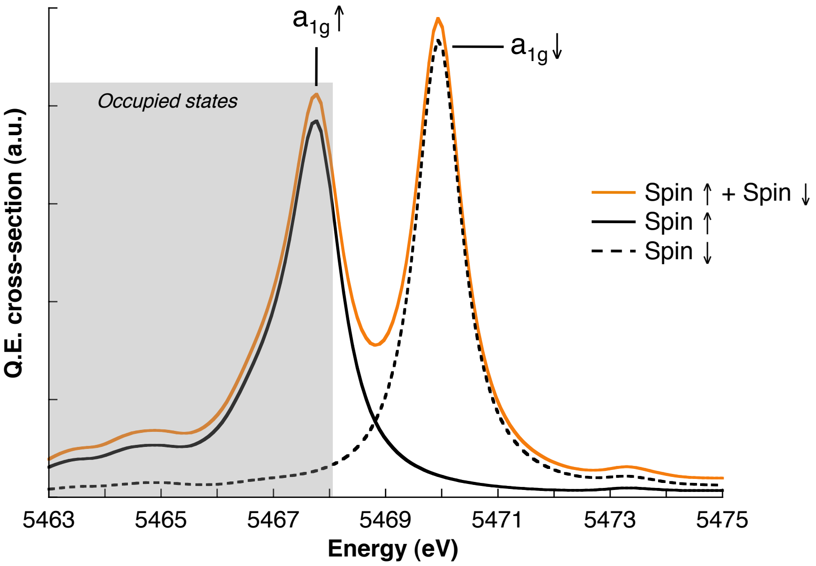

Figure 3.8: Calculated electric quadrupole cross-section with the spin-polarization, for the ($\hat{\boldsymbol{\varepsilon}} = [-\frac{1}{\sqrt{3}}, \frac{1}{\sqrt{3}}, \frac{1}{\sqrt{3}}]$, $\hat{\mathbf{k}} = [-\frac{1}{\sqrt{3}}, \frac{1}{\sqrt{3}}, \frac{1}{\sqrt{3}}]$) configuration.

The probing by DFT calculations of a specific orbital therefore permits the determination of the electronic configuration of V^{3+} in tsavorite. This result was obtained within the intrisic limits and approximations of the DFT and hence has to be considered with caution as it cannot be confirmed experimentally. Nevertheless, for a C_{3v} trigonal symmetry, the predicted splitting of the t_{2g} is described with the a_{1g} orbital as the lowest orbital [27]. The symmetry elements of the C_{3v} point group are the C_3 axis and three vertical mirrors, whereas the C_{3i} point group has a C_3 axis and an inversion center. That observation tends to confirm the results of the DFT calculations for the C_{3i} symmetry.

3.3 Multielectronic calculations

The spectral signature of V^{3+} in a slightly distorted centrosymmetric octahedron has been determined by HERFD-XAS experiments and DFT calculations. The results and the precise knowledge of the spectral signature of V^{3+} show that tsavorite can be used as a reliable V^{3+}-dilute reference compound when V K-edge XANES spectra are interpreted with the fingerprint method.

A more dedicated method to calculate transitions to localized states is the Ligand Field Multiplet (LFM) theory. The multielectronic calculations usually better take into account the *d*-*d* electronic interactions. To complete the DFT calculations described in the two previous sections, I thus performed multielectronic calculations. In LFM calculations, the ion is considered with all its electrons and as embedded in a ligand field. This method is also parameterized: some parameters (the crystal field, $10Dq$, and the distortion parameters D_σ and D_τ) have to be fitted to the experiments and compared to those obtained by optical spectroscopy. An important point is that the LFM theory enables to calculate only the pre-edge features.

Prior to the presentation of the multielectronic calculations results, details concerning the expression of the electric quadrupole cross-section are needed. In LFM theory, the ion is considered as embedded in a ligand field and the calculations are thus performed for a single site in the local point group symmetry. In the case of tsavorite, the V^{3+} ion sits in a C_{3i} site and the calculations are performed for a ligand field corresponding to the distorted octahedral symmetry. Since V^{3+} sits in a centrosymmetric site, the pre-edge arises from pure electric quadrupole transitions and only the electric quadrupole cross-section is calculated. However, the total absorption cross-section for the cubic crystal, *i.e.* with the eight different sites of the unit cell taken into account, is needed to compare the calculations with the experiments. The important points of the determination of the absorption cross-section of the cubic crystal are the determination of:

- the cross-section for a cubic crystal,
- the cross-section for a C_{3i} site,
- the relation between the C_{3i} site and the cubic crystal,
- the cross-sections for the experimental orientations for a cubic crystal.

In the second part of this section, the multiplet results are presented.

3.3.1 The eletric quadrupole cross-section

Absorption cross-section for a cubic crystal

In the electric quadrupole cross-section, the total absorption cross-section for a cubic compound is given by [24]:

$$\begin{aligned}\sigma^Q_{cube}(\hat{\varepsilon},\hat{\mathbf{k}}) = \sigma^Q_{cube}(0,0) + \frac{1}{\sqrt{14}}[&35\sin^2\theta\cos^2\theta\cos^2\psi + 5\sin^2\theta\sin^2\psi - 4\\ &+ 5\sin^2\theta(\cos^2\theta\cos^2\psi\cos(4\varphi) - \sin^2\psi\cos(4\varphi)\\ &- 2\cos\theta\sin\psi\cos\psi\sin 4\varphi)]\sigma^Q_{cube}(4,0) \qquad (3.9)\end{aligned}$$

The electric quadrupole cross-section σ^Q is expressed here as a function of 4^{th}-rank tensor components $\sigma^Q(\ell,m)$. σ^Q(0,0) is the isotropic electric quadrupole cross-section and σ^Q(4,0) an anisotropic term. The latter depends on the polarization $\hat{\boldsymbol{\varepsilon}}$ and direction $\hat{\boldsymbol{k}}$ of the incident X-rays beam, which are defined by the Euler angles $(\theta,\ \varphi,\ \psi)$:

$$\hat{\boldsymbol{\varepsilon}} = \begin{pmatrix} \sin\theta\ \cos\varphi \\ \sin\theta\ \sin\varphi \\ \cos\theta \end{pmatrix}, \tag{3.10}$$

and

$$\hat{\mathbf{k}} = \begin{pmatrix} \cos\theta\ \cos\varphi\ \cos\psi - \sin\varphi\ \sin\psi \\ \cos\theta\ \sin\varphi\ \cos\psi + \cos\varphi\ \sin\psi \\ -\sin\theta\ \cos\psi \end{pmatrix}. \tag{3.11}$$

The total absorption cross-section can also be expressed as [122, 32] :

$$\sigma^Q_{cube}(\hat{\boldsymbol{\varepsilon}}, \hat{\mathbf{k}}) = \sigma^Q_{cube}(0,0) + (\varepsilon_x^2 k_x^2 + \varepsilon_y^2 k_y^2 + \varepsilon_z^2 k_z^2 - \frac{1}{5})\ \sigma^Q_{cube}(4,0), \tag{3.12}$$

where $(\varepsilon_x,\ \varepsilon_y,\ \varepsilon_z)$ are the coordinates of the polarization $\hat{\boldsymbol{\varepsilon}}$ and $(k_x,\ k_y,\ k_z)$ the coordinates of the direction $\hat{\boldsymbol{k}}$. It is important to notice that the coordinates of $\hat{\boldsymbol{\varepsilon}}$ and $\hat{\boldsymbol{k}}$ are expressed in the Cartesian reference frame of the cube.

Absorption cross-section for a C_{3i} site

In the C_{3i} symmetry, the expression of the electric quadrupole cross-section is [24] :

$$\begin{aligned} \sigma^Q_{C_{3i}}(\hat{\boldsymbol{\varepsilon}}, \hat{\mathbf{k}}) = {} & \sigma^Q_{C_{3i}}(0,0) + \sqrt{\frac{5}{14}}(3\sin^2\theta\sin^2\psi - 1)\sigma^Q_{C_{3i}}(2,0) \\ & + \frac{1}{\sqrt{14}}(35\sin^2\theta\cos^2\theta\cos^2\psi + 5\sin^2\theta\sin^2\psi - 4)\sigma^Q_{C_{3i}}(4,0) \\ & - \sqrt{10}\sin\theta[(2\cos^2\theta\cos^2\psi - 1)\cos\theta(\sigma^{Qr}_{C_{3i}}(4,3)\cos(3\varphi) + \sigma^{Qi}_{C_{3i}}(4,3)\sin(3\varphi)) \\ & - (3\cos^2\theta - 1)\sin\psi\cos\psi(\sigma^{Qr}_{C_{3i}}(4,3)\sin(3\varphi) - \sigma^{Qi}_{C_{3i}}(4,3)\cos(3\varphi))]. \end{aligned} \tag{3.13}$$

$\sigma^Q_{C_{3i}}$(0,0) is the isotropic electric quadrupole cross-section. $\sigma^Q_{C_{3i}}$(2,0), $\sigma^Q_{C_{3i}}$(4,0), $\sigma^{Qr}_{C_{3i}}$(4,3) and $\sigma^{Qi}_{C_{3i}}$(4,3) are anisotropic terms and they depend on the polarization $\hat{\boldsymbol{\varepsilon}}$ and direction $\hat{\boldsymbol{k}}$ of the incident X-ray beam. Here the coordinates of $\hat{\boldsymbol{\varepsilon}}$ and $\hat{\boldsymbol{k}}$ are expressed in the Cartesian reference frame of the site, with the z-axis along the $[\bar{1}11]$ direction of the cube.

To determine $\sigma^Q_{C_{3i}}(\hat{\boldsymbol{\varepsilon}}, \hat{\boldsymbol{k}})$ for any configuration, $\sigma^Q_{C_{3i}}$(0,0), $\sigma^Q_{C_{3i}}$(2,0), $\sigma^Q_{C_{3i}}$(4,0), $\sigma^{Qr}_{C_{3i}}$(4,3) and $\sigma^{Qi}_{C_{3i}}$(4,3) must be determined by performing calculations for five independent configurations $(\hat{\boldsymbol{\varepsilon}},\hat{\boldsymbol{k}})$.

From a single site to the crystal

In order to reconstruct the angular dependence of the crystal from that of a single site with C_{3i} symmetry, a relation between the [$\sigma^Q_{C_{3i}}$(0,0), $\sigma^Q_{C_{3i}}$(2,0), $\sigma^Q_{C_{3i}}$(4,0), $\sigma^{Qr}_{C_{3i}}$(4,3), $\sigma^{Qi}_{C_{3i}}$(4,3)] and [σ^Q_{cube}(0,0), σ^Q_{cube}(4,0)] is needed. To do so, the formula given in the "Symmetry considerations: The coset method" section of Chap. 2 are used [25] .

However, another set of site parameters can be used to reconstruct the angular dependence of the cubic crystal. When a site has the C_{3i} symmetry, the z-axis of the orthonormal site frame is specified by the rotation axis but the y-axis is arbitrary in the plane perpendicular to the rotation axis. Because of this arbitrary nature, the parametrization of the crystal-field Hamiltonian can be simplified by choosing the y-axis so that a crystal-field parameter is set to zero ([29], p. 121 and 184). By doing this choice, the calculation of the eigenstates is simplified but the crystal-field parameter set to zero reappears as the angle α between the y-axis and the [110] direction of the cube in the plane perpendicular to the $[\bar{1}11]$direction[1]. In Chap. 2, the crystal-field Hamiltonian in the $O_3 \supset O_h \supset D_{3d} \supset C_{3i}$ subduction was shown to be:

$$\begin{aligned} H_{crystal} = {} & X^{4^+(O_3)0^+(O_h)0^+(D_{3d})0^+(C_{3i})} U^{4^+(O_3)0^+(O_h)0^+(D_{3d})0^+(C_{3i})} \\ & + X^{4^+(O_3)\tilde{1}^+(O_h)0^+(D_{3d})0^+(C_{3i})} U^{4^+(O_3)\tilde{1}^+(O_h)0^+(D_{3d})0^+(C_{3i})} \\ & + X^{4^+(O_3)1^+(O_h)\tilde{0}^+(D_{3d})0^+(C_{3i})} U^{4^+(O_3)1^+(O_h)\tilde{0}^+(D_{3d})0^+(C_{3i})} \\ & + X^{2^+(O_3)\tilde{1}^+(O_h)0^+(D_{3d})0^+(C_{3i})} U^{2^+(O_3)\tilde{1}^+(O_h)0^+(D_{3d})0^+(C_{3i})}. \end{aligned} \tag{3.14}$$

Therefore, if the $X^{41\tilde{0}0}$ parameter is set to zero, the crystal-field Hamiltonian has therefore the same expression than in a D_{3d} symmetry. The three branchings in the $O_3 \supset O_h \supset D_{3d} \supset C_{3i}$ subduction which have the $\mathbf{0}$ representation in D_{3d} are:

$$\begin{aligned} &\mathbf{4}^+(O_3) \to \mathbf{0}^+(O_h) \to \mathbf{0}^+(D_{3d}) \to \mathbf{0}^+(C_{3i}) \\ &\mathbf{4}^+(O_3) \to \tilde{\mathbf{1}}^+(O_h) \to \mathbf{0}^+(D_{3d}) \to \mathbf{0}^+(C_{3i}) \\ &\mathbf{2}^+(O_3) \to \tilde{\mathbf{1}}^+(O_h) \to \mathbf{0}^+(D_{3d}) \to \mathbf{0}^+(C_{3i}). \end{aligned}$$

The crystal-field Hamiltonian in a D_{3d} symmetry is therefore a function of the X^{4000}, $X^{4\tilde{1}00}$ and $X^{2\tilde{1}00}$ crystal-field parameters.

Consequently, the [σ^Q_{cube}(0,0), σ^Q_{cube}(4,0)] parameters can be expressed as functions of the [$\sigma^Q_{D_{3d}}$(0,0), $\sigma^Q_{D_{3d}}$(2,0), $\sigma^Q_{D_{3d}}$(4,0), $\sigma^{Qr}_{D_{3d}}$(4,3)] parameters and of the α angle [25]. The isotropic cross-sections are identical:

$$\sigma^Q_{cube}(0,0) \;=\; \sigma^Q_{D_{3d}}(0,0). \tag{3.15}$$

The second term of the cubic electric quadrupole cross-section, σ^Q_{cube}(4,0), is a function of two site parameters and the angle α:

$$\sigma^Q_{cube}(4,0) = -\frac{1}{18}[7\sigma^Q_{D_{3d}}(4,0) + 2\sqrt{70}\cos(3\alpha)\sigma^Q_{D_{3d}}(4,3)] \tag{3.16}$$

$\sigma^Q_{D_{3d}}$(0,0), $\sigma^Q_{D_{3d}}$(4,0) and $\sigma^Q_{D_{3d}}$(4,3) must therefore be determined to reconstruct the angular dependence of the cubic crystal.

The absorption cross-section can be computed in a D_{3d} site symmetry is given by [24]:

$$\begin{aligned} \sigma^Q_{D_{3d}}(\hat{\boldsymbol{\varepsilon}}, \hat{\mathbf{k}}) = {} & \sigma^Q_{D_{3d}}(0,0) + \sqrt{\frac{5}{14}}(3\sin^2\theta\sin^2\psi - 1)\sigma^Q_{D_{3d}}(2,0) \\ & + \frac{1}{\sqrt{14}}(35\sin^2\theta\cos^2\theta\cos^2\psi + 5\sin^2\theta\sin^2\psi - 4)\sigma^Q_{D_{3d}}(4,0) \\ & - \sqrt{10}\sin\theta[(2\cos^2\theta\cos^2\psi - 1)\cos\theta\cos(3\varphi) \\ & - (3\cos^2\theta - 1)\sin\psi\cos\psi\sin(3\varphi)]\sigma^{Qr}_{D_{3d}}(4,3). \end{aligned} \tag{3.17}$$

---

[1] This α angle is completely different from the α_{rot} angle defined in the angular dependence experiments

$\sigma^Q_{D_{3d}}$(0,0) is the isotropic electric quadrupole cross-section. $\sigma^Q_{D_{3d}}$(2,0), $\sigma^Q_{D_{3d}}$(4,0) and $\sigma^{Qr}_{D_{3d}}$(4,3) are anisotropic terms. They depend on the polarization $\hat{\boldsymbol{\varepsilon}}$ and direction $\hat{\boldsymbol{k}}$ of the incident X-rays beam. Here, the coordinates of $\hat{\boldsymbol{\varepsilon}}$ and $\hat{\boldsymbol{k}}$ are expressed in the Cartesian reference frame of the D_{3d} site, with the z-axis along the [$\bar{1}$11] direction of the cube and the y-axis alond the [110] direction.

$\sigma^Q_{D_{3d}}$(0,0), $\sigma^Q_{D_{3d}}$(2,0), $\sigma^Q_{D_{3d}}$(4,0) and $\sigma^Q_{D_{3d}}$(4,3) are needed to calculate the cubic electric quadrupole cross-section. They are determined by a linear combination of four independent values of the electric quadrupole cross-section, σ^Q_1, σ^Q_2, σ^Q_3 and σ^Q_4, which are calculated for arbitrary ($\hat{\varepsilon}$, $\hat{\boldsymbol{k}}$) configurations. From the expression of $\hat{\varepsilon}$ and $\hat{\boldsymbol{k}}$, the values of the Euler angles (θ, φ, ψ) are determined and then inserted in the expression of the absorption cross-section $\sigma^Q_{D_{3d}}$($\hat{\boldsymbol{\varepsilon}}$,$\hat{\boldsymbol{k}}$). Finally, the system of equations which gives the expression of σ^Q_1, σ^Q_2, σ^Q_3 and σ^Q_4 as functions of $\sigma^Q_{D_{3d}}$(0,0), $\sigma^Q_{D_{3d}}$(2,0), $\sigma^Q_{D_{3d}}$(4,0) and $\sigma^Q_{D_{3d}}$(4,3) is inversed.

For the first orientation, chosen as $\hat{\boldsymbol{\varepsilon}}_1$=[-$\frac{1}{\sqrt{6}}$, -$\frac{1}{\sqrt{2}}$, $\frac{1}{\sqrt{3}}$] and $\hat{\boldsymbol{k}}_1$= [$\frac{1}{\sqrt{6}}$, -$\frac{1}{\sqrt{2}}$, -$\frac{1}{\sqrt{3}}$], with the corresponding Euler angles ($\theta_1 = \arccos(\frac{1}{\sqrt{3}})$, $\varphi_1 = -\frac{2\pi}{3}$, $\psi_1 = \frac{\pi}{4}$), the absorption cross-section σ^Q_1 is:

$$\sigma^Q_1 = \sigma^Q_{D_{3d}}(0,0) + \frac{\sqrt{14}}{9}\sigma^Q_{D_{3d}}(4,0) + \frac{4\sqrt{5}}{9}\sigma^Q_{D_{3d}}(4,0). \tag{3.18}$$

For the second orientation, chosen as $\hat{\boldsymbol{\varepsilon}}_2$=[$\frac{-1+\sqrt{2}}{\sqrt{6}}$, 0, $\frac{1+\sqrt{2}}{\sqrt{6}}$] and $\hat{\boldsymbol{k}}_2$=[$\frac{1+\sqrt{2}}{\sqrt{6}}$, 0, $\frac{1-\sqrt{2}}{\sqrt{6}}$], with the corresponding Euler angles ($\theta_2 = \arccos(\frac{1}{\sqrt{3}} + \frac{1}{\sqrt{6}})$, $\varphi_2 = 0$, $\psi_2 = 0$), the absorption cross-section σ^Q_2 is:

$$\sigma^Q_2 = \sigma^Q_{D_{3d}}(0,0) - \sqrt{\frac{5}{14}}\sigma^Q_{D_{3d}}(2,0) - \frac{109}{36\sqrt{14}}\sigma^Q_{D_{3d}}(4,0) - \frac{2\sqrt{5}}{9}\sigma^Q_{D_{3d}}(4,3). \tag{3.19}$$

For the third orientation, chosen as $\hat{\boldsymbol{\varepsilon}}_3$=[0, 1, 0] and $\hat{\boldsymbol{k}}_3$=[$\bar{1}$, 0, 0], with the corresponding Euler angles ($\theta_3 = \frac{\pi}{2}$, $\varphi_3 = \frac{\pi}{2}$, $\psi_3 = \frac{\pi}{2}$), the absorption cross-section σ^Q_3 is:

$$\sigma^Q_3 = \sigma^Q_{D_{3d}}(0,0) + \sqrt{\frac{10}{7}}\sigma^Q_{D_{3d}}(2,0) + \frac{1}{\sqrt{14}}\sigma^Q_{D_{3d}}(4,0). \tag{3.20}$$

For the fourth orientation, chosen as $\hat{\boldsymbol{\varepsilon}}_4$=[0, $\frac{1}{\sqrt{2}}$, -$\frac{1}{\sqrt{2}}$] and $\hat{\boldsymbol{k}}_2$=[0, $\frac{1}{\sqrt{2}}$, $\frac{1}{\sqrt{2}}$], with the corresponding Euler angles ($\theta_4 =\frac{3\pi}{4}$, ϕ_4=$\frac{\pi}{2}$, ψ_4= π), the absorption cross-section σ^Q_4 is:

$$\sigma^Q_4 = \sigma^Q_{D_{3d}}(0,0) - \sqrt{\frac{5}{14}}\sigma^Q_{D_{3d}}(2,0) + \frac{19}{4\sqrt{14}}\sigma^Q_{D_{3d}}(4,0). \tag{3.21}$$

After the inversion of the system of equations 3.18, 3.19, 3.20 and 3.21, the expression of the D_{3d} site parameters are :

$$\sigma^Q_{D_{3d}}(0,0) = \frac{1}{5}\sigma^Q_1 + \frac{2}{5}\sigma^Q_2 - \frac{4}{15}\sigma^Q_3 + \frac{2}{15}\sigma^Q_4 \tag{3.22}$$

$$\sigma^Q_{D_{3d}}(2,0) = -\frac{1}{\sqrt{70}}\sigma^Q_1 - \sqrt{\frac{2}{35}}\sigma^Q_2 + \sqrt{\frac{5}{14}}\sigma^Q_3 - \sqrt{\frac{2}{35}}\sigma^Q_4 \tag{3.23}$$

$$\sigma^Q_{D_{3d}}(4,0) = -\frac{2\sqrt{14}}{35}\sigma^Q_1 - \frac{4\sqrt{14}}{35}\sigma^Q_2 + \frac{2\sqrt{14}}{105}\sigma^Q_3 + \frac{16\sqrt{14}}{105}\sigma^Q_4 \tag{3.24}$$

$$\sigma^Q_{D_{3d}}(4,3) = \frac{2}{\sqrt{5}}\sigma^Q_1 - \frac{1}{2\sqrt{5}}\sigma^Q_2 - \frac{2}{3\sqrt{5}}\sigma^Q_3 - \frac{5}{6\sqrt{5}}\sigma^Q_4 \tag{3.25}$$

σ^Q_{cube}(0,0) and σ^Q_{cube}(4,0) defined in Eq. 3.16 can thus be determined for any ($\hat{\boldsymbol{\varepsilon}}$, $\hat{\boldsymbol{k}}$) configuration.

Calculation of the absorption cross-sections for the experimental configuration

The two experimental orientations are $\alpha_{rot} = 0°$ and $\alpha_{rot} = 90°$. The cubic electric quadrupole cross-section for each configuration can be expressed from equation 3.12. In the case of $\alpha_{rot} = 0°$, $\hat{\boldsymbol{\varepsilon}}_1$=[0, 1, 0] and $\hat{\boldsymbol{k}}_1$= [$\bar{1}$, 0, 0] so:

$$\sigma^Q_{cube}(\alpha_{rot} = 0°) = \sigma^Q_{cube}(0,0) - \frac{4}{\sqrt{14}}\sigma^Q_{cube}(4,0) \tag{3.26}$$

In the case of $\alpha_{rot} = 90°$, $\hat{\boldsymbol{\varepsilon}}_1$=[$\frac{1}{2}$, $\frac{1}{2}$, $\frac{1}{\sqrt{2}}$] and $\hat{\boldsymbol{k}}_1$= [-$\frac{1}{2}$, -$\frac{1}{2}$, $\frac{1}{\sqrt{2}}$] so:

$$\sigma^Q_{cube}(\alpha_{rot} = 90°) = \sigma^Q_{cube}(0,0) + \frac{7}{2\sqrt{14}}\sigma^Q_{cube}(4,0) \tag{3.27}$$

The isotropic cubic cross-section can be deduced from Eq. 3.26 and 3.27:

$$\sigma^Q_{cube}(0,0) = \frac{1}{15}[7\sigma^Q_{cube}(\alpha_{rot} = 0°) + 8\sigma^Q_{cube}(\alpha_{rot} = 90°)], \tag{3.28}$$

and so can the dichroic term, which corresponds to the difference between the two orientations:

$$\sigma^Q_{dich} = \sigma^Q_{cube}(\alpha_{rot} = 90°) - \sigma^Q_{cube}(\alpha_{rot} = 0°) = \frac{15}{2\sqrt{14}}\sigma^Q_{cube}(4,0). \tag{3.29}$$

To summarize, the electric quadrupole absorption cross-section for the two experimental configurations is done in four steps. First, the four σ^Q_1, σ^Q_2, σ^Q_3 and σ^Q_4 cross-sections are calculated. Then the D_{3d} cross-sections, $\sigma^Q_{D_{3d}}$(0,0), $\sigma^Q_{D_{3d}}$(2,0), $\sigma^Q_{D_{3d}}$(4,0) and $\sigma^Q_{D_{3d}}$(4,3), are determined. In the third step, σ^Q_{cube}(4,0) is calculated from $\sigma^Q_{D_{3d}}$(0,0) and $\sigma^Q_{D_{3d}}$(4,0), with the angle α as a parameter. Finally, the two experimental cross-sections are determined from Eq. 3.26 and 3.27.

3.3.2 Transition operators

To perform the multielectronic calculations, a package developed by Thole [203] determines the eigenvalues of the Hamiltonian and then calculates the transitions. Both the Hamiltonian and the transition operator are expressed in the subduction of the local point group. In the case of tsavorite, vanadium is considered in a D_{3d} symmetry site and therefore, the subduction $O_3 \supset O_h \supset D_{3d} \supset C_{3i}$ is used (Chap. 2). The Hamiltonian is identical for the four configurations previously determined (σ^Q_1, σ^Q_2, σ^Q_3 and σ^Q_4) and is expressed as (Chap. 2) :

$$\begin{aligned} H_{crystal} = {} & X^{4^+(O_3)0^+(O_h)0^+(D_{3d})0^+(C_{3i})}U^{4^+(O_3)0^+(O_h)0^+(D_{3d})0^+(C_{3i})} \\ & + X^{4^+(O_3)\tilde{1}^+(O_h)0^+(D_{3d})0^+(C_{3i})}U^{4^+(O_3)\tilde{1}^+(O_h)0^+(D_{3d})0^+(C_{3i})} \\ & + X^{4^+(O_3)1^+(O_h)\tilde{0}^+(D_{3d})0^+(C_{3i})}U^{4^+(O_3)1^+(O_h)\tilde{0}^+(D_{3d})0^+(C_{3i})} \\ & + X^{2^+(O_3)\tilde{1}^+(O_h)0^+(D_{3d})0^+(C_{3i})}U^{2^+(O_3)\tilde{1}^+(O_h)0^+(D_{3d})0^+(C_{3i})}. \end{aligned} \tag{3.30}$$

Nevertheless, the transition operators for the four cross-sections σ_1^Q, σ_2^Q, σ_3^Q and σ_4^Q are different. They must be expressed in the site frame, then as the corresponding linear combination of the $|\alpha JM\rangle$ partners and finally as $|k(SO_3)\rho(O)\sigma(D_{3d})\lambda(C_{3i})\rangle$ states in the chosen subduction, using the Eq. 3.17 and 3.18 of Chap. 2. I give here their expressions for the $(\hat{\boldsymbol{\varepsilon}},\hat{\boldsymbol{k}})$ configurations used to reconstruct the total angular dependence of the pre-edge.

Orientation : $\hat{\boldsymbol{\varepsilon}}_1$=[-$\frac{1}{\sqrt{6}}$, -$\frac{1}{\sqrt{2}}$, $\frac{1}{\sqrt{3}}$] and $\hat{\boldsymbol{k}}_1$= [$\frac{1}{\sqrt{6}}$, -$\frac{1}{\sqrt{2}}$, -$\frac{1}{\sqrt{3}}$]

The transition operator is:

$$\hat{O}_1^Q = (\hat{\boldsymbol{\varepsilon}}_1 \cdot \boldsymbol{r})(\hat{\boldsymbol{k}}_1 \cdot \boldsymbol{r}) = -\frac{1}{6}\, x^2 + \frac{1}{2}\, y^2 - \frac{1}{3}\, z^2 + \frac{2}{\sqrt{18}}\, xz \tag{3.31}$$

Hence,

$$\hat{O}_1^Q = -\frac{1}{3}\, |22\rangle - \frac{1}{3}\, |2\bar{2}\rangle - \frac{1}{\sqrt{6}}\, |20\rangle - \frac{1}{3\sqrt{2}}\, |22\rangle - \frac{1}{3\sqrt{2}}\, |2\bar{2}\rangle \tag{3.32}$$

and

$$\hat{O}_1^Q = \frac{1}{3}\, U^{2\tilde{1}00} + \frac{1}{3}\, U^{2\tilde{1}11} + \frac{1}{3}\, U^{2\tilde{1}1\bar{1}} \tag{3.33}$$

Orientation 2: $\hat{\boldsymbol{\varepsilon}}_2$=[$\frac{-1+\sqrt{2}}{\sqrt{6}}$, 0, $\frac{1+\sqrt{2}}{\sqrt{6}}$] and $\hat{\boldsymbol{k}}_2$=[$\frac{1+\sqrt{2}}{\sqrt{6}}$, 0, $\frac{1-\sqrt{2}}{\sqrt{6}}$]

The transition operator is:

$$\hat{O}_2^Q = (\hat{\boldsymbol{\varepsilon}}_2 \cdot \boldsymbol{r})(\hat{\boldsymbol{k}}_2 \cdot \boldsymbol{r}) = \frac{1}{6}\, (x^2 - z^2) + \frac{2\sqrt{2}}{3}\, xz \tag{3.34}$$

Hence,

$$\hat{O}_2^Q = -\frac{1}{2\sqrt{6}}\, |20\rangle + \frac{1}{12}\, (|22\rangle + |2\bar{2}\rangle) + \frac{\sqrt{2}}{3}\, (|2\bar{1}\rangle - |21\rangle) \tag{3.35}$$

and

$$\hat{O}_2^Q = \frac{1}{6}\, U^{2\tilde{1}00} + \frac{1}{2\sqrt{2}}\, U^{2211} + \frac{1}{2\sqrt{2}}\, U^{221\bar{1}} + \frac{1}{6}\, U^{2\tilde{1}11} + \frac{1}{6}\, U^{2\tilde{1}1\bar{1}} \tag{3.36}$$

Orientation 3: $\hat{\boldsymbol{\varepsilon}}_3$=[0, 1, 0] and $\hat{\boldsymbol{k}}_3$=[$\bar{1}$, 0, 0]

The transition operator is:

$$\hat{O}_3^Q = (\hat{\boldsymbol{\varepsilon}}_3 \cdot \boldsymbol{r})(\hat{\boldsymbol{k}}_3 \cdot \boldsymbol{r}) = -xy \tag{3.37}$$

Hence,

$$\hat{O}_3^Q = \frac{1}{2i}\, (|2\bar{2}\rangle + |22\rangle) \tag{3.38}$$

and

$$\hat{O}_3^Q = -i\, (\frac{\sqrt{2}}{6}\, U^{2211} - \frac{\sqrt{2}}{6}\, U^{221\bar{1}} - \frac{1}{3}\, U^{2\tilde{1}11} + \frac{1}{3}\, U^{2\tilde{1}1\bar{1}}) \tag{3.39}$$

Orientation 4: $\hat{\boldsymbol{\varepsilon}}_4$=[0, $\frac{1}{\sqrt{2}}$, -$\frac{1}{\sqrt{2}}$] and $\hat{\boldsymbol{k}}_2$=[0, $\frac{1}{\sqrt{2}}$, $\frac{1}{\sqrt{2}}$],

The transition operator is:

$$\hat{O}_4^Q = (\hat{\boldsymbol{\varepsilon}}_4 \cdot \boldsymbol{r})(\hat{\boldsymbol{k}}_4 \cdot \boldsymbol{r}) = \frac{1}{2}\,(y^2 - z^2) \tag{3.40}$$

Hence,

$$\hat{O}_4^Q = -\frac{1}{4}\,(|22\rangle + |2\bar{2}\rangle) + \frac{\sqrt{6}}{4}\,|20\rangle) \tag{3.41}$$

and

$$\hat{O}_4^Q = \frac{1}{2}\,U^{2\tilde{1}00} - \frac{1}{6\sqrt{2}}\,U^{2211} - \frac{1}{6\sqrt{2}}\,U^{221\bar{1}} + \frac{1}{6}\,U^{2\tilde{1}11} + \frac{1}{6}\,U^{2\tilde{1}1\bar{1}} \tag{3.42}$$

3.3.3 Results

The transition operators have been given for the four orientations previously described and needed to determine the D_{3d} parameters $\sigma^Q_{D_{3d}}$(0,0), $\sigma^Q_{D_{3d}}$(2,0), $\sigma^Q_{D_{3d}}$(4,0) and $\sigma^Q_{D_{3d}}$(4,3). In a first step, the multielectronic calculations are therefore performed for these four orientations, thus giving the value of σ^Q_1, σ^Q_2, σ^Q_3 and σ^Q_4, with the methodology described in chapter 3. The cross-section is then computed for the two experimental configurations with Eq. 3.26 and 3.27. The results obtained for the K pre-edge of tsavorite are now presented. However, this study is still under progress and the results described in the following correspond to the most advanced work. A good agreement between the experimental and calculated spectra was not achieved yet. The determination of the α parameter is first described and then the influence of each crystal-fied parameter. The κ parameter is fixed to $\kappa = 0.7$, which is a reasonnable value for an oxide.

The experimental spectrum for the two orientations $\alpha_{rot} = 0°$ and $\alpha_{rot} = 90°$ are displayed in Fig. 3.9, with the X-ray Natural Linear Dichroism (XNLD). The XNLD signal corresponds to the difference between the signals recorded for $\alpha_{rot} = 90°$ and $\alpha_{rot} = 0°$. It is characterized by two peaks. The first peak has a negative intensity and represents approximately one third of the total intensity of the signal. The second peak has a positive intensity and represents approximately two thirds of the total intensity. The first parameter determined was the α parameter, by comparing the experimental and calculated dichroic signal. In particular, the 1/3-2/3 partition observed for the intensity of the experimental signal was used as a fingerprint to determine the α parameter. The effect of the different values of α is illustrated in Fig. 3.10. Only one angle corresponds approximately to the 1/3-2/3 partition: $3\alpha = \pi/3$, corresponding to $\alpha = \pi/9$ (Eq. 3.16). This is observed for almost all the sets of (X^{4000}, $X^{4\tilde{1}00}$, $X^{2\tilde{1}00}$) crystal-field parameters.

The influence of the crystal-field parameters X^{4000}, $X^{4\tilde{1}00}$ and $X^{2\tilde{1}00}$ was then studied for the value of the α parameter $3\alpha = \pi/3$. The value of the octahedral crystal-field splitting is set to a constant value of 1.97 eV, which corresponds to the experimental value determined by Mazurak *et al.* [145]. The two other parameters were varied one after the other. The first parameter kept fixed is $X^{2\tilde{1}00} = 1.0$ eV and $X^{4\tilde{1}00}$ is varied (Fig. 3.11). Only two values ($X^{4\tilde{1}00} = 1.2$, 1.5 eV) allowed the 1/3-2/3 partition of the intensity to be obtained. Six values of $X^{2\tilde{1}00}$ were tested while $X^{4\tilde{1}00}$ was kept fixed to 1.2 eV. The two highest values do not display the 1/3-2/3 partition. These observations from the comparison between the experimental and calculated dichroic signal suggest that the best set of crystal-field parameters is $X^{4000} = 7.2$ eV, $X^{4\tilde{1}00} = 1.2$ eV,

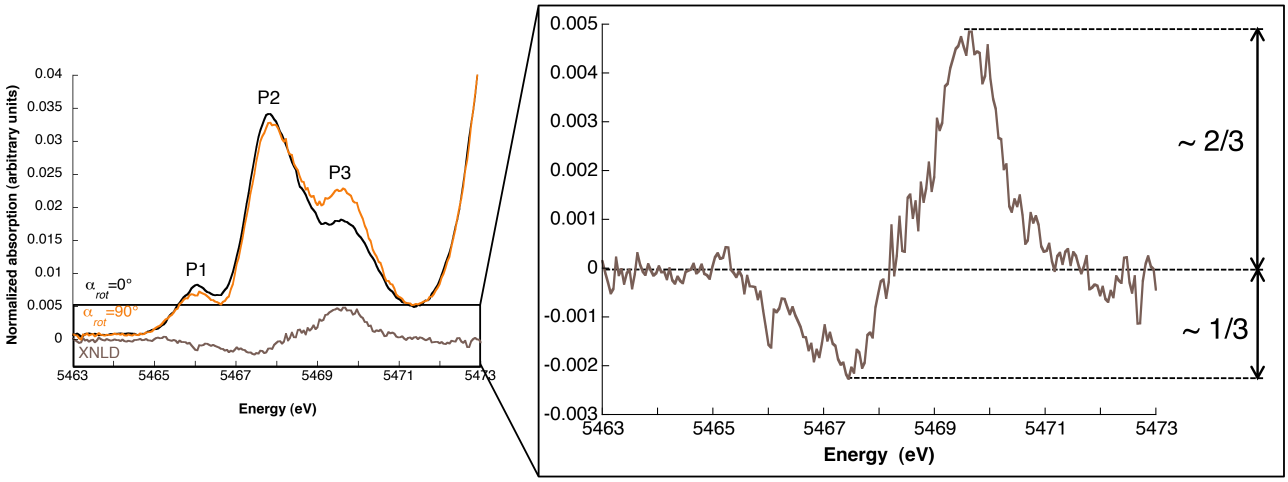

Figure 3.9: The experimental spectrum of the two orientations $\alpha_{rot} = 0°$ and $\alpha_{rot} = 90°$, with a zoom on the XNLD signal.

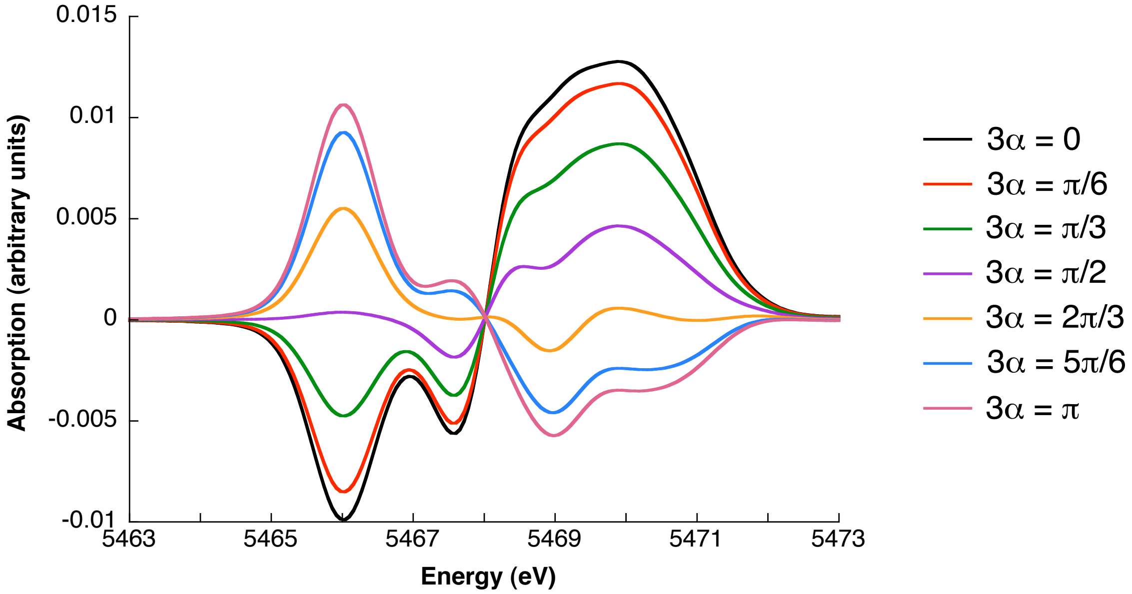

Figure 3.10: The effect on the dichroic signal of the α parameter. The dichroic signal was obtained for the parameters set ($X^{4000} = 7.2$ eV, $X^{4\tilde{1}00} = 1.2$ eV, $X^{2\tilde{1}00} = 1.0$ eV), corresponding to $10Dq = 1.97$ eV (Sec. 3.2.2) [145], $D\sigma = 0.06$ eV and $D\tau =$ -0.12 eV.

$X^{2\tilde{1}00} = 1.0$ eV, corresponding to $10Dq = 1.97$ eV, $D\sigma = 0.06$ eV and $D\tau =$ -0.12 eV, with $3\alpha = \pi/3$. Nevertheless, these values need to be refined and the calculated spectra for each orientation need to be compared to the experimental ones.

The calculated spectra for the two experimental orientations $\alpha_{rot} = 0°$ and $\alpha_{rot} = 90°$ are displayed in Fig. 3.12, for the parameters $3\alpha = \pi/3$, $X^{4000} = 7.2$ eV and $X^{4\tilde{1}00} = 1.2$ eV. They do not represent the three peaks observed in the experimental one. In particular, peak P3 is missing in the calculations for both orientations in the case of $X^{2\tilde{1}00} = 1.0$ eV. For $X^{2\tilde{1}00} = 3.0$ eV, peak P3 is present for the $\alpha_{rot} = 90°$ orientation but not for the $\alpha_{rot} = 0°$ one. Therefore, even if the set of crystal-field parameters $X^{4000} = 7.2$ eV, $X^{4\tilde{1}00} = 1.2$ eV, $X^{2\tilde{1}00} = 1.0$ eV and $3\alpha = \pi/3$

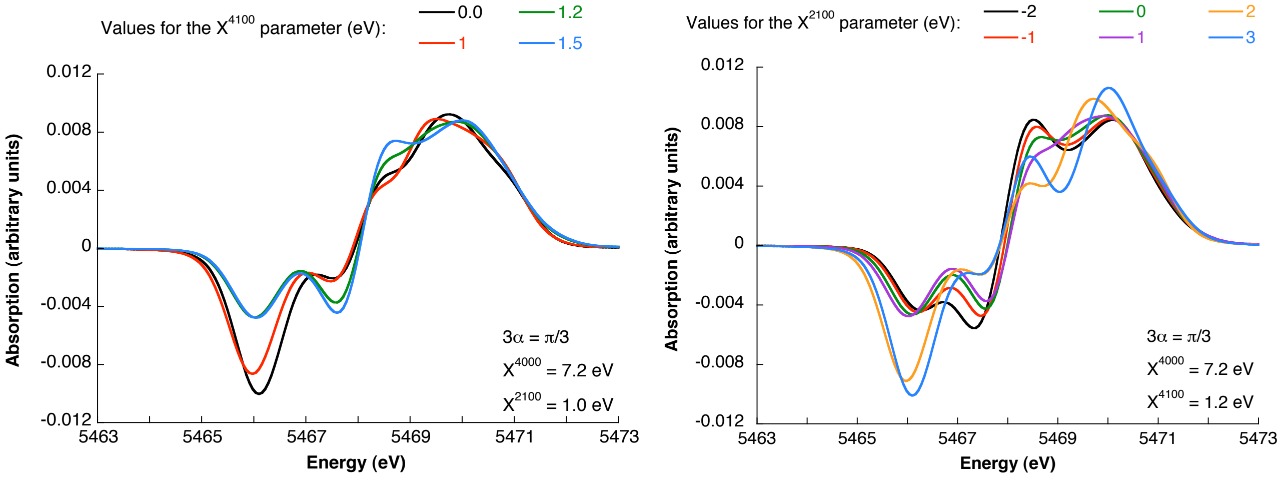

Figure 3.11: The influence of the $X^{4\tilde{1}00}$ *left* and $X^{2\tilde{1}00}$ *right* parameters on the dichroic signal for a fixed value of X^{4000} and 3α parameters.

gives a dichroic signal with the good 1/3-2/3 partition of the intensity, the comparison of the spectra for the two experimental orientations indicates that the set of parameters retained in the first place are not suitable.

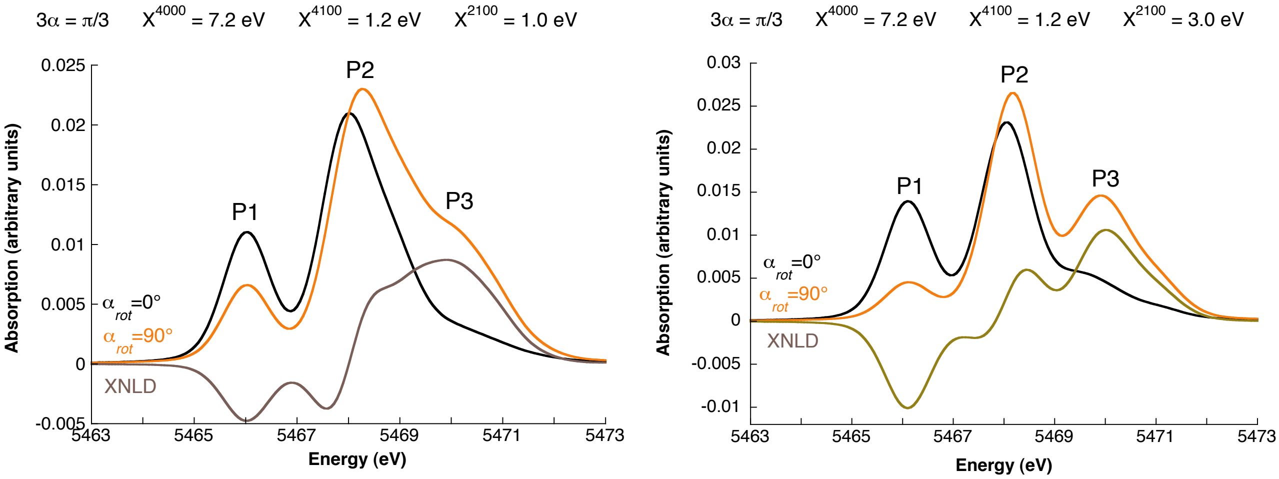

Figure 3.12: The spectra of the experimental $\alpha_{rot} = 0°$ and $\alpha_{rot} = 90°$ orientations for two sets of crystal-field parameters, illustrating the influence of the $X^{2\tilde{1}00}$ parameter on the spectra, for $X^{4000} = 7.2$ eV, $X^{4\tilde{1}00} = 1.2$ eV and $3\alpha = \pi/3$.

The evaluation of the crystal-field parameters was then done by directly comparing the calculated spectra with the experimental ones for each experimental orientation. Only a high value of the $X^{2\tilde{1}00}$ parameter allowed peak P3 to be present in the calculated spectra. This parameter has no influence on peaks P1 and P2, which are present in the calculated spectra for the X^{4000} and $X^{4\tilde{1}00}$ parameters determined by the investigation of the dichroic signal. The three crystal-field parameters were then set to a constant value: $X^{4000} = 7.2$ eV, $X^{4\tilde{1}00} = 1.2$ eV, $X^{2\tilde{1}00} = 3.0$ eV, and the α parameter was varied. The spectra for four values ($3\alpha = \pi/2, 2\pi/3, 5\pi/6, \pi$) are displayed in Fig. 3.13. The two highest values ($3\alpha = 2\pi/3, 5\pi/6$) do not reproduce the experimental spectra, since the $\alpha_{rot} = 0°$ orientation has a higher intensity than the $\alpha_{rot} = 90°$ one for peak P3. In the case $3\alpha = 2\pi/3$, the intensity of the $\alpha_{rot} = 90°$ orientation is slightly higher than the one of $\alpha_{rot} = 0°$ but the two intensities of peak P3 are too close compared to the experimental spectra. The most suitable α parameter is therefore $3\alpha = \pi/2$.

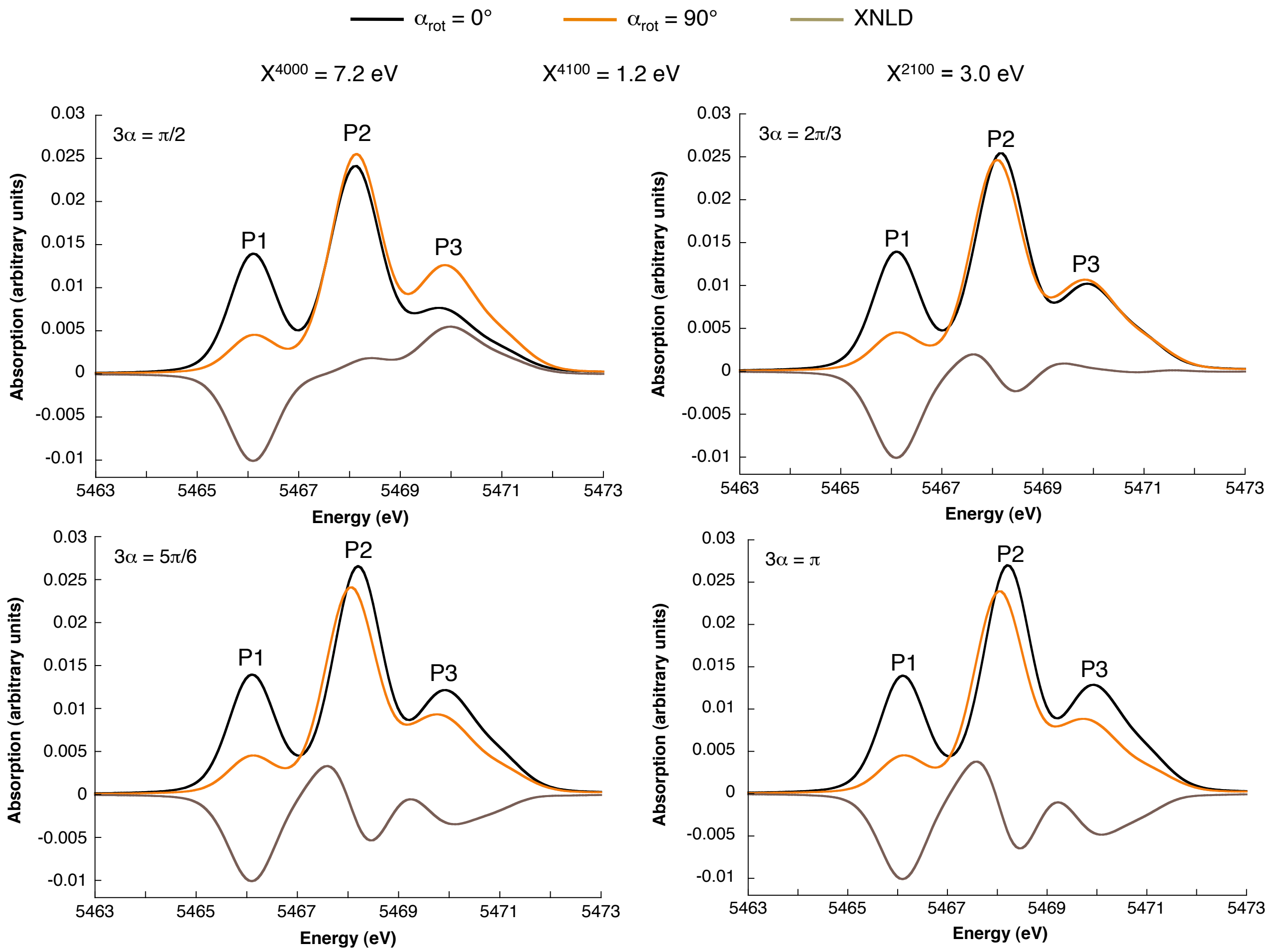

Figure 3.13: Influence of the 3α parameter on the spectra for the $\alpha_{rot} = 0°$ and $\alpha_{rot} = 90°$ orientations for a strong distortion: $X^{4000} = 7.2$ eV, $X^{4\tilde{1}00} = 1.2$ eV, $X^{2\tilde{1}00} = 3.0$ eV.

The influence of the different parameters that have to be fitted in the multielectronic calculations was studied and a first set of parameters can be retained: $3\alpha = \pi/2$, $X^{4000} = 7.2$ eV, $X^{4\tilde{1}00} = 1.2$ eV, $X^{2\tilde{1}00} = 3.0$ eV , corresponding to $10Dq = 1.97$ eV (Sec. 3.2.2) [145], $D\sigma = 0.06$ eV and $D\tau =$ -0.36 eV. However, they do not allow the experimental spectra to be well reproduced, in particular peak P1 which is too intense in the calculations for the $\alpha_{rot} = 0°$ orientation. It was not possible to go further in the refinement of the parameters mainly because of the absence of experimental values for the $D\sigma$ and $D\tau$ parameters. Optical absorption spectroscopy at low temperature may permit to determine these parameters and therefore to evaluate the reliability of the parameters set theoretically determined here. However, it was not possible to perform these experiments during the time of my thesis. Another important point to investigate concerning the reliability of the parameters set concerns the α parameter. It was defined after an interpretation of symmetry rules given by Butler [29] but its validity has to be checked. To do so, the multielectronic calculations have to be performed with the four parameters of the C_{3i}

symmetry (Sec. 3.3.1) and compared with the calculations done with the three D_{3d} parameters and the α one.

3.4 Conclusion

Tsavorite is used as a reference compound in the study of the titanomagnetites from the Bushveld Complex (Chap. 5). A detailed knowledge of the spectral signature of vanadium under the +III oxidation state and in an octahedral site with an inversion center is therefore needed. Its determination was the main purpose of the experiments and calculations described here.

V *K*-edge HERFD-XAS were performed on a tsavorite single-crystal for different orientations with respect to the polarisation and direction of the X-ray incident beam. As expected, an angular dependence of the pre-edge was observed. A RIXS plane was recorded as a complement to determine whether the HERFD spectrum is similar to the conventional XANES one. This point is important because the theoretical methods used to calculate the experimental spectra are dedicated to the conventional XANES spectroscopy. The analysis of the RIXS plane features demonstrated that the HERFD-XAS spectra are enough similar to conventional XANES ones to calculate the spectra with the methods described in Chap. 2.

To better understand the measured features, the experimental spectra were calculated with two different theoretical methods, based on the Density Functional Theory and on the Ligand Field Multiplet theory, respectively. For both methods, the coset method described in Chap. 2 was used to reduce the computational time in the case of the DFT calculations, and to determine the spectra for the crystal from those of a single site in the case of LFM calculations. For the DFT calculations, a structural model was first determined by substituting a vanadium atom for an aluminum one in the grossular structure and allowed the atomic positions to vary while the lattice parameter was kept fixed. The C_{3i} local symmetry was retained during the relaxation process, which showed a dilation of the first coordination shell around vanadium. The XANES spectra calculated from this structural model reproduced well the experimental spectra, including the angular dependence of the pre-edge. The experimental pre-edge features were interpreted within a monoelectronic view of the transitions. The electronic structure of V^{3+} in tsavorite was theoretically determined by calculating a specific $(\hat{\boldsymbol{\epsilon}},\hat{\boldsymbol{k}})$ configuration. The spectral signature was therefore determined and tsavorite can be used as a represnetative reference compound in the study of the titanomagnetite from the Bushveld Complex.

The multielectronic calculations are still under progress. The expression of the electric quadrupole cross-section was given for the crystal and each experimental orientation from the cross-section of a single site. The influence of the crystal-field parameters that have to be fitted to the experiments was investigated and a set of parameters was defined. However, this set does not allow the experimental spectra to be well reproduced and has to be more refined. The experimental determination of the crystal-field parameters D_σ and $D\tau$ with optical absorption measurements at low temperature may provide a reliable set of parameters. It should allow the multielectronic calculations to well reproduce the angular dependence of the pre-edge, with correct energy and relative intensity. A simplification in the crystal-field parameters was also done from symmetry rules given by Butler [29] and it has to be checked, by performing the calculations without the simplification.

Chapter 4

The incorporation of vanadium in anatase (TiO_2:V^{4+})

This chapter is dedicated to the study of V-doped anatase. TiO_2 is a widely studied material because of its good performance in photocatalytic oxidation of organic molecules, its application in solar cells, thin-film optical devices and as a gas sensor [16]. Among TiO_2 polymorphs, the activity of anatase in the photodegradation of various pollutants is, in general, much higher than that of rutile [48]. TiO_2 has the main advantage of its good chemical stability, its absence of toxicity and photocorrosivity, and its relative low price, but a serious disadvantage is its large band gap ($E_g = 3.2$ eV) [201]. This has prevented its use in some photocatalytic applications as it required UV irradiation to be photocatalytically active. Some attempts have been made to develop TiO_2 photocatalysts with a photoresponse in the visible spectrum by doping with various transition metal ions [220]. Vanadium was shown to increase the photocatalytic activity [62] and its role as a dopant in TiO_2 is widely studied. For instance, the effect of V^{4+} substitution in anatase nanowires on their hydrogen production by water photosplitting is under investigation, as it seems a promising way to produce hydrogen with water splitting on a photocatalyst. An important question concerning the vanadium doping in anatase is the incorporation site of vanadium. In the anatase structure, an element can indeed be incorporated in two different ways: by substituting a Ti atom or in an empty interstitial site. Both sites are distorted octahedron but the distortion of the interstitial site is more important: an element initially incorporated at the center of the octahedron is usually slightly displaced along the c direction and thus see a fivefold-coordination environment [204]. Numerous studies have been done on the incorporation of elements (Cu, Li, Al,...) in the anatase structure and the site incorporation depends on the element and on the way the doped anatse was synthesized [100, 133, 195, 204]. In the case of vanadium, an early study of V-doped anatase by electron paramagnetic resonance (EPR) spectroscopy had shown that in anatase, V^{4+} ions are incorporated in an interstitial site. An EPR signal for V^{4+} in anatase was indeed measured whereas the substitional V^{4+} ions can not be observed by EPR spectroscopy [82]. This result on the vanadium incorporation in anatase needs to be confirmed by other studies. A partition of the incoporated vanadium between the Ti-substitutional and interstitial sites can indeed not be excluded.

A powerful method to investigate the incorporation of an element in a host-structure is X-ray Absorption Spectroscopy (XAS). I thus collaborated on the study of the effect of V^{4+} substitution in anatase nanowires on their hydrogen production by watter photosplitting by measuring V K-edge XAS spectra on some V-doped anatase nanowires. The experimental spectra are presented in the first section of this chapter. The analysis of the spectra allowed a first interpretation of the incorporation site of vanadium. To go further in the interpretation, DFT calculations of the V K-edge spectrum with a V-atom substituted to a Ti-atom were performed. This theoretical study was completed by the determination of the Ti K-edge spectrum in undoped anatase TiO_2. Computational details are also given in this section, with a particular emphasis on the reconstruction of the isotropic spectrum. The available experimental data for both Ti K-edge of undoped anatase and V K-edge of V-doped anatase were indeed obtained for powder samples and hence the theoretical isotropic spectrum had to be determined.

4.1 V K-edge HERFD-XAS experiments on synthesized TiO_2:V^{4+}

4.1.1 HERFD-XAS measurements

Three synthesized anatase nanowires samples were studied, with three vanadium concentrations (V/Ti = 0.5%, 1% and 2%), in order to confirm the V^{4+} oxidation state and to determine the incorporation site of vanadium in the anatase structure. The preparation of the samples and their characterization are described in App. B. HERFD-XAS spectra were recorded at room temperature using the high-resolution spectrometer of the ID26 beamline. Indeed, as titanium is the major constituant, the fluorescence detection mode can not be used and HERFD-XAS is essential. The spectra corresponding to the three concentrations were normalized so that the intensity is 1 at $E = 5700$ eV.

Figure 4.1 (top) shows the normalized HERFD-XANES spectrum of the sample doped with 2% of vanadium. The edge spectrum displays three features at 5486.4 eV (P_3), 5491.3 eV (P_4) and 5504.0 eV (P_5). The edge shape is similar to that of Ti K-edge in anatase (Fig. 4.1 bottom) [180, 225], and it significantly differs from that of Ti in rutile or that of V in rutile-type VO_2 [93]. This first observation suggests that vanadium in the investigated samples is incorporated at the Ti site of the anatase structure. The pre-edge displays a strong feature at 5470.0 eV (P_1) and a smaller one at 5473. eV (P_2) (Fig. 4.1 top). It is different from the Ti K-edge in anatase, which is characterized by three structures, the intensity of which is similar to peak P2 (Fig. 4.1 bottom).

4.1.2 The RIXS plane

Because titanium is a major element of anatase, HERFD-XAS measurements were performed. However, as said in Chap. 1 and 3, an HERFD-XAS spectrum can be different from a conventional XANES spectrum. A RIXS plane of V-doped anatase was thus recorded in parallel to the HERFD-XAS measurements. Figure 4.2 (left) displays the RIXS plane. A strong feature is visible along the vanadium $K\alpha_1$ fluorescence line (~4952 eV emission energy, displayed by a dashed line) at an incident energy of 5470.0 eV, followed by feature with a weak intensity around 5473 eV. The $K\alpha_2$ line (~4945 eV emission energy, displayed by a dotted line) presents similar features: the main feature at 4970 eV visible in the case of the $K\alpha_1$ line is present at the same energy on the $K\alpha_2$ line. It is to be noted that no additional structure appears along the $K\alpha_2$ line and that the structures occur in both cases along the horizontal line, with no significant distortion. However, between these two sets of well-defined features, a weak broad feature is visible at an incident energy of 5466 eV. To check the influence of this broadening on the pre-edge features, an integration over the emission energies was done. The corresponding spectrum is plotted in Fig. 4.2 (right). The corresponding pre-edge spectrum is identical to the one measured with only the $K\alpha_1$ fluorescence line (Fig. 4.1).

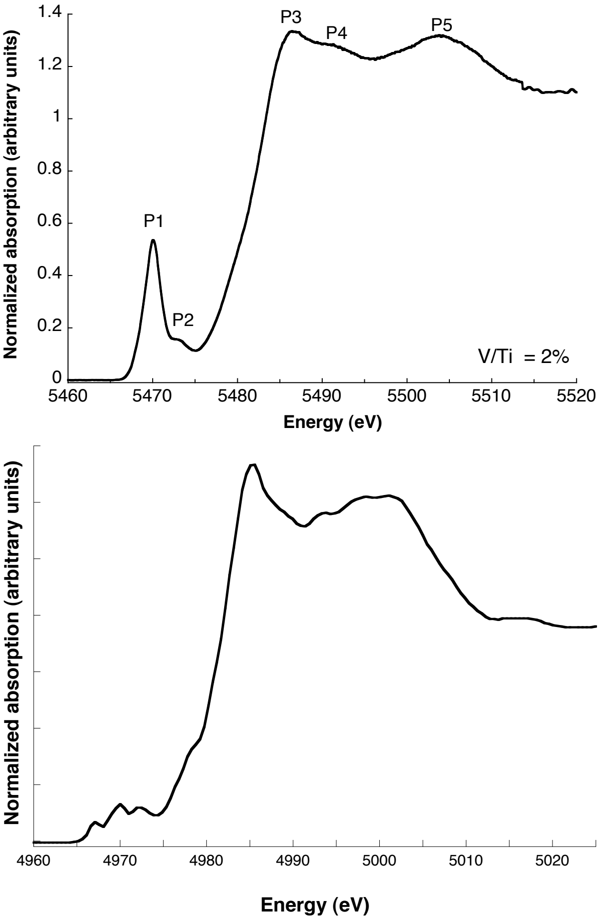

Figure 4.1: (*Top*) Experimental V K-edge HERFD-XANES spectrum of 2% V-doped anatase (TiO$_2$:V^{4+}). The spectrum was measured during my thesis. (*Bottom*) Experimental Ti K-edge XANES spectrum of undoped anatase (TiO$_2$). The spectrum is reproduced from Ref. [180].

Therefore, in the case of V-doped anatase, the selection of the Kα_1 fluorescence line to perform HERFD-XAS measurements results in a spectrum similar to that of the conventional XAS in terms of number of features, energy position and relative intensitites of these features. The HERFD-XAS pre-edges are hence reliable and can be trusted to determine the oxidation state and incorporation site of vanadium in V-doped anatase. They can also be simulated using the Xspectra code dedicated to conventional XANES calculations.

4.1.3 The influence of the concentration

The edge and pre-edge spectral features display no significant change with the doping level in vanadium (Fig. 4.3). Peak P$_1$ intensity increases slightly with the vanadium concentration but the number and energy position of the pre-edge features do not change, and neither do those of the edge. Therefore the vanadium oxidation state and site incorporation is identical whatever the vanadium concentration is.

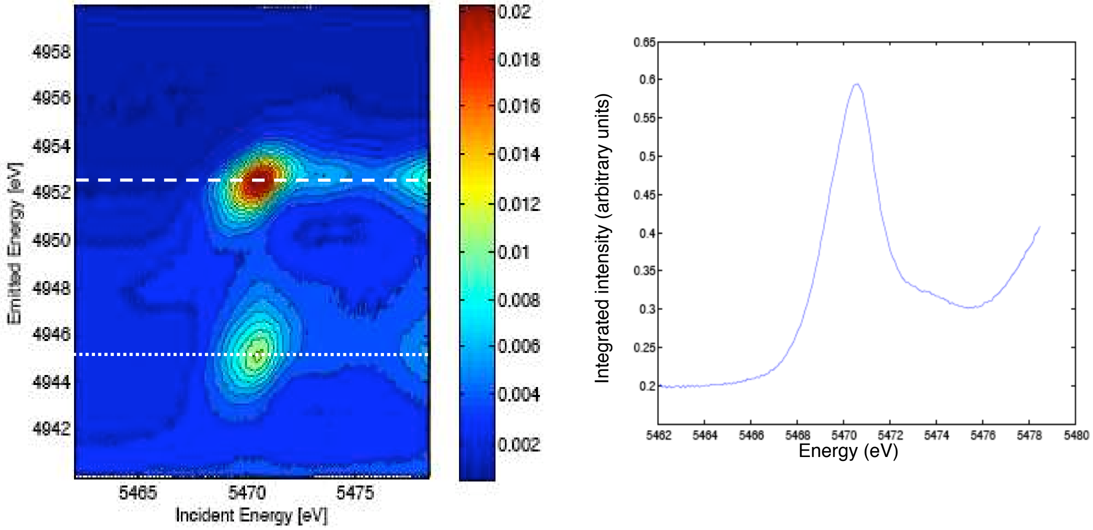

Figure 4.2: (*Left*) RIXS plane at the V K-edge in anatase and (*Right*) the corresponding spectrum obtained by integrating over the emitted energies.

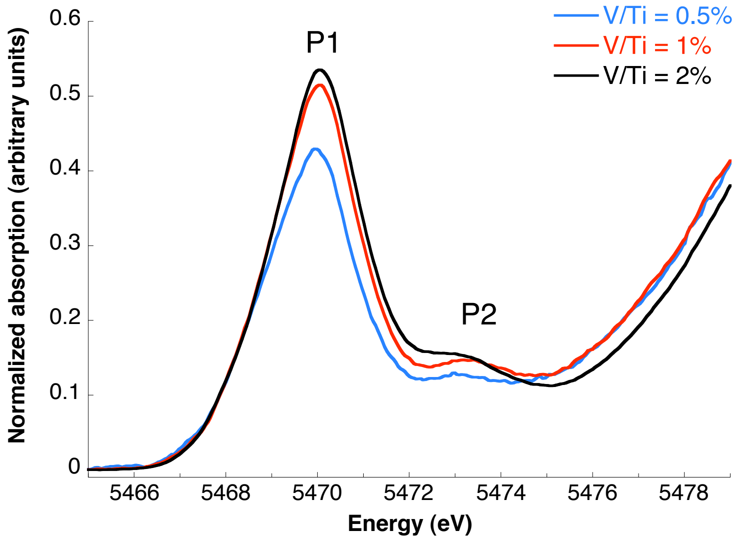

Figure 4.3: Experimental HERFD-XANES pre-edges at the V K-edge in V-doped anatase (TiO_2:V^{4+}) for the different dopings (V/Ti = 0.5 %, 1 % and 2%).

4.1.4 Interpretation of the experimental data

The energy position and intensity of the pre-edge features can be compared to the numerous data existing on vanadium in reference compounds [197, 224]. Fig. 4.4 displays the pre-edge energy centroid and intensity of some V-bearing compounds. The definition of "intensity" is not well defined in the publications, so I considered here that it refers to the intensity of the highest peak. It is reproduced from Ref. [197] and the data corresponding to the three synthesized V-doped anatase were then added. Regions corresponding to an oxidation state and a coordination number are thus defined: V^{3+} in an octahedral site, V^{4+} in an octahedral site, V^{4+} in a five-fold coordinated site, V^{5+} in a five-fold coordinated site and V^{5+} in a tetrahedral site. The position in this graph of the samples under investigation provides information about its oxidation state and coordination number. The relative intensity of the pre-edges of the V-doped TiO_2 samples is thus characteristic of a +IV oxidation state of vanadium. Nevertheless, the energy is too low for a regular octahedral environment and seems to better correspond to a strongly distorted octahedron or to a fivefold coordination. Raman spectroscopy measurements showed that no V^{5+} is present in the samples (App. B). The high relative intensity of the pre-edge features can not thus be assigned to a small amount of V^{5+} which would have superposed the signal of V^{4+}.

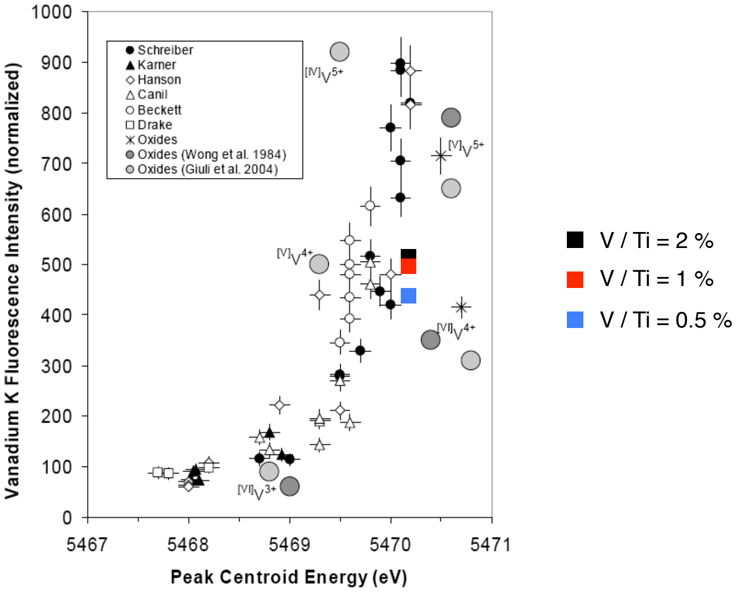

Figure 4.4: Pre-edge intensity *vs* peak energy of V-bearing compounds, illustrating the variation of the pre-edge features with the oxidation state and coordination number of vanadium (after [197]). The black, red and blue squares represent the three TiO_2:V^{4+} samples (V/Ti = 0.5 %, 1 % and 2%). The Schreiber, Karner, Hanson, Canil, Beckett and Drake samples are glasses synthesized under different oxidizing conditions for oxidation state and oxygen fugacity valence calibration. The "oxides" samples are natural glasses from Earth, Moon and Mars containing vanadium, the oxidation state of which was determined by comparison with the synthesized glasses. The two other sets of data display on the figure are reference crystallized minerals which were respectively studied by Wong *et al.* (V_2O_3, V_2O_4 and V_2O_5) [224] and Giuli *et al.* (V-bearing magnetite Fe_3O_4:V, V_2O_4, cavansite $Ca(VO)Si_4O_{10}(H_2O)_4$, V_2O_5 and vanadinite $Pb_5(VO_4)_3Cl$) [93].

The oxidation state of vanadium in the V-doped anatase was shown to be + IV but its incorporation site is not well-defined. The pre-edge intensity in the experimental spectrum is too high for a regular or slightly distorted (*i.e.* with an inversion center) octahedral and tends to indicate that vanadium is incorporated in a strongly distorted octahedral site or in a fivefold-coordinated one. For a given oxidation state, the intensity of the pre-edge increases when the coordination number decreases: if the absorbing atom is a fourfold, fivefold or strongly distorted sixfold site, *i.e.* when the site presents no inversion center, the pre-edge arises from electric dipole and quadrupole transitions and is therefore more intense. This hypothesis of the vanadium in a site with a lower coordination number, which would increases its pre-edge intensity, is coherent with the anatase structure, which presents several possible interstitial sites, with tetrahedral and octahedral symmetries. The interstitial octahedra are distorted and larger in size than the Ti ones. Inserting impurities into these substitutional sites leads to an increase of the distortion and a modification of the coordination. The octahedron is indeed elongated along the c axis so that an atom inserted exactly in the center would be only fourfold-coordinated. If the impurity does not occupy the exact center of the octahedron but is displaced along the c direction, its environment would be fivefold-coordinated [204].The incorporation of various elements in anatase has been widely investigated and the studies showed that the incorporation site depends on the incorporated element and on the synthesis protocol. The incorporation of the impurity in the intersitial octahedral site was observed for a low doping in Li^+ [133, 204]. In the case of aluminum-doped anatase, the most favorable situation is Ti-substitutional Al atoms [195]. For copper-doped anatase, stabilized by adding aluminum, the Al atoms were found to fill Ti-substitutional sites adjacent to interstitial sites which incorporated Cu atoms. With different doping methods, Ti-substitutional Cu atoms were also formed [100]. Finally, an early study of V-doped anatase by electron paramagnetic resonance (EPR) spectroscopy had shown that in anatase, V^{4+} ions are incorporated in an interstitial site. They indeed measured an EPR signal for V^{4+} in anatase whereas the Ti-substitutional V^{4+} ions can not be observed by EPR spectroscopy [82]. This last observation tends to confirm the first conclusion on the incorporation site of vanadium in V-doped anatase deduced from the analyses of the HERFD-XAS spectra, *i.e.* that vanadium may not be incorporated in the Ti-substitutional site.

The experimental HERFD-XAS study of V-doped anatase nanowires has shown that vanadium is incorporated under the +IV oxidation state but its incorporation site in the anatase structure is not well-defined. It could be either an interstitial site or a strongly distorted Ti-substitutional site. The HERFD-XAS experiments by themselves do not allow the incorporation site to be firmly determined. DFT calculations should provide complementary information. Concerning the study of the V-doped anatase photocatalytic properties, the determination of the vanadium incorporation site in not a crucial point. Indeed, the experiments performed by D. d'Elia and J-F. Hochepied on the V-doped anatase photocatalytic activity showed that the vanadium doping is highly detrimental to photoactivity and can not be used for water photosplitting (App. B).

4.2 DFT calculations at the Ti *K*-edge of anatase and at the V *K*-edge of V-doped anatase

To characterize the spectral signature of V^{4+} in the Ti-substitutional site in the anatase structure and thus to get complementary information on the incorporation site of vanadium, DFT calculations were performed at the V K-edge in the case of a vanadium incorporated in the Ti-substitutional site of V-doped anatase. Prior to the vanadium calculations, the Ti K-edge in undoped anatase was calculated and compared to the experimental spectrum measured by M.F. Ruiz-Lopez and A. Munoz-Páez [180]. The Ti K-edge spectrum in anatase is well-known and this comparison permits the methodology and the results to be validated, to then perform reliable calculations for the V K-edge. Indeed, to my knowledge, no experimental data on the V K-edge XANES of V-doped anatase, with a well-defined V^{4+} site symmetry, are available.

I first give the computational details and then describe the results in the case of the Ti K-edge in anatase and of the V K-edge in V-doped anatase.

4.2.1 Computational details

Parameters of the Xspectra code

The monoelectronic calculations were done with the methodology described in Chap. 2 and applied in Chap. 3 to the case of tsavorite. The code PARATEC was used for the relaxation, and the PWscf and Xspectra codes from Quantum Espresso for the XANES spectrum calculation.

The structure relaxation calculations started from the experimental structure of anatase TiO_2 [111], with the origin choice 1 for the point group symmetry. From the experimental unit cell, containing 12 atoms (4 Ti and 8 O), a 3×3×1 supercell was built. The lattice parameters for this supercell are $a = 11.35$ Å and $c = 9.51$ Å. It contains 108 atoms: 36 titanium and 72 oxygen. For the calculation at the V K-edge, a vanadium was substituted for one titanium in the supercell, which thus contains 1 vanadium, 35 titanium and 72 oxygen. The supercell was relaxed using a single **k**-point sampling in the Brillouin zone and a 110 Ry energy cutoff. Then, for the XANES calculation, a 90 Ry cutoff energy was used for the plane-wave expansion, one **k**-point for the self-consistent spin-polarized calculation of the charge density with a core-hole on vanadium and a Monkhorst-Pack grid of 4×4×4 points in the Brillouin zone for the absorption cross-section calculation. These parameters, as those of the relaxation, are identical for the Ti and V K edges calculation. An energy dependent broadening parameter γ is used in the continued fraction. For vanadium, the parameters used for the tsavorite calculations: γ=0.5 eV up to 5472 eV and γ=1 eV from 5485 eV, with a linear variation between these two energies, were taken. For titanium, the values γ=0.47 eV up to 4974 eV and γ=1.2 eV from 4991 eV were chosen. The DFT calculations were performed in the GGA approximation [160], with the spin-polarization taken into account in the case of vanadium calculations.

The theoretical spectrum at the Ti K-edge of undoped anatase must be compared to the experimental one to validate the calculations. Nevertheless, I did not measure the Ti K-edge of undoped anatase and the theoretical calculations are thus compared to spectra from literature and especially from Ref. [180]. This spectrum was measured on powder and is isotropic (Fig. 4.1 down). Consequently, the theoretical spectrum needs to be isotropic too. However, the calculation of the cross-section within Xspectra is not fully symmetrized. That means that the calculation does not take into account the various possible equivalent crystallographic sites which could give different signals with respect to the polarization $\hat{\varepsilon}$ and the direction $\hat{\boldsymbol{k}}$ of the incident X-ray beam. The determination of the isotropic spectrum is hence not straightforward. The space group of anatase is $I4_1/amd$, which corresponds to the D_{4h} point group. Both electric dipole and quadrupole cross-sections thus present a dependence with the incident X-rays beam [24]. The spectral features are expected to be different when the orientation of the sample with respect to the incident X-ray beam varies, for the pre-edge and edge regions. However, this angular dependence is different for the electric dipole and quadrupole cross-sections as the former depends only on the polarization $\hat{\varepsilon}$ and the latter on the polarization $\hat{\varepsilon}$ and direction $\hat{\boldsymbol{k}}$ of the beam. The total spectrum for a given ($\hat{\varepsilon}$, $\hat{\boldsymbol{k}}$) configuration is the sum of the corresponding electric dipole and quadrupole cross-sections. The isotropic absorption cross-section, $\sigma(0,0)$, is thus the sum of the electric dipole isotropic cross-section, $\sigma^D(0,0)$, and of the electric quadrupole one, $\sigma^Q(0,0)$:

$$\sigma(0,0) = \sigma^D(0,0) + \sigma^Q(0,0) \tag{4.1}$$

The case of Ti K-edge in undoped anatase is described here but the situation is identical in the case of the V K-edge in V-doped anatase, since the spectra were also measured on powder samples.

In the next section the angular dependence of the absorption cross-section are given, in both electric dipole and quadrupole approximations. Then I detail how the reconstruction of the isotropic cross-section can be done from the absorption cross-sections of a given number of ($\hat{\boldsymbol{\varepsilon}}$,$\hat{\boldsymbol{k}}$) configurations. The given formulas also permit the isotropic spectrum to be reconstructed and also the spectrum for any experimental ($\hat{\boldsymbol{\varepsilon}}$,$\hat{\boldsymbol{k}}$) configuration to be determined. The methodology used to do this reconstruction is identical to those described in Chap. 3 in the case of the multielectronic calculations of the V^{3+} pre-edge spectrum in tsavorite:

- for each ($\hat{\boldsymbol{\varepsilon}}$,$\hat{\boldsymbol{k}}$) configuration, the values of the Euler angles (θ, φ, ψ) are determined,
- then (θ, φ, ψ) are injected in the expression of the absorption cross-section,
- and finally the resulting equation system is inversed.

It is to be noted that the absorption cross-sections $\sigma(0,0)$, $\sigma^D(0,0)$ and $\sigma^Q(0,0)$, as well as all the absorption cross-sections defined in the following, are spherical tensors which transform under rotation like the spherical harmonics Y_ℓ^m [24, 25].

The angular dependence of the absorption cross-section

The D_{4h} group is a dichroic group and therefore the electric dipole cross-section $\sigma^D(\hat{\boldsymbol{\varepsilon}})$ is not isotropic [24]. It is expressed as :

$$\sigma^D(\hat{\boldsymbol{\varepsilon}}) = \sigma^D(0,0) - \frac{1}{\sqrt{2}}(3\cos^2\theta - 1)\sigma^D(2,0) \tag{4.2}$$

It depends on an isotropic term, $\sigma^D(0,0)$, and an anisotropic one, $\sigma^D(2,0)$. The formula 4.2 is also often written as $\sigma^D(\hat{\boldsymbol{\varepsilon}}) = \sigma_\parallel \sin^2\theta + \sigma_\perp \cos^2\theta$. The $\sigma_\parallel$ and $\sigma_\perp$ absorption cross-sections correspond to the beam polarization $\hat{\boldsymbol{\varepsilon}}$ orientated parallel and perpendicular to the four-fold axis, respectively. The angle θ defined the orientation of $\hat{\boldsymbol{\varepsilon}}$ with respect to the four-fold axis. If $\sigma_\parallel$ and $\sigma_\perp$ are known, the angular dependence of the electric quadrupole cross-section can thus be determined for any experimental configuration.

The electric quadrupole cross-section depends on both the polarisation $\hat{\boldsymbol{\varepsilon}}$ and direction $\hat{\boldsymbol{k}}$ of the incident beam and is expressed in the local frame of the site (here symmetry D_{2d}) as:

$$\begin{aligned}\sigma^Q(\hat{\boldsymbol{\varepsilon}},\hat{\mathbf{k}}) &= \sigma^Q(0,0) + \sqrt{\frac{5}{14}}(3\sin^2\theta\sin^2\psi - 1)\sigma^Q(2,0)\\ &+ \frac{1}{\sqrt{14}}(35\sin^2\theta\cos^2\theta\cos^2\psi + 5\sin^2\theta\sin^2\psi - 4)\sigma^Q(4,0)\\ &+ \sqrt{5}\sin^2\theta[(\cos^2\theta\cos^2\psi - \sin^2\psi)\cos 4\varphi - 2\cos\theta\sin\psi\cos\psi\sin 4\varphi]\sigma^{Qr}(4,4)\end{aligned} \tag{4.3}$$

$\sigma^Q(\hat{\boldsymbol{\varepsilon}})$ depends on an isotropic term, $\sigma^Q(0,0)$, and three anisotropic ones, $\sigma^Q(2,0)$, $\sigma^Q(4,0)$ and $\sigma^{Qr}(4,4)$.

The angles (θ, φ, ψ) which are present in Eq. 4.2 an 4.3 are the Euler angles, defined by:

$$\hat{\boldsymbol{\varepsilon}} = \begin{pmatrix} \sin\theta\ \cos\varphi \\ \sin\theta\ \sin\varphi \\ \cos\theta \end{pmatrix} \tag{4.4}$$

and

$$\hat{\mathbf{k}} = \begin{pmatrix} \cos\theta\ \cos\varphi\ \cos\psi - \sin\varphi\ \sin\psi \\ \cos\theta\ \sin\varphi\ \cos\psi + \cos\varphi\ \sin\psi \\ -\sin\theta\ \cos\psi \end{pmatrix}. \tag{4.5}$$

The reconstruction of the isotropic spectrum

The electric dipole cross-section $\sigma^D(\hat{\varepsilon})$ depends on two terms and therefore, two orientations are needed to determine $\sigma^D(0,0)$. Two orientations $\hat{\varepsilon}_1$ and $\hat{\varepsilon}_2$ were arbitrarily chosen with the polarization aligned respectively along the $\vec{a}$ and $\vec{c}$ axis of the tetragonal frame.

For the first orientation, as $\hat{\varepsilon}_1$=[100], the Euler angle is θ=$\pi/2$ and the corresponding absorption cross-section, σ_1^D, is:

$$\sigma_1^D = \sigma^D(0,0) + \frac{1}{\sqrt{2}}\sigma^D(2,0). \tag{4.6}$$

For the second orientation, as $\hat{\varepsilon}_2$=[001], the Euler angle is θ=0 and the corresponding absorption cross-section, σ_2^D, is:

$$\sigma_2^D = \sigma^D(0,0) - \frac{2}{\sqrt{2}}\sigma^D(2,0). \tag{4.7}$$

A linear combination of Eq. 4.6 and 4.7 gives the isotropic dipole cross-section $\sigma^D(0,0)$:

$$\sigma^D(0,0) = \frac{1}{3}(2\sigma_1^D + \sigma_2^D). \tag{4.8}$$

The σ_1^D and σ_2^D cross-sections and the corresponding isotropic one $\sigma^D(0,0)$, in the case of Ti K-edge, are displayed in Fig. 4.5, which clearly illustrates the anisotropic behavior of the electic dipole cross-section.

The electric quadrupole cross-section $\sigma^Q(\hat{\varepsilon},\hat{\boldsymbol{k}})$ depends on four terms and therefore, four orientations are needed to determine $\sigma^D(0,0)$. They were chosen arbitrarily. For the first orientation, $\hat{\varepsilon}_1$=[100] and $\hat{\boldsymbol{k}}_1$=[00$\bar{1}$], the corresponding Euler angles are (θ_1=$\pi/2$, φ_1=0, ψ_1=0) and the absorption cross-section σ_1^Q is:

$$\sigma_1^Q = \sigma^Q(0,0) - \sqrt{\frac{5}{14}}\sigma^Q(2,0) - \frac{4}{\sqrt{14}}\sigma^Q(4,0). \tag{4.9}$$

For the second orientation, $\hat{\varepsilon}_2$=[100] and $\hat{\boldsymbol{k}}_2$=[0$\bar{1}$0], the corresponding Euler angles are (θ_2=$\pi/2$, φ_2=0, ψ_2=- $\pi/2$) and the absorption cross-section σ_2^Q is:

$$\sigma_2^Q = \sigma^Q(0,0) + \sqrt{\frac{10}{7}}\sigma^Q(2,0) + \frac{1}{\sqrt{14}}\sigma^Q(4,0) - \sqrt{5}\sigma^Q(4,4). \tag{4.10}$$

For the third orientation, $\hat{\varepsilon}_3$=[1/2, 1/2, 1/$\sqrt{2}$] and $\hat{\boldsymbol{k}}_3$=[-1/2, -1/2, 1/$\sqrt{2}$], the corresponding Euler angles are (θ_3=$\pi/4$, φ_3=$\pi/4$, ψ_3=π) and the absorption cross-section σ_3^Q is:

$$\sigma_3^Q = \sigma^Q(0,0) - \sqrt{\frac{5}{14}}\sigma^Q(2,0) + \frac{19}{4\sqrt{14}}\sigma^Q(4,0) - \frac{\sqrt{5}}{4}\sigma^Q(4,4). \tag{4.11}$$

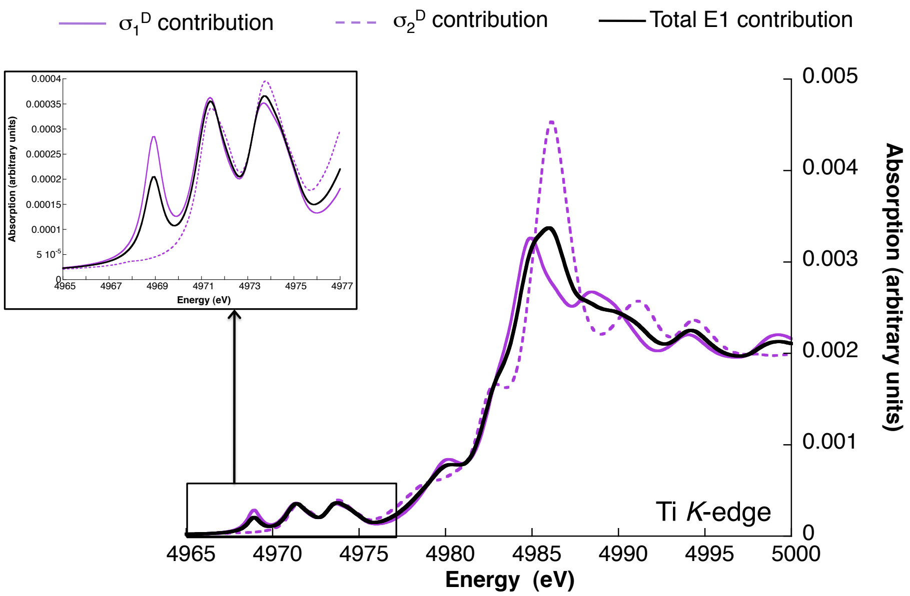

Figure 4.5: Electric dipole cross-sections calculated for the two different orientations (purple lines) in the whole XANES region of the spectrum, with the the pre-edge region displayed in the inset. The black line presents the isotropic dipole spectrum calculated from the two orientations $\hat{\varepsilon}_1$=[100] and $\hat{\varepsilon}_2$=[001].

For the fourth orientation, $\hat{\varepsilon}_4$=[0, $1/\sqrt{2}$, -$1/\sqrt{2}$] and $\hat{\boldsymbol{k}}_2$=[0, $1/\sqrt{2}$, $1/\sqrt{2}$], the corresponding Euler angles are (θ_4=$3\pi/4$, ϕ_4=π, ψ_4= $\pi/2$) and the absorption cross-section σ_4^Q is:

$$\sigma_4^Q = \sigma^Q(0,0) - \sqrt{\frac{5}{14}}\sigma^Q(2,0) + \frac{19}{4\sqrt{14}}\sigma^Q(4,0) + \frac{\sqrt{5}}{4}\sigma^Q(4,4). \tag{4.12}$$

Figure 4.6 shows the different cross-sections σ_1^Q, σ_2^Q, σ_3^Q and σ_4^Q and the isotropic one $\sigma^Q(0,0)$ in the case of Ti K-edge.

The equations 4.9, 4.10, 4.11 and 4.12 form an equation system, the inversion of which gives $\sigma^Q(0,0)$, $\sigma^Q(2,0)$, $\sigma^Q(4,0)$ and $\sigma^Q(4,4)$ as functions of the four independent cross-sections σ_1^Q, σ_2^Q, σ_3^Q and σ_4^Q:

$$\sigma^Q(0,0) = \frac{1}{15}(6\sigma_1^Q + 5\sigma_2^Q - 8\sigma_3^Q + 12\sigma_4^Q) \tag{4.13}$$

$$\sigma^Q(2,0) = \frac{1}{3}\sqrt{\frac{2}{35}}(-3\sigma_1^Q + 7\sigma_2^Q - 16\sigma_3^Q + 12\sigma_4^Q)$$

$$\sigma^Q(4,0) = \frac{2}{5}\sqrt{\frac{2}{7}}(-2\sigma_1^Q + \sigma_3^Q + \sigma_4^Q)$$

$$\sigma^Q(4,4) = \frac{2}{\sqrt{5}}(-\sigma_3^Q + \sigma_4^Q)$$

Particular attention has to be given here to the coordinates of $\hat{\varepsilon}$ and $\hat{\boldsymbol{k}}$ in the expression of the electric quadrupole cross-section. In equation 4.3, they are not expressed in the crystallographic

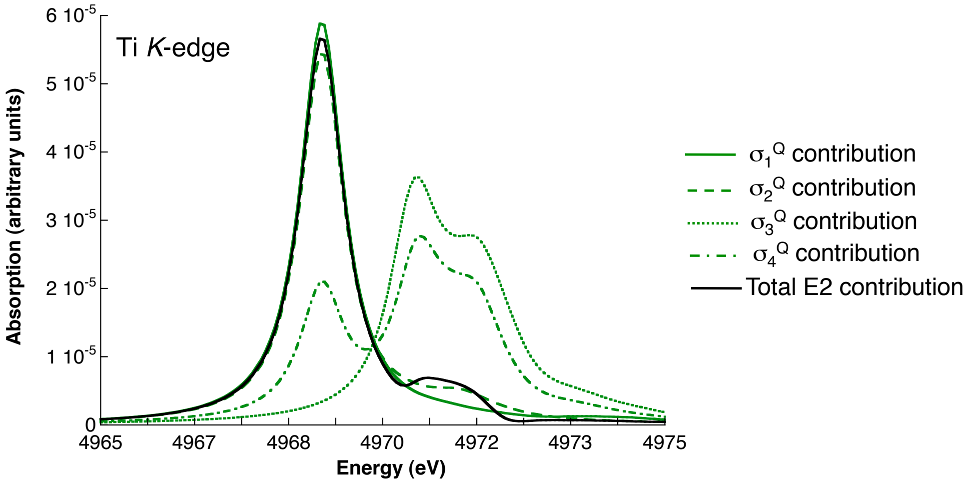

Figure 4.6: Electric quadrupole cross-sections calculated for the four different orientations (green lines). The black line presents the isotropic quadrupole spectrum calculated from the four ($\hat{\varepsilon}_1$=[100],$\hat{\boldsymbol{k}}_1$=[00$\bar{1}$]), ($\hat{\varepsilon}_2$=[100] and $\hat{\boldsymbol{k}}_2$=[0$\bar{1}$0]), ($\hat{\varepsilon}_3$=[1/2, 1/2, 1/$\sqrt{2}$] and $\hat{\boldsymbol{k}}_3$=[-1/2, -1/2, 1/$\sqrt{2}$]) and ($\hat{\varepsilon}_4$=[0, 1/$\sqrt{2}$, -1/$\sqrt{2}$] and $\hat{\boldsymbol{k}}_4$=[0, 1/$\sqrt{2}$, 1/$\sqrt{2}$]) orientations.

frame but in a local frame ($\vec{x}_s$, $\vec{y}_s$, $\vec{z}_s$) which is related to the D_{2d} symmetry (the local point group of the titanium site). This site frame is different from the crystal frame, ($\vec{x}_{crys}$, $\vec{y}_{crys}$, $\vec{z}_{crys}$), which is defined along the crystallographic axes and that is used in the Xspectra code. Therefore, to compute the isotropic quadrupole cross-section with Xspectra, the four ($\hat{\varepsilon}$, $\hat{\boldsymbol{k}}$) configurations used to describe $\sigma^Q(0,0)$, $\sigma^Q(2,0)$, $\sigma^Q(4,0)$ and $\sigma^Q(4,4)$ must be expressed in the crystallographic frame. To do so, the angle θ between the two frames must be determined. It is defined by the following matrix:

$$\mathrm{Rot} = \begin{pmatrix} \cos\theta & \sin\theta & 0 \\ -\sin\theta & \cos\theta & 0 \\ 0 & 0 & 1 \end{pmatrix} \tag{4.14}$$

which must obey this relation:

$$\mathrm{Rot}^{\mathrm{T}} \cdot \begin{pmatrix} \textit{Symmetry operations} \\ \textit{of the site} \end{pmatrix} \cdot \mathrm{Rot} = \begin{pmatrix} \textit{Symmetry operations} \\ \textit{of the crystal} \end{pmatrix} \tag{4.15}$$

where $\mathrm{Rot}^{\mathrm{T}}$ is the transpose matrix of the Rot matrix.

The symmetry operations of the D_{2d} site are (x,y,z), (y,$\bar{x}$,$\bar{z}$), ($\bar{y}$,x,$\bar{z}$), ($\bar{x}$,$\bar{y}$,z), ($\bar{x}$,y,$\bar{z}$), (x,$\bar{y}$,$\bar{z}$), (y,x,z) and ($\bar{y}$,$\bar{x}$,z). The symmetry operations of the crystal are the same. Therefore, the corresponding angle is θ=π/4. In the Xspectra code, the coordinates of $\hat{\varepsilon}$ and $\hat{\boldsymbol{k}}$ are therefore [Rot($\hat{\varepsilon}_{site}$), Rot($\hat{\boldsymbol{k}}_{site}$)], with:

$$\mathrm{Rot} = \begin{pmatrix} \frac{1}{\sqrt{2}} & \frac{1}{\sqrt{2}} & 0 \\ -\frac{1}{\sqrt{2}} & \frac{1}{\sqrt{2}} & 0 \\ 0 & 0 & 1 \end{pmatrix}. \tag{4.16}$$

In the Xspectra input file to calculate the electric dipole cross-section, the value of the polarization is therefore $\hat{\varepsilon}_{input} = \mathrm{Rot}(\hat{\varepsilon})$, and that for each value of $\hat{\varepsilon}$ needed to reconstruct the isotropic cross-section. In the case of electric quadrupole cross-section, the values of $\hat{\varepsilon}$ and $\hat{\boldsymbol{k}}$ are $\hat{\varepsilon}_{input} = \mathrm{Rot}(\hat{\varepsilon})$ and $\hat{\boldsymbol{k}}_{input} = \mathrm{Rot}(\hat{\boldsymbol{k}})$, respectively.

4.2.2 The theoretical Ti K-edge spectrum of anatase

The total isotropic spectrum calculated at the Ti K-edge is shown in Fig. 4.7, along with the experimental spectrum from Ref. [180]. The pre-edge displays three contributions at 4968.9 eV (peak A_1), 4971.3 eV (peak A_2) and 4973.8 eV (peak A_3). The main edge peak is at 4986 eV (peak C_1) with a peak at 4989.6 eV (peak C_2), followed by three contributions at 4994.2 eV (peak D_1), 4999.2 eV (peak D_2) and 5002.7 eV (peak D_3). An additional feature is present in the edge jump at 4980.1 eV (peak B) and one at 5015.3 eV (peak E). The theoretical spectrum reproduces all the experimental features. The theoretical and experimental edge peaks are in good agreement concerning the energy positions and relative intensity of the peaks. The relative energy and intensity of the pre-edge peaks are also in good agreement between theory and experiment. The absolute energy of the pre-edge is slightly higher in the theoretical spectrum (~1 eV) with respect to the main edge. This is due to the limit of the DFT-GGA theory to model the interaction between the core-hole and the $3d$ empty states, as mentioned in chapter 5.

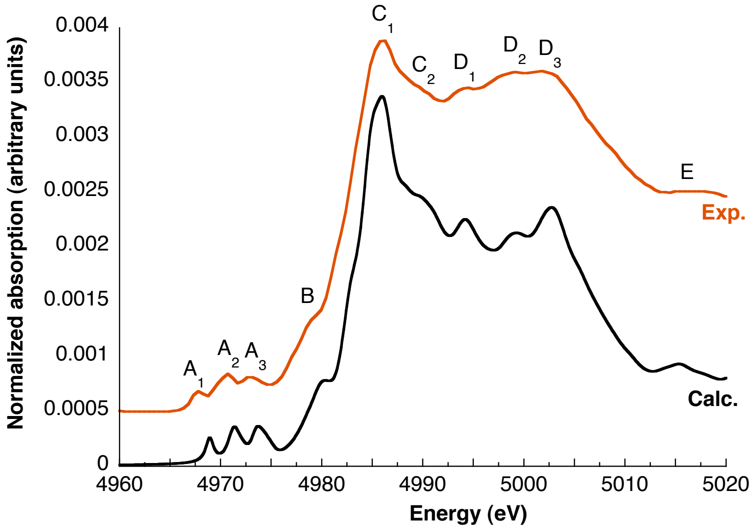

Figure 4.7: Comparison between experimental (orange) and calculated (black) isotropic spectra at the Ti K-edge in anatase. The experimental spectrum is reproduced from [180].

The electric dipole and quadrupole contributions of the pre-edge region are plotted in Fig. 4.8. The electric dipole cross-section shows three contributions, whereas the electric quadrupole one displays one contribution at 4968.9 eV and a really small one at 4971.1 eV. The first quadrupole peak represents 22% of the peak A_1 total intensity and the second 2% of the peak A_2 total intensity. The quadrupole contribution is therefore weak compared to the dipole one, as expected in a non-centrosymmetric site. The absence of an inversion center indeed permits the p-d intrasite hybridization, leading to a major dipole contribution..

4.2.3 The theoretical V K-edge spectrum of V-doped anatase with V incorporated in the Ti-substitutional site

The relaxation process around vanadium

The V^{4+} and Ti^{4+} ions in a octahedral environment have different radii: $r_{V^{4+}} = 0.58$ Å and $r_{Ti^{4+}} = 0.605$ Å [189]. A modification of the local structure around the substituted vanadium

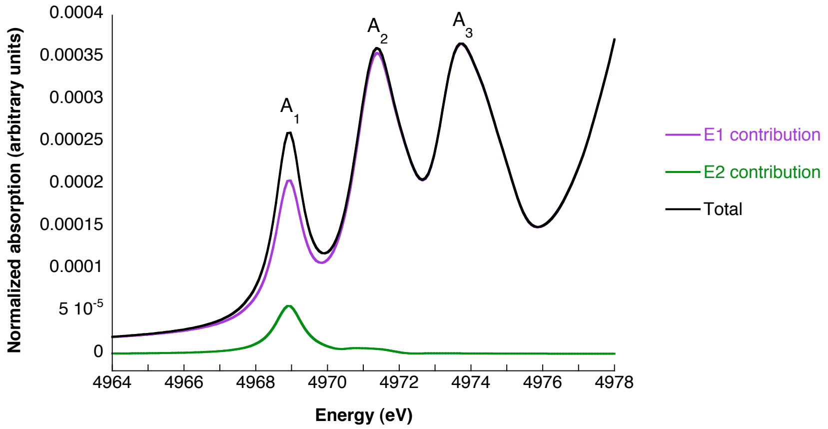

Figure 4.8: Calculated Ti *K* pre-edge in anatase, with the electric dipole (E1, purple line) and quadrupole (E2, green line) contributions.

atom is therefore expected in order to accomodate this smaller cation. Shorter cation-oxygens distances are observed after the relaxation process: the four distances at 1.934 Å and the two ones at 1.980 Å decrease to 1.918 Å and 1.888 Å, respectively. The angular relaxation is small: the variations range between 0.2° and 0.5°. The variations of the distances and the angles during the relaxation are summarized in Table 4.1 and illustrated in Fig. 4.9, which clearly indicates that the symmetry around vanadium is retained during the relaxation. The main effect of the substitution of a titanium atom by a vanadium one is thus a small contraction of the first coordination shell with the conservation of the initial D_{2d} symmetry.

	V-O distances (Å)		V-O-V angles (°)		
Before relaxation	1.934	1.980	92.44	78.09	101.91
After relaxation	1.918	1.888	92.25	78.58	101.42

Table 4.1: Structural parameters of the first coordination sphere of vanadium before and after relaxation.

The isotropic theoretical spectrum

Figure 4.10 presents the calculated spectrum at the V *K*-edge of anatase, with a vanadium atom substituted to a titanium one. The calculated spectrum was scaled in energy so that peak P_3 of the experimental spectrum coincides with peak C_1 of the calculated one, at 5486.3 eV. The experimental spectra was normalized so that its most intense peak has the same intensity than peak C1. The pre-edge displays four peaks at 5468.4 eV (peak A_0), 5469.2 eV (peak A_1), 5471.6 eV (peak A_2) and 5473.9 eV (peak A_4). A structure is present at 5480.7 eV (peak B) in the edge jump. The main peak is at 5486.3 eV (peak C_1), with a small shoulder at 5485.5 eV and followed by four peaks at 5490.0 eV (peak C_2), 5494.1 eV (peak D_1), 5499.5 eV (peak D_2) and 5503.1 eV (peak D_3). The calculated pre-edge for vanadium in a Ti-substitutional site does not reproduce the experimental spectrum (Fig. 4.10), suggesting that vanadium is not incorporated in the Ti-substitutional site in the anatase structure.

The spectra calculated at the Ti and V *K*-edge are compared in Fig. 4.11. The global shape of the V *K*-edge spectrum is similar to the Ti *K*-edge one, indicating that the V *K*-edge

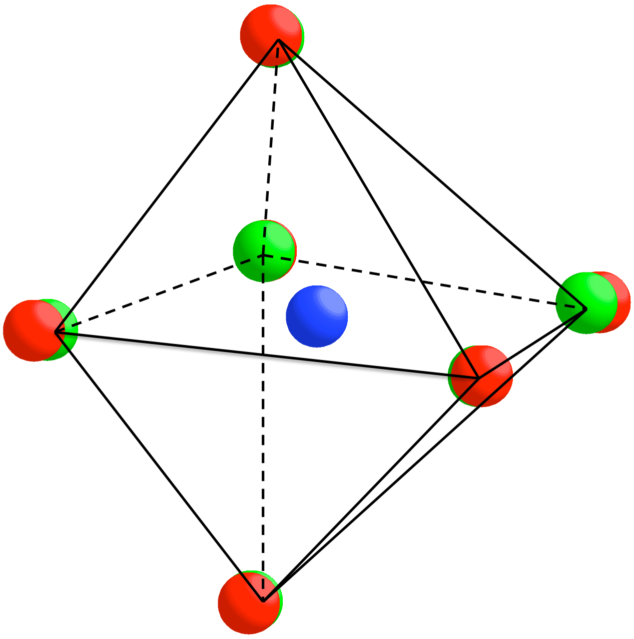

Figure 4.9: First atomic shell around vanadium (blue). The red oxygen atoms represent the shell before relaxation, and the green ones after relaxation.

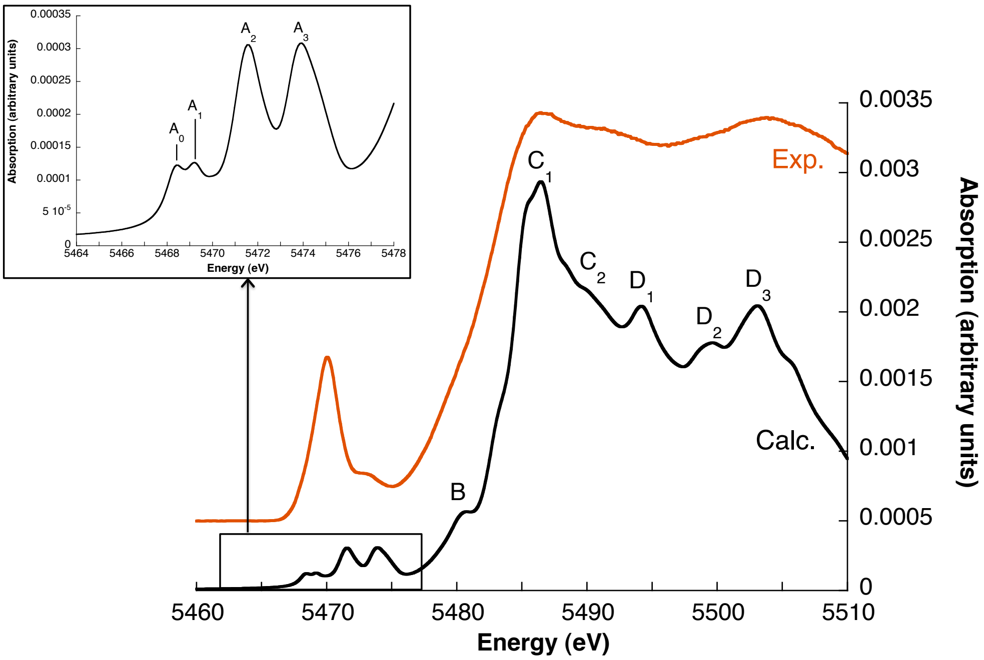

Figure 4.10: Isotropic calculated V *K*-edge spectrum in anatase. The calculated pre-edge is displayed in the inset.

calculations are reliable. The main difference between the two edges lies in the pre-edge region: the first peak of the Ti *K*-edge (peak A_1) is split in the case of the V *K* pre-edge (peaks A_0 and A_1). The energy and relative intensity of the peaks are however similar. The calculated V *K*-edge spectrum is therefore representative of the spectral signature of V^{4+} in the Ti octahedral site of the anatase structure.

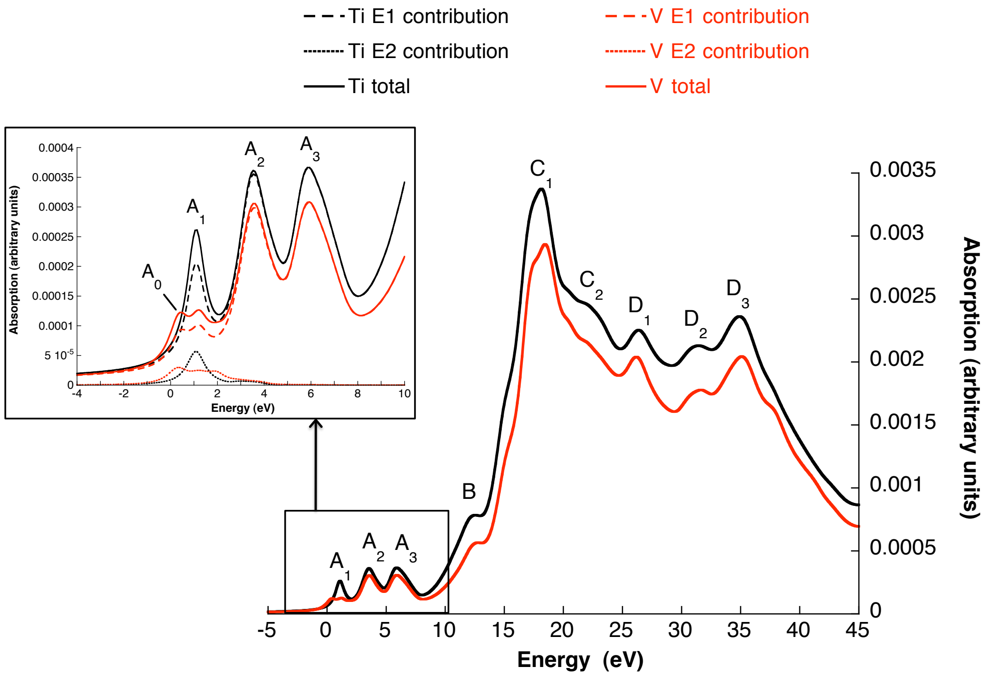

Figure 4.11: Comparison between the isotropic calculated spectra of anatase at the V (red) and Ti (black) K-edge. The pre-edges are displayed in the inset.

4.2.4 Interpretation of the theoretical data: Assignment of the transition in a monoelectronic framework

A splitting of peak A$_1$ of the Ti K pre-edge is observed in the case of the V K pre-edge and a first interpretation is given here. Figure 4.12 displays the isotropic absorption cross-sections at the Ti K-edge (left) and at the V K-edge (right) with the virtual transitions towards the occupied states. Three graphs are represented for each edge: the electric quadrupole cross-section E2 (down), the electric dipole cross-section E1 (middle) and the total absorption cross-section, corresponding to the sum of the E1 and E2 contributions. The broadening used in the calculations (0.47 eV in the pre-edge region for the Ti K-edge and 0.5 eV for the V K-edge) does not allow the observation of a gap between the occupied and empty states. This gap would be visible in the case of the Ti K-edge if a smaller broadening is chosen, but not in the case of the V K-edge. As for tsavorite, the vanadium $3d$ orbitals are partially occupied and they can not be well separated by the calculations, *i.e.* the calculations do not permit the creation of a significant splitting between the $3d$ occupied and empty orbitals. Indeed, the V^{4+} ion has an electronic configuration $3d^1$ and therefore only one electron (up in the calculations) occupies the $3d$ orbitals. In the case of the Ti K-edge in TiO2, the $3d$ orbitals of the Ti^{4+} ion are all empty, which makes it a favorable case to perform monoelectronic calculations. It is to be noted that the transition assignments to the peaks is done by considering a splitting of the $3d$ orbitals in an octahedral field. The degeneracy breaking resulting from the D_{2d} symmetry of the Ti and V site is neglected here.

The transition assignments in the case of the Ti K-edge in anatase is well understood because the situation is similar to the case of rutile [34, 120]. Two peaks are thus visible on the graph corresponding to the E2 cross-section (Fig. 4.12 left, down). The most intense peak is assigned to transitions from the 1*s* orbital to the 3*d* (t_{2g}) ones and it is followed by a less intense and broader peak assigned to transitions from the 1*s* orbital to the 3*d* (e_g) ones. The interpretation made by Joly *et al.* [120] and Cabaret *et al.* is used to interpret the peaks observed for the E1 cross-section (Fig. 4.12 left, middle). Peak A_1 corresponds to $1s \rightarrow p$ transitions hybridized with the t_{2g} orbitals of the Ti absorbing atom. Peak P2 corresponds to $1s \rightarrow p$ transitions hybridized with the e_g orbitals of the Ti absorbing atom and also to $1s \rightarrow p$ transitions hybridized with the t_{2g} orbitals of the Ti neighbor atoms through the 2*p* orbitals of the oxygen neighbor atoms. Peak A3 corresponds to $1s \rightarrow p$ transitions hybridized with the e_g orbitals of the Ti neighbor atoms through the 2*p* orbitals of the first oxygen neighbor atoms.

In the case of the V *K*-edge, the situation is more complicated. Indeed, on the one hand, spin up and spin down contributions must be individually considered and, on the other hand, the t_{2g} orbitals are partially occupied by a spin up electron, as said earlier. Nevertheless, a comparison with the case of the Ti *K*-edge allowed an first assignment of the peaks to be given. Some points remain unclear. In particular, a splitting of the E2 cross-section (Fig. 4.12 right, down) is observed for the peak assigned to transitions towards the e_g down orbitals and still needs to be understood. More calculations are therefore required to fully understand the electronic structure of V^{4+} in anatase. The determination of the partial and local densities of states for the oxygen and titanium neighbor atoms has to be done, as well as the calculations of the absorption cross-sections for specific orientations of the polarization and direction of the incident beam in order to probe specific 3*d* orbitals, as previously done for V^{3+} in tsavorite (Chap. 3). The latter would permit the splitting of the 3*d* orbitals for a D_{2d} symmetry to be taken into account.

4.3 Conclusion

I have determined by DFT calculations the spectrum at the Ti *K*-edge in anatase, and at the V *K*-edge in V-doped anatase. The Ti *K*-edge calculations were compared to an isotropic experimental spectrum [180] and a good agreement was found. As no experimental data for the V-doped anatase in which the incorporation site of vanadium is well-known are available, the calculated spectrum is validated only by the similarity with the Ti-*K*-edge spectrum. The comparison can be done because in the calculations, the absorbing atom (Ti or V) is in the same site with an identical coordination and site symmetry. The relaxation showed that the symmetry is retained when a vanadium atom is incorporated in a Ti-substitutional site. The V *K*-edge spectrum calculated from this relaxed structural model hence corresponds to the spectral signature of a V^{4+} in a slightly distorted six-fold environment.

However, the calculated V *K* pre-edge for vanadium in the Ti-substitutional site is in disageement with experiments (Fig. 4.1). This is a strong confirmation that in the V-doped anatase, vanadium may not be incorporated in the Ti-substitutional site. Nevertheless, a partition of vanadium among Ti-substitutional and interstital sites can not be excluded. DFT calculations with a vanadium atom incorporated in an interstitial site should provide the spectral signature of V^{4+} in an interstitial site in the anatase structure and thus give information on the incorporation site of vanadium in V-doped anatase. Nevertheless these calculations are not straightforward to perform. The incoporation of V^{4+} in an interstitial site indeed needs a charge compensation to maintain the global neutrality of anatase. This charge compensation has to be carefully taken into account in the calculations to get reliable results. It was not possible to do these calculations during my thesis because of its limited time, but they will be soon performed.

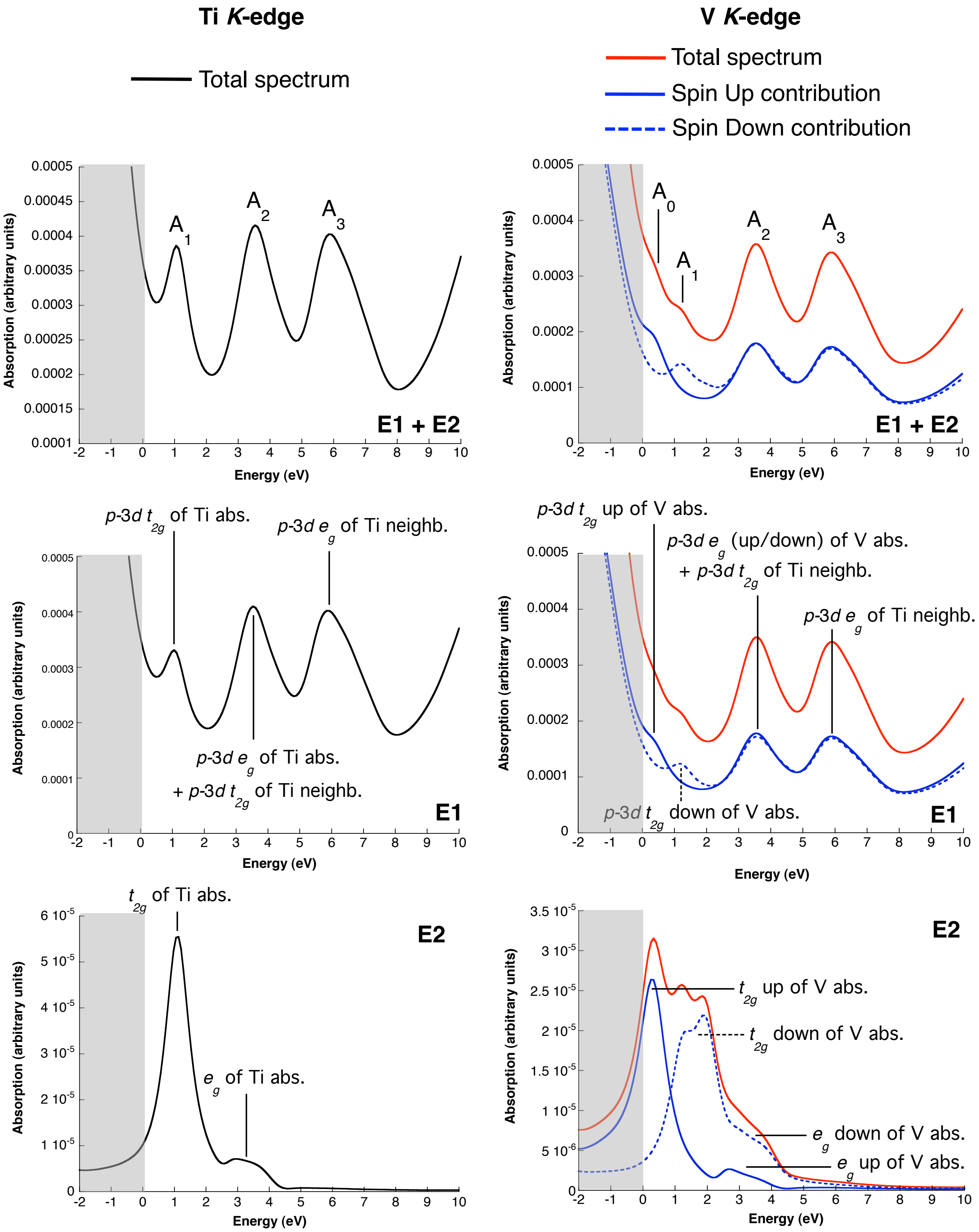

Figure 4.12: Isotropic calculated total spectrum, electric dipole (E1) transitions and electric quadrupole (E2) transitions, with an interpretation of the transitions within a mono-electronic framework. The grey region corresponds to the virtual transitions towards the occupied states. For the V K-edge, the respective contribution of the two spins are plotted (blue solid line for spin up, blue dashed line for spin down), as well as the sum (red line).

Chapter 5

The oxidation state of vanadium in titanomagnetites $Fe_{3-x}Ti_xO_4$ from the Bushveld Complex

Vanadium oxidation states range from +III to +V in terrestrial magmatic systems, which makes it a valuable geochemical probe, used to get information on rock formation processes. In particular, the determination of its oxidation state in V-bearing titanomagnetites is a potential window into the processes leading to the formation of the massive monomineralic layers of titanomagnetite in the Bushveld Complex in South Africa. This chapter is thus dedicated to the study of the vanadium oxidation state in natural and synthetic samples. The approach adopted for this investigation is based on a previous study on vanadium in titanomagnetites from the Bushveld Complex by Balan *et al.* [10]. They studied titanomagnetites from two localities in the Bushveld Complex. I applied their methodology and used their hypothesis to determine if their conclusions could also be applied to samples taken at different depths in a third locality of the Bushveld Complex. The first section therefore summarizes the work of Balan *et al.* and presents their main conclusions, which are needed for the present study. The second section is thus dedicated to the results obtained during this thesis on the titanomagnetite natural samples from the Bushveld Complex. To complete the investigation of the natural titanomagnetites from the Bushveld Complex, syntheses of V-bearing magnetite (without titanium) were performed. The synthesis protocol and the results obtained on these synthetic samples are described in a third section. These two sections only detail the results and their interpretation within the framework of the conclusions made by Balan *et al.* The fourth section is dedicated to a discussion on the results in a larger view than the framework of the conclusions made by Balan *et al.*

5.1 The initial idea

My work is based on a first study on titanomagnetite samples by Balan et *al.* [10]. Their publication being a fundamental basis on the following work, it is entirely reproduced in App. C but I summarize here the main information needed in the following. Balan et *al.* studied by V K-edge HERFD-XAS five samples from the Bushveld Complex (two from the main magnetite seam, Mapochs mine, and three from the BK1 Bierkraal borehole), one from the mine of Mustavaara (Koillismaa layered igneous complex, Finland) and one from the Skaergaard intrusion (Greenland). Five reference samples representative of the different vanadium oxidation states and coordination numbers were also investigated.

Significant variations were observed for the pre-edge features among the samples, whereas the edges were similar. The last contribution of the three features characterizing the measured pre-edges displays a variable intensity among the samples, leading to a significant increase of the pre-edge area with the pre-edge intensity increase. Orientational effects were not considered as the reason of these variations, neither was the incorporation of vanadium in a tetrahedral site. Because of the non-centrosymmetric character of a tetrahedron, the K pre-edge arises from both electric dipole ($1s \rightarrow p$) and quadrupole ($1s \rightarrow 3d$) transitions, which leads to an increase of the pre-edge intensity. However, the crystal-field energy stabilization favors the incorporation of vanadium in an octahedral site [27], as in normal spinel coulsonite (FeV_2O_4) and vuorelainenite MnV_2O_4 [108]. The hypothesis of the presence of two vanadium oxidation states, +III and +IV, in the titanomagnetite structure was put forward. The variations of the pre-edge intensity would therefore result from a variable proportion of the +IV oxidation state with respect to the +III one, the increase of the intensity corresponding to an higher content in V^{4+}. The presence of a +V oxidation state was not retained as a theory because V^{5+} is not expected to substitute into the magnetite [115]. The proportion of vanadium occuring as V^{4+} was determined by comparison with octahedral V^{3+} and V^{4+} references, respectively tsavorite and cavansite. It was found to range from 2% up to 17% of the total vanadium content.

The variations in the V^{4+} content were then interpreted in terms of formation conditions of V-rich titanomagnetite layers. As the proportion of V^{4+} is similar in the samples from different localities, the extreme enrichment of vanadium in magnetite should only occur within a small range of oxygen fugacities. At the scale of the Bushveld Complex magma chamber, the similar proportions of V^{4+} in the samples from Mapochs mine and Bierkraal borehole suggest that similar f_{O_2} conditions prevailed during the formation of these two layers. This contrasts with the observation at the scale of a single layer: an upward decrease in the f_{O_2} can be inferred from the decrease in the V^{4+}/V^{3+} ratio observed in the BK1 samples.

The main information to retain from this first study on the vanadium oxidation state in the titanomagnetite from the Bushveld Complex is that vanadium occurs under two oxidation states, +III and +IV. Variations observed among the V K-edge HERFD-XAS pre-edges are due to variable proportions of V^{4+}. These conclusions were the guiding principles of the new study on titanomagnetite samples from another locality of the Bushveld Complex, in order to complete the observations made by Balan et *al.*

5.2 The natural titanomagnetite samples from BK2 borehole

Natural titanomagnetite samples from the Main Magnetite Layer, taken in the BK2 borehole, in the Bushveld Complex, were investigated. The first part of this section is thus dedicated to a description of the borehole and to the chemical characterization of the samples. They were analyzed by Scanning Electron Microscopy (SEM) and microprobe analyses, the results of which were used to estimate the oxygen fugacity. The second part deals with the V K-edge HERFD-XAS investigation of the samples. The measured pre-edges were used to determine the oxidation state of titanomagnetite in the samples. The methodology used for this determination is presented.

5.2.1 Samples characterization

Geological settings

The Bierkraal borehole 2 (BK2) is situated in the north-east of Pretoria and Johannesburg, in the northern part of the Rustenburg layered suite in the western Bushveld Complex, and is close to the BK1 borehole studied by Balan et *al.* [10] (Fig. 5.1). The BK1 borehole is stratigraphically higher than the BK2 one and consequently closer to the surface. The study of the BK2 borehole thus allowed a deeper layer to be investigated [202]. The Bierkraal boreholes were drilled in the first place to provide a complete succession of the Rustenburg Layered Suite [216]. The Main Magnetite Layer (MML) of the Bushveld Complex was thus shown to appear at a depth of 171m in the BK2 borehole [135, 202]. A vertical continuous sequence of eleven polished thin sections of titanomagnetites from the MML in the BK2 borehole was studied. This sequence is 3m thick and located at depth ranging from 170.61m to 167.7m (Fig. 5.2).

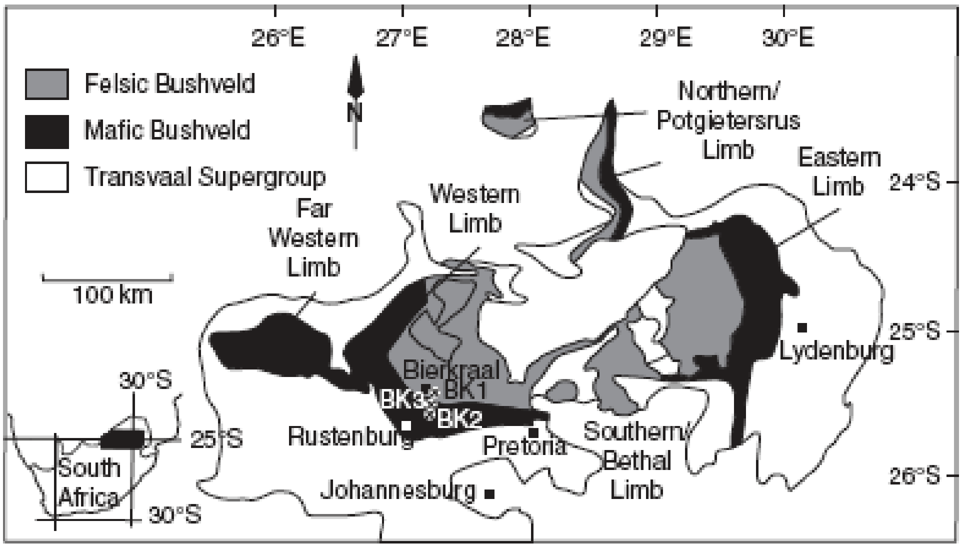

Figure 5.1: Map of the Bushveld Complex showing the location of the BK1 borehole studied by Balan et *al.* [10] and the BK2 borehole (Figure reproduced from Ref. [202]).

Scanning Electron Microscopy

The SEM images show broadly the same features for all the analyzed samples and therefore only a few have been selected for presentation here (Fig. 5.3). The observations are similar to the microscopic features of titaniferous iron ores described in previous studies: the titanomagnetite crystals are characterized by the development of typical ulvöspinel ($TiFe_2O_4$) cloth textures [174, 176, 214]. It consists of networks of micrometer- to submicrometer-sized ulvspinel lamellae that are oriented parallel to the [100] direction of magnetite (Fig. 5.3 c,d). The lamellae were formed from the exsolution of a magnetite-ulvöspinel solid solution under conditions of relatively low oxygen fugacity [176]. Broader ulvöspinel lamellae can also form distinct rectangular frames around pleonast, which is Fe-rich Al-Mg spinel (Fig. 5.3 a,b) [28, 214] .

A selected zone of the BK2-3 sample is situated near a fracture and presents a different texture. Chemical analysis by Energy Dispersive Spectoscopy show the presence of a significant amount of silica and calcium, which are absent in the case of the other samples.

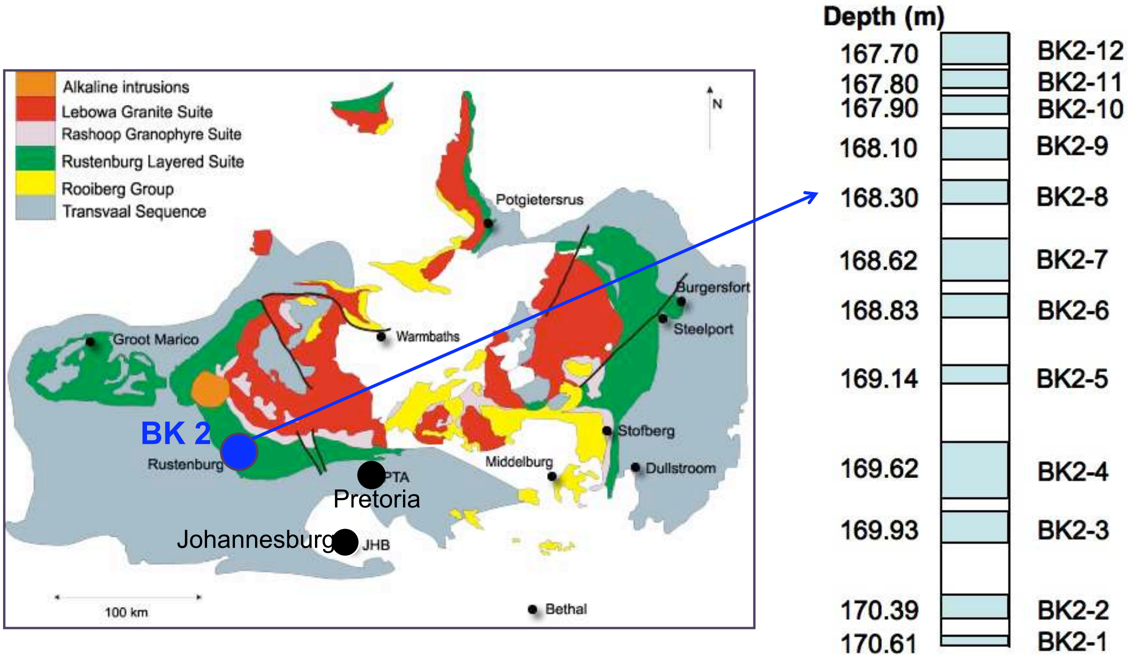

Figure 5.2: The BK2 vertical sequence. The 11 thin sections come from the blue zones of the sequence.

5.2.2 Determination of the oxygen fugacity

The oxygen fugacity was calculated with a Fe-Ti oxide geothermometer, which uses the chemical composition of the samples determined from microprobe analyses. The microprobe analyses are first detailed, then how the geothermometer determines the oxygen fugacity and finally the evolution of the oxygen fugacity through the BK2 sequence.

Microprobe analysis

Chemical analyses were performed on several points per thin section. The microprobe results presented here correspond to the average value per thin section and the complete data set is given in App. D.

The BK2 samples have a high content vanadium, ∼0.7 at% V, i.e. ∼1.47 wt% V_2O_3 (Table 5.1). This content varies between 0.64 and 0.78 at% V, the highest values being at the bottom of the profile. This general decrease in V concentration of titanomagnetites as a function of depth is a well-known feature of the Bushveld Complex, and is most likely the result of a progressive V-depletion of the liquid caused by crystallization of the lower magnetites [50, 54]. The high content in Ti (∼5.4 at% Ti), eight times higher than the V one, demonstrates the necessity to perform HERFD-XAS experiments instead of conventional (total fluorescence yield) XANES. The evolution of Ti content in the profile is opposit to that of vanadium: when V content increases, Ti content decreases (Fig. 5.4 a and b). This behaviour is reinforced by the very low vanadium content (∼0.07 at% V) in coexisting grains of ilmenite ($FeTiO_3$). This antipathetic relation between vanadium and titanium has already been described [50, 151, 175, 176, 184]. A rapid depletion of the Cr content is observed at the bottom of the profile, from 1.17 at% Cr down to 0.21 at% Cr over a depth decrease of only 20 cm. This brutal depletion is followed by a quite stable concentration in Cr (5.4c). This behaviour of Cr in titanomagnetites is characteristic of the magnetites from the Bushveld Complex [50, 51, 147, 52]. Local increases in Al and Mg

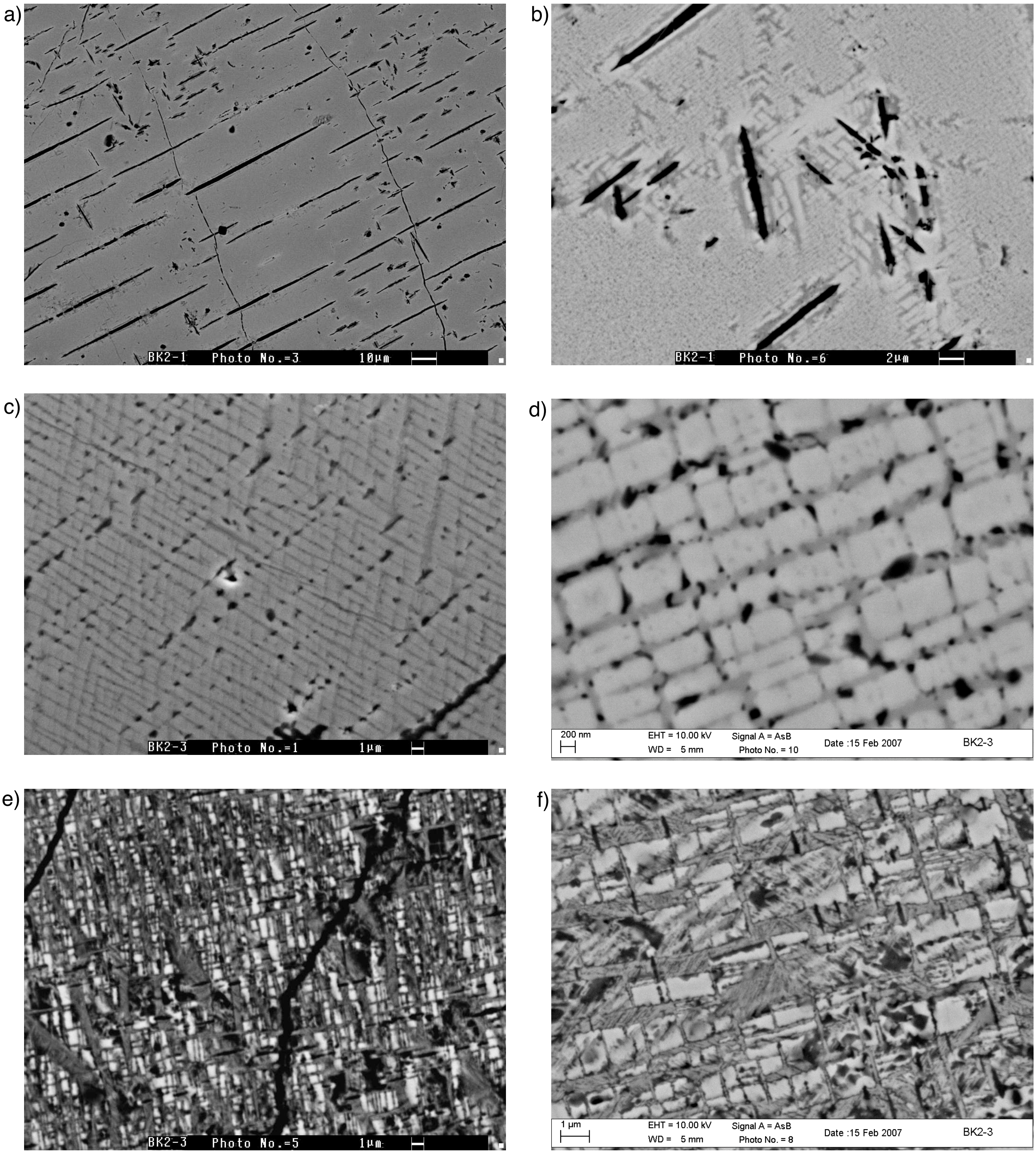

Figure 5.3: Typical SEM images of the BK2 samples. a,b: BK2-1, c,d: BK2-3, e-f: BK2-3 near a fracture. On images c and d, the grey matrix is magnetite and the dark lamellae parallel to the [100] direction of magnetite are ulvöspinel exsolutions. On image a and b, the dark lamellae are pleonaste exsolutions surrounded by broad ulvöspinel lamellae (dark grey), both in the titanomagnetite matrix (light grey).

concentrations were observed in the zone selected for the measurements, likely related to the exsolution of pleonaste, which are Fe-rich Al-Mg spinel [28].

Section	O at. %	Fe at. %	Ti at. %	V at. %	Cr at. %	Mn at. %	Mg at. %	Al at. %
BK2-12	53.3	39.0	5.6	0.70	0.14	0.15	0.15	0.96
BK2-11	53.4	37.7	5.3	0.68	0.15	0.12	0.57	2.07
BK2-9	53.4	38.0	5.5	0.66	0.17	0.14	0.52	1.48
BK2-8	53.5	37.6	5.8	0.64	0.18	0.15	0.57	1.32
BK2-7	53.6	37.4	5.8	0.67	0.14	0.13	0.51	1.80
BK2-6	53.2	39.2	5.4	0.74	0.13	0.11	0.12	0.88
BK2-5	53.4	38.5	5.6	0.71	0.14	0.13	0.22	0.94
BK2-4	53.6	37.3	5.6	0.66	0.13	0.14	0.47	2.08
BK2-3	53.4	38.0	5.2	0.68	0.14	0.12	0.29	1.69
BK2-2	53.1	38.9	4.8	0.78	0.21	0.12	0.40	1.67
BK2-1	53.6	36.5	5.2	0.76	1.17	0.14	0.47	2.04

Table 5.1: Average chemical composition per thin section of titanomagnetite, determined by microprobe analysis.

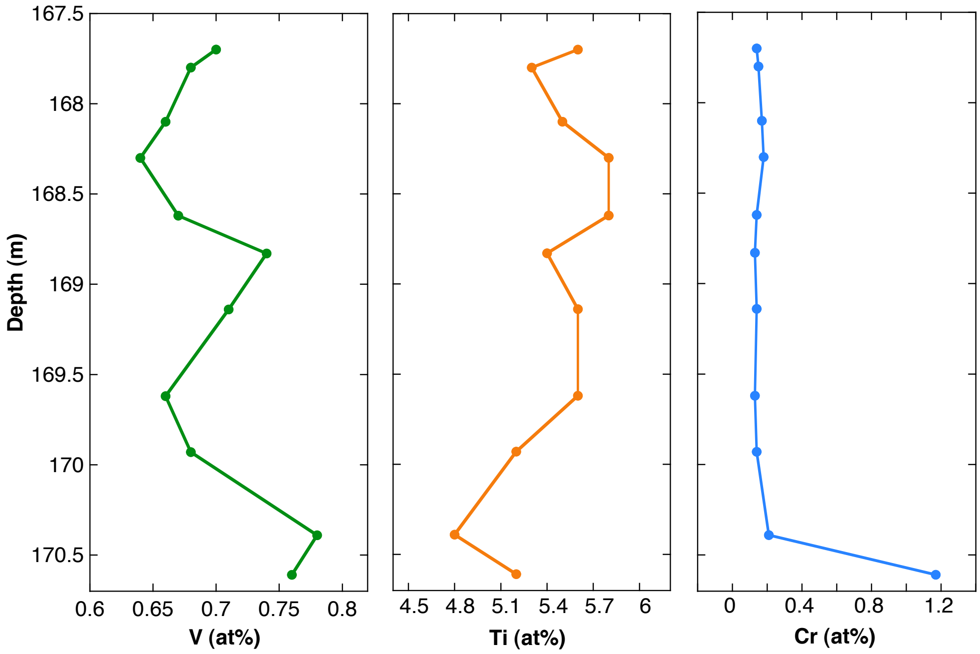

Figure 5.4: Evolution of the V(a), Ti (b) and Cr (c) content through the BK2 profile.

The Fe-Ti oxide geothermometer

The oxygen fugacity is an important parameter in the study of a crystallization process. In natural systems, it is usually controlled by the equilibrium between the silicate and oxide minerals and the magma, and can thus vary with the mineralogical composition. The oxygen fugacity has been calibrated as a function of the temperature for various assemblages of minerals or compounds, called buffers, representing different sets of oxidizing conditions. As an example, iron occurs under two oxidation state in natural systems: ferric iron (+III) and ferrous iron (+II). The relative proportion of each oxidation state in a mineral depends on the oxidizing conditions during the crystallization and therefore on the oxygen fugacity. Iron-bearing minerals form several buffers:

- iron-wüstite (IW) : $2(1\text{-x})\ \mathrm{Fe} + \mathrm{O_2} = 2\ \mathrm{Fe_{1-x}O}$
- wüstite-magnetite (WM) : $\frac{6}{4x-3}\ \mathrm{Fe_xO} + \mathrm{O_2} = \frac{2x}{4x-3}\ \mathrm{Fe_3O_4}$
- magnetite-hematite (HM) : $\mathrm{Fe_2O_3} + \mathrm{O_2} = \mathrm{Fe_3O_4}$
- fayalite-magnetite-quartz (FMQ) : $3\ \mathrm{Fe_2SiO_4} = 2\ \mathrm{Fe_3O_4} + 3\ \mathrm{SiO_2}$

another commonly used buffer is the nickel-nickel oxide (NNO) buffer : $\mathrm{Ni} + \mathrm{O_2} = 2\ \mathrm{NiO}$. The FMQ, IW and NNO buffers are shown in figure 5.5.

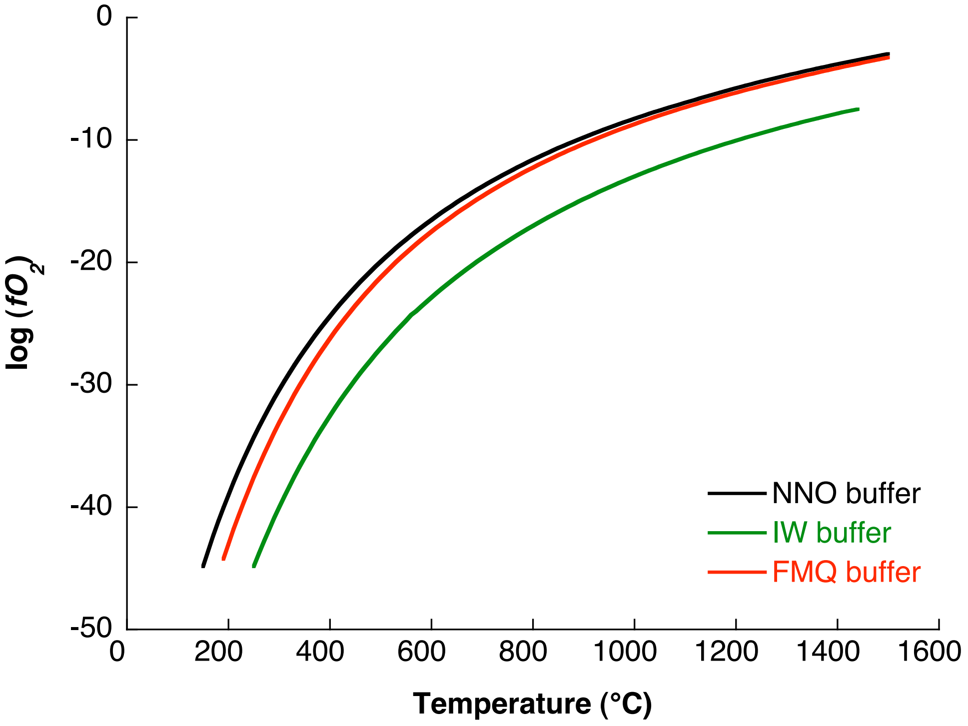

Figure 5.5: Evolution of the oxygen fugacity as a function of the temperature for the Faylaite-Magnetite-Quartz (FMQ), Iron-Wüstite (IW) and Nickel-Nickel Oxide (NNO) buffers

The range of temperature and oxygen fugacity in magmas is most conveniently obtained from the composition of coexisting Fe-Ti oxides [47]. Fe-Ti oxides geothermometry have thus been developed to be used in igneous and metamorphic petrology and several models have been proposed [167, 193, 4] to determine the equilibrium temperature. The ILMAT Excel worksheet [138] summarizes some of these models in a user-friendly program, oriented on the ilmenite-magnetite geothermometer. It calculates the equilibrium temperature and the oxygen fugacity using the electron microprobe data for Fe-Ti oxides. The magnetite and ilmenite oxide values in weight percent are first summed. The total iron is partitioned into FeO and $\mathrm{Fe_3O_4}$, using the method of Carmichael [45] and the sum of atomic molecular proportion is then calculated. After the calculation of the cation proportion for ulvöspinel and ilmenite, it determines the molecular fraction of ulvöspinel and ilmenite with respect to their solid solutions for four models [45, 5, 140, 196]. Finally, the equilibrium temperatures and oxygen fugacity are calculated using the geothermometer from Spencer and Lindsley [193] and Andersen and Lindsley [4].

Results

The oxygen fugacity in the BK2 samples was determined with the geothermometer from Spencer and Lindsley [193]. It was also calculated with the geothermometer from Andersen and Lindsley [4] but no significant differences were observed in the oxygen fugacities. The equilibrium temperatures determined by the program vary between 200°C and 610°C, depending on the model used to calculate the molecular fraction of ulvöspinel and ilmenite. The complete set of results is presented in App. D. The oxygen fugacities so obtained and the NNO buffer are compared in Fig. 5.6. The oxygen fugacities determined for the BK2 samples are far from the NNO and FMQ buffers whereas it was expected that they would be close to these buffers. Indeed the estimated oxygen fugacity at the time of saturation of magnetites from the Bushveld Complex is close to the FMQ buffer [174, 54].

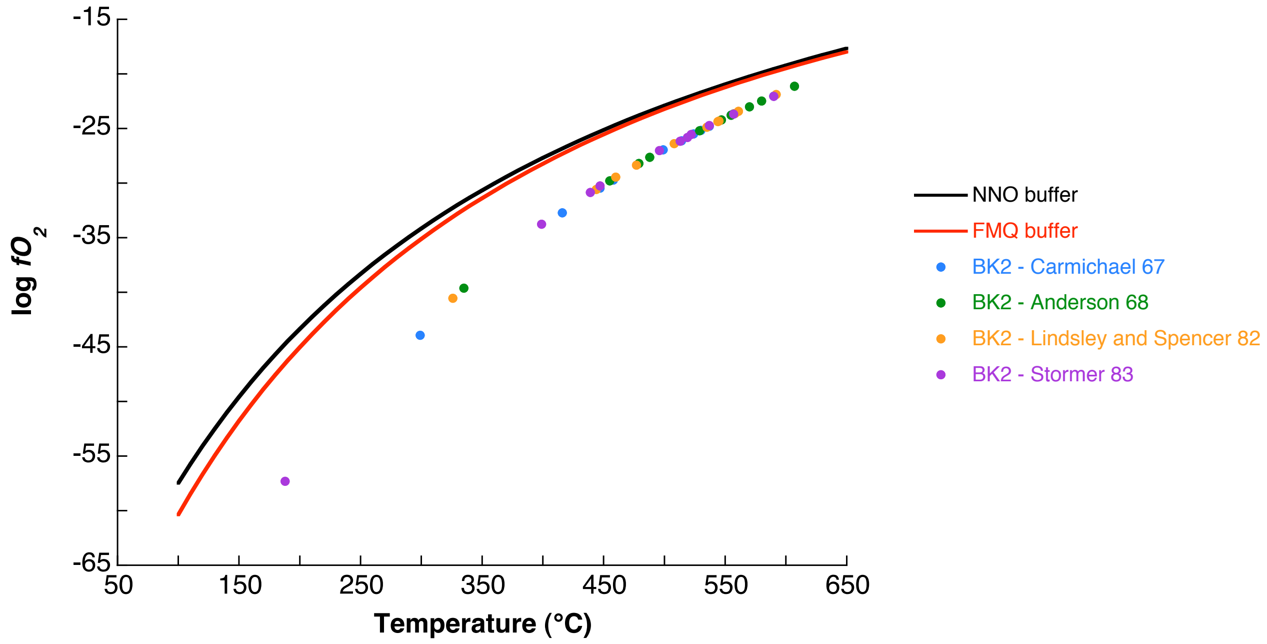

Figure 5.6: Comparison between the NNO buffer, the FMQ one and the oxygen fugacities of the BK2 samples determine with the geothermometer from Spencer and Lindsley [193] for the four models used to calculate the molecular fraction of ulvöspinel and ilmenite.

These differences can be explained by the fact that ILMAT's applicability is more for lavas than slowly cooling igneous bodies like the Bushveld Complex [174]. Indeed, as the Bushveld Complex cooled down very slowly, the reacting minerals continuously adapted their compositions as the temperature decreased [28]. The composition of minerals and therefore the temperature and oxygen fugacity that are calculated from the magnetite-ilmenite pairs were recorded when there was no further reaction between the minerals, i.e. when the reaction kinetics become negligible.

To follow the evolution of the oxygen fugacity throughout the BK2 borehole, the oxygen fugacities were recalibrated to standard temperatures of 500°C, 1000°C and 1200°C (Table 5.2). The molecular fraction of ulvöspinel and ilmenite was calculated with the procedure described by Lindsley and Spencer [140]. The oxygen fugacity thus varies between $log\ f_{O_2}$ = -34.9 and $log\ f_{O_2} = -23.8$. The evolution of the oxygen fugacity through the profile is illustrated in Fig. 5.7 for an equilibrium temperature of 1200°. This temperature was chosen in order to compare the natural and synthetic samples (Section 5.3.4), the reaction temperature of which being 1195°. The oxygen fugacity significantly increases at the bottom of the profile, from $log\ f_{O_2} = -25.57$ down to $log\ f_{O_2} = -15.9$. Variations between $log\ f_{O_2} = -15.9$ and $log\ f_{O_2} = -19.9$ are then observed, with an important decrease at 168.3 m, followed by a slight increase up to $log\ f_{O_2} = -16.5$.

Sample	Depth (m)	500°C	1000°C	1200°C
BK2-12	167.7	-25.33	-18.00	-16.47
BK2-11	167.8	-27.76	-20.23	-18.65
BK2-9	168.1	-28.40	-20.83	-19.24
BK2-8	168.3	-26.58	-19.0	-17.41
BK2-7	168.62	-29.06	-21.47	-19.88
BK2-6	168.83	-25.36	-18.13	-16.62
BK2-5	169.14	-23.84	-16.55	-15.02
BK2-4	169.62	-24.94	-17.50	-15.94
BK2-3	169.93	-25.7	-18.21	-16.91
BK2-2	170.39	-24.79	-17.48	-15.94
BK2-1	170.61	-34.86	-27.19	-25.57

Table 5.2: Oxygen fugacity of the BK2 samples for three equilibrium temperatures, determined with the geothermometer from Spencer and Lindsley [193]. The molecular fraction of ulvöspinel and ilmenite was calculated with the procedure described by Lindsley and Spencer [140].

5.2.3 V *K*-edge HERFD-XAS measurements

In order to determine the oxidation state of vanadium in the BK2 samples, HERFD-XAS experiments at the V *K*-edge were performed. The pre-edge features were analyzed to determine the vanadium oxidation state in the titanomagnetites. The spectra are first described, then the methodology used to analyze the pre-edge spectral features and finally the so-determined oxidation state of vanadium. Spectra were not recorded for all the points of the thin sections. Only from two to six points per thin section were analyzed by HERFD-XAS because of the limited time available to perform the experiments on the beam-line. The spectrum of each analyzed point was normalized to 1 at 5560 eV and the spectra of a thin section were then averaged to obtain the mean spectrum of the thin section. The pre-edge features were extracted from this mean spectrum. The energy was also rescaled for some samples so that the spectral features have the same energy as in Ref. [10].

The normalized BK2 spectra display the same features through the profile, and no significant variation is observed (Fig. 5.8). The normalized XANES spectrum of BK2-1 is taken as an example to describe the spectral features (Fig. 5.9). The spectrum displays an intense line at 5485.6±0.05 eV and two shoulders at 5475.9±0.1 eV and 5480.9±0.1 eV (Fig. 5.9). An additional feature is present at higher energy (5499.5 eV). The identical edge features suggest that the crystallographic environment of vanadium does not change through the profile. The pre-edge shows three weak contributions: peak A at 5465.6±0.1 eV, peak B at 5467.6±0.2 eV and peak C at 5469.0±0.1 eV (Fig. 5.9, inset). These spectra are characteristic of vanadium in titanomagnetite and are similar to those obtained for titanomagnetites from Mapochs Mine and

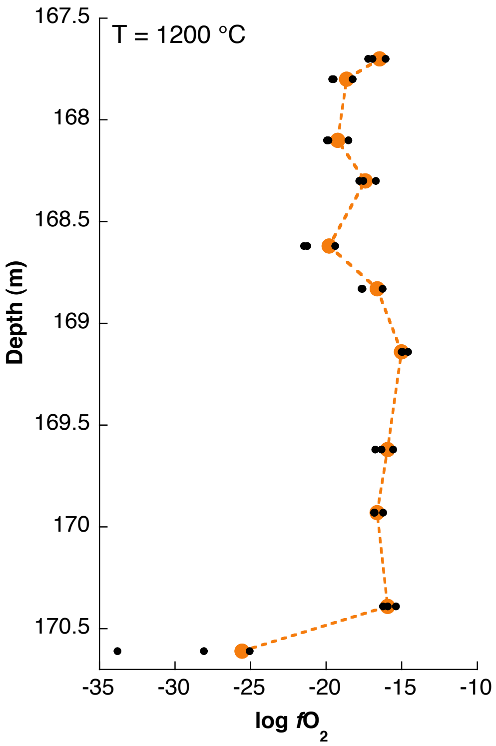

Figure 5.7: Evolution through the BK2 profile of the oxygen fugacity determined for T = 1195°C with the geothermometer from Spencer and Lindsley [193]. The molecular fraction of ulvöspinel and ilmenite was calculated with the procedure described by Lindsley and Spencer [140] (orange point). The black points represents the oxygen fugacity determined with the molecular fraction determined from the three other procedures proposed in the ILMAT program.

BK1 borehole [10]. The vanadium incorporation site in the BK2 samples was thus supposed to be an octahedral site (Sec. 5.1).

However, significant variations are observed among the pre-edge features. To better compare the features through the profile, the pre-edges were extracted from the spectra so that the background is zero before and after the pre-edge. To do so, in the pre-edge region, the edge tail was fitted by a Gaussian which was then subtracted from the measured pre-edge. This process is illustrated in Fig 5.10. Exactly the same procedure was applied to all the samples so that no artefact due to the fit would interfere in the comparison of the extracted pre-edges through the profile. The parameters of each Gaussian are given in App. D.

The extracted pre-edges are displayed in Fig. 5.11. Variations are clearly observed among the samples, in particular for peaks B and C which present an increasing contribution for some samples. The area under the extracted pre-edge (between 5463 and 5472 eV) was then determined in order to quantify these variations. The corresponding values are indicated in Fig. 5.11. The most significant variations are observed in the case of samples BK2-2 and BK2-3.

Following the hypothesis made by Balan *et al.* [10], these variations of the pre-edge area were interpreted as the presence of two different vanadium oxidation states in various proportions. The extracted pre-edges were thus compared to the pre-edge of V-bearing reference compounds: tsavorite and cavansite. As said in Chap. 1 and 3, tsavorite is a V-bearing grossular where vanadium sits in a slightly distorted octahedron and occurs only in the +III oxidation state. In cavansite ($Ca(VO)Si_4O_{10}(H_2O)_4$), vanadium occurs in the +IV oxidation state and sits in a

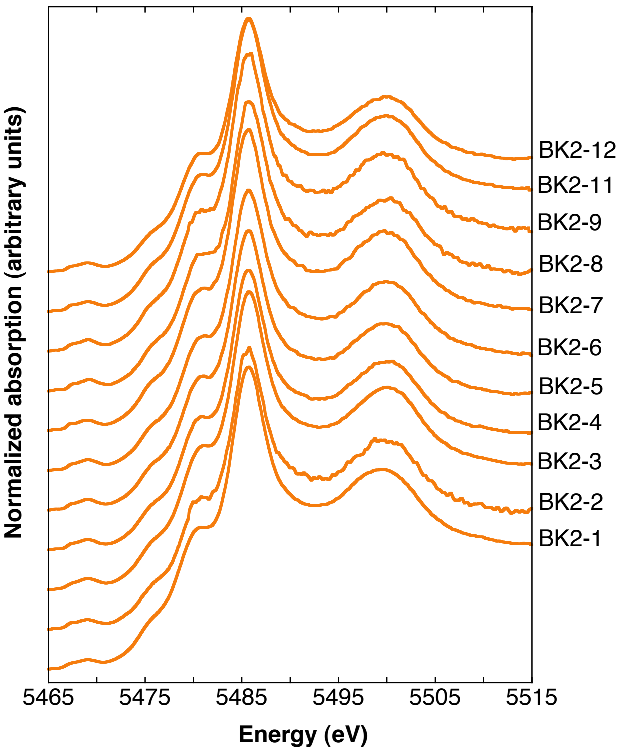

Figure 5.8: Evolution of the V K-edge spectra of BK2 samples through the profile. Each spectrum represents the average spectrum of the thin section.

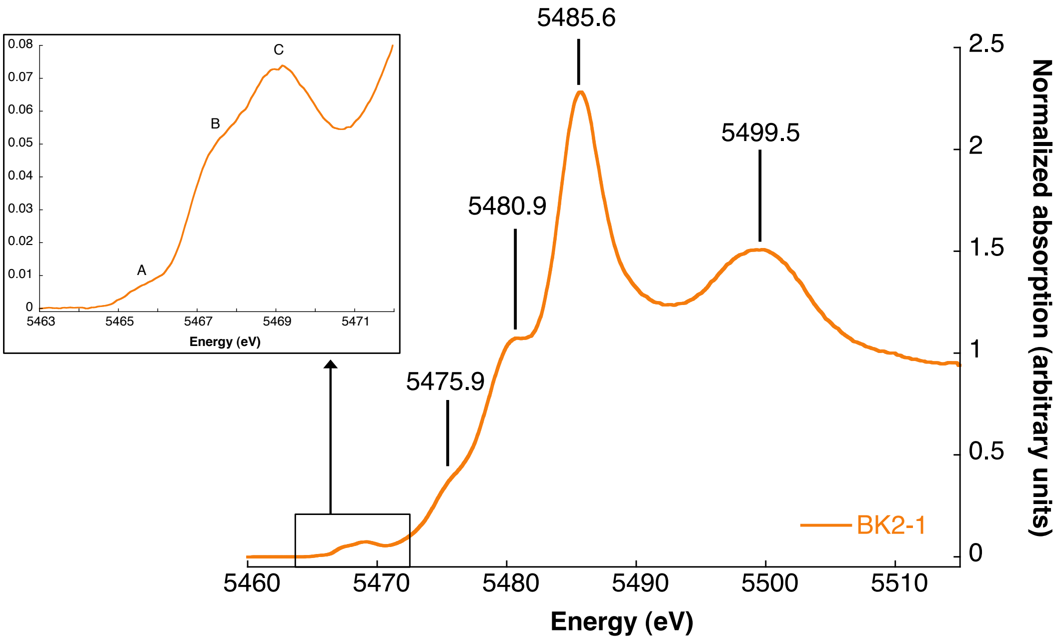

Figure 5.9: Normalized V K-edge spectrum of BK2-1 thin section. The inset represents the pre-edge features.

distorted six-fold environment. The pre-edges of the two reference compounds and of the BK2-1 sample are displayed in Fig. 5.12. The pre-edges of tsavorite and cavansite were extracted with the same methodology than for the BK2 samples. Peak A and B have the same energy as the

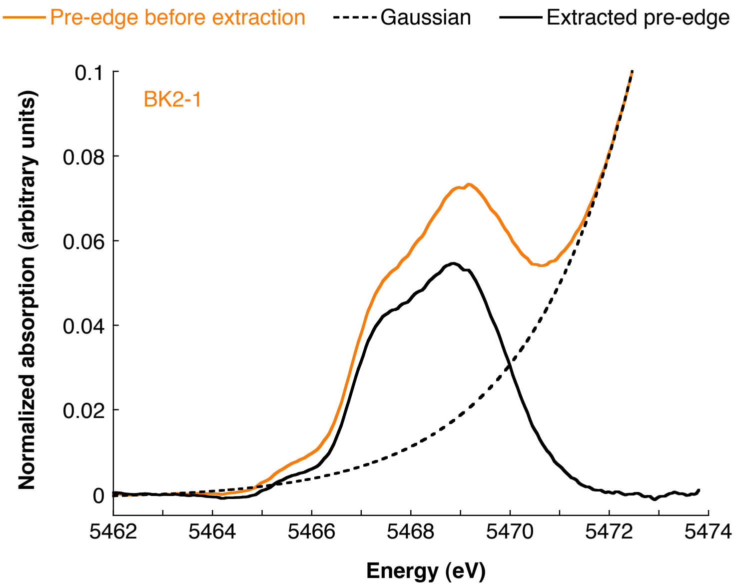

Figure 5.10: Extraction of the pre-edge of the BK2-1 sample. The extracted pre-edge (black solid line) corresponds to the subtraction of a gaussian (black dashed line) to the measured pre-edge (orange line). The gaussian fits the edge tail in the pre-edge region of the spectra.

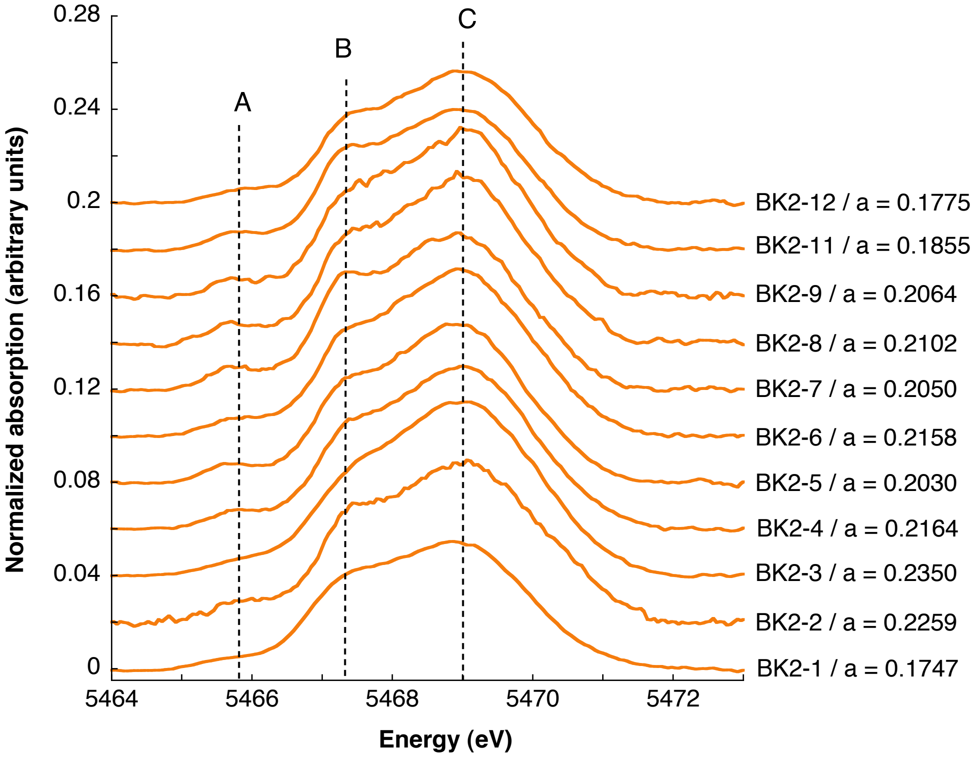

Figure 5.11: Evolution of the V *K* pre-edge spectra of BK2 samples through the profile. Each spectrum represents the average extracted pre-edge of the thin section. The area under each pre-edge is indicated in the right part of the figure.

first two features of the tsavorite pre-edge, which tends to indicate the presence of V^{3+}. However, peak C is significantly more intense than in tsavorite and this feature of the BK2 pre-edges is attributed to the presence of V^{4+}. The variations of the pre-edge area are therefore explained as various proportions of V^{3+} and V^{4+} oxidation states, the increasing of peak C meaning an increase in the V^{4+} content with respect to the V^{3+} one.

To determine the quantity of V^{4+} in the samples, the area under the extracted pre-edge of the BK2 samples was compared to the area under the extracted pre-edge of the two reference samples. The area under the pre-edge of tsavorite and cavansite was determined for the same energy range (9 eV). For tsavorite, the pre-edge was extracted from the isotropic spectrum, which was obtained from the two spectra presented in Chap. 3. The measurements were indeed performed on a single-crystal and the isotropic signal had to be reconstructed from those of two orientations. For cavansite, the pre-edge was extracted from the spectrum measured by Balan *et al.* and presented in Ref. [10]. The resulting areas are $\mathrm{a}_{tsavorite} = 0.0899$ and $\mathrm{a}_{cavansite} = 0.88946$. A linear variation of the pre-edge area as a function of the V^{4+} content was assumed and the following relation was thus established:

$$\mathrm{a}_{BK2} = \mathrm{a}_{tsavorite} \times V^{3+} + \mathrm{a}_{cavansite} \times V^{4+} \tag{5.1}$$

where a_{BK2}, $\mathrm{a}_{tsavorite}$ and $\mathrm{a}_{cavansite}$ are the area under the extracted pre-edge of each BK2 sample, of tsavorite and of cavansite respectively, V^{3+} and V^{4+} the content of the +III and +IV oxidation states. The V^{4+} content in the BK2 samples can thus be calculated with:

$$V^{4+} = \frac{\mathrm{a}_{BK2} - \mathrm{a}_{tsavorite}}{\mathrm{a}_{cavansite}} \tag{5.2}$$

The assumption that no V^{5+} is present is consistent with the temperatures and oxidizing conditions for the crystallization of magnetite.

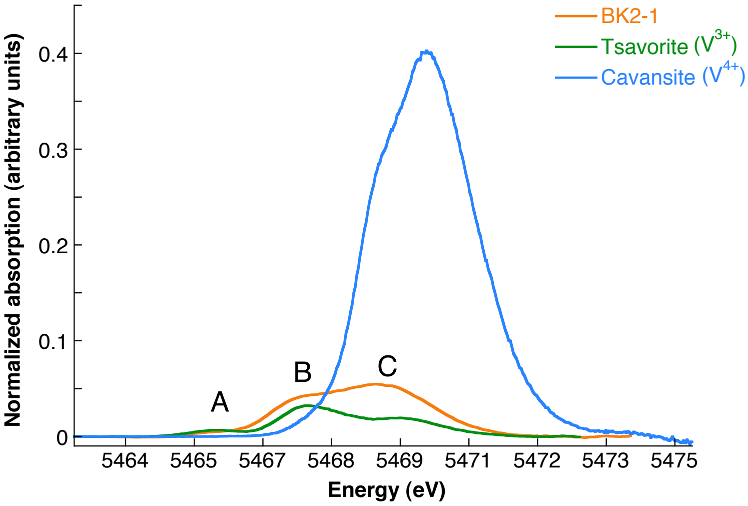

Figure 5.12: Extracted pre-edges of the BK2-1 sample (the orange line), the V^{3+} reference compound (tsavorite, the green line) and the V^{4+} reference compound (cavansite, the blue line).

The V^{4+} content determined from the comparison with the pre-edges of tsavorite and cavansite areas varies between 9.5 % and 16.3 % (Fig. 5.13). The V^{4+} content of each thin section is given in Table 5.3. This V^{4+} content is similar to those determined in the case of the Mapochs Mine and BK1 samples, where it was found to range between 11 % and 17 %. The evolution of the V^{4+} content through the profile is interesting: the V^{4+} content has the lowest values at the bottom and the top of the profile. It increases in the first 0.68 m of the profile from 9.5 % up to 16.3 %, then slightly varies between 13.1 % and 14.3% and finally decreases down to 9.8 % in the last 0.4 m of the profile. The V^{4+} content in the titanomagnetites thus seems to follow the crystallization of the profile: it increases (decreases) at the lower (upper) boundary of the titanomagnetite layer.

Sample	Depth (m)	V^{4+} content (%)
BK2-12	167.7	9.8
BK2-11	167.8	10.7
BK2-9	168.1	13.1
BK2-8	168.3	13.5
BK2-7	168.62	12.9
BK2-6	168.83	14.3
BK2-5	169.14	12.7
BK2-4	169.62	14.2
BK2-3	169.93	16.3
BK2-2	170.39	15.3
BK2-1	170.61	9.5

Table 5.3: V^{4+} content of the BK2 samples determined from the pre-edge area of the V *K*-edge spectra.

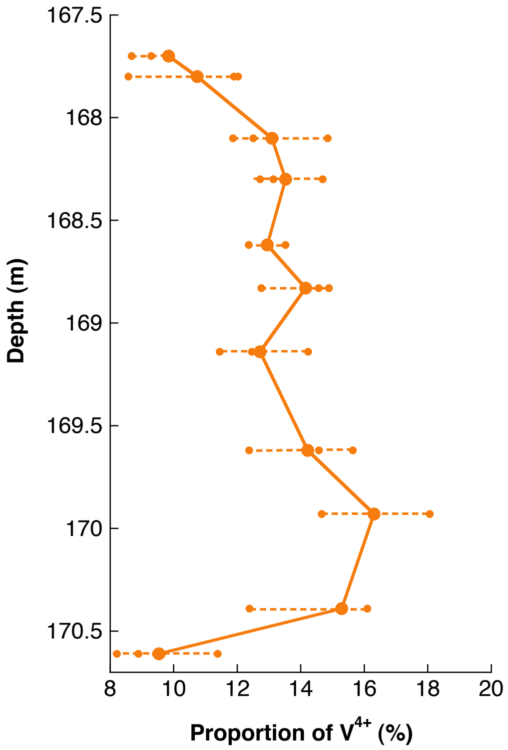

Figure 5.13: Evolution of the V^{4+} content through the BK2 profile, as determined from the pre-edge of the V *K*-edge HERFD-XAS spectra. The big point corresponds to the average value, and eahc small point to an analyzed point of the thin section.

5.2.4 Summary of the natural samples results

The natural samples from the BK2 borehole were characterized by scanning electron microscopy and microprobe analyses. The latter allowed the oxygen fugacity in the samples to be determined using the geothermobarometer from Spencer and Lindsley [193] (Fig. 5.14). HERFD-XAS measurements were performed at the V K-edge of the samples, which display similar features in the edge part. Concerning the pre-edge features, their number is identical for all the samples. A comparison with V^{3+} and V^{4+} allowed the features to be attributed to the presence of two oxidation states, +III and +IV. However, variations in the pre-edge intensity, and especially for peak C, are observed. These variations were attributed to various proportions of the two oxidation states. The V^{4+} content was thus found to vary between 9.5 % and 16.3 %, with the two lowest values found at the bottom and the top of the sequence. Fig. 5.14 presents the evolution through the layer of the oxygen fugacity determined from the microprobe analyses and the V^{4+} content determined from the HERFD-XAS pre-edges. The evolution of the oxygen fugacity follows the variation of the V^{4+} content, indicating that the V^{4+} content in the titanomagnetites may be correlated to the oxygen fugacity. The major differences between the evolution of the V^{4+} content and the oxygen fugacity occur at 169.1 m and at the very top part of the layer (167.7 m), where these two features display an opposite behavior.

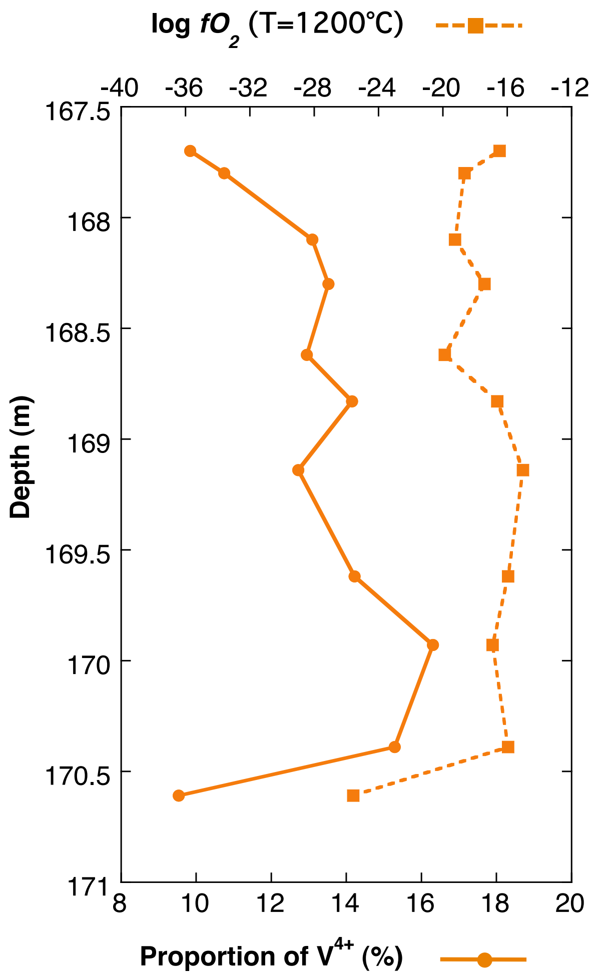

Figure 5.14: Comparison through the BK2 profile of the V^{4+} content, determined from HERFD-XAS experiments, and the oxygen fugacity, determined from microprobe analysis.

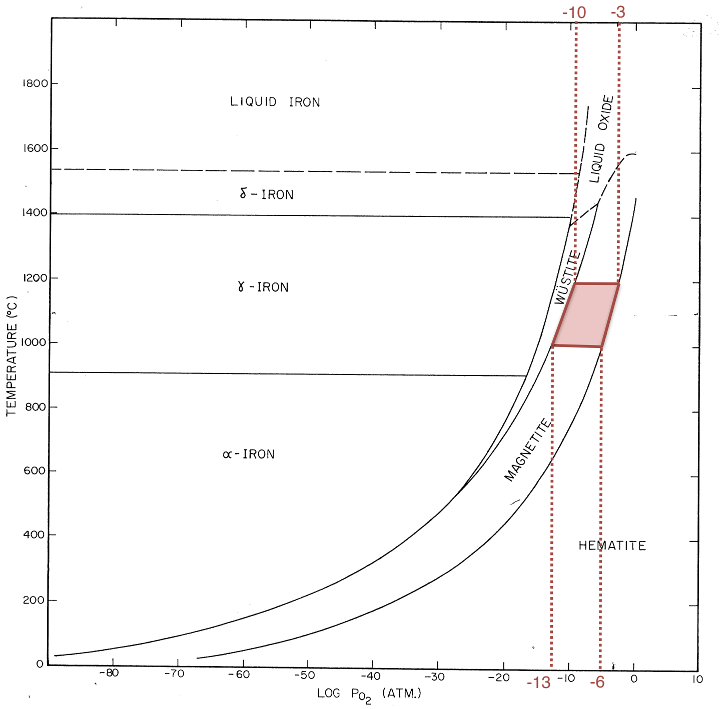

Figure 5.15: Phase diagram of the iron oxides, as a function of temperature and oxygen fugacity. The red zone corresponds to the synthesis conditions.

5.3 The synthesized magnetite samples

Natural titanomagnetite samples from the Bushveld Complex are chemically complex and the interpretation of their XAS spectrum is not obvious. To get information with a simpler, yet similar mineral, synthetic magnetites without Ti were studied. I performed these syntheses at the University of Pretoria (South Africa), in the Department of Materials Science and Metallurgical Engineering. The synthesis procedure consists of heating pellets of hematite (Fe_2O_3) mixed with V_2O_5 under controlled oxygen conditions. I present here the choice of these conditions and the experimental protocol. The final products were characterized by X-ray Diffraction, Scanning Electron Microscopy and microprobe analysis, and V *K*-edge HERFD-XAS measurements were then performed. A comparison between the spectra measured for the natural titanomagnetite and synthetic magnetite is finally presented.

5.3.1 The protocol for the synthesis of vanadiferous magnetite

The magnetite is stable over a determined range of oxygen fugacities (f_{O_2}) and temperatures. The oxygen fugacity is the partial pressure of oxygen. The magnetite stability zone, represented in the phase diagram of the Fe-O system (Fig. 5.15), determines the conditions for which the magnetite crystallizes or also for which an iron oxide evolves to the magnetite phase. For reaction kinetic reasons, two series of syntheses were performed at high temperature: 1000°C and 1200°C. In the case of T=1000°C, the corresponding f_{O_2} range is -13 atm < log f_{O_2} < -6 atm and in the case of T=1200°C, it is -10atm < log f_{O_2} < -3 atm (Fig. 5.15).

The oxygen conditions during the syntheses were controlled with a CO-CO_2 gas mixer. The two gases are mixed in various proportions, depending on the chosen oxygen fugacity, and then injected in the furnace. For a given temperature, the relative proportions of the two gases are tabulated by Deines et al. [70]. However, the maximal gas flow of the gas mixer did not allow the complete oxygen fugacity range to be covered, which had to be substantially reduced. Four syntheses were therefore realized for each temperature (1000°C and 1200°C). Two syntheses were performed in the stability zone and two at its borders : one in very reducing conditions, near the wüstite (FeO)-magnetite buffer and the other in very oxidizing conditions, near the magnetite-hematite buffer.

Pellets of hematite were prepared from a mixture of hematite and 2 wt% V_2O_5. After grinding to a very fine powder, a pellet was pressed (Fig. 5.16) and placed into the furnace during 24h to 72h, depending on the temperature and the oxygen fugacity. During the reaction, the temperature was controlled by a thermocouple (type S) placed in the furnace at the same height as the pellet. The sample was rapidly quenched in air at the end of the reaction. Prior to the syntheses, the gas flow indicated by the gas mixer had been calibrated for each gas. Tests were running to check the absence of O_2 leaks in the furnace and gas mixer, in order to avoid a change in the f_{O_2} value with respect to the one defined by the calibrated proportions of CO and CO_2. The temperature of the furnace was also calibrated as a function of the sample height in the furnace. Indeed, since the furnace is high ($\sim$ 1 m), the precise determination of the hottest zone and most stable in temperature was needed. For the wustite-magnetite buffer, Ar gas was injected in the gas mixer instead of the CO-CO_2 mixture. For the very oxidizing conditions, pure CO_2 (without CO) was injected in the furnace. For the two intermediate f_{O_2} conditions, a CO-CO_2 mixture was injected. The experimental setup is shown in Fig. 5.17: the temperature indicator is on the left, the furnace is the 1m-high vertical tube and the gas mixer is on the right. Table 5.4 presents the experimental conditions of the syntheses (temperature, f_{O_2}, time and CO-CO_2 proportions).

Temperature	1000°				1195°C			
log f_{O_2} (atm)	Ar	-12	-10.7	CO_2	Ar	-9	-7.7	CO_2
CO_2 proportion (%)	0	92	98	100	0	91.4	98	100
Time	72h	72h	48h	72h	24h	24h	24h	24h

Table 5.4: The different synthesis conditions.

5.3.2 Sample analyses by XRD, SEM and microprobe

Eight syntheses were done:

- four at T = 1000°C in the following conditions: one in pure Ar, one in pure CO_2 and two in various proportions of CO/CO_2 mixing, corresponding to log f_{O_2} = -12 and -10.7,
- four at T = 1195°C in the following conditions: one in pure Ar, one in pure CO_2 and two in various proportions of CO/CO_2 mixing, corresponding to log f_{O_2} = -9 and -7.7,

and they were characterized by X-ray Diffraction, Scanning Electron Microscopy and microprobe analysis.

The first analyses performed were the phase identification of the resulting products of the eight syntheses. The identification was done through the qualitative analyses of the XRD patterns (Fig. 5.18). Among the eight syntheses, six resulting samples are magnetite (Fig. 5.18

Figure 5.16: A hematite pellet before heating. The red fine rod is the thermocouple used to measure the temperature inside the furnace

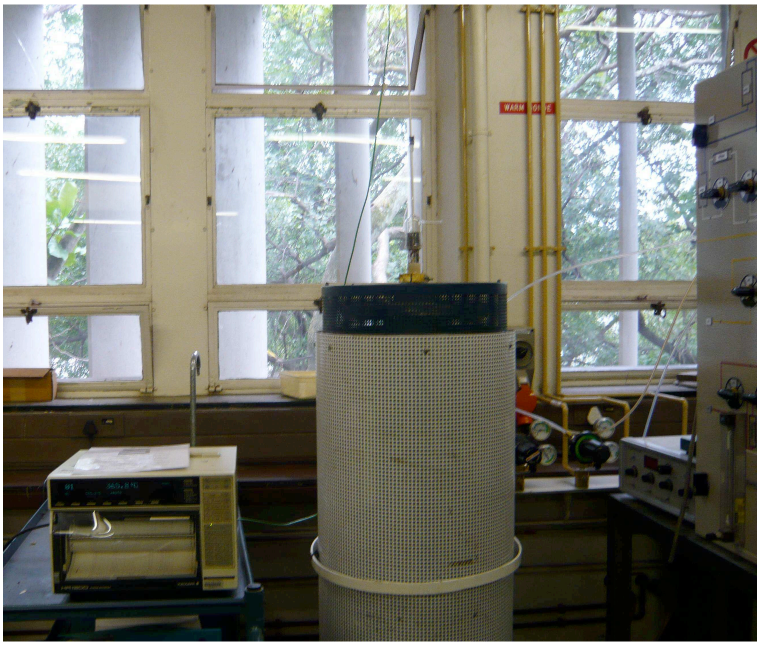

Figure 5.17: Furnace used for the magnetite syntheses (the white cylinder in the center), with the temperature indicator (on the left) and the gas mixer (on the right). The gas was injected from the bottom of the furnace.

a). Two synthesis conditions did not allow magnetite to be obtained as the final product. For T = 1000°C with pure Ar, the hematite evolutes to wüstite FeO, meaning that the conditions were too reducing to obtain magnetite (Fig. 5.18 b). On the contrary, for T = 1000°C with pure CO_2, the conditions were too oxidizing to fully reduce the hematite into magnetite. Both phases are therefore present in the sample (Fig. 5.18 c).

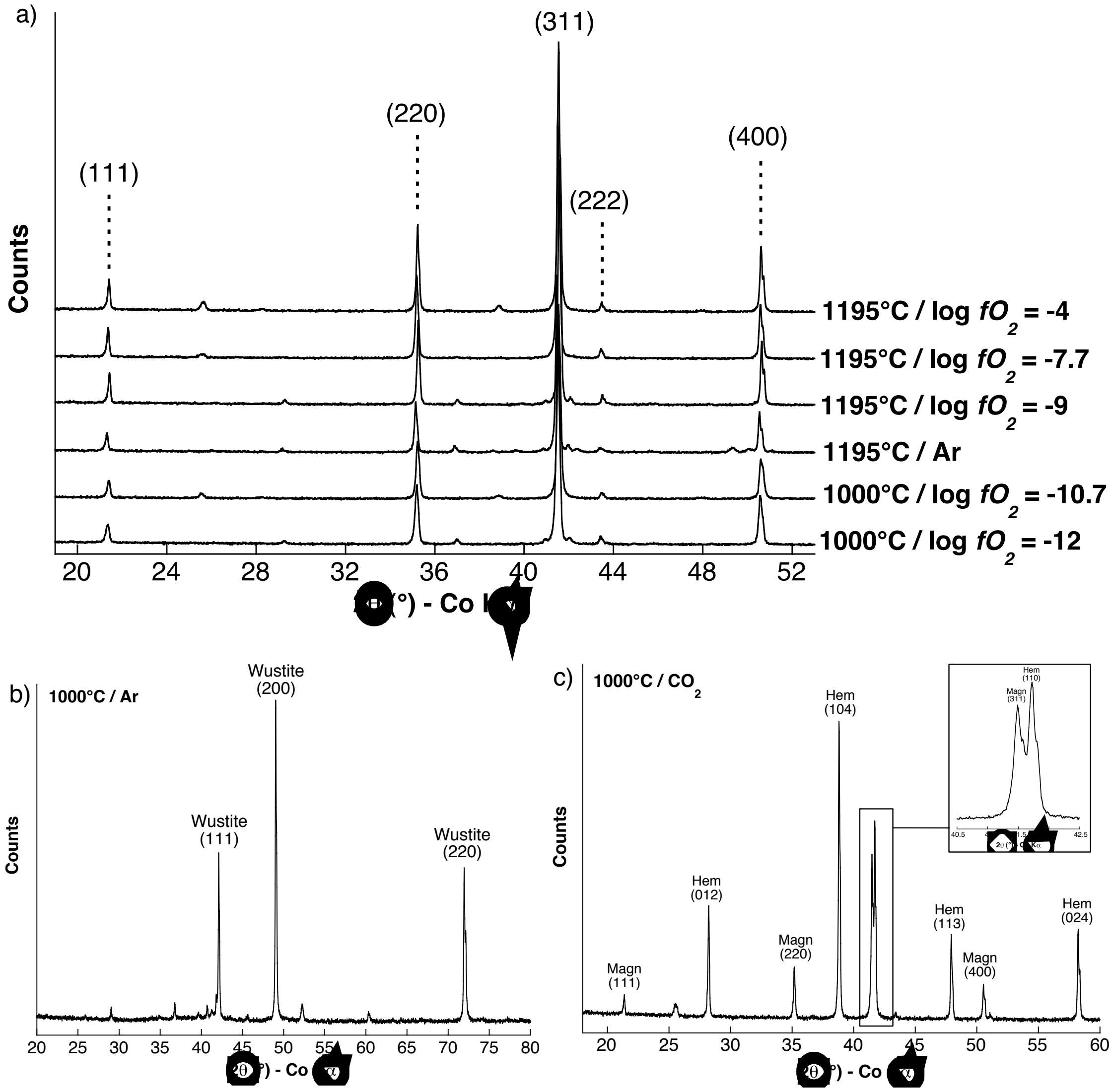

Figure 5.18: X-ray diffraction patterns of the synthesis products. *(a)* Samples with magnetite (Fe_3O_4) as the resulting phase. *(b)* Sample with wüstite (FeO) as a final product. *(c)* Sample with hematite (Fe_2O_3) and magnetite as final products.

The homogeneity of the samples was checked by performing Scanning Electron Microscopy. Images were taken for the eight samples and EDS analyses were performed for preliminary chemical analyses, in particular to see if the vanadium was incorporated in the present mineral phases. All the samples present homogeneous features, and the chemical analyses confirmed the presence of the phases identified by XRD. Fig. 5.19 illustrates the homogeneity of the synthesized samples through the example of the synthesis performed at 1195°C and log f_{O_2} = -7.7.

Microprobe analysis was finally performed on three samples obtained for the following synthesis conditions: T = 1195°C, log f_{O_2} = -9, -7.7, -4 (the latter corresponds to the synthesis

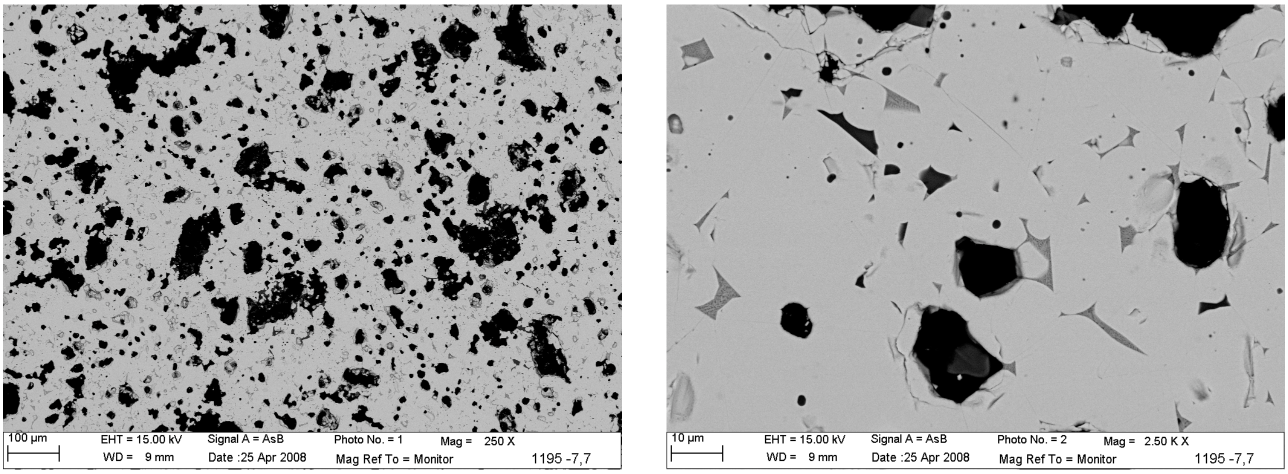

Figure 5.19: SEM images of the sample synthesized at T = 1195°C and log f_{O_2} = -7.7, illustrating the texture of the synthesized samples.

done in pure CO_2). The vanadium is present in similar concentration as in the natural samples:

- T = 1195°C, log f_{O_2} = -9 : V = 1.07 at%,
- T = 1195°C, log f_{O_2} = -7.7 : V = 1.25 at%,
- T = 1195°C, log f_{O_2} = -4 : V = 0.9 at%.

The two major components are iron and oxygen. Calcium, titanium, manganese and magnesium were found as trace elements, *i.e.* with a concentration lower than 0.05 at%. A small contamination by silica, aluminum and chromium was also observed, with a concentration lower than 1 at%. The homogeneity of the chemical composition of the samples was carefully checked by analyzing different points across the samples.

5.3.3 V *K*-edge HERFD-XAS measurements

Since the synthesized samples are well characterized, the V *K*-edge measurements can now be described. Measurements were performed for the eight syntheses. The six samples containing magnetite present identical features, whereas the sample containing wüstite and the one containing hematite and magnetite display significantly different spectra (Fig. 5.20). The spectrum of the magnetite samples, illustrated in Fig. 5.21 through the example of the sample synthesized at T = 1195°C and log f_{O_2} = -7.7, displays an intense line at 5485.6±0.05 eV and two shoulders at 5475.9±0.1 eV and 5480.9±0.1 eV. An additional feature is present at higher energy (5499.5 eV). These features are characteristic of magnetite and similar to the spectra measured by Balan *et al.* [10]. The vanadium incorporation site in the BK2 samples was thus supposed to be an octahedral site (Sec. 5.1). Only three samples were retained for the analyses of the pre-edge features, corresponding to the synthesized conditions T = 1195°C, log f_{O_2} = -9, -7.7, -4. The sample synthesized at T = 1195°C and in pure Ar is not presented with the three other members of the series because the oxygen fugacity could not be precisely determined. The series synthesized at T = 1000°C was not retained because half its samples are not magnetite. The pre-edge of the three retained samples were extracted using the same methodology than for the BK2 samples, and so was determined the V^{4+} content. The three pre-edges are displayed in Fig. 5.22 and the corresponding area is indicated. The V^{4+} content was found to be 19.7 % for the (T = 1195°C, log f_{O_2} = -9) sample, 22.4 % for the (T = 1195°C, log f_{O_2} = -7.7) sample and 23.6 % for the (T = 1195°C, log f_{O_2} = -4) sample. This increase of the V^{4+} content is consistent with the increase of the oxygen fugacity: the more the syntheses conditions were oxidizing, the higher the V^{4+} content is.

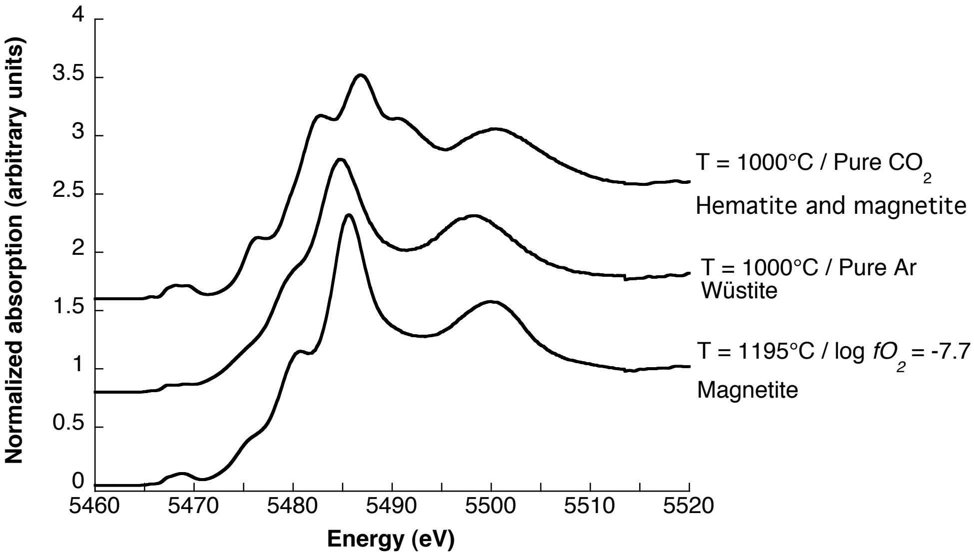

Figure 5.20: V *K*-edge HERFD-XAS spectra of the three samples containing respectively magnetite (T = 1195°C, log f_{O_2} = -7.7), wustite (T = 1000°C, pure Ar) and hematite + magnetite (T = 1000°C, pure CO_2).

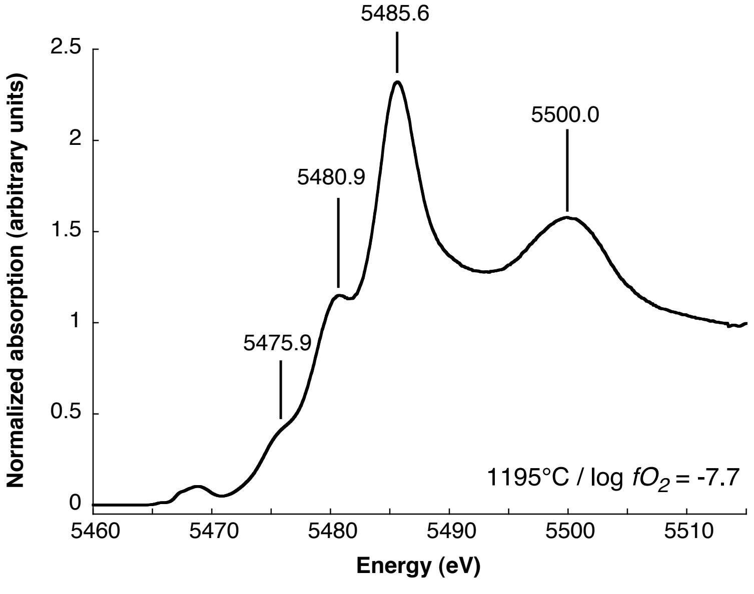

Figure 5.21: V *K*-edge HERFD-XAS spectrum of the (T = 1195°C, log f_{O_2} = -7.7) sample, illustrating the features observed in the six synthesized samples containing magnetite.

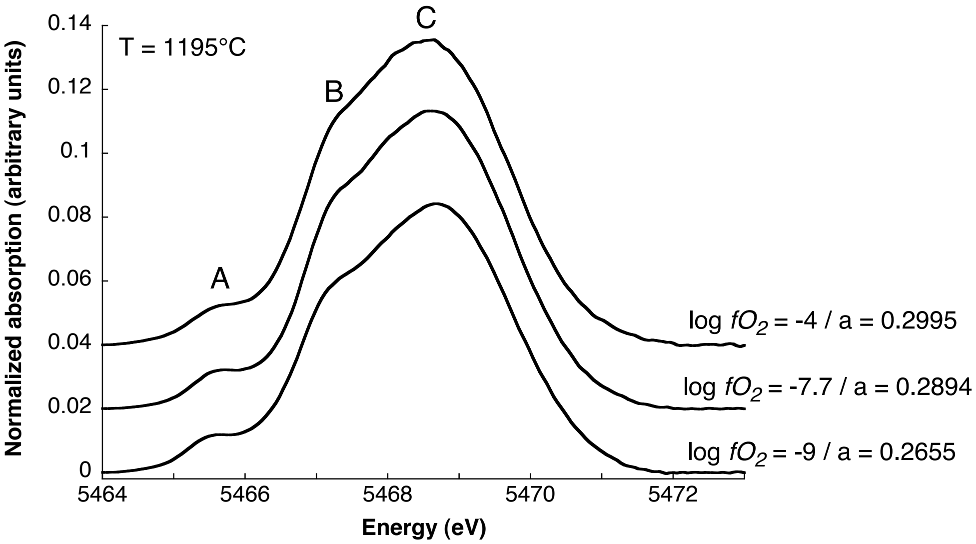

Figure 5.22: The V *K* pre-edges measured for the (T = 1195°C, log f_{O_2} = -9), (T = 1195°C, log f_{O_2} = -7.7) and (T = 1195°C, log f_{O_2} = -4) samples.

5.3.4 Comparison between the natural titanomagnetite and synthetic magnetite spectra

The studied natural samples are titanomagnetites $Fe_{3-x}Ti_xO_4$ whereas the synthetic samples are pure magnetite Fe_3O_4. Two representative spectra of the natural titanomagnetite and synthesized magnetite samples are compared in Fig. 5.23. The edge features are identical in energy and relative intensity, except for the structure at 5499.5 eV, the energy of which increasing of 0.5 eV in the case of magnetite samples. The three peaks (A,B and C) of the pre-edge are also present for both titanomagnetite and magnetite samples, with similar energy position and intensity. Therefore the oxidation state of vanadium and the symmetry of its incorporation site do not change in the natural titanomagnetite and synthetic magnetite samples. Two interpretations of this similarity can be given. The first one is that titanium has no influence on the vanadium incorporation in the magnetite structure. The oxidation state and local environment would not be conditioned by the presence of titanium. The second possible interpretation uses the SEM images of the natural samples of the titanomagnetites from the Bushveld Complex presented previously (Sec. 5.2.1). The similarity between the spectra of the synthetic and natural samples seems consistent with the SEM observation of the natural samples of the titanomagnetites from the Bushveld Complex. The macroscopic titanomagnetite indeed presents at a micrometric level a matrix of magnetite with ulvöspinel exsolutions (Sec. 5.2.1 and Fig. 5.3). These observations suggest that in the natural samples, vanadium is preferentially incorporated only in the magnetite and not in the ulvöspinel, which would explain why the natural and synthetic spectra are similar.

5.4 Discussion and prospects

V *K*-edge HERFD-XAS measurements were performed for the natural titanomagnetite samples from the BK2 borehole and the synthesized magnetite ones. The experimental spectra were interpreted in the framework of the conclusions made by Balan *et al.* [10]. Variations were observed in the pre-edge features: the intensity of one of the three peaks increases in some

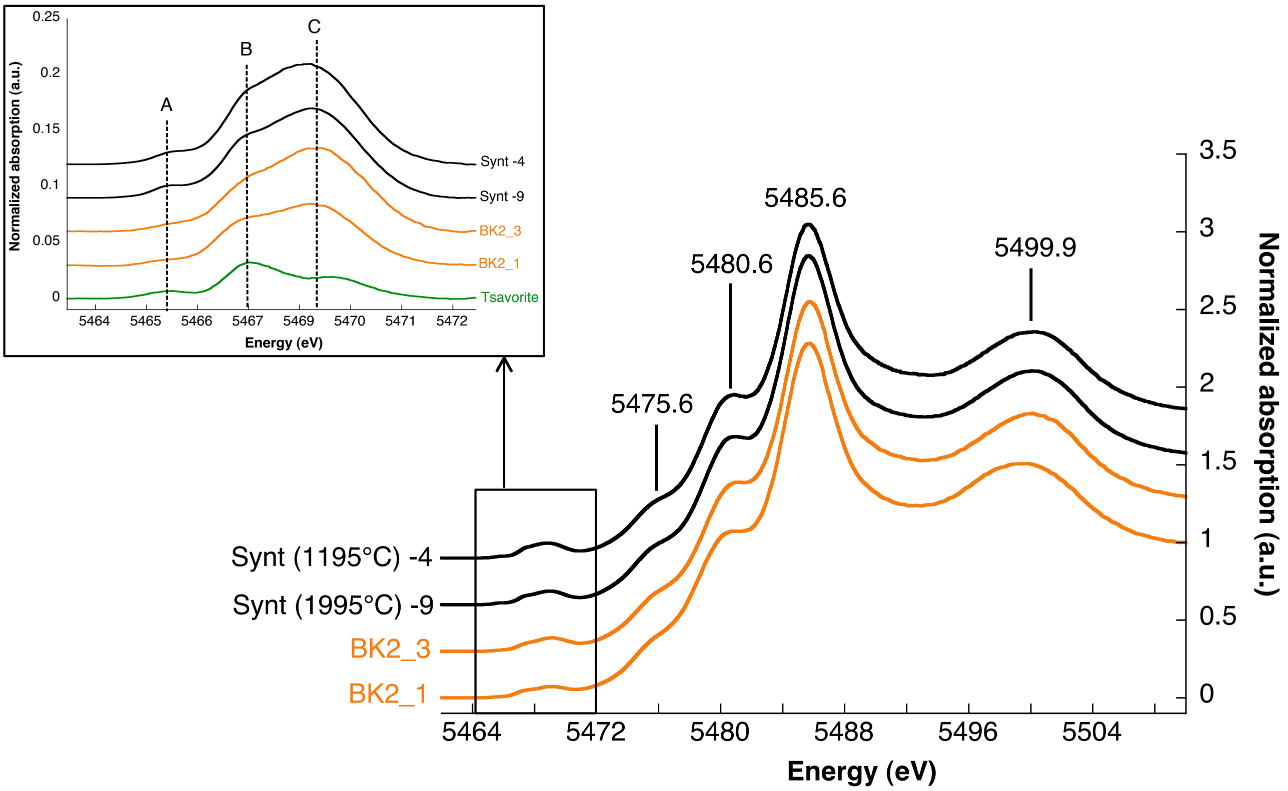

Figure 5.23: Comparison between V *K*-edge spectra of natural titanomagnetites and synthetic magnetites, illustrating the absence of the titanium influence on the vanadium incorporation.

samples. The presence of the +III and +IV oxidation states was deduced from the comparison of the pre-edges features with those of two reference compounds, tsavorite and cavansite, containing respectively only V^{3+} and V^{4+} (Fig. 5.12). The comparison of the respective pre-edge area of the magnetite samples and the two reference compounds allowed the proportion of V^{4+} with respect to the V^{3+} one to be determined. The same analyses were done for the synthetic magnetite samples. The results are consistent between the two kinds of samples.

The interpretation was done under the assumption that the conclusions made by Balan *et al.* were right, and they are not contradicted by the results presented here. Nevertheless it is necessary to complete this interpretation by analyzing some points more in detail and by considering other possibilities. First, there is still some doubt concerning the presence of V^{4+} in the magnetite and a discussion is needed. The references used to infer the vanadium oxidation state are then discussed. Their choice indeed conditiones all the conclusions about the oxidation state and the relative proportions of V^{4+} and V^{3+} (under the assumption that these two oxidation states are present). The symmetry around vanadium also needs to be more precisely characterized, to determine whether the high intensity of the pre-edge is not only related to the symmetry of the vanadium site. Finally, some theoretical and experimental prospects are presented. In particular, the spectral signature of V^{3+} and V^{4+} in magnetite has to be theoretically determined by DFT calculations and the first theoretical results obtained with the FDMNES code are presented. Some experiments are proposed, corresponding to the different questions still open on the vanadium oxidation state in (titano)magnetite. The crucial point for a geological interpretation of the data is indeed to know whether the V^{4+} content in the titanomagnetites provide information on the oxidizing conditions during the crystallization of the layer or was fixed during subsolidus reequilibration.

5.4.1 The remaining doubt about the presence of V^{4+} in magnetite

There is still a doubt concerning the presence of V^{4+} in the octahedral site of magnetite. Indeed the pre-edge peak assigned to the V^{4+} contribution is situated at too low an energy with respect to the energy of the octahedral V^{4+} reference compound. The pre-edge energy and intensity of several reference compounds is reported in Fig. 5.24, which is reproduced from Ref. [197] and completed with the data from Ref. [149] (roscoelite) and from this study (tsavorite, magnetite and cavansite). The position of the magnetite in this graph could suggest that vanadium may occur only as V^{3+} in magnetite, but in a octahedron more distorted than in tsavorite. The high energy of the third pre-edge peak could also indicate the presence of V^{4+} in a strongly distorted octahedron, which would explain the lower energy than in the case of V_2O_4. The incorporation of V^{4+} in the magnetite structure may indeed lead to a distortion of the octahedron and in particular to the loss of the inversion center, since the ionic radius of V^{4+} is much smaller that the Fe^{3+}: $r_{V^{4+}} = 0.58$ Å and $r_{Fe^{3+}} = 0.645$ Å, respectively [189]. Consequently, if the V^{4+} content is small and that the V^{3+} is the dominant oxidation state, the influence of V^{4+} may not be significant enough to slightly shift the pre-edge energy towards higher energy and increase the pre-edge intensity so that the magnetite point would be between the roscoelite and V_2O_4 ones. In this view, the position of the magnetite pre-edge could also correspond to an intermediate oxidation state between V^{3+} and V^{4+}, with vanadium incorporated in a distorted octahedron.

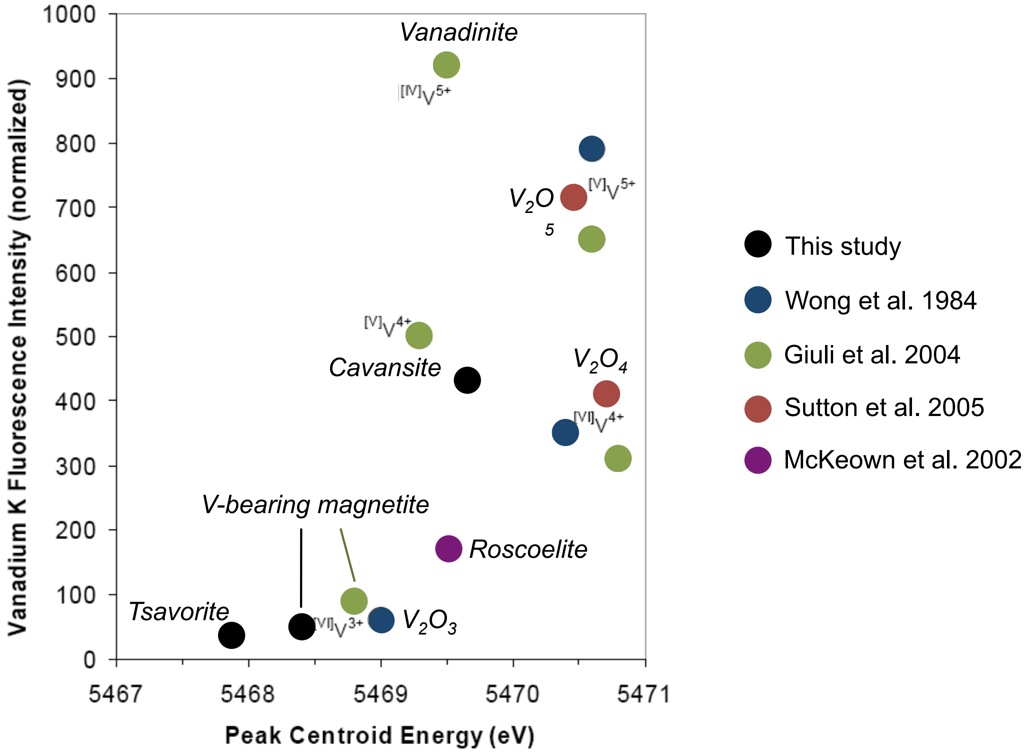

Figure 5.24: Pre-edge intensity *vs.* peak energy of V-bearing compounds, illustrating the variation of the pre-edge features with the oxidation state and coordination number of vanadium (after [197]).

5.4.2 The choice of reference compounds

The two references used to quantify the V^{4+} content in the titanomagnetite samples are tsavorite and cavansite. They were chosen in the first place because the oxidation state and site symmetry of vanadium is well-defined. The choice of these references are discussed here and which other ones could be used. The pre-edge intensity and energy of the reference compounds discussed herefater are illustrated in Fig. 5.24, with the results from Ref. [93], [149] and [224]. The pre-edges of tsavorite and magnetites are also indicated. In the following I talk about titanomagnetite or magnetite without distinction, since the oxidation state and site symmetry of vanadium are not influenced by the presence of titanium (Fig. 5.23).

In tsavorite($Ca_3Al_2(SiO_4)_3$:V^{3+}), vanadium occurs as V^{3+} and is present as a dilute element in the grossular structure. The V-atoms sit in a centrosymmetric octahedron, meaning that the pre-edge arises from pure electric quadrupole transitions and has therefore a weak intensity compared to that of the main edge. A detailed study of the tsavorite pre-edge is presented in Chap.3. This mineral is adapted for a comparison with magnetite because vanadium is present as a diluted element in both minerals and sits in an octahedron with an inversion center. Two other reference compounds could be used: V_2O_3 and roscoelite $K(V,Mg,Al)_2AlSi_3O_{10}(OH)_2$. In both these references, vanadium has the +III oxidation state and sits in an octahedral site. However, in both compounds, the octahedron does not have an inversion center [224]. The pre-edge thus arises from electric dipole and quadrupole transitions and is more intense than in the case of tsavorite [149, 224] (Fig. 5.24). These two compounds are therefore more adapted for the study of the vanadium incorporation in non-centrosymmetric octahedral sites. Moreover, the vanadium is present in concentration much more higher in V_2O_3 and roscoelite, where the vanadium concentration is ∼17 wt% V_2O_3, than in magnetite, where it is lower than 2 wt% V_2O_3. Tsavorite thus offers the advantage to incorporate vanadium in similar proportions as in magnetite.

In cavansite ($CaVOSi_4O_{10}\cdot 4H_2O$), vanadium has the +IV oxidation state and sits in a strongly distorted octahedron with no inversion center. A more detailed presentation of the vanadium octahedron in cavansite is needed here. The octahedron edges consists of five oxygen atoms, with V-O = 1.597 Å, 1.976 Å (×2) and 1.973 Å (×2), and a water molecule, with V-O = 2.887 Å [74]. The octahedron is therefore extremely distorted and the vanadium coordination number is even sometimes considered as only five-fold coordinated [60, 93, 149, 197]. The pre-edge has thus a relatively high intensity since it arises from electric quadrupole and dipole transitions. V_2O_4 may also be used as a reference compound [60, 93, 166, 224]. The vanadium atoms sit in a C_1 symmetry site [224], corresponding to an octahedron without an inversion center. The pre-edge has a lower intensity than cavansite but still significantly higher than V^{3+}-bearing compounds (Fig. 5.24). V-bearing rutile is also a potential reference compound for V^{4+} in an octahedral site. In the rutile structure, vanadium is incorporated in a non-centrosymmetric distorted octahedron (site symmetry D_{2h}). The V K-edge XANES spectra of $Ti_{1-x}V_xO_2$ were recorded for different vanadium substitution rates [166]. Thus a spectrum for a low content in vanadium ($Ti_{0.9}V_{0.1}O_2$, $x = 0.1$) is available for comparison. The latter compound would be more suitable in the case of magnetite where vanadium is present as a diluted element.

The choice of the reference compounds changes the determination of the vanadium oxidation states in magnetite, qualitatively and quantitatively. I consider for the following discussion that vanadium is incorporated in the octahedral site of the magnetite structure and that its incorporation does not change the local symmetry, *i.e.* the octahedron keeps its inversion center.

The local environment around vanadium will be discussed in the next section. Since vanadium is incorporated in a centrosymmetric site and in low concentrations, the pre-edge of magnetite should be similar in position and intensity as that of tsavorite. The comparison with the tsavorite pre-edge shows that the pre-edge of magnetite is slightly more intense, which tends to indicate that vanadium occurs also under the +IV oxidation state in magnetite. However, if roscoelite or V_2O_3 are chosen as reference compounds, their pre-edge intensity is similar to the one of magnetite and the following conclusion is that vanadium occurs only as V^{3+} in magnetite. Besides, magnetite was used as a reference compound for V^{3+} in an octahedral site in a study on synthetic and natural basaltic glasses [93]. On the other hand, if the presence of the +III and +IV oxidation states is retained as the right conclusion, the proportions of V^{4+} and V^{3+} may vary with the references used for each oxidation state. For instance, if V_2O_4 is chosen as the reference compound, the proportion of V^{4+} will increase with respect to the proportion determined from the pre-edge of cavansite, which is more intense than for V_2O_4. Nevertheless, whatever the reference compound chosen for V^{4+}, the relative variations of the V^{4+} content in the synthetic and natural magnetite samples will be identical since the same reference compounds are used for all the samples. The evolution of the V^{4+} content through the BK2 layer determined in Sec. 5.2.3 will therefore remain identical. Only the absolute values of the V^{4+} content will change.

5.4.3 The local environment around vanadium in magnetite

The choice of the reference is therefore crucial to determine the oxidation state of vanadium. However, an important point also to consider is the local symmetry around vanadium in the magnetite structure. The intensity of the pre-edge features indeed varies with the local symmetry, the more significant variations being between a six-fold, five-fold and four-fold coordination. However, in the case of a six-fold coordination, two situations occur and the corresponding pre-edge intensity is different. If the octahedron has an inversion center, the pre-edge arises from electric quadrupole transitions and has a very weak intensity compared to that of the main edge. This is the case of tsavorite. On the contrary, in the absence of an inversion center, the pre-edge arises from both electric dipole and quadrupole transitions and is significantly more intense, as in V_2O_3 and roscoelite. Thus the symmetry of the vanadium site has to be well characterized.

In the magnetite structure, the tetrahedral and octahedral sites are available for cation incorporation. The first point to consider is thus whether vanadium can be incorporated in both sites or in only one of them. Vanadium was shown experimentally and theoretically to incorporate a spinel structure only in the octahedral site [27]. The crystal-field stabilization energy of V^{3+} in oxide structures is indeed lower for an octahedral site (E_o = -160.2 kJ.mol^{-1}) than for a tetrahedral one (E_t = -106.7 kJ.mol^{-1}) [27]. The corresponding octahedral site preference energy, which may be regarded as the affinity of a transition metal ion for an octahedral site in oxide structures such as spinel, is -53.5 kJ.mol^{-1}, indicating a strong affinity of V^{3+} for the octahedral site. The same trend is observed in the case of V^{4+}. Another confirmation that V^{3+} and V^{4+} enter only in an octahedral site is the absence of values for their ionic radii [189]. Therefore, in magnetite vanadium is incorporated in the octahedral site of the spinel structure whatever its oxidation state is (V^{5+} can enter in a tetrahedral site but this oxidation state is not considered here). The second point to consider is the presence of an inversion center in the octahedron, since it changes the transitions involved in the pre-edge. The octahedron of the spinel structure has an inversion center (Chap. 1) and is expected to keep it when vanadium is incorporated in the structure. The ionic radii are indeed close : $r_{Fe^{3+}} = 0.645$ Å, $r_{V^{3+}} = 0.64$ Å and $r_{V^{4+}} = 0.58$ Å, and a strong distortion of the site during the incorporation is not expected. It was indeed shown in several studies that the symmetry was conserved when a cation substitutes for a cation with a similar ionic radius (Chap. 3 and 4) [88, 87, 86, 85, 121, 122, 124, 123, 166]. This conservation of the local symmetry means that the pre-edge intensity is very small compared to that of the main edge, and that consequently both V^{3+} and V^{4+} are present in magnetite. However, if the inversion center is lost during the substitution, the intensity of the pre-edge would be related to a distorted environment around vanadium and not to the presence of two oxidation states.

5.4.4 Theoretical prospects

A theoretical study on the oxidation state of vanadium is also under progress. DFT calculations were performed with the FDMNES code developed by Yves Joly [118, 119]. The purpose of this theoretical study is to characterize the spectral signature of V^{3+} and V^{4+} in magnetite. I present here some calculated results but they are only a preliminary investigation. The calculations were indeed performed with a non-relaxed structure, *i.e.* a vanadium atom was substituted for an aluminum atom without relaxing the atomic positions to fully accommodate the vanadium atom. Tests were conducted for vanadium in a tetrahedral and octahedral sites, and for different oxidation states with vanadium incorporated in the octahedral site. The calculations were performed using the multiple scattering (MS) theory, corresponding to the Green option in the FDMNES code. A calculation was also performed using the Finite Difference Method (FDM). Since the spectra obtained using FDM and MS were similar, the choice was made to perform all the calculations with the MS option to save computational time. A MS calculation was also performed self-consistently to evaluate the reliability of the MS calculations. Since the spectrum was similar to the one obtained without the self-consistency, calculations were not performed afterwards self-consistently. Tests were also performed for four different cluster radii (with V^{3+} in an octahedral site) to determine the most convenient size. The cluster must indeed be large enough to present all the features but small enough so the calculations are reasonably time-consuming. Moreover, for large clusters, features that are not observed in the experimental spectrum can be present in the theoretical spectrum. A compromise has therefore to be found for the cluster radius between, on the one hand, the good agreement with the experimental spectrum in terms of number of features, their energy position and their relative intensity, and on the other hand, the time needed to perform the calculations. The effect of the cluster radius is illustrated in Fig. 5.25. In the case of $r_{cluster} = 4$ Å, the relative intensities of the peaks are not in good agreement with the experiments,and no feature is present in the edge rising at ∼-3 eV for the calculation. The $r_{cluster} = 5$ Å and $r_{cluster} = 6$ Å spectra displays all the experimental features. However, too many features are present in the $r_{cluster} = 7$ Å spectrum, indicating that this value is too large. Since no significant difference is observed between the $r_{cluster} = 5$ Å and $r_{cluster} = 6$ Å spectra, I chose to perform the calculation for a cluster radius of $r_{cluster} = 5$ Å, because the smaller the cluster radius, the faster the calculations.

The first point analyzed with the FDMNES calculations was the vanadium incorporation site. Two calculations were performed for a +III oxidation state with vanadium incorporated in a tetrahedral site and an octahedral one (Fig. 5.26). The tetrahedral spectrum displays an intense pre-edge at -8.2 eV (peak T1) followed by two features in the edge rising at 0.2 eV (peak T2) and 4.9 eV (peak T3), the more intense peak being at 11 eV (peak T4). An additional shoulder is present at 17.4 eV. The octahedral spectrum displays four defined features at -7.9 eV (peak O1), 4.1 eV (peak O2), 9.5 eV (peak O3) and 23.5 eV (peak O4). The two spectra thus present really

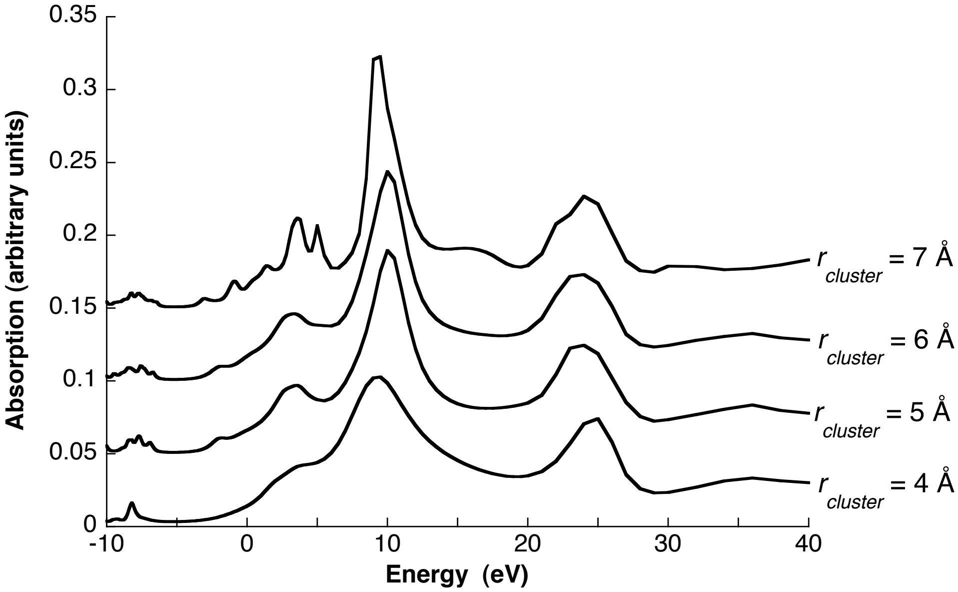

Figure 5.25: Comparison of V K-edge theoretical spectra in magnetite, in the case of V^{3+} in an octahedral site, for different cluster radii.

different features. It is also to be noted that the intensity of the main peak for the tetrahedral spectrum (peak T4) is less intense than for the octahedral one (peak O3). The pre-edge is also significantly more intense in the case of vanadium in tetrahedral site. This is consistent with the absence of an inversion center whereas in the case of vanadium in the octahedral site, the local symmetry is retained and an inversion center is present. The spectrum calculated for vanadium in the octahedral site was then compared to the experimental spectrum. The experimental spectrum was normalized so that the intensity of peak E4 is identical to that of the calculated spectrum (peak O4). The global shape of the edge is well-reproduced with vanadium in the octahedral site, in particular for the energy positions. All the experimental features are reproduced by the octahedral calculations, which confirms that vanadium is incorporated in the octahedral site of the magnetite structure.

In the calculations described below, vanadium is incorporated only in the octahedral site. The second point analyzed with the FDMNES calculations was the influence of the vanadium oxidation state on the pre-edge features. Calculations were thus performed for V^{3+}, V^{4+} and $V^{3.5+}$. The latter oxidation state was calculated because in magnetite, above the Verwey temperature ($T_V = 120$ K), an average $+2.5$ oxidation state is considered for the octahedral iron atoms, related to an electron hopping between the Fe^{2+} and Fe^{3+} ions [213, 226]. The following exchange could thus be expected:

$$Fe^{3+} + V^{3+} \Longleftrightarrow Fe^{2+} + V^{4+},$$

leading to an average oxidation state $+3.5$ for vanadium. The calculated spectra for these three valences are shown in Fig. 5.27. Their energy was not rescaled and corresponds to the one directly given by the calculations. The global shape of the edge and pre-edge features do not vary significantly. The main differences are a shift of the edge features to the higher energies with decreasing the oxidation state, especially for peak O3. The relative intensities between on the one hand, peaks O2 and O3, and on the other hand, peaks O1 and O4, also vary with the vanadium oxidation state. On the contrary, no shift of the pre-edge energy is observed (Fig. 5.27,

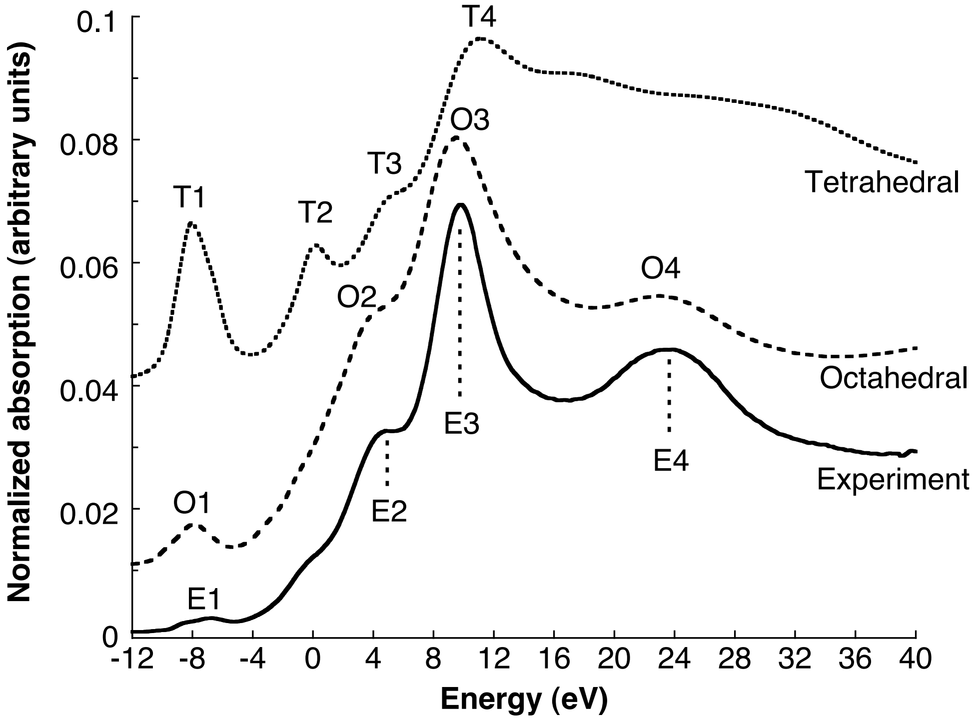

Figure 5.26: Comparison between the V K-edge experimental spectrum of V-bearing magnetite and the calculated spectra for a vanadium in a tetrahedral site and in an octahedral one.

inset). A feature at ~10 eV is present for the V^{3+} pre-edge whereas it is absent for the two other oxidation states. A small similar features was also observed in the pre-edge of tsavorite and in magnetite (Fig. 5.12) and thus could be defined as a signature of the presence of V^{3+} in the octahedral site of magnetite. This would confirm the presence of only V^{3+} in magnetite, but the presence of V^{4+} can not be completely excluded yet.

Nevertheless, in several studies on the vanadium oxidation state determined from XANES experiments, the edge main peaks of the spectra are positioned at the same energy and the pre-edge shifts are discussed (Fig. 5.24) [60, 93, 197]. The theoretical pre-edges of V^{3+}, $V^{3.5+}$ and V^{4+} in the case of an identical edge energy are displayed in Fig. 5.28. The V^{4+} pre-edge is at higher energy than for V^{3+}, as already observed experimentally for reference compounds (Fig. 5.24). The $V^{3.5+}$ pre-edge features are in agreement with this intermediate oxidation state, *i.e.* a continuous evolution can be deduced between the +III and +IV oxidation states. These observations are consistent with the general trend observed for the increase of the vanadium oxidation state in an octahedral site.

The theoretical calculations presented here are the first results of a study still under progress. Some parameters of the FDMNES code need to be tested more in detail. For instance, in these calculations, the oxidation state of iron in the octahedral site was defined as $Fe^{2.5+}$ and no test was performed with two distincts iron with the +III and +II oxidation states. The convergence parameters were also roughly determined. A more detailed investigation of the pre-edge features for the different oxidation states is therefore needed before being able to use the calculations in the interpretation of the V K-edge experimental spectra in magnetite.

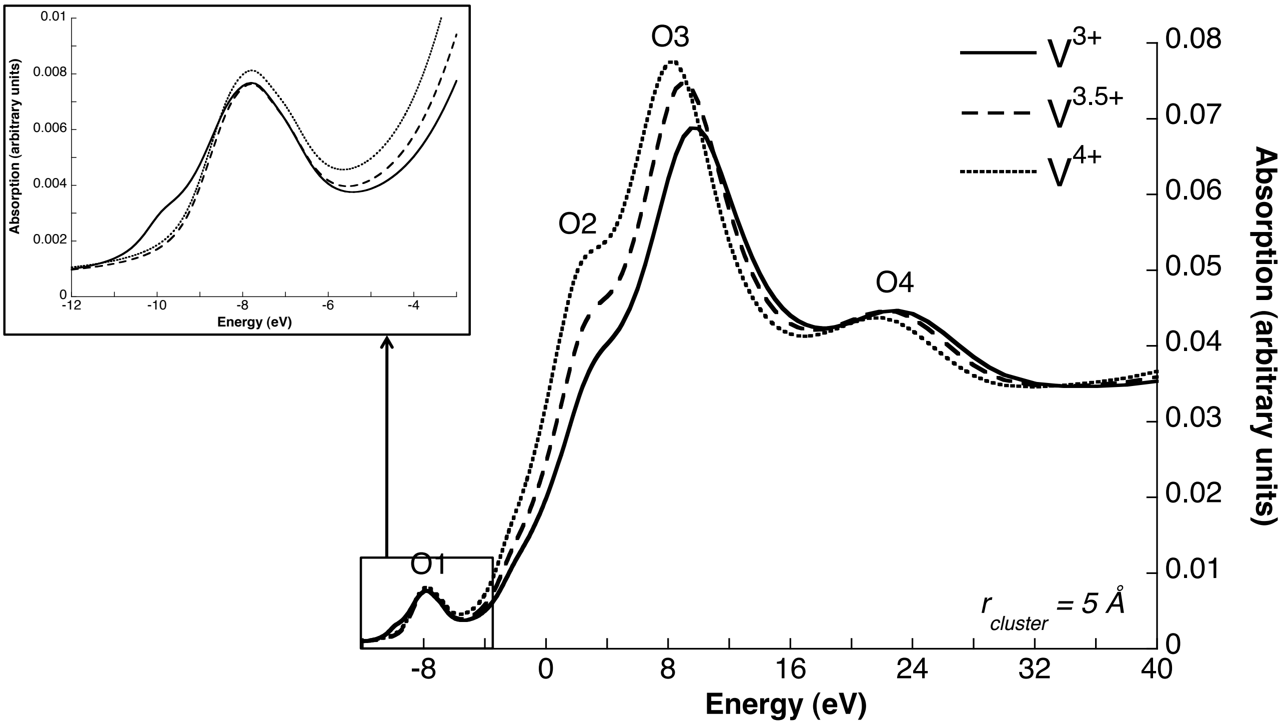

Figure 5.27: Comparison between the calculated spectra for octahedral V^{3+}, $V^{3.5+}$ and V^{4+} in the octahedral site. The energies given here are those calculated by the codes, with no rescaling.

5.4.5 Experimental prospects

A possible way to determine the oxidation state of vanadium is to analyze the V Kβ emission lines. Several studies show that the position of the Kβ emission lines is related to the oxidation state of the investigated element [14, 15, 94, 159, 209]. In particular, Ref. [80] and [84] showed that the energy of the Kβ emission lines for the +III, +IV and +V oxidation states of vanadium present interesting variations. Recording the V Kβ emission lines for reference compounds and natural and synthetic magnetite samples would enable to better characterize the vanadium oxidation state.

This structural characterization of the local environment around vanadium in magnetite still has to be done, experimentally and theoretically. V K-edge EXAFS could provide information on the distances between vanadium and its surrounding oxygen neighbors. The presence of an inversion center could thus be determined. A theoretical relaxation of the magnetite structure with substituted vanadium by an *ab initio* energy minimization calculation (Chap. 2) would also provide information on the distances between the vanadium atom and its neighbors and on the symmetry of the vanadium site. However, these two investigations of the local environment around vanadium in magnetite are not straightforward to perform. For the calculations, the structural relaxation can be done with the PARATEC and Quantum-Espresso codes. However, reproducing the magnetic structure of magnetite is a very challenging task for band-structure codes and requires too much computation time. It was thus not possible to reach a good convergence of the calculations during the time of the thesis and this theoretical study of the local environment around vanadium is still under progress.

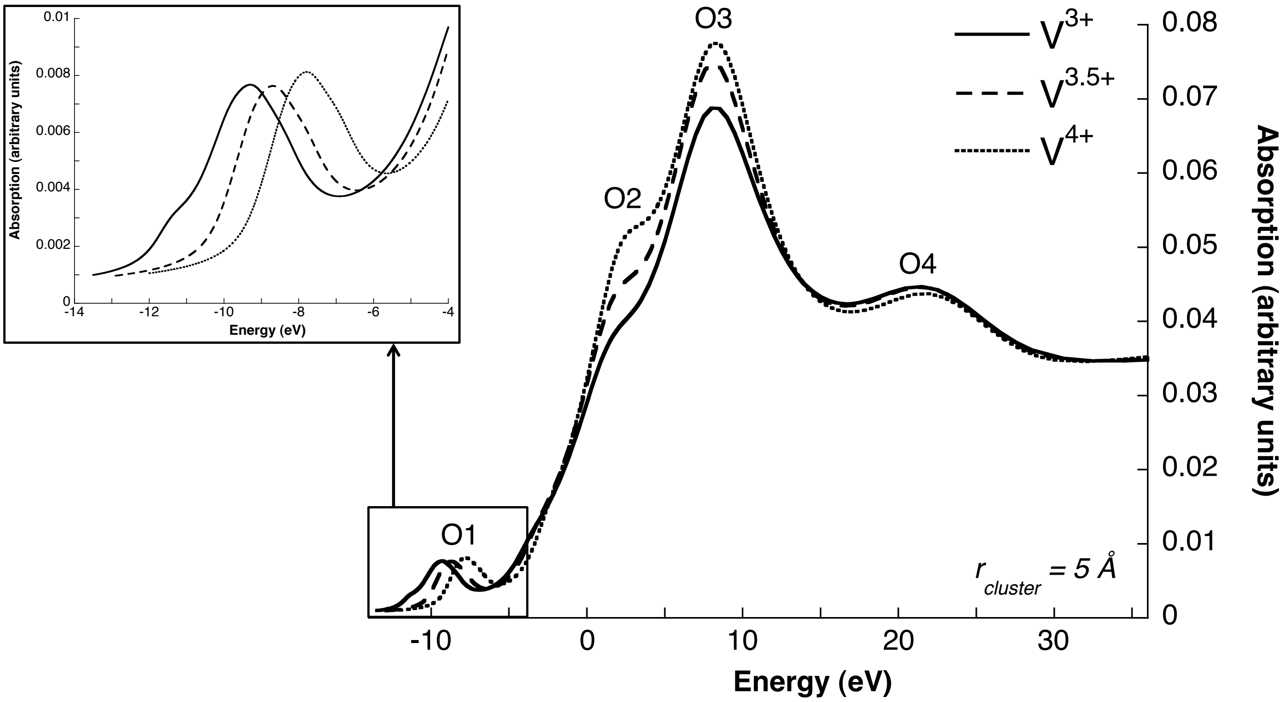

Figure 5.28: Comparison between the calculated spectra for octahedral V^{3+}, $V^{3.5+}$ and V^{4+} in the octahedral site. The spectra were aligned with the V^{3+} energy so that the main edge peak arises at an identical energy.

To complete these experiments and calculations which concentrate on the electronic structure and local environment of vanadium in magnetite, the natural and synthetic magnetite samples could be investigated by Mössbauer spectroscopy at room temperature in order to determine the Fe^{2+}/Fe^{3+} ratio. This technique is indeed sensitive to the iron oxidation state and can distinguish on the one hand between the octahedral and tetrahedral iron sites, and on the other hand between the +II and +III oxidation states in the octahedral site [23, 132, 146, 154, 194]. The Fe^{2+}/Fe^{3+} ratio would provide complementary information on the oxygen fugacity in the samples. In particular, under the assumption that both V^{3+} and V^{4+} are present in magnetite, a relation between the V^{4+}/V^{3+} and Fe^{2+}/Fe^{3+} ratios would indicate whether variations in the vanadium oxidation state reflect variations of the oxygen fugacity during the crystallization of the magnetite layer or whether they are related to a subsolidus reequilibration during the slow cooling of the layer. In that case, the V^{4+}/V^{3+} ratio could only be buffered by the Fe^{2+}/Fe^{3+} ratio in magnetite and provide no information on the layer crystallization. This hypothesis is reinforced by the fact that the variations observed for the V^{4+}/V^{3+} ratio in the titanomagnetite and magnetite samples are are too small with respect to the variations of the oxygen fugacity. More significant variations are expected in the V^{4+}/V^{3+} ratio in the case that this ratio reflects the oxygen fugacity during the crystallization [206, 143]. The determination of the Fe^{2+}/Fe^{3+} ratio in the titanomagnetite and magnetite would thus permit a clear interpretation of the V^{4+} content variations.

5.5 Conclusion

A complete sequence of natural titanomagnetite samples, taken from the BK2 borehole of the Main Magnetite Layer in the Bushveld Complex was studied by microprobe analysis and V K-edge HERFD-XAS experiments. The microprobe analysis allowed the observation that vanadium, titanium and chromium have the general behavior already observed for these elements incorporated in the titanomagnetites from the Bushveld Complex. The microprobe results were used to determine the oxygen fugacity and to follow its evolution through the BK2 sequence. The HERFD-XAS spectra display identical edge features, indicating a similar crystallographic environment around vanadium at the scale of the full crystal. The pre-edge features are also similar for all the samples, in particular in terms of energy position and number of peaks. This suggests that vanadium is incorporated in the titanomagnetite structure with the same local environment and oxidation state. However, variations in the intensity of the third pre-edge peak were observed and interpreted as the presence of vanadium under two oxidation states (+III and +IV) in various proportions, the more intense peak being related to an highest content in V^{4+}. This interpretation of the pre-edge features was done in the framework of the conclusions made by Balan *et. al.* (App. C, [10]). A series of synthesized V-bearing magnetite (without titanium) was then investigated. The study of the V K-edge HERFD-XAS spectra led to identical conclusions as concerning the natural titanomagnetite samples. On the one hand, this similarity suggests that the presence of titanium does not influence the incorporation of vanadium in the magnetite structure. On the other hand, this similarity is also consistent with the SEM observations showing a magnetite matrix with ulvöspinel exsolutions. The vanadium could be preferentially incorporated in magnetite in the natural BK2 samples, which are titanomagnetite at the macroscopic scale. The vanadium site was besides clearly determined: the vanadium is incorporated in the octahedral site of the magnetite structure. This is confirmed by the literature on the cation incorporation in the spinel structure, the pre-edge analysis and DFT calculations with the FDMNES code.

Nevertheless, some questions remained after this interpretation of the pre-edge variations and the presence of two oxidation states may not be the right conclusion. The feature attributed to the V^{4+} signature in the magnetite is situated at too low an energy when compared with octahedral V^{4+} reference compounds. The increase of the pre-edge intensity with respect to the V^{3+} reference compound (tsavorite) could also be explained by the presence of only V^{3+} in the octahedron without an inversion center . The local environment around vanadium has therefore to be precisely determined, by V K-edge EXAFS experiments and DFT relaxation calculations. On the other hand, the presence of only one oxidation state for vanadium would not explain the variations of the pre-edge area (interpreted here as variations in the V^{4+} content) in the BK2 sequence. These variations may however only reflect the Fe^{2+}-Fe^{3+} equilibration in the magnetite during the slow cooling of the layer. Indeed, the variations of the V^{4+} content with the oxygen fugacity do not respect the thermodynamical modeling of the titanomagnetite crystallization. Mössbauer spectroscopy could provide information on the Fe^{2+}/Fe^{3+} ratio and therefore bring complementary information on the phenomenon that the V^{4+} content variations really illustrate. This would also permit the determination whether the vanadium oxidation state is a reliable geochemical probe for the study of the V-bearing titanomagnetites.

Conclusion

The purpose of this thesis was to investigate the oxidation state of vanadium in the titanomagnetites from the Bushveld Complex (South Africa). This study required the study of the electronic and crystallographic structures of vanadium in tsavorite, a V-bearing grossular ($Ca_3Al_2(SiO_4)_3$:V^{3+}). These two studies belong to a more general question, the incorporation of impurities in a host-structure. This general problem of the vanadium incorporation in minerals and synthetic compounds was also tackled through the case of V-doped anatase (TiO_2:V^{4+}).

X-ray absorption spectroscopy is a powerful tool to determine the oxidation state and site incorporation of an impurity in a host structure. To investigate those of vanadium, High-Energy Resolution Fluorescence Detected X-ray Absorption Spectroscopy (HERFD-XAS) experiments were performed at the V K-edge of the three investigated minerals: tsavorite, V-doped anatase and (titano)magnetite. HERFD-XAS is a particular detection mode used to record the XANES spectra: the vanadium Kα_1 fluorescence line was recorded using a high-resolution spectrometer while scanning the incident energy range. It has the main advantage of filtering out the fluorescence which would be present in a conventional XANES spectrum and would interfere in the spectrum of the investigated element. For instance, in the case of titanomagnetites, the Ti K-edge EXAFS signal interferes with the background in the pre-edge of the V K-edge spectrum. Another effect of the HERFD mode is a sharpening effect on the spectral features, leading to better resolved spectra. However, the HERFD spectral features may differ from those measured in a conventional XANES detection mode. Recording a RIXS plane shows whether all the conventional XANES spectral features are detected with the good energy and relative intensity with HERFD. The V K-edge spectra were thus shown to be similar for the three minerals studied during this thesis, but it may not always be such a favorable case. It is to be noted that HERFD-XAS experiments on a single-crystal allow us to take advantage of the natural anisotropy that exists for all the crystals [24] and therefore to obtain a detailed knowledge of the crystallographic and electronic structures of the investigated element.

The analyses of the HERFD-XAS spectra focused on the pre-edge region, as the pre-edge features depend on the oxidation state and site symmetry of the absorbing atom. The interpretation of the experimental pre-edges were done with a fingerprint approach and a coupled experiment-calculation one. In the case of the titanomagnetite samples, the oxidation state had to be determined. The corresponding pre-edge spectra were thus compared to those of reference compounds. This fingerprint method is widely used to determine the speciation (oxidation state and incorporation site) of elements incorporated in glasses or minerals. This method thus requires the oxidation state and site symmetry of the investigated element in the reference compound to be well defined. Indeed a good knowledge of the spectral signature of the reference compound used to infer the speciation of the investigated element is mandatory since it influences the interpretation of the investigated sample spectrum. Variations of the pre-edge intensity can be related to a different oxidation state but also to different a site symmetry (for an identical oxidation state). This importance of the reference compounds characterization was discussed in the particular case of the titanomagnetite samples (Chap. 5) but concerns any investigation on the element speciation in a mineral or a glass.

The fingerprint method is used if the speciation of the investigated element has to be determined. In the case of a mineral in which the oxidation state and site symmetry of the investigated element is well known, a fine interpretation of the XAS spectral features can be obtained by coupling the experiments to a theoretical study. The transitions involved in the pre-edge and edge region of the spectrum can thus be determined, which allows an accurate determination of the spectral signature of the element in the mineral. Two theoretical approaches were presented to calculate the K pre-edge spectrum: the Ligand Field Multiplet Theory was used in the case of tsavorite and the Density Functional Theory for both tsavorite and V-doped anatase. The multielectronic approach is usually dedicated to the localized final states as the $3d$ orbitals and allows only the pre-edge to be calculated. The calculations are indeed performed for an ion embedded in a crystal field and consequently consider only the local symmetry around the ion. On the contrary, the monoelectronic approach enables the calculation of the complete XANES spectrum since it takes into account the complete crystal structure. This approach provides information on the structural relaxation process that occurs when an impurity is incorporated in a mineral. The study of vanadium in tsavorite and V-doped anatase (Chap. 3 and 4) thus showed that during this relaxation process, the local symmetry is retained. The knowledge of the relaxed structure is also of first importance to correctly reproduce the experimental spectrum if no reliable experimental structure is available. The monoelectronic method allowed information to be obtained on the incorporation of vanadium in tsavorite and V-doped anatase since a clear picture of the involved transitions was determined. The multielectronic and monoelectronic calculations also required general theoretical developments based on the spherical tensors formalism. The spherical tensor analysis was applied to the case of X-ray Absorption Spectroscopy in order to get the spectroscopic properties of an individual site from those of the full crystal and vice-versa. The combined use of the spherical tensors analysis, the multielectronic and the monoelectronic approaches is very powerful to get an accurate knowledge of the spectral signature of an element.

The importance of the experiment-calculation coupling was well illustrated for two compounds investigated during this thesis (tsavorite and V-doped anatase). The use of these two approaches allowed us to get an accurate knowledge of the spectral signature of V^{3+} in an octahedral site with an inversion center (Chap. 3). V K-edge HERFD-XAS experiments were performed on a oriented single-crystal in order to measure the angular dependence of the pre-edge. Monoelectronic calculations were performed to get a fine interpretation of the experimental angular dependence. They reproduce well the experiments and the relaxation process showed that the local C_{3i} symmetry is retained when a vanadium atom is substituted for an aluminum one. Multielectronic calculations were also performed but they are still in progress and they do not reproduce well the pre-edge angular dependence yet. A full advantage was taken from the spherical tensors analysis for both calculations.

Information on the incorporation site of vanadium in V-doped anatase were obtained (Chap. 4). The V K-edge HERFD-XAS experiments showed that vanadium is incorporated under the +IV oxidation state but they do not permit a clear determination of the vanadium incorporation site. Monoelectronic calculations were performed at the Ti K-edge of undoped anatase: the isotropic spectrum was calculated and reproduced well the experimental spectrum. The calculations at the V *K*-edge of V-doped anatase were then done for a vanadium incorporated in the Ti-substitutional site of the anatase structure. The calculated isotropic spectrum does not reproduce the experimental pre-edge measured by HERFD-XAS. This observation suggests that vanadium is incorporated in the interstitial site of the anatase structure. Calculations to investigate this hypothesis are under progress.

The oxidation state of vanadium in titanomagnetite from the Bushveld Complex was investigated using the fingerprint method (Chap. 5). Some questions remain open on this last study. The retained conclusion from the investigation of the natural samples taken in the BK2 layer is that vanadium is incorporated in the octahedral site of the magnetite structure under a mixing of +III and +IV oxidation states. This conclusion is consistent with a previous study on the oxidation state of vanadium in the titanomagnetite from other layers of the Bushveld Complex [10] However, the variations observed at the scale of a layer for the V^{4+}/V^{3+} ratio determined from HERFD-XAS experiments and the oxygen fugacity determined from microprobe analyses do not allow us to understand the geological implications of these variations. Further experimental (EXAFS, Mössbauer spectroscopy, emission spectroscopy) and theoretical (monoelectronic calculations with the FDMNES code) studies are needed to correctly interpret the variations in terms of crystallization conditions of the titanomagnetite giant layers in the Bushveld Complex.

The electronic and crystallographic structures of vanadium in minerals is only a small part of the general question on the impurity incorporation in minerals. The approaches used during this thesis to investigate vanadium can bring information to better understand the general process since they can be used for a wide range of minerals and impurities. This problem indeed concerns various domains such as the Earth sciences, materials science or gemology. For instance, in the case of gems, criteria are needed to differentiate their origin, whether they are natural or synthetic, if a treatment was applied to change the color... The coloring impurity content of a gem is related to the geological history of the host-rocks. A detailed study of the incorporation of the coloring impurity in the mineral may bring some answers to these gemological questions. For instance, pegmatitic minerals from the Minaas Gerais region, in Brazil, contain Fe and Cr. The determination of the Fe and Cr incorporation sites may help to understand coloring phenomena. The partitioning of Fe and Cr between co-genetic minerals (*e.g.* emerald $Be_3Al_2(SiO_3)_6$:Cr^{3+} and tourmaline, a silicate mineral) may provide information on the geological processes involved in the ore deposit formation and the general chemistry of pegmatites. The general understanding of the incorporation process of Cr and Fe in these pegmatitic minerals and the related coloration process may enable to propose new criteria to classify gems and also artificial treatments of natural stones in order to enhance their commercial value. Coupled with the geological considerations, clues for an optimal mining exploration may also be found to determine the most valuable ore deposit. The experimental and theoretical methods presented here, with the information provided by the study of the vanadium incorporation in minerals, are the most suitable tools for these investigations.

Appendixes

Appendix A

The characters tables of some groups and the notation of their representations

This appendix presents the equivalences between the Butler's notation that I used in the framework of the Ligand Field Multiplet theory, and the Mulliken's and Koster's notations. The character tables of the O_h, C_{3i} and D_{3d} groups. The table of the O_h is given for the z axis orientated along the four-fold axis of the group symmetry operations. The table of the C_{3i} and D_{3d} groups are given for the z axis orientated along the three-fold axis of the group symmetry operations.

The O_h group is built from the O group with the addition of an inversion center: $O_h = O \times C_i$. The C_{3i} and D_{3d} groups are determined in the same way: $C_{3i} = C_3 \times C_i$ and $D_{3d} = D_3 \times C_i$. The addition of the inversion center results in the distinction between the even irreducible representations (denoted with g) and the odd ones (denoted with$u$).

The complete character tables are given in Ref. [29] and [3].

A.1 The O group

	O		E	$\overline{E}$	$8C_3$	$8\overline{C}_3$	$6C_4$	$6\overline{C}_4$	$3C_2$,$3\overline{C}_2$	$6C_2'$,$6\overline{C}_2'$
0	A_1	Γ_1	1	1	1	1	1	1	1	1
$\tilde{0}$	A_2	Γ_2	1	1	1	1	-1	-1	1	-1
2	E	Γ_3	2	2	-1	-1	0	0	2	0
1	T_1	Γ_4	3	3	0	0	1	1	-1	-1
$\tilde{1}$	T_2	Γ_5	3	3	0	0	-1	-1	-1	1
$\frac{1}{2}$	$E_{1/2}$	Γ_6	2	-2	1	-1	$\sqrt{2}$	$-\sqrt{2}$	0	0
$\tilde{\frac{1}{2}}$	$E_{5/2}$	Γ_7	2	-2	1	-1	$-\sqrt{2}$	$\sqrt{2}$	0	0
$\frac{3}{2}$	$F_{3/2}$	Γ_8	4	-4	-1	1	0	0	0	0

A.2 The D_3 group

D_3			E	$\overline{E}$	$2C_3$	$2\overline{C}_3$	$3C'_2$	$3\overline{C}'_2$
0	A_1	Γ_1	1	1	1	1	1	1
$\tilde{0}$	A_2	Γ_2	1	1	1	1	-1	-1
1	E	Γ_3	2	2	-1	-1	0	0
$\frac{1}{2}$	$E_{1/2}$	Γ_4	2	-2	1	-1	0	0
$\frac{3}{2}$	$^1E_{3/2}$	Γ_5	1	-1	-1	1	-i	i
$-\frac{3}{2}$	$^2E_{3/2}$	Γ_6	1	-1	-1	1	i	-i

A.3 The C_3 group

C_{3z}			E	$\overline{E}$	C_{3z}	$\overline{C}_{3z}$	C_{3z}^{-1}	$\overline{C}_{3z}^{-1}$
0	A	Γ_1	1	1	1	1	1	1
1	^1E	Γ_2	1	1	ω^2	ω^2	ω^4	ω^4
-1	^2E	Γ_3	1	1	ω^4	ω^4	ω^2	ω^2
$\frac{1}{2}$	$^2E_{1/2}$	Γ_4	1	-1	ω	ω^4	ω^5	ω^2
-$\frac{1}{2}$	$^1E_{1/2}$	Γ_5	1	-1	ω^5	ω^2	ω	ω^4
$\frac{3}{2}$	$A_{3/2}$	Γ_6	1	-1	-1	1	-1	1

$\omega = \exp(i\pi/3)$, $\omega^3 =$ -1

Appendix B

The synthesis of V-doped anatase

I collaborated on a study on the effect of V^{4+} substitution in anatase nanowires on their hydrogen production by water photosplitting, which seems a promising way to produce hydrogen with water splitting on photocatalyst. As explained in Chap.4, I performed HERFD-XAS measurements at the V K-edge of the samples, to determine the incorporation site of vanadium in the anatase structure. However, I did not synthesize the samples, neither did I perform the chemical characterization and the photocatalytic experiments. This work is a part of Daniela D'Elia's thesis. She works at the "Ecole des Mines" of Paris, in the "Centre Energétique et Procédés - Laboratoire Systèmes Colloidaux dans les Procédés Industriels", with Jean-Francois Hochepied as a PhD advisor.

The synthesis protocol and the results of the chemical characterization and the photocatalytic experiments are presented in a publication in preparation (for submission in *Journal of Hydrogen Energy*). The HERFD-XAS experiments are included in this publication. To get a complete view of this work, with all the studies of the co-workers, I entirely reproduce the publication hereafter.

Anatase nanowires: effect of V^{4+} substitution on their hydrogen production by water photosplitting.

D'Elia D, Suzuki Y, Berger M-H, Valmalette J-C, Bordage A, Balan E. , Achard P, Beauger C, Rigacci A, Hochepied J-F

(a) Mines ParisTech, CEP/*SCPI* - Center for Energy and Processes, 60 Bd St Michel 75272 Paris Cedex 06, France
(b) Mines ParisTech, CEP/*EM&P*- Center for Energy and Processes, BP 207 1 rue Claude Daunesse 06904 Sophia Antipolis Cedex, France

(c) University of Kyoto, Institute of Advanced Energy, Uji, Kyoto 611-0011, Japan

(d) Mines ParisTech, MAT-Center of Materials, CNRS UMR 7633 BP 87 91003 Evry Cedex, France

(e) University of Toulon and of Var, Laboratory of materials and microelectronic, CNRS UMR 6137 BP 132 F-83957 La Garde Cedex, France

(f) Institut de Minéralogie et Physique des Milieux Condensés (IMPMC), UMR CNRS 7590, Université Pierre et Marie Curie, Université Paris Diderot, IRD UMR 206, IPGP, 140 rue de Lourmel, 75015 Paris, France

Abstract

In this work anatase nanowires have been doped with vanadium by wet impregnation technique using $VO(acac)_2$. After calcination treatment the samples have been characterized by X-ray diffraction, nitrogen adsorption/desorption isotherms applying BET model, Transmission Electron Microscopy, UV-vis diffuse reflectance, Raman spectroscopy, Infrared spectroscopy, HT-XRD, HERFD-XANES. Photocatalytic H_2 production reaction was carried out on TiO_2 suspensions with methanol as electron donor in a closed gas-circulation system using a high-pressure Hg lamp as the light source. Undoped nanowires exhibit a significantly better dihydrogen production as compared to nanoparticles, but V^{4+} substitution practically annihilates water splitting.

1.Introduction

When the first petroleum crisis finished, the researcher focused its attention on environmental problems. The recent increase of worldwide energy demand has obliged to reconsider water splitting on photocatalyst as a promising way to produce hydrogen.

Among many candidates (TiO_2 photocatalysis: Fundamentals and Applications), TiO_2 is the most promising photocatalyst because it is not photocorrosive, it has a strong chemical stability and a photocatalytic activity in the UV due to the value of its band gap. Titania has different polymorphs. The most active is the anatase (Stafford) phase and recently tubular morphology (nanotubes, nanowires…) has received much attention for its very good performance (Kuchibhatla).

The activity of a photocatalyst is affected by its ability to absorb light. Since the UVs represent only 3% of the solar spectrum radiation, shifting the photo-response of the active material in the visible region is the first challenge of the photocatalysis. The second one is to avoid the fast recombination of the photo-generated electron/hole pairs. Concerning the water splitting, the rapidity of the backward reaction should also be also considered:

$H_2 + \frac{1}{2} O_2 \rightarrow H_2O$

Ion doping is one of the most classical technique to improve the photo-response of TiO_2 into visible spectrum. It may as well avoid the fast recombination of the carriers . Among the 21 metal ions studied, (ref. Choi) Fe, Mo, Ru, Os, Re, V and Rh ions have been reported to increase the photocatalytic activity.

Particularly important is the effect of the introduction of V in the TiO_2 lattice (Bettinelli, Zhao, Zhao, Klosek). Wu et al.(Journal of Photochemistry and Photobiology A: Chemistry 163 (2004) 509–515) introduced V^{4+} up to 8% at. in anatase particles by sol-gel method followed by calcination and evidenced a red-shifted absorption responsible of the enhancement of the photocatalytic reactions under visible light. B. Tian et al. (Chemical Engineering Journal, in press) prepared up to 5% V^{4+} doped nanoparticles (90% anatase-10% rutile) by flame spray pyrolysis and evidenced an increased rate of methylene blue photodegradation by 1% V-TiO_2 under visible light.

In the Honda-Fujishima (Fujishima A., Nature 1972) model, TiO_2 was used as the photoactive part of the photoanode, while Pt represented the cathode. TiO_2 nanoparticles can also be directly dispersed in water. Recently, the appealing ease of a suspension system has gained academic interest. In this paper photoactivity tests have been carried out in this kind of reactor (Craig A. Grimes, Springer 2008).

Introducing an electron donor in water is one of the standard technique to avoid the concomitant formation of H_2 and O_2 as well as carriers recombination. In our case, we have used methanol. Possible reactions with methanol are the following (Galinska A. Energy & Fuel 2005):

$CH_3OH \rightarrow HCHO + H_2$
$HCHO + H_2O \rightarrow HCO_2H + H_2$
$HCO_2H \rightarrow CO_2 + H_2$

Hence, hydrogen (from our tests) may be produced both by water and methanol.

In this work anatase nanowires have been used because of the reported activity of tubular morphologies. In order to increase their visible light absorption, they have been doped with V^{4+}, by wet impregnation of protonated titanates followed by calcination. The samples have been tested for water splitting application.

2. Experimental session

The Figure 1 summarizes the TiO_2 doped vanadium nanowires process (références des travaux pionniers). A commercial, fine TiO_2 (anatase) powder (Alfa Aesar, 99.9% purity) was used as a starting material (préciser taille particules). A total of 2 g of TiO_2 powder and 25mL of 10M NaOH aqueous solution were put into a Teflon lined Hastelloy autoclave. The autoclave was heated and stirred at 150°C for 72 h. After cooling down to room temperature, precipitate was washed three times by distilled water. The pH of the suspension was lowered to 2 using a solution 2 M of HCl. After 4 h stirring the solution was centrifuged and washed three times with distilled water. The HCl treatment followed by distilled water treatment was repeated three times.

The particles were doped with V^{4+} by impregnating with $VO(acac)_2$ (Sigma Aldrich 99.99% purity) in order to have the atomic ratio V/Ti = 0.5, 1 and 2%. Three samples have been prepared: S1 (undoped nanowires), S2 (0.5%), S3 (1%), S4 (2%). The suspensions were stirred until the complete dissolution of $VO(acac)_2$ then heated at 100 °C until complete water evaporation. At the end of this stage titanate doped nanowires were obtained.

V-doped titanates were converted to anatase by calcination. The S1 sample was heated in air at 400 °C, S2 at 500 °C and S3 at 600 °C, during 2 h. The ramp was 2 °C/min.

Several techniques were employed for the characterization of the resulting samples.

Dried-powder X-ray diffraction patterns were recorded on a Bruker D8 diffractometer in θ–θ configuration, with Co K_a radiation (λ = 1.789 A°), and equipped with a position-sensitive detector. The HT-XRD measurements were carried out using a Rigaku RINT-2500 multifluex diffractometer (semi-vertical-type goniometer, a PSPC detector, Cu K_radiation operated at 40 kV and 40 mA) with a platinum direct heating stage. A surrounding heater was added to extend the soaking zone, which allowed a sufficient amount of powder to be put on the direct heating stage, and to improve signal/noise ratio. XRD patterns were acquired between room temperature and 800 °C in air after 3 min holding at each temperature (ramp rate: 10 °C/min).

Transmission electron microscopy (TEM Tecnai 20F ST) was used in the analysis of nanowires morphology and the EELS analysis has been used to check the presence of vanadium in the structure. Nitrogen adsorption/desorption isotherms were measured at 77 K using a Micromeritics ASAP2010 model. Specific surface area and pore size distribution were calculated applying the Brunauer–Emmet–Teller (BET) model and Barett–Joyner–Halenda (BJH) method on the desorption branch.

We performed Raman spectroscopy using a Labram HR800 spectrometer. The excitation wavelength used was 514.5 nm (green); laser power 3.2 mW.

Cary 500 UV-VIS-NIR Spectrophotometer has been used to determine the band gap.using the Kubelka-Munch theory.

V-doped anatase nanowires were studied by High-Energy Resolution Fluorescence Detection X-ray Absorption Near Edge Spectroscopy (HERFD-XANES). This technique consists in recording the X-ray fluorescence of the investigated element at a selected emitted energy while scanning the incident energy range, using an energy analyzer with a resolution similar to the core-hole lifetime broadening (De Groot et al. 2009; Glatzel and Bergmann, 2005). Compared with conventional XANES, HERFD-XANES leads to a sharpening of the pre-edge features and filters out the fluorescence of the other elements (e.g. Ti Kβ line), leading to a very low background. Vanadium *K*-edge HERFD-XANES spectra were collected at room temperature at high-brilliance beam line ID26 of the ESRF (European Synchrotron Radiation Facility) (Gauthier et al., 1999). The energy of the incident radiation was selected using a pair of N-cooled Si crystals with a (311) orientation. The spot size of the incident X-ray beam on the sample was 250 x 60 μm^2. Spectra were recorded in a quick scan mode between 5460 and 5815 eV and were normalized to the K-edge jump. The incident X-ray flux was monitored by detecting the radiation scattered by a thin Kapton foil in the incident beam path. The emission $K\alpha_1$ line of vanadium at 4952 eV was selectively detected by employing a spherical bent Ge crystal (R=855mm) with (331) orientation in Rowland geometry and an avalanche photodiode was used as a fast detector to avoid non-linear effects. Self-absorption effects were negligible because of the low V-content of the samples, and no photoreduction effect was observed.

Photocatalytic H_2 production reaction was carried out in a closed gas-circulation system (Figure 2). TiO_2 photocatalyst (0.5 g) was suspended in methanol water solution (10 % vol.); by means of magnetic stirrer within an inner irradiation-type reactor (1000 mL) made of Pyrex (borosilicate glass). A high-pressure Hg lamp (Ushio, UM-452 450 W) was used as the light source. To maintain the temperature constant during the course of reaction, cooling water circulated through a cylindrical Pyrex jacket located around the light source. The gaseous H_2 produced was periodically analysed by an on-line gas chromatograph.

3. Results and discussion

After calcination, samples are single-phased and identified as anatase (Figure 3; JCPDS card n° 71-1166) with cell parameters and crystallite sizes (according to Scherrer) summarized in Table 1. Excepted for S2 which has smaller crystallite sizes (around 17 nm) all the samples have crystallite sizes between 40 and 50 nm. Their specific surface areas are in the range [150-180 m^2/g].

3.1 Microscopic analyses

TEM (Figure 4) shows that 1D morphology was globally maintained after thermal treatment. Nanowires may be found in bundles. According to TEM, wires length ranged from 0.6 to 2 μm and their diameter was around 70 nm. A specific surface area between 150 and 180 m^2/g corresponds to wires diameter around 6.0 (+/-0.5) nm. HRTEM observations (Figure 5) of the wires reveal some dislocations. Although this difference may be due to overlap of structures, we cannot affirm nanowires are monocrystalline. For all the samples, the electron energy loss spectroscopy has been carried out. As shown in the Figure 6, the peaks of Ti, V and

O are present on the same spectrum, proving the presence of vanadium in the structure. A more precise description of the doping was obtained by HERFD-XANES.

3.2 HERFD-XANES results

The normalized HERFD-XANES spectrum of the sample doped with 2% of V (Figure 7) displays two features at 5486.4 and 5504.0 eV, and an additional feature at 5491.3 eV. The shape of the absorption edge is thus similar to that of Ti in anatase (Ruiz-Lopez, 1991; Wu et al., 2002). It significantly differs from that of Ti in rutile or that of V in rutile-type VO_2 (Giuli et al. 2004). This observation suggests that V in the investigated samples is incorporated at the Ti site of the anatase structure.

The pre-edge features observed at the low energy side of the absorption K-edge are related to dipole and quadrupole transitions from 1*s* core states to final states with 3*d* and 4*p* contributions, depending on the local symmetry (Calas and Petiau 1983). The energy and intensity of these transitions depend on the cation oxidation state and site symmetry. They are therefore used to determine the redox state of cations of transition elements in solids (e.g. Giuli et al. 2004; Sutton et al. 2005; Balan et al. 2006). The pre-edge of the V-doped anatase samples displays a strong contribution at 5470.0 eV, with a smaller contribution at 5473.1 eV. Comparing with the numerous data existing on vanadium in reference compounds (Wong et al. 1984; Sutton et al. 2005; Poumellec et al. 1987), the relative intensity of the pre-edge in the V-doped TiO_2 samples are characteristic of a +IV oxidation state (Figure 8). Nevertheless, the energy is too low for a weakly distorted octahedral coordination. The pre-edge energy and intensity better corresponds to a fivefold environment. This suggests that a fraction of V^{4+} ions could be located in interstitial sites of the anatase structure. The interstitial sites in the anatase structure are indeed strongly distorted octahedra. The incorporation of an impurity in this site leads to an even stronger distortion up to a fivefold coordination (Tielens et al. 2005). A partition of V^{4+} ions among substitutional and interstitial sites could thus be inferred by combining edge and pre-edge analysis. Note that the sharpening of pre-edge features in HERFD-XANES spectra may slightly increase their relative intensity, compared with that observed in previous studies performed using classical XANES measurements.

The edge and pre-edge features display no significant change with lower doping levels. It is a strong indication that the vanadium is incorporated in the same sites, whatever the doping level is. The minor differences observed in the spectra are likely related to variations in the sample crystallinity.

3.3 Raman Spectroscopy measurements

Shapes of Raman spectra give informations on effect of doping element in the matrix. The analyses were carried out with a wavelength (λ) of 14.5nm, a laser power (P) of 3.2 mW and for 30 s. Five samples have been analyzed: undoped and doped vanadium nanowires plus commercial V_2O_5. Figure 9 shows spectrum of undoped nanowires while figure 10 shows spectra of doped ones.

Results for undoped nanowires are in agreement with literature (Lei 2001, Chemical Physical Letters). The characteristic mode of V_2O_5 is at 141 cm^{-1}. This mode is absent in any doped materials spectrum. So we can affirm that no V_2O_5 is present in our samples. However the presence of a peak at 1000 cm^{-1} can be ascribed to a V-O bond.

(à compléter)

3.4 Band gap calculation

UV-Vis spectra obtained in diffuse reflectance mode can lead to estimation of the bandgap of semiconductors. This absorption edge corresponds indeed to the photoinduced transfer of an electron from the highest level of the valence band to the lowest level of the conduction band (figure x.x). Such a transition can be direct or indirect, corresponding to a direct or an indirect bandgap. The reflectance essentially depends on three parameters: the absorption coefficient, the scattering coefficient and the thickness of the sample. It is given by the formula:

$$R = (1 - Rg(a - b\coth(bSx)))/(a - Rg + b\coth(bSx))$$

where

- K = absorption coefficient
- S = scattering coefficient
- x = thickness
- $a = 1 + K/S$
- $b = (a^2-1)^2$
- Rg = reflectance of the support

In the case of a thick powder bed, the sample holder (support) has no effect on the reflectance of the sample, which can then be simplified as:

$$R\infty = 1 + K/S - [(K/S)^2 + 2K/S]^{1/2}$$

Where $R\infty$ is the reflectance at infinite thickness.

Solving this equation for (K/S) gives the Kubelka-Munk function:

$$F(R) = K/S=(1 - R\infty)^2/2R\infty$$

The absorption coefficient K can be expressed as*:

$$K \alpha (h\nu - Eg)^n/(h\nu)$$

n = 0.5 for a direct bandgap / n = 2 for an indirect bandgap

where

- h = Planck's constant
- λ = wave number (cm^{-1})
- Eg = bandgap energy value (eV)

Making the assumption that the Kubelka-Munk function F(R) is proportional to the absorption coefficient, we have:

- $[F(R). h\nu]^{0.5} \alpha (h\nu - Eg)$ for a direct bandgap
- $[F(R) h\nu]^2 \alpha (h\nu - Eg)$ for an indirect bandgap

Plotting $[F(R). h\nu]^n$ vs hν gives the the Kubelka-Munck equation as function of hν. The curve presents a linear part. We consider the linear interpolation of this linear part. Intersecting the linear interpolation with x-axis gives value of bandgap. Some authors report that for anatase nanoparticles, equation for direct bandgap fits perfectly (Diamandescu et al. 2008, Murphy 2007, Lin 2006). First we have applied both equations for undoped nanowires, as shown in fig. 11 and fig. 12. Assuming direct transition, bang gap is 3.25 eV, assuming indirect transition it is 3.68 eV. Since 3.25 eV is close to admitted values, we have decided to consider a direct transition for all our samples. Fig. 11, 13-15 are the diagrams of the plotting. Results of band gap evaluations are summed up in Table 1. Bandgaps are in the range from 3.23 to 3.30 eV. For comparing optical behaviour of samples, we have plotted all the curves on the same graph (Fig. 16). The curves indicate that linear part does not shift. These data leads to state that there is not a real reduction of bandgap, in spite of the absorption in the visible light region. Presence of mid gap levels could explain these results.

3.5 High temperature x-ray diffraction

Even if no precise transition temperature from anatase to rutile was searched for, our study evidenced a spectacular transition temperature change with substitution level. The higher the doping level, the lower the transition temperature is. Indeed, for the undoped sample, anatase disappears at 900°C (Figure 17), as well known by the literature, while for 0.5, 1 and 2% doped samples, the anatase disappears (roughly) at 800, 700 and 600 °C respectively (Figure 18 to 20). This may be explained by segregation and nucleation of rutile

VO_2 very small nanodomains that would act as germs accelerating the crystallization, and/or a lowering of rutile critical germ size. Hence, $V4^+$ substitution may promote the transformation of anatase to rutile, occurring at lower temperature than for pure TiO_2.

Note that the conditions of the high temperature x-ray diffraction analyses are different from the calcination conditions of our materials. The heating rate of the calcinations procedure is 2 °C/min, while that of the HT-XRD is 10 °C/min. This is why even though the 2% doped sample has been calcined at 600 °C, it has not lost the 1 D morphology and anatase phase.

3.6 Photocalatytic test for hydrogen evolution

The photocatalytic tests have been performed on doped and undoped nanowires (Figure 21). Degussa P25 (ref: Aerosil Evonik Degussa Co., Ltd.**)** and commercial anatase particles ST-01 (ref: ST-01, Ishihara Sangyo Co., Ltd.) have been tested as reference materials

With our experimental conditions the photoactivity of the tested materials ranges as follows:

Undoped nanowires >> Commercial anatase ST-01 > Degussa P25 >> doped nanowires

It is noteworthy that the most active materials are the undoped nanowires, according to the literature (Yoshikazu 2008, Catalysis Communications). Such an increase of photoactivity is probably due to the better crystalline structure of 1 D materials. Photoactivity of nanowires seems to be also more efficient in other applications (Aimin Yu et al., 2009, Catalysis Letters).

Despite this exciting behavior of undoped nanowires, vanadium doped nanowires have a very low activity, which wipes out any hope to use them as visible light photocatalyst for water splitting.

Recent studies have actually demonstrated that cation doping can significantly lower the flat band potential of the conduction band of titania, under the critical value of 0 eV (NagaveniK. Et al. 2004, J. Phys. Chem. B), but according to our results there is no significant band gap modification and we rather think that mid-gap levels act as recombination centers of electron/hole couples. In addition, we cannot totally discard that vanadium doped semiconductors could photocatalyse the competitive backward reaction (that produces water from H_2 and O_2), as already demonstrated for ethanol degradation (ref. Masih: Applied Catalysis A: General 325 (2007) 276–282).

Photoactivity of TiO_2 based nanomaterials depends also on testing conditions. Li L. (Li L. 2009, Materials Chemistry and Physics) reports that undoped catalysts are active under UV light, while vanadium doped materials are more active under visible light. Nevertheless, the activity under UV light is too low in our case to be compensated by a hypothetical additional activity under visible light.

4. Conclusion

As observed for other photocatalytic reactions, anatase nanowires suspensions are more efficient than nanoparticles for dihydrogen photoproduction under UV light.

In order to get activity in the visible part of the spectrum, V^{4+} doped anatase nanowires were produced by impregnating titanates nanowires and calcination in cautiously chosen conditions, depending on the dopant level, to keep 1D morphology. V^{4+} was proved to subsitute Ti^{4+} in anatase structure by different techniques supporting one another as HERFD-XANES and Raman spectroscopy. Unfortunately, V^{4+} subsitution is highly detrimental to photoactivity, probably due to the creation of recombination centers. To circumvent this effect, anionic doping should prove more relevant.

Table

Sample name	**V/Ti (%)**	**Heat treatment**	**BET (m^2g^{-1})**	**Crystallite size* (nm)**	**Band gap (eV)**	**Photoactivity** (H_2/µmol)**
S1	0	400 °C 2 h	180	43	3.25	280.31
S2	0.5	400 °C 2 h	165	17	3.30	6.52
S3	1	500 °C 2 h	182	49	3.30	8.93
S4	2	600 °C 2 h	154	43	3.23	0.8

*by Scherrer formula on A (101)

**after 300 min of irradiation

Table 1. Summarize of structural results

Sample name	**V/Ti (%)**	**Lattice parameters**
S1	0	a=b=3.753; c=9.492
S2	0.5	a=b=3.757; c=9.542
S3	1	a=b=3.755; c=9.454
S4	2	a=b=3.744; c=9.505

Ταβλε 2. Λαττιχε παραμετερσ

Figures

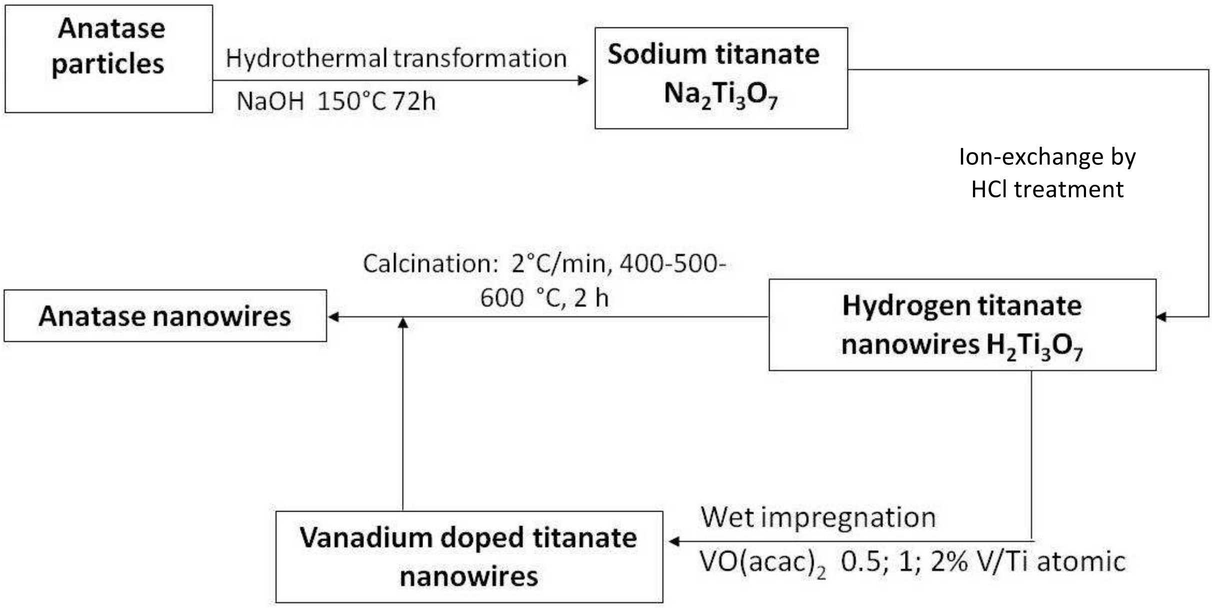

Figure 1. Synthesis of vanadium doped anatase nanowires

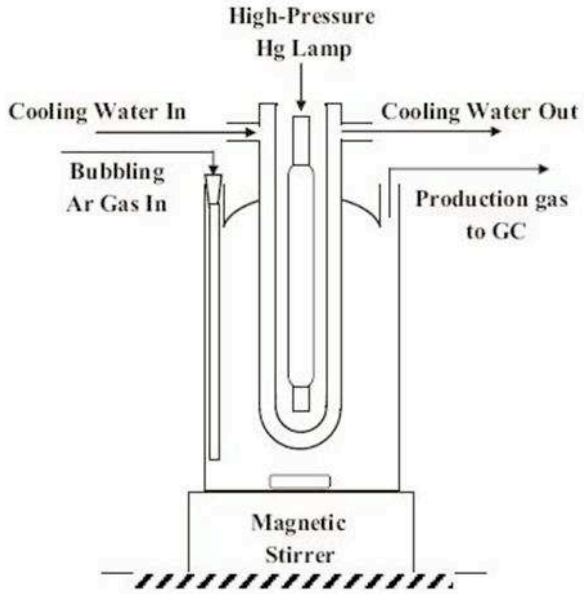

Figure 2.Photoreactor used for our H_2 production tests (Jitputti 2007)

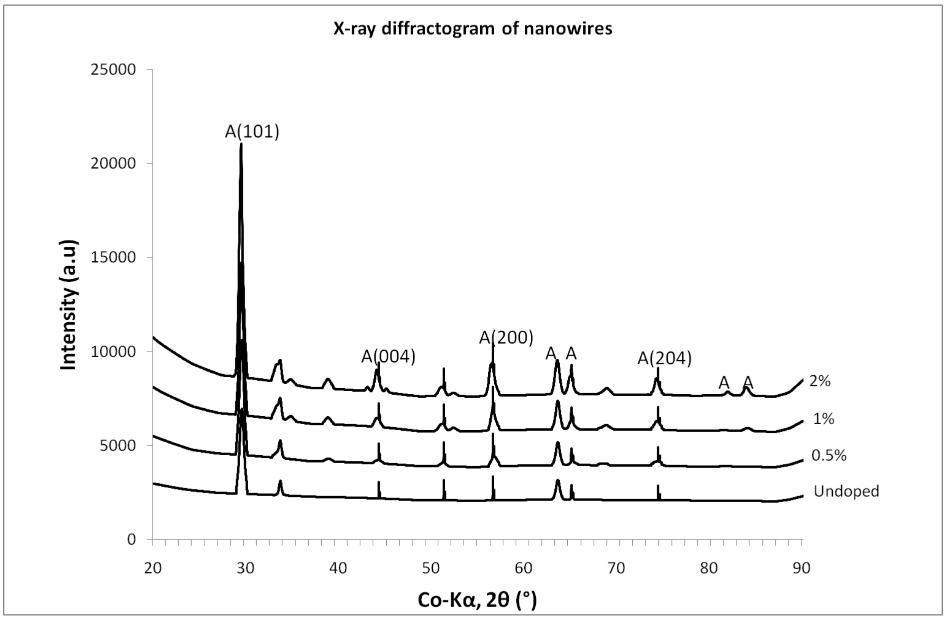

Figure 3. X-Rays Diffractograms of undoped and doped samples

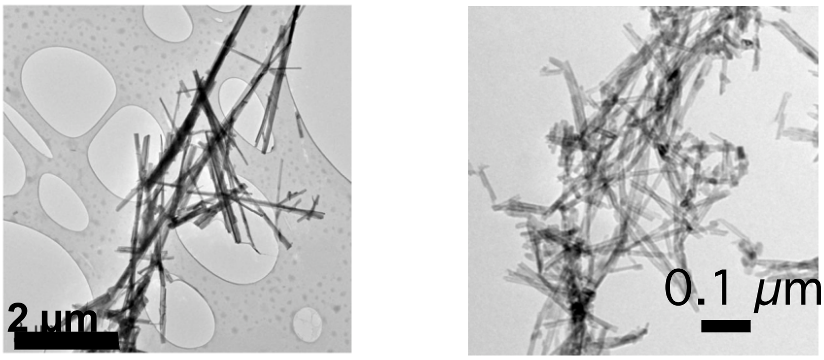

Anatase nanowires

0.5% vanadium anatase nanowires

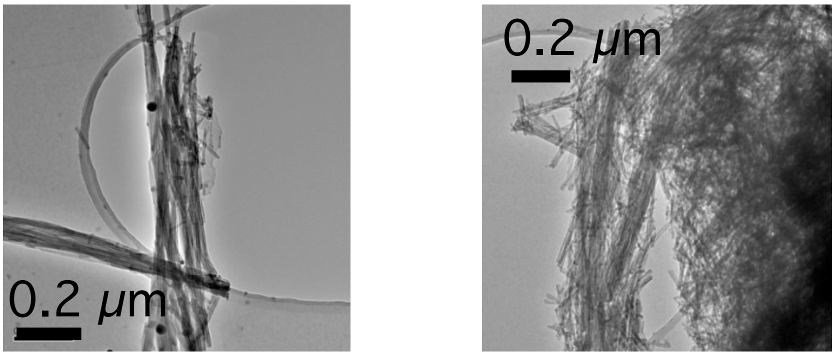

1% vanadium anatase nanowires

2% vanadium anatase nanowires

Figure 4. Transmission Electron Microscopy investigation

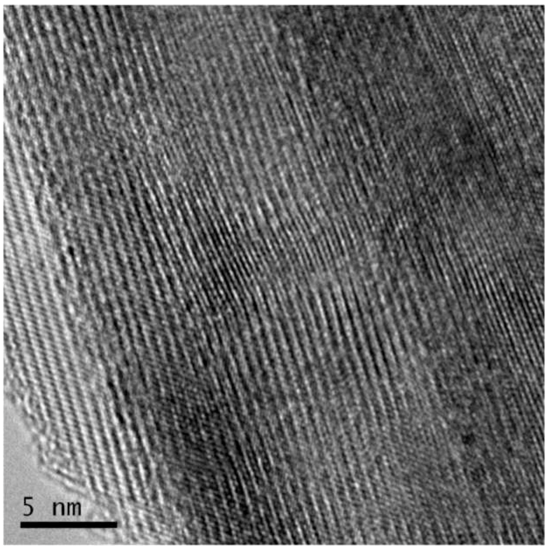

Figure 5. High Resolution Transmission Electron Microscopy on 2% doped sample

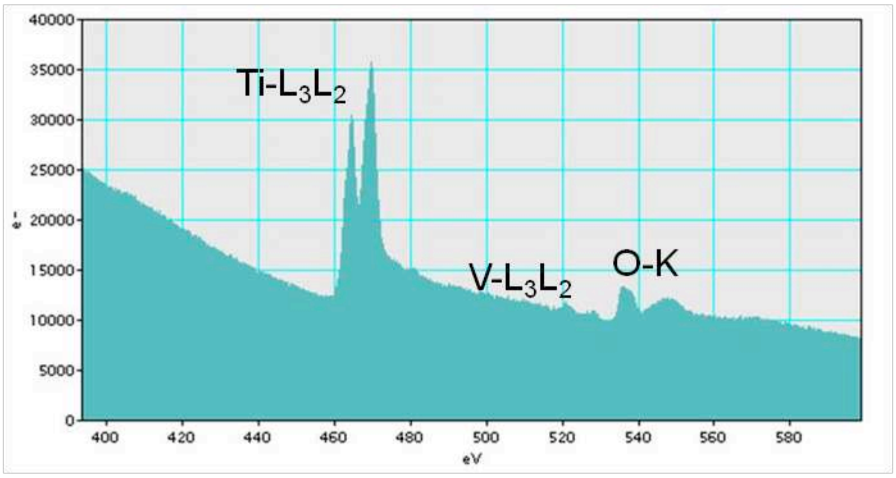

Figure 6. Electron Energy Loss Spectroscopy on 1% sample

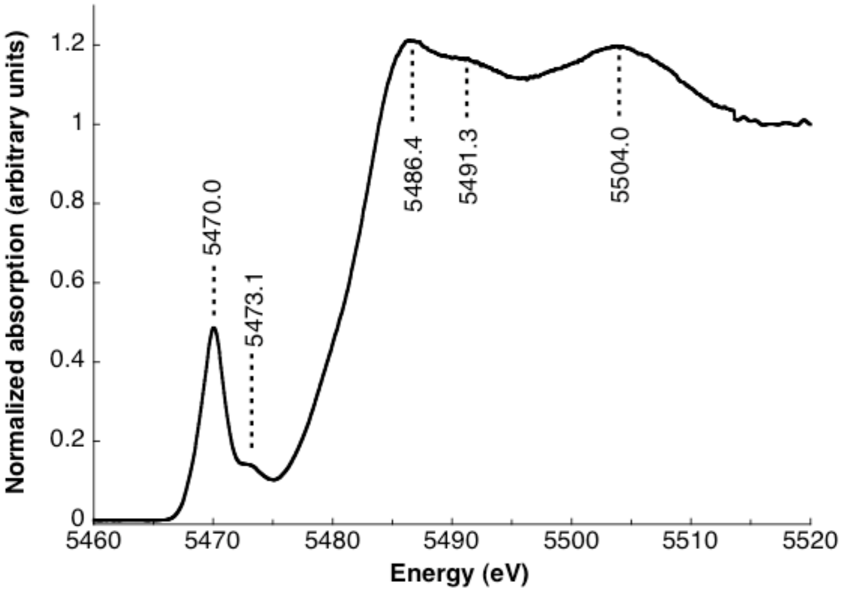

Figure 7. Normalized V K-edge HERFD-XAS spectra of TiO_2:V^{4+}

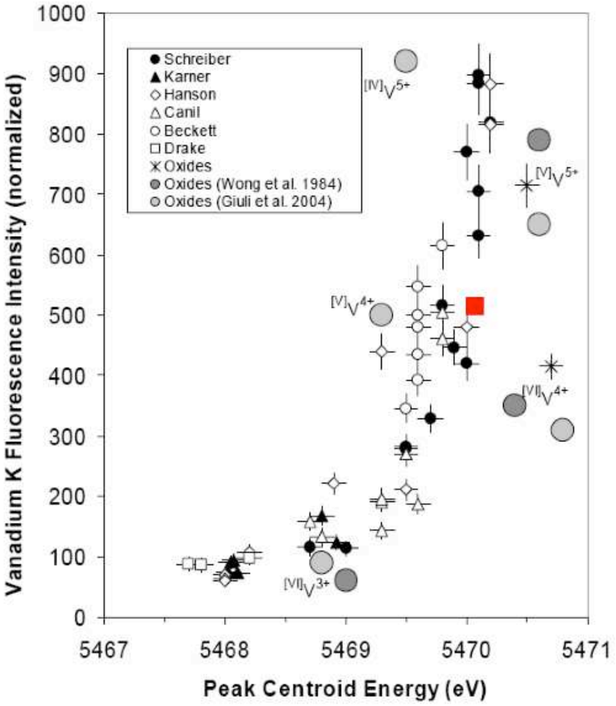

Figure 8. Pre-edge intensity vs. peak energy (after Sutton et al., 2005). The parameters measured on the V-doped sample are characteristic of V^{4+} in octahedral coordination.

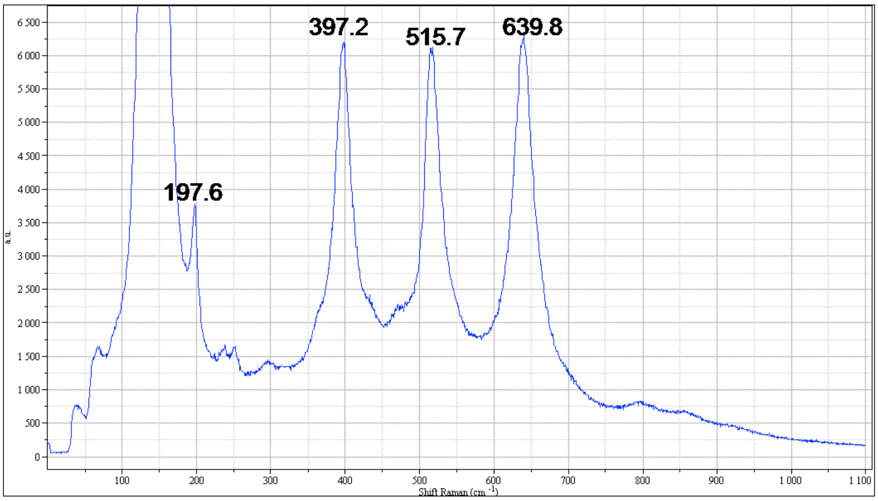

Figure 9. Raman Spectroscopy on undoped nanowires

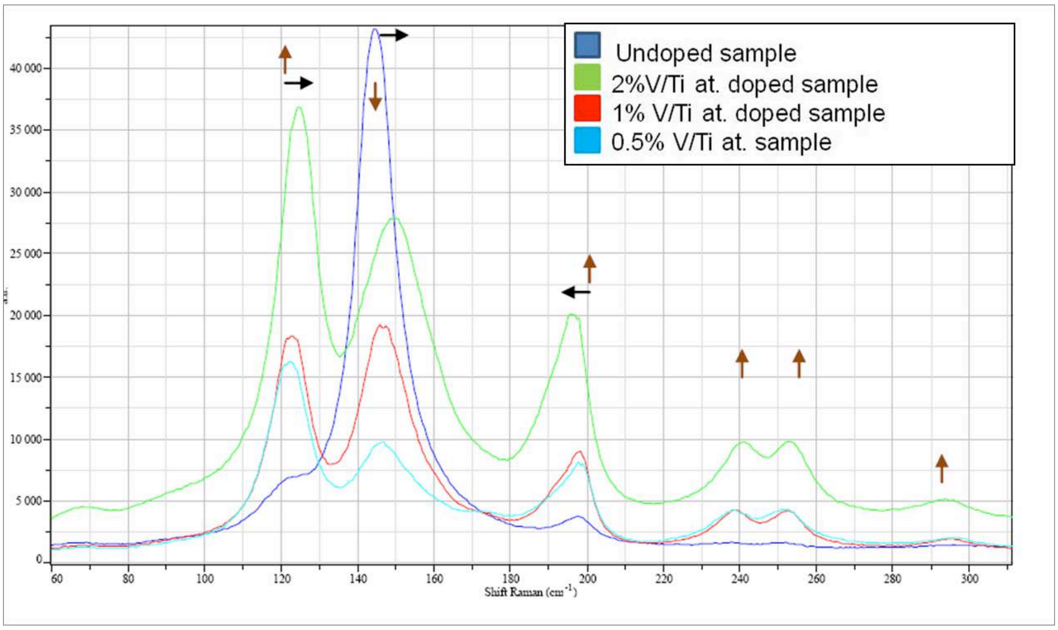

Figure 10. Raman Spectra of both undoped and doped nanowires. Arrows indicate modes changes

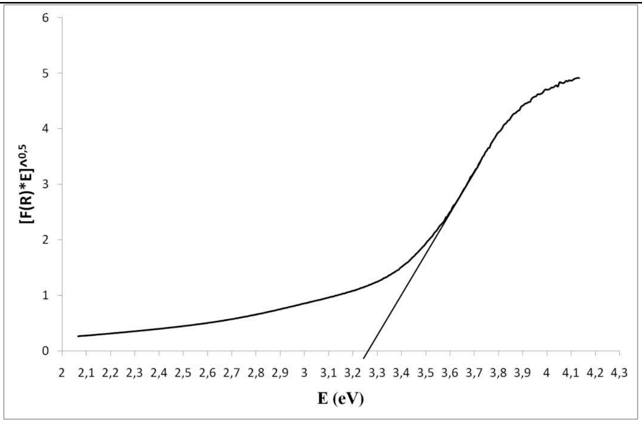

Figure 11. Kubelka-Munk function and bandgap estimation for undoped anatase nanowires assuming direct bandgap

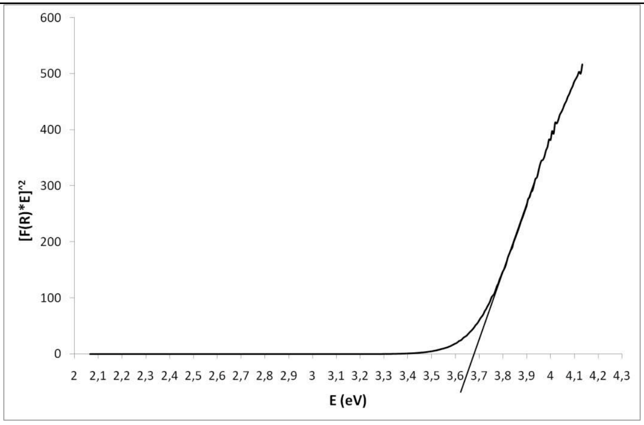

Figure 12. Kubelka-Munk function and bandgap estimation of undoped anatase nanowires assuming indirect bandgap

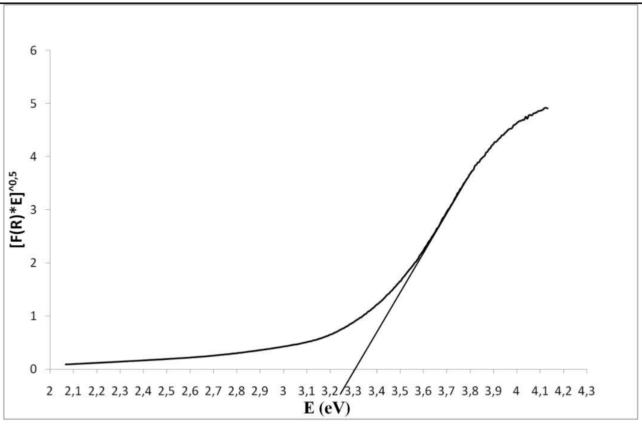

Figure 13. Kubelka-Munk function and bandgap estimation of 0.5% at. vanadium doped anatase nanowires

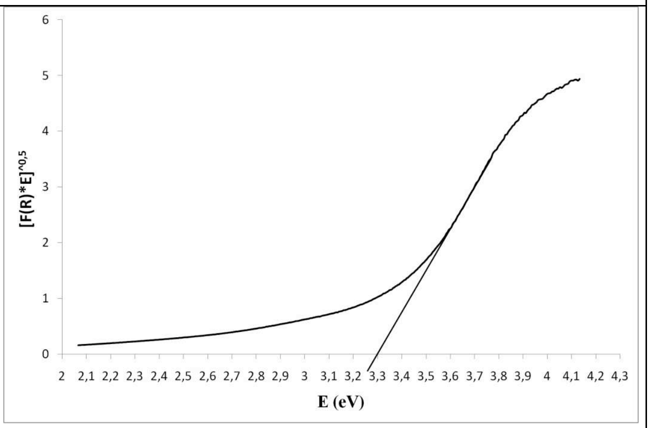

Figure 14. Kubelka-Munk function and bandgap estimation of 1% at. vanadium doped anatase nanowires

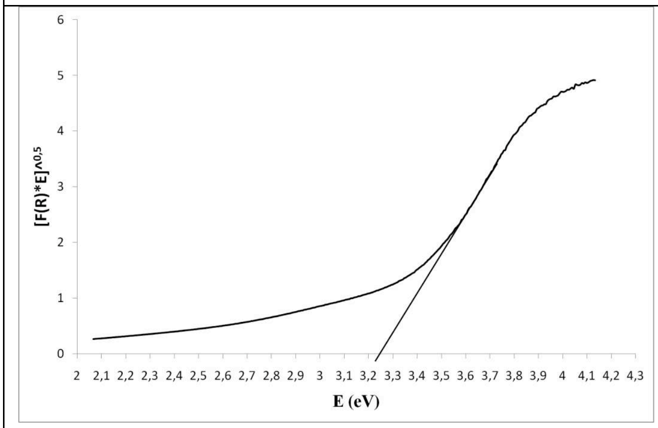

Figure 15. Kubelka-Munk function and bandgap estimation of 2% at. vanadium doped anatase nanowires

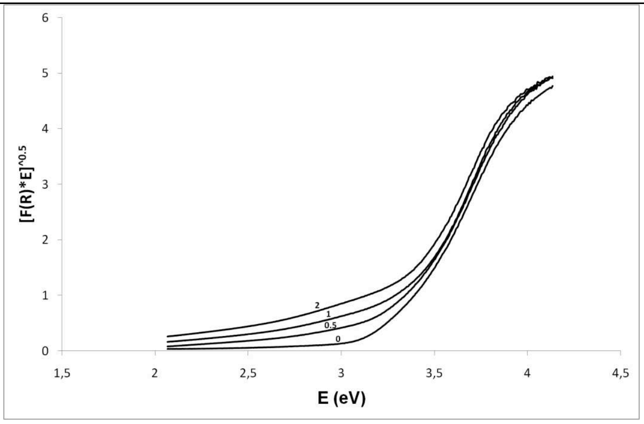

Figure 16. All the curves together

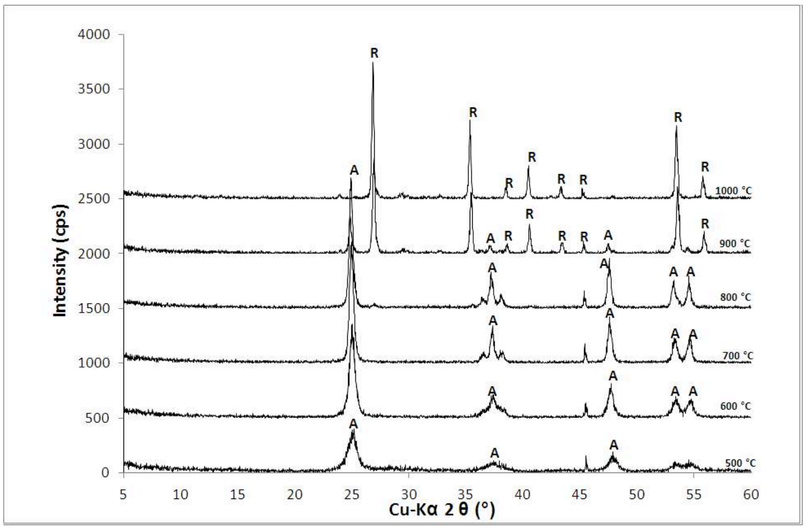

Figure 17. High Temperature X-Ray Diffractograms of undoped nanowires (A=anatase, R=rutile)

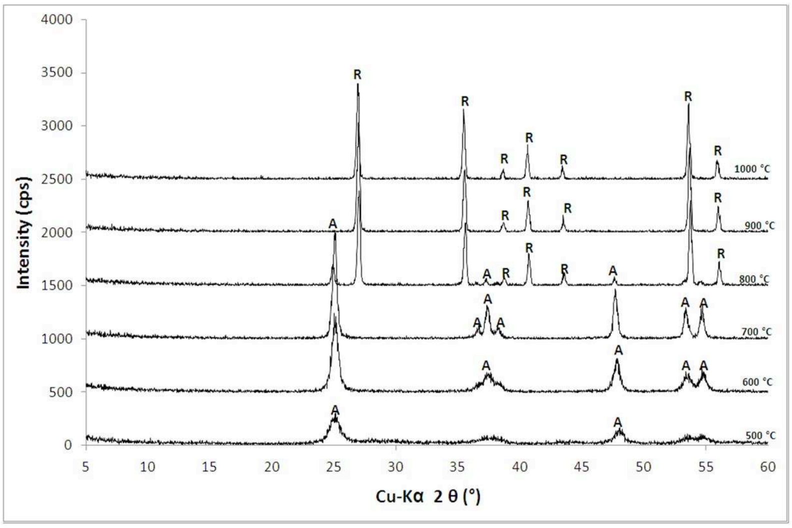

Figure 18. High Temperature X-Ray Diffractograms of 0.5% doped nanowires (A=anatase, R=rutile)

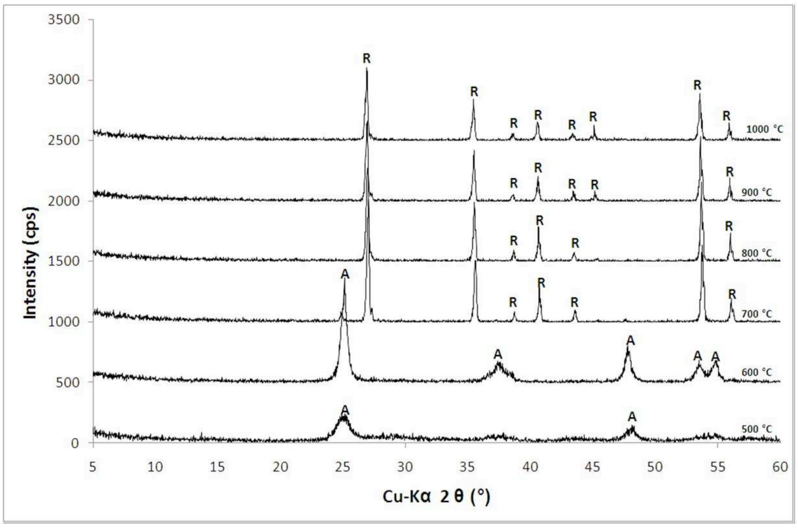

Figure 19. High Temperature X-Ray Diffractograms of 1% doped nanowires (A=anatase, R=rutile)

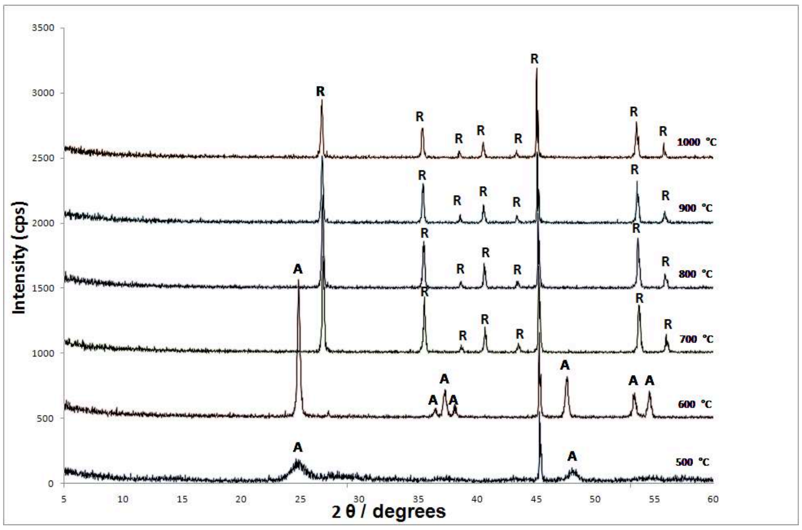

Figure 20. High Temperature X-Ray Diffractograms of 2% doped nanowires (A=anatase, R=rutile)

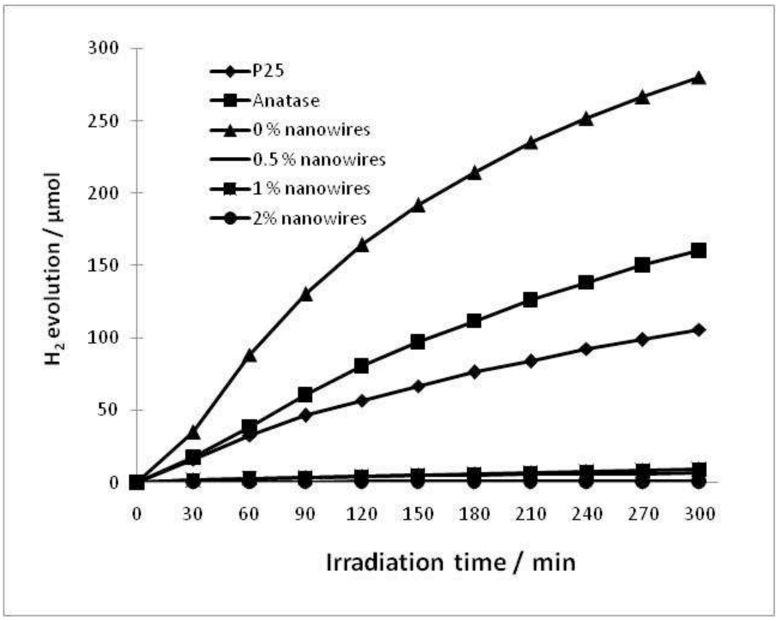

Figure 21. Hydrogen evolution

References:

Balan E., De Villiers J.P.R., Eeckhout S., Glatzel P., Toplis M.J., Firtsch E., Allard T., Galoisy L., Calas G. (2006) The oxidation state of vanadium in titanomagnetite from layered basic intrusions. American Mineralogist, 91, 953-956.

Bettinelli M et al., (2007) Photocatalytic activity of TiO_2 doped with boron and vanadium, Journal of Hazardous Materials, 146, 529-534.

Calas, G. and Petiau, J. (1983) Coordination of iron in oxide glasses through high-resolution K-edge spectra: information from the pre-edge. Solid State Communication, 48, 625-629.

Choi WY, Termin A, Hoffmann MR, (1995) The role of metal-ion dopants in quantum-sized TiO_2 . Correlation between photoreactivity and charge-carrier recombination dynamics, J. Phys. Chem. , 98, 13669-13679.

Craig A. Grimes et al., 2008, Light, Water, Hydrogen, Springer.

De Groot F.M.F., Vanko G. and Glatzel P. (2009) The 1s X-ray absorption pre-edge structures in transition metal oxides. Journal of Physics: Condensed Matter, 21, 104207.

Diamandescu L. et al., Structural and photocatalytic properties of iron- and europium-doped TiO2 nanoparticlesobtained under hydrothermal conditions, Materials Chemistry and Physics 112 (2008) 146-153.

Fujishima A., Honda K., 1972, Electrochemical Photolysis of water at a semiconductor electrode, Nature, 238.

Fujishima A. et al. (1999), TiO_2 Photocatalysis: Fundamentals and Applications, BKc Inc.

Galinska A., Walendziewski J., (2005), Photocatalytic water splitting over Pt-TiO_2 in the presence of sacrificial reagents, Energy & Fuels, 19, 1143-1147.

Gauthier C., Solé V.A., Signorato R., Goulon J. and Moguiline E. (1999) The ESRF beamline ID26: X-ray absorption on ultra dilute sample. Journal of Synchrotron Radiation 6, 164-166

Giuli, G., Paris, E., Mungall, J., Romano, C., and Dingwell, D. (2004) V oxidation state and coordination number in silicate glasses by XAS. American Mineralogist, 89, 1640-1646.

Glatzel P. and Bergmann U. (2005) High-resolution 1s core hole X-ray spectroscopy in 3d transition metal complexes – Electronic and structural information. Coordination Chemistry Review 249, 65-95.

Klosek S. and Raftery D., (2001) Visible light driven V-Doped TiO_2 photocatalyst and its photooxidation of ethanol,Journal of Physical Chemistry B, 105, 2815-2819

Kuchibhatla (2007), One dimensional nanostructured materials. Progress in Materials Science, 52, 699–913.

Jitputti J., Suzuki Y., Yoshikawa S., 2008, Synthesis of TiO_2 nanowires and their photocatalytic activity for hydrogen evolution, Catalysis Communications, 9, 1265–1271.

Lei Y. et al., 2001, Fabrication, characterization and Raman study of TiO_2 nanowire arrays prepared by anodic oxidative hydrolysis of $TiCl_3$, Chemical Physics Letters, 338, 231-236.

Li L., et al., 2009, Study on activities of vanadium (IV/V) doped TiO_2(R) nanorods induced by UV and visible light, Materials Chemistry and Physics , 113 , 551–557.

Lin H. et al., Size dependency of nanocrystalline TiO2 on its optical property and photocatalytic reactivity exemplified by 2-chlorophenol, Applied Catalysis B: Environmental 68 (2006) 1-11.

Masih D et al. , 2007, Photo-oxidation of ethanol on mesoporous vanadium-titanium oxide catalysts and the relation to vanadium(IV) and (V) sites. Applied Catalysis A: General, 325, 276–282.

Murphy A.B. , Band gap determination from diffuse reflectance measurements of semiconductor films, and application to photoelectrochemical water-splitting. Solar Energy Materials & Solar Cells 91 (2007), 1326-1327.

Nagaveni K et al. , 2004, Structure and Photocatalytic Activity of $Ti_{1-x}M_xO_2\pm\delta$ (M = W, V, Ce, Zr, Fe, and Cu) Synthesized by Solution Combustion Method, J. Phys. Chem. B, 108, 20204-20212.

Poumellec B., Marucco J.F. and Touzellin B. (1987) X-ray absorption near-edge structure of titanium and vanadium in $(Ti,V)O_2$ rutile solid solutions. Physical Review B, 32 (5), 2284-2294.

Ruiz-Lopez M.F. and Munoz-Paez A. (1991) A theoretical study of the XANES spectra of rutile and anatase. J. Phys. Cond. Matter 3, 8981-8890.

Stafford U. et al. (1993), An in situ diffuse reflectance FTIR investigation of photocatalytic degradation of 4-Chlorophenol on a TiO2 powder, Chem. Phys.Lett., 205, 55.

Sutton S.R., Karner J., Papike J., Delaney J.S., Shearer C., Newville M., Eng P., Rivers M., and Dyar M.D. (2005) Vanadium K-edge XANES of synthetic and natural basaltic glasses and application to microscale oxygen barometry. Geochimica et Cosmochimica Acta 69, 2333-2348.

Tielens F., Catalayud M., Baltran A., Minot C. and Andres J. (2005) Lithium insertion and mobility in the TiO2-anatase/titanate structures: A periodic DFT study. Journal of Electroanalytical Chemistry, 581, 216-223.

Yu A. et al., 2009, Synthesis and Characterization of N-doped TiO_2 Nanowires with Visible Light Response, Catalysis Letters, 129, 507–512

Wu Z.Y., Zhang J., Ibrahim K., Xian D.C., Li G., Tao Y., Hu T.D., Bellucci S., Marcelli A., Zhang Q.H., Gao L. and Chen Z.Z. (2002) Structural determination of titanium-oxide nanoparticles by X-ray absorption spectroscopy. *Applied Physics Letters* **80 (16)**, 2973-2975.

Wong, J., Lytle, F.W., Messmer, R.P., and Maylotte, D.H. (1984) K-edge absorption spectra of selected vanadium compounds. Physical Review B, 30, 5596-5610.

Zhao G. et al., (1999), Sol-gel preparation of $Ti_{1-2x}V_xO_2$ solid solution for electrodes with conspicuous photoresponse in the visible region," Thin Solid Films, 339, 123-128.

Appendix C

A previous study on the oxidation state of vanadium in titanomagnetites by XAS experiments

Before my thesis, a study on the oxidation state of vanadium in titanomagnetites from the Bushveld Complex was done by Etienne Balan and co-workers. They performed XAS measurements at the V K-edge of titanomagnetites from different locations in the Bushveld Complex and also in two other layered intrusions. The main conclusions were that :

- vanadium is incorporated in the octahedral site of the titanomagnetite structure,
- the variations observed in the pre-edge are related to the presence of V^{3+} and V^{4+} in various proportions.

At the beginning of my thesis, the starting hypotheses about the oxidation states of vanadium in titanomagentites were the two conclusions of this work, which was published in *American Mineralogist* [10]. The publication is thus entirely reproduced hereafter, to get a complementary picture of the starting hypotheses.

American Mineralogist, Volume 91, pages 953–956, 2006

LETTER

The oxidation state of vanadium in titanomagnetite from layered basic intrusions

ETIENNE BALAN,[1,2,*] JOHAN P.R. DE VILLIERS,[3] SIGRID GRIET EECKHOUT,[4] PIETER GLATZEL,[4]
MICHAEL J. TOPLIS,[5] EMMANUEL FRITSCH,[1,2] THIERRY ALLARD,[2] LAURENCE GALOISY,[2] AND
GEORGES CALAS[2]

[1]UR T058, Institut de Recherche pour le Développement (IRD), 213 rue La Fayette, 75480, Paris cedex 10, France
[2]Institut de Minéralogie et Physique des Milieux Condensés (IMPMC), UMR CNRS 7590, Universités Paris VI et VII, IPGP, 4 Place Jussieu, 75252 Paris Cedex 05, France
[3]Department of Materials Science and Metallurgical Engineering, University of Pretoria, Pretoria 0002, South Africa
[4]European Synchrotron Radiation Facility, 6 rue Jules Horowitz, 38043 Grenoble, France
[5]Laboratoire Dynamique Terrestre et Planétaire UMR CNRS 5562, Observatoire Midi-Pyrénées, 14 Avenue Edouard Belin 31400 Toulouse, France

ABSTRACT

The redox conditions prevailing during the formation of vanadiferous titanomagnetites from three layered intrusions (Bushveld; Koillismaa; Skaergaard) have been estimated from the valence state of vanadium using synchrotron X-ray absorption near edge structure spectroscopy (XANES). Using a high energy-resolution X-ray emission spectrometer, we show that vanadium occurs mostly as V^{3+}, with minor V^{4+}. The most concentrated samples (up to 2.4 wt% V_2O_3) contain approximately 10% of vanadium as V^{4+}. Both V^{3+} and V^{4+} occur in the octahedral site of the spinel structure. Considering the low magnetite/melt V^{4+} partition coefficients, this suggests that vanadium ores crystallized under specific oxidizing conditions.

Keywords: Trace elements, XAS (XANES), igneous petrology, new technique

INTRODUCTION

Vanadium oxidation state ranges from trivalent to pentavalent in terrestrial magmatic systems. This feature makes vanadium a valuable geochemical indicator, providing information on the oxygen fugacity (f_{O_2}) prevailing during the formation of igneous rocks (Irving 1978; Canil 2002; Papike et al. 2004, 2005; Karner et al. 2006). It is also a strategic metal, being used in high-performance steels. It does not form specific ore minerals, but is extracted from V-rich titanomagnetite ($Fe_{3-x}Ti_xO_4$) cumulates in the upper part of layered basic intrusions. The largest vanadium ore deposit in the world is the main magnetite layer of the Bushveld Complex (South Africa). In this giant layered intrusion ($450 \times 370 \times 7$ km^3), vanadium is encountered in meter-thick discrete layers of massive titanomagnetite. However, the formation of these layers is poorly understood, and has been variably attributed to pressure fluctuations (Cawthorn and McCarthy 1980), episodic increases in f_{O_2} (Reynolds 1985), or periodic mixing of compositionally different liquids (Harney and Von Gruenewaldt 1995). On the other hand, geochemical modeling based upon experimental data suggests that for fractional crystallization of basaltic melts, V-rich magnetites will only appear in a narrow range of f_{O_2} conditions, close to the Ni-NiO buffer (Toplis and Corgne 2002).

One potential window into the processes leading to the formation of V-bearing magnetites is the oxidation state of vanadium. However, at the present time the valence state of V in magnetites from layered intrusions is largely unknown. We present here the first data on the crystal-chemistry of vanadium in natural titanomagnetites using XANES spectroscopy. Focusing on the pre-edge features, which depend on the valence state and site symmetry of transition elements (Calas and Petiau 1983a; Wong et al. 1984; Giuli et al. 2004; Sutton et al. 2005; Karner et al. 2006), we show the coexistence of tri- and tetravalent vanadium in the titanomagnetite samples. The most concentrated samples, used as ore minerals, contain the highest V^{4+} proportion, an indication of their formation under specific oxidizing conditions.

METHODS

The chemical composition of the samples (Table 1), including oxygen concentration, was determined by electron microprobe analysis using a CAMECA SX50 instrument operated at 15 kV and 40 nA, with counting times varying from 10 to 30 s depending on the element. For each sample, about ten measurements were performed on the area selected for spectroscopic measurements (~1 mm^2). Concentrations are reported in at%, such that no assumption concerning the redox state of transition elements is necessary.

High energy-resolution XANES spectra were collected at beam line ID26 of the ESRF (European Synchrotron Radiation Facility) (Gauthier et al. 1999). The energy of the incident radiation beam was selected using a pair of He-cooled Si crystals with a (2 2 0) orientation. Using the fundamental undulator peak, the total incident flux on the sample was 10^{13} photons/second in a spot size of 0.3×1.2 mm^2. Spectra ranging from 5460 to 5550 eV incident energy were recorded in quick scan mode. Additional scans were performed between 5460 and 6200 eV to normalize the XANES spectra to the K-edge jump. The incident flux was monitored by detecting the X-ray scattering from a thin Kapton foil in the incident beam path. Self-absorption effects can be neglected due to the low V concentration in the samples. High energy-resolution emission detection was achieved by employing a spherically bent Ge crystal (R = 850 mm, 89 mm diameter) with a (3 3 1) orientation in Rowland geometry. The energy bandwidth of the emission spectrometer was ~0.8 eV. An avalanche photo diode (APD) was used as a fast detector for emission detection to avoid non-linear effects. XANES spectra with sharper spectral features can be obtained by recording the $K\alpha_1$ emission line intensity while scanning the incident

---

[*] E-mail: balan@lmcp.jussieu.fr

0003-004X/06/0506–953$05.00/DOI: 10.2138/am.2006.2192

Table 1. Chemical composition of the titanomagnetite samples (standard deviation in italics)

Sample	Origin	O (at%)	Fe (at%)	Ti (at%)	V (at%)	Cr (at%)	Mn (at%)	Mg (at%)	Al (at%)	%V^{3+} *	%V^{4+} *
M4	BK1 borehole 1457.25 m	59.7	30.2	7.3	0.09	0.05	0.18	0.53	1.9	98	2
		0.3	*0.6*	*0.4*	*0.02*	*0.02*	*0.02*	*0.05*	*0.1*		
M6	BK1 borehole 1466.6 m	60.4	28.7	7.9	0.14	0.01	0.17	0.86	1.8	89	11
		0.2	*0.6*	*0.1*	*0.02*	*0.02*	*0.05*	*0.12*	*0.4*		
M1	BK1 borehole 1469.9 m	60.8	29.0	7.3	0.19	0.02	0.17	0.71	1.8	87	13
		0.3	*0.5*	*0.3*	*0.02*	*0.01*	*0.04*	*0.01*	*0.1*		
M5	Mapochs mine Site 2 6A	59.5	30.1	5.5	0.58	0.08	0.12	1.55	2.6	83	17
		0.5	*1.8*	*0.6*	*0.02*	*0.01*	*0.02*	*0.28*	*1.2*		
M2	Mapochs mine Site 2 1A	58.1	30.0	5.2	0.63	0.27	0.11	2.36	3.4	86	14
		0.4	*2.8*	*0.1*	*0.04*	*0.02*	*0.02*	*0.92*	*2.2*		
M3	Mustavaara Mine Finland	56.6	41.1	1.2	0.69	0.01	0.06	0.16	0.2	85	15
		1.3	*3.1*	*1.6*	*0.06*	*0.01*	*0.09*	*0.15*	*0.2*		
S2	Skaergaard intrusion	58.3	32.2	5.3	1.1	0.04	0.12	0.69	2.2	87	13
		0.3	*0.6*	*0.4*	*0.1*	*0.01*	*0.01*	*0.13*	*0.1*		

* As assessed from XANES measurements (see text).

energy (Glatzel and Bergmann 2005). These XANES spectra also present a low background because the fluorescence of other elements (e.g., Ti) is filtered out. In the analysis of pre-edge features, a baseline subtraction was performed by fitting a Gaussian function on the low-energy tail of the edge, using data a few eV before and after the pre-edge. Gaussian profiles were then used to determine the energy position of pre-edge components.

SAMPLES

Samples M5 and M2 have been collected from the main magnetite seam of the Bushveld Complex. They contain ~0.6 at% vanadium (Table 1), i.e., 1.4 wt% V_2O_3. They display a fracture pattern with altered rims surrounding millimeter size homogeneous zones. Local increases in Al and Mg concentration were observed in the zones selected for the measurements, likely related to the exsolution of Fe-rich Al-Mg spinel (Butcher and Merkle 1987). Samples M1, M4, and M6 are from layer 21 of the Bushveld complex (Bierkraal borehole, BK1), a stratigraphic horizon well above the main seam. These magnetites are chemically more homogeneous than those from samples M5 and M2 (Table 1), but display much lower V concentration, ranging from 0.1 to 0.2 at%. The general decrease in V concentration of magnetites as a function of stratigraphic height is a well known feature of the Bushveld complex, and is most likely the result of progressive V-depletion of the liquid caused by crystallization of the lower magnetite layers (Cawthorn and McCarthy 1980). An upward decrease in V concentration is also observed at the scale of this single magnetite layer. Considering the large size of titanomagnetite grains (>1 mm), these samples have probably experienced some high-temperature textural re-equilibration (Reynolds 1985). Sample M3 comes from the vanadium mine of Mustavaara (Koillismaa layered igneous complex, Finland). It presents titanomagnetite grains (>1 mm) with a V concentration of 0.7 at%. Sample S2 is an unlayered rock from the Lower Zone c of the Skaergaard intrusion (Greenland), a stratigraphic horizon characterized by the appearance of titanomagnetite as an abundant cumulus phase (Wager and Brown 1968). For this more finely grained sample, spectroscopic measurements were performed on an oxide-rich zone containing vanadiferous titanomagnetite and ilmenite. Titanomagnetite displays the highest V concentration (ca. 2.4 wt% V_2O_3), whereas coexisting ilmenite has a much lower V content (0.1 at%).

Reference samples included tsavorite (a V-bearing garnet with octahedral V^{3+}), cavansite [$Ca(VO)Si_4O_{10}(H_2O)_4$] and synthetic VOSO4.5H_2O (both with distorted octahedral V^{4+}), and descloizite [$PbZn(VO_4)(OH)$] and synthetic Na_3VO4.10H_2O (both with tetrahedral V^{5+}).

RESULTS AND DISCUSSION

The pre-edge features observed at the low energy side of the absorption K-edge (Fig. 1a) are related to dipole and quadrupole transitions from 1*s* core states to 3*d* final states having some 4*p* contribution, depending on the local symmetry (Calas and Petiau 1983a). The energy and intensity of these transitions depend on the cation oxidation state and site symmetry. The reference XANES spectrum of V^{3+} displays small pre-edge features at 5465.7, 5467.5, and 5469.2 eV. XANES spectra of V^{4+} exhibit more intense pre-edge features at 5468.9 and 5469.8 eV and at 5467.8, 5469.2, and 5470.2 eV for cavansite and hydrous vanadyl sulfate, respectively. The pre-edge area is similar for both samples. The most intense pre-edge features are observed for tetrahedral vanadates in descloizite and hydrous sodium orthovanadate. A major peak is observed at 5469.8 eV in the descloizite spectrum. The sodium orthovanadate spectrum exhibits three peaks at 5468.1, 5469.8, and 5472.1 eV and a larger pre-edge area.

The normalized XANES spectra of the titanomagnetite samples typically display an intense line at 5485.6 eV and two shoulders at 5476.0 and 5480.9 eV (Fig. 1b). Small shifts of the edge are observed, reaching ~ 0.2 eV between M4 and M5. An additional feature at ~5500 eV presents greater variation in position (from 5498.0 to 5500.3 eV). The pre-edge shows three weak contributions at 5465.7 ± 0.2, 5467.3 ± 0.1, and 5469.0 ± 0.1 eV (Fig. 2a), an indication that vanadium mainly occurs as octahedral V^{3+}. However, significant variations are observed among the samples. The pre-edge of M4 shares the strongest similarity with that of the V^{3+} reference compound. The other samples display an increasing contribution at 5469.0 eV, leading to a significant increase of their pre-edge area (Fig. 2b). Orientational effects, which may influence the intensity of the anisotropic quadrupolar contribution in cubic crystals (Brouder 1990), cannot explain the simultaneous shift of the edge (Fig. 1b). The observed variations are therefore interpreted in terms of a variable proportion of V^{4+} ions in the magnetite structure. The incorporation of V^{4+} ions in octahedral sites of titanomagnetite is consistent with the similar ionic radius of Ti^{4+} and V^{4+} (Toplis and Corgne 2002). Tetravalent vanadium has also been observed in spinels crystallizing in oxidizing conditions (Righter

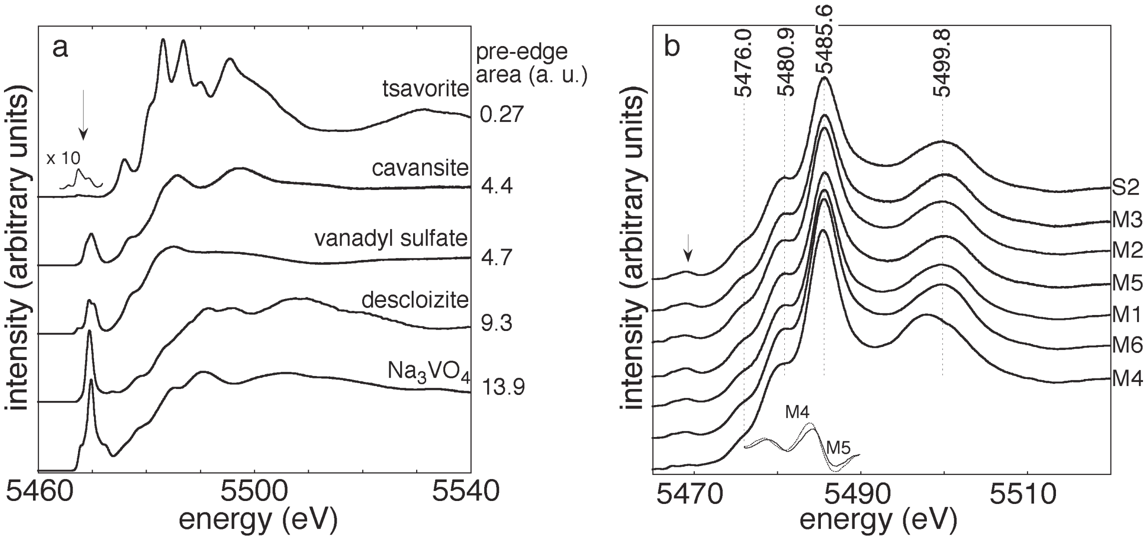

FIGURE 1. (**a**) Normalized V K-edge XANES spectra of reference compounds. The tsavorite sample (cubic garnet structure) is a single crystal, whereas other samples are powders. (**b**) Normalized V K-edge XANES spectra of titanomagnetite samples. Derivative curves evidencing an edge shift of ~0.2 eV between the M4 (dotted line) and M5 (plain line) spectra are reported at the bottom. Arrows = position of the pre-edge features.

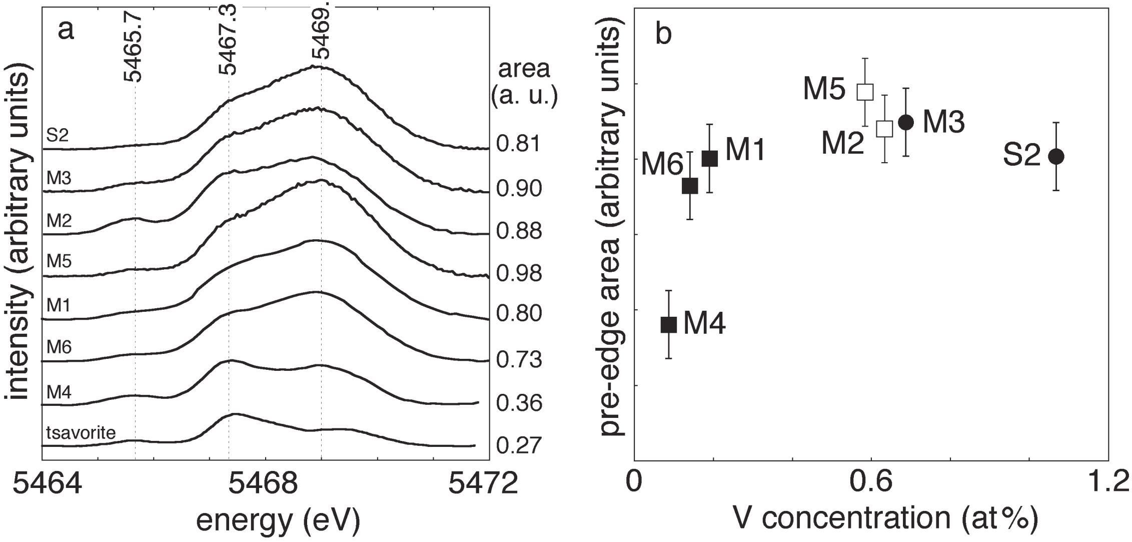

FIGURE 2. (**a**) Pre-edge peaks of titanomagnetite samples after baseline subtraction. For comparison, the pre-edge peaks of tsavorite are reported at the bottom. (**b**) Pre-edge area as a function of the vanadium concentration in titanomagnetite. Full squares = Bushveld samples (BK1); empty squares = Bushveld samples (main magnetite layer); circles = Finland (M3) and Skaergaard (S2) samples.

et al. 2005) and is a stable oxidation state in silicate melts near the Ni-NiO and QFM buffers (Schreiber and Balazs 1982; Calas and Petiau 1983b). In contrast, vanadate groups, although present in oxidized silicate melts (Giuli et al. 2004), are magmatophile (Irving 1978) and are not expected to substitute into the magnetite structure. The presence of tetrahedral V^{3+} is unlikely because the crystal field stabilization energy of V^{3+} favors octahedral coordination (Burns 1993), as in the normal spinels coulsonite (FeV_2O_4) and vuorelainenite (MnV_2O_4) (Hill et al. 1979).

The proportion of V occurring as V^{4+} has been calculated by comparison with octahedral V^{3+} and V^{4+} references, assuming a linear variation of the total pre-edge area as a function of the V^{4+} proportion (Table 1). In M4, the V^{4+} concentration does not exceed a few percent of the total vanadium. In the other samples, it is significantly higher and may represent up to ~17% of the total V content in M5. Considering that shifts of 2.5 to 3.2 eV per valence unit increase have been observed on the XANES spectrum of vanadium oxides (Wong et al. 1984), the amount of V^{4+} inferred from the pre-edge area of sample M5 is roughly consistent with the ~+0.2 eV shift observed on its edge.

Our data provide insights into the formation conditions of V-rich titanomagnetites. The proportion of V^{4+} (~10%) being similar in the V-rich samples from the three different localities suggests that extreme enrichments of V in magnetite only occur within a small range of f_{O_2} (Toplis and Corgne 2002). Furthermore, following those authors, the ratio of V^{4+} and V^{3+} magnetite/melt partition coefficients is about 10^{-3}. A V^{4+}/V^{3+} ratio of ~0.1 in magnetite thus corresponds to a ratio of ~10^2 in a coexisting melt, which compares favorably with the ratio expected in basaltic melts at conditions around the NNO buffer where V-enrichment is predicted (Toplis and Corgne 2002).

The valence state of vanadium in magnetite also provides insights into magmatic processes at several different length scales. At the scale of the Bushveld magma chamber, the similar proportion of V^{4+} in samples from the main magnetite layer (M2; M5) and the base of layer 21 (M1) suggests that similar f_{O_2} conditions prevailed during their formation. This implies that the observed upward decrease of the V content in magnetite is the consequence of progressive V-depletion of the liquid rather than of a significant change in f_{O_2}. This contrasts with the observations at the scale of a single magnetite layer, where an upward decrease in the f_{O_2} can be inferred from the decrease in the V^{4+}/V^{3+} ratio observed in the BK1 samples (Fig. 2b). In this case, the local variation of f_{O_2} is consistent with magmatic differentiation under conditions closed to oxygen sources, during which magnetite crystallization preferentially removes Fe^{3+} from the melt, thus lowering f_{O_2} (e.g., Toplis and Carroll 1996). In addition to the importance of f_{O_2}, the V^{4+}/V^{3+} ratio in the magnetite layers may also be affected by the local availability of V^{3+}. Indeed, a boundary layer depleted in V^{3+} may form in the liquid in the crystallization zone because of the high affinity of V^{3+} for the magnetite structure, leading in turn to an increase in the V^{4+}/V^{3+} ratio of the magnetite. A similar behavior has been inferred for Cr^{3+} in the Bushveld magnetites (McCarthy and Cawthorn 1983). Further work involving a combination of microscale trace-element analysis and X-ray absorption spectroscopy of vanadium in magnetite may provide new insights into the magmatic evolution of large basic intrusions, and a better understanding of the complex interplay between diffusion, convection, and fractional crystallization in those environments.

ACKNOWLEDGMENTS

We thank D. Dutton of Highveld Steel Corporation for the Mapochs Mine samples and the South African Council for Geoscience for the BK1 samples. We thank A. Djemai (ENSMP) for the M3 (ref. 41130) and descloizite (ref. 17208) samples. We thank F. Couffignal and M. Fialin (CAMPARIS, University of Paris VI), and C. Lapras (ESRF) for assistance during the experiments. D. Cabaret, C. Brouder, and Ph. Sainctavit (IMPMC, University of Paris VI) are thanked for fruitful discussions about XANES spectroscopy. Constructive comments by an anonymous reviewer, J. Papike, and C.-T. Lee were appreciated. This work was supported by the NRF-CNRS project 18383. This is IPGP contribution 2113.

REFERENCES CITED

Brouder, C. (1990) Angular dependence of X-ray absorption spectra. Journal of Physics: Condensed Matter, 2, 701–738.

Burns, R.G. (1993) Mineralogical application of crystal field theory (2nd edition), 224 p. Cambridge University Press, U.K.

Butcher, A.R. and Merkle, R.K.W. (1987) Postcumulus modifications of magnetite grains in the upper zone of the Bushveld Complex, South Africa. Lithos, 20, 247–260.

Calas, G. and Petiau, J. (1983a) Coordination of iron in oxide glasses through high-resolution K-edge spectra: information from the pre-edge. Solid State Communications, 48, 625–629.

——— (1983b) Structure of oxide glasses: spectroscopic studies of local order and crystallochemistry. Geochemical implications. Bulletin de Minéralogie, 106, 33–55.

Canil, D. (2002) Vanadium in peridotites, mantle redox and tectonic environments: Archean to present. Earth and Planetary Science Letters, 195, 75–90.

Cawthorn, R.G. and McCarthy, T.S. (1980) Variations in Cr content of magnetite from the upper zone of the Bushveld complex—Evidence for heterogeneity and convection currents in magma chambers. Earth and Planetary Science Letters, 46, 335–343.

Gauthier, C., Solé, V.A., Signorato, R., Goulon, J., and Moguiline, E. (1999) The ESRF beamline ID26: X-ray absorption on ultra dilute sample. Journal of Synchrotron Radiation, 6, 164–166.

Giuli, G., Paris, E., Mungall, J., Romano, C., and Dingwell, D. (2004) V oxidation state and coordination number in silicate glasses by XAS. American Mineralogist, 89, 1640–1646.

Glatzel, P. and Bergmann, U. (2005) High-resolution 1s core hole X-ray spectroscopy in 3d transition metal complexes—electronic and structural information. Coordination Chemistry Review, 249, 65–95.

Harney, D.M.W. and Von Gruenewaldt, G. (1995) Ore-forming processes in the upper part of the Bushveld complex, South Africa. Journal of African Earth Sciences, 20, 77–89.

Hill, R.J., Craig, J.R., and Gibbs, G.V. (1979) Systematics of the spinel structure type. Physics and Chemistry of Minerals, 4, 317–339.

Irving, A.J. (1978) A review of experimental studies of crystal/liquid trace element partitioning. Geochimica et Cosmochimica Acta, 42, 743–770.

Karner, J.M., Sutton, S.R., Papike, J.J., Shearer, C.K., Jones, J.H., and Newville, M. (2006) Application of a new vanadium valence oxybarometer to basaltic glasses from the Earth, Moon, and Mars. American Mineralogist, 91, 270–277.

McCarthy, T.S. and Cawthorn, R.G. (1983) The geochemistry of vanadiferous magnetite in the Bushveld complex: Implications for crystallization mechanisms in layered complexes. Mineralium Deposita, 18, 505–518.

Papike, J.J., Karner, J.M., and Shearer, C.K. (2004) Comparative planetary mineralogy: V/(Cr+Al) systematics in chromite as an indicator of relative oxygen fugacity. American Mineralogist, 89, 1557–1560.

——— (2005) Comparative planetary mineralogy: Valence state partitioning of Cr, Fe, Ti, and V among crystallographic sites in olivine, pyroxene, and spinel from planetary basalts. American Mineralogist, 90, 277–290.

Reynolds, I.M. (1985) The nature and origin of titaniferous magnetite-rich layers in the upper zone of the Bushveld complex: A review and synthesis. Economic Geology, 80, 1089–1108.

Righter, K., Sutton, S.R., Newville, M., Le, L., and Schwandt, C.S. (2005) Micro-XANES measurements on experimental spinels and the oxidation state of vanadium in coexisting spinel and silicate melt. Lunar and Planetary Science, XXXVI, 1140.

Schreiber, H.D. and Balazs, G.B. (1982) Vanadium as an oxygen geobarometer in basaltic magmas: the further development of a geochemical electromotive force series in silicate melts. Lunar and Planetary Science, XIII, 692–693.

Sutton, S.R., Karner, J., Papike, J., Delaney, J.S., Shearer, C., Newville, M., Eng, P., Rivers, M., and Dyar, M.D. (2005) Vanadium K-edge XANES of synthetic and natural basaltic glasses and application to microscale oxygen barometry. Geochimica et Cosmochimica Acta, 69, 2333–2348.

Toplis, M.J. and Carroll, M.R. (1996) Differentiation of ferro-basaltic magmas under conditions open and closed to oxygen: implications for the Skaergaard intrusion and other natural systems. Journal of Petrology, 37, 837–858.

Toplis, M. and Corgne, A. (2002) An experimental study of element partitioning between magnetite, clinopyroxene and iron-bearing silicate liquids with particular emphasis on vanadium. Contributions to Mineralogy and Petrology, 144, 22–37.

Wager, L.R. and Brown, G.M. (1968) Layered Igneous Rocks. Oliver and Boyd, Edinburgh.

Wong, J., Lytle, F.W., Messmer, R.P., and Maylotte, D.H. (1984) K-edge absorption spectra of selected vanadium compounds. Physical Review B, 30, 5596–5610.

MANUSCRIPT RECEIVED DECEMBER 15, 2005
MANUSCRIPT ACCEPTED FEBRUARY 23, 2006
MANUSCRIPT HANDLED BY BRYAN CHAKOUMAKOS

Appendix D

Chemical data on the titanomagnetite samples from the Bushveld Complex

In Chap. 5, a study of natural titanomagnetite samples from the Bushveld Complex is presented. The samples are thin sections and microprobe analyses were performed for five points per thin section. The average chemical analyses per investigated thin section are presented in Chap. 5 so the microprobe results for all the points of the thin sections are given here. HERFD-XAS spectra were not recorded for all the points. Consequently, the Gaussian parameters used to extract the pre-edges are given when possible, with the corresponding V^{4+} content. The methodology for the pre-edge extraction and the calculation of the V^{4+} content are given in Chap. 5.

D.1 Microprobe analyses

The following table presents the chemical composition per analyzed point of the titanomagnetite thin sections, determined by microprobe analysis.

Section	O at. %	Fe at. %	Ti at. %	V at. %	Cr at. %	Mn at. %	Mg at. %	Al at. %
BK2-1 / 169.61 m								
BK2-1/1	53.5	36.8	4.7	0.63	1.42	0.13	0.08	2.61
BK2-1/2	53.8	35.9	5.3	0.75	1.30	0.15	0.52	2.26
BK2-1/3	53.5	36.4	4.8	0.81	1.31	0.14	0.54	2.44
BK2-1/4	53.6	36.4	5.0	0.72	1.15	0.14	0.69	2.13
BK2-1/5	53.6	36.9	5.1	0.73	1.07	0.14	0.35	2.05
BK2-1/6	53.7	37.0	5.7	0.80	1.00	0.14	0.33	1.24
BK2-2 / 170.39 m								
BK2-2/1	53.0	38.9	4.5	0.80	0.22	0.11	0.45	1.94
BK2-2/2	53.3	38.1	5.0	0.73	0.17	0.11	0.40	2.20
BK2-2/3	53.1	38.8	4.7	0.78	0.20	0.12	0.45	1.81
BK2-2/4	52.9	39.5	4.6	0.84	0.25	0.12	0.34	1.30
BK2-2/5	53.1	39.3	5.0	0.75	0.19	0.12	0.39	1.11

Section	O at. %	Fe at. %	Ti at. %	V at. %	Cr at. %	Mn at. %	Mg at. %	Al at. %
BK2-3 / 169.93m								
BK2-3/1	53.4	37.9	5.4	0.67	0.13	0.12	0.50	1.59
BK2-3/2	53.5	37.9	5.2	0.67	0.13	0.13	0.30	1.37
BK2-3/3	53.3	38.3	5.1	0.71	0.14	0.11	0.08	2.12
BK2-4 / 169.62 m								
BK2-4/1	53.7	37.1	5.8	0.64	0.13	0.14	0.17	2.31
BK2-4/2	53.4	38.0	5.4	0.63	0.12	0.15	0.47	1.76
BK2-4/3	53.7	36.4	5.9	0.65	0.13	0.15	0.67	2.33
BK2-4/4	53.6	37.0	5.7	0.68	0.13	0.14	0.49	2.27
BK2-4/5	53.4	37.8	5.5	0.69	0.15	0.13	0.56	1.74
BK2-5 / 169.14 m								
BK2-5/1	53.9	36.8	6.3	0.65	0.12	0.15	0.44	1.08
BK2-5/2	53.3	38.9	5.4	0.71	0.13	0.12	0.20	0.95
BK2-5/3	53.2	39.5	5.6	0.70	0.12	0.13	0.05	0.60
BK2-5/4	53.5	38.7	6.0	0.70	0.13	0.14	0.10	0.61
BK2-5/5	53.2	38.8	4.8	0.78	0.17	0.11	0.31	1.48
BK2-6 / 168.83 m								
BK2-6/1	53.7	37.6	6.1	0.69	0.14	0.13	0.25	0.95
BK2-6/2	53.2	39.7	5.6	0.79	0.14	0.11	0.03	0.43
BK2-6/3	53.4	38.7	5.6	0.77	0.13	0.11	0.11	1.10
BK2-6/4	53.2	39.0	5.3	0.72	0.13	0.12	0.15	1.16
BK2-6/5	52.7	40.8	4.6	0.73	0.13	0.10	0.05	0.76
BK2-7 / 168.62 m								
BK2-7/1	53.3	38.4	5.2	0.69	0.13	0.13	0.37	1.77
BK2-7/2	54.1	35.9	6.8	0.66	0.12	0.13	0.41	1.87
BK2-7/3	53.6	37.2	6.1	0.67	0.14	0.15	0.58	1.47
BK2-7/4	53.2	38.2	4.9	0.72	0.18	0.13	0.45	2.07
BK2-7/5	53.6	37.0	5.9	0.67	0.13	0.13	0.71	1.77
BK2-8 / 168.30 m								
BK2-8/1	53.6	37.1	5.8	0.67	0.19	0.14	0.63	1.70
BK2-8/2	53.5	37.3	5.6	0.63	0.18	0.15	0.74	1.40
BK2-8/3	53.5	38.0	6.0	0.64	0.19	0.15	0.29	1.13
BK2-8/4	53.6	37.4	6.0	0.61	0.18	0.15	0.57	1.31
BK2-8/5	53.4	38.3	5.9	0.65	0.18	0.16	0.45	0.84
BK2-8/6	53.4	37.7	5.6	0.64	0.18	0.13	0.70	1.57
BK2-9 / 168.10 m								
BK2-9/1	53.5	37.4	5.5	0.64	0.17	0.13	0.83	1.44
BK2-9/2	53.4	38.3	5.7	0.65	0.17	0.16	0.31	1.17
BK2-9/3	53.4	38.5	5.7	0.64	0.17	0.14	0.37	0.95
BK2-9/4	53.2	38.6	5.1	0.70	0.19	0.13	0.40	1.72
BK2-9/5	53.5	37.3	5.4	0.67	0.16	0.13	0.70	2.11

Section	O at. %	Fe at. %	Ti at. %	V at. %	Cr at. %	Mn at. %	Mg at. %	Al at. %
BK2-11 / 167.80 m								
BK2-11/1	53.5	37.5	5.4	0.69	0.16	0.12	0.45	2.12
BK2-11/2	53.4	38.1	5.7	0.66	0.15	0.12	0.43	1.44
BK2-11/3	53.0	38.7	4.4	0.74	0.18	0.10	0.51	2.31
BK2-11/4	53.4	37.2	5.1	0.65	0.14	0.13	0.78	2.57
BK2-11/5	53.6	36.9	5.8	0.66	0.13	0.13	0.68	1.92
BK2-12 / 167.70 m								
BK2-12/1	53.1	39.6	5.3	0.71	0.14	0.14	0.08	0.92
BK2-12/2	53.0	39.9	5.2	0.72	0.15	0.14	0.07	0.71
BK2-12/3	53.5	38.0	6.0	0.70	0.13	0.17	0.23	1.17
BK2-12/4	53.3	38.8	5.6	0.72	0.14	0.14	0.19	1.06
BK2-12/5	53.3	38.9	5.6	0.65	0.14	0.15	0.19	0.95

D.2 Gaussian parameters used for the pre-edge extraction and determination of the corresponding V^{4+} content in the case of the natural BK2 titanomagnetite samples

The following table presents the Gaussian parameters used to extract the pre-edge of the natural BK2 titanomagnetite samples. The pre-edge area of the extracted pre-edge and the corresponding V^{4+} content are also given.

Section	Background	Amplitude	Position x_0 (eV)	s	Pre-edge area	V^{4+} content (%)
BK2-1 / 170.61 m						
BK2-1/1	-1.232 .10^{-3}	6.911 .10^{33}	5829.2964	28.239169	0.1755829	9.63
BK2-1/2	-1.1089 .10^{-3}	1.7106 .10^{36}	5841.8189	28.2752	0.1629272	8.21
BK2-1/3	-1.0418 .10^{-3}	1.0306 .10^{37}	5845.7930	28.2871	0.1689908	8.89
BK2-1/4	-1.0913 .10^{-3}	1.2453 .10^{39}	5857.2134	28.3810	0.175221	9.59
BK2-1/5	-1.2835 .10^{-3}	2.5011 .10^{38}	5852.8344	28.3028	0.1738569	9.44
BK2-1/6	-7.2522 .10^{-3}	2.9791 .10^{38}	5853.494	28.319	0.1911647	11.39
BK2-1/average	-1.0738 .10^{-3}	1.3484 .10^{37}	5846.4465	28.2885	0.1746992	9.53
BK2-2 / 170.39 m						
BK2-2/1	7.1258 .10^{-4}	0.1589	5473.8803	1.9189	0.233081	16.10
BK2-2/4	-3.3605 .10^{-4}	5.4791 .10^{19}	5663.7845	19.6313	0.2000939	12.4
BK2-2/average	5.0784 .10^{-4}	0.2857	5476.1507	2.8694	0.2259172	15.29
BK2-3 / 169.93 m						
BK2-3/1	-5.3141 .$^{-4}$	7.9588 .10^{24}	5706.4464	21.4848	0.220301	14.66
BK2-3/2	8.7661 .10^{-5}	0.6478	5478.973	3.7173	0.505365	18.06
BK2-3/3	-4.2050 .10^{-5}	1.8077	5482.7705	4.5504	0.2354331	16.36
BK2-3/average	-3.7092 .10^{-5}	3.6759	5485.7222	5.189	0.2349736	16.31

Section	Background	Amplitude	Position x_0 (eV)	s	Pre-edge area	V^{4+} content (%)
BK2-4 / 169.62 m						
BK2-4/1	$1.2355\ .10^{-4}$	0.5907	5478.5699	3.5083	0.2290245	15.64
BK2-4/4	$-3.2550\ .10^{-4}$	$5.2284\ .10^{20}$	5672.8293	20.0878	0.1999972	12.38
BK2-4/5	$6.3590\ .10^{-5}$	1.2630	5481.7445	4.3460	0.2194875	14.57
BK2-4/average	$1.0088\ .10^{-4}$	2.7014	5484.6882	4.9598	4.9598	14.22
BK2-5 / 169.14 m						
BK2-5/1	$-8.0398\ .10^{-4}$	$2.8262\ .10^{29}$	5759.4296	24.2842	0.2030374	11.45
BK2-5/2	$-8.8972\ .10^{-4}$	$2.0563\ .10^{33}$	5788.0305	25.1576	0.1917463	14.23
BK2-5/4	$-7.8038\ .10^{-4}$	$1.7327\ .10^{29}$	5458.3925	24.2807	0.2007194	12.46
BK2-5/average	$-8.2058\ .10^{-4}$	$2.8262\ .10^{29}$	5759.4296	24.2842	0.2030374	12.72
BK2-6 / 168.83 m						
BK2-6/1	$3.685\ .10^{-4}$	0.5531	5478.7876	3.6675	0.2194638	14.57
BK2-6/2	$-2.6944\ .10^{-4}$	453.266	5504.8559	8.0220	0.2034131	12.76
BK2-6/4	$-4.4212\ .10^{-4}$	$4.457\ .10^{10}$	5578.8894	14.6218	0.222332	14.89
BK2-6/average	$2.7483\ .10^{5}$	8.4233	5489.3715	5.8626	0.2157705	14.15
BK2-7 / 168.62 m						
BK2-7/3	$-3.5088\ .10^{-4}$	$3.9471\ .10^{4}$	5524.1658	10.3281	0.2101544	13.52
BK2-7/5	$-5.5866\ .10^{-4}$	$3.1739\ .10^{4}$	5523.6897	10.3221	0.1998963	12.37
BK2-7/average	$-5.5866\ .10^{-4}$	$3.5347\ .10^{4}$	5523.9229	10.3220	0.2050491	12.95
BK2-8 / 168.30 m						
BK2-8/3	$-6.5832\ .10^{-4}$	$3.589\ .10^{54}$	6020.7928	34.3211	0.2205624	14.69
BK2-8/4	$-6.0039\ .10^{-4}$	$1.1376\ .10^{59}$	6043.3975	34.3677	0.2030742	12.72
BK2-8/5	$-9.007\ .10^{-4}$	$2.5064\ .10^{60}$	6050.5497	34.4150	0.2067732	13.14
BK2-8/average	$-7.1448\ .10^{-4}$	$1.0040\ .10^{58}$	6038.4608	34.3743	0.2101996	13.53
BK2-9 / 168.10 m						
BK2-9/1	$-7.37\ .10^{-4}$	$1.0427\ .10^{68}$	6129.6781	36.9035	0.2219524	14.85
BK2-9/2	$-9.9645\ .10^{-4}$	$1.8224\ .10^{59}$	6083.0110	36.6996	0.2011398	12.51
BK2-9/3	$-6.2672\ .10^{-4}$	$9.8682\ .10^{70}$	6138.4192	36.6015	0.1954424	11.87
BK2-9/average	$-7.7102\ .10^{-4}$	$1.1940\ .10^{66}$	6119.0612	36.8279	0.2063554	13.09
BK2-11 / 167.80 m						
BK2-11/2	$-1.7005\ .10^{-4}$	2063.1520	5512.0751	9.0259	0.1968567	12.03
BK2-11/3	$-3.1605\ .10^{-4}$	12.6581	5492.3422	6.5585	0.1661566	8.57
BK2-11/4	$-4.0812\ .10^{-4}$	$3.6711\ .10^{7}$	5549.7691	12.4104	0.1957102	11.90
BK2-11/average	$-3.2237\ .10^{-4}$	1894.173	5511.9049	9.0252	0.1854599	10.74
BK2-12 / 167.70 m						
BK2-12/4	$-6.2323\ .10^{-4}$	$6.526\ .10^{7}$	5556.5252	13.2338	0.1670802	8.68
BK2-12/5	$4.2503\ .10^{-5}$	0.831	5481.0445	4.2876	0.1774602	9.29
BK2-12/average	$-1.6022\ .10^{-4}$	5.8095	5489.0909	5.9196	0172549	9.8442

Résumé de la thèse en français

L'objectif de cette thèse est d'étudier les propriétés spectroscopiques et la structure électronique du vanadium dans des matériaux complexes. L'étude s'est focalisée sur trois minéraux présentant un intérêt géologique ou technologique. Un minéral est un composé inorganique naturel se présentant sous forme de solide cristallin. En minéralogie, les éléments présents en faible concentration dans le minéral sont qualifiés de trace, alors qu'ils sont appelés impureté en science des matériaux. La présence d'une impureté dans un minéral modifie plusieurs de ses propriétés, comme par exemple la couleur: le corundum α-Al_2O_3 est transparent mais devient rouge si du chrome est présent (α-Al_2O_3:Cr^{3+}), jaune avec du fer α-Al_2O_3:Fe^{3+}, violet avec du vanadium α-Al_2O_3:V^{3+} et bleu s'il y a à la fois du titane et du fer (α-Al_2O_3:Fe^{2+}, Ti^{4+}). Les mécanismes d'incorporation des élélement-traces et leur influence sur les propriétés du minéral sont donc très étudiés en gémologie, géologie et science des matériaux.

Dans une première partie, le contexte de l'étude est présenté, puis les méthodes expérimentales et théoriques utilisées pour déterminer l'incorporation du vanadium dans les trois minéraux. Ensuite, les résultats obtenus pour chaque minéral sont donnés: la tsavorite, l'anatase dopée au vanadium et la titanomagnétite vanadifère.

Contexte de la thèse Le vanadium est un métal de transition (3*d*) et il est présent dans de nombreux minéraux en tant qu'impureté ou élément principal. Il est responsable d'une grande variété de couleurs dans les minéraux: le vert de la tsavorite $Ca_3Al_2(SiO_4)_3$:V^{3+}, le bleu de la cavansite $CaVOSi_4O_{10}\cdot 4H_2O$, l'orange de la lasalite $Na_2Mg_2[V_{10}O_{28}] \cdot 20H_2O$ ou encore le rouge de la vanadiite $Pb_5(VO_4)_3Cl$ (Fig. D.1).


Tsavorite Cavansite Vanadinite Lasalite

Figure D.1: Quelques minéraux devant leur couleur au vanadium: la tsavorite (verte), la cavansite (bleue), la vanadinite (rouge) et la lasalite (orange).

En plus de son rôle d'impureté colorante dans les minéraux, il possède de nombreuses applications industrielles. Il est ainsi utilisé comme catalyseur [73, 1] ou encore comme colorant dans des pigments ou des cristaux synthétiques. Il donne par exemple une large gamme de couleurs jaunes dans les pigments à base de zircone ZrO_2 pour les céramiques [61]. La couleur bleue ou verte des zircons ($ZrSiO_4$) synthétiques dépend ainsi des conditions de synthèse qui modifient l'incorporation du vanadium et par conséquent la couleur [6]. Le vanadium est aussi utilisé pour renforcer les aciers. Sa première utilisation industrielle dans l'acier fut dans la fabrication de la Ford T: l'utilisation d'un acier renforcé au vanadium permit d'alléger le poids d'un tiers pour une même résistance [17]. Cependant, le vanadium ne forme pas de minérai par lui même et il a besoin d'être extrait d'un minéral ou chimiquement isolé [144].

La principale source naturelle de vanadium est la titanomagnétite vanadifère $Fe_{3-x}Ti_xO_4$:V. Le gisement le plus important dans le monde est constitué par les couches de titanomagnétites dans le Bushveld Complex, en Afrique du Sud [215, 176, 54]. L'épaisseur de ces couches de titanomagnétites varie de quelques centimètres à plusieurs kilomètres, et certaines s'étendent latéralement sur plus de 100 km [54]. Des affleurements de ces couches sont visibles à différents endroits du Bushveld Complex et les couches sont bien observées dans les mines à ciel ouvert (Fig. D.2). Le Bushveld Complex, découvert en 1897 [150], est la plus grande intrusion litée dans le monde, avec une surface totale d'environ 66000 km^2 [222]. Son âge est estimé à 2058.9 ± 0.8 Ma [26] et il appartient au Bassin du Transvaal, en Afrique du Sud. Le Bushveld Complex est en fait une ancienne chambre magmatique géante qui a lentement cristallisé en formant une succession de couches. Il est composé de cinq lobes reliés les uns aux autres en profondeur [53, 57]: les lobes Ouest lointain, Ouest, Sud-Est(ou Bethal), Est et Nord (ou Potgietesrus) (Fig. D.3) [56]. Les roches litées sont divisées en quatre zones en fonction de la hauteur stratigraphique: inférieure, critique, principale et supérieure [187]. Deux principales familles de minéraux sont présentes dans les roches du Bushveld Complex. La première est constituée de chromitites, qui sont des cumulats de roches ignées composés majoritairement de chromite ($FeCr_2O_4$), dans la Zone Critique. La deuxième famille est composée de couches de titanomagnétite vanadifère dans la partie supérieure du Bushveld Complex [38]. Les roches du lobe Ouest riches en magnétite vanadifère sont regroupées sous le nom de Bierkraal Magnetite Gabbro.

Figure D.2: (*Gauche*) Affleurement d'une couche de titanomagnétite, à Mapochs Mine. (*Droite*) Une couche de titanomagnétite dans la mine de Vametco, située dans le lobe Est du Bushveld Complex.

Malgré de nombreuses études sur la formation du Bushveld Complex, la cristallisation des couches de titanomagnétite est encore mal comprise. Plusieurs modèles ont été proposés depuis les années 1920 mais aucun n'a trouvé un consensus général. Une revue des modèles proposés à été faite par Reynolds en 1985 [175], dans laquelle Reynolds concluait que la plupart des modèles reconnaissent que la précipitation d'importantes quantités de titanomagnétites nécéssaire

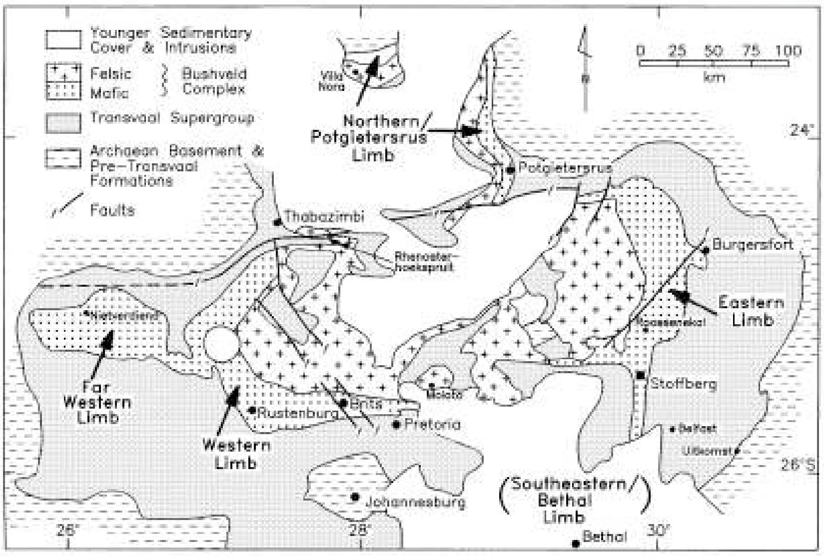

Figure D.3: Carte de la géologie générale du Bushveld Complex, représentant les affleurements des lobes Nord, Est, Ouest and Ouest lointain, ainsi que la position du lobe Sud-Est non exposé (il est complètement recouvert par des roches sédimentaires plus jeunes). La carte provient de la Ref. [56].

au développement de ces couches est déclenchée par une augmentation de la fugacité en oxygène [113, 172, 173, 152, 130, 129], mais que le processus par lequel cette augmentation a lieu est mal compris. Plusieurs explications ont été proposées: un mélange de magmas [114, 103], des changements de pression [50, 210], des injections régulières de nouveaux magmas [56]. Pour comprendre la cristallisation des couches de titanomagnétite, des analogies ont souvent été faites entre les couches de chromite et de magnétites [37, 39, 49, 71], et le chrome dans ces deux minéraux a été particulièrement étudié [28, 36, 52, 51, 50, 136, 148, 147]. Le vanadium a cependant moins retenu l'attention [54, 55, 175] et une étude détaillée du vanadium dans les titanomagnétites vanadifères est nécéssaire. En particulier, le degré d'oxydation du vanadium pourrait apporter des informations sur les processus qui ont mené à la cristallisation de ces couches géantes de titanomagnétites.

Le vanadium peut se trouver sous différents degrés d'oxydation: +II, +III, +IV and +V. Les ions V^{3+}, V^{4+} et V^{5+} existent dans une importante gamme d'environnements géologiques sur Terre, alors que V^{2+} ne se trouve que dans des systèmes très réducteurs comme ceux qui existaient dans la nébuleuse solaire primitive [192, 199]. La détermination de la fugacité en oxygène des magmas est capital pour la compréhension de la génèse et de la différentiation des magmas ainsi que de la nature et de l'évolution des couches internes des planètes [46, 11]. Les différents degrés d'oxydation du vanadium en font une sonde géochimique intéressante pour obtenir des informations sur les conditions en fugacité en oxygène prévalant durant la formation des roches terrestres et planétaires. Les proportions relatives entre les différents dégrés d'oxydation du vanadium dépendent en effet de la fugacité en oxygène du liquide fondu à partir duquel les minéraux ont cristallisé [41, 42]. La quantité de V^{4+} dans le liquide fondu est faible, mais il a été observé que le rapport V^{4+}/V^{3+} diminue significativement avec l'augmentation de la fugacité en oxygène [44]. Par exemple, pour des conditions en fugacité en oxygène correspondant aux systèmes basaltiques terrestres, il est attendu que V^{4+} soit la principale valence d'un magma ferrobasaltique, alors que pour des conditions plus oxydantes, V^{5+} devient la valence dominante (Fig. D.4) [206].

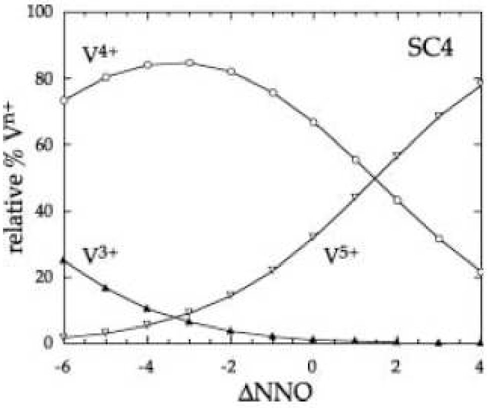

Figure D.4: Variations théoriques des proportions relatives des différents degrés d'oxydation du vanadium (V^{n+}) en fonction de la fugacité en oxygène pour un liquide ferrobasaltique, appelé SC4. Les conditions en fugacité en oxygène correspondant aux systèmes terrestres basaltiques varient de ΔNNO = -3 à ΔNNO = +1, où ΔNNO représente les conditions en oxygène par rapport au tampon NNO (Nickel-Nickel Oxide). La figure provient de la Ref. [206].

A partir de ces relations entre les degrés d'oxydation du vanadium et la fugacité en oxygène, des oxybaromètres basés sur la valence du vanadium ont été développés [107, 158]. Ils sont basés sur les variations du coefficient de partage entre un minéral et le magma parent, ce coefficient repésentant l'affinité d'un élément pendant la cristallisation ou la fonte pour la phase solide ou liquide [40, 43, 143]. Ces oxybaromètres peuvent enregistrer au moins huit ordres de grandeurs de fugacité en oxygène, ce qui permet de les utliser à la fois pour des magmas réduits et oxydés. Leur applicabilité pour des basses fugacités en oxygène est particulièrement importante car les baromètres traditionnels basés sur le rapport Fe^{2+}/Fe^{3+} sont inutilisables s'il n'y a pas de Fe^{3+} présent [125] et que peu d'oxydes Fe-Ti sont préservés sans altération. Des oxybaromètres basés sur la valence du vanadium ont été développés pour des verres basaltiques [197, 127], des spinelles [157, 177, 178], des olivines [198, 190] et des pyroxènes [125, 126]. Le degré d'oxydation du vanadium est par conséquent une sonde potentielle permettant d'obtenir des informations sur les processus qui ont abouti à la formation des couches de titanomagnétites vanadifères dans le Bushveld Complex, et en particulier sur la fugacité en oxygène pendant leur cristallisation.

Cependant, à l'heure actuelle, le degré d'oxydation du vanadium dans les titanomagnétites du Bushveld Complex n'est pas encore bien connu. Une première étude par spectroscopie d'absorption des rayons X (XAS) a été faite par Balan *et al.* [10]. La spectroscopie d'absorption des rayons X est une technique très utilisée pour déterminer le degré d'oxydation d'un élément dans un composé. Elle est en effet chimiquement sélective et les structures observées sur un spectre d'absorption des rayons X dépend de l'environnement cristallographique et électronique de l'élément étudié. Ces structures résultent de l'interaction entre le faisceau de rayons X incidents et les électrons du système. Plus particulièrement, les structures observées à une énergie inférieure à celle du seuil, appelées le préseuil, donnent des informations sur le degré d'oxydation et l'environnement local autour de l'atome absorbeur [35]. Pour déduire le degré d'oxydation de l'élément des structures du préseuil, la méthode la plus couramment utilisée est la comparaison du spectre de l'élément étudié avec ceux de composés de référence dans lesquels le degré d'oxydation et la coordinence sont bien déterminés. Cette méthode *fingerprint* a été utilisée dans l'étude de minéraux et de verres pour plusieurs éléments de transition comme le titane [79, 75, 78, 217], le fer [35, 83, 116, 161, 218, 219, 221], le chrome [72], le nickel [77], le manganèse [59, 76, 110] ou le magnésium [168, 207]. Concernant le vanadium, la première étude a été faite par Wong *et al.* [224] et de nombreuses études ont suivi, *e.g.* Ref [18, 10, 60, 93, 127, 149, 156, 166, 171, 197].

L'utilisation de cette méthode *fingerprint* nécessite une connaissance précise de la signature spectrale de la valence et de la coordination de l'élément dans le composé de référence. L'énergie et l'intensité du préseuil dépendent en effet des deux. Cette connaissance précise du préseuil peut être obtenue de manière expérimentale et théorique. Les mesures d'absorption des rayons X sur un monocristal permettent d'obtenir des informations plus précises que dans le cas d'une poudre pour lequel les informations obtenues sont moyennées sur tout le cristal. La plupart des cristaux présentent en effet une anisotropie naturelle, appelée X-ray Natural Linear Dichroism. La dépendance angulaire du spectre d'absorption X qui en résulte [24] est aussi observée pour le préseuil de composés cubiques [32, 122].

Les mesures d'absorption X sur un monocristal ne sont cependant pas aisées à réaliser. Une détermination théorique du spectre d'absorption des rayons X peut apporter des informations qualitatives et quantitatives supplémentaires. La relaxation structurale autour d'une impureté dans une structure-hôte peut par exemple être déterminée par un calcul de minimisation de l'énergie de la structure. Deux approches peuvent être utilisées pour calculer le spectre expérimental, leur choix dépendant de la nature des états finaux (localisés ou délocalisés). Dans le cas d'états localisés, l'approche multiplets est utilisé (on parle de calculs multiélectroniques) alors que la méthode utilisée pour les états délocalisés est basée sur la théorie de la fonctionnelle de la densité (on parle de calculs monoélectroniques). Cette dernière approche a l'avantage de ne pas être paramétrée et permet le calcul de tout le spectre d'absoprtion X, et pas uniquement le préseuil comme dans le cas de l'approche multiélectronique. Une seule des deux méthodes est souvent utilisée mais une étude récente sur le préseuil K du chrome dans le spinelle ($MgAl_2O_4$) a montré que le couplage de ces deux méthodes permet de complètement caractériser les structures cristallographiques et électroniques de l'atome absorbeur.

Au cours de cette thèse, j'ai cherché à déterminer les structures cristallographiques et électroniques du vanadium en impureté dans des minéraux en utilisant la spectroscopie d'absorption des rayons X. La question principale portait sur la spéciation, *i.e.* le degré d'oxydation et le site d'incorporation, du vanadium dans les titanomagnétites du Bushveld Complex dans le but de comprendre la formation des couches géantes de titanomagntétites au niveau de cette ancienne chambre magmatique. Des échantillons naturels et synthétiques ont été analysés principalement par spectroscopie d'absorption des rayons X. Les spectres obtenus au seuil K du vanadium ont ainsi été analysés par la méthode *fingerprint*. Une étude approfondie du préseuil K d'un des composés de référence utilisé, la tsavorite $Ca_3Al_2(SiO_4)_3$:V^{3+}, a alors été entreprise afin de caractériser complètement la signature spectrale du vanadium trivalent dans un octèdre légèrement distordu. Un couplage entre la théorie et l'expérience d'une part, et entre les différentes approches théoriques d'autre part, a été utilisé. En parallèle, une étude expérimentale et théorique de la spéciation du vanadium dans l'anatase a été menée. L'anatase dopée au vanadium est étudiée pour ses propriétés de photocatalyseur. Ce dernier thème de thèse permet de considérer la question de l'incorporation du vanadium dans des minéraux d'une manière plus large.

Méthodes expérimentales Deux types d'expériences ont été réalisées dans l'étude des trois minéraux vanadifères. La première série d'expériences menées est un ensemble de techniques de caractérisation très utilisées en Sciences de la Terre et en minéralogie: la diffraction des rayons X (DRX), la microsonde et la microscopie électronique à balayage (MEB). Le deuxième (et principal) type d'expériences ménées pendant cette thèse est l'enregistrement de spectres d'absorption des rayons X au seuil K du vanadium.

La DRX permet une analyse qualitative et quantitative de l'échantillon. Elle permet en effet de déterminer les phases présentes. Elle donne aussi accès à des paramètres structuraux (paramètre de maille, positions atomiques, ...) et à des informations sur la texture de l'échantillon. Dans le cadre de cette thèse, seule une analyse qualitative a été faite sur des échantillons synthétiques de magnétites vanadifères. L'enregistrement des diffractogrammes a été fait à l'Institut de Minéralogie et de Physique des Milieux Condensés (Paris, France). La microsonde fournit la composition chimique de l'échantillon. C'est une méthode non-destructive qui permet de détecter tous les éléments à partir du beryllium pour une concentration d'environ 100 ppm minimum. Les analyses ont été effectuées sur tous les échantillons étudiés au cours de cette thèse, au laboratoire CAMPARIS de l'Université Pierre et Marie Curie (Paris, France). Le MEB permet d'obtenir des informations topographiques et chimiques sur un échantillon (taille des grains, porosité, distribution de taille de particules,...) grâce à la prise d'images de l'échantillon à l'échelle micrométrique. Une analyse de la composition chimique de l'échantillon peut aussi être réalisée; on parle dans ce cas de spectroscopie dispersive en énergie (EDS). Les échantillons naturels et synthétiques de titanomagnétites ont été analysés au MEB et par EDS au Laboratoire Interfaces et Systèmes Electrochimiques de l'Université Pierre et Marie Curie (Paris, France) et à l'Industrial Minerals and Metals Research Institute, du Department of Materials Science and Metallurgical Engineering de l'Université de Pretoria (Pretoria, Afrique du Sud).

La spectroscopie d'absorption des rayons X est un outil puissant pour l'étude de la structure électronique et cristallographique d'une impureté dans une structure-hôte. Elle a le double avantage d'être sélective chimiquement et orbitalairement. On peut en effet sélectionner l'élément étudié grâce à l'énergie des rayons X incidents, chaque élément ayant une énergie bien définie. De même, on peut choisir dans quelle couche l'électron est excité et donc quels états vides sont sondés. On parle de seuils K si l'électron excité provient de la couche $1s$, $L_{2,3}$ s'il vient de la couche $2p$, etc. Dans le cas de l'approximation dipolaire électrique, les transitions doivent obéir à la règle de sélection $\Delta\ell = \pm 1$. L'approximation quadrupolaire électrique est définie par $\Delta\ell = \pm 2$ et le seuil K correspond alors à des transitions des états $1s$ vers d. Un autre avantage de l'absorption des rayons X est que cette technique ne nécessite pas d'ordre à longue distance et permet donc l'étude des verres et des matériaux amorphes. Toutes les expériences réalisées au cours de cette thèse ont été faites au seuil K du vanadium (situé à 5465 eV). Toutes les explications que je donne par la suite concernent donc uniquement les seuils K des éléments de transition.

Le principe de l'absorption des rayons X est le suivant. Les rayons X excitent un électron de cœur qui transite dans des états vides grâce à l'absorption d'un photon d'énergie $\hbar\omega$. Les variations du coefficient d'absorption des rayons X sont alors mesurées en fonction de l'énergie incidente. Dans le cas d'échantillons dilués, *e.g.* pour les impuretés incorporées dans une structure hôte, on enregistre le rendement de fluorescence. Un spectre d'absorption des rayons X comprend trois régions. La première se situe avant le seuil d'absorption de l'élément étudié et constitue la ligne de base du spectre. La deuxième région, le XANES (X-ray Absorption

Near-Edge Structure), s'étend environ 50 eV après le seuil d'absorption. Pour une énergie incidente légèrement inférieure à celle du seuil, le photoélectron est injecté dans des états localisés $3d$ et les structures enregistrées constituent le préseuil. Celui-ci préseuil résulte de transitions électriques dipolaires ($1s \rightarrow p$) et quadrupolaires ($1s \rightarrow 3d$) électriques. Dans le cas d'un site centrosymétrique, seules les transitions électriques quadrupolaires sont à l'origine des structure observées dans le préseuil. La partie du spectre XANES qui suit le préseuil constitue le seuil et résulte de l'éjection du photoélectron dans le continuum. Le seuil est composé de transitions dipolaires électriques. Le XANES donne accès à l'ordre à courte et moyenne distance autour de l'atome absorbeur. Le préseui donne plus particulièrement des informations sur la symétrie locale autour de l'atome absorbeur et son degré d'oxydation. Deux méthodes d'analyse sont possibles pour le XANES (préseuil et seuil). La première est dite *fingerprint* et consiste à comparer le spectre mesuré avec ceux de composés de référence afin de tirer des information qualitatives sur l'environnement de l'atome absorbeur; cette méthode a été appliquée au cours de cette thèse à la détermination du degré d'oxydation du vanadium dans les titanomagnétites du Bushveld. La deuxième méthode consiste à reproduire le spectre expérimental afin d'obtenir des informations fines sur les structures cristallographique et électronique de l'atome absorbeur. Elle a été utilisée au cours de l'étude sur la tsavorite et l'anatase dopée au vanadium. La dernière région du spectre est la partie EXAFS (Extended X-ray Absorption Fine Structure) qui fournit des informations locales sur l'atome absorbeur: sa coordinence, la nature de ses voisins, leurs distances et le désordre structural. Le XANES et l'EXAFS sont différenciés car leur méthode d'analyse sont très différentes mais c'est le même processus physique qui est en cause.

La présence de titane en quantité supérieure à celle de vanadium dans les titanomagnétites a nécessité l'usage d'un mode particulier d'enregistrement de la fluorescence afin de filtrer la fluorescence du titane. Ce mode de détection est appelé HERFD-XAS (High Energy-Resolution Fluorescence Detected X-ray Absorption Spectroscopy) [66, 69, 97, 96]. Une raie de fluorescence de l'atome absorbeur est enregistrée grâce à un spectromètre à haute résolution. Le HERFD a l'avantage de filtrer la fluorescence des autres éléments présents dans l'échantillon, ainsi que celui d'augmenter la résolution spectrale [94, 65, 104, 102]. Le montage particulier nécessaire à l'enregistrement du HERFD est illustré sur la figure D.5, ainsi que la géométrie dans laquelle est installé le spectromètre. La partie centrale du spectromètre est un cristal analyseur qui analyse la fluorescence émise par l'échantillon et la réfléchit sur le détecteur. Il faut cependant rester vigilant lors de l'analyse des spectres HERFD et vérifier que ceux-ci sont similaires à un spectre XANES enregistré de manière conventionnelle. Ceux-ci peuvent en effet différer d'un spectre XANES enregistré de manière conventionnelle par le nombre de structures et de leurs intensités relatives [94, 66]. Il est alors utile d'enregistrer aussi un plan RIXS (Resonant Inelastic X-ray Scattering), ce qui consiste à faire varier l'énergie incidente (Ω) et d'émission(ω). L'intensité est alors tracée sur un plan 2D en fonction de ces deux énergies, ou alors en fonction de l'énergie incidente et de l'énergie de transfert $\Omega - \omega$. Le spectre HERFD correspond alors à une coupe selon la diagonale de ce plan RIXS. Il est d'autant plus important de vérifier que toutes les structures visibles sur le spectre XANES conventionnel sont présentes sur le spectre HERFD à la bonne énergie que les méthode théoriques utilisées pour calculer les spectres XANES sont dédiées au XANES classique.

Trois campagnes de mesures ont été menées au cours de cette thèse afin d'enregistrer les spectres HERFD au seuil K du vanadium pour les trois types d'échantillons. Tous les spectres ont été enregistrés avec le spectromètre à haute résolution, en sélectionnant la raie $K\alpha_1$ du vanadium (4952 eV). Les mesures ont été réalisées sur la ligne ID26 [90] de l'ESRF (Grenoble, France).

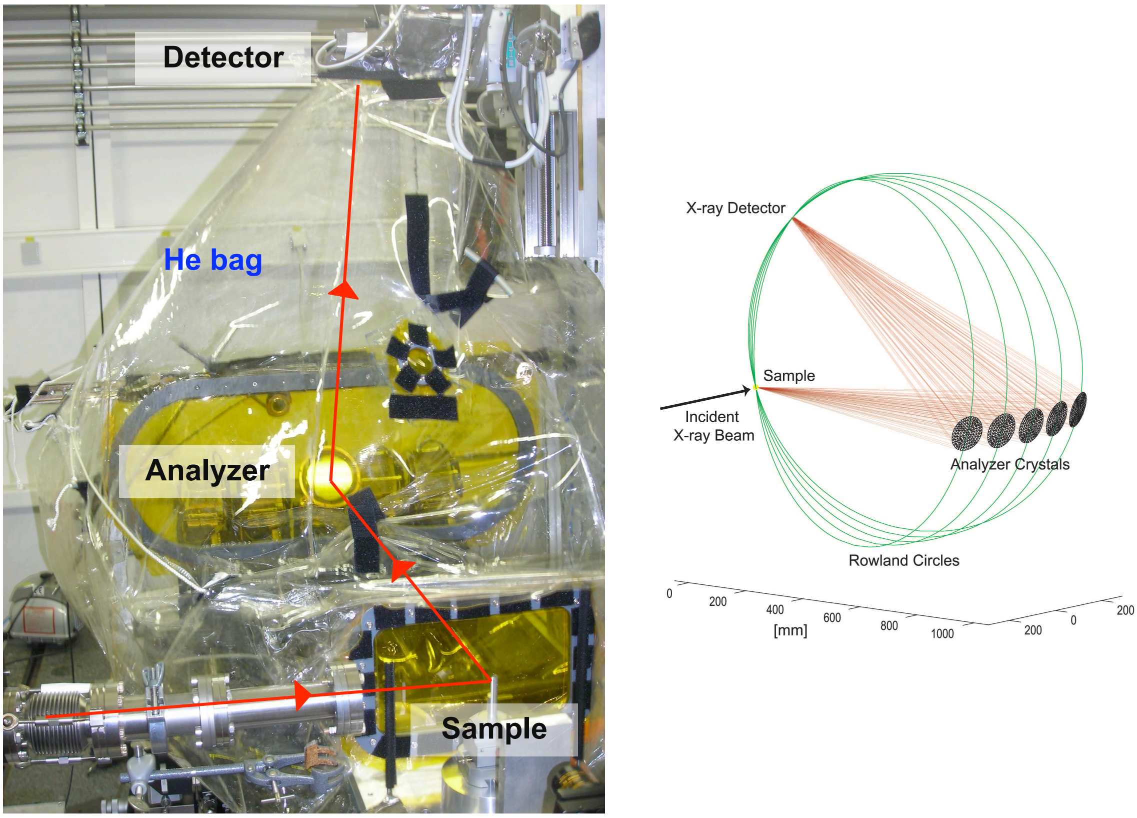

Figure D.5: Montage expérimental de la ligne ID26 de l'ESRF (gauche), permettant d'enregistrer le spectre HERFD, et géométrie du spectromètre à haute résolution (droite). Nous n'avons utilisé qu'un cristal analyseur pendant nos expériences. La figure provient de la Ref. [97].

Méthodes théoriques Deux approches théoriques ont été utilisées au cours de cette thèse afin de reproduire les spectres expérimentaux une approche monoélectronique et une approche multiélectronique. Elles consistent toutes les deux à calculer la section efficace d'absorption:

$$\sigma(\hbar\omega) = 4\pi^2\alpha\hbar\omega \sum_{i,f} |\langle\psi_f|\hat{O}|\psi_i\rangle|^2 \delta(E_f - E_i - \hbar\omega), \tag{D.1}$$

où α est la constante de structure fine ($\alpha = \frac{e^2}{4\pi\epsilon_0\hbar c}$(unités S.I.) et $\alpha \simeq \frac{1}{137}$), $\hbar\omega$ l'énergie des photons incidents et $\hat{O}$ un opérateur de transition couplant l'état initial $|\psi_i\rangle$, d'énergie E_i, et les états finaux $|\psi_f\rangle$ d'énergie E_f. La fonction de Dirac $\delta(E_f - E_i - \hbar\omega)$ assure la conservation de l'énergie. Dans le cas de l'approximation dipolaire électrique, l'opérateur de transition dépend de la polarisation $\hat{\boldsymbol{\varepsilon}}$ des rayons X incidents et s'exprime comme:

$$\hat{O}_{dip} = \hat{\boldsymbol{\varepsilon}} \cdot \boldsymbol{r}. \tag{D.2}$$

Dans la cas de l'approximation quadrupolaire électrique, l'opérateur de transition dépend cette fois de la polarisation $\hat{\boldsymbol{\varepsilon}}$ et de la direction $\hat{\mathbf{k}}$ du faisceau incident. Il est défini par:

$$\hat{O}_{quad} = \frac{i}{2}(\hat{\boldsymbol{\varepsilon}} \cdot \boldsymbol{r})(\hat{\boldsymbol{k}} \cdot \boldsymbol{r}). \tag{D.3}$$

Les opérateurs de transition dans ces deux approximations sont dérivés de l'expression générale du hamiltonien décrivant l'interaction rayonnement-matière. Les détails de la dérivation sont donnés dans la référence [24]. L'expression détaillée de la section efficace d'absorption dépend du groupe ponctuel du cristal étudié. La référence [24] en donne l'expression pour les groupes ponctuels dans chaque approximation de la section efficace d'absorption. La section efficace d'absorption totale est la somme des sections efficaces déterminées dans chaque approximation:

$$\sigma(\hat{\boldsymbol{\varepsilon}}, \hat{\mathbf{k}}) = \sigma^D(\hat{\boldsymbol{\varepsilon}}) + \sigma^Q(\hat{\boldsymbol{\varepsilon}}, \hat{\mathbf{k}}), \tag{D.4}$$

où $\sigma^D(\hat{\boldsymbol{\varepsilon}})$ est la section efficace électrique dipolaire et $\sigma^Q(\hat{\boldsymbol{\varepsilon}}, \hat{\mathbf{k}})$ celle électrique quadrupolaire.

L'approche monoélectronique est basée sur la théorie de la fonctionnelle de la densité (DFT) et consiste en une détermination *ab initio* des spectres XANES. Cette méthode se place dans l'espace réciproque et permet de déterminer par un calcul de minimisation d'énergie un modèle structural du minéral contenant une impureté. A partir de la structure expérimentale, une supercellule est construite de manière à contenir entre 100 et 200 atomes. Un atome d'impureté est alors incorporé dans cette structure et les positions atomiques des voisins de l'impureté peuvent varier de manière à minimiser l'énergie totale du système. A partir de cette structure relaxée, le spectre XANES est alors calculé. Deux étapes sont nécessaires : la densité de charge avec un trou $1s$ sur l'atome absorbeur est calculé puis le spectre lui-même dans les approximations dipolaire et quadrupolaire électriques. Le spectre total correspond à la somme des deux. Les calculs monoélectroniques prennent en compte la polarisation en spin, ce qui permet d'obtenir des informations fines sur la structure électronique de l'atome absorbeur.

L'approche monoélectronique a été adoptée pour l'étude de la tsavorite et de l'anatase dopé au vanadium. Deux codes ont été utilisés: PARATEC (PARAllel Total Energy Code) [163] et l'ensemble de codes Quantum-Espresso [92], incluant les programmes PWscf [12] et Xspectra [99]. Ces deux codes calculent l'énergie totale du système, ils utilisent des ondes planes et des pseudopotentiels (*norm-conserving* de type Troullier-Martins [208], dans la forme Kleinman-Bylander [128]). L'utilisation des pseudopotentiels nécessitent la reconstruction d'une fonction d'onde *all electron*, ce qui a été fait en utilisant la méthode PAW (Projector Augmented Wave). La méthode récursive de Haydock, Heine et Kelly [105, 106] a été utilisée; elle fait appel au formalisme de Green pour reécrire la section efficace d'absorption sous forme d'une fraction continue, ce qui permet de réduire les temps de calcul.

Un autre type de calculs monoélectroniques a été utilisé pour l'étude de l'incorporation du vanadium dans les titanomagnétites. Les deux codes cités précédemment n'ont pas pu être utilisés car ils reproduisent difficillement la structure magnétique complexe de la magnétite. Des calculs ont donc été faits avec le code FDMNES (Finite Difference Method for Near-Edge Structure) développé par Yves Joly [118]. J'ai utilisé le code dans le formalisme de la diffusion multiple. Les calculs se font dans l'espace réel, pour un cluster (et non pour la structure périodique du cristal) [119].

L'approche multiélectronique est une approche semi-empirique dédiée aux systèmes avec de fortes interactions électroniques. Elle est basée sur le théorie des multiplets dans un champ de ligands (Ligand Field Multiplet, LFM) et donne généralement de meilleurs résultats que l'approche monoélectronique dans le cas où les transitions ont lieu vers des états localisés, comme par exemple dans le cas des seuils $L_{2,3}$ des éléments de transition [8, 67]. Elle a été appliquée avec succès au préseuil K des éléments de transition [9, 85, 122, 219]. La principale caractéristique de la méthode LFM est que l'ion est considéré avec tous ses électrons et comme isolé dans un champ de ligands. Les calculs multiplets ne prennent en effet pas en compte toute la structure du cristal mais juste la symétrie autour de l'atome absorbeur. De ce fait, seul le préseuil K peut être calculé. Une autre caractéristique importante est que certains paramètres, en particulier les paramètres de champ cristallin définissant la symétrie locale autour de l'ion, doivent être ajustés par rapport au spectre expérimental. Les calculs multiélectroniques permettent d'obtenir des analyses quantitatives sur l'atome absorbeur, comme par exemple l'hybridation *p-d*. Le code utilisé st celui développé par Thole [203] dans le formalisme établi par Cowan [64] et Butler [29]. Dans le cadre de cette thèse, les calculs multiélectroniques n'ont été réalisés que pour l'étude du préseuil K du vanadium dans la tsavorite.

Dans les deux approches monoélectronique et multiélectronique, les calculs sont réalisés pour un site unique et le spectre du cristal doit être déduit de celui du site. Il est donc nécessaire de connaître les relations permettant de déduire le spectre du cristal à partir de celui du site. De même, dans un cristal, un site cristallographique n'est souvent pas unique. Il est donc nécessaire d'établir les relations permettant de déduire soit le spectre d'un site à partir de celui d'un autre site, soit celui le spectre moyen sur tous les sites possibles. Les relations entre sites ou entre site et cristal ne sont cependant pas triviales et et leur détermination nécessite un important développement théorique basé sur les tenseurs sphériques. Ce développement a été fait par Brouder *et al.* [25] et traite l'exemple du grenat et du spinelle. Les formules ainsi développées ont été alors appliquées aux calculs monoélectroniques et multiélectroniques du vanadium dans la tsavorite.

La tsavorite $\mathbf{Ca_3Al_2(SiO_4)_3{:}V^{3+}}$ La tsavorite a été utilisée comme composé de référence pour la détermination du degré d'oxydation du vanadium dans les titanomagnétites. C'est un grossulaire (grenat) vanadifère, donc un minéral cubique (de groupe pontuel $Ia\bar{3}d$), de couleur verte dans lequel le vanadium trivalent est incorporé en substitution de l'aluminium. Le vanadium se trouve donc dans un site de symétrie C_{3i}, correspondant à un octaèdre légèrement distordu avec un centre d'inversion. Le préseuil K résulte donc uniquement de transitions quadrupolaires électriques et une dépendance angulaire du préseuil K est attendue: selon l'orientation du cristal par rapport au faisceau de rayons X incidents, les structures observées dans le préseuil sont différentes.

Pour évaluer l'influence de la dépendance angulaire sur le préseuil K du vanadium dans la tsavorite, des spectres HERFD-XAS au seuil K du vanadium ont été enregistrés sur un monocristal pour différentes orientations de l'échantillon par rapport au faisceau incident (Fig. D.6). La dépendance angulaire a été bien observée expérimentalement. Le préseuil mesuré comprend trois pics qui possèdent des intensités relatives différentes selon l'orientation de l'échantillon. L'effet, bien que significatif, reste cependant faible et le spectre expérimental a été calculé dans l'approche monoélectronique afin de tirer des informations fines sur la structure électronique du vanadium dans la tsavorite. Cependant, les codes utilisés pour calculer le spectre XANES sont dédiés à l'absoprtion des rayons X mesurée de façon conventionnelle. Un plan RIXS du vanadium dans la tsavorite a été donc été enregistré dans la région du préseuil de manière à vérifier que le spectre HERFD enregistré est similaire à celui qui aurait été enregistré de manière conventionnelle. Le plan RIXS représentant l'énergie de transfert $\Omega - \omega$ en fonction de l'énergie incidente Ω est représenté sur la figure D.7 (gauche). Comme toutes les structures sont présentes selon la diagonale du plan, le préseuil enregistré avec le HERFD est identique à celui donné par le XANES conventionnel. La comparaison entre les spectres HERFD et conventionnel enregistrés au seuil K du vanadium dans la tsavorite montrent clairement leur similitude dans le cas de la tsavorite (Fig. D.7 droite). Le spectre expérimental pourra donc être comparé à celui calculé.

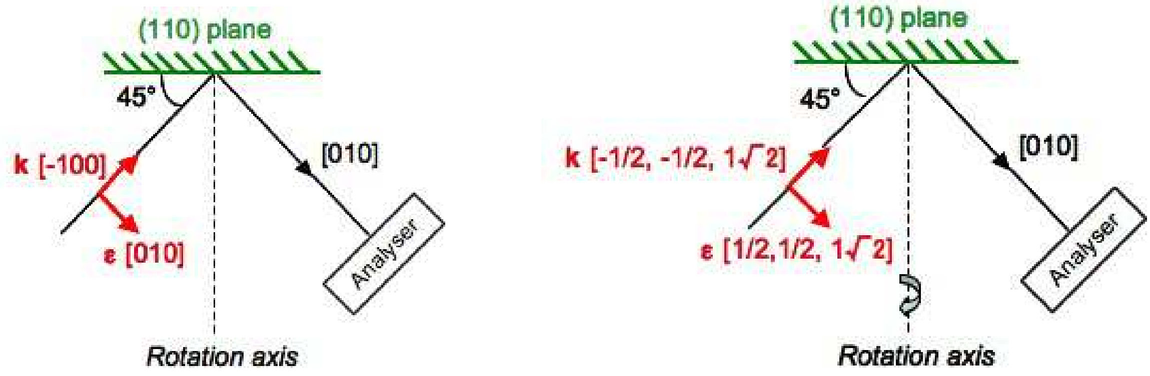

Figure D.6: Les deux configurations experimentales utilisées pour enregistrer les spectres HERFD-XAS au seuil K du vanadium dans la tsavorite. L'échantillon a été tourné de 90° entre les deux.

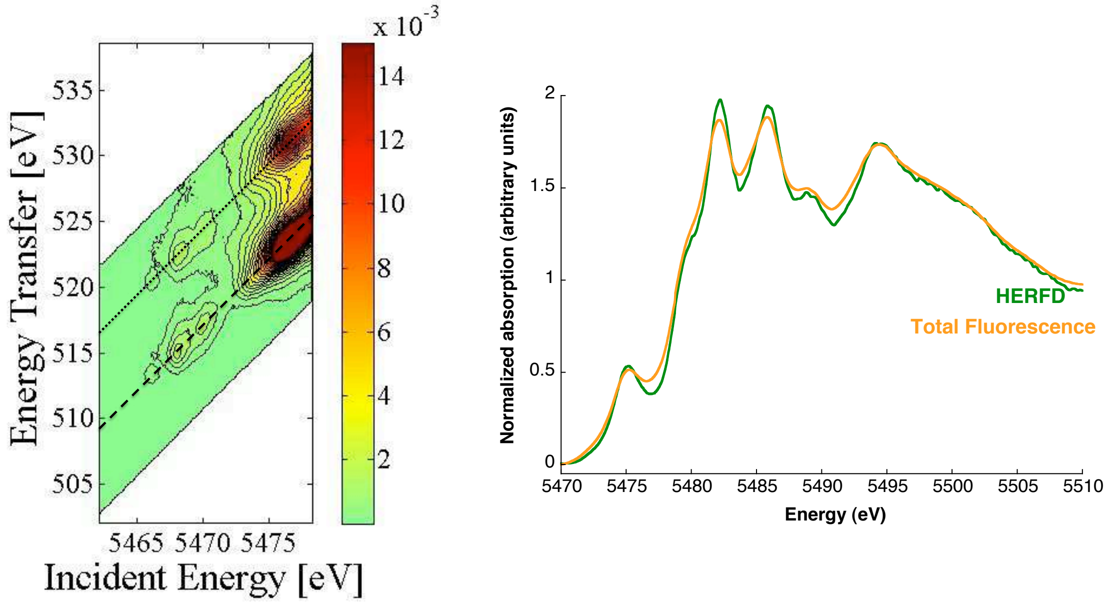

Figure D.7: (*Gauche*) Plan RIXS de la tsavorite enregistré dans la région du préseuil K du vanadium. La ligne tiretée correspond à la raie de fluorescence Kα_1 et celle pointillée à la raie de fluorescence Kα_2. (*Droite*) Comparaison entre le spectre XANES enregistré en fluorescence de manière conventionnelle (orange) et en HERFD (vert).

.

La structure relaxée a été déterminée de manière *ab initio*. La substitution de l'aluminium par le vanadium dans le site octaédrique entraîne en fait une dilatation de l'octaèdre, avec une augmentation de la distance V-O par rapport à celle Al-O du grossulaire. La symétrie C_{3i} est conservée au cours de la relaxation. Le spectre XANES calculé est représenté sur le figure D.8. Toutes les structures expérimentales sont présentes sur le spectre calculé, avec les positions en énergie et les intensités relatives correctes, y compris la dépendance angulaire du préseuil. Ce bon accord entre expérience et théorie a permis de donner une interprétation fine des structures observées. Les structures du préseuil ont été interpretées dans une vision monoélectronique des transitions $1s \rightarrow 3d$ mises en jeu. La séparation en énergie entre orbitales $3d$ sous l'effet du champ cristallin est similaire aux valeurs déterminées par spectroscopie optique. La signature spectrale du vanadium trivalent dans un site octaédrique centrosymétrique a donc pu être déterminée de manière précise et la tsavorite peut donc être utilisée de manière fiable comme composé de référence dans l'étude sur les titanomagnétites du Bushveld Complex.

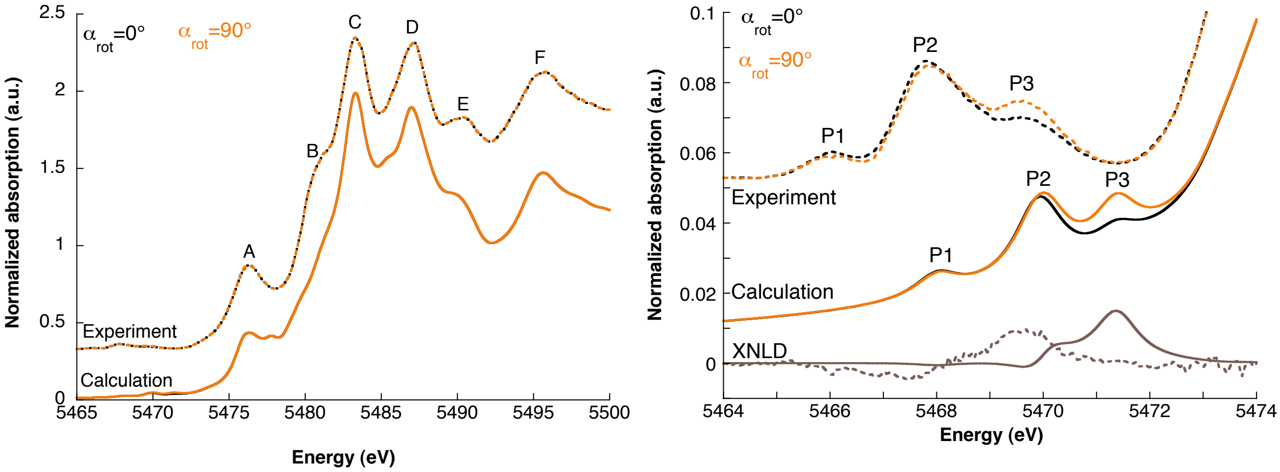

Figure D.8: Comparaison entre les spectres expérimentaux et théoriques du vanadium dans la tsavorite (*gauche*), avec un zoom sur le préseuil et la dépendance angulaire observée (*droite*).

.

Des calculs multiplets ont aussi été réalisés pour étudier le préseuil mais cette étude est encore en cours. L'expression de la section efficace d'absorption quadrupolaire a été donnée pour tout le cristal et pour les deux orientations expérimentales à partir de celui d'un site unique. L'influence des paramètres qui doivent être ajustés par rapport à l'expérience a été étudiée et un jeu de paramètres a été défini. Ce jeu de paramètres ne permettant pas de reproduire correctement le préseuil et sa dépendance angulaire, il doit encore être affiné. Des mesures de spectroscopie optique à basse température devrait permettre d'obtenir un jeu de paramètres expérimentaux permettant de reproduire les spectres expérimentaux et la dépendance angulaire avec les bonnes énergies et intensités relatives. Dans le calcul, une simplification a été faite dans les paramètres en interprétant des règles de symétrie données par Butler [29]. Des calculs doivent donc être réalisés sans simplification afin de tester celle-ci.

L'incorporation du vanadium dans l'anatase synthétique L'anatase TiO_2 est un matériau très étudié car il est un puissant catalyseur [16] et il est utilisé aussi comme photodégradant de nombreux polluants [48]. Il a été montré que le vanadium augmente l'activité photocatalytique [62]. Une étude est en cours sur l'effet de l'incorporation de vanadium dans des nanofilaments d'anatase sur la production d'hydrogène par dissociation de l'eau sous l'effet photocatalytique de l'anatase. Une des questions posées au cours de cette étude est le site d'incorporation du vanadium dans l'anatase au cours de la synthèse. Deux sites différents d'incorporation du vanadiumvexistent dans la structure de l'anatase: le site du titane (substitution) ou un site octaédrique interstitiel. Une étude par spectroscopie d'absorption des rayons X a été menée afin de déterminer le site d'incorporation du vanadium.

Des spectres HERFD au seuil *K* du vanadium ont été enregistrés pour des échantillons synthétiques contenant différentes concentrations de vanadium (V/Ti = 0.5%, 1% and 2%). Ils ont montré que le vanadium était incorporé sous forme de V^{4+}. Les spectres présentent des structures identiques quelle que soit la concentration. La figure D.9 montre le spectre mesuré pour l'échantillon contenant 2 % de vanadium, ainsi que le préseuil K au seuil du vanadium pour les trois concentrations. Elle indique clairement que la concentration n'influe pas sur le préseuil et donc que l'incorporation du vanadium se fait dans le même site. Le préseuil des spectres mesurés est cependant différent du préseuil du titane dans l'anatase. Cela suggère que le vanadium n'est peut-être pas incorporé en substitution du titane dans la structure de l'anatase [180].

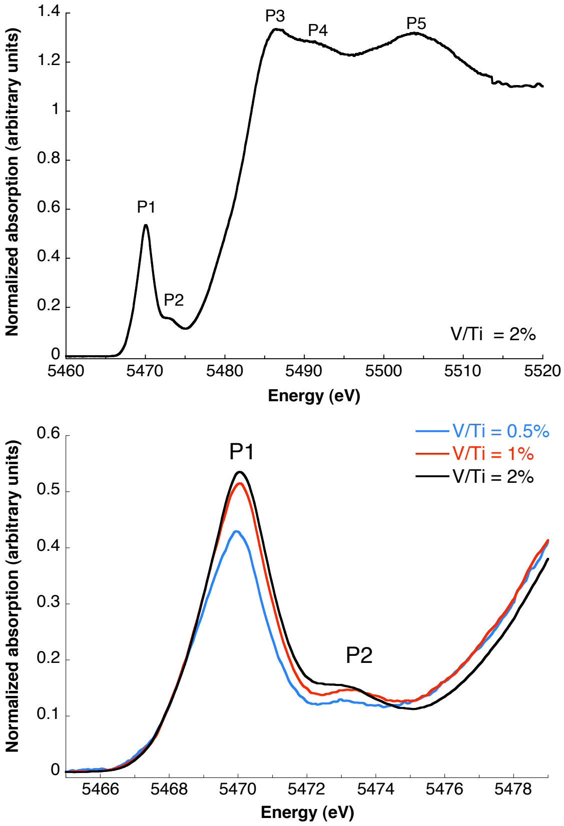

Figure D.9: (*Gauche*) Spectre HERFD au seuil K du vanadium pour l'échantillon d'anatase dopée avec 2% de vanadium. (*Droite*) Préseuils mésurés pour les différentes concentrations de vanadium.

Une étude théorique a donc été faite afin de caractériser la signature spectrale du vanadium tétravalent en substitution du titane et des calculs monoélectroniques ont été réalisés. Préalablement au calcul au seuil du vanadium, le spectre théorique isotrope au seuil K du titane dans l'anatase a été déterminé et comparé au spectre expérimental mesuré par Ruiz-Lopez *et al.* [180]. Cette étape a été faite afin de valider la méthodologie adopté pour la détermination du spectre théorique au seuil K du vanadium. Le groupe ponctuel de l'anatase est en effet $I4_1/amd$ et donc à la fois le seuil et le préseuil présentent une dépendance angulaire [24]. Les calculs sont en très bon accord avec l'expérience (Fig. D.10 gauche), toutes les structures du seuil et du préseuil sont reproduites avec la bonne énergie et intensité relative. Le spectre au seuil du vanadium a ensuite été calculé. La relaxation montre que la symétrie D_{2d} du site est conservée au cours de la relxation. Une contraction des distances V-O est observée par rapport à la distance Ti-O dans l'anatase pure. Le spectre calculé à partir de ce modèle relaxé d'anatase avec du vanadium substitué ne reproduit cependant pas le spectre expérimental (Fig. D.10 droite). Cette différence ne provient pas du fait que le spectre expérimental est du HERFD et non du XANES conventionnel car un plan RIXS au seuil du vanadium de l'anatase dopée a été enregistré et a permis de conclure que le spectre HERFD était similaire à celui que donne la mesure en mode de fluorescence conventionnel. Les spectres calculés au seuil du titane et du vanadium ont alors été comparés entre eux et les structures observées diffèrent uniquement dans le préseuil: un pic du spectre au seuil du vanadium est splitté par rapport à celui du titane. Cela indique que le spectre calculé au seuil du vanadium correspond bien à la signature spectrale du vanadium tétravalent incorporé en substitution dans le site du titane. Le calcul doit donc maintenant être fait pour une incorporation du vanadium dans un site interstitiel, afin d'interpréter sans ambiguïté le spectre expérimental.

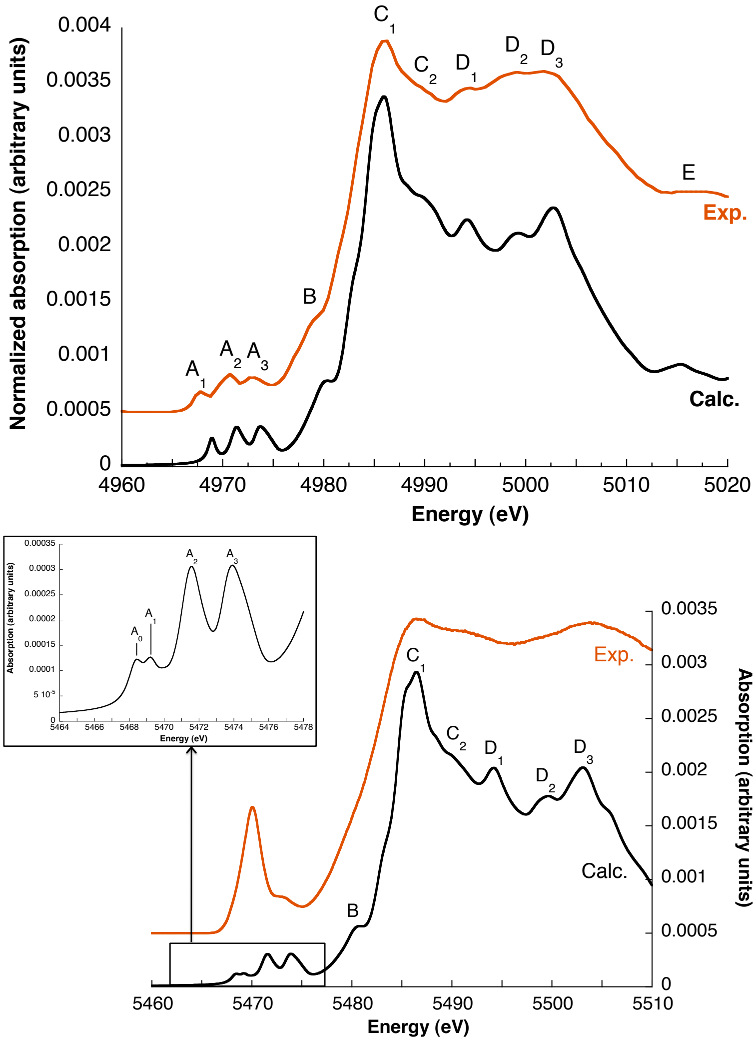

Figure D.10: Comparaison entre les spectres isotropes expérimentaux (oranges) et calculés (noirs) de l'anatase au seuil K du titane (*haut*) et du vanadium (*bas*). Le spectre expérimental au seuil du titane est reproduit de la référence [180].

Le degré d'oxydation du vanadium dans les titanomagnétites du Bushveld Complex en Afrique du Sud Les différents degrés d'oxydation du vanadium (+III, +IV et +V) dans les systèmes magmatiques terrestres en font une sonde géochimique particulièrement intéressante pour l'étude des processus de formation des roches. La détermination des degrés d'oxydation du vanadium dans les titanomagnétites du Bushveld Complex permettrait ainsi d'obtenir des informations sur les conditions de formation des couches géantes de titanomagnétites. Une première étude par spectroscopie d'absorption des rayons X du degré d'oxydation du vanadium a été faite par Balan *et. al.* sur des échantillons provenants de différentes localités du Bushveld Complex [10]. Ils ont montré d'une part que le vanadium s'incorpore dans le site octaédrique de la structure de la magnétite, qui est une structure spinelle. Ils concluent d'autre part que deux degrés d'oxydation du vanadium coexistent dans les titanomagnétites (+III et +IV). Ils ont en effet observé des variations dans l'intensité du préseuil et les ont interprétées comme étant liées à des proportions relatives de ces deux degrés d'oxydation.

Au cours de cette thèse, des échantillons naturels de titanomagnétite vanadifère d'un même gisement (BK2) ont été analysés de deux manières différentes. Ces échantillons se présentent sous forme de lames minces et ont été prélevés à onze profondeurs différentes (Fig. **??**). Des analyses microsonde ont tout d'abord été faites afin de déterminer la composition chimique des échantillons. Elles ont montré que le vanadium, le titane et le chrome présentent à travers le profil un comportement caractéristiques des titanomagnétites du Bushveld Complex [50, 51, 147, 52, 151, 175, 176, 184]. L'analyse des images MEB a aussi montré les structures typiques observées pour les titanomagnétites du Bushveld Complex [28, 214, 176]. Les analyses microsonde ont alors servi à déterminer la fugacité en oxygène des échantillons à partir des compositions chimiques de la titanomagnétite et de l'ilmenite coexistantes. Des géobaromètres basés sur les oxydes de fer-titane ont en effet été développés et sont couramment utilisés dans l'étude des roches ignées et métamorphiques [167, 193, 4]. La fugacité en oxygène des échantillons BK2 a été déterminée en utilisant le programme ILMAT [138] et son évolution à travers le profil BK2 est montré sur la figure D.12.

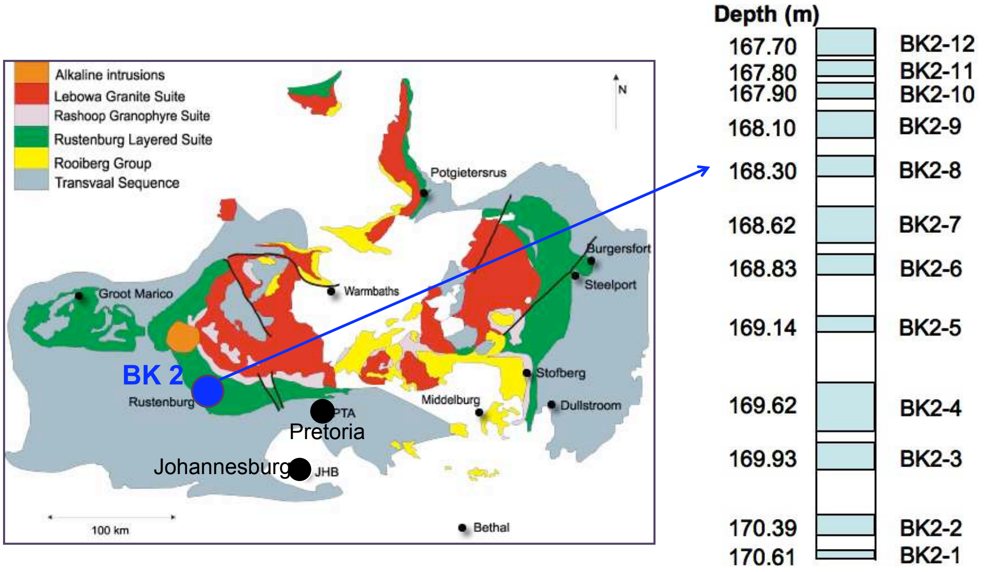

Figure D.11: Emplacement du profil BK2 dans le Bushveld Complex et schéma vertical du profil. Les onze lames minces ont été prélevées dans les zones bleutées.

Afin de déterminer le degré d'oxydation du vanadium dans les titanomagnétites, des spectres HERFD au seuil *K* du vanadium ont été enregistrés sur les échantillons du profil BK2. Les structures du seuil sont identiques quel que soit l'échantillon, ce qui indique que l'environnement cristallographique autour du vanadium est identique à l'échelle du cristal. Concernant le préseuil, un nombre identique de structures (trois) situées à une même énergie suggère que le vanadium est incorporé dans les titanomagnétites sous un même degré d'oxydation et avec la même symétrie locale. Deux spectres caractéristiques des structures observées pour le seuil et le préseuil sont reproduits sur le figure D.13. Cependant, des variations dans l'intensité du préseuil sont observées, en particulier pour la troisième structure (Fig. D.13, encart). Ces variations ont été interprétées dans le cadre des conclusions tirées par Balan *et al.*, *i.e.* que le vanadium est incorporé dans le site octaédrique de la structure de la titanomagnétite sous formes trivalente et tétravalente. Les proportions relatives de V^{3+} et V^{4+} ont été calculées en supposant une relation linéaire entre le degré d'oxydation et l'aire sous le préseuil. Celle-ci a donc été déterminée pour chaque échantillon du profil BK2 ainsi que pour deux composés de référence: la tsavorite, qui ne contient que du V^{3+}, et la cavansite ($CaVOSi_4O_{10}{\cdot}4H_2O$), qui ne contient que du V^{4+}. La proportion de V^{4+} augmente significativement dans le bas de la couche et diminue significativement dans le haut (Fig. D.12). La comparaison entre la fugacité en oxygène déterminée grâce aux analyses microsonde et la quantité de V^{4+} déterminée à partir des spectres d'absorption des rayons X montre que ces deux grandeurs varient de manière semblable à travers le profil BK2.

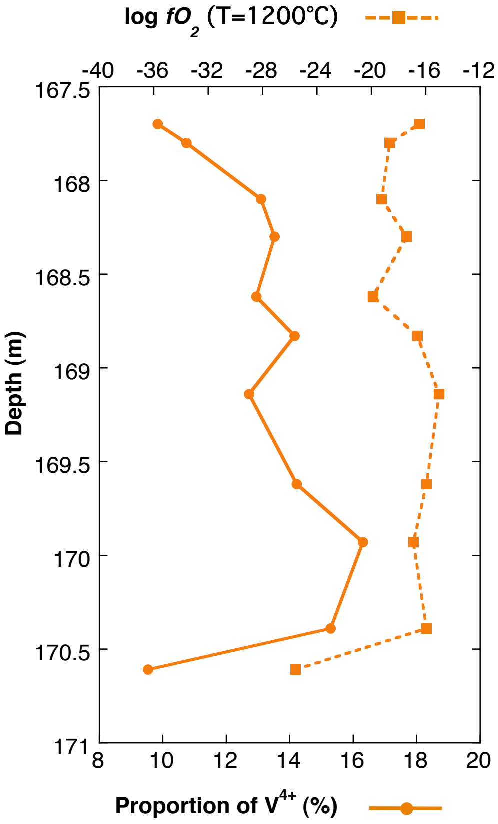

Figure D.12: Comparaison à travers le profile BK2 de la fugacité en oxygène déterminée à partir des analyses microsonde et de la propostion de V^{4+} déterminée à partir des spectres d'absorption des rayons X.

Une série de magnétites vanadifères synthétisées en conditions contrôlées en oxygène a ensuite été étudiée par spectroscopie d'absorption des rayons X. J'ai réalisé ces synthèses au Department of Materials Science and Metallurgical Engineering de l'Université de Pretoria. Des pastilles d'hématite mélangée avec~2wt % de V_2O_5 ont été chauffées à 1200°C pendant 24 heures pour différentes conditions en oxygène. L'analyse par diffraction des rayons X des synthèses a montré que la magnétite était bien la phase produite au cours de la synthèse, et des analyses MEB ont montré que les échantillons étaient homogènes. Les spectres HERFD enregistrés au seuil *K* du vanadium des magnétites synthétiques présentent des structures identiques aux spectres des échantillons naturels, que ce soit au niveau du seuil ou du préseuil. Cette similitude suggère que l'incorporation du vanadium se fait sous le même degré d'oxydation et dans le même site pour les deux types d'échantillon. L'intensité du préseuil est cependant plus intense dans le cas des échantillons synthétiques, ce qui indique une quantité de V^{4+} plus importante pour ces derniers. La similitude entre les échantillons de titanomagnétite naturels et de magnétite synthétiques peut être expliquée de deux manières, la première étant simplement que le titane n'a aucune influence sur l'incorporation du vanadium dans la magnétite. La similitude entre les deux types d'échantillon est d'autre part cohérente avec les observation MEB des échantillons naturels, dans lesquelles des exsolutions d'ulvöspinel sont observées dans une matrice de magnétite. Le vanadium serait donc incorporé préférentiellement dans la magnétite des échantillons naturels, qui sont des titanomagnétites à l'échelle macroscopique.

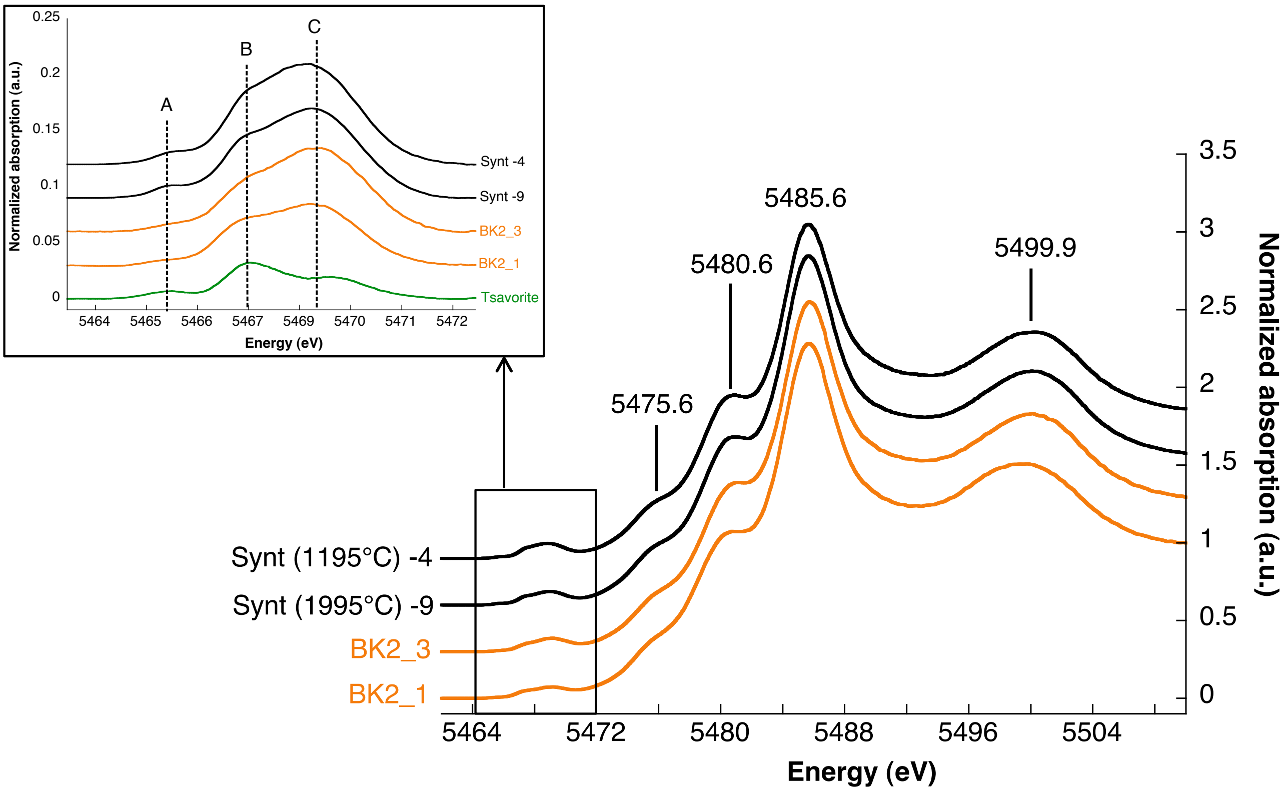

Figure D.13: Comparaison des spectres enregistrés au seuil *K* du vanadium des échantillons naturels de titanomagnétites provenant du profil BK2 et des échantillons de magnétites synthétiques.

Des calculs monoélectroniques ont été réalisés avec le code FDMNES afin de mieux interpréter les spectres expérimentaux. Ces calculs confirment que l'incorporation du vanadium se fait bien dans le site octaédrique de la structure spinelle. Des calculs complémentaires sont en cours afin de déterminer les spectres théoriques du vanadium trivalent et tétravalent dans la magnétite. L'influence de relaxation autour du vanadium lors de son incorporation doit encore être étudié. L'intensité du préseuil pourrait en effet être expliqué par la perte du centre de symétrie de l'octaèdre au cours de l'incorporation du vanadium dans la structure de la magnétite. Un autre point qui n'a pas été éclairci au cours de cette thèse est que la structure attribuée à la signature du vanadium tétravalent dans la magnétite se situe à une énergie trop basse par rapport à celle des préseuils des composés de référence du V^{4+}. La présence da vanadium sous un unique degré d'oxydation dans un site non- centrosymétrique n'explique cependant pas les variations observées au niveau du profil BK2. Ces variations pourraient refléter l'équilibre entre Fe^{2+} et Fe^{3+} dans la magnétite au cours du refroidissement de la couche ou les conditions en oxygène au moment de la cristallisation de la couche. Des mesures de spectroscopie Mössbauer permettraient de définir le rapport Fe^{2+}/Fe^{3+} dans les échantillons et ainsi de déterminer quel phénomène est vraiment reflété par les variations des proportions de V^{4+}.

Conclusion Le but de cette thèse était d'étudier le degré d'oxydation du vanadium dans les titanomagnétites ($Fe_{3-x}Ti_xO_4$:V) du Bushveld Complex et de manière plus générale son incorporation comme impureté dans des minéraux. Un grenat vanadifère, la tsavorite ($Ca_3Al_2(SiO_4)_3$:V^{3+}, a ainsi été étudié, de même que l'anatase dopée au vanadium (TiO_2:V^{4+}).

L'absorption des rayons X a été utlisée comme outil principal pour déterminer la spéciation, *i.e.* le degré d'oxydation et le site d'incorporation, du vanadium dans ces trois composés. Un mode particulier d'enregistrement des spectres, appelé High Energy-Resolution Fluorescence Detection (HERFD), a été utilisé pour enregistrer les spectres au seuil K du vanadium des différents composés. Cependant, un spectre HERFD peut différer d'un spectre XANES classique et l'enregistrement d'un plan RIXS a été nécessaire afin de déterminer si les deux modes d'enregistrement du XANES (HERFD et conventionnel) donne un spectre similaire. Les spectres HERFD enregistrés au seuil K du vanadium au cours de cette thèse sont similaires à un spectre mesuré de façon conventionnelle. Il faut aussi retenir que les mesures d'absorption des rayons X sur un monocristal permettent de tirer avantage de l'anisotropie naturelle qui existe pour tous les cristaux [24] afin d'obtenir une connaissance fine des structures cristallographique et électronique de l'élément étudié et de son environnement local.

Les analyses des spectres HERFD se sont concentrées sur la région du préseuil puisque les structures observées dans celle-ci dépendent du degré d'oxydation et de la symétrie du site de l'atome absorbeur. L'interprétation des préseuils expérimentaux des titanomagnétites vanadifères a été faite en utilisant la méthode *fingerprint*, *i.e.* en comparant les préseuils mesurés à ceux de composés de référence. Ces derniers doivent être bien connus car leur comparaison avec l'échantillon étudié est conditionné par les composés de référence choisis. Les variations observées dans l'intensité du préseuil peuvent par exemple être dues à un degré d'oxydation différent ou à une symétrie du site différente pour un même degré d'oxydation. Leur choix est donc un point capital dans l'utilisation de la méthode *fingerprint*. Une deuxième méthode d'analyse des préseuils consiste en un couplage théorie-expérience. Cette méthode est plutôt utilisée dans le cas où le degré d'oxydation et la symétrie du site de l'élément étudié sont bien connus et qu'une interprétation fine de la structure électronique ou cristallographique est recherchée. Les transitions impliquées dans le préseuil peuvent par exemple être déterminées. Cette méthode a été utilisée pour l'étude de la tsavorite et de l'anatase dopée au vanadium. Pour la partie théorie, deux approches existent pour calculer le préseuil: les calculs multiplets, basés sur la théorie LFM, et les calculs monoélectronique, basés sur la DFT. Les calculs multiplets sont une approche paramétrée dédiés aux cas des états finaux localisés et ils ne permettent de calculer que le préseuil, contrairement aux calculs monoélectroniques. Ces deux approches théoriques ont nécessité un développement théorique général basé sur les tenseurs sphériques. Appliqué au cas de la spectroscopie d'absorption des rayons X, il permet de déterminer le spectre d'un cristal à partir de celui d'un site unique de la maille et inversement.

Les questions développées au cours de cette thèse représentent seulement une petite partie de la question générale posée en Sciences de la Terre ou en gémologie sur l'incorporation des impuretés dans un minéral et ses conséquences. Par exemple, en gémologie, l'étude de l'incorporation d'une impureté permet de définir des critères pour différencier les origines géographiques des gemmes, pour définir leur caractère naturel ou synthétique ou encore si un traitement leur a été appliqué afin de modifier leur couleur. L'incorporation de l'impureté est aussi liée à l'histoire géologique de la roche-mère. En plus de son intérêt au niveau des gemmes eux-mêmes, une étude approfondie de l'incorporation de l'impureté ainsi couplée à des considérations géologiques fournit des informations précieuses pour l'exploitation et la recherche de gisements.

Bibliography

[1] M. Abon and J-C. Volta. Vanadium phosphorus oxides for n-butane oxidation to maleic anhydre. *Applied Catalysis A: General*, 157:173–193, 1997.

[2] H.R. Adam. The constitution of the titaniferous magnetites from the Pretoria district. *J. S. Afr. Chem. Inst.*, 6:3–7, 1923.

[3] S.L. Altmann and P. Herzig. *Point-group theory tables.* Oxford University Press, 1994.

[4] D.J. Andersen and D.H. Lindsley. New (and final!) models for the Ti-magnetite/ilmenite geothermometer and oxygen barometer. In *AGU 1985 Spring Meeting Eos Transactions. American Geophysical Union*, volume 66, page 416, 1985.

[5] A.T. Anderson. Oxidation of the La Blanche Lake titaniferous magnetite deposit, Quebec. *Journal of Geology*, 76:528–547, 1968.

[6] S. Ardizzone, G. Cappelletti, C. Oliva, M. Scavini, and F. Scime. Structural and spectroscopic investigations of blue vanadium doped $ZrSiO_4$ pigments prepared by a sol-gel route. *Journal of Physical Chemistry B*, 109:22112–22119, 2005.

[7] H. Arnold, E.F. Bertaut, Y. Billiet, M.J. Buerger, H. Burzlaff, J.D.H. Donnay, W. Fischer, D.S. Fokkema, T. Hahn, H. Klapper, E. Koch, G.A. Langlet, A.Vos, P.M. de Wolff, H. Wondratschek, and H. Zimmermann. *International Tables for Crystallography. Volume A: Space-group symmetry.* For The International Union of crystallography, by D. Reidel Publishing Company, 1987.

[8] M-A. Arrio. *Dichroïsme circulaire magnétique d'aimants à base moléculaire par absorption des rayons X.* PhD thesis, Université Paris Sud (France), 1995.

[9] M-A. Arrio, S. Rossano, Ch. Brouder, L. Galoisy, and G. Calas. Calculation of multipole transitions at the Fe K pre-edge through p-d hybridization in the Ligand Field Multiplet model. *Europhysics Letters*, 51:454–460, 2000.

[10] E. Balan, J.P.R. de Villiers, S.G. Eeckhout, P. Glatzel, M.J. Toplis, E. Fritsch, T. Allard, L. Galoisy, and G. Calas. The oxidation state of vanadium in titanomagnetite from layered basic intrusions. *American Mineralogist*, 91:953–956, 2006.

[11] C. Ballhaus. Redox states of litospheric and asthenospheric upper-mantle. *Contributions to Mineralogy and Petrology*, 114:331–348, 1993.

[12] S. Baroni, S. de Gironcoli, A. Dal Corso, and P. Gianozzi. $http://www.quantum-espresso.org$.

[13] A.M. Bateman. The formation of late magmatic ores. *Economic Geology*, 46:404–426, 1951.

[14] U. Bergmann, P. Glatzel, F.M.F. de Groot, and S.P. Cramer. High resolution K capture X-ray fluorescence spectroscopy: A new tool for chemical characterization. *Journal of American Chemical Society*, 121:4926–4927, 1999.

[15] U. Bergmann, C.R. Horne, T.J. Collins, J.M. Workman, and S.P. Cramer. Chemical dependence of interatomic X-ray transition energies and intensities - A study of Mn $K\beta''$ and $K\beta_{2,5}$ spectra. *Chemical Physics Letters*, 302:119–124, 1999.

[16] M. Bettinelli, V. Dallacasa, D. Falcomer, P. Fornasiero, V. Gombac, T. Montini, L. Romanò, and A. Speghini. Photocatalytic activity of TiO_2 doped with boron and vanadium. *Journal of hazardous materials*, 146:529–534, 2007.

[17] F. Betz. *Managing technological innovation: Competitive advantage from change.* John Wiley & Sons Inc., Hokoben, New Jersey, 1937.

[18] A. Bianconi, E. Fritsch, G. Calas, and J. Petiau. X-ray Absorption Near-Edge Structure of $3d$ transition elements in tetrahedral coordination: The effect of bond-length variation. *Physical Review B*, 32:4292–4295, 1985.

[19] W. Bleloch. The electric smelting of iron ore for production of alloy iron and steel and recovery of chromium and vanadium. *J. Chem. Metal. Min. Soc.*, 48–49:363–408, 1949.

[20] P.E. Blochl. Projector augmented-wave method. *Physical Review B*, 50(24):17953–17979, 2008.

[21] A.A Borisov, A.A Kadik, Y.V. Zharova, and N.V. Kalinichenko. Effects of oxygen fugacity on the ratio between valency forms of vanadium in magmas. *Geochem.J. Int.*, 24:15–20, 1988.

[22] J.H. Braun, A. Baidins, and R.E. Marganski. TiO_2 pigment technology: a review. *Progress in organic coatings*, 20(2):105–138, 1992.

[23] S. Brice-Profeta. *Etude de l'ordre chimique et magnétique d'oxydes spinelles de taille nanométrique par dichroïsme magnétique circulaire des rayons X.* PhD thesis, Université Pierre et Marie Curie (Paris, France), 2004.

[24] Ch. Brouder. Angular dependence of X-ray absorption spectra. *Journal of Physics: Condensed Matter*, 2:701–738, 1990.

[25] Ch. Brouder, A. Juhin, A. Bordage, and M.-A. Arrio. Site symmetry and crystal symmetry: a spherical tensor analysis. *Journal of Physics: Condensed Matter*, 20:455205, 2008.

[26] I.S. Buick, R. Maas, and R. Gibson. Precise U-Pb titanite age constraints on the emplacement of the Bushveld Complex, South Africa. *Journal of the Geological Society*, 158:3–6, 2001.

[27] R.G. Burns. *Mineralogical applications of crystal field theory.* Cambridge topics in mineral physics and chemistry, 1993.

[28] A.R. Butcher and R.K.W. Merkle. Postcumulus modification of magnetite grains in the upper zone of the Bushveld Complex, South Africa. *Lithos*, 20:247–260, 1987.

[29] P.H. Butler. *Point group symmetry: Applications, methods and tables*. Plenum, New York, 1981.

[30] D. Cabaret. *Théorie de la diffusion multiple comme modèle de l'absorption des rayons X. Applications au seuil K de l'aluminium et du magnésium dans des géomatériaux*. PhD thesis, Université Pierre et Marie Curie (Paris, France), 1997.

[31] D. Cabaret. XANES: approche monoélectronique. Ecole thématique du CNRS Aussois, 2006.

[32] D. Cabaret, Ch. Brouder, M-A. Arrio, Ph. Sainctavit, Y. Joly, A. Rogalev, and J. Goulon. Natural linear dichroism in pyrite (FeS_2): Experiments and calculations. *Journal of Synchrotron Radiation*, 8:460–462, 2001.

[33] D. Cabaret, E. Gaudry, M. Taillefumier, Ph. Sainctavit, and F. Mauri. XANES calculation with an efficient "non muffin-tin" method: Application to the angular dependence of the Al K-edge in corundum. *Physica Scripta*, T115:131–133, 2005.

[34] D. Cabaret, Y. Joly, H. Renevier, and C.R. Natoli. Pre-edge structure analysis of K-edge polarized X-ray absorption spectra in TiO_2 by full-potential XANES calculations. *Journal of Synchrotron Radiation*, 6:258–260, 1999.

[35] G. Calas and J. Petiau. Coordination of iron in oxide glasses through high-resolution K-edge spectra: Information from the pre-edge. *Solid State Communications*, 48:625–629, 1983.

[36] E.N. Cameron. Unusual titanian-chromian spinels from the Eastern Bushveld Complex. *American Mineralogist*, 58:172–188, 1973.

[37] E.N. Cameron. Chromite in the central sector of the Eastern Bushveld Complex, South Africa. *American Mineralogist*, 62:1082–1096, 1977.

[38] E.N. Cameron. Titanium-bearing oxide minerals of the Critical Zone of the Eastern Bushveld Complex. *American Mineralogist*, 64:140–150, 1979.

[39] E.N. Cameron and G.A. Desborough. Occurence and characteristics of chromite deposits - Eastern Bushveld Complex. *Economic Geology Monograph*, 4:23–40, 1969.

[40] D. Canil. Vanadium partitioning and the oxidation state of Archean komatiite magmas. *Nature*, 389:842–8452, 1997.

[41] D. Canil. Vanadium partitioning between orthopyroxene, spinel and silicate melt and the redox states of mantle source regions for primary magma. *Geochimica et Cosmochimica Acta*, 63:557–572, 1999.

[42] D. Canil. Vanadium in peridotites, mantle redox and tectonic environments: Archean to present. *Earth and Planetary Science Letters*, 195:75–90, 2002.

[43] D. Canil and Y. Fedortchouk. Clinopyroxene-liquid partitioning for vanadium and the oxygen fugacity during formation of cratonic and oceanic mantle litosphere. *Journal of Geophysical Research*, 105:26003–26016, 2000.

[44] D. Canil and Y. Fedortchouk. Olivine-liquid partitioning of vanadium and other trace elements, with applications to modern and ancient pycrites. *The Canadian Mineralogist*, 39:319–330, 2001.

[45] I.S.E. Carmichael. The iron-titanium oxides of salic volcanic rocks and their associated ferromagnesian silicates. *Contributions to Mineralogy and Petrology*, 14:36–64, 1967.

[46] I.S.E. Carmichael. The redox states of basic and silicic magmas: a reflection of their source regions? *Contributions to Mineralogy and Petrology*, 106:129–141, 1991.

[47] I.S.E. Carmichael and M.S Ghiorso. The effect of oxygen fugacity on the redox state of natural liquids and their crystallizing phases. *Reviews in Mineralogy*, 24:191–212, 1990.

[48] O. Carp, C.L. Huisman, and A. Reller. Photoinduced reactivity of titanium dioxide. *Progress in Solid State Chemistry*, 32:33–177, 2004.

[49] R.G. Cawthorn. Pressure fluctuation and the formation of the PGE-rich Merensky and chromitite reefs, Bushveld Complex. *Mineralium Deposita*, 40:231–235, 2005.

[50] R.G. Cawthorn and T.S. McCarthy. Variations in Cr content of magnetite from the upper zone of the Bushveld Complex - evidence for heterogenity and convection currents in magma chambers. *Earth and Planetary Science Letters*, 46:335–343, 1980.

[51] R.G. Cawthorn and T.S. McCarthy. Bottom crystallization and diffusion control in layered complexes: Evidence from Cr distribution in magnetite from the Bushveld Complex. *Trans. geol. Soc. S. Afr.*, 84:41–50, 1981.

[52] R.G. Cawthorn, T.S. McCarthy, and G. Davies. Vertical chemical gradients in a single grain of magnetite from the Bushveld Complex, South Africa. *Mineralogical Magazine*, 47:27–34, 1983.

[53] R.G. Cawthorn and N. McKenna. The extension of the western limb, Bushveld Complex (South Africa), at Cullinan Diamond Mine. *Mineralogical Magazine*, 70:241–256, 2006.

[54] R.G. Cawthorn and T.G. Molyneux. Vanadiferous magnetite deposits of the Bushveld Complex. *Mineral deposits of Southern Africa*, pages 1251–1266, 1986.

[55] R.G. Cawthorn and J. Street. Vertical migration of residual magma in the Upper Zone of the Bushveld Complex. *Mineralogy and Petrology*, 51:345–354, 1994.

[56] R.G. Cawthorn and F. Walraven. Emplacement and crystallization time for the Bushveld Complex. *Journal of Petrology*, 39:1669–1687, 1998.

[57] R.G. Cawthorn and S.J. Webb. Connectivity between the eastern and western limbs of the Bushveld Complex. *Tectonophysics*, 330:195–209, 2002.

[58] D.M. Ceperley and B.J. Alder. Ground state of the electron gas by a stochastic method. *Physical Review Letters*, 45:566–569, 1980.

[59] E. Chalmin, F. Farges, and G.E. Brown Jr. A pre-edge analysis of Mn K-edge XANES spectra to help determine the speciation of manganese in minerals and glasses. *Contributions to Mineralogy and Petrology*, 157:111–126, 2009.

[60] P. Chaurand, J. Rose, V. Briois, M. Salome, O. Proux, V. Nassif, L. Olivi, J. Susini, J-L. Hazemann, and J-Y. Bottero. New methodological approach for the vanadium K-edge X-ray Absorption Near-Edge Structure interpretation: Application to the speciation of vanadium in oxide phases from steel slag. *Journal of Physical Chemistry B*, 111:5101–5510, 2007.

[61] E.B.S Cherepanov. Peculiarities in the formation of zirconium-vanadium colors. *Steklo i Keramika*, 22:367–370, 1965.

[62] W.Y. Choi, A. Termin, and M.R. Hoffmann. The role of metal-ion dopants in quantum-sized TiO_2. Correlation between photoreactivity and charge-carrier recombination dynamics. *Journal of Physical Chemistry*, 98:13669–13779, 1995.

[63] F.J. Coertze. The genesis and geological environment of the Bushveld Complex in the area southwest of the Leolo Mountains. *South African Geological Survey Bulletin*, 47, 1966.

[64] R.D. Cowan. *The theory of atomic structure and spectra.* University of California Press, Berkeley, 1981.

[65] F. de Groot, M.H. Krisch, and J. Vogel. Spectral sharpening of the Pt L edges by high-resolution X-ray emission. *Physical Review B*, 66:195112, 2002.

[66] F. de Groot, G. Vankó, and P. Glatzel. The 1s X-ray absorption pre-edge structures in transition metal oxides. *Journal of Physics: Condensed Matter*, 21:104207, 2009.

[67] F.M.F. de Groot. *X-ray absorption of transition metal oxides.* PhD thesis, University of Nijmegen (The Netherlands), 1991.

[68] F.M.F de Groot. Invisible peaks and the relation between RIXS, fluorescence and Auger. In *Resonant Inelastic X-ray Scattering workshop, Grenoble (France)*, june 2009.

[69] F.M.F de Groot and Kotani. *Corelevel spectroscopy of solids.* New York:Taylor and Francis, 2009.

[70] P. Deines, R.H. Nafziger, G.C. Ulmer, and E. Woermann. Temperature-oxygen fugacity tables for selected gas mixtures in the system C-H-O at one atmosphere total pressure. *Bulletin of the Earth and Mineral Sciences: Experiment station*, 88, 1974.

[71] J. Van der Merwe and R.G. Cawthorn. Structures at the base of the Upper Group 2 chromitite layer, Bushveld Complex, South Africa, on Karee Mine (Lonmin Platinum). *Lithos*, 83:214–228, 2005.

[72] S.G. Eeckhout, N. Bolfan-Casanova, C. McCammon, S. Klemme, and E. Amiguet. XANES study of the oxidation state of Cr in lower mantle phases: Periclase and magnesium silicate perovskite. *American Mineralogist*, 92:966–972, 2007.

[73] K.M. Eriksen, D.A. Karydis, S. Bogoshian, and R. Fehrmann. Deactivation and compound formation in sulfuric acid catalysts and model systems. *Journal of Catalysis*, 155:32–42, 1995.

[74] H.T. Evans. The crystal structure of cavansite and pentagonite. *American Mineralogist*, 58:412–424, 1973.

[75] F. Farges. Coordination of Ti^{4+} in silicate glasses: A high-resolution XANES spectroscopy study at the Ti K edge. *American Mineralogist*, 82:36–43, 1997.

[76] F. Farges. *Ab initio* and experimental pre-edge investigations of the Mn K-edge XANES in oxide-type materials. *Physical Review B*, 71:155109, 2005.

[77] F. Farges, G.E. Brown Jr, P-E. Petit, and M. Munoz. Transition elements in water-bearing silicate glasses/melts. Part I. A high-resolution and anharmonic analysis of Ni coordination environments in crystals, glasses and melts. *Geochimica et Cosmochimica Acta*, 65:1665–1678, 2001.

[78] F. Farges, G.E. Brown Jr, and J.J Rehr. Coordination chemistry of Ti (IV) in silicate glasses and melts: I. XAFS study of titanium coordination in oxide model compounds. *Geochimica et Cosmochimica Acta*, 60:3023–3038, 1996.

[79] F. Farges, G.E. Brown Jr, and J.J. Rehr. Ti K-edge XANES studies of Ti coordination and disorder in oxide compounds: Comparison between theory and experiment. *Physcial Review B*, 56:1809–1819, 1997.

[80] S. Fazinic, M. Jaksic, L. Mandic, and J. Dobrinic. Chemical dependence of second-order radiative contributions in the Kβ x-ray spectra of vanadium and its compounds. *Physcial Review A*, 74:062501, 2006.

[81] L.W. Finger, R.M. Hazen, and A.M. Hofmeister. High-pressure crystal chemistry of spinel ($MgAl_2O_4$) and magnetite (Fe_3O_4): Comparison with silicate spinels. *Physics and Chemistry of Minerals*, 13:215–220, 1986.

[82] R. Gallay, J.J. van der Klink, and J. Moser. EPR study of vanadium (4+) in the anatase and rutile phase of TiO_2. *Physical Review B*, 34:3060–3068, 1986.

[83] L. Galoisy, G. Calas, and M-A. Arrio. High-resolution XANES spectra of iron in minerals and glasses: Structural information from the pre-edge region. *Chemical Geology*, 174:307–319, 2001.

[84] S.D. Gamblin and D.S. Urch. Metal Kβ x-ray emission spectra of first row transition metal compounds. *Journal of Electron Spectroscopy and Related Phenomena*, 113:179–192, 2001.

[85] E. Gaudry. *Structure locale autour des impuretés dans les gemmes, étudiée par spectroscopies et calculs ab initio.* PhD thesis, Université Pierre et Marie Curie (Paris, France), 2004.

[86] E. Gaudry, D. Cabaret, Ch. Brouder, I. Letard, A. Rogalev, F. Wilhlem, N. Jaouen, and Ph. Sainctavit. Relaxation around the substitutional chromium site in emerald: X-ray absorption experiments and density functional calculations. *Physical Review B*, 76:094110, 2007.

[87] E. Gaudry, D. Cabaret, Ph. Sainctavit, Ch. Brouder, F. Mauri, J. Goulon, and A. Rogalev. Structural relaxations around Ti, Cr and Fe impurities in α-Al_2O_3 probed by X-ray absorption near-edge structure combined with first-principles calculations. *Journal of Physics: Condensed Matter*, 17:5467–5480, 2005.

[88] E. Gaudry, A. Kiratisin, Ph. Sainctavit, Ch. Brouder, F. Mauri, A. Ramos, A. Rogalev, and J. Goulon. Structural and electronic relaxations around Cr^{3+} and Fe^{3+} ions in corundum. *Physical Review B*, 67:094108, 2003.

[89] E. Gaudry, Ph. Sainctavit, F. Juillot, F. Bondioli, Ph. Ohresser, and I. Letard. From the green color of eskolaite to the red color of ruby: an X-ray absorption spectroscopy study. *Physics and Chemitsry of Minerals*, 32:710–720, 2006.

[90] Ch. Gauthier, V.A. Solé, R. Signorato, J. Goulon, and E. Moguiline. The ESRF beamline ID26 : X-ray absorption on ultra dilute sample. *Journal of Synchrotron Radiation*, 6:164–166, 1999.

[91] C.A. Geiger and T. Armbruster. $Mn_3Al_2Si_3O_{12}$ spessartine and $ca_3Al_2Si_3O_{12}$ grossular garnet: Structural dynamic and thermodynamic properties. *American Mineralogist*, 82:740–747, 1997.

[92] P. Gianozzi, S. Baroni, N. Bonini, M. Calandra, R. Car, C. Cavazzoni, D. Ceresoli, G.L. Chiarotti, M. Cococcioni, I. Dabo, A. Dal Corso, S. de Gironcoli, R. Gebauer, U. Gerstmann, Ch. Gougoussis, A. Kokalj, M. Lazzeri, L. Martin Samos Colomer, N. Marzari, F. Mauri, S. Paolini, A. Pasquarello, L. Paulatto, C. Sbraccia, S. Scandolo, G. Sclauzero, A.P. Seistsonen, A. Smogunov, P. Umari, and R.M. Wentzcovitch. QUANTUM ESPRESSO: a modular and open-source software project for quantum simulations of materials. *Journal of Physics: Condensed Matter*, 2009.

[93] G. Giuli, E. Paris, J. Mungall, C. Romano, and D. Dingwell. V oxidation state and coordination number in silicate glasses by XAS. *American Mineralogist*, 89:1640–1646, 2004.

[94] P. Glatzel and U. Bergmann. High-resolution $1s$ core-hole spectroscopy in $3d$ transition metal complexes - electronic and structural information. *Coordination Chemistry Review*, 249:65–95, 2005.

[95] P. Glatzel, U. Bergmann, J.Yano, H. Visser, J.H. Robblee, W. Gu, F.M.F. de Groot, G. Christou, V.L. Pecoraro, S.P. Cramer, and V.K. Yachandra. The electronic structure of Mn oxides, coordination complexes and the oxygen-evolving complex of photosystem II studied by Resonant Inelastic X-ray Scattering. *Journal of the American Chemical Society*, 126:9946–9959, 2004.

[96] P. Glatzel, F.M.F de Groot, and U. Bergmann. Hard X-ray photon-in photon-out spectroscopy. *Synchrotron Radiation News*, 22:12–16, 2009.

[97] P. Glatzel, M. Sikora, G. Smolentsev, and M. Feranàndez-García. Hard X-ray photon-in photon-out spectroscopy. *Catalysis Today*, 145:294–299, 2009.

[98] J.B. Goedkoop. *X-ray dichroism of rare-earth materials.* PhD thesis, University of Nijmegen (The Nethelands), 1989.

[99] C. Gougoussis, M. Calandra, A. Seitsonen, Ch. Brouder, A. Shukla, and F. Mauri. Intrinsic charge transfer gap in NiO from Ni K-edge X-ray absorption spectroscopy. *Physical Review B*, 79:045118, 2009.

[100] V.S. Grunin, G.D. Davtyan, V.A. Ioffe, and I.B. Patrina. EPR of Cu^{2+} and radiation centres in anatase (TiO_2). *Physica Status Solidi B*, 77:85–92, 1976.

[101] N. Hadjisavas and A. Theophilou. Rigorous formulation of the Kohn and Sham theory. *Physical Review A*, 30:2183–2186, 1984.

[102] K. Hamalinen, D.P. Siddons, J.B. Hastings, and L.E. Berman. Elimination of the inner-shell lifetime broadening in X-ray absorption spectroscopy. *Physical Review Letters*, 67:2850–2853, 1991.

[103] D.M.W. Harney and G. von Gruenewaldt. Ore-forming processes in the upper part of the Bushveld Complex, South Africa. *Journal of African Earth Sciences*, 20:77–89, 1995.

[104] H. Hayashi, Y. Udagawa, W.A. Caliebe, and C-C. Kao. Lifetime-broadening removed X-ray absorption near-edge structure by resonant inelastic X-ray scattering spectroscopy. *Chemical Physics Letters*, 371:125–130, 2003.

[105] R. Haydock, V. Heine, and J. M. Kelly. Electronic structure based on the local atomic environment for tight-binding bands. *Journal of Physics C: Solid State Physics*, 5:2845, 1972.

[106] R. Haydock, V. Heine, and J. M. Kelly. Electronic structure based on the local atomic environment for tight-binding bands (II). *Journal of Physics C: Solid State Physics*, 8:2591–2605, 1975.

[107] C.D.K. Herd. Insights into the redox history of the NWA1068/1110 martian basalt from mineral equilibria and vanadium oxybarometry. *American Mineralogist*, 91:1616–1627, 2006.

[108] R.J. Hill, J.R. Craig, and G.V. Gibbs. Systematics of the spinel structure type. *Physics and Chemistry of Minerals*, 4:317–339, 1979.

[109] P. Hohenberg and W. Kohn. Inhomogeneous electron gas. *Physical Review B*, 136:864–871, 1964.

[110] C.R. Horne, U. Bergmann, M.M. Grush, R.C.C. Perera, D.L. Ederer, T.A. Callcott, E.J. Cairns, and S.P. Cramer. Electronic structure of chemically-prepared LiMnO determined by Mn X-ray Absorption and Emission Spectroscopies. *The Journal of Physical Chemistry B*, 104:9587–9596, 2000.

[111] C.J. Howard, T.M. Sabine, and F. Dickson. Structural and thermal parameters for rutile and anatase. *Acta Crystallographica B*, 47:462–468, 1991.

[112] M. Iizumi, T.F. Koetzle, G. Shirane, S. Chikazumi, M. Matsui, and S. Todo. Structure of magnetite (Fe_3O_4) below the Verwey transition temperature. *Acta Crystallographica B*, 38:2121–2133, 1982.

[113] T.N. Irvine. Crystallization sequences in the Muskox intrusion and other layered intrusions - II. Origin of chromitite layers and similar deposits of other magmatic ores. *Geochimica et Cosmochimica Acta*, 39:991–1020, 1975.

[114] T.N. Irvine. Origin of chromitite layers in the Muskox intrusion and other layered intrusions. *Geology*, 5:273–277, 1977.

[115] A.J. Irving. A review of experimental studies of crystal/liquid trace element partitioning. *Geochimica et Cosmochimica Acta*, 42:743–770, 1978.

[116] W.E. Jackson, F. Farges, M. Yeager, P.A Mabrouk, S. Rossano, G.A. Waychunas, E.I. Solomon, and G.E. Brown Jr. Multi-spectroscopic study of Fe(II) in silicate glasses: Implications for the coordination environment of Fe(II) in silicate melts. *Contributions to Mineralogy and Petrology*, 144:22–37, 2002.

[117] Y. Joly. Les spectroscopies d'absorption X. $http://www.neel.cnrs.fr/fdmnes$.

[118] Y. Joly. X-ray absorption near edge structure calculations beyond the muffin-tin approximation. *Physical Review B*, 63:125120, 2001.

[119] Y. Joly. Les méthodes de simulation de spectres XANES au-delà de l'approximation *muffin-tin* (Partie I). Ecole thématique du CNRS Aussois, 2004.

[120] Y. Joly, D. Cabaret, H. Renevier, and C.R. Natoli. Electron population analysis by full potential X-ray absorption simulations. *Physical Review Letters*, 82:2398, 1999.

[121] A. Juhin. *Propriétés électroniques et structurales du chrome en impureté dans les cristaux. Approche expérimentale et théorique.* PhD thesis, Université Pierre et Marie Curie (Paris, France), 2008.

[122] A. Juhin, Ch. Brouder, M.-A. Arrio, D. Cabaret, Ph. Sainctavit, E. Balan, A. Bordage, A.P. Seitsonen, G. Calas, S.G. Eeckhout, and P. Glatzel. X-ray linear dichroism in cubic compounds: The case of Cr^{3+} in $MgAl_2O_4$. *Physical Review B*, 78:195103, 2008.

[123] A. Juhin, G. Calas, D. Cabaret, L. Galoisy, and J-L. Hazemann. Structural relaxation around substitutional Cr^{3+} in $MgAl_2O_4$. *Physical Review B*, 76:054105, 2007.

[124] A. Juhin, G. Calas, D. Cabaret, L. Galoisy, and J-L. Hazemann. Structural relaxation around substitutional Cr^{3+} in pyrope garnet. *American Mineralogist*, 93:800–805, 2007.

[125] J.M. Karner, J.J. Papike, and C.K. Shearer. Comparative planetary mineralogy: Pyroxene major- and minor-element chemistry and partitioning of vanadium between pyroxene and melt in planetary basalts. *American Mineralogist*, 91:1574–1582, 2006.

[126] J.M. Karner, J.J. Papike, C.K. Shearer, G. McKay, L. Le, and P. Burger. Valence state partitioning of Cr and V between pyroxene-melt: Estimates of oxygen fugacity for martian basalt QUE94201. *American Mineralogist*, 92:1238–1241, 2007.

[127] J.M. Karner, S.R. Sutton, J.J. Papike, C.K. Shearer, J.H. Jones, and M. Newville. Application of a new vanadium valence oxybarometer to basaltic glasses from the Earth, Moon and Mars. *American Mineralogist*, 91:270–277, 2006.

[128] L. Kleinman and D.M. Bylander. Efficacious form for model pseudopotentials. *Physical Review Letters*, 48:1425–1428, 1982.

[129] D.D Klemm, J. Henckel, R. Dehm, and G. von Gruenewaldt. The geochemistry of titanomagnetite in magnetite layers and their host-rocks of the Eastern Bushveld Complex. *Economic Geology*, 80:1075–1088, 1985.

[130] D.D Klemm, R. Snethlage, R. Dehm, J. Henckel, and R. Schmidt-Thome. The formation of the chromite and titanomagnetite deposits within the Bushveld Igneous Complex. *Ore genesis - the state of the art. Berlin, Springer Verlag*, pages 351–370, 1982.

[131] W. Kohn and L.J. Sham. Self-consistent equations including exchange and correlation effects. *Physical Review A*, 140:1133–1138, 1965.

[132] J. Korecki, B. Handke, N. Spiridis, T. Slezak, I. Flis-Kabulska, and J. Haber. Siez effects in epitaxial films of magnetite. *Thin Solid FIlms*, 412:14–23, 2002.

[133] M.V. Koudriachova, S.W. de Leeuw, and N.H. Harrison. Orthorhombic distortion on Li intercalation in anatase. *Physical Review B*, 69:054106, 2004.

[134] M.O. Krause and J.H. Oliver. Natural widths of atomic K and L levels, K_α X-ray lines and several KLL Auger lines. *Journal of Physical and Chemical Reference Data*, 8:329–338, 1979.

[135] F.J. Kruger, R.G. Cawthorn, and K.L. Walsh. Strontium isotopic evidence against magma addition in the Upper Zone of the Bushveld Complex. *Earth and Planetary Science Letters*, 84:51–58, 1987.

[136] F.J. Kruger and J.S. Marsh. The mineralogy, petrology and origin of the Merensky cyclic unit in the Western Bushveld Complex. *Economic Geology*, 80:958–974, 1985.

[137] M. Lazzeri, A. Vittadini, and A. Selloni. Structure and energetics of stoichiometric TiO_2 anatase surfaces. *Physical Review B*, 63:155409, 2001.

[138] L.D Lepage. ILMAT: an Excel worksheet for ilmenite-magnetite geothermometry and geobarometry. *Computers and Geosciences*, 29:673–678, 2003.

[139] A.B.P. Lever and J. Lascombe. *Inorganic Electronic Spectroscopy.* Elsevier, 1984.

[140] D.H. Lindsley and K.J. Spencer. Fe-Ti oxide geothermometry: Reducing analyses of coexisting Ti-magnetite (Mt) and ilmenite (Ilm). In *AGU 1982 Spring Meeting Eos Transactions. American Geophysical Union*, volume 63, page 471, 1982.

[141] G.F. Lister. The composition and origin of selected iron-titanium deposits. *Economic Geology*, 61:275–310, 1966.

[142] R. Long, Y. Dai, and B. Huang. Structural and electronic properties of iodone-doped anatase and rutile TiO_2. *Computational Materials Science*, 45:223–228, 2009.

[143] G. Mallmann and H.S.C. O'Neill. The crystal/melt partitioning of V during mantle melting as a function of oxygen fugacity compared with some other elements Al, P, Ca, Sc, Ti, Cr, Fe, Ga, Y, Zr and Nb. *Journal of Petrology*, 50:1765–1794, 2009.

[144] J.W. Marden and M.N. Rich. Vanadium. *Industrial and Engineering Chemistry*, 19:786–788, 1927.

[145] Z. Mazurak and M. Czaja. Optical properties of tsavorite $Ca_3Al_2(SiO_4)_3$:Cr^{3+},V^{3+} from Kenya. *Journal of Luminescence*, 65:335–340, 1996.

[146] C.A. McCammon. Mössbauer spectroscopy: Applications. *EMU Notes in Mineralogy*, 6:369–398, 2004.

[147] T.S. McCarthy and R.G. Cawthorn. The geochemistry of vanadiferous magnetite in the Bushveld Complex: Implications for crystallization mechanisms in layered complexes. *Mineralium Deposita*, 18:505–518, 1983.

[148] T.S. McCarthy, R.G. Cawthorn, C.J. Wright, and J.R. McIver. Mineral layering in the Bushveld Complex: Implications of Cr abundances in magnetite from closely spaced magnetitite and intervening silicate-rich layers. *Economic Geology*, 80:1062–1074, 1985.

[149] D.A. McKeown, I.S. Muller, K.S. Matlack, and I.L. Pegg. X-ray absorption studies of vanadium valence and local environment in borosilicate waste glasses using vanadium sulfide, silicate, and oxide standards. *Journal of Non-Crystalline Solids*, 298:160–175, 2002.

[150] G.A.F. Molengraaf. *Geology of the Transvaal.* T. & A. Constable, 1904.

[151] T.C. Molyneux. X-ray data and chemical analyses of some titanomagnetite and ilmenite samples from the Bushveld Complex, South Africa. *Mineralogical Magazine*, 38:863–871, 1972.

[152] T.G. Molyneux. The geology of the area in the vicinity of Magnet Heights, eastern Transvaal, with special reference to the magnetite iron ore. *Geol. Soc. South Africa Spec. Pub.*, 1:228–241, 1970.

[153] H.J. Monkhorst and J.D. Pack. Special points for Brillouin-zone integrations. *Physical Review B*, 13:5188–5192, 1976.

[154] E. Murad. Magnetic properties of microcrystalline iron (III) oxides and related materials as reflected in their Mössbauer spectra. *Physics and Chemistry of MInerals*, 23:248–262, 1996.

[155] G.A. Novak and G.V. Gibbs. The crystal chemistry of the silicate garnets. *American Mineralogist*, 56:791–825, 1971.

[156] M. Ocana, A.R. Gonzalèz-Elipe, V.M. Orera, P. Tartaj, and C.J. Serna. Spectroscopic studies on the localization of vanadium(IV) in vanadium-doped zircon pigments. *Journal of American Ceramics Society*, 82:395–400, 1998.

[157] J.J. Papike, J.M. Karner, and C.K. Shearer. Comparative planetary mineralogy: V/(Cr + Al) systematics in chromite as an indicator of relative oxygen fugacity. *American Mineralogist*, 89:1557–1560, 2004.

[158] J.J. Papike, J.M. Karner, and C.K. Shearer. Comparative planetary mineralogy: Valence state partitioning of Cr, Fe, Ti and V among crystallographic sites in olivine, pyroxene, and spinel from planetary basalts. *American Mineralogist*, 90:277–290, 2005.

[159] G. Peng, F.M.F de Groot, K. Hamaläinen, J.A. Moore, X. Wang, M.M Grush, J.B. Hastings, D.P. Siddons, W.H. Armstrong, O.C. Mullins, and S.P. Cramer. High-resolution manganese X-ray fluorescence spectroscopy. Oxidation state and spin state sensitivity. *Journal of American Chemical Society*, 116:2914–2920, 1994.

[160] J. P. Perdew, K. Burke, and M. Ernzerhof. Generalized Gradient Approximation made simple. *Physical Review Letters*, 77:3865–3868, 1996.

[161] P-E. Petit, F. Farges, M. Wilke, and V.A Solé. Determination of the iron oxidation state in Earth materials using XANES pre-edge information. *Journal of Synchrotron Radiation*, 8:952–954, 2001.

[162] R.F. Pettifer, Ch. Brouder, M. Benfatto, C.R. Natoli, C. Hermes, and M.F. Ruiz López. Magic-angle theorem in powder X-ray absorption spectroscopy. *Physical Review B*, 42:37–42, 1990.

[163] B. Pfrommer, D. Raczkowski, A. Canning, S. G. Louie, and (Lawrence Berkeley National Laboratory, with contributions from F. Mauri, M. Cote, Y. Yoon, Ch. Pickard and P. Haynes.). *www.nersc.gov/projects/paratec.*

[164] B. Poumellec, R. Cortes, G. Tourillon, and J. Berthon. Angular dependence of the Ti K edge in rutile TiO_2. *Phys. Stat. Sol. (b)*, 164:319–326, 1991.

[165] B. Poumellec, V. Kraizman, Y. Aifa, R. Cotrès, A. Novakovich, and R. Vedrinskii. Experimental and theoretical studies of dipole and quadrupole contributions to the vanadium K-edge XANES for $VOPO_4$ *cdot* $2H_2O$ xerogel. *Physical Review B*, 58:6133–6146, 1998.

[166] B. Poumellec, J.F. Marucco, and B. Touzelin. X-ray absorption near-edge structure of titanium and vanadium in $(Ti,V)O_2$ rutile solid solutions. *Physical Review B*, 35:2284–2294, 1987.

[167] R. Powell and M. Powell. Geothermometry and oxygen barometry using coexisting iron-titanium oxides: a reappraisal. *Mineralogical Magazine*, 41:257–263, 1977.

[168] S. Quartieri, M. Triscari, G. Sabatino, F. Boscherini, and A. Sani. Fe and Mn K-edge XANES study of ancient Roman glasses. *European Journal of Mineralogy*, 14:749–756, 2002.

[169] J.J. Rehr, R.C. Albers, C.R. Natoli, and E.A. Stern. New high-energy approximation for X-ray absorption near-edge structure. *Physical Review B*, 34:4350–4353, 1986.

[170] J.J. Rehr, Z.I. Zabinsky, and R.C. Albers. High-order multiple scattering calculations of X-ray absorption fine structure. *Physical Review Letters*, 69:3397–4000, 1992.

[171] T. Ressler, O. Timpe, F. Girgsdies, J. Wienold, and T. Neisus. In situ investigations of the bulk structural evolution of vanadium-containing heteropolyoxomolybdate catalysts during thermal activation. *Journal of Catalysis*, 231:279–291, 2005.

[172] I.M. Reynolds. Ore petrography and mineralogy of the vanadium-bearing titaniferous magnetite layer of the Kaffirskraal intrusion, Heidelberg district, Transvaal. *Geol. Soc. South Africa Trans.*, 83:221–230, 1980.

[173] I.M. Reynolds. The mineralogy and petrography of some titaniferous iron-ores from the Ushushwana Complex. *Geol. Soc. South Africa Trans.*, 84:261–269, 1981.

[174] I.M. Reynolds. Contrasted mineralogy and textural relationships in the uppermost titaniferous magnetite layers of the Bushveld Complex in the Bierkraal area north of Rustenburg. *Economic Geology*, 80:1027–1048, 1985.

[175] I.M Reynolds. The nature and origin of titaniferous magnetite-rich layers in the upper zone of the Bushveld Complex: A review and synthesis. *Economic Geology*, 80:1089–1108, 1985.

[176] I.M. Reynolds. The mineralogy and ore petrography of the Bushveld titaniferous magnetite-rich layers. *Mineral Deposits of Southern Africa*, pages 1267–1286, 1986.

[177] K. Righter, S.R. Sutton, and M. Newville. Micro-XANES measurements on experimental spinels and the oxidation state of vanadium in spinel-melt pairs. In *Oxygen in the Terrestrial Planets workshop, no.3010*, 2004.

[178] K. Righter, S.R. Sutton, M. Newville, L. Le, C.S. Schwandt, H. Uchida, B. Lavina, and R.T. Downs. An experimental study of the oxidation state of vanadium in spinel and basaltic melt with implications for the origin of planetary basalts. *Geol. Soc. South Africa Trans.*, 83:221–230, 1980.

[179] G.R. Rossman. $http://minerals.gps.caltech.edu.$

[180] M.F. Ruiz-López and A. Munoz-Páez. A theoretical study of the XANES spectra of rutile and anatase. *Journal of Physics: Condensed Matter*, 3:8981–8990, 1991.

[181] Ph. Sainctavit. Multiple scattering theory applied to X-ray absorption spectroscopy. Ecole thématique du CNRS Aussois, 2004.

[182] Ph. Sainctavit, J. Petiau, M. Benfatto, and C.R. Natoli. Comparison between XAFS experiment and multiple-scattering calculations in silicon and zincblende. *Physica B: Condensed Matter*, 158:347–350, 1987.

[183] D.G. Schulze. The influence of aluminum on iron oxides. VIII. Unit-cell dimensions of Al-substituted goethites and estimation of Al from them. *Clays and Clay Minerals*, 32:36–44, 1984.

[184] C.M. Schwellnus and J. Willemse. Titanium and vanadium in the magnetic iron ores of the Bushveld Complex. *Geol. Soc. South Africa Trans.*, 46:23–28, 1943.

[185] U. Schwertmann, R.W. Fitzpatrick, R.M. Taylor, and D.G. Lewis. The influence of aluminum on iron oxides. Part II. Preparation and properties of al-substituted hematites. *Clays and Clay Minerals*, 27:105–112, 1979.

[186] A. Sclafani, P. Palmisano, and E. Davi. Photocatalytic degradation of phenol in aqueous polycrystalline TiO_2 dispersions: the influence of Fe^{3+}, Fe^{2+} and Ag^+ on the reaction rate. *Journal of photochemistry and photobiology*, 56:113–123, 1991.

[187] C.L. Seabrook, R.G. Cawthorn, and F.J. Kruger. The Merensky Reef, Bushveld Complex: Mixing of minerals, not mixing of magmas. *Economic Geology*, 100:1191–1206, 2005.

[188] N.G. Sefström. Ueber das Vanadin, ein neues Metall, gefunden im Stangeneisen von Eckersholm, einer Eisenhütte, die ihr Erz von Tabgerg in Smaland bezieht. *Annalen der Physik*, 97:43–49, 1831.

[189] R.D. Shannon. Revised effective ioni radii and systematic studies of interatomic distances in halides and chalcogenides. *Acta Crystallograhica A*, 32:751–767, 1976.

[190] C.K. Shearer, G. McKay, J.J. Papike, and J.M. Karner. Valence state partitioning of vanadium between olivine-liquid: Estimates of the oxygen fugacity of Y980459 and application to other olivine-phyric martian basalts. *American Mineralogist*, 91:1657–1663, 2006.

[191] J.W. Shervais. Ti-V plots and the petrogenesis of modern and ophiolitic lavas. *Earth and Planetary Science Letters*, 59:101–118, 1982.

[192] S.B. Simon, S.R. Sutton, and L. Grossman. Valence of titanium and vanadium in pyroxene in refractory inclusion interiors and rims. *Geochimica et Cosmochimica Acta*, 71:3098–3118, 2007.

[193] K.J. Spencer and D.H. Lindsley. A solution model for coexisting iron-titanium oxides. *American Mineralogist*, 66:1189–1201, 1981.

[194] N. Spiridis, B. Handke, T. Slezak, J. Barbasz, M. Zajac, J. Haber, and J. Korecki. Surface structure of epitaxial magnetite Fe_3O_4 (001) films: In situ STM and CEMS studies. *Journal of Physical Chemistry B*, 108:14356–14361, 2004.

[195] M. Steveson, T. Bredow, and A.R. Gerson. MSINDO quantum chemical modelling study of the structure of aluminium-doped anatase and rutile titanium dioxide. *Physical Chemistry and Chemical Physics*, 4:358–365, 2002.

[196] J.C. Stormer. The effects of recalculation on estimates of temperature and oxygen fugacities from analyses of multicomponent iron-titanium oxides. *American Mineralogist*, 68:586–594, 1983.

[197] S.R. Sutton, J. Karner, J. Papike, J.S. Delaney, C. Shearer, M. Newville, P. Eng, M. Rivers, and M.D. Dyar. Vanadium K edge XANES of synthetic and natural basaltic glasses and application to microscale oxygen barometry. *Geochimica et Cosmochimica Acta*, 69:2333–2348, 2005.

[198] S.R. Sutton and M. Newville. Vanadium K-edge XANES of synthetic olivine: Valence determinations and crystal orientation effects. In *Lunar and Planetary Science Conference XXXVI*, 2005.

[199] S.R. Sutton, S. Simon, L. Grossman, J.S. Delaney, J. Beckett, M. Newville, P. Eng, and M. Rivers. Evidence for divalent vanadium in Allende CAI fassaite and implications for formation conditions. In *Lunar and Planetary Science Conference XXXIII*, 2002.

[200] M. Taillefumier, D. Cabaret, A-M. Flank, and F. Mauri. X-ray absorption near-edge structure calculations with the pseudopotentials: Application to the K edge in diamond and α-quartz. *Physical Review B*, 66:195107, 2002.

[201] H. Tang, H. Berger, P.E. Schmid, F. Lévy, and G. Burri. Photoluminescence in TiO_2 anatase single crystals. *Solid State Communications*, 87:847–850, 1993.

[202] C. Tegner, R.G. Cawthorn, and F.J. Kruger. Cyclicity in the Main and Upper Zones of the Bushveld Complex, South Africa: Crystallization from a zoned magma sheet. *Journal of Petrology*, 47:2257–2279, 2006.

[203] T. Thole, G. van der Laan, J.C. Fuggle, G. Sawatzky, R.C. Karnatak, and J-M. Estava. $3d$ X-ray absorption lines and the $3d^94f^{n+1}$ multiplets of the lanthanides. *Physical Review B*, 32:5107–5118, 1985.

[204] F. Tielens, M. Catalayud, A. Beltrán, C. Minot, and J. Andrés. Lithium insertion and mobility in the TiO_2-anatase/titanate structure: A periodic DFT study. *Journal of Electroanalytical Chemistry*, 581:216–223, 2005.

[205] A.L. Du Toit. Plumasite (corundum-aplite) and titaniferous magnetite rocks from Natal. *Geol. Soc. South Africa Trans.*, 21:53–73, 1918.

[206] M.J. Toplis and A. Corgne. An experimental study of element partitioning between magnetite, clinopyroxene and iron-bearing silicate liquids with particular emphasis on vanadium. *Contributions to Mineralogy and Petrology*, 144:22–37, 2002.

[207] N. Trcera, D. Cabaret, S. Rossano, F. Farges, A-M. Flanck, and P. Lagarde. Experimental and theoretical study of the structural environment of magnesium in minerals and silicate glasses using X-ray absorption near edge structure. *Physics and Chemistry of Minerals*, 36:241–257, 2009.

[208] N. Troullier and J.L. Martins. Efficient pseudopotentials for plane-wave calculations. *Physical Review B*, 43:1993–2006, 1991.

[209] T.A. Tyson, Q. Qian, C-C. Kao, J-P. Rueff, F.M.F de Groot, M. Croft, S-W. Cheong, M. Greenblatt, and M.A. Subramanian. Valence state of Mn in Ca-doped $LaMnO_3$ studied by high-resolution Mn $K\beta$ emission spectroscopy. *Physical Review B*, 60:4665–4674, 1999.

[210] G.C. Ulmer. Experimental investigation of chromite spinels. *Economic Geology Monograph*, 4:114–131, 1969.

[211] C. Di Valentin, E. Finazzi, G. Pacchioni, A. Selloni, S. Lovraghi, M.C. Paganini, and E. Giamello. N-doped TiO_2: Theory and experiment. *Chemical Physics*, 339:44–56, 2007.

[212] E.J.W. Verwey and P.W. Haayman. Electronic conductivity and transition point of magnetite (Fe_3O_4). *Physic*, 9:979–987, 1941.

[213] E.J.W. Verwey, P.W. Haayman, and F.C. Romeijn. Physical properties and cation arrangement of oxides with spinel structures. *The Journal of Chemical Physics*, 13:181–187, 1947.

[214] G. von Gruenewaldt, D.D Klemm, J. Henckel, and R.M. Dehm. Exsolution features in titanomagnetites from massive magnetite layers and their host rocks of the Upper Zone, Eastern Bushveld Complex. *Economic Geology*, 80:1049–1061, 1985.

[215] P.A. Wagner. The iron ore ressources of the Union of South Africa. *Mem. Geol. Surv. S. Afr.*, 26, 1938.

[216] F Walraven and L.G. Wolmarans. Stratigraphy of the upper part of the Rustenburg layered suite, Bushved Complex, in western Transvaal. *Annals of the geological survey of South Africa*, 13:109–114, 1979.

[217] G.A. Waychunas. Synchrotron radiation XANES spectroscopy of Ti in minerals: Effects of Ti bonding distances, Ti valence, and site geometry on absorption edge structure. *American Mineralogist*, 72:89–101, 1987.

[218] G.A. Waychunas, M.J. Apted, and G.E Brown Jr. X-ray K-edge Absorption Spectra of Fe minerals and model compounds: Near-Edge Structure. *Physics and Chemistry of Minerals*, 10:1–9, 1983.

[219] T.E. Westre, P. Kennepohl, J.G. DeWitt, B. Hedman, K.O. Hodgson, and E.L. Solomon. A multiplet analysis of Fe K-edge $1s \rightarrow 3d$ pre-edge features of iron complexes. *Journal of the American Chemical Society*, 119:6297–6314, 1997.

[220] K. Wilke and H.D. Breuer. Transition metal doped titania: physical properties and photocatalytic behaviour. *Z. Phys. Chem. - Int. J. Res. Phys. Chem. Chem. Phys.*, 213:135–140, 1999.

[221] M. Wilke, F. Farges, P-E. Petit, G.E. Brown Jr, and F. Martin. Oxidation state and coordination of Fe in minerals: An Fe K-XANES spectroscopic study. *American Mineralogist*, 86:714–730, 2001.

[222] J. Willemse. The geology of the Bushveld igneous Complex, the largest repository of magmatic ore deposits in the world. *Economic Geology Monograph*, 4:1–22, 1969.

[223] J.C. Woicik, E.L. Shirley, C.S. Hellberg, K.E. Andersen, S. Sambasivan, D.A. Fischer, B.D. Chapman, E.A. Stern, P. Ryan, D.L. Elderer, and H. Li. Ferroelectric distortion in $SrTiO_3$ thin films on Si(001) by x-ray absorption fine structure spectroscopy: Experiments and first-principles calculations. *Physical Review B*, 75:140103, 2007.

[224] J. Wong, F.W. Lytle, R.P. Messmer, and D.H. Maylotte. K-edge absorption spectra of selected vanadium compounds. *Physical Review B*, 30:5596–5510, 1984.

[225] Z.Y. Wu, J. Zhang, K. Ibrahim, D.C. Xian, G. Li, Y. Tao, T.D. Hu, S. Bellucci, A. Marcelli, Q.H. Zhang, and Z.Z. Chen. Structural determination of titanium-oxide nanoparticles by X-ray absorption spectroscopy. *Applied Physics Letters*, 80:2973–2975, 2002.

[226] J.M. Zuo, C.H. Spence, and W. Petuskey. Charge ordering in magnetite at low temperatures. *Physical Review B*, 42:8451–8464, 1990.

That's all, folks!